

IMPACT FACTOR  
**11.082**

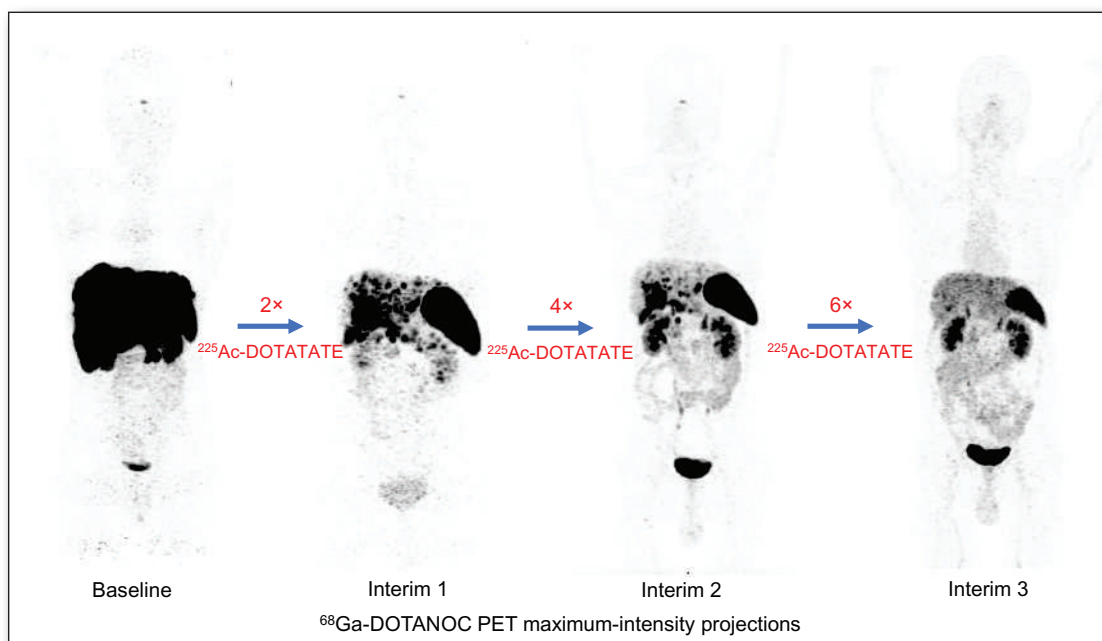
#1 NUCLEAR MEDICINE,  
MOLECULAR IMAGING  
AND MOLECULAR  
RADIOTHERAPY JOURNAL

# JNM

The Journal of Nuclear Medicine

## FEATURED ARTICLE

Survival Outcomes in Metastatic Gastroenteropancreatic Neuroendocrine Tumor Patients Receiving Concomitant  $^{225}\text{Ac}$ -DOTATATE-Targeted  $\alpha$ -Therapy and Capecitabine: A Real-World-Scenario Management-Based Long-Term Outcome Study. Sanjana Ballal et al. See page 211.



Enhanced  $^{68}\text{Ga}$ -radiopharmaceutical availability: assessing clinical safety and PET imaging efficacy of integrated cyclotron-produced  $^{68}\text{Ga}$ -DOTATATE. Sébastien Tremblay et al. See page 232.

# Thank You to our 2022 SNMMI Annual Fund, Heritage Fund, Women in Nuclear Medicine (WINM), PDEF, and Value Initiative: Transformative Leadership Donors

- Twyla B. Bartel, DO, FACNM, FSNMMI
- Tina M. Buehner, PhD, CNMT, FSNMMI-TS
- John C. Carney
- Deborah Charych, PhD
- John and Bonnie Clarke
- Troy Cox
- Cathy Sue Cutler, PhD, FSNMMI
- Paresh B. Desai, MD
- Subodh M. Duggal, BSc, CNMT, RT(N)
- Dennis Kiyoshi Fujii, PhD
- Brett Gerberman, CNMT
- Global Advanced Imaging, PLLC
- Michael M. Graham, PhD, MD, FACR, FSNMMI
- Frederick D. Grant, MD
- Bennett S. Greenspan, MD, FACNM, FACR, FSNMMI
- Madeline Greth, BS, CNMT, RT(CT), PET
- Lucas J. Gross, MS, CNMT, RT(N)
- Paul Hamel
- Michael E. Harvey, CNMT
- Jose de Jesus Herrera, MD
- Tyese Hodges, CNMT
- Mark C. Hyun, CNMT, NCT, RT, FASNC
- Arnold F. Jacobson, MD, PhD
- Courtney Krug, MD
- Kanchan Kulkarni, MD
- Steven M. Larson, MD, FACNM
- Joe and Karen Leonard Charitable Fund
- Mykol Larvie, MD, PhD
- Myung Soon Lee
- Maria L. Mackin, BS, MS, CNMT, RT(N)
- Michael Maslanka
- Alan H. Maurer, MD, FSNMMI
- Eileen M. Mercado-Yap, MD
- Beth T. Meysenburg, CNMT, PET, RT(N)(CT)
- Joseph K. Oni
- Orhan Kemal Oz, MD, PhD
- Erika Padilla-Morales, CNMT, NMTCB(CT)
- Christopher J. Palestro, MD, FSNMMI, FACNM
- Scott B. Perlman, MD
- Rachael L. Picchi
- Vincent A. Pistilli, CPA, CGMA
- Lalitha Ramanna, MD, FACNM
- Michael B. Ryan, CNMT
- The Sipra and Gopal Saha Scholarship
- Irene Saranteas
- Sonnet L. Schulz
- George M. Segall, MD, FACNM, FSNMMI
- Barry L. Shulkin, MD, MBA
- Tamara Sloper
- Rodger A. Stinson, MS, CNMT, RT(N)
- Larisa Toderas, MBA, CNMT, PET, NMTCB(RS), ARRT(CT)
- Jaco Van Niekerk
- Jean-Luc VANDERHEYDEN, PhD
- Joseph T. Viggiano, MD
- John Viscovic
- Sean X. YAN, MD
- Hyungtae Yim, CNMT, NMTCB(CT)



## Tc 99m: The **core** of nuclear medicine imaging<sup>1,2</sup>

### EFFICIENT AND RELIABLE<sup>3</sup>

- Greater than 50 years of TechneLite<sup>®</sup> generator manufacturing expertise<sup>3</sup>
- Our 5th generation of dry-column technetium-99m generator advances<sup>3</sup>
- 100% Assay and Mo-99 breakthrough testing<sup>3</sup>
- 100% terminal sterilization following filling and in-process test elutions<sup>3</sup>



#### INDICATIONS AND USAGE:

The TechneLite<sup>®</sup> generator is a source of sodium pertechnetate Tc 99m for use in the preparation of FDA-approved diagnostic radiopharmaceuticals, as described in the labeling of these diagnostic radiopharmaceutical kits.

Sodium Pertechnetate Tc 99m Injection is used IN ADULTS as an agent for:

- Thyroid Imaging
- Salivary Gland Imaging
- Urinary Bladder Imaging (direct isotopic cystography) for the detection of vesico-ureteral reflux
- Nasolacrimal Drainage System Imaging

Sodium Pertechnetate Tc 99m Injection is used IN CHILDREN as an agent for:

- Thyroid Imaging
- Urinary Bladder Imaging (direct isotopic cystography) for the detection of vesico-ureteral reflux

**CONTRAINDICATIONS:** None known.

#### Important Safety Information:

Allergic reactions including anaphylaxis have been reported infrequently following the administration of Sodium Pertechnetate Tc 99m Injection.

#### WARNINGS:

Radiation risks associated with the use of Sodium Pertechnetate Tc 99m Injection are greater in children than in adults and, in general, the younger the child, the greater the risk owing to greater absorbed radiation doses and longer life expectancy. These greater risks should be taken firmly into account in all benefit-risk assessments involving children. Long-term cumulative radiation exposure may be associated with an increased risk of cancer.

#### PRECAUTIONS:

Since the eluate does not contain an antimicrobial agent, it should not be used after 12 hours from the time of TechneLite<sup>®</sup>, Technetium Tc 99m Generator, elution. After the termination of the nasolacrimal imaging procedure, blowing the nose and washing the eyes with sterile distilled water or an isotonic sodium chloride solution will further minimize the radiation dose. As in the use of any radioactive material, care should be taken to minimize radiation exposure to patients and occupational workers. Radiopharmaceuticals should be used only by physicians who are qualified by training and experience and who are licensed in the safe handling of radionuclides.

Please see following page(s) for brief Prescribing Information. Full Prescribing Information may be accessed at <https://www.lantheus.com/assets/TechneLite-PI-513160-0719mktg.pdf>

#### References:

1. World Nuclear Association, <http://www.world-nuclear.org/information-library/non-power-nuclear-applications/radioisotopes-research/radioisotopes-in-medicine.aspx> Accessed April 1, 2019 2. FDA News Release, February 8, 2018, <https://www.fda.gov/news-events/newsroom/press-announcements/ucm595990.htm> Accessed April 1, 2019 3. Quality data on file, Lantheus Medical Imaging, Inc.

**TechneLite**<sup>®</sup>  
Technetium Tc 99m Generator

FOR DIAGNOSTIC USE

## BRIEF SUMMARY

Please see Full Prescribing Information available at [https://www.lantheus.com/assets/TechneLite-PI-\\_513160-0719mktg.pdf](https://www.lantheus.com/assets/TechneLite-PI-_513160-0719mktg.pdf) for complete information.

## INDICATIONS AND USAGE:

The Technelite generator is a source of sodium pertechnetate Tc 99m for use in the preparation of FDA-approved diagnostic radiopharmaceuticals, as described in the labeling of these diagnostic radiopharmaceutical kits. Sodium Pertechnetate Tc 99m Injection is used IN ADULTS as an agent for:

- Thyroid Imaging
- Salivary Gland Imaging
- Urinary Bladder Imaging (direct isotopic cystography) for the detection of vesico-ureteral reflux.
- Nasolacrimal Drainage System Imaging

Sodium Pertechnetate Tc 99m Injection is used IN CHILDREN as an agent for:

- Thyroid Imaging
- Urinary Bladder Imaging (direct isotopic cystography) for the detection of vesico-ureteral reflux.

**CONTRAINDICATIONS:** None known.

**WARNINGS:** Radiation risks associated with the use of Sodium Pertechnetate Tc 99m Injection are greater in children than in adults and, in general, the younger the child, the greater the risk owing to greater absorbed radiation doses and longer life-expectancy. These greater risks should be taken firmly into account in all benefit-risk assessments involving children.

Long-term cumulative radiation exposure may be associated with an increased risk of cancer.

## PRECAUTIONS:

### General

As in the use of any radioactive material, care should be taken to minimize radiation exposure to the patient consistent with proper patient management and to ensure minimum radiation exposure to occupational workers.

Since the eluate does not contain an antimicrobial agent, it should not be used after 12 hours from the time of TECHNELITE<sup>®</sup>, Technetium Tc 99m Generator elution.

After the termination of the nasolacrimal imaging procedure, blowing the nose and washing the eyes with sterile distilled water or an isotonic sodium chloride solution will further minimize the radiation dose.

Radiopharmaceuticals should be used only by physicians who are qualified by training and experience in the safe handling of radionuclides and whose experience and training have been approved by the appropriate government agency authorized to license the use of radionuclides.

## Carcinogenesis, Mutagenesis, Impairment of Fertility

No animal studies have been performed to evaluate carcinogenic potential or whether Sodium Pertechnetate Tc 99m affects fertility in males or females.

## Pregnancy

Animal reproductive studies have not been conducted with Sodium Pertechnetate Tc 99m. It is also not known whether Sodium Pertechnetate Tc 99m can cause fetal harm when administered to a pregnant woman or can affect reproduction capacity. Sodium Pertechnetate Tc 99m Injection should be given to a pregnant woman only if clearly needed.

Ideally examinations using radiopharmaceuticals, especially those elective in nature, of a woman of childbearing capability should be performed during the first few (approximately 10) days following the onset of menses.

## Nursing Mothers

Sodium Pertechnetate Tc 99m is excreted in human milk during lactation; therefore formula feedings should be substituted for breast feeding.

This radiopharmaceutical preparation should not be administered to pregnant or lactating women unless expected benefits to be gained outweigh the potential risks.

## Pediatric Use

See INDICATIONS and DOSAGE AND ADMINISTRATION sections. Also see the description of additional risks under WARNINGS.

## Geriatric Use

Clinical studies of Technelite<sup>®</sup> did not include sufficient numbers of subjects aged 65 and over to determine whether they respond differently from younger subjects. Other reported clinical experience has not identified differences in responses between the elderly and younger patients. In general, dose selection for an elderly patient should be cautious, usually starting at the low end of the dosing range, reflecting the greater frequency of decreased hepatic, renal, or cardiac function, and of concomitant disease or other drug therapy.

**ADVERSE REACTIONS:** Allergic reactions including anaphylaxis have been reported infrequently following the administration of Sodium Pertechnetate Tc 99m Injection.

Lantheus Medical Imaging

331 Treble Cove Road

N. Billerica, MA 01862 USA

For Ordering Call Toll-Free: 800-299-3431

All other business: 800-362-2668

(In Massachusetts and International, call 978-667-9531)

Patent: <http://www.lantheus.com/patents/index.html>



**LANTHEUS**<sup>™</sup>

513160-0719  
PM-US-TE-0004

Printed in U.S.A.

July 2019

## DISCUSSIONS WITH LEADERS

- 185** Advancing Clinical Trial Innovation in Pancreatic Cancer: A Conversation Between Diane Simeone, Ken Herrmann, and Johannes Czernin  
Diane M. Simeone, Ken Herrmann, and Johannes Czernin

## THE STATE OF THE ART

- 188** Artificial Intelligence in Nuclear Medicine: Opportunities, Challenges, and Responsibilities Toward a Trustworthy Ecosystem  
Babak Saboury, Tyler Bradshaw, Ronald Boellaard, Irène Buvat, Joyita Dutta, Mathieu Hatt, Abhinav K. Jha, Quanzheng Li, Chi Liu, Helena McMeekin, et al.

## HOT TOPICS

- 197** Whole-Body PET Imaging: A Catalyst for Whole-Person Research?  
Lalith Kumar Shiyam Sundar, Marcus Hacker, and Thomas Beyer

## ISSUES AND CONTROVERSIES

- 200** Scientific Fraud, Publication Bias, and Honorary Authorship in Nuclear Medicine  
Thomas C. Kwee, Maan T. Almaghrabi, and Robert M. Kwee

## PROCEDURE STANDARD

- 204** SNMMI Procedure Standard/EANM Practice Guideline for SSTR PET: Imaging Neuroendocrine Tumors  
Thomas A. Hope, Martin Allen-Auerbach, Lisa Bodei, Jeremie Calais, Magnus Dahlbom, Lisa K. Dunnwald, Michael M. Graham, Heather A. Jacene, Courtney Lawhn Heath, Erik S. Mittra, et al.

## THERANOSTICS

### Clinical

- 211** ■ **FEATURED ARTICLE OF THE MONTH.** Survival Outcomes in Metastatic Gastroenteropancreatic Neuroendocrine Tumor Patients Receiving Concomitant <sup>225</sup>Ac-DOTATATE-Targeted  $\alpha$ -Therapy and Capecitabine: A Real-World-Scenario Management-Based Long-Term Outcome Study  
Sanjana Ballal, Madhav P. Yadav, Madhavi Tripathi, Ranjit Kumar Sahoo, and Chandrasekhar Bal
- 219** ■ **INVITED PERSPECTIVE.** The Future of Targeted  $\alpha$ -Therapy Is Bright, but Rigorous Studies Are Necessary to Advance the Field  
Jonathan Strosberg, Ken Herrmann, and Lisa Bodei
- 221** Evaluation of <sup>177</sup>Lu-PSMA-617 SPECT/CT Quantitation as a Response Biomarker Within a Prospective <sup>177</sup>Lu-PSMA-617 and NOX66 Combination Trial (LuPIN)  
Sarennya Pathmanandavel, Megan Crumbaker, Bao Ho, Andrew O. Yam, Peter Wilson, Remy Niman, Maria Ayers, Shikha Sharma, Adam Hickey, Peter Eu, et al.

- 227** Eligibility for <sup>177</sup>Lu-PSMA Therapy Depends on the Choice of Companion Diagnostic Tracer: A Comparison of <sup>68</sup>Ga-PSMA-11 and <sup>99m</sup>Tc-MIP-1404 in Metastatic Castration-Resistant Prostate Cancer  
Gary J.R. Cook, Wai-Lup Wong, Bal Sanghera, Stephen Mangar, Amarnath Challapalli, Amit Bahl, Paul Bassett, Darren Leaning, and Christian Schmidkonz

### Translational

- 232** ■ **FEATURED TRANSLATIONAL SCIENCE ARTICLE.** <sup>68</sup>Ga-DOTATATE Prepared from Cyclotron-Produced <sup>68</sup>Ga: An Integrated Solution from Cyclotron Vault to Safety Assessment and Diagnostic Efficacy in Neuroendocrine Cancer Patients  
Sébastien Tremblay, Jean-François Beaudoin, Ophélie Bélissant Benesty, Samia Ait-Mohand, Véronique Dumulon-Perreault, Étienne Rousseau, Éric E. Turcotte, and Brigitte Guérin

## ONCOLOGY

### Clinical

- 239** Application of the Lugano Classification for Initial Evaluation, Staging, and Response Assessment of Hodgkin and Non-Hodgkin Lymphoma: The PROLoG Consensus Initiative (Part 2—Technical)  
Fabien Ricard, Sally Barrington, Ron Korn, Guenther Brueggenwerth, Judith Trotman, Bruce Cheson, Gilles Salles, Larry Schwartz, Greg Goldmacher, Rudresh Jarecha, et al.
- 244** Static and Dynamic <sup>68</sup>Ga-FAPI PET/CT for the Detection of Malignant Transformation of Intraductal Papillary Mucinous Neoplasia of the Pancreas  
Matthias Lang, Anna-Maria Spletter, Thomas Hielscher, Jorge Hoppner, Frederik M. Glatting, Felix Bicu, Thilo Hackert, Ulrike Heger, Thomas Pausch, Ewgenija Gutjahr, et al.
- 252** Prospective Phase II Trial of [<sup>68</sup>Ga]Ga-NODAGA-E[c(RGDyK)]<sub>2</sub> PET/CT Imaging of Integrin  $\alpha_v\beta_3$  for Prognostication in Patients with Neuroendocrine Neoplasms  
Esben Andreas Carlsen, Mathias Loft, Annika Loft, Dorota Czyzewska, Mikkel Andreassen, Seppo W. Langer, Ulrich Knigge, and Andreas Kjaer

## CARDIOLOGY

### Clinical

- 260** Precision of Myocardial Blood Flow and Flow Reserve Measurement During CZT SPECT Perfusion Imaging Processing: Intra- and Interobserver Variability  
Matthieu Bailly, Frédérique Thibault, Gilles Mettrard, Maxime Courtehoux, Denis Angoulvant, and Maria Joao Ribeiro

## NEUROLOGY

### Clinical

- 266** Early-Phase <sup>18</sup>F-Florbetapir and <sup>18</sup>F-Flutemetamol Images as Proxies of Brain Metabolism in a Memory Clinic Setting  
Cecilia Boccalini, Débora Elisa Peretti, Federica Ribaldi, Max Scheffler, Sara Stampacchia, Szymon Tomczyk, Cristelle Rodriguez, Marie-Louise Montandon, Sven Haller, Panteleimon Giannakopoulos, et al.

**274 Differential Effects of Tau Stage, Lewy Body Pathology, and Substantia Nigra Degeneration on <sup>18</sup>F-FDG PET Patterns in Clinical Alzheimer Disease**

Jesús Silva-Rodríguez, Miguel A. Labrador-Espinosa, Alexis Moscoso, Michael Schöll, Pablo Mir, and Michel J. Grothe; for the Alzheimer's Disease Neuroimaging Initiative

**281 Longitudinal Tau PET Using <sup>18</sup>F-Flortaucipir: The Effect of Relative Cerebral Blood Flow on Quantitative and Semiquantitative Parameters**

Denise Visser, Hayel Tuncel, Rik Ossenkoppele, Maqsood Yaqub, Emma E. Wolters, Tessa Timmers, Emma Weltings, Emma M. Coomans, Marijke E. den Hollander, Wiesje M. van der Flier, et al.

**287 Investigating Tau and Amyloid Tracer Skull Binding in Studies of Alzheimer Disease**

Shaney Flores, Charles D. Chen, Yi Su, Aylin Dincer, Sarah J. Keefe, Nicole S. McKay, Angela M. Paulick, Gloria Guzman Perez-Carrillo, Liang Wang, Russ C. Hornbeck, et al.

**294 ■ SPECIAL CONTRIBUTION. The RSNA QIBA Profile for Amyloid PET as an Imaging Biomarker for Cerebral Amyloid Quantification**

Anne M. Smith, Nancy A. Obuchowski, Norman L. Foster, Gregory Klein, P. David Mozley, Adriaan A. Lammertsma, Richard L. Wahl, John J. Sunderland, Jean-Luc Vanderheyden, Tammie L.S. Benzinger, et al.

**AI/ADVANCED IMAGE ANALYSIS**

**Clinical**

**304 Clinical Decision Support for Axillary Lymph Node Staging in Newly Diagnosed Breast Cancer Patients Based on <sup>18</sup>F-FDG PET/MRI and Machine Learning**

Janna Morawitz, Benjamin Sigl, Christian Rubbert, Nils-Martin Bruckmann, Frederic Dietzel, Lena J. Häberle, Saskia Ting, Svyetlana Mohrmann, Eugen Ruckhäberle, Ann-Kathrin Bittner, et al.

**RADIOBIOLOGY/DOSIMETRY**

**Clinical**

**312 Fetal Dose from PET and CT in Pregnant Patients**

Christiane Sarah Burton, Kirk Frey, Frederic Fahey, Mark S. Kaminski, Richard K.J. Brown, Judith M. Pohlen, and Barry L. Shulkin

**Translational**

**320 First-in-Humans Evaluation of Safety and Dosimetry of <sup>64</sup>Cu-LLP2A for PET Imaging**

Richard Laforest, Anchal Ghai, Tyler J. Fraum, Reiko Oyama, Jennifer Frye, Helen Kaemmerer, Greg Gaehele, Tom Voller, Cedric Mpoy, Buck E. Rogers, et al.

**329 Lesion Quantification Accuracy of Digital <sup>90</sup>Y PET Imaging in the Context of Dosimetry in Systemic Fibroblast Activation Protein Inhibitor Radionuclide Therapy**

David Kersting, Walter Jentzen, Daniel Jeromin, Elektra-Antonia Mavroedi, Maurizio Conti, Florian Büther, Ken Herrmann, Christoph Rischpler, Rainer Hamacher, Wolfgang P. Fendler, et al.

**ILLUSTRATED POST**

**Clinical**

**337 First-in-Humans PET/MRI of In Vivo GD2 Expression in Osteosarcoma**

Nils Florian Trautwein, Gerald Reischl, Christian Seitz, Helmut Dittmann, Ferdinand Seith, Sophia Scheuermann, Tobias Feuchtinger, Frank Dombrowski, Rupert Handgretinger, Jörg Fuchs, et al.

**LETTERS TO THE EDITOR**

**339 Dosimetry in Radiopharmaceutical Therapy**

Michael Stabin

**339 Reply: Dosimetry in Radiopharmaceutical Therapy**

Joe O'Donoghue, Pat Zanzonico, John Humm, and Adam Kesner

**DEPARTMENTS**

**8A This Month in JNM**

**341 Book Review**

**342 In Memoriam**

The Official Publication of **SNMMI**

## Publications Committee

TODD E. PETERSON, PhD, FSNMMI  
*Chair*

CAROLYN J. ANDERSON, PhD, FSNMMI

PAIGE B. BENNETT, MD

JOYITA DUTTA, PhD

MICHAEL M. GRAHAM, PhD, MD, FACR,  
FSNMMI

HOSSEIN JADVAR, MD, PhD, FACNM,  
FSNMMI

STEVEN M. LARSON, MD, FACNM

HEINRICH R. SCHELBERT, MD, PhD, FSNMMI

HEIKO SCHÖDER, MD, MBA, FSNMMI

DAVID M. SCHUSTER, MD

JESSICA WILLIAMS, CNMT, RT(N),  
FSNMMI-TS

HARVEY A. ZIESSMAN, MD, FSNMMI

## *Ex officio*

JOHANNES CZERNIN, MD, FSNMMI

MUNIR GHESANI, MD, FACNM, FACR

ARNOLD M. STRASHUN, MD, FSNMMI

KATHY S. THOMAS, MHA, CNMT,  
PET, FSNMMI-TS

HENRY F. VANBROCKLIN, PhD, FSNMMI

## Associate Director of Communications

SUSAN ALEXANDER

## Senior Copyeditor

SUSAN NATH

## Senior Publications & Marketing Service Manager

STEVEN KLEIN

## Editorial Production Manager

PAULETTE MCGEE

## Editorial Project Manager

MARK SUMIMOTO

## Director of Communications

REBECCA MAXEY

## CEO

VIRGINIA PAPPAS

**MISSION STATEMENT:** *The Journal of Nuclear Medicine* advances the knowledge and practice of molecular imaging and therapy and nuclear medicine to improve patient care through publication of original basic science and clinical research.

*JNM* (ISSN 0161-5505 [print]; ISSN 2159-662X [online]) is published monthly by SNMMI, 1850 Samuel Morse Drive, Reston, VA 20190-5316. Periodicals postage is paid at Herndon, VA, and additional mailing offices. Postmaster, send address changes to *The Journal of Nuclear Medicine*, 1850 Samuel Morse Drive, Reston, VA 20190-5316. The costs of publication of all nonsolicited articles in *JNM* were defrayed in part by the payment of page charges. Therefore, and solely to indicate this fact, these articles are hereby designated "advertisements" in accordance with 18 USC section 1734.

**DISCLOSURE OF COMMERCIAL INTEREST:** Johannes Czernin, MD, editor-in-chief of *The Journal of Nuclear Medicine*, has indicated that he is a founder of Sofie Biosciences and holds equity in the company and in intellectual property invented by him, patented by the University of California, and licensed to Sofie Biosciences. He is also a founder and board member of Trethera Therapeutics and holds equity in the company and in intellectual property invented by him, patented by the University of California, and licensed to Triangle. He also serves on the medical advisory board of Actinium Pharmaceuticals and on the scientific advisory boards of POINT Biopharma, RayzeBio, and Jubilant Pharma and is a consultant for Amgen. No other potential conflicts of interest were reported. Manuscripts submitted to *JNM* with potential conflicts are handled by a guest editor.

**EDITORIAL COMMUNICATIONS** should be sent to: Editor-in-Chief, Johannes Czernin, MD, *JNM* Office, SNMMI, 1850 Samuel Morse Drive, Reston, VA 20190-5316. Phone: (703) 326-1185; Fax: (703) 708-9018. To submit a manuscript, go to <https://submit-jnm.snmjournals.org>.

**BUSINESS COMMUNICATIONS** concerning permission requests should be sent to the publisher, SNMMI, 1850 Samuel Morse Drive, Reston, VA 20190-5316; (703) 708-9000; home page address: [jnm.snmjournals.org](http://jnm.snmjournals.org). Subscription requests and address changes should be sent to Membership Department, SNMMI at the address above. Notify the Society of change of address and telephone number at least 30 days before date of issue by sending both the old and new addresses. Claims for copies lost in the mail are allowed within 90 days of the date of issue. Claims are not allowed for issues lost as a result of insufficient notice of change of address. For information on advertising, contact Team SNMMI (Kevin Dunn, Rich Devanna, and Charlie Meitner; (201) 767-4170; fax: (201) 767-8065; [TeamSNMMI@cunasso.com](mailto:TeamSNMMI@cunasso.com)). Advertisements are subject to editorial approval and are restricted to products or services pertinent to nuclear medicine. Closing date is the first of the month preceding the date of issue.

**INDIVIDUAL SUBSCRIPTION RATES** for the 2023 calendar year are \$633 within the United States and Canada; \$680 elsewhere. Make checks payable to the SNMMI. CPC IPM Sales Agreement No. 1415158. Sales of individual back copies from 1999 through the current issue are available for \$60 at <http://www.snmml.org/subscribe> (subscriptions@snmml.org; fax: (703) 667-5134). Individual articles are available for sale online at <http://jnm.snmjournals.org>.

COPYRIGHT © 2023 by the Society of Nuclear Medicine and Molecular Imaging. All rights reserved. No part of this work may be reproduced or translated without permission from the copyright owner. Individuals with inquiries regarding permission requests, please visit <http://jnm.snmjournals.org/site/misc/permission.xhtml>. Because the copyright on articles published in *The Journal of Nuclear Medicine* is held by the Society, each author of accepted manuscripts must sign a statement transferring copyright (available for downloading at <http://jnm.snmjournals.org/site/misc/ifora.xhtml>). See Information for Authors for further explanation (available for downloading at <http://www.snmjournals.org/site/misc/ifora.xhtml>).

The ideas and opinions expressed in *JNM* do not necessarily reflect those of the SNMMI or the Editors of *JNM* unless so stated. Publication of an advertisement or other product mentioned in *JNM* should not be construed as an endorsement of the product or the manufacturer's claims. Readers are encouraged to contact the manufacturer with any questions about the features or limitations of the products mentioned. The SNMMI does not assume any responsibility for any injury or damage to persons or property arising from or related to any use of the material contained in this journal. The reader is advised to check the appropriate medical literature and the product information currently provided by the manufacturer of each drug to be administered to verify the dosage, the method and duration of administration, and contraindications.

**EDITOR-IN-CHIEF**

**Johannes Czernin, MD**  
University of California at Los Angeles  
Los Angeles, California

**IMMEDIATE PAST EDITOR**

**Dominique Delbeke, MD, PhD**  
Vanderbilt University Medical Center  
Nashville, Tennessee

**ASSOCIATE EDITORS, CONTINUING EDUCATION**

**Hossein Jadvar, MD, PhD, MPH, MBA, FACNM, FSNMMI**  
University of Southern California  
Los Angeles, California  
**Lale Kostakoglu, MD, MPH**  
University of Virginia Health System  
Charlottesville, Virginia

**ASSOCIATE EDITORS**

**Ramsey Derek Badawi, PhD**  
UC Davis Medical Center  
Sacramento, California  
**Henryk Barthel, MD, PhD**  
Leipzig University  
Leipzig, Germany  
**Frank M. Bengel, MD**  
Hannover Medical School  
Hannover, Germany  
**Lisa Bodei, MD, PhD**  
Memorial Sloan Kettering Cancer Center  
New York, New York  
**Irene Buvat, PhD**  
Université Paris Sud  
Orsay, France  
**Jérémie Calais, MD**  
University of California at Los Angeles  
Los Angeles, California  
**Sharmila Dorbala, MBBS**  
Brigham and Women's Hospital  
Lexington, Massachusetts  
**Alexander E. Drzezga, MD**  
University Hospital of Cologne  
Cologne, Germany  
**Jan Grimm, MD, PhD**  
Memorial Sloan Kettering Cancer Center  
New York, New York  
**Ken Herrmann, MD, MBA**  
Universitätsklinikum Essen  
Essen, Germany  
**Thomas A. Hope, MD**  
University of California, San Francisco  
San Francisco, California  
**Jason S. Lewis, PhD**  
Memorial Sloan Kettering Cancer Center  
New York, New York  
**David A. Mankoff, MD, PhD**  
University of Pennsylvania  
Philadelphia, Pennsylvania  
**Heiko Schöder, MD**  
Memorial Sloan Kettering Cancer Center  
New York, New York  
**Wolfgang Weber, MD**  
Technical University of Munich  
München, Germany

**SERIES EDITOR, FOCUS ON MI**

**Carolyn J. Anderson, PhD**  
University of Missouri  
Columbia, Missouri

**SERIES EDITOR, HOT TOPICS**

**Heinrich R. Schelbert, MD, PhD**  
University of California at Los Angeles  
Los Angeles, California

**CONSULTING EDITORS**

**Nancy Knight, PhD**  
University of Maryland School of Medicine  
Baltimore, Maryland  
**Barry A. Siegel, MD**  
Mallinckrodt Institute of Radiology  
St. Louis, Missouri  
**Arnold M. Strashun, MD**  
SUNY Downstate Medical Center  
Scarsdale, New York  
**H. William Strauss, MD**  
Memorial Sloan Kettering Cancer Center  
New York, New York

**ASSOCIATE EDITORS (INTERNATIONAL)**

**Gerald Antoch, MD**  
Dusseldorf, Germany  
**Richard P. Baum, MD, PhD**  
Bad Berka, Germany  
**Ambros J. Beer, MD**  
Ulm, Germany  
**François Bénard, MD, FRCPC**  
Vancouver, Canada  
**Thomas Beyer, PhD**  
Vienna, Austria  
**Andreas K. Buck, MD, PhD**  
Würzburg, Germany  
**Ignasi Carrió, MD**  
Barcelona, Spain  
**June-Key Chung, MD**  
Seoul, Korea  
**Stefano Fanti, MD**  
Bologna, Italy  
**Markus Hacker, MD**  
Wien, Austria  
**Rodney J. Hicks, MD, FRACP**  
Melbourne, Australia  
**Michael S. Hofman, MBBS, FRACP**  
Melbourne, Australia  
**Ora Israel, MD**  
Haifa, Israel  
**Andreas Kjaer, MD, PhD, DMSc**  
Copenhagen, Denmark  
**Adriaan A. Lammertsma, PhD**  
Amsterdam, The Netherlands  
**Michael Lassman, PhD**  
Würzburg, Germany  
**Helmut R. Mäcke, PhD**  
Freiburg, Germany  
**Wim J.G. Oyen, MD, PhD**  
Milan, Italy  
**John O. Prior, MD, PhD**  
Lausanne, Switzerland  
**Osman Ratib, MD, PhD**  
Geneva, Switzerland  
**Mike Sathekge, MBChB, MMed, PhD**  
Pretoria, South Africa  
**Markus Schwaiger, MD**  
München, Germany  
**Andrew M. Scott, MD**  
Heidelberg, Australia  
**Nagara Tamaki, MD, PhD**  
Kyoto, Japan  
**Jia-He Tian, PhD**  
Beijing, China  
**Mei Tian, MD, PhD**  
Hangzhou, China

**EDITORIAL CONSULTANTS**

**Martin S. Allen-Auerbach, MD**  
Los Angeles, California  
**Magnus Dahlbom, PhD**  
Los Angeles, California  
**Andrew Quon, MD**  
Los Angeles, California  
**Christiaan Schiepers, MD, PhD**  
Los Angeles, California  
**Daniel H. Silverman, MD, PhD**  
Los Angeles, California  
**Roger Slavic, PhD**  
Winterthur, Switzerland

**EDITORIAL BOARD**

**Diane S. Abou, PhD**  
St. Louis, Missouri  
**Valentina Ambrosini, MD, PhD**  
Bologna, Italy  
**Norbert Avril, MD**  
Cleveland, Ohio  
**Shadfar Bahri**  
Los Angeles, California  
**Jacques Barbet, PhD**  
Saint-Herbalin, France  
**Bradley Jay Beattie, PhD**  
New York, New York  
**Matthias Richard Benz, MD**  
Los Angeles, California  
**Elie Besserer-Offroy, PhD, FACS**  
Los Angeles, California

**Pradeep Bhambhani, MD**  
Birmingham, Alabama  
**Angelika Bischof-Delaloye, MD**  
Lausanne, Switzerland  
**Christina Bluemel, MD**  
Würzburg, Germany  
**Ronald Boellaard, PhD**  
Groningen, The Netherlands  
**Nicolaas Bohnen, MD**  
Ann Arbor, Michigan  
**Wesley E. Bolch, PhD**  
Gainesville, Florida  
**Elias H. Botvinick, MD**  
San Francisco, California  
**Winfried Brenner, MD, PhD**  
Berlin, Germany  
**Richard C. Brunken, MD**  
Cleveland, Ohio  
**Ralph Buchert, PhD**  
Hamburg, Germany  
**Alfred Buck, MD**  
Menzingen, Switzerland  
**Denis B. Buxton, PhD**  
Bethesda, Maryland  
**Weibo Cai, PhD**  
Madison, Wisconsin  
**Federico Caobelli, MD**  
Basel, Switzerland  
**Giuseppe Carlucci, PhD**  
Los Angeles, California  
**Richard E. Carson, PhD**  
New Haven, Connecticut  
**Paolo Castellucci, MD**  
Bologna, Italy  
**Francesco Ceci, MD, PhD**  
Turin, Italy  
**Juliano J. Cerri**  
Curitiba, Brazil  
**Delphine Chen, MD**  
Seattle, Washington  
**Xiaoyuan Chen, PhD**  
Singapore  
**Simon R. Cherry**  
Davis, California  
**Arturo Chiti, MD**  
Rozzano, Italy  
**Peter M. Clark, PhD**  
Los Angeles, California  
**Christian Cohade, MD**  
Montreal, Canada  
**Ekaterina (Kate) Dadachova, PhD**  
Saskatoon, Canada  
**Issa J. Dahabreh, MD**  
Boston, Massachusetts  
**Heike Elisabeth Daldrop-Link, MD, PhD**  
Stanford, California  
**Farrokh Dehdashti, MD**  
St. Louis, Missouri  
**Robert C. Delgado-Bolton, MD, PhD**  
Logroño, Spain  
**Thorsten Derlin, MD**  
Hannover, Germany  
**Elisabeth G.E. de Vries, PhD**  
Groningen, The Netherlands  
**Marcelo F. Di Carli, MD**  
Boston, Massachusetts  
**David W. Dick, PhD**  
Iowa City, Iowa  
**Vasken Dilsizian, MD**  
Baltimore, Maryland  
**Jacob Dubroff, MD, PhD**  
Philadelphia, Pennsylvania  
**Janet F. Eary, MD**  
Bethesda, Maryland  
**W. Barry Edwards, PhD**  
Columbia, Missouri  
**Matthias Eiber, MD**  
Munich, Germany  
**David Eidelberg, MD**  
Manhasset, New York  
**Georges El Fakhri, PhD**  
Boston, Massachusetts  
**Peter J. Ell, MD**  
London, United Kingdom



**EDITORIAL BOARD, continued**

**Keigo Endo, MD**  
Nantan, Japan

**Einat Even-Sapir, MD, PhD**  
Tel Aviv, Israel

**Frederic H. Fahey, DSc**  
Boston, Massachusetts

**Melpomeni Fani, PhD, MSc**  
Basel, Switzerland

**Andrea Farolfi, MD**  
Bologna, Italy

**Wolfgang Peter Fendler, MD**  
Essen, Germany

**James W. Fletcher, MD**  
Indianapolis, Indiana

**Amy M. Fowler, MD, PhD**  
Madison, Wisconsin

**Kirk A. Frey, MD, PhD**  
Ann Arbor, Michigan

**Andrei Gafita**  
Los Angeles, California

**Victor H. Gerbaudo, PhD, MSHCA**  
Boston, Massachusetts

**Frederik L. Giesel, MD, PhD, MBA**  
Düsseldorf, Germany

**Serge Goldman, MD, PhD**  
Brussels, Belgium

**Stanley J. Goldsmith, MD**  
New York, New York

**Martin Gotthardt, MD, PhD**  
Nijmegen, The Netherlands

**Michael Graham, MD, PhD**  
Iowa City, Iowa

**David Groheux, MD, PhD**  
Paris, France

**Uwe A. Haberkorn, MD**  
Heidelberg, Germany

**Mathieu Hatt, PhD, HDR**  
Brest, France

**Wolf-Dieter Heiss, MD**  
Cologne, Germany

**Karl Herholz, MD**  
Manchester, United Kingdom

**Thomas F. Heston, MD**  
Las Vegas, Nevada

**John M. Hoffman, MD**  
Salt Lake City, Utah

**Carl K. Hoh, MD**  
San Diego, California

**Jason P. Holland, DPhil**  
Zurich, Switzerland

**Roland Hustinx, MD, PhD**  
Liege, Belgium

**Andrei H. Iagaru, MD**  
Stanford, California

**Masanori Ichise, MD**  
Chiba, Japan

**Heather A. Jacene, MD**  
Boston, Massachusetts

**Francois Jamar, MD, PhD**  
Brussels, Belgium

**Jae Min Jeong, PhD**  
Seoul, Korea

**John A. Katzenellenbogen, PhD**  
Urbana, Illinois

**Zohar Keidar, MD, PhD**  
Haifa, Israel

**Kimberly A. Kelly, PhD**  
Charlottesville, Virginia

**Laura M. Kenny, MD, PhD**  
London, United Kingdom

**Fabian Kiessling, MD**  
Aachen, Germany

**E. Edmund Kim, MD, MS**  
Orange, California

**Francoise Kraeber-Bodéré, MD, PhD**  
Nantes, France

**Clemens Kratochwil, MD**  
Heidelberg, Germany

**Kenneth A. Krohn, PhD**  
Portland, Oregon

**Brenda F. Kurland, PhD**  
Pittsburgh, Pennsylvania

**Constantin Lapa, MD**  
Augsburg, Germany

**Suzanne E. Lapi, PhD**  
Birmingham, Alabama

**Steven M. Larson, MD**  
New York, New York

**Dong Soo Lee, MD, PhD**  
Seoul, Korea

**Jeffrey Leyton, PhD**  
Sherbrooke, Canada

**Xiang-Guo Li, PhD**  
Turku, Finland

**Hannah M. Linden, MD**  
Seattle, Washington

**Martin A. Lodge, PhD**  
Baltimore, Maryland

**Katharina Lückerath, PhD**  
Los Angeles, California

**Susanne Lütje, MD, PhD**  
Bonn, Germany

**Umar Mahmood, MD, PhD**  
Boston, Massachusetts

**H. Charles Manning, PhD**  
Nashville, Tennessee

**Giuliano Mariani, MD**  
Pisa, Italy

**Chester A. Mathis, PhD**  
Pittsburgh, Pennsylvania

**Alan H. Maurer, MD**  
Philadelphia, Pennsylvania

**Jonathan McConathy, MD, PhD**  
Birmingham, Alabama

**Alexander J.B. McEwan, MD**  
Edmonton, Canada

**Yusuf Menda, MD**  
Iowa City, Iowa

**Philipp T. Meyer, MD, PhD**  
Freiburg, Germany

**Matthias Miederer, MD**  
Mainz, Germany

**Erik Mittra, MD, PhD**  
Portland, Oregon

**Christine E. Mona, PhD**  
Los Angeles, California

**Dae Hyuk Moon, MD**  
Seoul, Korea

**Jennifer Murphy, PhD**  
Los Angeles, California

**Helen Nadel, MD, FRCPC**  
Stanford, California

**Matthias Nahrendorf, MD, PhD**  
Boston, Massachusetts

**Yuji Nakamoto, MD, PhD**  
Kyoto, Japan

**David A. Nathanson, PhD**  
Los Angeles, California

**Nghi C. Nguyen, MD, PhD**  
Dallas, Texas

**Sridhar Nimmagadda, PhD**  
Baltimore, Maryland

**Egbert U. Nitzsche, MD**  
Aarau, Switzerland

**Medhat M. Osman, MD, PhD**  
Saint Louis, Missouri

**Christopher J. Palestro, MD**  
New Hyde Park, New York

**Miguel Hernandez Pampaloni, MD, PhD**  
San Francisco, California

**Neeta Pandit-Taskar, MD**  
New York, New York

**Ashwin Singh Parihar, MBBS, MD**  
Saint Louis, Missouri

**Michael E. Phelps, PhD**  
Los Angeles, California

**Gerold Porenta, MD, PhD**  
Vienna, Austria

**Sophie Poty, PhD**  
Montpellier, France

**Edwin (Chuck) Pratt, PhD, MS Eng**  
New York, New York

**Daniel A. Pryma, MD**  
Philadelphia, Pennsylvania

**Valery Radchenko, PhD**  
Vancouver, Canada

**Caius G. Radu, MD**  
Los Angeles, California

**Isabel Rauscher, MD**  
Munich, Germany

**Nick S. Reed, MBBS**  
Glasgow, United Kingdom

**Mark Rijpkema, PhD**  
Nijmegen, The Netherlands

**Steven P. Rowe, MD, PhD**  
Baltimore, Maryland

**Mehran Sadeghi, MD**  
West Haven, Connecticut

**Rozio Schillaci, MD**  
Rome, Italy

**Charles Ross Schmidlein, PhD**  
New York, New York

**David M. Schuster, MD**  
Atlanta, Georgia

**Travis Shaffer, PhD**  
Stanford, California

**Sai Kiran Sharma, PhD**  
New York, New York

**Anthony F. Shields, MD, PhD**  
Detroit, Michigan

**Barry L. Shulkin, MD, MBA**  
Memphis, Tennessee

**Yu Shyr, PhD**  
Nashville, Tennessee

**Albert J. Sinusas, MD**  
New Haven, Connecticut

**Riener H.J.A. Slart, MD, PhD**  
Groningen, The Netherlands

**Piotr Slomka, PhD, FACC**  
Los Angeles, California

**Simon John Christoph Soerensen, MD**  
Stanford, California

**Ida Sonni, MD**  
Los Angeles, California

**Michael G. Stabin, PhD**  
Richland, Washington

**Lisa J. States, MD**  
Philadelphia, Pennsylvania

**Sven-Erik Strand, PhD**  
Lund, Sweden

**Rathan M. Subramaniam, MD, PhD, MPH**  
Dunedin, New Zealand

**John Sunderland, PhD**  
Iowa City, Iowa

**Suleman Surti, PhD**  
Philadelphia, Pennsylvania

**Julie Sutcliffe, PhD**  
Sacramento, California

**David Taieb, MD, PhD**  
Marseille, France

**Laura H. Tang, MD, PhD**  
New York, New York

**Ukiihide Tateishi, MD, PhD**  
Tokyo, Japan

**James T. Thackeray, PhD**  
Hannover, Germany

**Mathew L. Thakur, PhD**  
Philadelphia, Pennsylvania

**Alexander Thiel, MD**  
Montreal, Canada

**Daniel L.J. Thorek, PhD**  
St. Louis, Missouri

**David W. Townsend, PhD**  
Singapore

**Timothy Turkington, PhD**  
Durham, North Carolina

**Gary A. Ulaner, MD, PhD**  
Irvine, California

**David Ulmert, MD, PhD**  
Los Angeles, California

**Christopher H. van Dyck, MD**  
New Haven, Connecticut

**Douglas Van Nostrand, MD**  
Washington, District of Columbia

**Patrick Veit-Haibach, MD**  
Toronto, Canada

**Nerissa Viola-Villegas, PhD**  
Detroit, Michigan

**John R. Votaw, PhD**  
Atlanta, Georgia

**Richard L. Wahl, MD**  
St. Louis, Missouri

**Anne Marie Wallace, MD**  
La Jolla, California

**Martin A. Walter, MD**  
Geneva, Switzerland

**Rudolf A. Werner, MD**  
Wuerzburg, Germany

**Andreas G. Wibmer, MD**  
New York, New York

**Anna M. Wu, PhD**  
Duarte, California

**Randy Yeh, MD**  
New York, New York

**Hyewon (Helen) Youn, PhD**  
Seoul, Korea

**Pat B. Zanzonico, PhD**  
New York, New York

**Brian M. Zeglis, PhD**  
New York, New York

**Robert Zeiser, MD**  
Freiburg, Germany

**Hong Zhang, MD, PhD**  
Hangzhou, China

**Hongming Zhuang, MD, PhD**  
Philadelphia, Pennsylvania

**Sibylle I. Ziegler, PhD**  
Munich, Germany

**ASSISTANT TO THE EDITOR**

**Joshua N. Wachtel**  
Los Angeles, California

**Discussions with leaders:** Herrmann and Czernin talk with Diane Simeone, MD, about her career achievements in advancing clinical research in pancreatic cancer. . . . . **Page 185**

**Trustworthy AI ecosystems:** Saboury and members of an SNMMI task force outline opportunities and challenges in creating strategic plans for establishment of trustworthy artificial intelligence ecosystems in nuclear medicine. . . . . **Page 188**

**WB PET and whole-person research:** Sundar and colleagues present a forward-looking assessment of the possibilities offered by total-body PET for investigating and illuminating multiorgan systemic interactions. . . . . **Page 197**

**Scientific integrity in nuclear medicine:** Kwee and colleagues report on the results of an international survey of nuclear medicine scientists' experience with scientific fraud, publication bias, and honorary authorship. . . . . **Page 200**

**SSTR procedure standard:** Hope and colleagues detail consensus procedure guidelines intended to assist physicians in recommending, performing, interpreting, and reporting the results of somatostatin-receptor PET imaging in patients with neuroendocrine tumors. . . . . **Page 204**

**<sup>225</sup>Ac-DOTATATE TAT in GEP NETs:** Ballal and colleagues evaluate long-term outcomes of targeted  $\alpha$ -therapy with <sup>225</sup>Ac-DOTATATE in patients with somatostatin receptor-expressing advanced-stage metastatic gastroenteropancreatic neuroendocrine tumors. . . . . **Page 211**

**Assessing <sup>225</sup>Ac-TAT studies:** Strosberg and colleagues offer perspective on results and analysis of a study in this issue of *JNM* reporting on real-world experience using targeted  $\alpha$ -therapy in neuroendocrine tumor patients by radiolabeling DOTATATE with <sup>225</sup>Ac. . . . . **Page 219**

**SPECT as <sup>177</sup>Lu-PSMA-617 response biomarker:** Pathmanandavel and colleagues investigate the predictive value of serial <sup>177</sup>Lu-PSMA SPECT imaging in monitoring treatment response to <sup>177</sup>Lu-PSMA-617 in metastatic castration-resistant prostate cancer. . . . . **Page 221**

**Eligibility for <sup>177</sup>Lu-PSMA-617 therapy in mCRPC:** Cook and colleagues compare lesion and lesion-to-normal-organ ratios between <sup>68</sup>Ga-PSMA-11 PET/CT and <sup>99m</sup>Tc-MIP-1404 SPECT/CT

to evaluate eligibility for <sup>177</sup>Lu-PSMA-617 therapy in metastatic castration-resistant prostate cancer. . . . . **Page 227**

**Cyclotron-produced <sup>68</sup>Ga tracer:** Tremblay and colleagues report on a comparison of DOTATATE labeling with <sup>68</sup>Ga produced by a cyclotron or eluted from a generator to demonstrate safety and diagnostic efficacy of the cyclotron-produced radiopharmaceutical as a routine diagnostic tool. . . . . **Page 232**

**PRoLoG initiative on Lugano classification:** Ricard and colleagues present the second in a 2-part series on consensus recommendations from academic and industry experts in lymphoma and imaging for consistent application of the Lugano lymphoma classification system. . . . . **Page 239**

**<sup>68</sup>Ga-FAPI PET/CT for IPMN:** Lang and colleagues describe the clinical feasibility of accurate additional identification of intraductal papillary mucinous neoplasms by <sup>68</sup>Ga-FAPI PET/CT in patients with MRI- or CT-proven cystic pancreatic lesions. . . . . **Page 244**

**Integrin  $\alpha_v\beta_3$  PET in NENs:** Carlsen and colleagues use <sup>68</sup>Ga-NODAGA-E[c(RGDyK)]<sub>2</sub> for PET/CT imaging of integrin  $\alpha_v\beta_3$  in patients with neuroendocrine neoplasms and explore its potential utility in disease prognosis. . . . . **Page 252**

**SPECT MBF and MFR variability:** Bailly and colleagues study intra- and interuser reproducibility of myocardial blood flow and myocardial flow reserve measurements in patients referred for dynamic cadmium zinc telluride-based pinhole cardiac SPECT. . . . . **Page 260**

**Early-phase amyloid PET and <sup>18</sup>F-FDG PET:** Boccalini and colleagues compare early-phase amyloid PET and <sup>18</sup>F-FDG PET imaging at the individual level and report on their relative abilities to identify typical neurodegenerative patterns. . . . . **Page 266**

**LB copathology and PET in AD:** Silva-Rodríguez and colleagues analyze relationships between neuropathologically assessed tau pathology, Lewy body pathology, substantia nigra neuronal loss, and antemortem <sup>18</sup>F-FDG PET hypometabolism in patients with clinical Alzheimer disease presentation. . . . . **Page 274**

**Relative cerebral blood flow effects:** Visser and colleagues compare semiquantitative and

quantitative parameters of longitudinal <sup>18</sup>F-flortaucipir PET scans in individuals with subjective cognitive decline or Alzheimer disease and explore the effects of changes in blood flow on these metrics. . . . . **Page 281**

**Skull binding in tau and amyloid PET:** Flores and colleagues characterize the frequency of off-target [<sup>18</sup>F]flortaucipir skull binding on PET, its influence on estimates of Alzheimer disease pathology, and whether skull uptake is a stable feature across time and tracers. . . . . **Page 287**

**RSNA QIBA profile for amyloid PET:** Smith and members of the Quantitative Imaging Biomarkers Alliance detail development and validation of a profile to characterize and reduce the variability of SUVs in amyloid PET imaging, increasing statistical power and utility. . . . . **Page 294**

**Machine learning in PET/MRI:** Morawitz and colleagues investigate whether machine learning prediction models based on simple assessable MRI or PET/MRI features can determine nodal status in newly diagnosed breast cancer for decision support in axillary lymph node staging. . . . . **Page 304**

**Fetal dose in PET/CT:** Burton and colleagues provide radiation dose estimates to the fetus from PET/CT with protocols that are adapted to University of Michigan low-dose protocols for patients known to be pregnant. . . . . **Page 312**

**<sup>64</sup>Cu-LLP2A in MM:** Laforest and colleagues report on preclinical and first-in-humans studies of safety and efficacy with this very late antigen 4-targeting radiopharmaceutical with promise for managing patients with multiple myeloma. . . . . **Page 320**

**<sup>90</sup>Y-FAPI PET quantification:** Kersting and colleagues explore the conditions needed for reliable lesion image quantification in <sup>90</sup>Y-FAPI radionuclide therapy using a digital PET/CT system. . . . . **Page 329**

**GD2 PET/MRI in sarcoma:** Trautwein and colleagues present details on clinical [<sup>64</sup>Cu]Cu-DOTAGA-ch14.18/CHO PET/MRI to evaluate expression of the disialoganglioside GD2 in an osteosarcoma patient with pulmonary metastasis. . . . . **Page 337**



## 2023 SNMMI/ACNM **HOT TOPICS** Webinar Series

SNMMI and ACNM are excited to announce the lineup for the 2023 Hot Topics Webinar Series. These informative webinars will take place at 12:00 pm ET on the second Tuesday of each month and are complimentary for SNMMI and ACNM members.

▶ **Theranostics for Pheochromocytoma/Paraganglioma**

February 14 | *Speaker: Erik Mittra, MD, PhD*

▶ **FDG PET/CT for Infection Imaging**

March 14 | *Speaker: Gad Abikhzer, MDCM, FRCPC*

▶ **From Beta to Alpha in Theranostics**

April 11 | *Speaker: Chandrasekhar Bal, MD*

▶ **Myocardial Flow Reserve**

May 9 | *Speaker: Ron Schwartz, MD*

▶ **PET/MR**

June 25 | *Speaker: Andrei Iagaru, MD*  
in-person during the SNMMI 2023 Annual Meeting

▶ **Theranostics for Neurodegenerative Disease- Final Frontier for Health Span**

July 11 | *Speaker: Phillip Kuo, MD, PhD*

▶ **Cardiac Infection and Inflammation Imaging**

August 8 | *Speaker: Vasken Dilsizian, MD*

▶ **Whole Body PET**

September 12 | *Speaker: Ramsey Badawi, PhD*

▶ **FAPI PET: Make it or break it?**

October 10 | *Speaker: Kenneth Herrmann, MD*

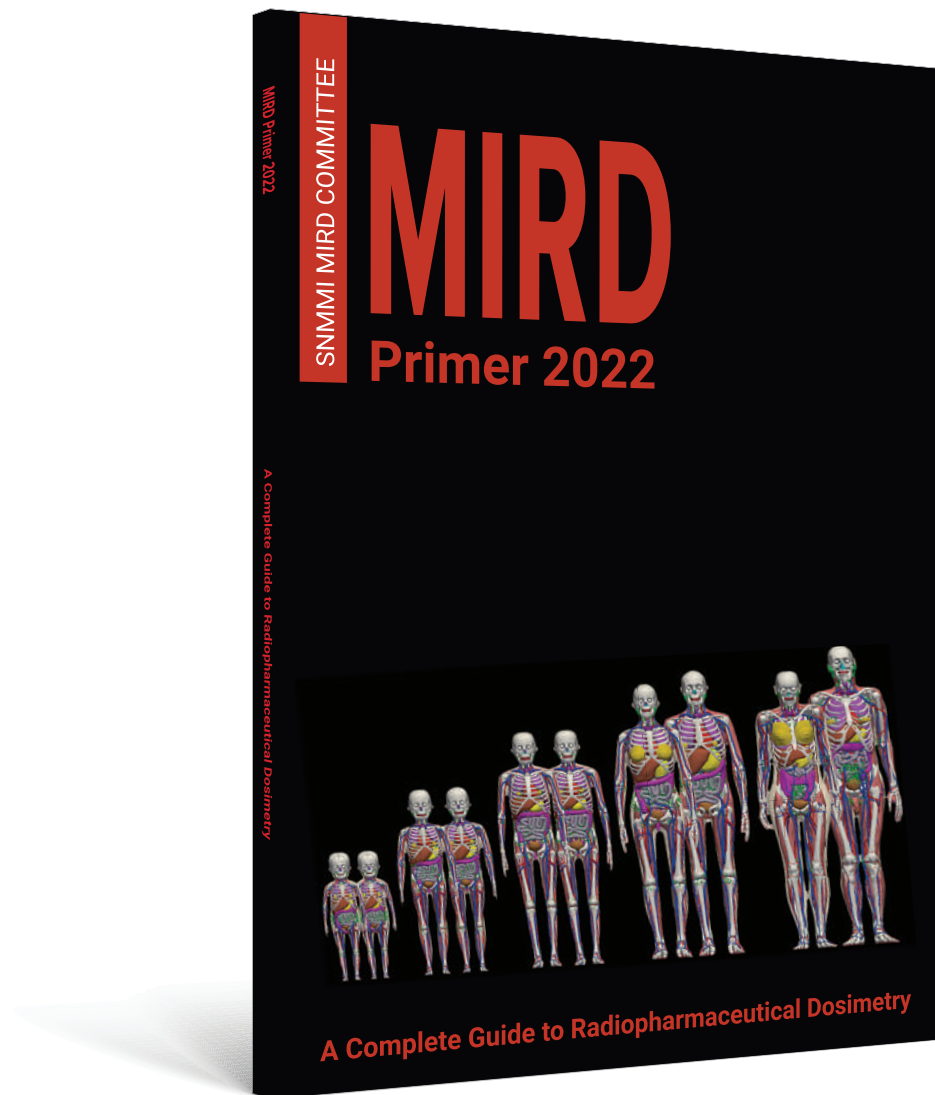
▶ **Landscape of Molecular Imaging and Fluid Biomarkers in Neurodegeneration**

November 14 | *Speaker: Alexander Drzezga, MD*

▶ **PSMA PET**

December 12 | *Speaker: Jeremy Calais, MD*





## MIRD Primer 2022

### A Complete Guide to Radiopharmaceutical Dosimetry

Richly illustrated and thoroughly referenced, the **MIRD Primer 2022** is a comprehensive, state-of-the-art guide to radiopharmaceutical dosimetry that reflects the dramatic evolution of the field of nuclear medicine, including molecular imaging and, increasingly, radiopharmaceutical therapy.

The MIRD Primer 2022 serves as

- a foundation for nuclear medicine and other medical professionals who require a working knowledge of internal radionuclide dosimetry and its radiobiological implications—without having to delve too deeply into the underlying mathematics.
- an authoritative reference on the latest, complete mathematical formulation of the MIRD schema for those seeking a more rigorous understanding of internal dosimetry.
- an invaluable teaching tool, with a large number and wide variety of clinically relevant calculational examples.

Order your copy today!

[WWW.SNMMI.ORG/MIRD2022](http://WWW.SNMMI.ORG/MIRD2022)

# Advancing Clinical Trial Innovation in Pancreatic Cancer

## A Conversation Between Diane Simeone, Ken Herrmann, and Johannes Czernin

Diane M. Simeone<sup>1</sup>, Ken Herrmann<sup>2</sup>, and Johannes Czernin<sup>3</sup>

<sup>1</sup>New York University Langone, New York, New York; <sup>2</sup>Universitätsklinikum Essen, Essen, Germany and <sup>3</sup>David Geffen School of Medicine at the University of California Los Angeles, Los Angeles, California

**K**en Herrmann, MD, from the Universitätsklinikum Essen, and Johannes Czernin, MD, from the David Geffen School of Medicine at the University of California Los Angeles, talked with Diane M. Simeone, MD, about her career advancing clinical research in pancreatic cancer. Dr. Simeone is the Laura and Isaac Perlmutter Professor of Surgery and Pathology and director of the Pancreatic Cancer Center at New York University (NYU), where she also serves as the associate director for Translational Research. An internationally recognized pancreatic surgeon and researcher with a longstanding focus on treatment of pancreatic neoplasms, she has been the recipient of numerous National Institutes of Health (NIH) grants investigating the molecular mechanisms of pancreatic metastasis and developing novel therapeutic strategies. She has a large clinical practice taking care of patients with pancreatic neoplasms and those at elevated risk of the disease. She first discovered pancreatic cancer stem cells, identified ATDC as a novel oncogene in human cancers, and defined for the first time unique populations of cancer-associated fibroblasts in pancreatic cancer. She has been an innovator in development of therapeutic clinical trials for pancreatic cancer and is currently the principal investigator of Precision Promise, an adaptive-platform clinical trial consortium focused on next-generation trials in pancreatic cancer. She also heads the Pancreatic Early Detection Consortium (PRECEDE), an international collaboration studying a large cohort of individuals at heritable risk for pancreatic cancer. She served as chair of the scientific and medical advisory board of the Pancreatic Cancer Action Network (PanCAN) and has previously served as president of the Society of University Surgeons (SUS) and the American Pancreatic Association, as well as on the National Cancer Institute (NCI) Pancreatic Cancer Task Force. Dr. Simeone is a member of the National Academy of Medicine.

**Dr. Herrmann:** You are a leading pancreatic cancer surgeon and also a translational researcher. Can you give us some highlights of your career?

**Dr. Simeone:** My father was an economics professor. Education was always strongly emphasized in my family. But I also played basketball at Brown University, which taught me that the whole team has to perform to be able to accomplish things. My parents strongly encouraged me to go for whatever I wanted to accomplish.

**Dr. Herrmann:** Your university major was very different from what you are doing now.

**Dr. Simeone:** Yes, I majored in neuroscience, because the brain was fascinating—a black box of connections that had not been untangled. But then I went to medical school at Duke University and realized that abdominal surgery was more interesting to me. I am a hands-on person; I like the idea of fixing things, and that is what led me to surgery: I felt I could do research but also have a tangible impact on patients' lives. I was actually deterred in medical school from pursuing a career in surgery, because I was told that the lifestyle was just too hard and I wouldn't have a chance to be a mother and have balance in my life. Luckily, I was strong willed and raised in a family that taught me not to accept what somebody else put on me. I remember thinking: Who are these guys to tell me what I can or can't do? I ended up at the University of Michigan for my surgical residency. Lazar Greenfield, MD, the inventor of the Greenfield filter, was the chair of surgery. In 1988, 7 of the interns in the department were women, which was unheard of at the time. Dr. Greenfield's mantra was to take the best talent. Then I did a 2-y research fellowship with John Williams, MD, PhD, one of the pioneers in pancreatology, and Craig Logsdon, PhD. As mentors, they started me on my research path.

**Dr. Czernin:** What does mentorship mean to you? What is good mentorship?

**Dr. Simeone:** A true mentor helps the mentee to thrive and succeed. It should be about what the mentor does for the mentee, not what the mentee can do for the mentor.

**Dr. Czernin:** Do you have a mentoring structure? How often do you meet with your trainees or your students or postdocs?

**Dr. Simeone:** I see my research mentees very often, multiple times a week, and we have a weekly lab meeting. I also mentor a whole team on the clinical and clinical research side. Many are young women who want to know how to best look for their first job, negotiate, and achieve balance. I'm good at negotiating now, because I was bad at negotiating early in my career and have learned to do it successfully. When I hire people, I push the institution to give them bigger packages and more resources, because I want them to be successful.

**Dr. Herrmann:** Before Johannes sidetracked us, we were in Michigan. How did you get from Michigan to NYU?

**Dr. Simeone:** I had a wonderful academic career at Michigan. Although I did not have a tenure track position in the beginning, I fought for and got it. I met with success gradually, with my first grant in 1997 or 1998, and then built on that. In 2001 I established



Diane M. Simeone, MD

a multidisciplinary pancreas tumor clinic at a time when there were not very many multidisciplinary clinics. Only 2 people were working on pancreatic cancer at the University of Michigan. The senior surgeons would say, “Oh, it’s resectable!” This was an imprecise approach to a complex problem, so I set up a database and a tumor board. We got the radiologists to join. The point I want to make is about valuing everyone who can contribute to the team. By the time I left, we had 60 people working on pancreas cancer. We had an NCI Specialized Programs of Research Excellence grant and helped recruit people from almost every department to work on pancreas cancer. Then, Pfizer moved out of Ann Arbor, and the University of Michigan bought the Pfizer campus. It was like the Louisiana Purchase—they bought 29 buildings and 2 million square feet of space for something like \$110 million. One signature project was a translational oncology program, which I was asked to run. I arm-twisted 6 colleagues to start this with me. Within 3 y, we had about 30 faculty. The premise of the program was to leverage the entire scientific strength at the University of Michigan to tackle cancer.

**Dr. Herrmann:** *So how did NYU poach you?*

**Dr. Simeone:** After a change in leadership at Michigan, I explored other professional options. The chief scientific officer at NYU reached out and asked me to join NYU, where I could continue to work on my passion, which is pancreas cancer.

**Dr. Herrmann:** *One intriguing aspect of your personality is passion. And 1 example is the PRECEDE project. Can you explain what this is about?*

**Dr. Simeone:** We need to take the imaging that is currently being done and make sure that it is standardized and state of the art. We assembled a working group that focuses mostly on MRI and endoscopic ultrasound (EUS). The other component is to create a data cloud into which we load deidentified and longitudinal imaging data. This is supported by participating companies. I also asked experts whether we can develop more sophisticated molecular imaging tools that pick up 3-mm pancreas lesions instead of the 1.5-mm range with MRI. I do think that by having this large cohort of patients we are in a position to develop strategies for new imaging approaches that might not have been possible previously.

**Dr. Czernin:** *What is your key expectation for imaging. Is it high sensitivity, specificity, or both?*

**Dr. Simeone:** We need high sensitivity to pick up small lesions. Will this be a molecular probe or something with EUS and microbubbles? Is it going to be nanodots? I don’t know the answer. I have had this idea to issue a \$1,000,000 challenge to imagers to come to the table with their next greatest ideas, so that we can help to test them.

**Dr. Herrmann:** *What kind of imaging tools, in addition to MRI, do you use for screening?*

**Dr. Simeone:** Mostly MRI, alternating with EUS, which, of course, is somewhat more invasive. The algorithm is usually to alternate them. But I do not think that we have engaged the brain trust of the imaging community to help us solve this; this is an opportunity. If we develop a blood test that can be, for example, a first sieve for identifying someone at risk, we then need a very sensitive early-detection imaging test to locate the source.

---

“The strategy was to take a group at sufficient heritable risk of pancreatic cancer, follow them, and enable development of blood-based biomarkers, more sophisticated imaging, or better multimodal data integration.”

---

**Dr. Simeone:** It all started at Michigan. I had been working on pancreatic cancer for some time but did not know if we would be able to change survival during my career. We needed to define the problems in order to solve them. I worked with PanCAN to develop a whole new platform for drug development. We developed a new approach to clinical trials called Precision Promise, a large-scale adaptive platform. Today it involves 30 centers, with 12 new innovations never done before in clinical trials. The other component is early detection, which is the key to improved survival. We resect when tumors are very small, and then, as needed, supplement with adjuvant treatment for micrometastatic disease. About 4 y ago, I started to work on PRECEDE. The key questions focused on obstacles to early detection. We used a nonprofit group called Arbor Research and then invited others to come to the table if they agreed to share data. We now have 40 centers and have enrolled close to 3,300 patients.

**Dr. Czernin:** *How do you go about early detection? What are your thoughts or plans?*

**Dr. Simeone:** The strategy was to take a group at sufficient heritable risk of pancreatic cancer, follow them, and enable development of blood-based biomarkers, more sophisticated imaging, or better multimodal data integration. That is what the PRECEDE study is. It is a heritable risk cohort study, and we are enrolling 100–150 each month. At this pace, we will be able to enroll 10,000 patients within 5 y and then follow them for another 5 y.

**Dr. Herrmann:** *Amazing strategy. What are your expectations for imaging in the next 5 to 10 y to help you accomplish your goals?*

**Dr. Herrmann:** *You talked about the importance of early detection for changing the outcome. Another opportunity is the development of improved therapies. What about the new drugs that come along, including KRAS inhibitors? How much can you improve 5-y survival by using these new drugs and identifying patients who would benefit?*

**Dr. Simeone:** That gets back to Precision Promise and setting up the platform. How do we “de-risk” bringing new therapies to pancreas cancer? We developed a pharma consortium. With the platform, cost and time to FDA approval can be cut, because it is a seamless phase II–III adaptive platform trial. You mentioned KRAS therapeutics, an area where several companies have pretty exciting new agents. With this platform, as soon as the safety studies are done, we have an accelerated testing path for a group of 30 centers around the country funded by PanCAN, the patient advocacy group that has made an investment of at least \$40 million in the platform to date.

**Dr. Herrmann:** *Before I switch to completely different areas, what do you think about immunotherapy and CAR-T cells in pancreatic cancer?*

**Dr. Simeone:** I do think now there are some interesting advances in approaches that may be quite effective in solid cancers. They just need to be tested. We are exploring that space. We know that pancreatic cancer is much more immunosuppressive than just about any other cancer. One thing we really pushed in Precision Promise was to get paired biopsies on patients before and on treatment as a critical piece that had never been done before, so that we can see

what is actually happening in the tumors. It is important to understand resistance to therapy. We are taking treatment biopsies at 8 wk for genomic and transcriptomic analyses. There are also some immune-based analyses. Of course, this is not done in isolation in humans, but in coordination with a whole preclinical research community.

**Dr. Herrmann:** *Let's talk about the role of women in medicine. How can we move forward to improve and support the careers of women in academia?*

**Dr. Simeone:** I'm disappointed that we have not seen the equity I thought we would have achieved by now. If you look at the top of every academic institution and of every co., men remain heavily dominant in leadership. We have to put women in leadership positions. I'll give you one example: When I was a member of the SUS, I was 1 of only 2 women among a group of 12–15 men. I gradually worked my way up to become president. By the time I finished being on the board and president, the board was composed equally of men and women. We had representation from minorities who had never had a seat at the table. You just have to have someone at the top who is paying attention. I give credit to Francis Collins, MD, PhD, who as NIH director announced that he would not participate in professional meetings that did not feature women in prominent speaker roles.

We need to address simple things like child care. When I was at the University of Michigan, which had thousands of employees, they had 18 slots for child care. After a positive pregnancy test, the first thing I did was put my name on the list for child care, which I never got. Better systems must be in place so that women have opportunities.

**Dr. Herrmann:** *Let's switch gears. We had a discussion with Declan Murphy, MBChB, a leading genitourinary surgeon at Peter MacCallum Cancer Centre. He said that he recently gave a talk on*

*"Avoiding obsolescence as a cancer surgeon." How do you avoid obsolescence?*

**Dr. Simeone:** I definitely have paid attention to that during my career. I am doing things now I never thought I would be doing, because I kept an open mind. I helped develop the largest clinical trial platform for pancreas cancer in the country and learned what I needed to learn to do this. Cancer surgeons should certainly make sure they educate themselves about precision oncology, genomics, clinical trials, and key trends in the basic sciences. The clinician/scientist is, unfortunately, a dying breed. Although we are drifting away a little from obsolescence, it is vital to sustain learning and keep an open mind. Academia must create a true continuum between basic science discovery and clinical applications. Our patients depend on us to drive change and improvement in their care, and that is what I encourage in all my colleagues, whether basic scientists or clinicians I mentor: Don't be afraid to do something big and to be ambitious, because people are counting on you to change how we care for patients.

**Dr. Czernin:** *Much of the academic mission is now replaced by relative value unit-driven business concepts.*

**Dr. Simeone:** I understand the statement "no margin, no mission," but I think we have to be true to what we're here for!

**Dr. Czernin:** *Maybe we should turn this around and promote the concept of "no academic mission, no margin"!*

**Dr. Herrmann:** *Do you have a take-home message for our young colleagues?*

**Dr. Simeone:** We should value everybody, every team member, who can contribute to tackling our major problems.

**Dr. Czernin:** *With this concise message, both Ken and I are grateful for your time and are sure that our readers will enjoy your insights.*

# Artificial Intelligence in Nuclear Medicine: Opportunities, Challenges, and Responsibilities Toward a Trustworthy Ecosystem

Babak Saboury<sup>1</sup>, Tyler Bradshaw<sup>2</sup>, Ronald Boellaard<sup>3</sup>, Irène Buvat<sup>4</sup>, Joyita Dutta<sup>5</sup>, Mathieu Hatt<sup>6</sup>, Abhinav K. Jha<sup>7</sup>, Quanzheng Li<sup>8</sup>, Chi Liu<sup>9</sup>, Helena McMeekin<sup>10</sup>, Michael A. Morris<sup>1</sup>, Peter J.H. Scott<sup>11</sup>, Eliot Siegel<sup>12</sup>, John J. Sunderland<sup>13</sup>, Neeta Pandit-Taskar<sup>14</sup>, Richard L. Wahl<sup>15</sup>, Sven Zuehlsdorff<sup>16</sup>, and Arman Rahmim<sup>17</sup>

<sup>1</sup>Department of Radiology and Imaging Sciences, Clinical Center, National Institutes of Health, Bethesda, Maryland; <sup>2</sup>Department of Radiology, University of Wisconsin–Madison, Madison, Wisconsin; <sup>3</sup>Department of Radiology and Nuclear Medicine, Cancer Centre Amsterdam, Amsterdam University Medical Centres, Amsterdam, The Netherlands; <sup>4</sup>Institut Curie, Université PSL, INSERM, Université Paris–Saclay, Orsay, France; <sup>5</sup>Department of Electrical and Computer Engineering, University of Massachusetts Lowell, Lowell, Massachusetts; <sup>6</sup>LaTIM, INSERM, UMR 1101, University of Brest, Brest, France; <sup>7</sup>Department of Biomedical Engineering and Mallinckrodt Institute of Radiology, Washington University, St. Louis, Missouri; <sup>8</sup>Department of Radiology, Massachusetts General Hospital and Harvard Medical School, Boston, Massachusetts; <sup>9</sup>Department of Radiology and Biomedical Imaging, Yale University, New Haven, Connecticut; <sup>10</sup>Department of Clinical Physics, Barts Health NHS Trust, London, United Kingdom; <sup>11</sup>Department of Radiology, University of Michigan Medical School, Ann Arbor, Michigan; <sup>12</sup>Department of Radiology and Nuclear Medicine, University of Maryland Medical Center, Baltimore, Maryland; <sup>13</sup>Departments of Radiology and Physics, University of Iowa, Iowa City, Iowa; <sup>14</sup>Department of Radiology, Memorial Sloan Kettering Cancer Center, New York, New York; <sup>15</sup>Mallinckrodt Institute of Radiology, Washington University, St. Louis, Missouri; <sup>16</sup>Siemens Medical Solutions USA, Inc., Hoffman Estates, Illinois; and <sup>17</sup>Departments of Radiology and Physics, University of British Columbia, Vancouver, British Columbia, Canada

Trustworthiness is a core tenet of medicine. The patient–physician relationship is evolving from a dyad to a broader ecosystem of health care. With the emergence of artificial intelligence (AI) in medicine, the elements of trust must be revisited. We envision a road map for the establishment of trustworthy AI ecosystems in nuclear medicine. In this report, AI is contextualized in the history of technologic revolutions. Opportunities for AI applications in nuclear medicine related to diagnosis, therapy, and workflow efficiency, as well as emerging challenges and critical responsibilities, are discussed. Establishing and maintaining leadership in AI require a concerted effort to promote the rational and safe deployment of this innovative technology by engaging patients, nuclear medicine physicians, scientists, technologists, and referring providers, among other stakeholders, while protecting our patients and society. This strategic plan was prepared by the AI task force of the Society of Nuclear Medicine and Molecular Imaging.

**Key Words:** artificial intelligence; trustworthy; nuclear medicine; ecosystem

**J Nucl Med 2023; 64:188–196**  
DOI: 10.2967/jnumed.121.263703

Received Feb. 13, 2022; revision accepted Dec. 6, 2022.  
For correspondence or reprints, contact Babak Saboury (sabouryb@nih.gov).

Published online Dec. 15, 2022.  
Immediate Open Access: Creative Commons Attribution 4.0 International License (CC BY) allows users to share and adapt with attribution, excluding materials credited to previous publications. License: <https://creativecommons.org/licenses/by/4.0/>. Details: <http://jnm.snmjournals.org/site/misc/permission.xhtml>.

COPYRIGHT © 2023 by the Society of Nuclear Medicine and Molecular Imaging.









**M**edicine uses science, practical wisdom, and the best available tools in the art of compassionate care. The necessity of dealing with maladies has motivated physicians to incorporate inventions into medical practice to decrease or eliminate patient suffering. During the past two centuries, along with technologic revolutions, new medical devices have become the standard of care, from the stethoscope and electrocardiogram to cross-sectional imaging (Fig. 1). The stethoscope, which arose out of the first industrial revolution, is so pervasive that it has become the symbol of health-care professionals today. Compared with other medical equipment, it has the highest positive impact on the perceived trustworthiness of the practitioner seen with it (1).

Nuclear medicine has always embraced the progress of technology. With the emergence of AI, we will again be poised to experience a modern renaissance, similar to the one experienced after David Kuhl's and Roy Edwards' groundbreaking work in the 1960s. By applying the concepts of radon transform through newly available computing technology, they introduced volumetric cross-sectional medical imaging with SPECT, which was subsequently followed by the development of x-ray–based CT and PET (2).

The past decades have seen tremendous advances in information technology and in its integration into the practice of medicine. The application of artificial intelligence (AI) to medicine represents the actualization of a new era. Such transformative technologies can affect all facets of society, yielding advances in space exploration, defense, energy, industrial processes, and finance; and even in cartography, transportation, and food service, among others.

The addition of AI into clinical practice in nuclear medicine poses opportunities and challenges. The full benefits of this new technology will continuously evolve. It is important to recognize that the nuclear medicine community must be actively involved to ensure safe and effective implementation. Establishing and maintaining AI



			
Steam engines	Light bulb	Computer	Self-driving car; IoT
<b>1<sup>st</sup> Industrial revolution</b> <b>Mechanization</b>	<b>2<sup>nd</sup> Industrial revolution</b> <b>Electricity</b>	<b>3<sup>rd</sup> Industrial revolution</b> <b>Digital and IT</b>	<b>4<sup>th</sup> Industrial revolution</b> <b>Big Data and AI</b>
Mechanical loom Late 18 <sup>th</sup> - Early 19 <sup>th</sup> Century	Mass production Late 19 <sup>th</sup> - Early 20 <sup>th</sup> Century	Computation and connectivity Latter half of 20 <sup>th</sup> Century	Hyperconnectivity, CNN Early 21 <sup>st</sup> Century-Now
Stethoscope	Electrocardiogram	Computed Tomography	Medical Imaging AI application
			

**FIGURE 1.** New technologies in medicine have coincided with each phase of industrial revolution. First industrial revolution was mechanization, with mechanical loom invented in 1784. The stethoscope was invented by René Laennec in 1816 and improved by Arthur Leared (1851) and George Philip Cammann (1852). Second industrial revolution was driven by advent of electricity, with the commercial light bulb (patented by Thomas Edison in 1879), telegram, and modern factory production line. Electrocardiogram was invented by Augustus Waller in 1887 by projecting the heartbeat captured by Lippmann capillary electrometer onto photographic plate, allowing heartbeat to be recorded in real time. Willem Einthoven (1895) assigned letters P, Q, R, S, and T to the theoretic waveform. Third industrial revolution, known as digital revolution, brought computing technology and refined it to personal computer. In 1960s, Kuhl and Edwards developed cross-sectional CT and implemented this in the SPECT scanner, which was later applied to CT scanner by Sir Godfrey Hounsfield and Allan Cormack in 1972. Fourth industrial revolution is that of modern day, with big data, hyperconnectivity, and neural networks, resulting in ability to propel self-driving cars and development of AI in nuclear medicine. CNN = convolutional neural network; IoT = Internet of things.

leadership in the realm of nuclear medicine requires a comprehensive strategy to promote the application of innovative technology while protecting our patients and society, executing our professional and ethical obligations, and promoting our values. A potential advantage of deploying AI techniques is that nuclear medicine methodologies may become more widely available, increasing the access of patients to high-quality nuclear medicine procedures.

Nuclear medicine professional societies such as the Society of Nuclear Medicine and Molecular Imaging (SNMMI) and others provide leadership to ensure that we recognize the benefits of technologic advances in a manner consistent with our core values, medical ethics, and society's best interests. In July 2020, the SNMMI formed an AI task force by bringing together experts in nuclear

#### NOTEWORTHY

- An appropriate AI ecosystem can contribute to enhancing the trustworthiness of AI tools throughout their life cycle through close collaboration among stakeholders.
- A trustworthy medical AI system depends on the trustworthiness of the AI system itself, as well as the trustworthiness of all people and processes that are part of the system's life cycle.
- By encouraging the establishment of trustworthy AI in nuclear medicine, SNMMI aims to decrease health disparity, increase health system efficiency, and contribute to the improved overall health of society using AI applications in the practice of nuclear medicine.

medicine and AI, including physicists, computational imaging scientists, physicians, statisticians, and representatives from industry and regulatory agencies. This article serves as both a strategic plan and a summary of the deliberations of the SNMMI AI task force over the past year in conjunction with other focused topics, including best practices for development (3) and evaluation (4) (Table 1).

## OPPORTUNITIES

### Quantitative Imaging and Process Improvement

Nuclear medicine is evolving toward even better image quality and more accurate and precise quantification in the precision medicine era, most recently in the paradigm of theranostics.

### Diagnostic Imaging

AI techniques in the patient-to-image subdomain improve acquisition, and models in the image-to-patient subdomain improve decision making for interventions on patients (Fig. 2) (3).

Image generation considerations are elaborated in the supplemental section "Opportunities," part A (supplemental materials are available at <http://jnm.snmjournals.org> (5–40)); however, examples include improved image reconstruction from raw data

(list-mode, sinogram); data corrections including for attenuation, scatter, and motion; and postreconstruction image enhancement, among others (41–43). These enhancements could impact PET and SPECT in clinical use today. Multiple-time-point acquisitions and PET/MRI may see improved feasibility.

Specific opportunities in image analysis are elaborated in the supplemental section "Opportunities," part B. A few examples include image registration, organ and lesion segmentation, biomarker measurements and multiomics integration, and kinetic modeling (44).

Opportunities for clinical use of AI in nuclear medicine practice were extensively reviewed recently, including brain imaging (45), head and neck imaging (46), lung imaging (47), cardiac imaging (48,49), vascular imaging (49,50), bone imaging (51), prostate imaging (52), and imaging of lymphoma (53). Neuroendocrine tumors, other cancers (including gastrointestinal, pancreatic, hepatobiliary, sarcoma, and hereditary), infection, and inflammation are some examples of additional areas requiring further consideration.

### Emerging Nuclear Imaging Approaches

New developments are also emerging such as total-body PET (54), which presents unique data and computational challenges. Another potential use of AI is to separate multichannel data from single-session multiisotope dynamic PET imaging. This pragmatic advancement could be valuable to extract greater phenotyping information in the evaluation of tumor heterogeneity (55).

### Radiopharmaceutical Therapies (RPTs)

There are several areas in which AI is expected to significantly impact RPTs.

**TABLE 1**  
Opportunities and Challenges Ahead for Nuclear Medicine Toward Achieving Trustworthy AI

Category	Domain	Subdomain
Opportunities	Diagnostic imaging	Emerging nuclear imaging approaches
	RPTs	AI-driven theranostic drug discovery and labeling
		Precision dosimetry
		Predictive dosimetry and digital twins
	Clinical workflow: increasing throughput while maintaining excellence	
Challenges	Development of AI applications/medical devices	Data
		Optimal network architecture
		Measurement and communication of uncertainty
		Clinically impactful use cases
		Team science
		Evaluation (verification of performance)
		Performance profiling through task-based evaluations
		Guidelines for validation
		Multicenter clinical trial network
		Ethical, regulatory, and legal ambiguities
		Ethical aspects
		Regulatory and legal aspects
		Implementation of clinical AI solutions and postimplementation monitoring
		AI platform
	Barriers of dissemination and implementation of AI technology in medicine	
	Postdeployment: change management and performance	
	Trust and trustworthiness	

*AI-Driven Theranostic Drug Discovery and Labeling.* The use of AI for molecular discovery has been explored to select the most promising leads to design suitable theranostics for the target in question. For example, machine learning models could be trained using parameters from past theranostic successes and failures (e.g., partition coefficient, dissociation constant, and binding potential) to establish which best predict a given outcome (e.g., specific binding, blood–brain barrier penetration, and tumor-to-muscle ratio). New AI approaches are revolutionizing our understanding of protein–ligand interactions (56). New hit molecules (e.g., from the literature or high-throughput screens) can then serve as the test set in such AI models to speed up hit-to-lead optimization. Subsequently, with lead molecules identified, AI could also predict optimal labeling precursors and synthesis routes to facilitate fast and efficient development of theranostic agents (57,58). By defining parameters from existing synthetic datasets (e.g., solvents, additives, functional groups, and nuclear magnetic resonance shifts), models can be trained to predict radiochemical yield for a given substrate using different precursors and radiosynthetic methods. Subjecting new lead candidates as test sets in the models will enable rapid identification of appropriate precursors and labeling strategies for new theranostics, minimizing resource-intensive manual synthetic development.

*Precision Dosimetry.* The field of radiopharmaceutical dosimetry is progressing rapidly. After administration of radiopharmaceuticals, dynamic and complex pharmacokinetics results in time-variable

biodistribution. Interaction of ionizing particles arising from the injected agent with the target and normal tissue results in energy deposition. Quantification of this deposited energy and its biologic effect is the essence of dosimetry, with opportunities to link the deposited energy to its biologic effect on diseased and normal tissues (Fig. 3).

In dosimetry, SPECT serves as a posttreatment quantitative measuring device. One challenge is the difficulty for patients to remain flat and motionless on the scanning table for the required time. AI-based image reconstruction or enhancement methods can reduce the required SPECT scanning time for patients while maintaining or enhancing the accuracy of quantification (59) and enable attenuation correction in SPECT (60).

Multiple steps in dosimetry potentially can be enhanced by AI methods, including multimodality and multiple–time-point image registration, segmentation of organs and tumors, time–activity curve fitting, time-integrated activity estimation, conversion of time-integrated activity into absorbed dose, linking macroscale dosimetry to microscale dosimetry, and arriving at comprehensive patient dose profiling (61).

*Predictive Dosimetry and Digital Twins.* Existing models can perform dosimetry before (e.g., <sup>131</sup>I-metaiodobenzylguanidine) or after treatment. Personalized RPTs require predictive dosimetry for optimal dose prescription in which AI can play a role. Pretherapy (static or dynamic) PET scans could model radiopharmaceutical pharmacokinetics and absorbed doses in tumors and normal organs.

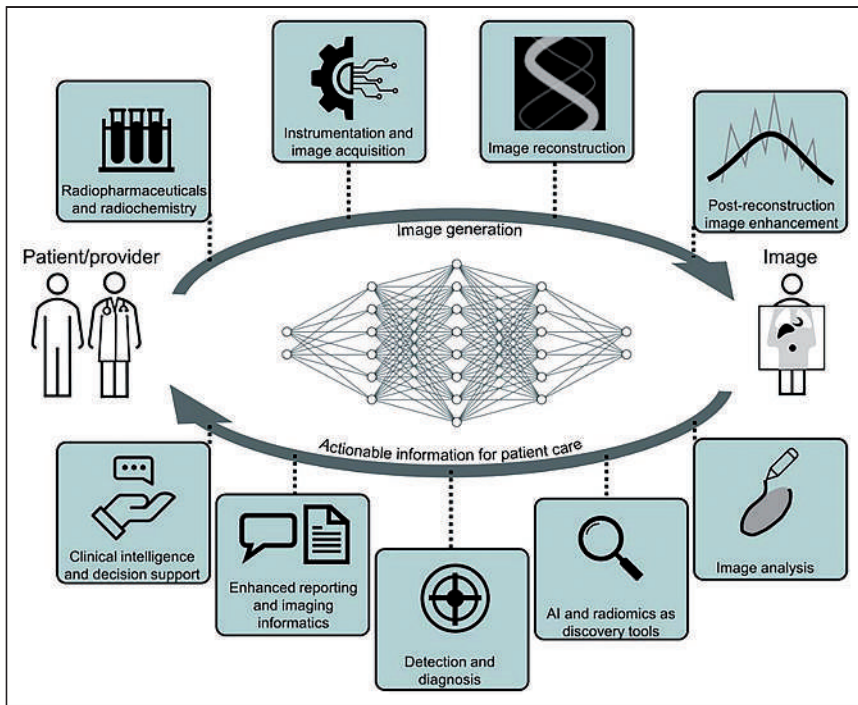


**FIGURE 2.** From patient to image creation and back to physician, there are opportunities for AI systems to act at nearly any step in medical imaging pipeline to improve our ability to care for patients and understand disease (3).

Furthermore, it is possible to additionally use intratherapy scans (e.g., single-time-point SPECT in the first cycle of RPTs) to better anticipate and adjust doses in subsequent cycles.

Overall, a vision of the future involves accurate and rapid evaluation of different RPT approaches (e.g., varying the injected

radioactivity dose and rate, site of injection, and injection interval and coupling with other therapies) using the concept of the theranostic digital twin. The theranostic digital twin can aid nuclear medicine physicians in complex decision-making processes. It enables experimentation (in the digital world) with different treatment scenarios, thus optimizing delivered therapies.

The opportunities discussed in the RPT section above are further described in the supplemental section “Opportunities,” part C.

**Clinical Workflow: Increase Throughput While Maintaining Excellence**

AI may impact operations in nuclear medicine, such as patient scheduling and resource use (62), predictive maintenance of devices to minimize unexpected downtimes, monitoring of quality control measurement results to discover hidden patterns and indicate potential for improvement, and monitoring of the performance of devices in real time to capture errors and detect aberrancies (62,63). These processes will make the practice of nuclear medicine safer, more reliable, and more valuable.

Triage of urgent findings and augmentation of time-consuming tasks could improve the report turnaround time for the most critical cases and increase the efficiency of nuclear medicine physicians, allowing them to more effectively care for patients. It is important to ensure that AI systems in nuclear medicine are sustainable through developing new current

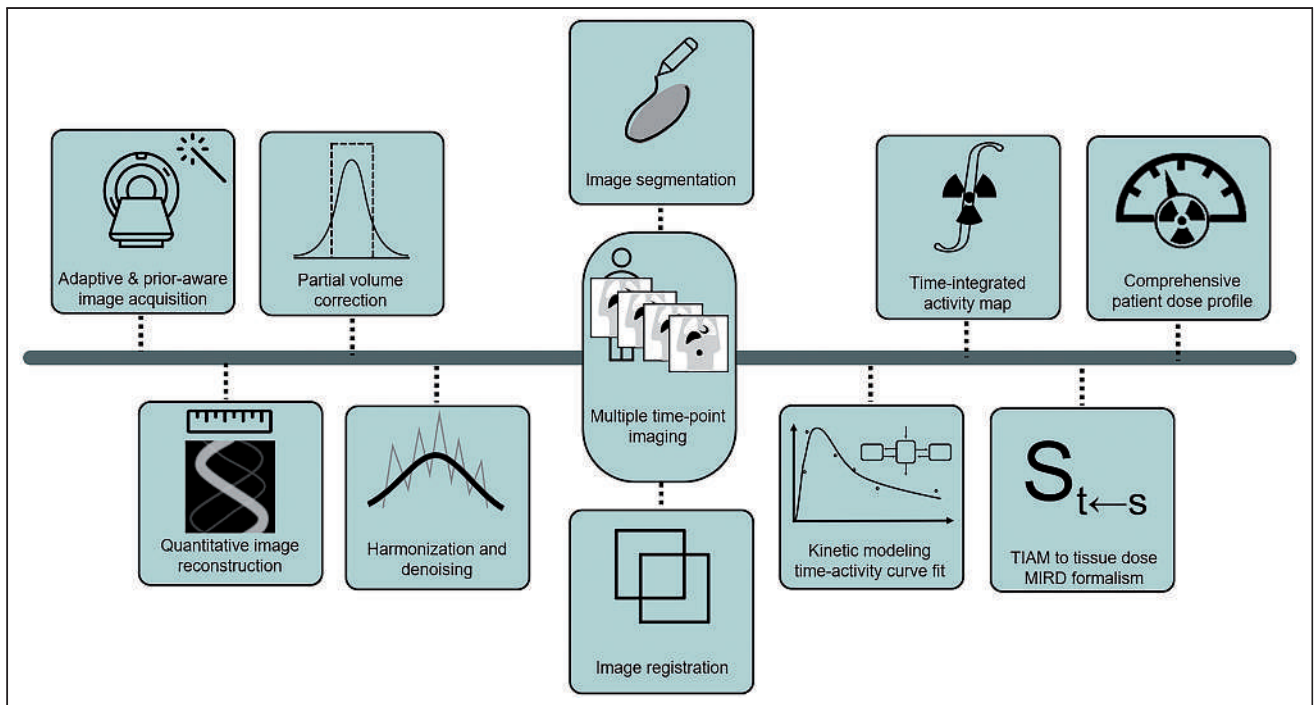


**FIGURE 3.** Dosimetry as major frontier supported by AI toward personalization of therapy: various contributions by AI to image acquisition, generation, and processing, followed by automated dose calculations, can enable routine deployment and clinical decision support. TIAM = Time Integrated Activity Map.

procedural terminology codes and assigning appropriate relative value units for the technical and professional components. It is also possible that increased efficiencies in interpretation (more cases read accurately per unit time) may allow AI to be deployed into clinical workflows in an overall cost-effective manner.

## AI ECOSYSTEM

### Actualization of Opportunities and Contextualization of Challenges

Although early nuclear medicine AI systems are already emerging, many opportunities remain in which the continuous propagation of AI technology could augment our precision patient care and practice efficiencies. The environment in which AI development, evaluation, implementation, and dissemination occurs needs a sustainable ecosystem to enable progress, while appropriately mitigating concerns of stakeholders.

The total life cycle of AI systems, from concept to appropriation of training data, model development and prototyping, production testing, validation and evaluation, implementation and deployment, and postdeployment surveillance, occurs within a framework that we call the AI ecosystem (Fig. 4). An appropriate AI ecosystem can contribute to enhancing the trustworthiness of AI tools throughout their life cycle through close collaboration among stakeholders.

### CHALLENGES FOR DEVELOPMENT, VALIDATION, DEPLOYMENT, AND IMPLEMENTATION

#### Development of AI Applications and Medical Devices

Five challenges that should be addressed include availability of curated data, optimization of network architecture, measurement and communication of uncertainty, identification of clinically impactful use cases, and improvements in team science approaches (supplemental section “Development Challenges”).

### Evaluation (Verification of Performance)

Theories on appropriate evaluation of AI software are a broad and active area of current investigation. Establishing clear and consistent guidelines for performance profiling remains challenging. Most current verification studies evaluate AI methods on the basis of metrics that are agnostic to performance on clinical tasks (64). Although such evaluation may help demonstrate promise, there is an important need for further testing on specific clinical tasks before the algorithms can be implemented. Failure-mode profiling is among the most important challenges (supplemental section “Evaluation Challenges”).

### Ethical, Regulatory, and Legal Ambiguities

Major ethical concerns include informed consent for data use, replication of historical bias and unfairness embedded in training data, unintended consequences of AI device agency, the inherent opaqueness of some algorithms, concerns about the impact of AI on health-care disparities, and trustworthiness (supplemental section “Ethical, Regulatory, and Legal Ambiguities”). AI in nuclear medicine has limited legal precedent (65).

### Implementation of Clinical AI Solutions and Postdeployment Monitoring

The lack of an AI platform integrating AI applications in the nuclear medicine workflow is among the most critical challenges of implementation (66). Barriers of dissemination can be categorized at the individual level (health-care providers), at the institutional level (organization culture), and at the societal level (67). Deployment is not the end of the implementation process (supplemental section “Implementation of Clinical AI Solutions and Post-Deployment Monitoring”).

### TRUST AND TRUSTWORTHINESS

In medicine, trust is the essence, not a pleasance.

Successful solutions to the above-mentioned challenges are necessary but not sufficient for the sustainability of AI ecosystems in medicine. Well-developed and validated AI devices with supportive regulatory context, appropriate reimbursement, and successful primary implementation may still fail if physicians, patients, and society lose trust because of lack of transparency and other critical elements of trustworthiness such as perceived inattention to health disparity or racial injustice. In a recent survey, Martinho et al. (68) found significant perceived mistrust among health-care providers with regard to AI systems and the AI industry while realizing the importance and benefits of this new technology. Responders also emphasized the importance of ethical use, and the need for physician-in-the-loop interactions with AI systems, among the other factors. There is a need for a comprehensive analysis of the AI ecosystem to define and clarify the core elements of trustworthiness in order to realize the benefits of AI in clinical practice.

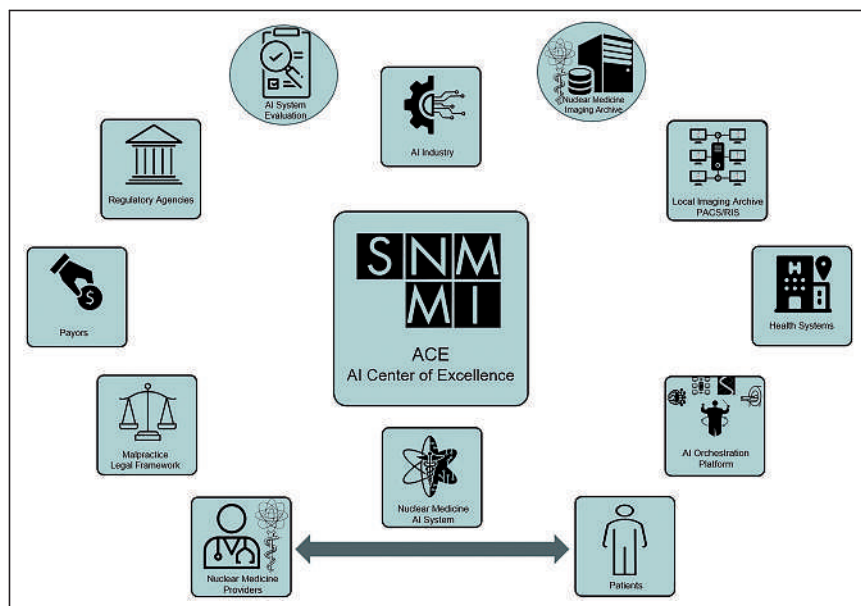


**FIGURE 4.** AI ecosystem is a complex environment in which AI system development occurs. The ecosystem connects stakeholders from industry to regulatory agencies, physicians, patients, health systems, and payers. Proposed SNMMI AI Center of Excellence can serve as an honest broker to empower the AI ecosystem from a neutral standpoint with focus on solutions. ACE = SNMMI AI Center of Excellence; RIS = radiology information system.

### RESPONSIBILITIES: TOWARD TRUSTWORTHY AI

When the safety, well-being, and rights of our patients are at stake, SNMMI should

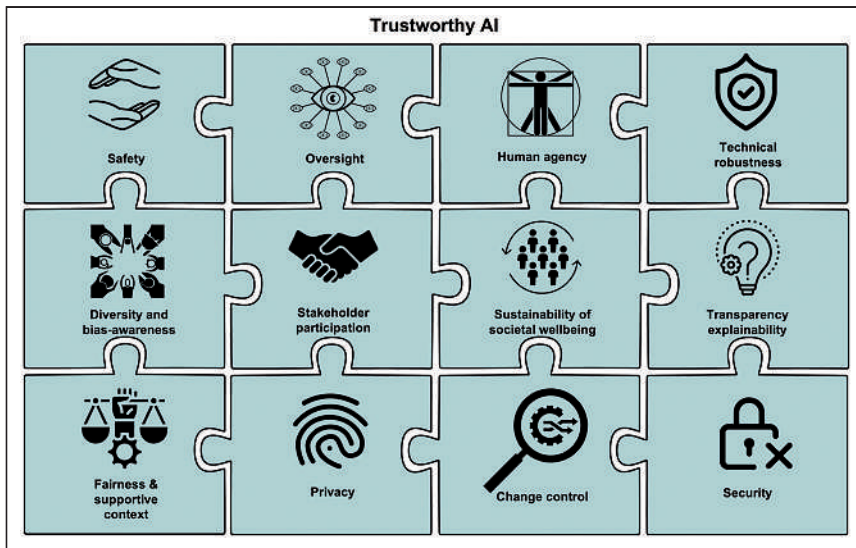


**FIGURE 5.** Twelve core concepts critical to trustworthy AI ecosystems.

be committed to support principles that are future-proof and innovation-friendly.

The willingness of physicians and patients to depend on a specific tool in a risky situation is the measure of the trustworthiness of that tool (69). In the case of AI systems, that willingness is based on a set of specific beliefs about the reliability, predictability, and robustness of the tool, as well as the integrity, competency, and benevolence of the people or processes involved in the AI system's life cycle (development, evaluation/validation, deployment/implementation, and use).

A trustworthy medical AI system depends on the trustworthiness of the AI system itself, as well as the trustworthiness of all people and processes that are part of the system's life cycle (Fig. 5).

Trustworthy medical AI systems require a societal and professional commitment to the ethical AI framework, which includes 4 principles rooted in the fundamentals of medical ethics: respect for patients' and physicians' autonomy, prevention of harm, beneficence to maximize the well-being of patients and society, and fairness. These principles should be observed in various phases of the AI system life cycle.

In what follows, we outline 12 key elements that need to be consistently present in AI systems.

### 12 Key Elements of Trustworthy AI Systems

**Human Agency.** AI systems should empower physicians and patients, allowing them to make better-informed decisions and foster their autonomy (70). Effects of the AI algorithms on human independence should be considered. It should be clear to patients and physicians the extent to which AI is involved in patient care and the extent of physician oversight. There must be checks to avoid automation bias, which is the propensity of humans to value and overly rely on observations and analyses from computers over those of human beings (71).

**Oversight.** There must be sufficient oversight of AI decision making, which can be achieved through human-in-the-loop and human-in-command approaches (72). AI systems that are involved in higher-risk tasks (e.g., those that drive clinical management and diagnose or treat disease) must be closely monitored through post-market surveillance by independent professional credentialing

organizations analogous to certification and recertification of medical professionals. Peer review processes in practices can be adapted to consider the combined physician–AI decision-making process.

**Technical Robustness.** AI systems must perform in a dependable manner (sufficient accuracy, reliability, and reproducibility) (73). This performance should be resilient to the breadth of clinical circumstances related to their prescribed use (generalizability). The AI tool should explicitly convey a degree of certainty about its output (confidence score) and have a mechanism in place to monitor the accuracy of outputs as part of a continuous quality assurance program. Failure modes of the algorithm should be well-characterized, documented, and understood by users.

**Safety and Accountability.** According to the concepts of safety-critical systems (74), AI systems should prioritize safety above

other design considerations (e.g., potential gains in efficiency, economics, or performance). When adverse events occur, mechanisms should be in place for ensuring accountability and redress. Vendors must be accountable for the claims made of their AI systems. Physicians must be accountable for the way in which AI systems are implemented and used in the care of patients. The ability to independently audit the root cause of a failure in an AI system is important. Protection must be provided for individuals or groups reporting legitimate concerns in accordance with the principles of risk management.

**Security and Data Governance.** AI systems must include mechanisms to minimize harm, as well as to prevent it whenever possible. They must comply with all required cybersecurity standards. There should be an assessment of vulnerabilities such as data poisoning, model evasion, and model inversion. Assurances should be made to mitigate potential vulnerabilities and avoid misuse, inappropriate use, or malicious use (such as a deep fake) (75).

**Predetermined Change Control Plan.** AI tools can be highly iterative and adaptive, which may lead to rapid continual product improvement. The plan should include types of anticipated modifications (software-as-a-medical-device prespecifications). There must be a clear and well-documented methodology (algorithm change protocol) to evaluate the robustness and safety of the updated AI system. The algorithm change protocol should include guidelines for data management, retraining, performance evaluation, and update procedures. Vendors should maintain a culture of quality and organizational excellence.

**Diversity, Bias Awareness, Nondiscrimination, and Fairness.** AI systems can be affected by input data maladies (incomplete data, inadvertent historically biased data), algorithm design insufficiencies, or suboptimal performance assessment or monitoring strategies. These issues may result in biases leading to unintended prejudice and cause harm to patients. Discriminatory bias should be removed from AI systems in the development phase when possible (67).

AI system performance should be evaluated in a wide spectrum of diseases and in patients with a particular condition regardless of extraneous personal characteristics. No particular group of patients should be systematically excluded from AI device development. Patients who are underrepresented or have rare diseases should not

be excluded from AI system development or evaluation—though such datasets will be sparse and most likely could be used in the evaluation of AI methods developed only in larger populations (for generalizability). Appropriate validation testing on standardized sets that incorporate patient diversity, including rare or unusual presentations of disease, are critical to evaluate the presence of bias in results regardless of the training data used (76).

AI systems should be user-centric and developed with an awareness of the practical limitations of the physician work environment. Accessibility features should be provided to those individuals with disabilities to the extent necessary according to universal design principles.

**Stakeholder Participation.** Throughout the life cycle of an AI system, all stakeholders who may directly or indirectly be affected should actively participate to help, advise, and oversee the developers and industry. Participation of patients, physicians, and all relevant providers, health-care systems, payors, regulatory agencies, and professional societies is imperative. This inclusive and transparent engagement is essential for a trustworthy AI ecosystem. Regular clinical feedback is needed to establish longer-term mechanisms for active engagement.

**Transparency and Explainability.** Vendors should openly communicate how an AI system is validated for the labeled claim (purpose, criteria, and limitations) by describing the clinical task for which the algorithm was evaluated; the composition of the patient population used for validation; the image acquisition, reconstruction, and analysis protocols; and the figure of merit used for the evaluation (4,73). There must be appropriate training material and disclaimers for health-care professionals on how to adequately use the system. It should be clear which information is communicated from the AI system and which information is communicated by a health-care professional. AI systems should incorporate mechanisms to log and review which data, AI model, or rules were used to generate certain outputs (auditability and traceability). The effect of the input data on the AI system's output should be conveyed in a manner whereby their relationship can be understood by physicians and, ideally, patients (explainability) in order to allow a mechanism to critically evaluate and contest the AI system outputs. For diagnostic applications, the AI system should communicate the degree of confidence (uncertainty) together with its decision. To the extent possible, in high-stakes tasks the use of black box AI systems without proper emphasis on transparency should be avoided (77).

**Sustainability of Societal Well-Being.** It is important to acknowledge that exposure to AI could negatively impact social relationships and attachment within the health-care system (social agency) (78). AI systems should be implemented in a manner that enhances the physician-patient relationship. AI systems should not interfere with human deliberation or deteriorate social interactions. The societal and environmental impact of an AI tool should be carefully considered to ensure sustainability. Health-care workers who are impacted by the implementation of AI systems should be given an opportunity to provide feedback and contribute to its implementation plan. Professional societies and training programs should take steps to ensure that AI systems do not result in deskilling of professionals, such as by providing opportunities for reskilling and upskilling. A new set of skills, including physician oversight and interaction with AI tools, will evolve and must be refined.

**Privacy.** AI systems should have appropriate processes in place to maintain the security and privacy of patient data. The amount of personal data used should be minimized (data minimization).

There should be a statement on measures used to achieve privacy by design, such as encryption, pseudoanonymization, aggregation, and anonymization. Systems should be aligned with standards and protocols for data management and governance.

**Fairness and Supportive Context of Implementation.** Early development efforts can pose more risk to developers and consumers. To address liability concerns, there have been successful programs in other industries to encourage adoption of new technology and support consumer protection, such as for vaccines and autonomous vehicles (65).

## STRATEGIES FOR SUCCESS

### Part 1: SNMMI Initiatives

In July 2022, SNMMI created an AI task force to strategically assess the emergence of AI in nuclear medicine (supplemental section "SNMMI Initiatives"). An area of important focus was to designate working groups, such as the AI and dosimetry working group for predictive dosimetry and treatment planning.

### Part 2: SNMMI Action Plan

The AI task force recommends the establishment of an SNMMI AI Center of Excellence to facilitate a sustainable AI ecosystem (supplemental section "SNMMI Action Plan"). A nuclear medicine imaging archive will address the need for meaningful data access. A coalition on trustworthy AI in medicine and society will address the need for an AI bill of rights (79).

### Part 3: SNMMI Recommendations

Recommendations for the future are also provided in the supplemental section "SNMMI Recommendations."

## CONCLUSION

There are immense and exciting opportunities for AI to benefit the practice of nuclear medicine. Meanwhile, there are challenges that must and can be addressed head-on. As current challenges are addressed and new AI solutions emerge, SNMMI and the nuclear medicine community have the responsibility to ensure the trustworthiness of these tools in the care of patients.

We can all benefit from efforts to ensure fairness, inclusion, and lack of bias in the entire life cycle of AI algorithms in different settings.

There are 3 levels of facilitation that can support and enable the appropriate environment for trustworthy AI. First, our community must establish guidelines, such as those referenced in this article, to promote the natural development of trustworthy AI. Second, we can facilitate trustworthy AI through an SNMMI AI Center of Excellence. Third, we can make trustworthy AI occur through active engagement and communicative actions.

By encouraging the establishment of trustworthy AI in nuclear medicine, SNMMI aims to decrease health disparity, increase health system efficiency, and contribute to the improved overall health of society using AI applications in the practice of nuclear medicine.

## DISCLOSURE

The views expressed in this article are those of the authors and do not necessarily reflect the views of the U.S. government, nor do they reflect any official recommendation or endorsement of the National Institutes of Health. Helena McMeekin is a part-time employee of Hermes Medical Solutions, Inc. Sven Zuehlsdorff is a

full-time employee of Siemens Medical Solutions, Inc. No other potential conflict of interest relevant to this article was reported.

## ACKNOWLEDGMENTS

We acknowledge Bonnie Clarke for her very valuable support of this project. We are grateful for the insightful comments of Dr. Roberto Maas-Moreno, particularly on the concept of theranostic digital twins (AI and RPT).

## REFERENCES

1. Jiwa M, Millett S, Meng X, Hewitt VM. Impact of the presence of medical equipment in images on viewers' perceptions of the trustworthiness of an individual on-screen. *J Med Internet Res*. 2012;14:e100.
2. Dunnick NR, David E, Kuhl, MD. *Radiology*. 2017;285:1065.
3. Bradshaw TJ, Boellaard R, Dutta J, et al. Nuclear medicine and artificial intelligence: best practices for algorithm development. *J Nucl Med*. 2022;63:500–510.
4. Jha AK, Bradshaw TJ, Buvat I, et al. Nuclear medicine and artificial intelligence: best practices for evaluation (the RELAINCE guidelines). *J Nucl Med*. 2022;63:1288–1299.
5. Saboury B, Rahmim A, Siegel E. PET and AI trajectories finally coming into alignment. *PET Clin*. 2021;16:15–16.
6. Saboury B, Rahmim A, Siegel E. Taming the complexity: using artificial intelligence in a cross-disciplinary innovative platform to redefine molecular imaging and radiopharmaceutical therapy. *PET Clin*. 2022;17:17–19.
7. Reader AJ, Schramm G. Artificial intelligence for PET image reconstruction. *J Nucl Med*. 2021;62:1330–1333.
8. Shiri I, Ghafarian P, Geramifard P, et al. Direct attenuation correction of brain PET images using only emission data via a deep convolutional encoder-decoder (Deep-DAC). *Eur Radiol*. 2019;29:6867–6879.
9. Yu Z, Rahman MA, Schindler T, Laforest R, Jha AK. A physics and learning-based transmission-less attenuation compensation method for SPECT. *Proc SPIE Int Soc Opt Eng*. 2021;11595.
10. Shiri I, Arabi H, Geramifard P, et al. Deep-JASC: joint attenuation and scatter correction in whole-body  $^{18}\text{F}$ -FDG PET using a deep residual network. *Eur J Nucl Med Mol Imaging*. 2020;47:2533–2548.
11. Liu F, Jang H, Kijowski R, Zhao G, Bradshaw T, McMillan AB. A deep learning approach for  $^{18}\text{F}$ -FDG PET attenuation correction. *EJNMMI Phys*. 2018;5:24.
12. Van Hemmen H, Massa H, Hurlley S, Cho S, Bradshaw T, McMillan A. A deep learning-based approach for direct whole-body PET attenuation correction [abstract]. *J Nucl Med*. 2019;60(suppl 1):569.
13. Rahman A, Zhu Y, Clarkson E, Kupinski MA, Frey EC, Jha AK. Fisher information analysis of list-mode SPECT emission data for joint estimation of activity and attenuation distribution. *Inverse Probl*. 2020;36:084002.
14. Qian H, Rui X, Ahn S. Deep learning models for PET scatter estimations. In: *2017 IEEE Nuclear Science Symposium and Medical Imaging Conference (NSS/MIC)*. IEEE; 2017:1–5.
15. Arabi H, Bortolin K, Ginovart N, Garibotto V, Zaidi H. Deep learning-guided joint attenuation and scatter correction in multitracer neuroimaging studies. *Hum Brain Mapp*. 2020;41:3667–3679.
16. Sanaat A, Arabi H, Maimta I, Garibotto V, Zaidi H. Projection space implementation of deep learning-guided low-dose brain PET imaging improves performance over implementation in image space. *J Nucl Med*. 2020;61:1388–1396.
17. Yu Z, Rahman MA, Schindler T, et al. AI-based methods for nuclear-medicine imaging: need for objective task-specific evaluation [abstract]. *J Nucl Med*. 2020; 61(suppl 1):575.
18. Fu Y, Lei Y, Wang T, Curran WJ, Liu T, Yang X. Deep learning in medical image registration: a review. *Phys Med Biol*. 2020;65:20TR01.
19. Yousefirizi F, Pierre Decazes, Amyar A, Ruan S, Saboury B, Rahmim A. AI-based detection, classification and prediction/prognosis in medical imaging: towards radiophenomics. *PET Clin*. 2022;17:183–212.
20. Cui J, Gong K, Guo N, Kim K, Liu H. CT-guided PET parametric image reconstruction using deep neural network without prior training data. In: *Proceedings of SPIE 10948, Medical Imaging 2019: Physics of Medical Imaging*. SPIE; 2019:109480Z.
21. Xie N, Gong K, Guo N, et al. Clinically translatable direct Patlak reconstruction from dynamic PET with motion correction using convolutional neural network. In: *Medical Image Computing and Computer Assisted Intervention: MICCAI 2020*. Springer International Publishing; 2020:793–802.
22. Gong K, Catana C, Qi J, Li Q. Direct reconstruction of linear parametric images from dynamic PET using nonlocal deep image prior. *IEEE Trans Med Imaging*. 2022;41:680–689.
23. Jackson P, Hardcastle N, Dawe N, Kron T, Hofman MS, Hicks RJ. Deep learning renal segmentation for fully automated radiation dose estimation in unsealed source therapy. *Front Oncol*. 2018;8:215.
24. Akhavanallaf A, Shiri I, Arabi H, Zaidi H. Whole-body voxel-based internal dosimetry using deep learning. *Eur J Nucl Med Mol Imaging*. 2021;48:670–682.
25. Langlotz CP, Allen B, Erickson BJ, et al. A roadmap for foundational research on artificial intelligence in medical imaging: from the 2018 NIH/RSNA/ACR/the Academy Workshop. *Radiology*. 2019;291:781–791.
26. Morris MA, Saboury B, Burkett B, Gao J, Siegel EL. Reinventing radiology: big data and the future of medical imaging. *J Thorac Imaging*. 2018;33:4–16.
27. Sitek A, Ahn S, Asma E, et al. Artificial intelligence in PET: an industry perspective. *PET Clin*. 2021;16:483–492.
28. Krizhevsky A, Sutskever I, Hinton GE. ImageNet classification with deep convolutional neural networks. In: *Advances in Neural Information Processing Systems 25 (NIPS 2012)*. MIT Press; 2012:1–9.
29. Ouyang D, He B, Ghorbani A, et al. Video-based AI for beat-to-beat assessment of cardiac function. *Nature*. 2020;580:252–256.
30. Huang S-C, Pareek A, Seyyedi S, Banerjee I, Lungren MP. Fusion of medical imaging and electronic health records using deep learning: a systematic review and implementation guidelines. *NPJ Digit Med*. 2020;3:136.
31. Kaissis G, Ziller A, Passerat-Palmbach J, et al. End-to-end privacy preserving deep learning on multi-institutional medical imaging. *Nat Mach Intell*. 2021;3:473–484.
32. Warnat-Herresthal S, Schultze H, Shastry KL, et al. Swarm Learning for decentralized and confidential clinical machine learning. *Nature*. 2021;594:265–270.
33. Begoli E, Bhattacharya T, Kusnezov D. The need for uncertainty quantification in machine-assisted medical decision making. *Nat Mach Intell*. 2019;1:20–23.
34. Poplin R, Varadarajan AV, Blumer K, et al. Prediction of cardiovascular risk factors from retinal fundus photographs via deep learning. *Nat Biomed Eng*. 2018;2:158–164.
35. Ghassemi M, Oakden-Rayner L, Beam AL. The false hope of current approaches to explainable artificial intelligence in health care. *Lancet Digit Health*. 2021;3:e745–e750.
36. Arun N, Gaw N, Singh P, et al. Assessing the trustworthiness of saliency maps for localizing abnormalities in medical imaging. *Radiol Artif Intell*. 2021;3:e200267.
37. Obermeyer Z, Powers B, Vogeli C, Mullainathan S. Dissecting racial bias in an algorithm used to manage the health of populations. *Science*. 2019;366:447–453.
38. Murray E, Treweek S, Pope C, et al. Normalisation process theory: a framework for developing, evaluating and implementing complex interventions. *BMC Med*. 2010;8:63.
39. Morris ZS, Wooding S, Grant J. The answer is 17 years, what is the question: understanding time lags in translational research. *J R Soc Med*. 2011;104:510–520.
40. May C. A rational model for assessing and evaluating complex interventions in health care. *BMC Health Serv Res*. 2006;6:86.
41. Gong K, Kim K, Cui J, Wu D, Li Q. The evolution of image reconstruction in PET: from filtered back-projection to artificial intelligence. *PET Clin*. 2021;16:533–542.
42. McMillan AB, Bradshaw TJ. Artificial intelligence-based data corrections for attenuation and scatter in position emission tomography and single-photon emission computed tomography. *PET Clin*. 2021;16:543–552.
43. Liu J, Malekzadeh M, Mirian N, Song T-A, Liu C, Dutta J. Artificial intelligence-based image enhancement in PET imaging: noise reduction and resolution enhancement. *PET Clin*. 2021;16:553–576.
44. Yousefirizi F, Jha AK, Brosch-Lenz J, Saboury B, Rahmim A. Toward high-throughput artificial intelligence-based segmentation in oncological PET imaging. *PET Clin*. 2021;16:577–596.
45. Cross DJ, Komori S, Minoshima S. Artificial intelligence for brain molecular imaging. *PET Clin*. 2022;17:57–64.
46. Gharavi SMH, Faghihimehr A. Clinical application of artificial intelligence in PET imaging of head and neck cancer. *PET Clin*. 2022;17:65–76.
47. Zukotynski KA, Gaudet VC, Uribe CF, Chiam K, Bénard F, Gerbaudo VH. Clinical applications of artificial intelligence in positron emission tomography of lung cancer. *PET Clin*. 2022;17:77–84.
48. Miller RJH, Singh A, Dey D, Slomka P. Artificial intelligence and cardiac PET/computed tomography imaging. *PET Clin*. 2022;17:85–94.
49. Slart RHJA, Williams MC, Juarez-Orozco LE, et al. Position paper of the EACVI and EANM on artificial intelligence applications in multimodality cardiovascular imaging using SPECT/CT, PET/CT, and cardiac CT. *Eur J Nucl Med Mol Imaging*. 2021;48:1399–1413.
50. Paravastu SS, Theng EH, Morris MA, et al. Artificial intelligence in vascular-PET: translational and clinical applications. *PET Clin*. 2022;17:95–113.
51. Paravastu SS, Hasani N, Farhadi F, et al. Applications of artificial intelligence in  $^{18}\text{F}$ -sodium fluoride positron emission tomography/computed tomography: current state and future directions. *PET Clin*. 2022;17:115–135.
52. Ma K, Harmon SA, Klyuzhin IS, Rahmim A, Turkbey B. Clinical application of artificial intelligence in positron emission tomography: imaging of prostate cancer. *PET Clin*. 2022;17:137–143.

53. Hasani N, Paravastu SS, Farhadi F, et al. Artificial intelligence in lymphoma PET imaging: a scoping review (current trends and future directions). *PET Clin.* 2022; 17:145–174.
54. Wang Y, Li E, Cherry SR, Wang G. Total-body PET kinetic modeling and potential opportunities using deep learning. *PET Clin.* 2021;16:613–625.
55. Ding W, Yu J, Zheng C, et al. Machine learning-based noninvasive quantification of single-imaging session dual-tracer  $^{18}\text{F}$ -FDG and  $^{68}\text{Ga}$ -DOTATATE dynamic PET-CT in oncology. *IEEE Trans Med Imaging.* 2022;41:347–359.
56. Tunyasuvunakool K, Adler J, Wu Z, et al. Highly accurate protein structure prediction for the human proteome. *Nature.* 2021;596:590–596.
57. Webb EW, Scott PJH. Potential applications of artificial intelligence and machine learning in radiochemistry and radiochemical engineering. *PET Clin.* 2021;16: 525–532.
58. Ataieina B, Heidari P. Artificial intelligence and the future of diagnostic and therapeutic radiopharmaceutical development: in silico smart molecular design. *PET Clin.* 2021;16:513–523.
59. Arabi H, AkhavanAllaf A, Sanaat A, Shiri I, Zaidi H. The promise of artificial intelligence and deep learning in PET and SPECT imaging. *Phys Med.* 2021;83:122–137.
60. Shi L, Onofrey JA, Liu H, Liu Y-H, Liu C. Deep learning-based attenuation map generation for myocardial perfusion SPECT. *Eur J Nucl Med Mol Imaging.* 2020; 47:2383–2395.
61. Brosch-Lenz J, Yousefirizi F, Zukotynski K, et al. Role of artificial intelligence in theranostics: toward routine personalized radiopharmaceutical therapies. *PET Clin.* 2021;16:627–641.
62. Beegle C, Hasani N, Maass-Moreno R, Saboury B, Siegel E. Artificial intelligence and positron emission tomography imaging workflow. *PET Clin.* 2022;17:31–39.
63. Ullah MN, Levin CS. Application of artificial intelligence in PET instrumentation. *PET Clin.* 2022;17:175–182.
64. Yang J, Sohn JH, Behr SC, Gullberg GT, Seo Y. CT-less direct correction of attenuation and scatter in the image space using deep learning for whole-body FDG PET: potential benefits and pitfalls. *Radiol Artif Intell.* 2020;3: e200137.
65. Mezrich JL. Demystifying medico-legal challenges of artificial intelligence applications in molecular imaging and therapy. *PET Clin.* 2022;17:41–49.
66. Saboury B, Morris M, Siegel E. Future directions in artificial intelligence. *Radiol Clin North Am.* 2021;59:1085–1095.
67. Yousefi Nooraie R, Lyons PG, Baumann AA, Saboury B. Equitable implementation of artificial intelligence in medical imaging: what can be learned from implementation science? *PET Clin.* 2021;16:643–653.
68. Martinho A, Kroesen M, Chorus C. A healthy debate: exploring the views of medical doctors on the ethics of artificial intelligence. *Artif Intell Med.* 2021;121: 102190.
69. Hasani N, Morris MA, Rhamim A, et al. Trustworthy artificial intelligence in medical imaging. *PET Clin.* 2022;17:1–12.
70. Kilbride MK, Joffe S. The new age of patient autonomy: implications for the patient-physician relationship. *JAMA.* 2018;320:1973–1974.
71. Lyell D, Coiera E. Automation bias and verification complexity: a systematic review. *J Am Med Inform Assoc.* 2017;24:423–431.
72. Vinuesa R, Azizpour H, Leite I, et al. The role of artificial intelligence in achieving the sustainable development goals. *Nat Commun.* 2020;11:233.
73. Jha AK, Myers KJ, Obuchowski NA, et al. Objective task-based evaluation of artificial intelligence-based medical imaging methods: framework, strategies, and role of the physician. *PET Clin.* 2021;16:493–511.
74. Grant ES. Requirements engineering for safety critical systems: an approach for avionic systems. In: *2016 2nd IEEE International Conference on Computer and Communications (ICCC).* IEEE; 2016:991–995.
75. Zhou Q, Zuley M, Guo Y, et al. A machine and human reader study on AI diagnosis model safety under attacks of adversarial images. *Nat Commun.* 2021;12:7281.
76. Hasani N, Farhadi F, Morris MA, et al. Artificial intelligence in medical imaging and its impact on the rare disease community: threats, challenges and opportunities. *PET Clin.* 2022;17:13–29.
77. Rudin C. Stop explaining black box machine learning models for high stakes decisions and use interpretable models instead. *Nat Mach Intell.* 2019;1:206–215.
78. Harvey DL. Agency and community: a critical realist paradigm. *J Theory Soc Behav.* 2002;32:163–194.
79. Science and Technology Policy Office. Notice of request for information (RFI) on public and private sector uses of biometric technologies. *Fed Regist.* 2021;86: 56300–56302.



# Whole-Body PET Imaging: A Catalyst for Whole-Person Research?

Lalith Kumar Shiyam Sundar<sup>1</sup>, Marcus Hacker<sup>2</sup>, and Thomas Beyer<sup>1</sup>

<sup>1</sup>Quantitative Imaging and Medical Physics Team, Medical University of Vienna, Vienna, Austria; and <sup>2</sup>Division of Nuclear Medicine, Department of Biomedical Imaging and Image-Guided Therapy, Medical University of Vienna, Vienna, Austria

*You don't understand anything until you learn it more than one way.*

—Marvin Minsky (1927–2016)

**L**iving organisms maintain homeostasis through dynamic multiorgan systemic interactions (1). Considerable energy is needed to fuel these interactions to promptly orchestrate multiple organs to respond to perturbations (allostatic load) (2). For example, inflammation in response to infection or tissue damage is a critical survival mechanism to return to the original homeostatic state. In the case of ill-compensated systemic feedback loops (allostatic overload), persistent disruptions in baseline homeostasis may occur, which gives rise to chronic diseases such as arthritis, cancer, cardiovascular disease, or diabetes (3). These pathologies can, in theory, be characterized by deviations in parameters that describe a normative multiorgan network and that extend beyond their usual range.

Molecular imaging modalities such as PET can provide valuable insights into the underlying homeostasis of living subjects using target-specific radiotracer imaging (4). After the commercial inception of PET, most of its clinical investigations focused on imaging with a single-organ field of view (FOV) (cardiology and neurology). With the introduction of a whole-body (WB) acquisition mode—that is, the successive translation of the subject through the axial FOV of a PET system with slightly overlapping bed positions (5)—the identification of hypermetabolic tumor lesions in oncology patients became the primary application of PET. Such a reductionist “lumpology” approach (6), however, caused a wealth of molecular information available from PET to be overlooked and the concept of human physiology imaging to be discarded.

The recent extension of the WB PET concept to extended axial-imaging ranges with larger-FOV systems, colloquially referred to as total-body (TB) PET, has sparked interest in the PET community to conduct multiorgan systemic investigations. TB PET systems cover axial scan ranges of 1 m (7,8) to 2 m (9), allowing synchronous measurement of signals from multiple organs. In addition, the richness of the multiorgan data derived from WB PET notwithstanding (10,11), TB PET is particularly unique as it satisfies

2 critical criteria for such causal investigations: the simultaneous acquisition of signals from multiple investigated distant organs and a high temporal resolution across the FOV (12). The combination of increased sensitivity and subsecond temporal sampling (13) provided by TB PET could potentially aid in probing real-time multiorgan interactions (Fig. 1).

## MULTIORGAN ANALYSIS WITH STANDARD WB PET

Traditional WB PET with an axial FOV of about 20 cm can already be used for multiorgan analysis. For example, simple intergroup comparisons of organ-based SUV can provide crucial information on the underlying pathology. A recent study demonstrated that in a patient cohort with resected breast cancer, a high metabolic tumor volume and increased spleen glucose metabolism at baseline were associated with poor 5-y recurrence-free survival (14). That study hinted toward a possible interaction between the tumor and the host immune system through upregulation of hematopoiesis. Diseases formerly conceived as focal, such as myocardial infarction, have distributed effects throughout the body that are mediated through disease-specific networks (15). And finally, mental and societal stress triggers have been linked to various diseases associated with chronic inflammation that can already be assessed by WB PET (16).

## INTERORGAN NETWORKS THROUGH PET

Current multiorgan network investigations using WB or TB PET are mostly fishing expeditions aiming to pinpoint stable correlations between organs (10,11). In general, correlation analyses explore gross systemic effects between 2 groups without causal explanation. When correlation analyses are performed, the chosen sample should represent the investigated population (e.g., healthy or pathologic) (17). Other factors, such as variability, linearity, and variance of the samples, must also be considered. Since most multiorgan correlation network studies seek to pinpoint monotonic relationships between investigated organs, Spearman correlation should be chosen over Pearson correlation, as the former is nonparametric and insensitive to the linearity and homogeneity of the variance of observed data.

The ultimate goal of interorgan analysis is to identify causal relationships between organs that can facilitate the development of impactful interventions in medicine. Here, structure learning of Bayesian networks (18) in combination with graph models as visual representations of causal links in complex processes can be an attractive approach (19), which, however, still mandates the integration of a clinical expert to denounce spurious causal links.

Received Oct. 6, 2022; revision accepted Nov. 17, 2022.

For correspondence or reprints, contact Lalith Kumar Shiyam Sundar (lalith.shiyamsundar@meduniwien.ac.at).

Published online Dec. 2, 2022.

COPYRIGHT © 2023 by the Society of Nuclear Medicine and Molecular Imaging.  
DOI: 10.2967/jnumed.122.264555

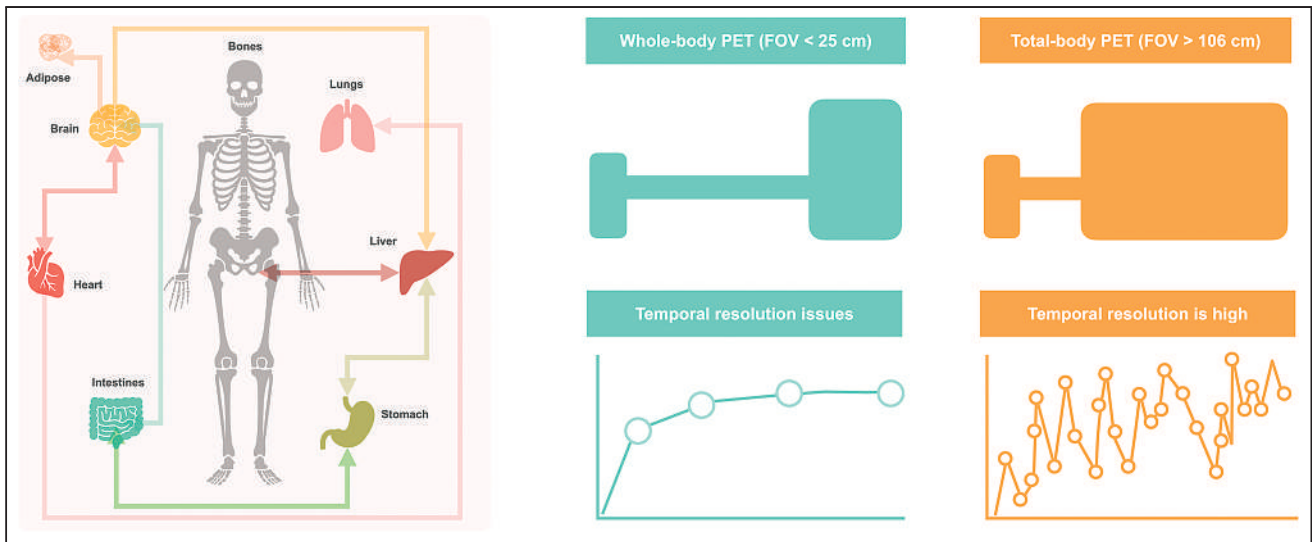


**FIGURE 1.** Thanks to markedly increased performance, TB PET allows assessment of multiple organs synchronously, giving way to noninvasive exploration of systemic, interorgan interactions.

Both causal and correlation networks should be considered hypothesis-generating tools rather than tools that provide solid endpoints. Such hypotheses must be proven or disproven in rigorous validation studies (Fig. 2) in which investigators should be conscious of the confounders affecting the accuracy of SUV or kinetic parameters as part of a multiorgan analysis (20).

#### THE PROMISE OF TB PET

Despite the increasing installed base of TB PET systems, the number of studies that explore TB PET beyond dose reduction and higher throughput for the sake of assessing the human connectome studies is limited. Preliminary studies have demonstrated the potential of using the temporal domain, namely raw time–activity curves, to derive metabolic associations between different bone compartments (21) or to construct normative networks for healthy male and female controls (22). Although neither study explained causality,

dynamic TB PET has the potential to create personalized causal networks from a single subject. Such a paradigm requires, however, the subject to be challenged by a task, pharmacologic intervention, or external stressor (e.g., pain or cold). By challenging (perturbing) the system, simultaneous or delayed changes in signals from different organs can be measured and used to establish causality.

For decades, such studies have been performed with functional MRI to derive effectivity connectivity by conducting baseline and task paradigms in a single imaging session (23). Recent innovative brain studies in functional PET have shown the possibility of using  $^{18}\text{F}$ -FDG PET to study dynamic changes in glucose metabolism within a single session with the aid of constant-infusion protocols (24). However, conducting such challenge-based studies is nontrivial in a TB PET setting, particularly in view of unknown response times and downstream interactions. Therefore, test studies on well-understood paradigms (25) should be performed before exploratory connectome investigations are conducted using TB PET.

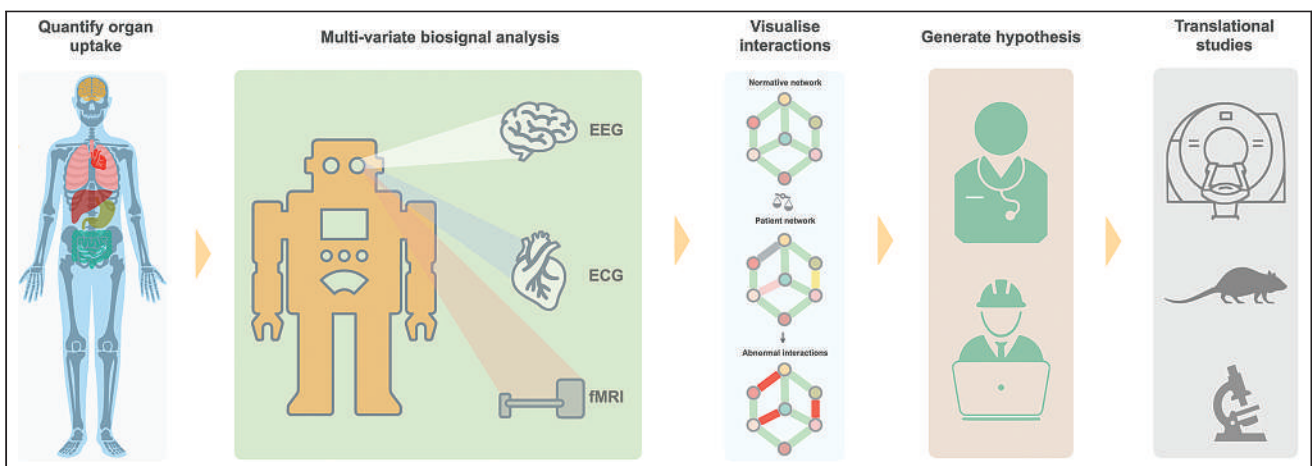


**FIGURE 2.** Categorical pathway to adopting WB or TB PET for exploring human connectome: several advanced and automated tools are required to extract robust data for hypothesis building and validation in translational setting. ECG = electrocardiography; EEG = electroencephalography; fMRI = functional MRI.

## ROAD MAP TO THE FUTURE: CONNECT TO THE CONNECTOME

To date, the PET imaging community is fragmented by vendor, geography, and skill set. There needs to be more meaningful sharing of code, data, and expertise to address the novel challenges and opportunities that arise with this technology. To fully leverage the potential of WB and TB PET alike for health care, new analysis methods are required, and new skills in the workforce are needed (Fig. 2). Automated data analytics pipelines, including automatic WB semantic segmentation (26) as well as WB and TB PET motion correction and spatial normalization, are prerequisites to robust TB PET connectome studies.

The community needs to be open to the repurposing of existing solutions (e.g., Statistical Parametric Mapping, version 12 (27)) and to be prepared to fail in this high-risk–high-gain approach to using PET far from the comfortable notion of a high-sensitivity lesion tracker. Fostering rigorous experiments to prove the validity of correlations and causalities while also sharing negative results must be encouraged. Also, rich data from healthy and pathologic cohorts should be pooled to amass large sample sizes that help us to better understand the actual distribution of the data and, therefore, to arrive at logical conclusions.

## CONCLUSION

The introduction of TB PET offers unique opportunities to investigate multiorgan interactions—the organ connectome for understanding human physiology and pathology. Novel study protocols and paradigms, and translational research pipelines, will be required to support causal interpretations of interorgan relationships. As a community, we should unite to prioritize progress over our vanities. The same was said in the early days of PET/CT and PET/MRI, and it still holds true. Novel and open-minded collaborative efforts beyond the nuclear medicine comfort zone are required to unlock the power of WB and TB PET imaging. Adopting this concept requires significant personal and infrastructural investments; the concept may fail, but if it does not, it will benefit our patients and medicine at large.

## DISCLOSURE

Research support was received from NIH R01CA29422, Era-PErMED PETictCAC, and ANR-FWF I-6174B. No other potential conflict of interest relevant to this article was reported.

## ACKNOWLEDGMENTS

We sincerely thank Irene Buvat (Paris), Ramsey Badawi (U.C. Davis), Simon Cherry (U.C. Davis), Terry Jones (U.K.), and Stefan Grünert (Vienna) for their continuous input and motivation.

## REFERENCES

1. Cannon WB. *The Wisdom of the Body*. Revised and enlarged ed. W.W. Norton and Co.; 1963.
2. Goodman L. Regulation and control in physiological systems: 1960–1980. *Ann Biomed Eng*. 1980;8:281–290.

3. Billman GE. Homeostasis: the underappreciated and far too often ignored central organizing principle of physiology. *Front Physiol*. 2020;11:200.
4. Phelps ME, Hoffman EJ, Mullani NA, Ter-Pogossian MM. Application of annihilation coincidence detection to transaxial reconstruction tomography. *J Nucl Med*. 1975;16:210–224.
5. Dahlbom M, Hoffman EJ, Hoh CK, et al. Whole-body positron emission tomography: part I. Methods and performance characteristics. *J Nucl Med*. 1992;33:1191–1199.
6. Hofman MS, Hicks RJ. Moving beyond “lumpology”: PET/CT imaging of pheochromocytoma and paraganglioma. *Clin Cancer Res*. 2015;21:3815–3817.
7. Karp JS, Viswanath V, Geagan MJ, et al. PennPET Explorer: design and preliminary performance of a whole-body imager. *J Nucl Med*. 2020;61:136–143.
8. Prenosil GA, Sari H, Fürstner M, et al. Performance characteristics of the Biograph Vision Quadra PET/CT system with a long axial field of view using the NEMA NU 2-2018 standard. *J Nucl Med*. 2022;63:476–484.
9. Spencer BA, Berg E, Schmall JP, et al. Performance evaluation of the uEXPLORER total-body PET/CT scanner based on NEMA NU 2-2018 with additional tests to characterize PET scanners with a long axial field of view. *J Nucl Med*. 2021;62:861–870.
10. Sun T, Wang Z, Wu Y, et al. Identifying the individual metabolic abnormalities from a systemic perspective using whole-body PET imaging. *Eur J Nucl Med Mol Imaging*. 2022;49:2994–3004.
11. Dias AH, Hansen AK, Munk OL, Gormsen LC. Normal values for <sup>18</sup>F-FDG uptake in organs and tissues measured by dynamic whole body multiparametric FDG PET in 126 patients. *EJNMMI Res*. 2022;12:15.
12. Bashan A, Bartsch RP, Kantelhardt JW, et al. Network physiology reveals relations between network topology and physiological function. *Nat Commun*. 2012;3:702.
13. Zhang X, Cherry SR, Xie Z, et al. Subsecond total-body imaging using ultrasensitive positron emission tomography. *Proc Natl Acad Sci USA*. 2020;117:2265–2267.
14. Seban R-D, Rouzier R, Latouche A, et al. Total metabolic tumor volume and spleen metabolism on baseline [<sup>18</sup>F]-FDG PET/CT as independent prognostic biomarkers of recurrence in resected breast cancer. *Eur J Nucl Med Mol Imaging*. 2021;48:3560–3570.
15. Thackeray JT. Imaging the molecular footprints of the heart–brain axis in cardiovascular disease. *J Nucl Med*. 2019;60:728–729.
16. Tawakol A, Ishai A, Takx RA, et al. Relation between resting amygdalar activity and cardiovascular events: a longitudinal and cohort study. *Lancet*. 2017;389:834–845.
17. Goodwin LD, Leech NL. Understanding correlation: factors that affect the size of r. *J Exp Educ*. 2006;74:249–266.
18. Scanagatta M, Salmerón A, Stella F. A survey on Bayesian network structure learning from data. *Prog Artif Intelligence*. 2019;8:425–439.
19. Zheng X, Aragam B, Ravikumar PK, Xing EP. DAGs with NO TEARS: continuous optimization for structure learning. In: Bengio S, Wallach H, Larochelle H, et al., eds. *Advances in Neural Information Processing Systems*. Vol 31. Curran Associates, Inc.; 2018:1–6.
20. Sarikaya I, Albatineh AN, Sarikaya A. Revisiting weight-normalized SUV and lean-body-mass-normalized SUV in PET studies. *J Nucl Med Technol*. 2020;48:163–167.
21. Suchacki KJ, Alcaide-Corral CJ, Nimale S, et al. A systems-level analysis of total-body PET data reveals complex skeletal metabolism networks in vivo. *Front Med (Lausanne)*. 2021;8:740615.
22. Sundar LS, Badawi RD, Spencer BA, et al. Enhance-PET: exploring the human functional connectome using total-body [<sup>18</sup>F] FDG-PET [abstract]. *Eur J Nucl Med Mol Imaging*. 2021;48(suppl):S201.
23. Glover GH. Overview of functional magnetic resonance imaging. *Neurosurg Clin N Am*. 2011;22:133–139.
24. Rischka L, Gryglewski G, Pfaff S, et al. Reduced task durations in functional PET imaging with [<sup>18</sup>F]FDG approaching that of functional MRI. *Neuroimage*. 2018;181:323–330.
25. Castellani JW, Young AJ. Human physiological responses to cold exposure: acute responses and acclimatization to prolonged exposure. *Auton Neurosci*. 2016;196:63–74.
26. Sundar LKS, Yu J, Muzik O, et al. Fully automated, semantic segmentation of whole-body <sup>18</sup>F-FDG PET/CT images based on data-centric artificial intelligence. *J Nucl Med*. 2022;63:1941–1948.
27. Ashburner J. SPM: a history. *Neuroimage*. 2012;62:791–800.

# Scientific Fraud, Publication Bias, and Honorary Authorship in Nuclear Medicine

Thomas C. Kwee<sup>1</sup>, Maan T. Almaghrabi<sup>1</sup>, and Robert M. Kwee<sup>2</sup>

<sup>1</sup>Medical Imaging Center, Department of Radiology, Nuclear Medicine, and Molecular Imaging, University Medical Center Groningen, University of Groningen, Groningen, The Netherlands; and <sup>2</sup>Department of Radiology, Zuyderland Medical Center, Heerlen, Sittard, and Geleen, The Netherlands

Our objective was to investigate nuclear medicine scientists' experience with scientific fraud, publication bias, and honorary authorship.

**Methods:** Corresponding authors who published an article in one of the 15 general nuclear medicine journals (according to Journal Citation Reports) in 2021 received an invitation to participate in a survey on scientific integrity. **Results:** In total, 254 (12.4%) of 1,897 corresponding authors completed the survey, of whom 11 (4.3%) admitted to having committed scientific fraud and 54 (21.3%) reported having witnessed or suspected scientific fraud by someone in their department in the past 5 y. Publication bias was considered present by 222 (87.4%) respondents, and honorary authorship practices were experienced by 100 (39.4%) respondents. Respondents assigned a median score of 8 (range, 2–10) on a 1- to 10-point scale for their overall confidence in the integrity of published work. On multivariate analysis, researchers in Asia had significantly more confidence in the integrity of published work, with a  $\beta$ -coefficient of 0.983 (95% CI, 0.512–1.454;  $P < 0.001$ ). A subset of 22 respondents raised additional concerns, mainly about authorship criteria and assignments, the generally poor quality of published studies, and perverse incentives of journals and publishers. **Conclusion:** Scientific fraud, publication bias, and honorary authorship appear to be nonnegligible practices in nuclear medicine. Overall confidence in the integrity of published work is high, particularly among researchers in Asia.

**Key Words:** fraud; medical imaging; nuclear medicine; research; scientific misconduct

J Nucl Med 2023; 64:200–203  
DOI: 10.2967/jnumed.122.264679

The contribution of nuclear medicine to health care has developed tremendously over the past decades (1). Continued innovations will further bolster the importance of the specialty in clinical medicine (1). Scientific publications can be considered paramount to proving the benefit of new technology and clinical applications to nuclear medicine patient care. They also provide an important source of information and inspiration to other researchers to initiate further studies in the same field. To avoid potential patient harm and futile investments, it is crucial that scientific publications be trustworthy and ethical.

Scientific fraud, defined as fabrication, falsification, or plagiarism in proposing, performing, or reviewing research, or in reporting

research results, has been around for many centuries and still persists (2,3). Publication bias, which refers to a greater likelihood that studies with positive results will be published than studies with negative results, is also considered a persistent problem (4). Both scientific fraud and publication bias lead to unreliable scientific data in medical journals. Honorary authorship, defined as the intentional misrepresentation of credit to an individual whose contributions to a biomedical article do not meet the criteria for authorship established by the International Committee of Medical Journal Editors (5), is a third major undesired phenomenon in the scientific community (6). Although honorary authorship may not undermine the validity of scientific data, it is still considered to be unethical and to represent scientific misconduct (6).

For nuclear medicine to prosper to its full potential, there should ideally be no place for scientific fraud, publication bias, and honorary authorship. Research into this topic in the field of nuclear medicine has been lacking so far.

The purpose of this study was to investigate nuclear medicine scientists' experience with scientific fraud, publication bias, and honorary authorship.

## MATERIALS AND METHODS

### Study Design and Participants

A survey study, which was approved by the institutional review board of the University Medical Center Groningen, was conducted among corresponding authors of all articles that were published in the 15 general nuclear medicine journals (according to Journal Citation Reports [https://jcr.clarivate.com]) in 2021. These 15 journals are displayed in Supplemental Table 1 (supplemental materials are available at <http://jnm.snmjournals.org>). Corresponding authors were excluded if their e-mail address could not be found, if a message could not be delivered to their e-mail address, or if they were from the same institution as the authors of the present work. The remaining corresponding authors received an e-mail with an invitation to participate in a survey on scientific integrity in the field of nuclear medicine, on a voluntary and anonymous basis. This e-mail contained a link to a digital survey that was composed with Qualtrics Core XM survey software (Qualtrics LLC). Eligible participants were first contacted on May 18, 2022, and received reminders on June 1, 2022, June 15, 2022, and August 26, 2022.

### Questionnaire

The survey contained 6 closed-ended or semi-closed-ended questions on participant's characteristics (age, sex, country of work, academic degree, academic position, and years of research experience), 2 semi-closed-ended questions on scientific fraud in the past 5 y (by the participant and by colleagues in the participant's department), 2 closed-ended questions on publication bias and honorary authorship

Received Jul. 16, 2022; revision accepted Sep. 6, 2022.  
For correspondence or reprints, contact Thomas Kwee (thomaskwee@gmail.com).  
Published online Sep. 8, 2022.  
COPYRIGHT © 2023 by the Society of Nuclear Medicine and Molecular Imaging.

in the past 5 y, and 1 closed-ended question on the participant's overall confidence in the integrity of published scientific work in the participant's field. Finally, all participants were given the opportunity to leave any comments in an open text field. All survey questions and possible answer options are displayed in Supplemental Table 2.

### Data Analysis

Participants' characteristics were descriptively summarized. Frequencies of reported scientific fraud, publication bias, and honorary authorship were calculated. Associations between overall confidence in the integrity of published work (1- to 10-point scale) versus participant's age, sex, continent (countries were merged into continents), academic degree, academic position, and years of research experience were determined using linear regression analysis. Variables that were significant on univariate analysis were subjected to multivariate analysis. The category with most observations was used as a reference for each nominal variable. Categories with fewer than 10 counts were excluded. All narrative comments provided by the participants in the open text field at the end of the survey were qualitatively analyzed to identify common topics of concern. *P* values of less than 0.05 were considered statistically significant. Statistical analyses were performed with the Statistical Package for the Social Sciences, version 26 (IBM).

## RESULTS

### Eligible Participants

A total of 2,111 corresponding authors published an article in the 15 journals in 2021. Of these corresponding authors, 185 were excluded because of undeliverable e-mails and 29 were excluded because they were from the same institution as the authors of the present work, leaving 1,897 individuals who were contacted to participate in the survey.

### Respondents

A total of 254 (12.4%) of the 1,897 invited corresponding authors completed the survey. Most respondents were aged 35–44 y (31.1%) and male (77.6%); their top-three countries of residence were the United States (16.5%), Italy (12.6%), and Germany (11.8%); and most respondents had a medical doctor degree (60.2%), were a full professor (32.7%), and had more than 10 y of research experience (71.3%) (Supplemental Table 3).

### Scientific Fraud

Eleven (4.3%) of the 254 respondents admitted to having committed scientific fraud in the past 5 y, with data manipulation or falsification and misleading reporting being the most common types of scientific fraud (Table 1). Fifty-four (21.3%) of the 254 respondents reported having witnessed or suspected scientific fraud by someone in their department in the past 5 y, with duplicate or redundant publication, misleading reporting, and data manipulation or falsification being the leading types of scientific fraud (Table 1).

### Publication Bias

Two hundred twenty-two (87.4%) of the 254 respondents thought that a study with positive results is more likely to be accepted by a journal than a similar study with negative results, 21 (8.3%) thought that this is not the case, and 11 (4.3%) were unsure as to whether there is publication bias.

### Honorary Authorship

One hundred (39.4%) of the 254 respondents indicated that they had an author on one of their publications in the past 5 y who actually did not deserve this coauthorship based on the International Committee of Medical Journal Editors criteria, 124 (48.8%) did not, and 30 (11.8%) were unsure as to whether they had experienced honorary authorship practices.

### Overall Confidence in the Integrity of Scientific Publications

Respondents assigned a median score of 8 (range, 2–10) on a 1- to 10-point scale for their overall confidence in the integrity of published work (Fig. 1). On multivariate regression, researchers in Asia had significantly more confidence in the integrity of published work, with a  $\beta$ -coefficient of 0.983 (95% CI, 0.512–1.454; *P* < 0.001) (Supplemental Table 4).

### Common Topics of Concern

Twenty-two respondents provided additional narrative comments, which are displayed in Supplemental Table 5. Authorship issues were most commonly addressed (with honorary authorship as the leading topic), followed by the generally poor quality of published studies (because of either unintentional or intentional scientific misconduct), and perverse incentives (e.g., financial) of journals and publishers that impede the publication and dissemination of unbiased, high-quality scientific work.

**TABLE 1**  
Types of Reported Scientific Fraud

Type	Among survey respondents ( <i>n</i> = 11)*	Among departmental coworkers ( <i>n</i> = 54)†
Data fabrication	2	10
Data manipulation or falsification	4	19
Misleading (e.g., selective) reporting	4	26
Plagiarism	2	16
Duplicate or redundant publication	3	28
Other type of publication fraud	1‡	3 <sup>¶</sup>

\*Three respondents indicated to have committed multiple types of scientific fraud.

†Twenty-eight respondents indicated to have witnessed or suspected multiple types of scientific fraud among departmental coworkers.

‡Including authors on papers that did not contribute enough to justify this."

¶"A doctoral candidate pulled together study plans of others and got a grant with his application. This was noticed and he had to withdraw his application," "Ghost authorship," and "Same as above."

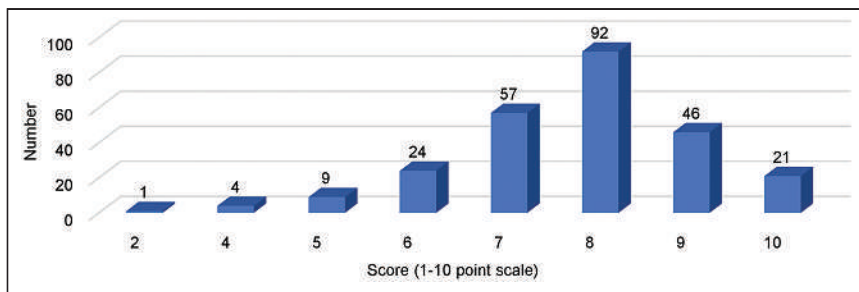


**FIGURE 1.** Distribution of scores assigned by 254 respondents to their overall confidence in integrity of published work in their scientific field.

## DISCUSSION

The reported scientific fraud rates, with duplicate or redundant publication, misleading reporting, and data manipulation or falsification being the leading types of scientific fraud, can be considered a reason for concern. These scientific integrity concerns are further aggravated by the fact that most respondents indicated that publication bias takes place and that a substantial proportion of respondents had faced honorary authorship practices. Overall confidence in the scientific integrity of published work in the field of nuclear medicine was generally high but was quite variable when considering the entire pool of survey participants. Interestingly, researchers from Asia had more confidence in the scientific integrity of published work. It can be speculated that Asian researchers generally regard scientific journals as authoritative (14 of the 15 journals used for the present study are based in Western countries) and therefore trust their publications. However, this finding applies only to the respondents who participated in this survey; more research is necessary to investigate whether this finding can be generalized.

Survey studies similar to the present one have been performed outside the medical imaging field. In a metaanalysis by Fanelli et al. (7) that included 18 such studies, 2.0% of scientists admitted to having fabricated, falsified, or modified data or results at least once, and up to 33.7% admitted to other questionable research practices. In addition, in surveys asking about the behavior of colleagues, admission rates were 14.1% for falsification and up to 72.0% for other questionable research practices (7). These percentages are considerably higher than those in the present study. This difference may be explained by the fact that the metaanalysis by Fanelli et al. (7) included studies that were not related to nuclear medicine and were published between 1998 and 2005. Publication bias and honorary authorship practices in nuclear medicine research have also been an unexplored field so far. Related studies in the specialty of radiology reported both phenomena to be widespread (8–10), in line with the results of the present study.

Publication pressure (“publish or perish”) and the scramble for research grants have been recognized as important factors that may give rise to fraudulent research (11–13), because grants and income, number of publications, publications in high-impact journals, and citations of published research are still regarded as important criteria (either explicit or implicit) for academic appointments and promotions (14). Funding bodies and medical journals are often driven by the desire for positive study results, which may also be detrimental to the scientific climate in which researchers have to operate. Banning scientific fraud and lifting the integrity and trustworthiness of nuclear medicine research and of research in general may require a system change taking into account all these different factors.

The present study had some limitations. First, the response rate was 12.4%, and it remains unclear whether this sample was representative of the whole population of nuclear medicine researchers. Second, it can be speculated that corresponding authors frequently also serve as senior authors, as a result of which there may have been under-reporting of scientific fraud. Further research is necessary to investigate this speculation. Interestingly, on univariate linear regression, researchers aged 55–64 y had significantly more confidence in the integrity of published

work, whereas the opposite was true for assistant professors and those with less than 5 y of research experience—a finding that feeds the hypothesis that there are differences in perceptions on this topic between junior and senior researchers. However, these associations did not remain significant on multivariate analysis. Third, only 11 respondents indicated that they themselves committed scientific fraud, which was too low to investigate which individual factors are associated with performing fraud. Fourth, the results of this study apply only to the past 5 y. Fifth, it remains unclear which publications contained fraudulent data and to what extent this inflicted patient harm and financial damage.

## CONCLUSION

Scientific fraud, publication bias, and honorary authorship appear to be nonnegligible practices in nuclear medicine. Overall confidence in the integrity of published work is relatively high, particularly among researchers aged 55–64 y and researchers in Asia.

## DISCLOSURE

No potential conflict of interest relevant to this article was reported.

## KEY POINTS

**QUESTION:** What is the experience of nuclear medicine scientists concerning scientific fraud, publication bias, and honorary authorship practices?

**PERTINENT FINDINGS:** In this survey study among 254 nuclear medicine scientists, 4.3% admitted to having committed scientific fraud in the past 5 y, 21.3% reported having witnessed or suspected scientific fraud by someone in their department in the past 5 y, 87.4% reported publication bias to be present, and 39.4% had experienced honorary authorship practices.

**IMPLICATIONS FOR PATIENT CARE:** There is considerable room for improvement when it comes to banning scientific fraud and lifting the integrity and trustworthiness of nuclear medicine research, which may be achieved by cultural and policy reforms that involve all stakeholders.

## REFERENCES

1. Weber WA, Czernin J, Anderson CJ, et al. The future of nuclear medicine, molecular imaging, and theranostics. *J Nucl Med.* 2020;61(suppl 2):263S–272S.
2. Bauchner H, Fontanarosa PB, Flanagin A, Thornton J. Scientific misconduct and medical journals. *JAMA.* 2018;320:1985–1987.
3. Broad W, Wade N. *Betrayers of the Truth.* Simon and Schuster.

4. Petticrew M. Diagoras of Melos (500 BC): an early analyst of publication bias. *Lancet*. 1998;352:1558.
5. Defining the role of authors and contributors. International Committee of Medical Journal Editors website. <http://www.icmje.org/recommendations/browse/roles-and-responsibilities/defining-the-role-of-authors-and-contributors.html>. Accessed October 17, 2022.
6. Quaia E, Crimi F. Honorary authorship: is there any chance to stop it? Analysis of the literature and a personal opinion. *Tomography*. 2021;7:801–803.
7. Fanelli D. How many scientists fabricate and falsify research? A systematic review and meta-analysis of survey data. *PLoS One*. 2009;4:e5738.
8. Treanor L, Frank RA, Cherpak LA, et al. Publication bias in diagnostic imaging: conference abstracts with positive conclusions are more likely to be published. *Eur Radiol*. 2020;30:2964–2972.
9. Eisenberg RL, Ngo L, Boisselle PM, Bankier AA. Honorary authorship in radiologic research articles: assessment of frequency and associated factors. *Radiology*. 2011;259:479–486.
10. Eisenberg RL, Ngo LH, Heidinger BH, Bankier AA. Honorary authorship in radiologic research articles: assessment of pattern and longitudinal evolution. *Acad Radiol*. 2018;25:1451–1456.
11. Angell M. Publish or perish: a proposal. *Ann Intern Med*. 1986;104:261–262.
12. Rawat S, Meena S. Publish or perish: where are we heading? *J Res Med Sci*. 2014;19:87–89.
13. Harvey L. Research fraud: a long-term problem exacerbated by the clamour for research grants. *Qual High Educ*. 2020;26:243–261.
14. Abbott A, Cyranoski D, Jones N, Maher B, Schiermeier Q, Van Noorden R. Metrics: do metrics matter? *Nature*. 2010;465:860–862.

# SNMMI Procedure Standard/EANM Practice Guideline for SSTR PET: Imaging Neuroendocrine Tumors

Thomas A. Hope<sup>1,2</sup>, Martin Allen-Auerbach<sup>3</sup>, Lisa Bodei<sup>4</sup>, Jeremie Calais<sup>3</sup>, Magnus Dahlbom<sup>3</sup>, Lisa K. Dunnwald<sup>5</sup>, Michael M. Graham<sup>5</sup>, Heather A. Jacene<sup>6</sup>, Courtney Lawhn Heath<sup>2</sup>, Erik S. Mittra<sup>7</sup>, Chadwick L. Wright<sup>8</sup>, Wolfgang P. Fendler<sup>9</sup>, Ken Herrmann<sup>9</sup>, David Taïeb<sup>10</sup>, and Andreas Kjaer<sup>11</sup>

<sup>1</sup>Department of Radiology, San Francisco VA Medical Center, San Francisco, California; <sup>2</sup>Department of Radiology and Biomedical Imaging, University of California San Francisco, San Francisco, California; <sup>3</sup>Ahmanson Translational Theranostics Division, Department of Molecular and Medical Pharmacology, UCLA, Los Angeles, California; <sup>4</sup>Molecular Imaging and Therapy Service, Department of Radiology, Memorial Sloan Kettering Cancer Center, Weill Medical College of Cornell University, New York, New York; <sup>5</sup>Department of Radiology, Roy J. and Lucille A. Carver College of Medicine, University of Iowa, Iowa City, Iowa; <sup>6</sup>Department of Imaging, Dana-Farber Cancer Institute, Department of Radiology, Brigham and Women's Hospital, Boston, Massachusetts; <sup>7</sup>Department of Diagnostic Radiology, Oregon Health & Science University, Portland, Oregon; <sup>8</sup>Wright Center of Innovation and Biomedical Imaging, Department of Radiology, The Ohio State University Wexner Medical Center, Columbus, Ohio; <sup>9</sup>Department of Nuclear Medicine, University of Duisburg-Essen and German Cancer Consortium (DKTK)-University Hospital Essen, Essen, Germany; <sup>10</sup>Department of Nuclear Medicine, La Timone University Hospital, CERIMED, Aix-Marseille University, Marseille, France; and <sup>11</sup>Department of Clinical Physiology, Nuclear Medicine & PET and Cluster for Molecular Imaging, Department of Biomedical Sciences, Rigshospitalet and University of Copenhagen, Copenhagen, Denmark

## PREAMBLE

The Society of Nuclear Medicine and Molecular Imaging (SNMMI) is an international scientific and professional organization founded in 1954 to promote the science, technology, and practical application of nuclear medicine. Its 18,000 members are physicians, technologists, and scientists specializing in the research and practice of nuclear medicine. In addition to publishing journals, newsletters, and books, the SNMMI also sponsors international meetings and workshops designed to increase the competencies of nuclear medicine practitioners and to promote new advances in the science of nuclear medicine. The European Association of Nuclear Medicine (EANM) is a professional non-profit medical association that facilitates communication worldwide between individuals pursuing clinical and research excellence in nuclear medicine. The EANM was founded in 1985.

The SNMMI/EANM will periodically define new standards/guidelines for nuclear medicine practice to help advance the science of nuclear medicine and to improve the quality of service to patients. Existing standards/guidelines will be reviewed for revision or renewal, as appropriate, on their fifth anniversary or sooner, if indicated. Starting February 2014, the SNMMI guidelines have been referred to as procedure standards. Any practice guideline or procedure guideline published before that date is now considered an SNMMI procedure standard.

Each standard/guideline, representing a policy statement by the SNMMI/EANM, has undergone a thorough consensus process in which it has been subjected to extensive review. The SNMMI/EANM recognizes that the safe and effective use of diagnostic

nuclear medicine imaging requires specific training, skills, and techniques, as described in each document.

The EANM and SNMMI have written and approved these standards/guidelines to promote the use of nuclear medicine procedures with high quality. These standards/guidelines are intended to assist practitioners in providing appropriate nuclear medicine care for patients. They are not inflexible rules or requirements of practice and are not intended, nor should they be used, to establish a legal standard of care. For these reasons and those set forth below, the SNMMI/EANM cautions against the use of these standards/guidelines in litigation in which the clinical decisions of a practitioner are called into question.

The ultimate judgment regarding the propriety of any specific procedure or course of action must be made by medical professionals taking into account the unique circumstances of each case. Thus, there is no implication that an approach differing from the standards/guidelines, standing alone, is below the standard of care. To the contrary, a conscientious practitioner may responsibly adopt a course of action different from that set forth in the standards/guidelines when, in the reasonable judgment of the practitioner, such course of action is indicated by the condition of the patient, limitations of available resources, or advances in knowledge or technology subsequent to publication of the standards/guidelines.

The practice of medicine involves not only the science but also the art of dealing with the prevention, diagnosis, alleviation, and treatment of disease. The variety and complexity of human conditions make it impossible to always reach the most appropriate diagnosis or to predict with certainty a particular response to treatment. Therefore, it should be recognized that adherence to these standards/guidelines will not ensure an accurate diagnosis or a successful outcome. All that should be expected is that the practitioner will follow a reasonable course of action based on current knowledge, available resources, and the needs of the patient to deliver effective and safe medical care. The sole purpose of these standards/guidelines is to assist practitioners in achieving this objective.

Received Aug. 30, 2022; revision accepted Aug. 30, 2022.  
For correspondence or reprints, contact Thomas A. Hope (Thomas.hope@ucsf.edu).  
COPYRIGHT © 2023 by the Society of Nuclear Medicine and Molecular Imaging.  
DOI: 10.2967/jnumed.122.264860



## I. INTRODUCTION

Somatostatin receptor (SSTR) imaging using PET has replaced scintigraphic imaging using  $^{111}\text{In}$ -pentetreotide (OctreoScan), unless PET is unavailable. Several benefits of SSTR PET compared with  $^{111}\text{In}$ -pentetreotide have driven this change: improved sensitivity of lesion detection; lower radiation dose; and shorter and more convenient study duration. Three SSTR PET radiotracers are currently available:  $^{68}\text{Ga}$ -DOTATATE approved by the Food and Drug Administration (FDA) in 2016,  $^{68}\text{Ga}$ -DOTATOC approved by the European Medicines Agency in 2016 and the FDA in 2019, and  $^{64}\text{Cu}$ -DOTATATE approved by the FDA in 2020.  $^{68}\text{Ga}$ -DOTANOC is also used at some institutions, although has not been approved by either the FDA or the EMA. The use of  $^{68}\text{Ga}$ -DOTANOC generally mirrors that of  $^{68}\text{Ga}$ -DOTATOC and  $^{68}\text{Ga}$ -DOTATATE and has similar accuracy at detecting SSTR-positive disease.

SSTRs are overexpressed on a wide range of neuroendocrine tumor (NET) cells and can be targeted using somatostatin analogs (SSAs). Initially, SSAs were used not only for treatment of hormone-based symptoms but also to prevent disease progression (1,2). The first imaging agent to target the SSTR was  $^{111}\text{In}$ -pentetreotide, and imaging included the use of SPECT or SPECT/CT. Imaging protocols typically required imaging 4 and 24 h after injection.

The development of the next generation of SSAs (DOTATATE and DOTATOC) resulted in faster tumor targeting and therefore enabled the use of positron emitters such as  $^{68}\text{Ga}$  for radiolabeling.  $^{68}\text{Ga}$  is most commonly produced using a  $^{68}\text{Ge}/^{68}\text{Ga}$  generator, which can yield several doses per synthesis. More recently, SSAs have been labeled with  $^{64}\text{Cu}$ , which is produced using a cyclotron.

## II. GOALS

The goal of providing guidelines is to assist physicians in recommending, performing, interpreting, and reporting the results of SSTR PET imaging studies for patients with NETs. This document aims to provide clinicians with the best available evidence, to inform where robust evidence is lacking, and to help them to deliver the best possible diagnostic efficacy and study quality for their patients. This guideline also presents standardized quality control/quality assurance (QC/QA) procedures and imaging procedures for SSTR PET. Adequate precision, accuracy, repeatability, and reproducibility are essential for the clinical management of patients and the use of SSTR PET within multicenter trials. A standardized imaging procedure will help to promote the appropriate use of SSTR PET and enhance subsequent research.

## III. DEFINITIONS

Definitions are based on the EANM procedure guidelines for tumor PET imaging, version 2.0 (3):

PET/CT: An integrated or multimodality PET/CT system is a physical combination of PET and CT that allows sequential acquisition of PET and CT portions. The patient remains in the same position within both examinations. SSTR PET/CT examination may cover various coaxial imaging ranges. These are described as follows:

- Whole-body PET: From the top of the head through the feet.
- Skull base to midthigh PET: Base of the skull to midthigh. Covers most of the relevant portions of the body in many oncologic diseases (standard for both Europe and the United States). If indicated, cranially extended imaging may also cover the brain in the same scan (vertex to midthigh). In PET/CT studies,

attenuation correction and scatter correction are performed using the CT data.

CT: a combined x-ray source and detector rotating around the patient to acquire tomographic data. CT generates 3-dimensional images of tissue density, which allows for attenuation correction of PET and tumor visualization with a high spatial resolution.

A PET/CT examination can include different types of CT scans depending on the CT characteristics, the dose, and the use (or not) of oral or intravenous contrast agents.

- Low-dose CT scan: CT scan that is performed only for attenuation correction (CT-AC) and anatomic correlation of PET findings (with reduced voltage or current of the x-ray tube settings), that is, a low-dose CT is not intended a priori for a dedicated radiologic interpretation.
- Diagnostic CT scan: CT scan with or without intravenous or oral contrast agents, commonly using higher x-ray doses than low-dose scans. Diagnostic CT scan should be performed according to applicable local or national protocols and guidelines.

## IV. COMMON CLINICAL INDICATIONS

Clinical indications for the use of SSTR PET have been previously discussed in the Appropriate Use Criteria (AUC) for SSTR PET, which has recently been updated (4). Common indications include initial staging at diagnosis, localization of primary tumor, staging before surgery, and selection of patients for peptide receptor radionuclide therapy (PRRT). Recently, the SSTR PET AUC was updated to include a post-PRRT study to serve as a new baseline 9–12 mo after the completion of treatment for future comparisons (5). Some NETs have lower expression of the SSTR, and therefore imaging using  $^{18}\text{F}$ -FDG PET may be more beneficial. Neuroendocrine neoplasms are broken down into NETs and neuroendocrine carcinomas (NECs). NETs are well differentiated and are classified based on Ki-67 staining, which is a marker of cellular proliferation: grade 1 with  $\leq 2\%$  Ki-67 staining, grade 2 with 3%–20% Ki-67 staining, and grade 3 with  $> 20\%$  Ki-67 staining (6). Poorly differentiated NECs typically have a Ki-67 greater than 55%. Although  $^{18}\text{F}$ -FDG uptake in well-differentiated NETs is only increased in part of the patients, the loss of differentiation and loss of SSTR expression in G3 NECs is generally associated with a significant increase in glycolytic metabolism and tumor aggressiveness. In general, G3 NECs rarely overexpress the SSTR and  $^{18}\text{F}$ -FDG PET is usually preferred, whereas in G3 NENs, SSTR PET may be helpful.

Additionally, benign, localized insulinomas usually lack SSTR overexpression. In such cases, SSTR PET may not be useful and alternative tracers, such as glucagonlike peptide-1 receptor PET and 6- $^{18}\text{F}$ -l-fluoro-l-3,4-dihydroxyphenylalanine ( $^{18}\text{F}$ -FDOPA) PET, are being tested in clinical trials (7). Also, medullary thyroid carcinomas frequently exhibit low-density and heterogeneous SSTR expression, resulting in a suboptimal imaging performance of SSTR PET, which is surpassed by that of  $^{18}\text{F}$ -FDOPA PET (8).

## V. QUALIFICATIONS AND RESPONSIBILITIES OF PERSONNEL

### A. Physician

SSTR PET examinations should be performed by, or under the supervision of, a physician specialized in nuclear medicine and certified by accrediting boards. Physicians who interpret SSTR

PET results should also complete appropriate training programs provided by the manufacturers of approved radiotracers.

### **B. Technologist**

SSTR PET examinations should be performed by qualified registered or certified nuclear medicine technologists. (see (9) for further details). According to location of practice, additional qualifications may be requested for technologists to use the CT and MR component of the scanner.

### **C. Medical Physicist**

PET systems should comply with the international standard of quality, including dosimetry and radiation protection procedure, to limit the irradiation exposure of patients and health care personnel. A medical physicist should optimize protocols, ensuring that the established standards are met. A medical physicist can assist physicians to adhere to and maintain good practice, by monitoring and optimizing radiation dose and developing algorithms to reduce the radiation exposure of the CT component.

## **VI. PROCEDURE/SPECIFICATIONS OF THE EXAMINATION**

As of the publication of this document, 3 SSTR-targeted radiotracers (including  $^{68}\text{Ga}$ -DOTATOC,  $^{68}\text{Ga}$ -DOTATATE, and  $^{64}\text{Cu}$ -DOTATATE) have been approved by the FDA and a  $^{68}\text{Ga}$ -DOTATOC kit has been approved by the EMA for imaging of SSTR-positive malignancies. Although these radiotracers share a common imaging target and similar imaging characteristics, SSTR PET radiotracers can differ in their binding affinity and optimal imaging parameters. Overall, these radiotracers can be considered equivalent in terms of their ability to detect SSTR-positive disease.

### **A. Request**

The nuclear medicine imaging facility should check with its local nuclear pharmacy provider as to the availability of the radiotracer before scheduling the examination. Advanced notice may be required for radiotracer delivery. The study requisition should include clinical information about the patient to justify the study and to allow coding of the examination or study, information about the ability of the patient to cooperate with the test, and information about current medications in case mild sedation is necessary. It is also helpful to know if the patient needs to be accompanied by a guardian.

### **B. Patient Preparation and Precautions**

*1. Prearrival and Patient Instructions.* It is generally recommended that before SSTR PET imaging, patients discontinue all short-acting SSAs 12 h prior. Referring physicians should be instructed to schedule SSTR PET imaging just before dosing with long-acting SSAs. The EANM procedure guidelines for SSTR PET suggest an interval of 3–4 wk after administration of long-acting SSAs to avoid potential SSTR blockade (10). However, a recent prospective study with lanreotide (somatuline) showed that treatment immediately before SSTR PET had minimal effect on normal organ and tumor uptake (11). Therefore, it may be less important to have a prolonged interval from the most recent administered SSA than previously thought in patients receiving stable doses of long-acting SSAs, although it is unclear if this is true with octreotide acetate LAR (sandostatin) as compared with lanreotide (11–13).

Patients should drink water to ensure adequate oral hydration before administration of SSTR-targeted radiotracers and to continue to drink and void frequently during the first hours after

administration to reduce radiation exposure to the bladder. The procedure should be carefully explained to the patient in an easily understandable manner, and patients may require reminders of the need for their cooperation during the scan from the technologist (i.e., limiting motion). For a variety of reasons, some patients may require sedation for the scan. The sedation method will vary by patient and may need to be determined on the basis of the information provided by the referring physician. Sedation should be arranged at the time an SSTR PET examination is scheduled so that the procedure will go smoothly and without delay.

It is not known whether SSTR PET radiotracers have harmful fetal effects. SSTR PET should be performed on a pregnant woman only if there is a clear clinical benefit. It is not known if SSTR PET tracers have harmful effects on infants or breast tissue. However, for caution in this rare instance and because of the potential for radiotracer excretion in human milk and potential radiation exposure to infants, either avoid performing SSTR PET imaging on a breastfeeding mother or have the mother interrupt breastfeeding for 24 h after administration of the radiotracer. SSTR PET is safe in the pediatric patient population (14,15), although in many countries pediatric use may be outside the marketing authorization.

### **C. Radiopharmaceuticals**

Several SSTR-targeting radiotracers have been investigated:  $^{68}\text{Ga}$ -DOTATOC,  $^{68}\text{Ga}$ -DOTATATE, and  $^{64}\text{Cu}$ -DOTATATE. Although these radiotracers share a common imaging target and similar imaging characteristics, they can differ in their binding affinity and optimal imaging parameters, and hence have different recommended injected activities, times to initiate imaging after injection, and scan durations. Each radiotracer should be prepared according to good manufacturing practice or other applicable good practices within national regulations; QC procedures should follow the pharmacopoeia standards or provisions of the competent pharmaceutical authorities. Recommendations for kit-based radiolabeling methods are outside the scope of this document.

### **D. Administered Activity**

All SSTR PET radiotracers are administered as an intravenous bolus injection. In adult patients, for  $^{68}\text{Ga}$ -DOTATOC the prescribed activity is 148 MBq (4 mCi), with a range of 111–185 MBq (3–5 mCi) based on the FDA prescribing information (16) and 100–200 MBq (2.7–5.4 mCi) based on the EMA product information (17). For  $^{68}\text{Ga}$ -DOTATATE, the prescribed administered activity is 2 MBq/kg of body weight (0.054 mCi/kg) up to 200 MBq (5.4 mCi) (18), and for  $^{64}\text{Cu}$ -DOTATATE the administered activity is 148 MBq (4 mCi) (19).  $^{68}\text{Ga}$ -DOTATOC has a separate weight-based dosing for pediatric patients: 1.59 MBq/kg (0.043 mCi/kg), with a range of 11.1 MBq (0.3 mCi) to 111 MBq (3 mCi).

### **E. Uptake Time**

In general, uptake times are similar for the 3 available SSTR-targeted radiotracers. The uptake times reported in the prescribing information for  $^{68}\text{Ga}$ -DOTATOC,  $^{68}\text{Ga}$ -DOTATATE, and  $^{64}\text{Cu}$ -DOTATATE are 55–90 min, 40–90 min, and 45–90 min, respectively (16–19). It should be noted that  $^{64}\text{Cu}$  has a longer half-life than  $^{68}\text{Ga}$  (12.7 h vs. 68 min), and therefore a later imaging time point with  $^{64}\text{Cu}$  may be feasible, although this is not acknowledged in the package insert. It is currently unclear if delayed imaging with  $^{64}\text{Cu}$ -DOTATATE provides benefit compared with standard imaging times, but it has recently been shown that imaging at 1 and 3 h have comparable lesion detection rates (20).

## F. Image Acquisition

Imaging should start at the vertex and extend to the midthighs. Although a small lesion seen on PET may be better characterized with a diagnostic-quality CT, both CT and PET acquisition parameters will be scanner- and institution-dependent. Intravenous CT contrast is optional; however, it can improve characterization of hepatic metastases and other soft-tissue lesions. If diagnostic CT is performed, water should be used as oral contrast, since it will not obscure the CT identification of gastrointestinal lesions.

Time-of-flight PET with a reconstruction method including modeling of resolution degradation, often referred to as point spread function reconstruction, may help with the detection of small lesions. PET data should be fused with both standard and bone CT reconstructions.

PET/MRI may be used instead of PET/CT and may be beneficial for patients with liver-dominant NETs due to the ability to perform hepatobiliary phase imaging. Details about acquisition protocol and reconstruction for PET/MRI are beyond the scope of this guideline. For details, see relevant literature (21).

## G. Impact of $^{64}\text{Cu}$ Versus $^{68}\text{Ga}$

The range of the positrons is one of several components that will affect the spatial resolution of PET images. The amount of image blurring due to the positron range depends on the energies of the positrons emitted from the particular isotope. Positron emitters such as  $^{18}\text{F}$  and  $^{64}\text{Cu}$  emit positrons of relatively low-energy (250 and 278 keV, average energy, respectively) and the amount of resolution loss from the positron range is 0.2 mm in full width half maximum (FWHM) or 1.3 mm in full width tenth maximum (FWTM). The energy of the positrons from  $^{68}\text{Ga}$  is significantly higher (836 keV, average energy) and the loss in spatial resolution is 0.8 mm FWHM or 4.7 mm FWTM. Any loss in spatial resolution will affect quantification and will underestimate activity concentration and SUV, particularly for small lesions. It is difficult to generalize how much of the greater positron range of  $^{68}\text{Ga}$  will affect quantification in small lesions compared with  $^{64}\text{Cu}$ . The reason for this is the complex interplay of the components that contributes to the final image resolution (i.e., the intrinsic detector resolution, system diameter, image reconstruction algorithm, and spatial filtering). Under typical

clinical imaging conditions, it is expected that there will be an additional 10%–20% underestimation in small lesions (10–15 mm diameter) when imaging with  $^{68}\text{Ga}$  compared with  $^{64}\text{Cu}$ .

Additionally, the positron emission yield of 17.4% for  $^{64}\text{Cu}$  is significantly lower than the yield 88.9% for  $^{68}\text{Ga}$ . To achieve the same number of counts in the study, it would be necessary to image for approximately 5 times longer, assuming the same injected activity. However, when taking into account the longer physical half-life of  $^{64}\text{Cu}$  (12.7 h) compared with  $^{68}\text{Ga}$  (68 min), the difference in scan time 55–90 min after injection for the same injected dose is reduced to approximately 2 times longer. However, for practical reasons the scan time is not increased as this may lead to patient motion during imaging. In theory, the injected activity could be increased instead, but one hesitation to doing this may be the dosimetry of  $^{64}\text{Cu}$ -DOTATATE as the radiation dose per injected activity for  $^{64}\text{Cu}$ -DOTATATE is 20%–25% higher than for  $^{68}\text{Ga}$ -DOTATATE (Table 1). The expected increase in image noise due to the lower positron yield of  $^{64}\text{Cu}$  can be reduced by applying a smoother spatial filter compared with the filter used for  $^{68}\text{Ga}$ . Nonetheless, using standard image acquisitions, the  $^{64}\text{Cu}$ -DOTATATE produces diagnostic scans equivalent to the 2 gallium-labeled compounds.

One of the main advantages of using  $^{64}\text{Cu}$  over  $^{68}\text{Ga}$  is the longer half-life. This makes the distribution logistics easier and delivery times less critical. Furthermore, the long half-life makes the  $^{64}\text{Cu}$  less susceptible to delays in imaging after a patient has been injected compared with  $^{68}\text{Ga}$ -DOTATATE or  $^{68}\text{Ga}$ -DOTATOC.

## VII. DOCUMENTATION AND REPORTING

### A. Study Identification

The final report should include the full name of the patient, sex assigned at birth, medical record number, date of birth, and date of the examination.

### B. Clinical Information

As a minimum, a summary of relevant clinical history should include reason for referral and the specific clinical question to be answered. If known, the primary location and grade of the tumor should be provided. The type and date of comparison studies should

**TABLE 1**  
Dosimetry for  $^{68}\text{Ga}$ -DOTATATE,  $^{68}\text{Ga}$ -DOTATOC,  $^{64}\text{Cu}$ -DOTATATE, and  $^{18}\text{F}$ -FDG

Organ	$^{68}\text{Ga}$ -DOTATATE (22)	$^{68}\text{Ga}$ -DOTATOC (48)	$^{64}\text{Cu}$ -DOTATATE (49)	$^{18}\text{F}$ -FDG (50)
<b>Organ (mSv/MBq)</b>				
Kidneys	9.2E-02	2.2E-01	1.4E-01	1.7E-02
Liver	4.5E-02	7.4E-02	1.6E-01	2.1E-02
Spleen	2.8E-01	2.4E-01	1.2E-01	1.1E-02
Bladder wall	1.3E-01	7.0E-02	3.7E-02	1.3E-01
<b>Dose</b>				
ED (mSv/MBq)	2.6E-02	2.3E-02	3.2E-02	1.9E-02
<b>Typical IA</b>				
MBq	200	185	148	370
mCi	5.4	5	4	10
Estimated ED per scan (mSv)	5.2	4.3	4.7	7.0

ED = effective dose; IA = injected activity.

be stated. If no comparison studies are available, a statement should be made to that effect. Finally, whether the patient is on SSA therapy and which therapy and duration of therapy should be noted.

### C. Technical Details

Study-specific information should include the radiopharmaceutical, the amount of injected activity in megabecquerels (MBq) or millicuries (mCi), the route (intravenous) and anatomic site of administration, and the date and time of administration. If extravasation is seen, it should also be noted. The uptake time interval between the administration of the radiopharmaceutical and the start time of the acquisition should be reported. The body parts covered by imaging should be described. Any nonstandard position of the patient should be stated.

The direction and range the patient image was acquired should be stated (i.e., “images were acquired from the vertex to the midthigh”). If a nonoptimized CT was performed for attenuation correction and anatomic registration of the emission images only, the description may be limited to a short statement including the mAs and kVp. If a diagnostic CT was performed, then a more detailed description of the CT protocol and anatomic findings should be provided. Dosimetry parameters should be included if required by national or local regulations. The report should state whether contrast-enhanced or nonenhanced CT was used for attenuation correction.

### D. Description of Findings

Quality issues of the PET, for example, motion artifacts, halo artifacts due to high activity in the collecting urinary system, or attenuation artifacts (from attenuating materials), should be reported.

### E. Interpretation

1. *Biodistribution.* Physiologic uptake is present and most intense in the kidneys and bladder, spleen, and liver (Fig. 1). Normal uptake is also seen in the pituitary, adrenal glands, salivary glands, and the thyroid (22).  $^{64}\text{Cu}$ -DOTATATE allows for late imaging. At 3 h after injection,  $^{64}\text{Cu}$ -DOTATATE uptake decreases for kidney and bladder, remains unchanged for spleen, and increases for liver, although differences in early versus late biodistribution do not impact lesion detection (20). At early time-point



FIGURE 1. Normal biodistribution of  $^{68}\text{Ga}$ -DOTATOC,  $^{68}\text{Ga}$ -DOTATATE, and  $^{64}\text{Cu}$ -DOTATATE.

acquisition, no clinically meaningful difference in organ uptake was demonstrated for  $^{68}\text{Ga}$ -DOTATOC versus  $^{64}\text{Cu}$ -DOTATATE (23) or  $^{68}\text{Ga}$ -DOTATATE versus  $^{68}\text{Ga}$ -DOTATOC, respectively (20). There are no major differences between physiologic uptake of  $^{64}\text{Cu}$ -DOTATATE and  $^{68}\text{Ga}$ -labeled DOTATATE (Table 2) (24).

2. *General Interpretation.* Images should be interpreted by a physician trained in SSTR PET/CT imaging and informed about the clinical context of the scan indication (e.g., staging, assessment for PRRT, restaging). Focal tracer uptake that cannot be explained by physiologic biodistribution or that is higher than organ background activity is to be considered pathologic, especially if there is a correlating abnormal structure on CT. Consistent qualitative grading of uptake (mild = blood pool, moderate = liver, intense = clearly above liver) can be used in addition to SUV-related measurements and modified Krenning score.

3. *Incidental Findings, Normal Variants, and Important Pitfalls.* Increased uptake on SSTR PET does not make the diagnosis of a NET, and care should be taken in interpretation. For example, physiologically increased uptake in the head/uncinate process of the pancreas is observed in a large portion of patients (diffuse or focal) and usually remains stable over time (25). This physiologic uptake in the head/uncinate process of the pancreas is thought to be caused by a higher concentration of pancreatic polypeptide producing cells in this region. There is a significant overlap between

TABLE 2  
Comparison of physiologic uptake of  $^{68}\text{Ga}$ -DOTATATE and  $^{64}\text{Cu}$ -DOTATATE

Organ SUV <sub>mean</sub> - mean (SD)	$^{68}\text{Ga}$ -DOTATATE (60–80 min after injection) (20)	$^{68}\text{Ga}$ -DOTATOC (50–70 min after injection) (51)	$^{64}\text{Cu}$ -DOTATATE (43–80 min after injection) (24)
Liver	4.5 (1.5)	5.7 (1.6)	4.0 (1.1)
Spleen	15.5 (5.5)	—	8.9 (3.4)
Pituitary gland	6.8 (2.3)	4.1 (1.8)	12.9 (6.1)
Adrenal gland	10.1 (3.7)	7.2 (3.1)	9.5 (4.4)
Uncinate process of pancreas	6.7 (2.2)	—	3.2 (0.5)

\*Median.

the SUVs of the physiologic pancreas and tumoral lesions of the head/uncinate process (26), which can result in false-positive interpretations. Correlation with MRI or multiphase CT, with subsequent follow-up with SSTR PET, may be useful in challenging cases.

Splenules demonstrate high levels of physiologic uptake, similar to the spleen (27). Avoiding a false-positive interpretation can be especially challenging in the setting of intrapancreatic splenules, or in differentiating peritoneal splenosis from new tumor deposits after a splenectomy. In these cases, heat-damaged red blood cell or sulfur colloid SPECT/CT may be useful to confirm the locations of ectopic splenic tissue.

Finally, SSTR2 is expressed by normal osteoblasts (28) and white blood cells including macrophages (29), which can lead to false-positive interpretations. Areas of high osteoblastic activity can have increased osseous uptake on SSTR PET and include degenerative changes, fractures, and benign lesions such as fibrous dysplasia (27). In challenging cases, correlation with dedicated CT or MRI can help distinguish tumor from nontumor pathology. Areas of high leukocyte activity can have increased uptake on SSTR PET and may be seen in postradiation changes and reactive lymphadenopathy including sarcoidosis and infections such as tuberculosis (27).

**4. Semiquantitative Analysis.** Quantification of uptake using PET is typically defined using SUV, but it should be noted that SUV measurements may not be reproducible across scanners and institutions without standardization of image protocols, scanner qualifications, and cross-calibrations. In addition, SUV can be affected by lesion size and uptake time among other issues. The Krenning score is the most common approach to qualitative interpretation and was originally developed for planar or SPECT imaging with  $^{111}\text{In}$ -pentetreotide. When using SSTR PET, lesional uptake is characterized using the modified Krenning score (24,27). Identical to the Krenning score, the modified Krenning score is based on the lesion with the highest SSTR uptake: 0, no uptake; 1, very low uptake; 2, uptake less than or equal to that of the liver; 3, uptake greater than the liver; and 4, uptake greater than that of the spleen. SSTR PET leads to higher Krenning scores than with  $^{111}\text{In}$ -pentetreotide, particularly in patients with small SSTR-avid lesions (<2 cm) (30). Additional SSTR PET-based lesion assessment methodologies described in the literature include the use of tumor-to-liver ratios (31) and the proposed SSTR-RADS reporting system (32). It should be noted that an increase or decrease in uptake within a lesion should not be taken as an indicator of response or progression as seen with other radiotracers.

**5. SSTR PET as a Predictive Biomarker for PRRT.** The indication for PRRT relies on sufficient target expression. SSTR PET can be used to assess the SSTR expression level based on the modified Krenning score. In the NETTER-1 trial, patients with a Krenning score > 2 were eligible, but the study used  $^{111}\text{In}$ -pentetreotide for enrollment and it is unclear how SSTR PET should be used for patient selection for PRRT (33). In general, the higher the uptake on SSTR PET, the better the expected response to PRRT (31,34).

**6. Disease Heterogeneity and False-Negatives.** SSTR expression generally correlates with the degree of tumor differentiation, with well-differentiated G1/G2 and even well-differentiated G3 tumors expressing the SSTR while poorly differentiated G3 NECs lack the SSTR (35,36). The heterogeneity of SSTR expression appears to be a poor prognostic factor in patients treated with PRRT (37–39). However, within grades, tumor behavior of NET can vary widely. Ki-67 is frequently determined based on a single metastatic lesion that may not reflect inpatient tumor heterogeneity. In

contrast, PET imaging provides a whole-body assessment of the SSTR expression.  $^{18}\text{F}$ -FDG PET provides information complementary to SSTR PET by helping identify lesions that have lost SSTR expression (40).  $^{18}\text{F}$ -FDG positivity is not rare in G1/G2 NET and is a stronger predictor of progression and prognosis than tumor grade (41,42). In particular,  $^{18}\text{F}$ -FDG PET can be useful in patients with a negative SSTR PET result or a well-differentiated G3 tumor (43). Combining  $^{18}\text{F}$ -FDG and SSTR PET imaging can identify the highest-grade, most aggressive lesion (i.e.,  $^{18}\text{F}$ -FDG-positivity and SSTR-negative) that may lead to better selection of biopsy site to identify the highest-grade disease (44). Of note, a combined  $^{18}\text{F}$ -FDG and SSTR PET grading system (NETPET grade) has been developed that relies not only on the lesion with the highest SSTR PET uptake but also on the SSTR/ $^{18}\text{F}$ -FDG phenotype across the entire tumor burden (41).

False-negatives, although uncommon, can occur. For example, G3 NECs (44), generally have lower uptake than well-differentiated G1/G2 tumors. The term “false-negative” in this case is relative, because the tumor has been accurately characterized versus being detected by SSTR PET. Medullary thyroid cancer and insulinomas also have variable expression of SSTR. Nonfunctional tumors may be more likely than functional NETs to be negative on SSTR PET (45). Like other radiotracer studies, lesions may be false-negative on SSTR PET due to small size or being within or in proximity to organs with high physiologic uptake. The higher sensitivity of SSTR PET compared with  $^{111}\text{In}$ -pentetreotide planar or SPECT/CT imaging has helped to overcome these limitations (46,47).

## VIII. DOSIMETRY

The estimated absorbed and effective radiation doses for adult patients after intravenous injection of  $^{68}\text{Ga}$ -DOTATATE,  $^{68}\text{Ga}$ -DOTATOC, and  $^{64}\text{Cu}$ -DOTATATE are shown in Table 1. For an adult weight of 75 kg based on the prescribing information, the effective radiation dose is 3.2 mSv for  $^{68}\text{Ga}$ -DOTATATE for a 150-MBq (4.1 mCi) administration, 3.1 mSv for  $^{68}\text{Ga}$ -DOTATOC for a 148-MBq (4 mCi) administration, and 4.7 mSv for a 148-MBq (4 mCi) administration of  $^{64}\text{Cu}$ -DOTATATE (16,18,19).

## IX. ACKNOWLEDGMENTS

This guideline summarizes the views of the EANM Physics, Dosimetry, Radiation Protection, Radiopharmacy, and Thyroid Committees and the Society of Nuclear Medicine and Molecular Imaging. It reflects recommendations for which the EANM cannot be held responsible. The recommendations should be taken into context of good practice of nuclear medicine and do not substitute for national and international legal or regulatory provisions. No other potential conflict of interest relevant to this article was reported. The guidelines were brought to the attention of the relevant EANM Committees and the National Societies of Nuclear Medicine. The comments and suggestions from the EANM Physics, Dosimetry, Radiation Protection, Radiopharmacy, and Thyroid Committees are highly appreciated and have been considered for this Guideline.

## X. REFERENCES

1. Rinke A, Müller H-H, Schade-Brittinger C, et al. Placebo-controlled, double-blind, prospective, randomized study on the effect of octreotide LAR in the control of tumor growth in patients with metastatic neuroendocrine midgut tumors: a report from the PROMID Study Group. *J Clin Oncol*. 2009;27:4656–4663.
2. Caplin ME, Pavel M, Cwikła JB, et al. Lanreotide in metastatic enteropancreatic neuroendocrine tumors. *N Engl J Med*. 2014;371:224–233.

3. Boellaard R, Delgado-Bolton R, Oyen WJG, et al. FDG PET/CT: EANM procedure guidelines for tumour imaging: version 2.0. *Eur J Nucl Med Mol Imaging*. 2015;42:328–54.
4. Hope TA, Bergsland EK, Bozkurt MF, et al. Appropriate use criteria for somatostatin receptor PET imaging in neuroendocrine tumors. *J Nucl Med*. 2018;59:66–74.
5. Hope TA. Updates to the appropriate-use criteria for somatostatin receptor PET [editorial]. *J Nucl Med*. 2020;61:1764.
6. Nagtegaal ID, Odze RD, Klimstra D, et al. The 2019 WHO classification of tumours of the digestive system. *Histopathology*. 2020;76:182–188.
7. Pattison DA, Hicks RJ. Molecular imaging in the investigation of hypoglycaemic syndromes and their management. *Endocr Relat Cancer*. 2017;24:R203–R221.
8. Treglia G, Castaldi P, Villani MF, et al. Comparison of <sup>18</sup>F-DOPA, <sup>18</sup>F-FDG and <sup>68</sup>Ga-somatostatin analogue PET/CT in patients with recurrent medullary thyroid carcinoma. *Eur J Nucl Med Mol Imaging*. 2012;39:569–580.
9. Society of Nuclear Medicine and Molecular Imaging Technologist Section. Nuclear Medicine Technologist Scope of Practice and Performance Standards. 2nd Edition. Amazon aws website. [http://s3.amazonaws.com/rdcms-snm/production/public/NMT%20Scope%20of%20Practice%20and%20Performance%20Standards%202nd%20Ed-2022%20Complete-Approved\\_6-9-22.pdf](http://s3.amazonaws.com/rdcms-snm/production/public/NMT%20Scope%20of%20Practice%20and%20Performance%20Standards%202nd%20Ed-2022%20Complete-Approved_6-9-22.pdf). Approved June 9, 2022. Accessed December 1, 2022.
10. Bozkurt MF, Virgolini I, Balogova S, et al. Guideline for PET/CT imaging of neuroendocrine neoplasms with <sup>68</sup>Ga-DOTA-conjugated somatostatin receptor targeting peptides and <sup>18</sup>F-DOPA. *Eur J Nucl Med Mol Imaging*. 2017;44:1588–1601.
11. Aalbersberg EA, de Wit-van der Veen BJ, Versleijen MWJ, et al. Influence of lanreotide on uptake of <sup>68</sup>Ga-DOTATATE in patients with neuroendocrine tumours: a prospective intra-patient evaluation. *Eur J Nucl Med Mol Imaging*. 2019;46:696–703.
12. Gálne A, Almquist H, Almquist M, et al. A Prospective observational study to evaluate the effects of long-acting somatostatin analogs on <sup>68</sup>Ga-DOTATATE uptake in patients with neuroendocrine tumors. *J Nucl Med*. 2019;60:1717–1723.
13. Ayati N, Lee ST, Zakavi R, et al. Long-acting somatostatin analog therapy differentially alters <sup>68</sup>Ga-DOTATATE uptake in normal tissues compared with primary tumors and metastatic lesions. *J Nucl Med*. 2018;59:223–227.
14. Kong G, Hofman MS, Murray WK, et al. Initial experience with gallium-68 DOTA-octreotate PET/CT and peptide receptor radionuclide therapy for pediatric patients with refractory metastatic neuroblastoma. *J Pediatr Hematol Oncol*. 2016;38:87–96.
15. Abongwa C, Mott S, Schafer B, et al. Safety and accuracy of <sup>68</sup>Ga-DOTATOC PET/CT in children and young adults with solid tumors. *Am J Nucl Med Mol Imaging*. 2017;7:228–235.
16. Ga 68 DOTATOC prescribing information. Food and Drug Administration; August 2019.
17. SomaKit TOC: European public assessment report—product information. European Medicines Agency; February 2017.
18. NETSPOT prescribing information. Food and Drug Administration; June 2016.
19. Detectnet prescribing information. Food and Drug Administration; September 2021.
20. Loft M, Carlsen EA, Johnbeck CB, et al. <sup>64</sup>Cu-DOTATATE PET in patients with neuroendocrine neoplasms: prospective, head-to-head comparison of imaging at 1 hour and 3 hours post-injection. *J Nucl Med*. 2021;62:73–80.
21. Hope TA, Pampaloni MH, Nakamura E, et al. Simultaneous <sup>68</sup>Ga-DOTA-TOC PET/MRI with gadoxetate disodium in patients with neuroendocrine tumor. *Abdom Imaging*. 2015;40:1432–1440.
22. Walker RC, Smith GT, Liu E, Moore B, Clanton J, Stabin M. Measured human dosimetry of <sup>68</sup>Ga-DOTATATE. *J Nucl Med*. 2013;54:855–860.
23. Johnbeck CB, Knigge U, Loft A, et al. Head-to-head comparison of <sup>64</sup>Cu-DOTATATE and <sup>68</sup>Ga-DOTATOC PET/CT: a prospective study of 59 patients with neuroendocrine tumors. *J Nucl Med*. 2017;58:451–457.
24. Kumikowska J, Króllicki L, Pawlak D, Zerizer I, Mikołajczak R. Semiquantitative analysis and characterization of physiological biodistribution of <sup>68</sup>Ga-DOTATATE PET/CT. *Clin Nucl Med*. 2012;37:1052–1057.
25. Virgolini I, Gabriel M, Kroiss A, et al. Current knowledge on the sensitivity of the <sup>68</sup>Ga-somatostatin receptor positron emission tomography and the SUVmax reference range for management of pancreatic neuroendocrine tumours. *Eur J Nucl Med Mol Imaging*. 2016;43:2072–2083.
26. Orci L, Malaisse-Lagae F, Baetens D, Perrelet A. Pancreatic-polypeptide-rich regions in human pancreas. *Lancet*. 1978;2:1200–1201.
27. Hofman MS, Lau WFE, Hicks RJ. Somatostatin receptor imaging with <sup>68</sup>Ga-DOTATATE PET/CT: clinical utility, normal patterns, pearls, and pitfalls in interpretation. *Radiographics*. 2015;35:500–516.
28. Mackie EJ, Trechsel U, Bruns C. Somatostatin receptors are restricted to a subpopulation of osteoblast-like cells during endochondral bone formation. *Development*. 1990;110:1233–1239.
29. Dalm VASH, van Hagen PM, van Koetsveld PM, et al. Expression of somatostatin, cortistatin, and somatostatin receptors in human monocytes, macrophages, and dendritic cells. *Am J Physiol Endocrinol Metab*. 2003;285:E344–E353.
30. Hope TA, Calais J, Zhang L, Dieckmann W, Millo C. <sup>111</sup>In-pentetreotide scintigraphy versus <sup>68</sup>Ga-DOTATATE PET: impact on Krenning scores and effect of tumor burden. *J Nucl Med*. 2019;60:1266–1269.
31. Kratochwil C, Stefanova M, Mavriopoulou E, et al. SUV of [<sup>68</sup>Ga]DOTATOC-PET/CT predicts response probability of PRRT in neuroendocrine tumors. *Mol Imaging Biol*. 2015;17:313–318.
32. Werner RA, Solnes L, Javadi M, et al. SSTR-RADS version 1.0 as a reporting system for SSTR-PET imaging and selection of potential PRRT candidates: a proposed standardization framework. *J Nucl Med*. 2018;59:1085–1091.
33. Strosberg J, El-Haddad G, Wolin E, et al. Phase 3 trial of <sup>177</sup>Lu-dotatate for midgut neuroendocrine tumors. *N Engl J Med*. 2017;376:125–135.
34. Öksüz MÖ, Winter L, Pfannenbergs C, et al. Peptide receptor radionuclide therapy of neuroendocrine tumors with <sup>90</sup>Y-DOTATOC: is treatment response predictable by pre-therapeutic uptake of <sup>68</sup>Ga-DOTATOC? *Diagn Interv Imaging*. 2014;95:289–300.
35. Squires MH, Volkan Adsay N, Schuster DM, et al. Octreoscan versus FDG-PET for neuroendocrine tumor staging: a biological approach. *Ann Surg Oncol*. 2015;22:2295–2301.
36. Reubi JC, Kvolis LK, Waser B, et al. Detection of somatostatin receptors in surgical and percutaneous needle biopsy samples of carcinoids and islet cell carcinomas. *Cancer Res*. 1990;50:5969–5977.
37. Graf J, Pape U-F, Jann H, et al. Prognostic significance of somatostatin receptor heterogeneity in progressive neuroendocrine tumor treated with Lu-177 DOTATOC or Lu-177 DOTATATE. *Eur J Nucl Med Mol Imaging*. 2020;47:881–894.
38. Werner RA, Ilhan H, Lehner S, et al. Pre-therapy somatostatin receptor-based heterogeneity predicts overall survival in pancreatic neuroendocrine tumor patients undergoing peptide receptor radionuclide therapy. *Mol Imaging Biol*. 2019;21:582–590.
39. Werner RA, Lapa C, Ilhan H, et al. Survival prediction in patients undergoing radionuclide therapy based on intratumoral somatostatin-receptor heterogeneity. *Oncotarget*. 2017;8:7039–7049.
40. Kayani I, Bomanji JB, Groves A, et al. Functional imaging of neuroendocrine tumors with combined PET/CT using <sup>68</sup>Ga-DOTATATE (DOTA-DPhe1, Tyr3-octreotate) and <sup>18</sup>F-FDG. *Cancer*. 2008;112:2447–2455.
41. Hindié E. The NETPET Score: combining FDG and somatostatin receptor imaging for optimal management of patients with metastatic well-differentiated neuroendocrine tumors. *Theranostics*. 2017;7:1159–1163.
42. Binderup T, Knigge U, Johnbeck CB, et al. <sup>18</sup>F-FDG-PET is superior to WHO grading as prognostic tool in neuroendocrine neoplasms and useful in guiding peptide receptor radionuclide therapy: a prospective 10-year follow-up study of 166 patients. *J Nucl Med*. 2021;62:808–815.
43. Hicks RJ. Use of molecular targeted agents for the diagnosis, staging and therapy of neuroendocrine malignancy. *Cancer Imaging*. 2010;10 Spec no A:S83–91.
44. Chan DL, Pavlakis N, Schembri GP, et al. Dual somatostatin receptor/FDG PET/CT imaging in metastatic neuroendocrine tumours: proposal for a novel grading scheme with prognostic significance. *Theranostics*. 2017;7:1149–1158.
45. Gabriel M, Decristoforo C, Kendler D, et al. <sup>68</sup>Ga-DOTA-Tyr3-octreotide PET in neuroendocrine tumors: comparison with somatostatin receptor scintigraphy and CT. *J Nucl Med*. 2007;48:508–518.
46. Pfeifer A, Knigge U, Binderup T, et al. <sup>64</sup>Cu-DOTATATE PET for neuroendocrine tumors: a prospective head-to-head comparison with <sup>111</sup>In-DTPA-octreotide in 112 patients. *J Nucl Med*. 2015;56:847–854.
47. Sadowski SM, Neychev V, Millo C, et al. Prospective study of <sup>68</sup>Ga-DOTATATE positron emission tomography/computed tomography for detecting gastro-enteropancreatic neuroendocrine tumors and unknown primary sites. *J Clin Oncol*. 2016;34:588–596.
48. Hartmann H, Zöphel K, Freudenberg R, et al. Radiation exposure of patients during <sup>68</sup>Ga-DOTATOC PET/CT examinations [in German]. *Nucl Med (Stuttg)*. 2009;48:201–207.
49. Pfeifer A, Knigge U, Mortensen J, et al. Clinical PET of neuroendocrine tumors using <sup>64</sup>Cu-DOTATATE: first-in-humans study. *J Nucl Med*. 2012;53:1207–1215.
50. Brix G, Lechel U, Glatting G, et al. Radiation exposure of patients undergoing whole-body dual-modality <sup>18</sup>F-FDG PET/CT examinations. *J Nucl Med*. 2005;46:608–613.
51. Kratochwil C, Mavriopoulou E, Rath D, et al. Comparison of <sup>68</sup>Ga-DOTATOC biodistribution in patients with and without splenectomy. *Q J Nucl Med Mol Imaging*. 2015;59:116–120.

# Survival Outcomes in Metastatic Gastroenteropancreatic Neuroendocrine Tumor Patients Receiving Concomitant <sup>225</sup>Ac-DOTATATE–Targeted α-Therapy and Capecitabine: A Real-World-Scenario Management-Based Long-Term Outcome Study

Sanjana Ballal\*<sup>1</sup>, Madhav P. Yadav\*<sup>1</sup>, Madhavi Tripathi<sup>1</sup>, Ranjit Kumar Sahoo<sup>2</sup>, and Chandrasekhar Bal<sup>1</sup>

<sup>1</sup>Department of Nuclear Medicine, All India Institute of Medical Sciences, New Delhi, India; and <sup>2</sup>Department of Medical Oncology, BR Ambedkar Rotary Cancer Hospital, All India Institute of Medical Sciences, New Delhi, India

See an invited perspective on this article on page 219.

Although the short-term results of targeted α-therapy (TAT) with <sup>225</sup>Ac-DOTATATE in gastroenteropancreatic neuroendocrine tumors (GEP-NETs) have proven the therapy to be effective, to our knowledge no one has assessed the long-term outcome results. In this study, we aimed to evaluate the long-term outcome of <sup>225</sup>Ac-DOTATATE TAT in patients with somatostatin receptor–expressing advanced-stage metastatic GEP-NETs. **Methods:** Patients with <sup>68</sup>Ga-DOTANOC PET/CT scans showing moderate-to-high somatostatin receptor expression were recruited. Systemic TAT was performed on 91 adults with GEP-NETs (54 men and 37 women; mean age, 54.3 y; range, 25–75 y) using <sup>225</sup>Ac-DOTATATE (100–120 kBq/kg of body weight). All patients were given capecitabine therapy as a radiosensitizer (2 g/d) from days 0 to 14 of every <sup>225</sup>Ac-DOTATATE treatment cycle. Patients were categorized into 3 groups based on the status of prior <sup>177</sup>Lu-peptide receptor radionuclide therapy (PRRT): a prior-<sup>177</sup>Lu-PRRT–refractory group; a prior-<sup>177</sup>Lu-PRRT disease-control group; and a <sup>177</sup>Lu-PRRT–naïve group. Primary endpoints were overall survival (OS), and secondary endpoints included progression-free survival (PFS), objective tumor response, clinical response, and assessment of treatment-related toxicities. **Results:** Among the 91 patients, 57 underwent prior <sup>177</sup>Lu-DOTATATE therapy (24 with controlled disease [partial response/stable disease] and 33 with progressive disease [PD]). In total, 453 <sup>225</sup>Ac-DOTATATE TAT cycles were administered (median, 4 cycles per patient; range, 1–10) in a median follow-up of 24 mo (range, 5–41 mo). Median OS was not attained, with a 24-mo OS probability of 70.8%. In multivariate analysis, prognostic factors associated with a poor OS included the presence bone metastases (hazard ratio [HR], 2.501; 95% CI, 1.826–5.791; *P* < 0.032) and <sup>225</sup>Ac-DOTATATE therapy–refractory disease (HR, 8.781; 95% CI, 3.843–20.062; *P* < 0.0001). Median PFS was also not reached, with a 24-mo PFS probability of 67.5%. The multivariate analysis revealed only <sup>177</sup>Lu-PRRT–refractory disease to be significantly associated with a reduced PFS (HR, 14.338; 95% CI, 1.853–97.698; *P* = 0.011). Two of 79 patients (2.5%) with assessable disease experienced a complete response, 38 (48%) had a partial response, 23 (29%) had stable disease, and 16 (20.2%)

had PD. PD was observed in more patients from the prior-<sup>177</sup>Lu-PRRT–refractory group (11/33, 34%) than in <sup>177</sup>Lu-PRRT–naïve patients (4/24, 11%; *P* = 0.056). Patients from the prior-<sup>177</sup>Lu-PRRT–refractory group had the highest risk of poor PFS (HR, 13.553; 95% CI, 4.343–42.271; *P* = 0.0009). A significant clinical benefit was achieved after <sup>225</sup>Ac-DOTATATE therapy with minimal treatment-related toxicities. **Conclusion:** In long-term results, <sup>225</sup>Ac-DOTATATE TAT showed promise and improved the OS, even in patients refractory to prior <sup>177</sup>Lu-DOTATATE treatment, with transient and acceptable adverse effects.

**Key Words:** <sup>225</sup>Ac-DOTATATE TAT; GEP-NETs; overall survival; progression-free survival; objective response

**J Nucl Med 2023; 64:211–218**

DOI: 10.2967/jnumed.122.264043

**E**xpanded treatment options have recently become available to patients with well-differentiated gastroenteropancreatic neuroendocrine tumors (GEP-NETs) (1). Surgery offers the best chance of curing patients with localized GEP-NETs; however, surgery is not feasible when extensive metastases are present. In such cases, other options include somatostatin analogs (SSAs; e.g., lanreotide and octreotide) (2,3), interferons, tyrosine kinase inhibitors (e.g., sunitinib) (4), mammalian-target-of-rapamycin inhibitors (e.g., everolimus) (5), peptide receptor radionuclide therapy (PRRT) (6), systemic chemotherapy, and liver-targeted therapies, depending on the extent, stage, and location of disease and the tumor grade (7). The phase III NETTER-1 trial provided evidence for the efficacy and safety of PRRT using <sup>177</sup>Lu in this setting (8). However, only 18% of patients achieved a partial or complete response, despite treatment with <sup>177</sup>Lu-DOTATATE, a β- and γ-emitting radionuclide, and most patients relapsed within 2–3 y of treatment (9,10).

One promising option that has gained interest is using high-linear-energy-transfer α-emitting radioisotopes such as <sup>225</sup>Ac and <sup>213</sup>Bi instead of low-linear-energy-transfer β-emitting radioisotopes such as <sup>90</sup>Y and <sup>177</sup>Lu. The theoretic physical advantages of α-radiation over β-radiation are an endearing option to further improve the efficacy of PRRT by labeling the peptides with α-particle emitters (11).

Results from preclinical and clinical studies have suggested that an alternative strategy using PRRT delivering an α-emitting radionuclide

Received Feb. 22, 2022; revision accepted Jul. 15, 2022.

For correspondence or reprints, contact Chandrasekhar Bal (csbal@hotmail.com).

\*Contributed equally to this work.

Published online Jul. 21, 2022.

COPYRIGHT © 2023 by the Society of Nuclear Medicine and Molecular Imaging.

such as  $^{213}\text{Bi}$  and  $^{225}\text{Ac}$ -DOTATOC may have promise in patients with advanced GEP-NETs refractory to  $^{177}\text{Lu}$ -PRRT (12–16).

One clinical study used  $^{213}\text{Bi}$ -DOTATOC in 7 patients with neuroendocrine tumor progression on  $\beta$ -PRRT (17). Although that study demonstrated the therapeutic potential of this approach,  $^{213}\text{Bi}$ -DOTATOC was administered via intraarterial delivery, limiting the more widespread application of  $\alpha$ -radionuclide therapy in the real-world setting.  $^{213}\text{Bi}$  also has a physical half-life of only 46 min, resulting in logistic challenges for broader adoption.

These studies prompted us to investigate the role of  $^{225}\text{Ac}$ -DOTATATE as salvage treatment for patients with GEP-NETs (18). Initial results from 32 patients who had previously received  $^{177}\text{Lu}$ -PRRT indicated that  $^{225}\text{Ac}$ -DOTATATE administered intravenously induced sustained responses. Approximately two thirds of the 24 patients (15/24, 62.5%) who underwent interim morphologic response analysis had a partial response, and the disease control rate was 100% (15 with PR and 9 with stable disease). Furthermore, there was no documented progressive disease (PD), and no deaths occurred during a median follow-up of 8 mo (range, 2–13 mo). We observed minimal and reversible toxicities and no life-threatening adverse events (AEs). These data suggested that multiple cycles of therapy could be safely administered without a significant risk of either acute or delayed radiation toxicity (18). Despite the favorable short-term results, as far as we are aware no comprehensive long-term outcome results have been extensively studied to demonstrate the survival benefit of  $^{225}\text{Ac}$ -DOTATATE therapy in both prior- $^{177}\text{Lu}$ -PRRT and  $^{177}\text{Lu}$ -PRRT-naïve groups of GEP-NET patients.

In the current study, we extensively studied the long-term follow-up data in an expanded cohort of patients to assess overall survival (OS), progression-free survival (PFS), factors predicting survival, response to treatment, and the patterns of the delayed AE profile in advanced metastatic GEP-NETs.

## MATERIALS AND METHODS

### Study Design

The independent institutional review board of All India Institute of Medical Sciences approved the study. All patients provided written informed consent before participating. Ethical clearance was received (reference number IEC-517). The study design and treatment regimen are depicted schematically in Figure 1. The methodology is detailed in the supplemental materials (available at <http://jnm.snmjournals.org>).

The study was on patients with histologically well-differentiated, inoperable, or metastatic GEP-NETs. Patients were included if they had a history of prior concomitant therapies, such as SSAs and chemotherapy, as well as  $^{177}\text{Lu}$ -DOTATATE therapy. Essential prerequisites were significant somatostatin receptor expression and at least 1 measurable lesion on the CT component of the baseline  $^{68}\text{Ga}$ -DOTANOC PET/CT scan (uptake  $\geq$  liver or Krenning score  $\geq$  2 as compared on maximum-intensity-projection, coronal, and transaxial images).

Patients with inadequate laboratory parameters (baseline hemoglobin  $<$  9 g/dL, platelet count  $<$  75,000/ $\mu\text{L}$ , serum creatinine  $>$  1.6 mg/dL, or serum bilirubin  $>$  3 mg/dL) or a Karnofsky performance status (KPS) of less than 40 were excluded.

### Treatment Planning and Follow-up

**Image Acquisition.** All patients underwent a baseline diagnostic  $^{68}\text{Ga}$ -DOTANOC PET/CT scan as a pretherapeutic work-up. For morphologic assessment, additional  $^{68}\text{Ga}$ -DOTANOC PET/CT scans were repeated within 6–8 wk after patients completed every 2–3 cycles of  $^{225}\text{Ac}$ -DOTATATE-targeted  $\alpha$ -therapy (TAT), when patients presented with clinical disease progression, or at the investigator's discretion.

**$^{68}\text{Ga}$ -DOTANOC PET/CT Imaging.** The  $^{68}\text{Ga}$ -DOTANOC PET/CT scans did not require special preparation. A mean activity of 111 MBq (3 mCi) was injected, and PET/CT scans were acquired between 45 and 60 min after injection. For the acquisition, the patient lay supine on the examination table. The protocol constituted of an initial

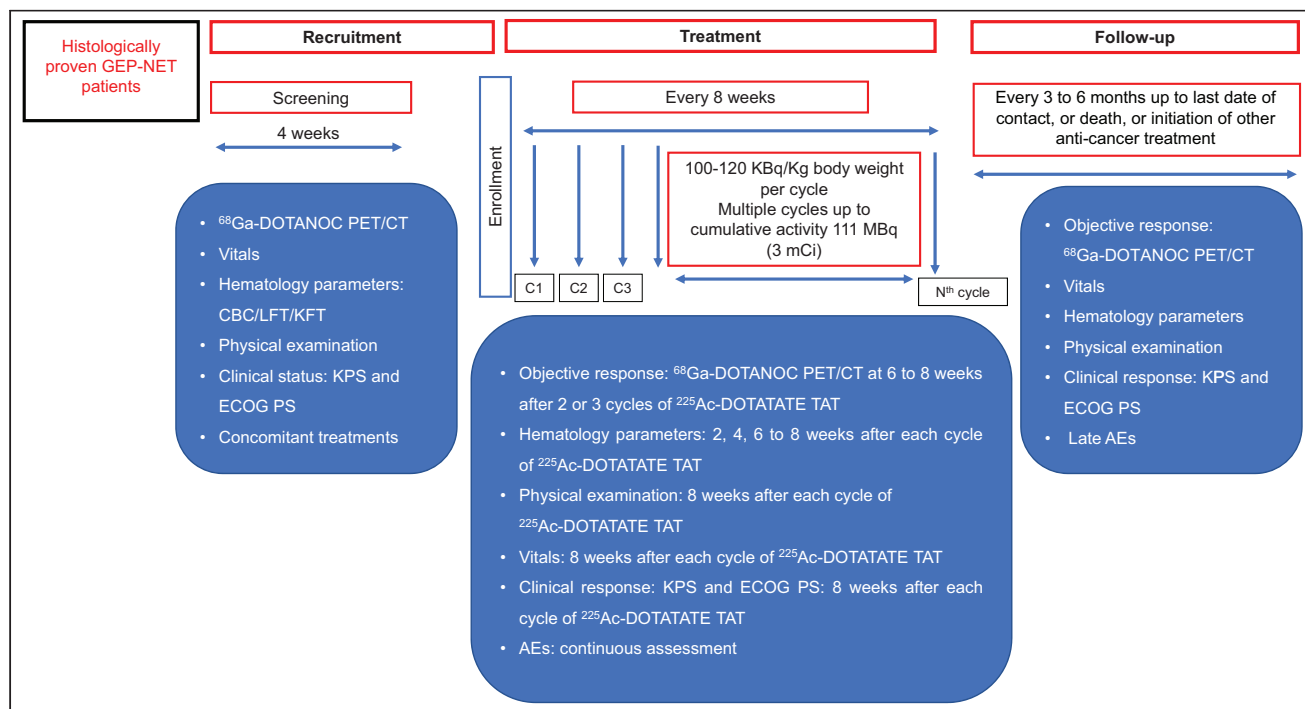


**FIGURE 1.**  $^{225}\text{Ac}$ -DOTATATE TAT treatment regimen and follow-up. CBC = complete blood count; ECOG = Eastern Cooperative Oncology Group; KFT = kidney function testing; LFT = liver function testing; PS = performance status.



scout image to define the field of view from vertex to mid thigh, followed by diagnostic CT and PET scans. The diagnostic whole-body CT scan parameters involved a diagnostic-dose CT scan with 300–380 mAs, 120 kVp, a slice thickness of 3.75 mm, and a pitch of 0.6. Additionally, spot views were acquired if required, with a slice thickness of 1.25 mm on CT at 120 kVp, 300–380 mAs, and a pitch of 0.6.

The administration and route of the contrast medium depended on the site of the tumor and scan indication. Generally, CT scans were acquired with a nonionic, isomolar contrast medium (iodixanol injection, U.S. Pharmacopeia; 1 mL/kg of body weight) containing 320 mg I/mL intravenously or orally and a neutral oral contrast medium (water). Fifty-six patients were injected with nonionic, isomolar contrast medium. Positive oral (iodixanol) and neutral (water) contrast media were administered when indicated. All tumors were visualized on the diagnostic CT scan, but only tumors with measurable dimensions according to RECIST, version 1.1, were included for the assessment of morphologic response.

**Treatment.** Long- and short-acting somatostatin agents were stopped 4–5 wk and 48–72 h, respectively, before  $^{225}\text{Ac}$ -DOTATATE therapy. Premedications, including an antiemetic (ondansetron) or corticosteroid (dexamethasone), were administered and repeated if necessary. For kidney protection, a single-day kidney protection protocol was followed, which consisted of an injection solution containing lysine (23.3 g) and arginine (8 g) in 1 L of water. This cocktail was infused over 4 h, starting 30–60 min before the  $^{225}\text{Ac}$ -DOTATATE infusion.

As previously described,  $^{225}\text{Ac}$ -DOTATATE (100–120 kBq/kg [3–3.2  $\mu\text{Ci}/\text{kg}$ ] of body weight per cycle diluted in 50 mL of saline) was administered over 30 min (flow rate, 1.6 mL/min) every 8 wk up to a maximum cumulative dose of 111 MBq (3 mCi). All patients received capecitabine as a radiosensitizer (2 g/d) from days 0 to 14 of every cycle. Patients were monitored for 24 h after  $^{225}\text{Ac}$ -DOTATATE TAT to observe any acute side effects. Patients on supportive care or octreotide continued to receive those treatments at the investigator's discretion.

Patients were withdrawn from the study in the event of any serious AEs; lack of adherence to the treatment protocol due to unavoidable pandemic conditions; demonstration of disease progression; withdrawal of consent to further treatment cycles; or death.

**Assessments.** Safety was monitored at baseline and at 8-wk intervals thereafter. Assessments included physical examination, vital parameters, laboratory tests (assessed at 2, 4, and 6- to 8-week intervals), and clinical evaluation via KPS and Eastern Cooperative Oncology Group (ECOG) performance status. Patients were given a diary to document any side effects or discomfort. With the exception of blood parameters, all other assessments were conducted at baseline and at 8 wk after each cycle of  $^{225}\text{Ac}$ -DOTATATE TAT or on withdrawal from the study or at treatment completion.

**Patient Groups.** On the basis of  $^{177}\text{Lu}$ -PRRT history, patients were categorized into 2 groups: a prior- $^{177}\text{Lu}$ -PRRT group and a  $^{177}\text{Lu}$ -PRRT-naïve group (Fig. 2). The prior- $^{177}\text{Lu}$ -PRRT group was further divided according to cancer status after  $^{177}\text{Lu}$ -PRRT, that is, those who were treatment-refractory and those who were stable or responded to  $^{177}\text{Lu}$ -PRRT (Fig. 2). Patients in the prior- $^{177}\text{Lu}$ -PRRT-refractory group ( $n = 33$ ) progressed during the  $^{177}\text{Lu}$ -DOTATATE treatment course or within 12 mo of completion of the  $^{177}\text{Lu}$ -DOTATATE treatment regimen. Patients in the prior- $^{177}\text{Lu}$ -PRRT disease-control group ( $n = 24$ ) completed the  $^{177}\text{Lu}$ -DOTATATE treatment regimen and achieved disease control (partial response or stable disease) but were further treated with  $^{225}\text{Ac}$ -DOTATATE because of the persistent high tumor burden. Patients in the  $^{177}\text{Lu}$ -PRRT-naïve group ( $n = 34$ ) did not receive  $^{177}\text{Lu}$ -DOTATATE therapy at any point in the treatment course.

## Outcomes

The primary endpoint was OS (defined as the time from initiation of  $^{225}\text{Ac}$ -DOTATATE TAT until death due to any cause or the date of the last contact). Patients who were lost to follow-up were considered alive but were censored (supplemental material). The key secondary endpoint was PFS (defined as the first observation of documented morphologic disease progression on diagnostic CT according to the assessment by RECIST 1.1 (19) or the development of pleural/pericardial effusion/malignant ascites or disease-specific death, whichever occurred first). Other secondary endpoints included objective tumor response by RECIST 1.1, clinical response assessment with KPS and ECOG performance status (20), and evaluation of treatment-related AEs using the National Cancer Institute Common Terminology Criteria for Adverse Events (version 5.0) and the Food and Drug Administration document entitled, "Guidance for Industry: Toxicity Grading Scale for Healthy Adult and Adolescent Volunteers Enrolled in Preventive Vaccine Clinical Trials" (21,22).

## Statistical Analysis

Univariate analysis was used to compare characteristics among patient groups. On the basis of the normality of parameters, continuous variables with a normal distribution were represented as mean, SD, range, median, and interquartile range. Parameters of the same population at different time points were compared using a paired  $t$ -test (parametric test) or Wilcoxon signed-rank test (nonparametric test). OS and PFS plots were constructed using the Kaplan–Meier methodology; a log-rank test was used to compare survival between groups. The Cox proportional-hazards regression model was performed to determine the predictive and prognostic factors associated with OS and PFS.  $P$  values of less than 0.05 were considered to be significant. The analysis was conducted using MedCalc statistical software (version 15.1; MedCalc Software Ltd).

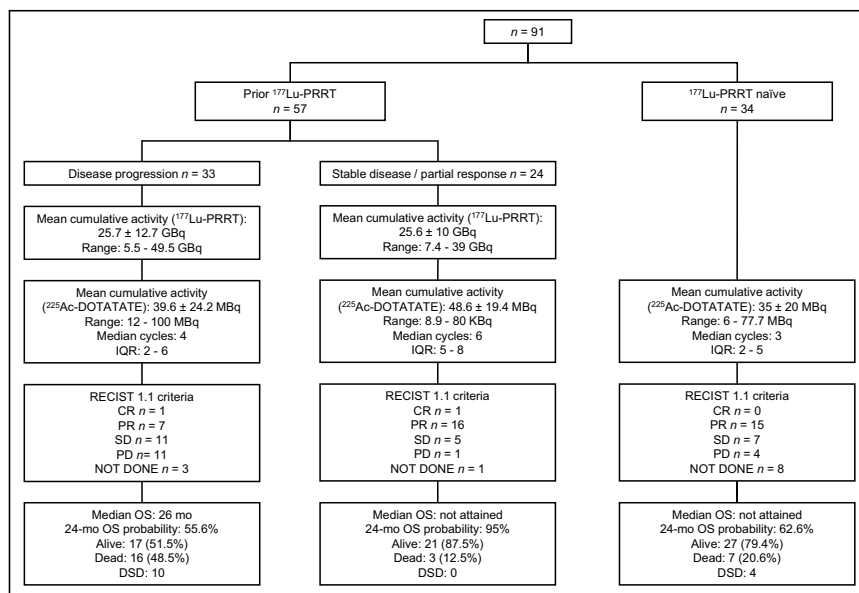


**FIGURE 2.** Flowchart depicting treatment details and response in various groups of patients. CR = complete response; DSD = disease-specific death; IQR = interquartile range; PR = partial response; SD = stable disease.

## RESULTS

### Baseline Demographic and Clinical Characteristics of Patients

Between April 2018 and February 2022, 91 consecutive GEP-NET patients (54 men and 37 women, mean [ $\pm$ SD] age, 54.3  $\pm$  11.6 y; range, 25–75 y) were enrolled. The first  $^{225}\text{Ac}$ -DOTATATE TAT treatment was administered in April 2018, and the last patient was recruited in October 2021. The last date for follow-up cutoff was February 20, 2022. The median follow-up duration was 24 mo (range, 5–41 mo) from the start of  $^{225}\text{Ac}$ -DOTATATE TAT.

Baseline characteristics are summarized in Table 1. The pancreas (33%) was the most common site of the primary tumor, followed by the duodenum (14.3%) and ileum (13%). GEP-NETs were World Health Organization grade 1 in 33 patients (36.2%), grade 2 in 48 (52.7%), and grade 3 in 7 (7%) (Table 1; Supplemental Table 1). Primary or residual tumor was noted in 55 patients (60.4%), and all patients demonstrated metastases on somatostatin receptor PET/CT, with the most common metastatic sites being the liver ( $n = 88$ , 96.7%), lymph nodes ( $n = 66$ , 72.5%), and bone ( $n = 25$ , 27.5%)

**TABLE 1**  
Patient Characteristics at Baseline ( $n = 91$ )

Characteristic	Value
Age (y)	
Mean $\pm$ SD	54.3 $\pm$ 11.6
Range	25–75
Sex	
Male	54 (59.4%)
Female	37 (40.6%)
Tumor location	
Pancreas	30 (33%)
Stomach	7 (7.7%)
Appendix	1 (1%)
Ileum	12 (13%)
Duodenum	13 (14.3%)
Jejunum	2 (2.2%)
Colon	2 (2.2%)
Rectum	8 (8.8%)
Abdominal neuroendocrine tumor with unknown primary	16 (17.6%)
WHO tumor grade (Ki-67 tumor proliferation index)	
Grade I (<2%)	33 (36.2%)
Grade II (3%–20%)	48 (52.7%)
Grade III (>20%)	7 (7%)
Not accessible	3 (3.3%)
Previous surgery	20 (22%)
Prior chemotherapy	20 (22%)
Prior $^{177}\text{Lu}$ -DOTATATE therapy	57 (62.6%)
ECOG status	
1–2	63 (69%)
3–4	28 (31%)

WHO = World Health Organization.

Data are number and percentage, except for age.

(Supplemental Table 2). Eighteen patients (20%) had received prior chemotherapy (Supplemental Table 3), most of whom had 1 previous line ( $n = 12$ , 66.6%); 4 patients (22.2%) had 2 prior lines, and 2 (11%) had at least 3 prior lines. Ten symptomatic patients were on long-acting SSAs, which were stopped 4 wk before commencing  $^{225}\text{Ac}$ -DOTATATE TAT.

### Treatment

The mean cumulative radioactivity administered was 35.52 MBq (range, 21.64–59.47 MBq [960  $\mu\text{Ci}$ ; range, 583.7–1,607.3  $\mu\text{Ci}$ ]). The median interval between treatment cycles was 8 wk. In total, 453 cycles of  $^{225}\text{Ac}$ -DOTATATE TAT were administered: 32 patients received 1–3 cycles, and the remaining 59 patients received 4–10 cycles (Supplemental Table 4). Three patients received a single cycle of  $^{225}\text{Ac}$ -DOTATATE TAT: the first patient died after the first cycle, the second was lost to follow-up, and the third withdrew consent.

### Efficacy Assessment

**OS and PFS.** Twenty-six patients (26.5%) died during follow-up. The causes of death are detailed in Supplemental Table 5. In the overall patient population, the median OS was not attained, with a 24-mo survival probability of 70.8% (Fig. 3A). On subcategory analysis, whereas 16 (16/33, 48.5%) deaths occurred in the prior- $^{177}\text{Lu}$ -PRRT-refractory group (median OS, 26 mo), 3 deaths (3/24, 12.5%) and 7 deaths (7/34, 20.6%) occurred in the prior- $^{177}\text{Lu}$ -PRRT disease-control group and  $^{177}\text{Lu}$ -PRRT naïve group, respectively ( $P = 0.0003$ ) (Fig. 3B). Interestingly, in patients who demonstrated disease control on  $^{177}\text{Lu}$ -PRRT, none of the 3 deaths was disease-specific (Supplemental Table 5). The prior- $^{177}\text{Lu}$ -PRRT disease-control group showed significantly better OS than the  $^{177}\text{Lu}$ -PRRT-naïve group (95% vs. 67%) (Fig. 2). We speculated that these differences might be due to inherent differences in the baseline demographic or clinical characteristics of the patient cohorts. However, univariate comparison between the groups did not reveal any differences in the demographic parameters (Supplemental Table 6).

On univariate analysis, the presence of bone metastases (Fig. 3C), a cumulative  $^{225}\text{Ac}$ -DOTATATE TAT dose of less than 37,000 kBq (Fig. 3D), and PD to  $^{225}\text{Ac}$ -DOTATATE TAT (Fig. 3E) were associated with significantly poorer OS (Supplemental Table 7). However, on multivariate analysis, the presence of bone metastases (hazard ratio [HR], 2.501; 95% CI, 1.826–5.791;  $P = 0.032$ ) and  $^{225}\text{Ac}$ -DOTATATE therapy-refractory disease (PD) persisted as significant prognostic factors associated with poor OS (HR, 8.781; 95% CI, 3.843–20.062;  $P < 0.0001$ ) (Fig. 3E).

At the time of this analysis, median PFS had not been attained in the overall patient population. The median PFS was 30 mo in the prior- $^{177}\text{Lu}$ -PRRT-refractory group and was not reached in the prior- $^{177}\text{Lu}$ -PRRT disease-control group (HR, 13.553; 95% CI, 4.343–42.271;  $P = 0.0009$ ) (Fig. 4A). Similarly, univariate analysis revealed an association between the presence of bone metastases (Fig. 4B) and a cumulative  $^{225}\text{Ac}$ -DOTATATE dose of less than 1 mCi and PD (HR, 2.718; 95% CI, 0.999–7.393;  $P = 0.028$ ) (Fig. 4C; Supplemental Table 8). However, on multivariate analysis, only  $^{177}\text{Lu}$ -PRRT-refractory disease was significantly associated with a significantly reduced PFS (HR, 14.3; 95% CI, 1.853–97.6;  $P = 0.011$ ).

**Objective Response.** Morphologic response to  $^{225}\text{Ac}$ -DOTATATE TAT according to the disease status on prior  $^{177}\text{Lu}$ -PRRT therapy is shown in Table 2. Two of the 79 evaluable patients (2.5%), both previously treated with  $^{177}\text{Lu}$ -PRRT, had a complete response; no complete responses were observed in the  $^{177}\text{Lu}$ -PRRT-naïve group.  $^{68}\text{Ga}$ -DOTANOC PET/CT revealed a partial response in 38

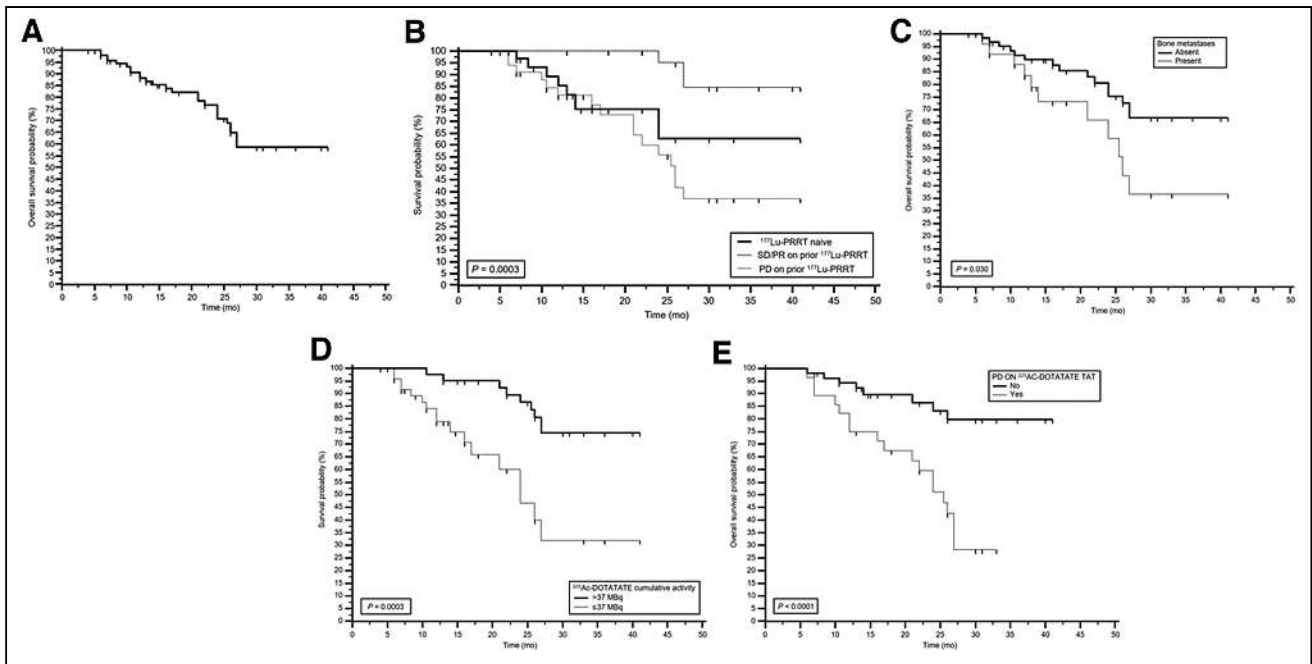


**FIGURE 3.** OA in entire cohort of 91 patients who had been treated with  $^{225}\text{Ac}$ -DOTATATE (A), based on disease status on prior  $^{177}\text{Lu}$ -PRRT (B), based on presence of bone metastases (C), based on cumulative dosage of  $^{225}\text{Ac}$ -DOTATATE received (D), and based on disease status on  $^{225}\text{Ac}$ -DOTATATE therapy (E). PR = partial response; SD = stable disease.

patients (48%) and stable disease in 23 (29%), for a disease control rate of 80%. Twelve and 4 progression events occurred in the prior- $^{177}\text{Lu}$ -PRRT and  $^{177}\text{Lu}$ -PRRT-naïve groups, respectively, representing a 40% lower estimated risk of progression in the  $^{177}\text{Lu}$ -PRRT-naïve group than in the prior- $^{177}\text{Lu}$ -PRRT group.

In the prior- $^{177}\text{Lu}$ -PRRT group, among 24 patients who experienced disease control with  $^{177}\text{Lu}$ -PRRT, 17 (74%) further showed a response to  $^{225}\text{Ac}$ -DOTATATE TAT. Promising response rates were also observed in 8 of 30 patients (27%; 1 complete response and 7 PRs) belonging to the prior- $^{177}\text{Lu}$ -PRRT-refractory group, with stable disease in a further 11 patients (36.6%; Fig. 1). PRs were observed in 15 of 27 patients (55.5%) in the  $^{177}\text{Lu}$ -PRRT-naïve groups.

Of the 17 patients with PD, 14 experienced disease-specific deaths, 2 have been rechallenged with an escalated 150 kBq/kg dose of  $^{225}\text{Ac}$ -DOTATATE and have shown disease stability, and the remaining patient refused to undergo any further treatment but is alive.

**Clinical Response.** Among the patients who were alive till the end of analysis, the median KPS significantly improved from 60 at baseline to 70 after treatment ( $P < 0.0001$ ), and the median ECOG score enhanced from 2 to 1 ( $P < 0.0001$ ). In the overall population, whereas the KPS improved from 60 to 70 ( $P = 0.053$ ), ECOG status remained the same as the median baseline value of 2.

#### Toxicity and AEs

Treatment-related AEs occurring during  $^{225}\text{Ac}$ -DOTATATE TAT are shown in Supplemental Table 9. No renal or liver toxicity and no tumor-lysis syndrome were observed. One patient had grade 3 thrombocytopenia. Clinical disease-related symptoms, such as fatigue, loss of appetite, nausea, gastritis, abdominal pain, abdominal distension, and myalgia, were caused mainly by the nature of the cancer and the site of metastasis and were prevalent before the initiation of  $^{225}\text{Ac}$ -DOTATATE treatment. All the above symptoms improved after treatment.

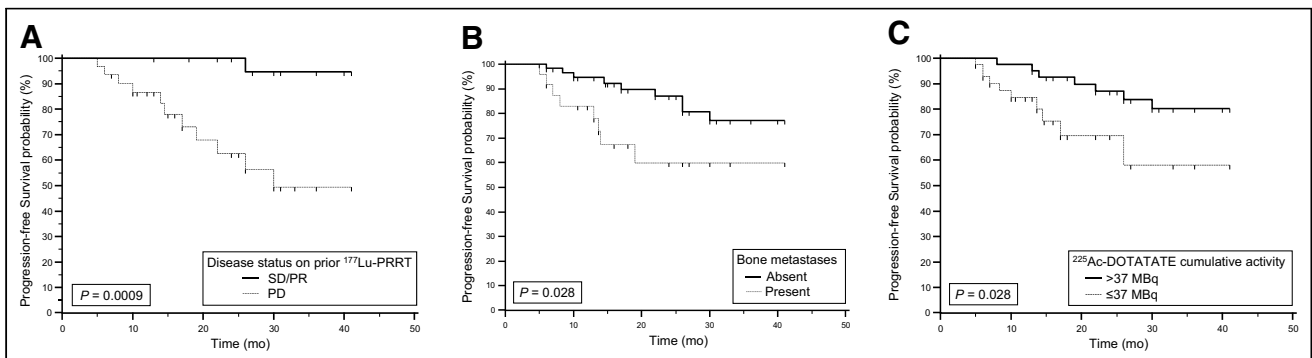


**FIGURE 4.** Radiologic PFS according to disease status on prior  $^{177}\text{Lu}$ -PRRT (A), presence or absence of bone metastases (B), and cumulative activity of  $^{225}\text{Ac}$ -DOTATATE received (C).

**TABLE 2**  
Morphologic Tumor Response Based on Primary Tumor Site

Site of primary	Prior <sup>177</sup> Lu-PRRT (n = 57)					<sup>177</sup> Lu-PRRT-naïve (n = 34)					
	CR	PR	SD	PD	Not assessed	Site of primary	CR	PR	SD	PD	Not assessed
Foregut (n = 32)	1 (3%)	13 (40.6%)	10 (31%)	6 (18.7%)	2 (6%)	Foregut (n = 15)	0	7 (46.6%)	2 (13.3%)	3 (20%)	3 (20%)
Midgut (n = 11)	0	6 (54.5%)	3 (27.3%)	1 (9%)	1 (9%)	Midgut (n = 9)	0	5 (55.6%)	2 (22.2%)	0	2 (22.2%)
Hindgut (n = 7)	1 (14.3%)	2 (28.6%)	2 (28.6%)	2 (28.6%)	0	Hindgut (n = 1)	0	0	1 (100%)	0	0
Unknown (n = 7)	0	2 (28.6%)	1 (14.3%)	3 (42.8%)	1 (14.3%)	Unknown (n = 9)	0	3 (33.3%)	2 (22.2%)	1 (11%)	3 (33.3%)
Total (n = 57)	2 (3.5%)	23 (40.3%)	16 (28%)	12 (21%)	4	Total (n = 34)	0	15 (44%)	7 (20.6%)	4 (11.8%)	8 (23.6%)

CR = complete response; PR = partial response; SD = stable disease.  
Data are number and percentage.

Malignant ascites and pleural effusion, which are signs of PD, were observed in 14 and 2 patients, respectively. Grade 1 of 2 malignant ascites was present in 8 patients at baseline. Eventually, 4 patients experienced grade 2 malignant ascites, and 10 experienced life-threatening malignant ascites and died. One patient with pleural effusion also died.

Before initiation of <sup>225</sup>Ac-DOTATATE, flushing was documented in 8 patients, 3 of whom had grade 3 flushing. After treatment, flushing improved to grade 1 in all patients.

Transient symptoms, including nausea, vomiting, and abdominal discomfort, were encountered in most patients during the amino acid infusion and <sup>225</sup>Ac-DOTATATE administration and settled within 24 h after treatment. Fatigue, myalgia, and loss of appetite were also observed and resolved within 1 wk after treatment.

## DISCUSSION

In our short-term analysis on the first clinical experience with the α-emitting conjugate <sup>225</sup>Ac-DOTATATE TAT in 32 patients with GEP-NETs who had exhausted or were refractory to β-emitting <sup>177</sup>Lu-DOTATATE therapy, we observed favorable responses with low toxicities (18). The study included an expanded cohort of 91 patients with an extended median follow-up of 24 mo, ranging from 5 to 41 mo. Our results provide further evidence that <sup>225</sup>Ac-DOTATATE is effective in patients with neuroendocrine tumors, a group with few therapeutic options, especially after progression on other therapies. Median OS and PFS were not attained. The objective response rate and disease control rates were 48% and 80%, respectively, and were lower than our previously reported short-term data showing a response rate of 63% and a disease control rate of 100%.

Though the current study had broad and heterogeneous inclusion criteria, it was conducted in a real-world setting based on everyday clinical practice that includes patients of poor performance status (31%) (ECOG status ≥ 3)—a critical and optimistic perspective of this study. We believe that real-world-based clinical study results can be extended and translated to the general population. Moreover, in this study, several demographic and clinical variables were compared among 3 groups of patients whose categorization was based on the status of prior <sup>177</sup>Lu-PRRT therapy and who were matched (Supplemental Table 6), which ruled out the potential inherent bias.

Comparisons with the NETTER-1 median long-term OS result (23), 48 mo, revealed that <sup>225</sup>Ac-DOTATATE provided an additive OS benefit of 26 mo in the worst-outcome patient cohort, who were refractory to prior <sup>177</sup>Lu-PRRT. Well in line with the phase III NETTER-1 (8) short-term result showing 14 deaths (12%) in the 116 neuroendocrine tumor patients who underwent <sup>177</sup>Lu-DOTATATE therapy as a first-line treatment option, our cohort of 34 <sup>177</sup>Lu-PRRT-naïve patients reported a similar disease-specific death rate of 11.7% (4/34) in a median follow-up of 24 mo.

Another finding meriting comment is that in this cohort of patients from our group and the NETTER 1 group, the median OS was not attained. An interpretation of this finding is that the upfront use of <sup>225</sup>Ac-DOTATATE therapy in advanced neuroendocrine tumors may not be necessary as a mainstay option. Irrespective of the disease burden, patients can first be challenged with <sup>177</sup>Lu-PRRT and eventually be rechallenged with α-based <sup>225</sup>Ac-DOTATATE therapy when a high disease burden is persistent despite attaining a maximum tolerable dose of <sup>177</sup>Lu (~1.2 Ci) or the patient is refractory to <sup>177</sup>Lu-PRRT.

Patients who achieved disease control (partial response or stable disease) with prior  $^{177}\text{Lu}$ -PRRT ( $n = 24$ ) followed by retreatment with  $^{225}\text{Ac}$ -DOTATATE showed the best outcome, with a 24-mo OS probability of 95%, which was remarkably higher than in the  $^{177}\text{Lu}$ -PRRT-refractory (55.6%) and -naïve (62.6%) groups. Moreover, only 3 deaths occurred in this group of patients, and none of the events was disease-specific. There may be 2 possible explanations for these findings. The first possibility is that  $^{225}\text{Ac}$ -DOTATATE significantly increased the OS as an adjuvant treatment option after  $^{177}\text{Lu}$ -PRRT. The alternative possibility is simply that patients had already achieved disease control on  $^{177}\text{Lu}$ -PRRT and could be followed up with a wait-and-watch approach until the disease progressed. However, only a double-arm randomized, controlled trial between the wait-and-watch group and the group receiving further  $^{225}\text{Ac}$ -DOTATATE treatment can be the definitive answer.

Rudisile et al. (24) studied the outcomes of  $^{177}\text{Lu}$ -PRRT retreatment in the salvage setting for all patients who responded to the initial standard 4 cycles of  $^{177}\text{Lu}$ -PRRT. They observed an additional response rate of 3%, PFS of 6 mo, and OS of 51 mo. The largest systematic review and metaanalysis, by Strosberg et al. (25), examined published evidence of  $^{177}\text{Lu}$ -PRRT retreatment efficacy and safety in patients with advanced progressive neuroendocrine tumors.  $^{177}\text{Lu}$ -PRRT retreatment provided encouraging results, with a median PFS of 12.5 mo and a median OS of 26.7 mo. In a similar salvage treatment setting, our results go beyond the previous reports, as we observed a remarkably higher response rate of 74% (17 with complete response and 23 with partial response), and promising prolonged survival benefits, as neither PFS nor OS was attained with  $^{225}\text{Ac}$ -DOTATATE therapy.

Although several groups reported variations in the site of metastases associated with poor survival, it is apparent that the presence of distant metastases has a significant impact on survival, irrespective of the treatment modality. Regarding the impact of bone metastases on survival, our results with  $^{225}\text{Ac}$ -DOTATATE TAT are similar to those reported by Rudisile et al. (24) and Swiha et al. (26), who demonstrated that the presence of bone metastases was associated with a shorter OS in patients with well-differentiated neuroendocrine tumors who received  $^{177}\text{Lu}$ -DOTATATE.

In addition to morphologic responses, improvements in overall patient well-being were observed, with the median KPS increasing from 60 before treatment (patients requiring medical care and much assistance with self-care) to 70 after treatment (patients being able to care for themselves but unable to do their usual activities or active work). This finding highlights the potential for  $^{225}\text{Ac}$ -DOTATATE to improve the quality of life in the worst-outcome patient population.

Treatment with  $^{225}\text{Ac}$ -DOTATATE TAT was well tolerated. As previously described, low-grade hematologic AEs were the most common side effect of treatment with  $^{225}\text{Ac}$ -DOTATATE. Grade 3 and higher AEs were uncommon and transient or unlikely to be treatment-related. The total amount of  $^{225}\text{Ac}$  administered ( $\leq 111$  MBq) did not correlate with AEs. Interestingly, AEs also did not correlate with  $^{177}\text{Lu}$ -naïve or prior  $^{177}\text{Lu}$ -PRRT therapy, which suggests that dosing with  $^{225}\text{Ac}$ -DOTATATE TAT should not be influenced by prior treatment with  $^{177}\text{Lu}$ . Moreover, similar to the short-term results (18) by our group on  $^{225}\text{Ac}$ -DOTATATE, there were minimal hematologic, kidney, and liver function toxicities. However, over time during the long-term follow-up, when making comparisons with our pilot results we observed a significantly high incidence of malignant ascites and pleural effusion; whether they were related to disease per se or

were TAT-related, longer follow-up of this cohort will clarify. In agreement with our findings, another study using  $^{225}\text{Ac}$ -DOTATOC reported that cumulative doses of 60,000–80,000 kBq were tolerated with minimal acute and chronic grade 3 or 4 hepatotoxicity in patients with advanced-stage malignancies (27). Looking at the toxicity profile, it seems that there is scope to further escalate the individual activity per kilogram or use higher cumulative activity of  $^{225}\text{Ac}$  in the future. Thus, the only approach is to rigorously follow these patients for long-term side effects of  $^{225}\text{Ac}$ -DOTATATE TAT.

High-level evidence for long-term safety and sustained benefits to OS and radiologic PFS in patients with GEP-NETs treated with  $^{225}\text{Ac}$ -DOTATATE is crucial and warrants well-controlled, multicenter, randomized trials to determine its role and the best treatment algorithm for this challenging disease.

Our study had some limitations. The results are exploratory and single-center and are based on a heterogeneous patient population. Although not conducted as a clinical trial with strict inclusion criteria, we believe the study had the advantage of enrolling the largest (to our knowledge) GEP-NET population treated with  $^{225}\text{Ac}$ -DOTATATE therapy, including poor-outcome patients, and better reflects the results of treatment-related toxicity, confirming the benefit of efficacy, survival, and improvement in quality of life in a real-world clinical setting. Though all the CT scans of the CT component of PET/CT were of diagnostic quality, contrast was not administered to all patients, resulting in suboptimal-quality images.

## CONCLUSION

$^{225}\text{Ac}$ -DOTATATE-based PRRT was effective in the heavily pretreated GEP-NET cohort of patients, with good survival rates, high response rates, improvements in KPS, and an acceptable toxicity profile.  $^{225}\text{Ac}$ -DOTATATE TAT may be a suitable treatment option for patients with stable disease or PD after  $^{177}\text{Lu}$ -DOTATATE  $\beta$ -therapy. Patients refractory to  $^{225}\text{Ac}$ -DOTATATE treatment have the worst outcome. We strongly advocate a large multicenter, randomized, controlled trial to assess the potential of this strategy as a new therapeutic paradigm for patients with GEP-NET who have exhausted all other options. Further, a balanced approach that exploits our long-term results and clinical trials can best aid the oncology community in delivering the most beneficial, individualized care to patients.

## DISCLOSURE

No potential conflict of interest relevant to this article was reported.

## KEY POINTS

**QUESTION:** What is the long-term outcome for GEP-NET patients treated with  $^{225}\text{Ac}$ -DOTATATE TAT?

**PERTINENT FINDINGS:** The median OS was not attained, and the 24-mo OS probability was 70.8%. Median PFS was also not reached, with a 24-mo PFS probability of 67.5%. A significant clinical benefit was achieved after  $^{225}\text{Ac}$ -DOTATATE therapy, with minimal treatment-related toxicities.

**IMPLICATIONS FOR PATIENT CARE:** Even in patients resistant to prior  $^{177}\text{Lu}$ -DOTATATE,  $^{225}\text{Ac}$ -DOTATATE TAT has shown promising long-term results, with transient and acceptable adverse effects.

## REFERENCES

- Fernandez CJ, Agarwal M, Pottakkat B, Haroon NN, George AS, Pappachan JM. Gastroenteropancreatic neuroendocrine neoplasms: a clinical snapshot. *World J Gastrointest Surg.* 2021;13:231–255.
- Rinke A, Müller HH, Schade-Brittinger C, et al. Placebo-controlled, double-blind, prospective, randomised study on the effect of octreotide LAR in the control of tumour growth in patients with metastatic neuroendocrine midgut tumors: a report from the PROMID Study Group. *J Clin Oncol.* 2009;27:4656–4663.
- Delavault P, Caplin ME, Liyanage N, et al. The CLARINET study: assessing the effect of lanreotide autogel on tumor progression-free survival in patients with non-functioning gastroenteropancreatic neuroendocrine tumors [abstract]. *J Clin Oncol.* 2017;30:TPS4153.
- Raymond E, Dahan L, Raoul JL, et al. Sunitinib malate for the treatment of pancreatic neuroendocrine tumors. *N Engl J Med.* 2011;364:501–513.
- Yao JC, Fazio N, Singh S, et al. Everolimus for the treatment of advanced, non-functional neuroendocrine tumours of the lung or gastrointestinal tract (RADIANT-4): a randomised, placebo-controlled, phase 3 study. *Lancet.* 2016;387:968–977.
- Camus B, Cottreau AS, Palmieri LJ, et al. Indications of peptide receptor radionuclide therapy (PRRT) in gastroenteropancreatic and pulmonary neuroendocrine tumors: an updated review. *J Clin Med.* 2021;10:1267.
- Yao JC. Molecular targeted therapy for carcinoid and islet-cell carcinoma. *Best Pract Res Clin Endocrinol Metab.* 2007;21:163–172.
- Strosberg J, El-Haddad G, Wolin E, et al. Phase 3 trial of <sup>177</sup>Lu-DOTATATE for midgut neuroendocrine tumors. *N Engl J Med.* 2017;376:125–135.
- Bodei L, Cremonesi M, Grana CM, et al. Peptide receptor radionuclide therapy with <sup>177</sup>Lu-DOTATATE: the IEO phase I-II study. *Eur J Nucl Med Mol Imaging.* 2011;38:2125–2135.
- Ballal S, Yadav MP, Damle NA, Sahoo RK, Bal C. Concomitant <sup>177</sup>Lu-DOTATATE and capecitabine therapy in patients with advanced neuroendocrine tumours: a long-term-outcome, toxicity, survival, and quality-of-life study. *Clin Nucl Med.* 2017;42:e457–e466.
- Navalkissoor S, Grossman A. Targeted alpha particle therapy for neuroendocrine tumours: the next generation of peptide receptor radionuclide therapy. *Neuroendocrinology.* 2019;108:256–264.
- Nayak TK, Norenberg JP, Anderson TL, Prossnitz ER, Stabin MG, Atcher RW. Somatostatin-receptor-targeted alpha-emitting <sup>213</sup>Bi is therapeutically more effective than beta(–)-emitting <sup>177</sup>Lu in human pancreatic adenocarcinoma cells. *Nucl Med Biol.* 2007;34:185–193.
- Miederer M, Henriksen G, Alke A, et al. Preclinical evaluation of the alpha-particle generator nuclide <sup>225</sup>Ac for somatostatin receptor radiotherapy of neuroendocrine tumors. *Clin Cancer Res.* 2008;14:3555–3561.
- Norenberg JP, Krenning BJ, Konings IR, et al. <sup>213</sup>Bi-[DOTA<sup>0</sup>, Tyr<sup>3</sup>]octreotide peptide receptor radionuclide therapy of pancreatic tumors in a preclinical animal model. *Clin Cancer Res.* 2006;12:897–903.
- Chan HS, Konijnenberg MW, de Blois E, et al. Influence of tumour size on the efficacy of targeted alpha therapy with <sup>213</sup>Bi- [DOTA<sup>0</sup>, Tyr<sup>3</sup>]-octreotate. *EJNMMI Res.* 2016;6:6.
- Chan HS, Konijnenberg MW, Daniels T, et al. Improved safety and efficacy of <sup>213</sup>Bi-DOTATATE-targeted alpha therapy of somatostatin receptor expressing neuroendocrine tumors in mice pre-treated with L-lysine. *EJNMMI Res.* 2016;6:83.
- Kratochwil C, Giesel FL, Bruchertseifer F, et al. <sup>213</sup>Bi-DOTATOC receptor-targeted alpha-radionuclide therapy induces remission in neuroendocrine tumours refractory to beta radiation: a first-in-human experience. *Eur J Nucl Med Mol Imaging.* 2014;41:2106–2119.
- Ballal S, Yadav MP, Bal C, Sahoo RK, Tripathi M. Broadening horizons with <sup>225</sup>Ac-DOTATATE targeted alpha therapy for gastroenteropancreatic neuroendocrine tumour patients stable or refractory to <sup>177</sup>Lu-DOTATATE PRRT: first clinical experience on the efficacy and safety. *Eur J Nucl Med Mol Imaging.* 2020;47:934–946.
- Wahl RL, Jacene H, Kasamon Y, et al. From RECIST to PERCIST: evolving considerations for PET response criteria in solid tumors. *J Nucl Med.* 2009;50(suppl 1):122S–150S.
- Crooks V, Waller S, Smith T, et al. The use of the Karnofsky Performance Scale in determining outcomes and risk in geriatric outpatients. *J Gerontol.* 1991;46:M139–M144.
- Toxicity grading scale for healthy adult and adolescent volunteers enrolled in preventive vaccine clinical trials. Food and Drug Administration website. <https://www.fda.gov/regulatory-information/search-fda-guidance-documents/toxicity-grading-scale-healthy-adult-and-adolescent-volunteers-enrolled-preventive-vaccine-clinical>. Published September 2007. Accessed November 15, 2022.
- Guidance for industry: toxicity grading scale for healthy adult and adolescent volunteers enrolled in preventive vaccine clinical trials; availability. *Fed Regist.* 2007;72:54917.
- Strosberg JR, Caplin ME, Kunz PL, et al.; NETTER-1 investigators. <sup>177</sup>Lu-Dotatate plus long-acting octreotide versus high-dose long-acting octreotide in patients with midgut neuroendocrine tumours (NETTER-1): final overall survival and long-term safety results from an open-label, randomised, controlled, phase 3 trial. *Lancet Oncol.* 2021;22:1752–1763.
- Rudisile S, Gosewisch A, Wenter V, et al. Salvage PRRT with <sup>177</sup>Lu-DOTATOC in extensively pretreated patients with metastatic neuroendocrine tumor (NET): dosimetry, toxicity, efficacy, and survival. *BMC Cancer.* 2019;19:788.
- Strosberg J, Leeuwenkamp O, Siddiqui MK. Peptide receptor radiotherapy re-treatment in patients with progressive neuroendocrine tumors: a systematic review and meta-analysis. *Cancer Treat Rev.* 2021;93:102141.
- Swiha MM, Sutherland DEK, Sistani G, et al. Survival predictors of <sup>177</sup>Lu-Dotatate peptide receptor radionuclide therapy (PRRT) in patients with progressive well-differentiated neuroendocrine tumors (NETS). *J Cancer Res Clin Oncol.* 2022;148:225–236.
- Kratochwil C, Apostolidis L, Rathke H, et al. Dosing <sup>225</sup>Ac-DOTATOC in patients with somatostatin-receptor-positive solid tumors: 5-year follow-up of hematological and renal toxicity. *Eur J Nucl Med Mol Imaging.* 2021;49:54–63.

# The Future of Targeted $\alpha$ -Therapy Is Bright, but Rigorous Studies Are Necessary to Advance the Field

Jonathan Strosberg<sup>1</sup>, Ken Herrmann<sup>2</sup>, and Lisa Bodei<sup>3</sup>

<sup>1</sup>Department of GI Oncology, Moffitt Cancer Center, Tampa, Florida; <sup>2</sup>Department of Nuclear Medicine, University of Duisburg–Essen and German Cancer Consortium (DKTK)–University Hospital Essen, Essen, Germany; and <sup>3</sup>Molecular Imaging and Therapy Service, Department of Radiology, Memorial Sloan Kettering Cancer Center, New York, New York

See the associated article on page 211.

Among the advances in radiopharmaceutical therapy, few innovations have shown more promise than targeted  $\alpha$ -therapy. By inducing double-strand DNA breaks, high-linear-energy-transfer isotopes such as <sup>213</sup>Bi, <sup>212</sup>Pb, and <sup>225</sup>Ac have the potential to produce substantially higher cytotoxicity than existing  $\beta$ -emitters (e.g., <sup>177</sup>Lu). Indeed, since approval of <sup>223</sup>Ra for castration-resistant prostate cancer metastatic to bone, there has been a 6-fold increase in the number of prospective trials of  $\alpha$ -emitters.

In this issue of *The Journal of Nuclear Medicine*, Dr. Ballal and colleagues (1) have accumulated the largest real-world experience using targeted  $\alpha$ -therapy in neuroendocrine tumor patients by radiolabeling DOTATATE with <sup>225</sup>Ac in-house and treating patients with multiple cycles ( $\leq 10$ ) at a dose of 100–120 kBq/kg per cycle. At the time of the most recent data analysis (cutoff, February 2022), 91 patients at the All India Institute of Medical Sciences had been treated with this therapy: a mixed population of patients who included peptide receptor radionuclide therapy (PRRT)–naïve individuals ( $n = 34$ ), patients refractory to <sup>177</sup>Lu-PRRT ( $n = 57$ ), patients with progressive disease, and patients with stable disease but presumably treated because of symptom burden or tumor volume.

The results have been encouraging. At the time of analysis, median PFS had not been reached in the overall patient population and was reported to be 30 mo in patients who had received prior <sup>177</sup>Lu-PRRT—patients who frequently do not exhibit long PFS intervals at the retreatment. Objective response rates were also impressive, at 44% both in patients who had received prior <sup>177</sup>Lu-PRRT (25/57) and in those who were <sup>177</sup>Lu-PRRT–naïve (15/34). No cases of myelodysplastic syndrome or acute leukemia have been reported as of yet, and treatment was described overall as tolerable.

Nevertheless, there are reasons to interpret these data with caution. The authors have, on occasion, described their work as a prospective phase II study (2). However, the term *phase II study*

implies certain prerequisites, including a predetermined sample size, strict eligibility criteria, a clear prospective treatment protocol, and strict criteria for interpretation of response. These criteria do not apply to this analysis, which is best described as a retrospective study of real-world experience. The eligibility criteria seem to have shifted between the initial analysis of 32 patients in 2019 (3) and the current analysis. For example, exclusion of patients with a European Cooperative Oncology Group status of more than 2 (3) seems to have been unheeded (31% of patients were described as having status 3 or 4, which is, in itself, remarkable). Disease response and progression were evaluated using RECIST, version 1.1, despite the fact that many patients lacked contrast-enhanced anatomic imaging and were evaluated for response based on PET findings.

A notable revelation in this paper is that patients received capecitabine concurrently with <sup>225</sup>Ac-DOTATATE. To our knowledge, this component of therapy was not reported in prior published analyses of the same patient cohort (2,3). While the contribution of radiosensitizing doses of capecitabine may have been minor, the display of this critical information is of the utmost importance to allow for reproducibility of the results.

Although many advances in nuclear medicine began with compassionate administration of in-house–radiolabeled drugs, drug approvals depend on prospective trials that are strictly followed. It is therefore fortunate that such trials are rapidly proliferating, including studies of targeted  $\alpha$ -therapy for patients with neuroendocrine tumors. Examples are a phase II study of <sup>212</sup>Pb-DOTAMTATE in <sup>177</sup>Lu-PRRT–naïve and –refractory patients (NCT05153772) and a phase I/III study of <sup>225</sup>Ac-DOTATATE in patients who have received prior <sup>177</sup>Lu-PRRT (NCT05477576). If the outcomes are nearly as favorable as those described by Dr. Ballal et al., the future of targeted  $\alpha$ -therapy in neuroendocrine tumors is promising.

## DISCLOSURE

This work was supported in part by NIH grant P30 CA008748. Jonathan Strosberg is on the speakers' bureau for Ipsen and Tersera. Ken Herrmann receives personal fees from Bayer, Sofie Biosciences, SIRTEX, Adacap, Curium, Endocyte, BTG, IPSEN, Siemens Healthineers, GE Healthcare, Amgen, Novartis, ymabs, Aktis Oncology, Theragnostics, and Pharma15; other fees from Sofie Biosciences; nonfinancial support from ABX; and grants from BTG, outside the submitted work. Lisa Bodei in a nonremunerated consultant for AAA-Novartis, Ipsen, Iba, Clovis Oncology, MTTI,

Received Aug. 16, 2022; revision accepted Aug. 22, 2022.

For correspondence or reprints, contact Lisa Bodei (bodeil@mskcc.org).

Published online Oct. 20, 2022.

COPYRIGHT © 2023 by the Society of Nuclear Medicine and Molecular Imaging.

DOI: 10.2967/jnumed.122.264805

and Great Point Partners. No other potential conflict of interest relevant to this article was reported.

## REFERENCES

1. Ballal S, Yadav MP, Tripathi M, Sahoo RK, Bal C. Survival outcomes in metastatic gastroenteropancreatic neuroendocrine tumor patients receiving concomitant  $^{225}\text{Ac}$ -DOTATATE-targeted  $\alpha$ -therapy and capecitabine: a real-world-scenario management-based long-term outcome study. *J Nucl Med.* 2023;64:211–218.
2. Bal C, Ballal S, Yadav M. A phase II clinical study on  $^{225}\text{Ac}$ -DOTATATE therapy in advanced stage gastroenteropancreatic neuroendocrine tumor patients [abstract]. *J Nucl Med.* 2022;63(suppl 2):2208.
3. Ballal S, Yadav MP, Bal C, Sahoo RK, Tripathi M. Broadening horizons with  $^{225}\text{Ac}$ -DOTATATE targeted alpha therapy for gastroenteropancreatic neuroendocrine tumour patients stable or refractory to  $^{177}\text{Lu}$ -DOTATATE PRRT: first clinical experience on the efficacy and safety. *Eur J Nucl Med Mol Imaging.* 2020;47:934–946.



# Evaluation of $^{177}\text{Lu}$ -PSMA-617 SPECT/CT Quantitation as a Response Biomarker Within a Prospective $^{177}\text{Lu}$ -PSMA-617 and NOX66 Combination Trial (LuPIN)

Sarennya Pathmanandavel<sup>1</sup>, Megan Crumbaker<sup>2-4</sup>, Bao Ho<sup>1</sup>, Andrew O. Yam<sup>2-4</sup>, Peter Wilson<sup>5</sup>, Remy Niman<sup>5</sup>, Maria Ayers<sup>1</sup>, Shikha Sharma<sup>1</sup>, Adam Hickey<sup>1</sup>, Peter Eu<sup>6</sup>, Martin Stockler<sup>7</sup>, Andrew J. Martin<sup>7</sup>, Anthony M. Joshua<sup>2-4</sup>, Andrew Nguyen<sup>1,4</sup>, and Louise Emmett<sup>1,3,4</sup>

<sup>1</sup>Department of Theranostics and Nuclear Medicine, St. Vincent's Hospital, Sydney, New South Wales, Australia; <sup>2</sup>Kinghorn Cancer Centre, St. Vincent's Hospital, Sydney, New South Wales, Australia; <sup>3</sup>Garvan Institute of Medical Research, Sydney, New South Wales, Australia; <sup>4</sup>St. Vincent's Clinical School, University of New South Wales, Sydney, New South Wales, Australia; <sup>5</sup>MIM Software, Inc., Cleveland, Ohio; <sup>6</sup>Peter MacCallum Cancer Centre, Melbourne, Victoria, Australia; and <sup>7</sup>NHMRC Clinical Trials Centre, University of Sydney, Sydney, New South Wales, Australia

$^{177}\text{Lu}$ -PSMA-617 is an effective and novel treatment in metastatic castration-resistant prostate cancer (mCRPC). Our ability to assess response rates and therefore efficacy may be improved using predictive tools. This study investigated the predictive value of serial  $^{177}\text{Lu}$ -PSMA-617 SPECT/CT ( $^{177}\text{Lu}$  SPECT) imaging in monitoring treatment response. **Methods:** Fifty-six men with progressive mCRPC previously treated with chemotherapy and novel androgen signaling inhibitor were enrolled into the LuPIN trial and received up to 6 doses of  $^{177}\text{Lu}$ -PSMA-617 and a radiation sensitizer (3-(4-hydroxyphenyl)-2H-1-benzopyran-7-ol [NOX66]).  $^{68}\text{Ga}$ -PSMA-11 and  $^{18}\text{F}$ -FDG PET/CT were performed at study entry and exit, and  $^{177}\text{Lu}$  SPECT from vertex to mid thighs was performed 24 h after each treatment. SPECT quantitative analysis was undertaken at cycles 1 (baseline) and 3 (week 12) of treatment. **Results:** Thirty-two of the 56 men had analyzable serial  $^{177}\text{Lu}$  SPECT imaging at both cycle 1 and cycle 3. In this subgroup, median prostate-specific antigen (PSA) progression-free survival (PFS) was 6.3 mo (95% CI, 5–10 mo) and median overall survival was 12.3 mo (95% CI, 12–24 mo). The PSA 50% response rate was 63% (20/32).  $^{177}\text{Lu}$  SPECT total tumor volume (SPECT TTV) was reduced in 68% (22/32; median,  $-0.20\text{ m}^3$  [95% CI,  $-1.4$  to  $-0.001$ ]) and increased in 31% (10/32; median,  $0.36$  [95% CI,  $0.1$ – $1.4$ ]). Any increase in SPECT TTV was associated with shorter PSA PFS (hazard ratio, 4.1 [95% CI, 1.5–11.2];  $P = 0.006$ ). An increase of 30% or more in SPECT TTV was also associated with a shorter PSA PFS (hazard ratio, 3.3 [95% CI, 1.3–8.6];  $P = 0.02$ ). Tumoral  $\text{SUV}_{\text{max}}$  was reduced in 91% (29/32) and  $\text{SUV}_{\text{mean}}$  in 84% (27/32); neither was associated with PSA PFS or overall survival outcomes. PSA progression by week 12 was also associated with a shorter PSA PFS (hazard ratio, 26.5 [95% CI, 5.4–131]). In the patients with SPECT TTV progression at week 12, 50% (5/10) had no concurrent PSA progression (median PSA PFS, 4.5 mo [95% CI, 2.8–5.6 mo]), and 5 of 10 men had both PSA and SPECT TTV progression at week 12 (median PSA PFS, 2.8 mo [95% CI, 1.8–3.7 mo]). **Conclusion:** Increasing SPECT TTV on quantitative  $^{177}\text{Lu}$  SPECT predicts a short PFS and may play a future role as an imaging response biomarker.

**Key Words:** metastatic prostate cancer; SPECT; lutetium-PSMA; response biomarker

Received May 10, 2022; revision accepted Jul. 22, 2022.  
For correspondence or reprints, contact Louise Emmett (louise.emmett@svha.org.au).  
Published online Aug. 25, 2022.  
COPYRIGHT © 2023 by the Society of Nuclear Medicine and Molecular Imaging.

J Nucl Med 2023; 64:221–226  
DOI: 10.2967/jnumed.122.264398

Although treatment resistance and short response duration remain common,  $^{177}\text{Lu}$ -PSMA-617 is an effective therapy in metastatic castration-resistant prostate cancer (mCRPC) (1–4). Accurate monitoring of response to  $^{177}\text{Lu}$ -PSMA-617 may improve patient outcomes by enabling treatment escalation, change in treatment, or a treatment holiday, dependent on imaging results. Interim and serial prostate-specific membrane antigen (PSMA) PET has recently been shown to be predictive of progression-free survival (PFS) with PSMA-targeted radionuclide therapy (5). Quantitative  $^{177}\text{Lu}$ -PSMA-617 SPECT/CT ( $^{177}\text{Lu}$  SPECT) imaging after each  $^{177}\text{Lu}$ -PSMA-617 dose may also be valuable in response monitoring in addition to providing dosimetric information. This LuPIN trial substudy aimed to determine whether quantitative parameters on serial  $^{177}\text{Lu}$  SPECT imaging 24 h after  $^{177}\text{Lu}$ -PSMA-617 therapy were predictive of treatment response and PFS.

## MATERIALS AND METHODS

The LuPIN trial is a prospective single-center phase I/II dose escalation and expansion trial of combination  $^{177}\text{Lu}$ -PSMA-617 and 3-(4-hydroxyphenyl)-2H-1-benzopyran-7-ol (NOX66) for men with mCRPC previously treated with at least 1 line of taxane chemotherapy and androgen signaling inhibitor. The clinical results have been previously published (6,7). The St. Vincent's Hospital institutional review board approved the study protocol (HREC/17/SVH/19 and ACTRN12618001073291), and all patients provided informed written consent.

## Screening

Men with progressive mCRPC, based on either conventional imaging (CT and bone scanning) or a rising prostate-specific antigen (PSA) level according to Prostate Cancer Working Group 3 criteria (8), were eligible for screening. Prior treatment with at least 1 line of taxane chemotherapy (docetaxel or cabazitaxel) and an androgen signaling inhibitor (abiraterone or enzalutamide) was required for inclusion. Men underwent screening with  $^{18}\text{F}$ -FDG and  $^{68}\text{Ga}$ -HBEDD-PSMA-11 PET/CT, bone scanning, and CT of the chest, abdomen, and pelvis.

Molecular screening criteria were based on  $SUV_{max}$  rather than physiologic activity (liver or parotid). Men were eligible if they had an  $SUV_{max}$  of more than 15 on PSMA PET at 1 or more sites, an  $SUV_{max}$  of more than 10 at all measurable sites, and no  $^{18}F$ -FDG avidity without corresponding PSMA uptake.

### Study Treatment

Men received up to 6 doses of  $^{177}Lu$ -PSMA-617 at 6-wk intervals, with 3 dose-escalated cohorts of NOX66 (400, 800, 1,200 mg). NOX66 suppositories were administered as a radiosensitizer on days 1–10 after each  $^{177}Lu$ -PSMA-617 injection. All cohorts were administered 7.5 GBq of  $^{177}Lu$ -PSMA-617 on day 1 via slow intravenous injection. The PSMA-617 precursor (AAA Novartis) was radiolabeled to no-carrier-added  $^{177}Lu$ -chloride according to the manufacturer's instructions. Quality control tests for radionuclide and radiochemical purity were performed using high-pressure liquid chromatography and thin-layer chromatography. Blood was prospectively collected before assessment of adverse events and biochemical responses. The patients were treated on trial until they were no longer clinically benefiting from treatment.

### Imaging Procedures and Analysis

$^{68}Ga$ -PSMA and  $^{18}F$ -FDG PET/CT scans were obtained at baseline and trial exit (after completing 6 cycles or when treatment was ceased), using the imaging acquisition and analysis parameters previously published (7).  $^{177}Lu$  SPECT (vertex to mid thighs) was performed 24 h after  $^{177}Lu$ -PSMA-617 injection using a Discovery 670 system (GE Healthcare) with the following parameters: medium-energy collimators, 3 bed positions, 60 projections over  $360^\circ$  with an acquisition time of 10 s per frame,  $128 \times 128$  matrix, and  $4.42 \times 4.42$  mm pixel size. An energy window centered on 208 keV  $\pm 10\%$  with a 165 keV  $\pm 6.5\%$  scatter window was used. An unenhanced low-dose CT scan was obtained immediately afterward using the following parameters: pitch of 1, tube voltage of 120 kV, automatic mAs control (reference mAs, 90), slice thickness of 3.7 mm, matrix of  $512 \times 512$ , and field of view of 40 cm. The SPECT projection images were reconstructed with an iterative ordered-subset estimation-maximum algorithm that used 4 iterations and 10 subsets using SPECTRA Quant (MIM Software, Inc.). No pre- or postreconstruction filters were applied. CT-based attenuation correction, dual-energy-window scatter correction, collimator-based resolution recovery, and quantitative conversion to SUV were performed during the reconstruction. The conversion from counts to units of activity was based on a cylinder phantom with known activity.

### Quantitative Analysis

$^{177}Lu$  SPECT and  $^{68}Ga$ -PSMA PET/CT were analyzed semiquantitatively by a nuclear medicine physician using MIM (LesionID; MIM Software Inc.) software and a standardized semiautomated workflow to delineate regions of interest with a minimum SUV cutoff of 3. All lesions identified quantitatively were manually reviewed and physiologic activity removed. Whole-body quantitation was used to derive total tumor volume (TTV),  $SUV_{max}$ , and  $SUV_{mean}$  for both  $^{68}Ga$ -PSMA PET and  $^{177}Lu$  SPECT (9).

### Statistical Analysis

We measured PSA decline from baseline ( $\geq 50\%$ ) at any time point, PSA PFS as defined by Prostate Cancer Working Group 3 criteria, and overall survival (8,10). The Kaplan–Meier method was used to characterize time-to-event endpoints and estimate medians (presented with 95% CIs). We correlated changes in TTV, PSMA intensity, clinical parameters, and biochemical parameters with time-to-event outcomes, using univariate Cox proportional-hazards regression models (11,12). Continuous variables included increase in TTV,  $SUV_{max}$ , and  $SUV_{mean}$ . *P* values below 5% were considered significant. We compared  $^{68}Ga$ -PSMA PET TTV with cycle 1 SPECT TTV using scatterplots and Pearson correlation coefficients. Reproducibility testing of SPECT TTV and PSMA  $SUV_{max}$

**TABLE 1**  
Baseline Patient Characteristics

Characteristic	Data
Total patients	32
Age (y)	69 (66–73)
ECOG	
0 or 1	25 (78)
2	7 (22)
Prior systemic treatments	
LHRH agonist/antagonist	32 (100)
Chemotherapy	32 (100)
Docetaxel	32 (100)
Cabazitaxel	29 (91)
Androgen signaling inhibitor	32 (100)
Sites of disease	
Lymph nodes	18 (56)
Bone	30 (94)
Viscera	6 (19)
Median PSMA tumor volume at screening (cm <sup>3</sup> )	670 (275–1,736)
Number of cycles of $^{177}Lu$ -PSMA-617 received	6 (3–6)

LHRH = luteinizing hormone-releasing hormone.  
Qualitative data are absolute counts and percentage;  
continuous data are median and interquartile range.

was undertaken using repeatability statistics calculated from a hierarchic linear mixed model that accounted for variance in score at the patient level (13). A 95% CI for the repeatability statistics was derived via bootstrapping. Analyses were performed using R (version 4.0.5).

## RESULTS

### Baseline Patient Characteristics

Of the men enrolled in LuPIN, 57% (32/56) had  $^{177}Lu$  SPECT imaging suitable for analysis, 30% (17/56) had incomplete SPECT data precluding analysis, and 13% (7/56) did not reach cycle 3 of treatment. Baseline characteristics are summarized in Table 1. In this LuPIN substudy, 53% (17/32) completed 6 cycles of treatment whereas 47% (15/32) completed between 3 and 5 cycles, and 63% (20/32) achieved at least a 50% PSA decline from baseline at any time point. At the time of analysis, 84% (27/32) were deceased.

**TABLE 2**  
Summary of  $^{177}Lu$  SPECT Quantitation at Cycles 1 and 3

Parameter	Cycle 1	Cycle 3
TTV (cm <sup>3</sup> )	787 (282–1,298)	492 (191–1,190)
$SUV_{max}$	70 (57–100)	36 (27–60)
$SUV_{mean}$	10.1 (8–12)	8 (6–9)

Data are median and interquartile range.

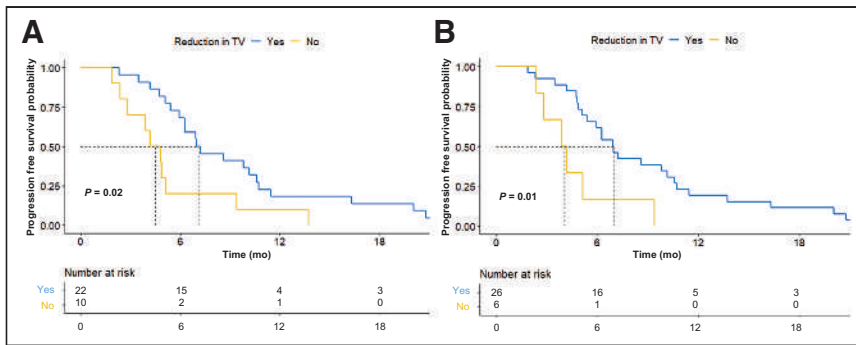


**FIGURE 1.** Kaplan–Meier curve for PSA PFS stratified by any increase in SPECT TTV at cycle 3 (A) or >30% increase in SPECT TTV at cycle 3 (B). TV = tumor volume.

There was no difference in either PSA PFS or overall survival based on NOX66 dose. Overall, median overall survival was 12.3 mo (95% CI, 11.7–23.6 mo). Median PSA PFS was 6.3 mo (95% CI, 5.1–9.8 mo).

### <sup>177</sup>Lu SPECT Quantitation

SPECT quantitation measures at baseline and week 12, including SPECT TTV, SUV<sub>max</sub>, and SUV<sub>mean</sub>, are summarized in Table 2. SPECT TTV was reduced between baseline and week 12 in 68% (22/32; median,  $-0.20 \text{ m}^3$  [95% CI,  $-1.4$  to  $-0.001$ ]) and increased in 31% (10/32; median,  $0.36$  [95% CI,  $0.1$ – $1.4$ ]). A 30% increase in SPECT TTV by week 12 was identified in 19% (6/32). SUV<sub>max</sub> was reduced between baseline and week 12 in 91% (29/32; median,  $-28.9$  [95% CI,  $-195$  to  $+42$ ]), and SUV<sub>mean</sub> was reduced in 84% (27/32; median,  $-2.6$  [95% CI,  $-12$  to  $+10$ ]).

### Correlation with Patient Outcomes

An increase in SPECT TTV between baseline and week 12 was associated with a significantly worse PSA PFS (hazard ratio, 4.1 [95% CI, 1.5–11.2];  $P = 0.006$ ). Median PSA PFS in those with an increase in SPECT TTV was 4.5 mo (95% CI, 2.8–5.6 mo), compared with 7.1 mo (95% CI, 6.3–10.7 mo) for those with no increase in SPECT TTV. A SPECT TTV increase of at least 30% was also associated with a shorter PSA PFS (hazard ratio, 3.3 [95% CI, 1.3–8.6],  $P = 0.02$ ) (Fig. 1). Increased SUV<sub>max</sub> or SUV<sub>mean</sub> between baseline and week 12 was not associated with PSA PFS or overall survival (Table 3). By week 12, 25% (8/32) of patients demonstrated PSA progression. PSA progression at week 12 was associated with significantly worse PSA PFS (hazard ratio, 26.5 [95% CI, 5.4–131];  $P < 0.001$ ). Patients with PSA progression at week 12 had a median

PSA PFS of 3.5 mo (95% CI, 1.1–4.5 mo), versus 7.9 mo (95% CI, 6.3–10.7 mo) in those without PSA progression. In the 10 patients with SPECT TTV progression at week 12, 50% (5/10) had no concurrent PSA progression (median PSA PFS, 4.5 mo [95% CI, 2.8–5.6 mo]), and 5 of 10 men had both PSA and SPECT TTV progression at week 12 (median PSA PFS, 2.8 mo [95% CI, 1.8–3.7 mo]) (Fig. 2).

### Reproducibility

TTV was compared between <sup>68</sup>Ga PSMA-11 PET/CT at screening (PSMA PET TTV) and the baseline <sup>177</sup>Lu SPECT (median time

between scans, 15 d [range, 6–56 d]). There was a strong correlation between PSMA PET TTV and cycle 1 SPECT TTV ( $R = 0.87$  [95% CI, 0.74–0.93],  $P < 0.001$ ) (Fig. 3). Mean TTV was similar between PSMA PET and SPECT (PET TTV,  $925 \pm 856 \text{ cm}^3$ ; SPECT TTV,  $949 \pm 852 \text{ cm}^3$ ).

The repeatability of <sup>177</sup>Lu SPECT quantitative analysis was assessed in all 32 patients. There was no evidence of a systematic difference between test and retest for SUV<sub>max</sub>, SUV<sub>mean</sub>, or TTV. The repeatability estimate was 0.99 for SUV<sub>max</sub> (95% CI, 0.97–0.99), 0.90 for SUV<sub>mean</sub> (95% CI, 0.81–0.95), and 0.99 for TTV (95% CI, 0.98–0.99) (Table 4).

### DISCUSSION

This study found that quantified changes in SPECT TTV between baseline and 12-wk <sup>177</sup>Lu-PSMA-617 predict PFS in men treated on a prospective PSMA-targeted therapy trial. To our knowledge, this was the first study to evaluate SPECT parameters for response biomarker capability, a potentially valuable development that uses a readily available tool to potentially enhance personalized treatment by directly assessing treatment response. <sup>177</sup>Lu-PSMA-617 has proven an effective therapy for mCRPC, with randomized trials demonstrating both improved overall survival and improved radiographic PFS compared with the standard of care (3), as well as increased PSA 50% response rates and improved patient-reported outcomes compared with cabazitaxel (2). However, responses can be heterogeneous, and PFS remains relatively short (2,3). Combination trials with <sup>177</sup>Lu-PSMA-617 are under way to investigate whether combining <sup>177</sup>Lu-PSMA-617 with other agents may deepen and prolong responses (NCT04419402, NCT03658447, and NCT03874884) (14).

**TABLE 3**

Univariable Analysis of Clinical and Imaging Markers and Association with PSA PFS and Overall Survival

Univariable analysis	Overall survival	PSA PFS
Increase in SPECT TTV ( $\text{m}^3$ )*	1.5 (0.6–4.1); $P = 0.40$	4.1 (1.5–11.2); $P = 0.006$
Increase in SPECT SUV <sub>max</sub> *	1.002 (0.99–1.01); $P = 0.75$	1.004 (0.99–1.02); $P = 0.51$
Increase in SPECT SUV <sub>mean</sub> *	1.11 (0.98–1.24); $P = 0.09$	1.11 (0.99–1.23); $P = 0.06$
PSA progression*	5.6 (2.1–14.8); $P < 0.001$	26.5 (5.4–131); $P < 0.001$
PSA decline $\geq 50\%$ *	0.31 (0.1–0.8); $P = 0.02$	0.40 (0.2–0.9); $P = 0.02$
Time since diagnosis	0.95 (0.88–1.03); $P = 0.18$	0.93 (0.87–1.01); $P = 0.09$

\*At week 12.

Data are hazard ratios and 95% CIs.

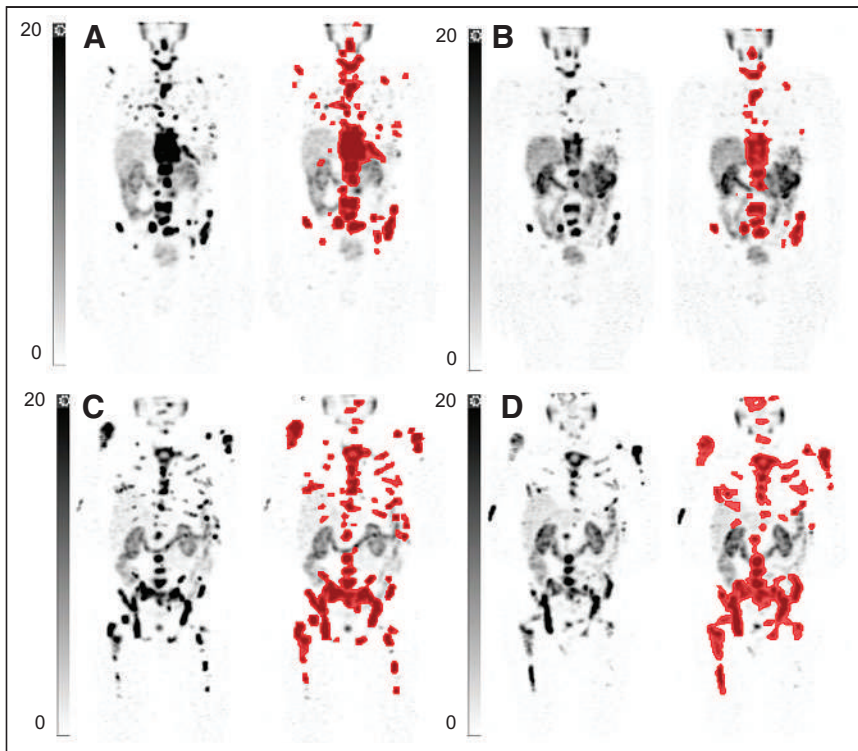


**FIGURE 2.** (A and B) Maximum-intensity projection and quantitation of  $^{177}\text{Lu}$  SPECT at cycle 1 (A) and cycle 3 (B) for patient with reduction in SPECT TTV and PSA and PSA PFS of 22 mo. (C and D) Maximum-intensity projection and quantitation of  $^{177}\text{Lu}$  SPECT at cycle 1 (C) and cycle 3 (D) for patient with increase in SPECT TTV > 30% but no increase in PSA and PSA PFS of 5 mo.

Predictive and interim response biomarkers, both imaging and genomic, will be critical in personalizing treatments to optimize longer-term responses to PSMA-targeted radionuclide therapy (5,7). Although there are limitations in spatial resolution with  $^{177}\text{Lu}$  SPECT, its elegant potential as a response biomarker warrants further evaluation. Molecular imaging as an interim response biomarker has been particularly successful in optimizing treatment responses with

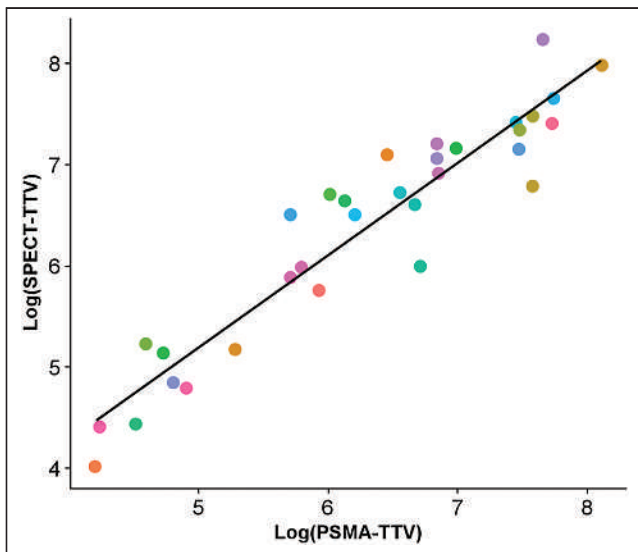


**FIGURE 3.** Scatterplot of  $\log(\text{PSMA TTV})$  at baseline vs.  $\log(\text{SPECT TTV})$  at cycle 1.

12-wk  $^{18}\text{F}$ -FDG PET in lymphoma (15–19). More recently, Gafita et al. proposed a 12-wk interim PSMA PET scan on the basis of its predictive value for early disease progression in a multicenter  $^{177}\text{Lu}$ -PSMA-617 therapy trial (RECIP 1.0) (5). Being able to identify treatment-resistant phenotypes early could allow either intensification with the addition of synergistic drugs or a change in treatment, thereby maximizing opportunities for treatment response in individuals and avoiding the clinical and financial costs of continuing futile treatment. Generally, this has been done in mCRPC by monitoring serum PSA response (20). Similarly to PSMA, there is heterogeneity of PSA expression, meaning it is not an accurate measure of disease volume in a significant proportion of men with mCRPC (21). In this study, both SPECT TTV and PSA progression were predictive of PFS. However, 21% of those in this study with no PSA progression had SPECT TTV progression. Gafita et al. had a similar finding, with 14% demonstrating PSMA PET progression before PSA progression (5). Larger numbers are required to determine whether use of SPECT TTV in combination with PSA can more effectively identify disease progression, but this study provides strong preliminary evidence, with  $^{177}\text{Lu}$  SPECT identifying progression in a subset of patients who had not yet experienced a PSA rise. These results raise the question of whether  $^{177}\text{Lu}$  SPECT or PSMA PET should be the preferred interim imaging response biomarker for  $^{177}\text{Lu}$ -PSMA-617 therapy.

Posttherapy imaging both with planar imaging and with  $^{177}\text{Lu}$  SPECT after radionuclide therapy has traditionally been used for dosimetric calculations to determine the dose to nontarget organs and tumor (22–25). Because of its significantly lower spatial resolution and inability to detect small lesions relative to PET imaging,  $^{177}\text{Lu}$  SPECT has not been considered for treatment response. In our direct comparison of quantitative findings between  $^{68}\text{Ga}$ -PSMA PET and  $^{177}\text{Lu}$  SPECT within 2 wk, TTV was very similar between  $^{177}\text{Lu}$  SPECT and PET, with a high correlation between the 2 modalities, although theoretically  $^{177}\text{Lu}$  SPECT will underestimate small-volume disease (26). However, evaluating disease progression requiring treatment change or intensification should not depend on identifying small-volume disease. A lesion that is below the spatial resolution for detection on  $^{177}\text{Lu}$  SPECT will become visible as its size increases. Although the findings from this trial confirm that  $^{177}\text{Lu}$  SPECT has potential for identifying clinically significant disease progression, the opposite may be a more difficult issue.  $^{177}\text{Lu}$  SPECT may struggle to confirm complete resolution of all sites of disease in men with exceptional responses to  $^{177}\text{Lu}$ -PSMA-617 therapy. Confirmation of an exceptional response may indeed require the spatial resolution of PSMA PET, and further research is required to more precisely define the limitations of  $^{177}\text{Lu}$  SPECT and appropriate minimal volume changes required to identify progression.

This study relied on quantitation of  $^{177}\text{Lu}$  SPECT data, rather than visual assessment, to determine an increase in TTV. It is becoming clear that assessment of treatment response using PSMA-based

**TABLE 4**  
Repeatability of <sup>177</sup>Lu SPECT Quantitation Measures

Parameter	Absolute test-retest difference	Repeatability estimate
SUV <sub>max</sub>	1.47 (−1.46 to 4.39)	0.99 (0.97–0.99); <i>P</i> < 0.001
SUV <sub>mean</sub>	−0.29 (−1.06 to 0.48)	0.90 (0.81–0.95); <i>P</i> < 0.001
Tumor volume (cm <sup>3</sup> )	34.21 (−14.62 to 83.03)	0.99 (0.98–0.99); <i>P</i> < 0.001

Data are estimate and 95% CIs.

imaging for PSMA-targeted therapy must focus on changes in volume rather than measures of intensity (27,28). Accurate visual assessment of changes in tumor volume can be difficult, especially in the presence of large-volume metastatic bone disease. We found that the repeatability of tumor volume on <sup>177</sup>Lu SPECT was high and comparable to PSMA PET/CT (29). However, quantitation remains outside routine reporting guidelines and is time-intensive. Further work is needed both to evaluate the accuracy of quantitation over visual assessment and to streamline quantitation to be more user-friendly for integration into routine clinical practice (9).

Changes in SPECT TTV were predictive of progression-free but not overall survival in this study. Although this finding may be due to the small patient cohort, it may also be due to the many patients with progressive disease on 12-wk posttherapy SPECT who were taken off trial and changed to an agent that proved effective. Further work is required to evaluate the benefit of <sup>177</sup>Lu SPECT as a prognostic biomarker.

There were several limitations to this study. First, the patient numbers were small, and a larger cohort is needed to validate these findings. This was a single-center study, and <sup>177</sup>Lu SPECT quantitative measures can vary significantly between centers and systems (30). Further evaluation is required to harmonize image acquisition and reconstruction across centers and imaging systems for results to be reproducible. Finally, appropriate volume cutoffs for a significant increase in SPECT TTV need to be defined. This will require trials with larger patient numbers and outcome data. However, this study provided a strong foundation on which to build further work.

## CONCLUSION

Increasing SPECT TTV on quantitative <sup>177</sup>Lu SPECT predicted a short PFS and identified progression in some men who had yet to demonstrate PSA progression. This tool shows promise as an imaging response biomarker.

## DISCLOSURE

This investigator-initiated study was sponsored by St. Vincent's Hospital, Sydney, and supported by a Cancer Institute NSW prostate translational research grant. Noxopharm Limited provided funding for drug and PET scans, and AAA/Novartis provided the PSMA-617 ligand. Louise Emmett has an advisory role with Noxopharm Limited, received grant funding support through St. Vincent's Clinic Foundation, and received trials support from Novartis and Astellas. Anthony Joshua has an advisory role with Noxopharm Limited and received institutional funding from Novartis. Peter Wilson and Remy Niman

are salaried employees of MIM Software, Inc. Sarennya Pathmanandavel received funding through the Cancer Institute NSW and St. Vincent's Clinic Foundation. No other potential conflict of interest relevant to this article was reported.

## ACKNOWLEDGMENTS

We thank the patients, as well as the clinical trials teams at the Department of Theranostics and Nuclear Medicine and the Kinghorn Cancer Centre, St. Vincent's Hospital, for their support.

## KEY POINTS

**QUESTION:** Do the SPECT images acquired 24 h after <sup>177</sup>Lu PSMA-617 therapy provide predictive information on patient outcomes?

**PERTINENT FINDINGS:** A change in SPECT TTV between dose 1 and dose 3 <sup>177</sup>Lu PSMA-617 is predictive of PFS.

**IMPLICATIONS FOR PATIENT CARE:** SPECT images early in treatment have the potential to predict the response to therapy, potentially allowing adjustment of treatment combinations or changes in therapy to improve patient outcomes.

## REFERENCES

- Emmett L, Crumbaker M, Ho B, et al. Results of a prospective phase 2 pilot trial of <sup>177</sup>Lu-PSMA-617 therapy for metastatic castration-resistant prostate cancer including imaging predictors of treatment response and patterns of progression. *Clin Genitourin Cancer*. 2019;17:15–22.
- Hofman MS, Emmett L, Sandhu S, et al. [<sup>177</sup>Lu]Lu-PSMA-617 versus cabazitaxel in patients with metastatic castration-resistant prostate cancer (TheraP): a randomised, open-label, phase 2 trial. *Lancet*. 2021;397:797–804.
- Sartor O, de Bono J, Chi KN, et al. Lutetium-177-PSMA-617 for metastatic castration-resistant prostate cancer. *N Engl J Med*. 2021;385:1091–1103.
- Violet J, Sandhu S, Irvani A, et al. Long-term follow-up and outcomes of retreatment in an expanded 50-patient single-center phase II prospective trial of <sup>177</sup>Lu-PSMA-617 theranostics in metastatic castration-resistant prostate cancer. *J Nucl Med*. 2020;61:857–865.
- Gafita A, Rauscher I, Weber M, et al. Novel framework for treatment response evaluation using PSMA PET/CT in patients with metastatic castration-resistant prostate cancer (RECIP 1.0): an international multicenter study. *J Nucl Med*. 2022;63:1651–1658.
- Crumbaker M, Pathmanandavel S, Yam AO, et al. Phase I/II trial of the combination of <sup>177</sup>lutetium prostate specific membrane antigen 617 and idronoxil (NOX66) in men with end-stage metastatic castration-resistant prostate cancer (LuPIN). *Eur Urol Oncol*. 2021;4:963–970.
- Pathmanandavel S, Crumbaker M, Yam AO, et al. <sup>177</sup>Lu-PSMA-617 and idronoxil in men with end-stage metastatic castration-resistant prostate cancer (LuPIN): patient outcomes and predictors of treatment response in a phase I/II trial. *J Nucl Med*. 2022;63(suppl 1):560–566.
- Scher HI, Morris MJ, Stadler WM, et al. Trial design and objectives for castration-resistant prostate cancer: updated recommendations from the prostate cancer clinical trials working group 3. *J Clin Oncol*. 2016;34:1402–1418.
- Niman R, Buteau JP, Kruzer A, Turcotte A, Nelson A. Evaluation of a semi-automated whole body PET segmentation method applied to diffuse large B cell lymphoma [abstract]. *J Nucl Med*. 2018;59(suppl 1):592.
- Eisenhauer EA, Therasse P, Bogaerts J, et al. New response evaluation criteria in solid tumours: revised RECIST guideline (version 1.1). *Eur J Cancer*. 2009;45:228–247.
- Halabi S, Lin CY, Kelly WK, et al. Updated prognostic model for predicting overall survival in first-line chemotherapy for patients with metastatic castration-resistant prostate cancer. *J Clin Oncol*. 2014;32:671–677.
- Gafita A, Calais J, Grogan TR, et al. Nomograms to predict outcomes after <sup>177</sup>Lu-PSMA therapy in men with metastatic castration-resistant prostate cancer: an international, multicentre, retrospective study. *Lancet Oncol*. 2021;22:1115–1125.
- Stoffel MA, Nakagawa S, Schielzeth H, Goslee S. rptR: repeatability estimation and variance decomposition by generalized linear mixed-effects models. *Methods Ecol Evol*. 2017;8:1639–1644.

14. Emmett L, Subramaniam S, Joshua AM, et al. ENZA-p trial protocol: a randomized phase II trial using prostate-specific membrane antigen as a therapeutic target and prognostic indicator in men with metastatic castration-resistant prostate cancer treated with enzalutamide (ANZUP 1901). *BJU Int.* 2021;128:642–651.
15. Gallamini A, Barrington SF, Biggi A, et al. The predictive role of interim positron emission tomography for Hodgkin lymphoma treatment outcome is confirmed using the interpretation criteria of the Deauville five-point scale. *Haematologica.* 2014;99:1107–1113.
16. Eertink JJ, Burggraaff CN, Heymans MW, et al. Optimal timing and criteria of interim PET in DLBCL: a comparative study of 1692 patients. *Blood Adv.* 2021;5:2375–2384.
17. Radford J, Illidge T, Counsell N, et al. Results of a trial of PET-directed therapy for early-stage Hodgkin's lymphoma. *N Engl J Med.* 2015;372:1598–1607.
18. Borchmann P, Goergen H, Kobe C, et al. PET-guided treatment in patients with advanced-stage Hodgkin's lymphoma (HD18): final results of an open-label, international, randomised phase 3 trial by the German Hodgkin Study Group. *Lancet.* 2017;390:2790–2802.
19. Johnson P, Federico M, Kirkwood A, et al. Adapted treatment guided by interim PET-CT scan in advanced Hodgkin's lymphoma. *N Engl J Med.* 2016;374:2419–2429.
20. Halabi S, Vogelzang NJ, Ou S-S, Owzar K, Archer L, Small EJ. Progression-free survival as a predictor of overall survival in men with castrate-resistant prostate cancer. *J Clin Oncol.* 2009;27:2766–2771.
21. Balk SP, Ko YJ, Bubley GJ. Biology of prostate-specific antigen. *J Clin Oncol.* 2003;21:383–391.
22. Fendler WP, Reinhardt S, Ilhan H, et al. Preliminary experience with dosimetry, response and patient reported outcome after <sup>177</sup>Lu-PSMA-617 therapy for metastatic castration-resistant prostate cancer. *Oncotarget.* 2017;8:3581–3590.
23. Jackson PA, Hofman MS, Hicks RJ, Scalzo M, Violet J. Radiation dosimetry in <sup>177</sup>Lu-PSMA-617 therapy using a single posttreatment SPECT/CT scan: a novel methodology to generate time- and tissue-specific dose factors. *J Nucl Med.* 2020; 61:1030–1036.
24. Violet J, Jackson P, Ferdinandus J, et al. Dosimetry of <sup>177</sup>Lu-PSMA-617 in metastatic castration-resistant prostate cancer: correlations between pretherapeutic imaging and whole-body tumor dosimetry with treatment outcomes. *J Nucl Med.* 2019;60:517–523.
25. Yadav MP, Ballal S, Tripathi M, et al. Post-therapeutic dosimetry of <sup>177</sup>Lu-DKFZ-PSMA-617 in the treatment of patients with metastatic castration-resistant prostate cancer. *Nucl Med Commun.* 2017;38:91–98.
26. Khalil MM, Tremoleda JL, Bayomy TB, Gsell W. Molecular SPECT imaging: an overview. *Int J Mol Imaging.* 2011;2011:796025.
27. Kurth J, Kretzschmar J, Aladwan H, et al. Evaluation of [<sup>68</sup>Ga]Ga-PSMA PET/CT for therapy response assessment of [<sup>177</sup>Lu]Lu-PSMA radioligand therapy in metastasized castration refractory prostate cancer and correlation with survival. *Nucl Med Commun.* 2021;42:1217–1226.
28. Grubmüller B, Senn D, Kramer G, et al. Response assessment using <sup>68</sup>Ga-PSMA ligand PET in patients undergoing <sup>177</sup>Lu-PSMA radioligand therapy for metastatic castration-resistant prostate cancer. *Eur J Nucl Med Mol Imaging.* 2019;46: 1063–1072.
29. Seifert R, Sandach P, Kersting D, et al. Repeatability of <sup>68</sup>Ga-PSMA-HBED-CC PET/CT-derived total molecular tumor volume. *J Nucl Med.* 2022;63:746–753.
30. Peters SMB, Meyer Viol SL, van der Werf NR, et al. Variability in lutetium-177 SPECT quantification between different state-of-the-art SPECT/CT systems. *EJNMMI Phys.* 2020;7:9.

---

---

# Eligibility for $^{177}\text{Lu}$ -PSMA Therapy Depends on the Choice of Companion Diagnostic Tracer: A Comparison of $^{68}\text{Ga}$ -PSMA-11 and $^{99\text{m}}\text{Tc}$ -MIP-1404 in Metastatic Castration-Resistant Prostate Cancer

Gary J.R. Cook<sup>1</sup>, Wai-Lup Wong<sup>2</sup>, Bal Sanghera<sup>2</sup>, Stephen Mangar<sup>3</sup>, Amarnath Challapalli<sup>4</sup>, Amit Bahl<sup>4</sup>, Paul Bassett<sup>5</sup>, Darren Leaning<sup>6</sup>, and Christian Schmidkonz<sup>7,8</sup>

<sup>1</sup>Cancer Imaging Department, School of Biomedical Engineering and Imaging Sciences, King's College London, London, United Kingdom; <sup>2</sup>Paul Strickland Scanner Centre, Mount Vernon Hospital, Northwood, Northwood, United Kingdom; <sup>3</sup>Department of Oncology, Charing Cross Hospital, Imperial College Healthcare NHS Trust, London, United Kingdom; <sup>4</sup>Department of Clinical Oncology, Bristol Cancer Institute, Bristol, United Kingdom; <sup>5</sup>Statsconsultancy Ltd, Amersham, United Kingdom; <sup>6</sup>Department of Clinical Oncology, James Cook University Hospital, South Tees NHS Trust, Middlesbrough, United Kingdom; <sup>7</sup>Department of Nuclear Medicine, University Hospital Erlangen, Erlangen, Germany; and <sup>8</sup>Department of Industrial Engineering and Health, Technical University of Applied Sciences Amberg-Weiden, Weiden, Germany

$^{177}\text{Lu}$ -prostate-specific membrane antigen-617 ( $^{177}\text{Lu}$ -PSMA-617) is an effective therapy for metastatic castration-resistant prostate cancer (mCRPC), with evidence of improved survival over standard care. The VISION trial inclusion criteria required a metastatic lesion-to-liver ratio of greater than 1 on  $^{68}\text{Ga}$ -PSMA-11 PET scans. We aimed to determine whether an equivalent ratio is suitable for a SPECT tracer,  $^{99\text{m}}\text{Tc}$ -MIP-1404, and to compare lesion and lesion-to-normal-organ ratios between the 2 radiotracers. **Methods:** Two cohorts of patients with mCRPC matched for age, prostate-specific antigen level, and total Gleason score, with either  $^{99\text{m}}\text{Tc}$ -MIP-1404 SPECT/CT ( $n = 25$ ) or  $^{68}\text{Ga}$ -PSMA-11 PET/CT ( $n = 25$ ) scans, were included for analysis. Up to 3 lesions in each site (prostate/prostate bed, lymph nodes, bone and soft-tissue metastases) as well as normal liver, parotid gland, spleen, and mediastinal blood-pool  $\text{SUV}_{\text{max}}$  were measured. **Results:**  $^{99\text{m}}\text{Tc}$ -MIP-1404 SPECT lesion  $\text{SUV}_{\text{max}}$  was not significantly different from  $^{68}\text{Ga}$ -PSMA-11 PET (median, 18.2 vs. 17.3;  $P = 0.93$ ). However,  $^{99\text{m}}\text{Tc}$ -MIP-1404 liver  $\text{SUV}_{\text{max}}$  was higher (median, 8.5 vs. 5.8;  $P = 0.002$ ) and lesion-to-liver ratios were lower (median, 2.7 vs. 3.5;  $P = 0.009$ ). There was no significant difference in parotid gland or splenic  $\text{SUV}_{\text{max}}$  or lesion-to-parotid gland ratios between the 2 tracers although there was a small difference in lesion-to-spleen ratios ( $P = 0.034$ ). **Conclusion:** There are differences in biodistribution and, in particular, liver activity, between  $^{68}\text{Ga}$ -PSMA-11 and  $^{99\text{m}}\text{Tc}$ -MIP-1404. Therefore, if  $^{99\text{m}}\text{Tc}$ -MIP-1404 is used to assess eligibility for  $^{177}\text{Lu}$ -PSMA-617 therapy, a lower adjusted lesion-to-liver ratio should be used.

**Key Words:**  $^{177}\text{Lu}$ -PSMA-617;  $^{68}\text{Ga}$ -PSMA-11;  $^{99\text{m}}\text{Tc}$ -MIP-1404

**J Nucl Med 2023; 64:227–231**

DOI: 10.2967/jnumed.122.264296

The therapeutic options for metastatic castration resistant prostate cancer (mCRPC) are rapidly expanding, especially in the area of targeted radionuclide therapy. In particular, exploiting prostate-specific membrane antigen (PSMA) overexpression in metastatic disease is an appealing option for targeted therapy (1). The recently reported VISION trial confirmed an improvement in progression-free survival and overall survival after treatment with radiolabeled PSMA therapy,  $^{177}\text{Lu}$ -PSMA-617 (2). In keeping with optimal practice and the principles of theranostics, and given the knowledge that some prostate cancers do not express PSMA, target expression was mandated by  $^{68}\text{Ga}$ -PSMA-11 PET imaging as an inclusion criterion (3). Specifically, the trial required at least 1 PSMA-positive metastasis, defined as uptake greater than liver with no PSMA-negative lesion (uptake  $\leq$  liver) in any measurable metastasis (lymph node  $> 2.5$  cm, solid organ  $> 1.0$  cm, bone  $> 1.0$  cm soft-tissue component). In the trial, 126 of 995 subjects did not meet imaging criteria.

The inclusion criteria were based on pragmatic reasons, including the widespread use and availability of  $^{68}\text{Ga}$ -PSMA-11 (2,3) and that screen failures were subsequently shown to have worse outcomes (4).

As eligibility for  $^{177}\text{Lu}$ -PSMA-617 therapy requires only a binary decision depending on the level of lesion uptake rather than requiring maximal sensitivity for lesion detection, several alternative PET and SPECT PSMA ligands exist that could potentially be used to confirm metastatic PSMA expression, some of which may be less costly or more readily available and accessible in different geographic areas of the world. These include other  $^{68}\text{Ga}$ -,  $^{18}\text{F}$ -, and  $^{99\text{m}}\text{Tc}$ -labeled ligands that have demonstrated utility in detection of PSMA-expressing metastases in prostate cancer (5–12). For example,  $^{99\text{m}}\text{Tc}$ -MIP-1404 has shown efficacy in patients with intermediate- and high-risk prostate cancer undergoing prostatectomy and extended pelvic lymph node dissection (5) and has favorable radiation dosimetry (0.0088 mSv/MBq) compared with  $^{68}\text{Ga}$ -PSMA-11 (0.022 mSv/MBq) (13,14). However, these ligands have biodistributions different from  $^{68}\text{Ga}$ -PSMA-11, and particularly in those where biliary rather than renal excretion predominates, the use of a

---

Received May 20, 2022; revision accepted Aug. 11, 2022.

For correspondence or reprints, contact Gary J.R. Cook (gary.cook@kcl.ac.uk).

Published online Oct. 27, 2022.

Immediate Open Access: Creative Commons Attribution 4.0 International License (CC BY) allows users to share and adapt with attribution, excluding materials credited to previous publications. License: <https://creativecommons.org/licenses/by/4.0/>. Details: <http://jnm.snmjournals.org/site/misc/permission.xhtml>.

COPYRIGHT © 2023 by the Society of Nuclear Medicine and Molecular Imaging.

lesion- to-liver ratio of greater than 1 may deny patients access to <sup>177</sup>Lu-PSMA-617 treatment when <sup>68</sup>Ga-PSMA-11 would have confirmed eligibility. There is therefore a need to determine appropriate quantitative criteria for different PSMA ligands to ensure equity of eligibility to <sup>177</sup>Lu-PSMA-617 therapy.

Our aim was to compare the biodistributions of <sup>68</sup>Ga-PSMA-11 and <sup>99m</sup>Tc-MIP-1404 (ROTOP Pharmaka GmbH) in metastases and potential reference organs in matched cohorts of patients with mCRPC. Our hypothesis was that differences in biodistributions would be present, requiring an appropriate equivalent metric for <sup>99m</sup>Tc-MIP-1404 to define treatment eligibility.

## MATERIALS AND METHODS

Institutional approval was acquired for analysis of anonymized retrospective data without the need for further consent. Two cohorts of 25 consecutive patients who had undergone <sup>68</sup>Ga-PSMA-11 PET/CT or <sup>99m</sup>Tc-MIP-1404 SPECT/CT scans were included in the analysis. Inclusion criteria were CRPC with metastatic disease being considered for systemic therapy including <sup>177</sup>Lu-PSMA-617. Patients were excluded if they did not have mCRPC or information on a prostate-specific antigen (PSA) level within 1 mo of the PSMA scan or no history of the original Gleason score. Age, PSA level closest to the time of scanning, and original Gleason score data were collected.

### <sup>68</sup>Ga-PSMA-11 PET/CT Scan

No specific patient preparation was required except bladder voiding immediately before imaging. All patients were injected intravenously with <sup>68</sup>Ga-PSMA-11 (mean, 169.6 ± 16.5 MBq). At 60 min, a scan was acquired from pelvis to skull base at 4 min per bed position with an axial field of view of 15.7 cm and an 11-slice overlap between bed positions, using a Discovery 710 PET/CT scanner (GE Healthcare). A low-dose CT scan (140 kV; mAs, 15–100; noise index, 40; rotation time, 0.5 s; and collimation, 40 mm) was obtained at the start of imaging to provide attenuation correction and an anatomic reference. PET image reconstruction used a Bayesian penalized likelihood algorithm (Q.CLEAR; GE Healthcare) with a β penalization factor of 800 as previously described (15,16).

### <sup>99m</sup>Tc-MIP-1404 SPECT/CT Scan

No specific patient preparation was required except bladder voiding immediately before imaging. All patients were injected intravenously with <sup>99m</sup>Tc-MIP-1404 (mean 705 ± 61 MBq). At 2–4 h, SPECT scans were acquired on a Symbia T2 SPECT/CT system (Siemens Healthcare) from midhigh to skull vertex with low-energy high-resolution collimation, a 128 × 128 matrix with 4.8-mm pixel size, and 120 projections over 360° for 15 s per projection. SPECT scans were followed by low-dose CT (130 kV, 30 mAs) using adaptive dose modulation (CAREdose 4D; Siemens Healthcare). CT data were reconstructed with 3- and 5-mm slice thicknesses using B70s and B41s kernels for image analysis. The SPECT dataset was reconstructed using an ordered-subset expectation maximization algorithm with 4 subsets and 8 iterations, including point-spread-function modeling with CT-based attenuation correction and dual-energy window scatter correction as previously described (10). Both PET and SPECT scanners underwent routine quality control measures.

### Scan Analysis

For each subject, SUV<sub>max</sub> was measured in any malignant lesion in the prostate or prostate bed and up to 3 lesions in each of pelvic nodes (N1), extrapelvic nodes (M1a), and skeletal (M1b) and visceral metastases (M1c) using Hermes Gold software (Hermes Medical Solution). A semiquantitative expression score was measured by comparison to normal tissues including the mediastinal blood pool (MBP), liver, spleen,

and parotid glands, according to the PROMISE proposed classification for PSMA ligand PET/CT interpretation (17). For the liver, a 3-cm spheric volume of interest was placed in the center of the right lobe avoiding metastases if present, with 2-cm volumes of interest used for spleen, MBP (aortic arch), and parotid glands. SUV<sub>max</sub> was calculated for each. For each malignant lesion, a lesion-to-liver, lesion-to-spleen, lesion-to-blood-pool, and lesion-to-parotid gland ratio was calculated.

## Statistical Analysis

Statistical analyses were performed using SPSS (version 27; IBM Corp). Data were tested for normality, and comparisons made with either the *t* test or the Mann–Whitney test and values presented as mean ± SD or median and range accordingly. A *P* value of < 0.05 was taken for statistical significance.

## RESULTS

The <sup>99m</sup>Tc-MIP-1404 group and the <sup>68</sup>Ga-PSMA-11 group of mCRPC patients were matched for age (median, 72 and 71 y, respectively), PSA level (mean, 413.4 and 415.6 ng/mL, respectively), and Gleason score (median, 9 and 9, respectively). The previous rates of androgen deprivation therapy and other local or systemic therapies (except prostatectomy rate) were also similar between the 2 groups (Table 1). The 2 groups showed a similar distribution of metastatic disease on either <sup>99m</sup>Tc-MIP-1404 SPECT or <sup>68</sup>Ga-PSMA-11 PET in the prostate/prostate bed (7 and 10 patients, respectively), N1 (8 and 13 patients, respectively), M1a (8 and 9 patients, respectively), M1b (23 and 23 patients, respectively), and M1c (4 and 4 patients, respectively).

Lesion SUV<sub>max</sub> measurements were not statistically different between the 2 groups (median, 18.2, range, 4.1–52.1 for the <sup>99m</sup>Tc-MIP-1404 group; and median, 17.3, range, 3.4–128 for the

**TABLE 1**  
Characteristics in <sup>99m</sup>Tc-MIP-1404 and <sup>68</sup>Ga-PSMA-11 Groups

Characteristic	<sup>99m</sup> Tc-MIP-1404	<sup>68</sup> Ga-PSMA-11
Median age (y)	72 (range, 62–91)	71 (range, 54–84)
Median Gleason score	9 (SD, 8–9)	9 (SD, 7–9)
Mean PSA	413.6 (SD, 581.6)	415.6 (SD, 1,101.7)
Prior ADT	24	25
Current ADT	6	8
Prior prostatectomy	14	4
Prior prostate radiotherapy	13	13
Prior chemotherapy	20	15
miTNM		
Prostate	7	10
N1	8	13
M1a	8	8
M1b	23	23
M1c	3	4

ADT = androgen deprivation therapy; miTNM = molecular imaging tumor, node and metastasis staging.



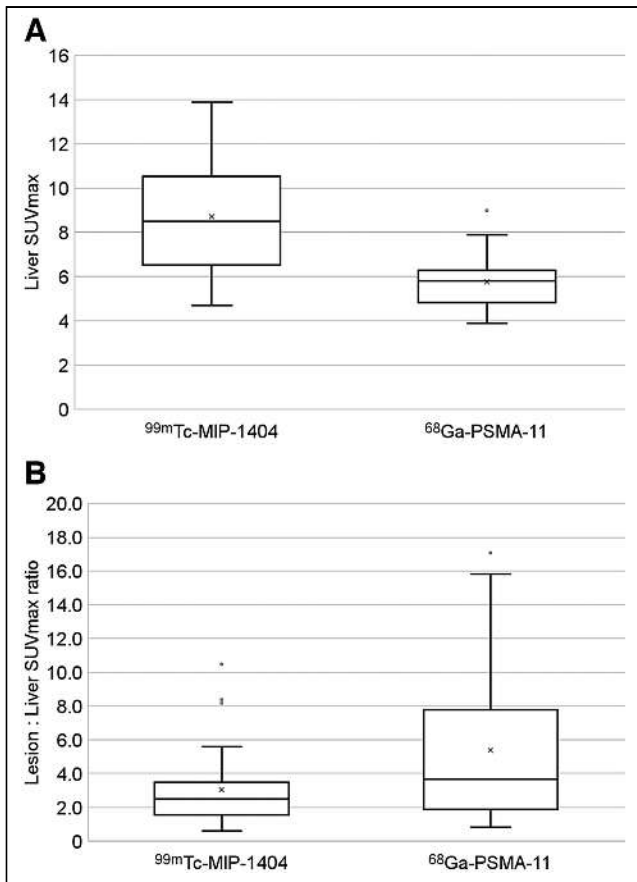


**FIGURE 1.** Box plots of  $^{99m}\text{Tc}$ -MIP-1404 and  $^{68}\text{Ga}$ -PSMA-11 liver  $\text{SUV}_{\text{max}}$  ( $P = 0.002$ ) (A) and lesion-to-liver  $\text{SUV}_{\text{max}}$  ratios ( $P = 0.009$ ) (B) in patients with mCRPC. median = central line; mean = X; box = interquartile range (IQR); whiskers = maximum and minimum values;  $\circ$  = outliers  $> 1.5$  IQR.

$^{68}\text{Ga}$ -PSMA-11 group;  $P = 0.93$ ). However, liver  $\text{SUV}_{\text{max}}$  was higher in the  $^{99m}\text{Tc}$ -MIP-1404 scans (median, 8.5, range, 4.7–13.9 for the  $^{99m}\text{Tc}$ -MIP-1404 group; and median, 5.8, range, 3.9–9.0 for

the  $^{68}\text{Ga}$ -PSMA-11 group;  $P = 0.002$ ) (Fig. 1A). Lesion-to-liver ratios were lower in the  $^{99m}\text{Tc}$ -MIP-1404 group (median 2.5, range 0.6–10.5 for the  $^{99m}\text{Tc}$ -MIP-1404 group; and median, 3.7, range, 0.8–17.1 for the  $^{68}\text{Ga}$ -PSMA-11 group;  $P = 0.009$ ) (Fig. 1B). Lesion-to-liver ratios of  $^{99m}\text{Tc}$ -MIP-1404 SPECT were on average 57% of those with  $^{68}\text{Ga}$ -PSMA-11 PET.

There was no significant difference in parotid gland  $\text{SUV}_{\text{max}}$  between the  $^{99m}\text{Tc}$ -MIP-1404 and the  $^{68}\text{Ga}$ -PSMA-11 group (mean,  $13.4 \pm 7.1$  and  $16.8 \pm 6.4$ , respectively;  $P = 0.23$ ) or lesion-to-parotid gland ratios (median, 1.8, range, 0.3–6.4; and median, 1.4, range, 0.3–7.0, respectively;  $P = 0.5$ ). Similarly, there was no difference between spleen  $\text{SUV}_{\text{max}}$  (median, 11.5, range, 5.4–22.5; and median, 9.3, range, 4.9–16.0, respectively;  $P = 0.072$ ), but there was a small difference in lesion-to-spleen ratios (median, 1.4, range, 0.3–6.1; and median, 2.0, range, 0.4–14.9, respectively;  $P = 0.034$ ). There was a difference between MBP  $\text{SUV}_{\text{max}}$  measurements (mean,  $1.1 \pm 0.3$  and  $1.6 \pm 0.3$ , respectively;  $P = 0.003$ ) and lesion-to-MBP ratios (median, 19.9, range, 3.8–114.5; and median, 13.5, range, 2.7–57.6, respectively;  $P = 0.011$ ) (Table 2).

## DISCUSSION

Although we have not measured a difference in lesion avidity between  $^{99m}\text{Tc}$ -MIP-1404 SPECT and  $^{68}\text{Ga}$ -PSMA-11 PET PSMA ligands in patients with mCRPC, there are differences in biodistribution. In particular, liver activity and hence lesion-to-liver ratios differ between the 2 tracers with higher liver uptake but lower lesion-to-liver ratios with  $^{99m}\text{Tc}$ -MIP-1404 SPECT. This is potentially of importance as the eligibility for  $^{177}\text{Lu}$ -PSMA-617 therapy in the VISION trial depended on a lesion-to-liver ratio greater than 1 using  $^{68}\text{Ga}$ -PSMA-11 (2,3). Another phase 2 study used a lesion-to-liver ratio of 1.5 and absence of  $^{18}\text{F}$ -FDG-positive and  $^{68}\text{Ga}$ -PSMA-11-negative lesions to determine eligibility (18).

Different eligibility criteria would therefore need to be considered for different PSMA ligands so that patients are not deemed ineligible from treatment when they may benefit if confirmation of PSMA expression at all metastatic sites is mandated by reimbursement guidelines before treatment.

**TABLE 2**

Lesion, Normal-Organ (Liver, Spleen, Parotid Gland, MBP), and Lesion-to-Normal-Organ Ratios Between  $^{99m}\text{Tc}$ -MIP-1404 and  $^{68}\text{Ga}$ -PSMA-11 mCRPC Patients

Parameter	$^{99m}\text{Tc}$ -MIP-1404		$^{68}\text{Ga}$ -PSMA-11		<i>P</i>
	Median	Mean $\pm$ SD	Median	Mean $\pm$ SD	
Lesion $\text{SUV}_{\text{max}}$	18.2 (4.1–52.1)		17.3 (3.4–128.0)		0.93
Liver $\text{SUV}_{\text{max}}$	8.5 (4.7–13.9)		5.8 (3.9–9.0)		0.002
Lesion-to-liver $\text{SUV}_{\text{max}}$ ratio	2.5 (0.6–10.0)		3.7 (0.8–17.1)		0.009
Parotid gland $\text{SUV}_{\text{max}}$		$13.4 \pm 7.1$		$16.8 \pm 6.4$	0.23
Lesion-to-parotid gland $\text{SUV}_{\text{max}}$ ratio	1.8 (0.3–6.4)		1.4 (0.3–7.0)		0.5
Spleen $\text{SUV}_{\text{max}}$	11.5 (5.4–22.5)		9.3 (4.9–16.0)		0.072
Lesion-to-spleen $\text{SUV}_{\text{max}}$ ratio	1.4 (0.3–6.1)		2.0 (0.4–14.9)		0.034
MBP $\text{SUV}_{\text{max}}$		$1.1 \pm 0.3$		$1.6 \pm 0.3$	0.003
Lesion-to-MBP $\text{SUV}_{\text{max}}$ ratio	19.9 (3.8–114.5)		13.5 (2.7–57.6)		0.011

Data in parentheses are ranges.

Although the predominant renal excretion route of  $^{99m}\text{Tc}$ -MIP-1404 is not dissimilar to that of  $^{68}\text{Ga}$ -PSMA-11 (10), there appear to be sufficient differences to provide variation in lesion-to-liver ratios between the 2 tracers. This is probably even more relevant for other PSMA ligands that have a predominant hepatobiliary route of excretion such as  $^{18}\text{F}$ -PSMA-1007, for which liver  $\text{SUV}_{\text{max}}$  has been shown to be more than double that of  $^{68}\text{Ga}$ -PSMA-11 in a comparative study (8). We found the mean  $^{99m}\text{Tc}$ -MIP-1404 lesion-to-liver ratio to be 57% of that of  $^{68}\text{Ga}$ -PSMA-11, suggesting that a correspondingly lower lesion-to-liver ratio would be required to achieve equitable eligibility for  $^{177}\text{Lu}$ -PSMA-617 therapy if applying the VISION trial, or other previously reported, eligibility criteria (2,18). Although an optimal level of lesion uptake has not been defined for  $^{177}\text{Lu}$ -PSMA-617 efficacy, it is generally accepted that a theranostic pair is required to ensure targetable disease and to avoid futile therapy in the minority of patients with non-PSMA-expressing disease (4,11).

To standardize PSMA ligand PET reporting, it has been suggested that uptake in metastatic lesions should be graded by comparison to blood pool, liver, or parotid gland (or spleen in liver-dominant excretion ligands) (17). We have therefore measured uptake in these organs in our series. Our results compare closely with another published series of  $^{68}\text{Ga}$ -PSMA-11 with respect to liver, spleen, and parotid gland  $\text{SUV}_{\text{max}}$  measurements with a small difference in blood-pool values, possibly due to methodologic differences in measurement of the latter (6). Interestingly, the  $^{99m}\text{Tc}$ -MIP-1404 ligand shows no significant difference from  $^{68}\text{Ga}$ -PSMA-11 with respect to lesion uptake, parotid gland uptake, lesion-to-parotid gland ratio, spleen, and lesion-to-MBP ratios. Apart from the previously mentioned lesion-to-liver ratio differences, lesion-to-spleen ratios and MBP  $\text{SUV}_{\text{max}}$  were lower for  $^{99m}\text{Tc}$ -MIP-1404, reflecting differences in biodistribution and pharmacokinetics of the 2 PSMA ligands. We also noted higher variability in splenic and parotid gland uptake between patients for both tracers compared with liver  $\text{SUV}_{\text{max}}$ , suggesting these organs may be less suitable than the liver as semiquantitative comparators. Rather than using a liver threshold, other studies have used a lesion  $\text{SUV}_{\text{max}}$  of 20 as an eligibility criterion (19,20), and it is possible that this would present an effective alternative treatment threshold. Indeed, our data show a similar  $\text{SUV}_{\text{max}}$  between  $^{99m}\text{Tc}$ -MIP-1404 and  $^{68}\text{Ga}$ -PSMA-11 (Table 2), but further work would be required to determine comparable lesion avidity in other PSMA tracers.

Our analysis has some limitations. First, the 2 types of PSMA scan were not performed in the same patients. Nevertheless, both the groups analyzed included patients with mCRPC who would potentially be eligible for  $^{177}\text{Lu}$ -PSMA-617 therapy and were reasonably well matched for age, PSA level, Gleason score, and other relevant characteristics. However, perfect matching is unlikely and a study of both scans in the same patients, or a study evaluating  $^{68}\text{Ga}$ -PSMA-11 uptake in  $^{99m}\text{Tc}$ -MIP-1404-negative patients, would provide more robust data. Second, not all of the patients in our cohorts received  $^{177}\text{Lu}$ -PSMA-617 therapy and so we do not know if potential differences in eligibility for therapy would have had an impact on clinical outcomes. In addition, we cannot exclude systematic differences in SUV calculation between the SPECT and PET modalities, weakening a comparison of  $\text{SUV}_{\text{max}}$  between lesions and organs in the 2 cohorts. However, the ratios that we measured would not be significantly affected by systematic differences.

## CONCLUSION

There are differences in biodistribution between  $^{99m}\text{Tc}$ -MIP-1404 and  $^{68}\text{Ga}$ -PSMA-11 in patients with mCRPC who might be

eligible for  $^{177}\text{Lu}$ -PSMA-617 therapy such that different semi-quantitative criteria may need to be adopted for different ligands if lesion-to-liver ratios are the main parameter under consideration. This is likely to be even more important for PSMA ligands that are predominantly excreted via the hepatobiliary route. Prospective analysis of the optimal imaging metrics to predict treatment outcomes will be an important goal in future trials, particularly if SPECT agents that offer increased availability and access with reduced costs are used.

## DISCLOSURE

Financial support was provided by the following: Cancer Research U.K. National Cancer Imaging Translational Accelerator (A27066), the Wellcome/Engineering and Physical Sciences Research Council Centre for Medical Engineering at King's College London (WT 203148/Z/16/Z), and National Institute for Health Research Biomedical Research Centre at Guy's & St Thomas' Hospitals and King's College London. No other potential conflict of interest relevant to this article was reported.

## KEY POINTS

**QUESTION:** Can differences in PSMA imaging tracer biodistribution affect selection of patients for  $^{177}\text{Lu}$ -PSMA-617 therapy if lesion-to-liver ratios are used for treatment selection?

**PERTINENT FINDINGS:** This comparison of retrospective matched  $^{68}\text{Ga}$ -PSMA-11 PET and  $^{99m}\text{Tc}$ -MIP-1404 SPECT data in 2 cohorts of 25 patients with mCRPC has shown differences in biodistribution that led to greater liver activity but lower lesion-to-liver ratios for  $^{99m}\text{Tc}$ -MIP-1404.

**IMPLICATIONS FOR PATIENT CARE:** Different semiquantitative data may be required for different PSMA imaging tracers used as companion diagnostics to ensure equal eligibility for  $^{177}\text{Lu}$ -PSMA-617 therapy in mCRPC.

## REFERENCES

1. Bois F, Noirot C, Dietemann S, et al. [ $^{68}\text{Ga}$ ]Ga-PSMA-11 in prostate cancer: a comprehensive review. *Am J Nucl Med Mol Imaging*. 2020;10:349–374.
2. Sartor O, de Bono J, Chi KN, et al. Lutetium-177-PSMA-617 for metastatic castration-resistant prostate cancer. *N Engl J Med*. 2021;385:1091–1103.
3. Kuo PH, Benson T, Messmann R, Groaning M. Why we did what we did: PSMA-PET/CT selection criteria for the VISION Trial. *J Nucl Med*. 2022;63:816–818.
4. Gafita A, Calais J, Grogan TR, et al. Nomograms to predict outcomes after  $^{177}\text{Lu}$ -PSMA therapy in men with metastatic castration-resistant prostate cancer: an international, multicentre, retrospective study. *Lancet Oncol*. 2021;22:1115–1125.
5. Goffin KE, Joniau S, Tenke P, et al. Phase 2 study of  $^{99m}\text{Tc}$ -Trofolastat SPECT/CT to identify and localize prostate cancer in intermediate- and high-risk patients undergoing radical prostatectomy and extended pelvic LN dissection. *J Nucl Med*. 2017;58:1408–1413.
6. Kalshetty A, Menon B, Rakshit S, et al. Correlation of lesional uptake parameters and ratios with miPSMA score and estimating normal physiologic concentration: an exploratory analysis in metastatic castration-resistant prostatic carcinoma patients with  $^{68}\text{Ga}$ -PSMA-11 PET/CT. *J Nucl Med Technol*. 2021;49:235–240.
7. Peters SMB, Hofferber R, Privé BM, et al. [ $^{68}\text{Ga}$ ]Ga-PSMA-11 PET imaging as a predictor for absorbed doses in organs at risk and small lesions in [ $^{177}\text{Lu}$ ]Lu-PSMA-617 treatment. *Eur J Nucl Med Mol Imaging*. 2022;49:1101–1112.
8. Pattison DA, Debowski M, Gulhane B, et al. Prospective intra-individual blinded comparison of [ $^{18}\text{F}$ ]PSMA-1007 and [ $^{68}\text{Ga}$ ]Ga-PSMA-11 PET/CT imaging in

- patients with confirmed prostate cancer. *Eur J Nucl Med Mol Imaging*. 2022;49:763–776.
9. Metser U, Zukotynski K, Mak V, et al. Effect of  $^{18}\text{F}$ -DCFPyL PET/CT on the management of patients with recurrent prostate cancer: results of a prospective multi-center registry trial. *Radiology*. 2022;303:414–422.
  10. Schmidkonz C, Hollweg C, Beck M, et al.  $^{99\text{m}}\text{Tc}$ -MIP-1404-SPECT/CT for the detection of PSMA-positive lesions in 225 patients with biochemical recurrence of prostate cancer. *Prostate*. 2018;78:54–63.
  11. Sheikh N, Younis MN, Mumtaz M, Shahid A. Tc-99m PSMA and Lu-177 PSMA theranostic pair in a patient of metastatic castration resistant prostate cancer. *JPMA J Pak Med Assoc*. 2021;71:2679–2682.
  12. Hillier SM, Maresca KP, Lu G, et al.  $^{99\text{m}}\text{Tc}$ -labeled small-molecule inhibitors of prostate-specific membrane antigen for molecular imaging of prostate cancer. *J Nucl Med*. 2013;54:1369–1376.
  13. Vallabhajosula S, Nikolopoulou A, Babich JW, et al.  $^{99\text{m}}\text{Tc}$ -labeled small-molecule inhibitors of prostate-specific membrane antigen: pharmacokinetics and biodistribution studies in healthy subjects and patients with metastatic prostate cancer. *J Nucl Med*. 2014;55:1791–1798.
  14. Sandgren K, Johansson L, Axelsson J, et al. Radiation dosimetry of [ $^{68}\text{Ga}$ ]PSMA-11 in low-risk prostate cancer patients. *EJNMMI Phys*. 2019;6:2.
  15. Chuah SJ, Kulkarni M, Pike L, et al. Bayesian penalised likelihood (“Q-clear”) reconstruction of  $^{68}\text{Ga}$ -THP-PSMA PET/CT in prostate cancer: a comparison with standard image reconstruction methods. *Nucl Med Commun*. 2019;40:416–417.
  16. Krokos G, Pike LC, Cook GJR, Marsden PK. Standardisation of conventional and advanced iterative reconstruction methods for gallium-68 multi-centre PET-CT trials. *EJNMMI Phys*. 2021;8:52.
  17. Eiber M, Herrmann K, Calais J, et al. Prostate cancer molecular imaging standardized evaluation (PROMISE): proposed miTNM classification for the interpretation of PSMA-ligand PET/CT. *J Nucl Med*. 2018;59:469–478.
  18. Hofman MS, Violet J, Hicks RJ, et al. [ $^{177}\text{Lu}$ ]-PSMA-617 radionuclide treatment in patients with metastatic castration-resistant prostate cancer (LuPSMA trial): a single-centre, single-arm, phase 2 study. *Lancet Oncol*. 2018;19:825–833.
  19. Hofman MS, Emmett L, Violet J, et al. ANZUP TheraP team, Davis ID. TheraP: a randomized phase 2 trial of  $^{177}\text{Lu}$ -PSMA-617 theranostic treatment vs cabazitaxel in progressive metastatic castration-resistant prostate cancer (Clinical Trial Protocol ANZUP 1603). *BJU Int*. 2019;124(suppl 1):5–13.
  20. Dhiantravan N, Emmett L, Joshua AM, et al. UpFrontPSMA: a randomized phase 2 study of sequential  $^{177}\text{Lu}$ -PSMA-617 and docetaxel vs docetaxel in metastatic hormone-naïve prostate cancer (clinical trial protocol). *BJU Int*. 2021;128:331–342.

# $^{68}\text{Ga}$ -DOTATATE Prepared from Cyclotron-Produced $^{68}\text{Ga}$ : An Integrated Solution from Cyclotron Vault to Safety Assessment and Diagnostic Efficacy in Neuroendocrine Cancer Patients

Sébastien Tremblay<sup>1</sup>, Jean-François Beaudoin<sup>2</sup>, Ophélie Bélissant Benesty<sup>1,2</sup>, Samia Ait-Mohand<sup>1</sup>, Véronique Dumulon-Perreault<sup>2</sup>, Étienne Rousseau<sup>1,2</sup>, Éric E. Turcotte<sup>1,2</sup>, and Brigitte Guérin<sup>1,2</sup>

<sup>1</sup>Department of Nuclear Medicine and Radiobiology, Université de Sherbrooke, Sherbrooke, Quebec, Canada; and <sup>2</sup>Sherbrooke Molecular Imaging Center of the CRCHUS, Sherbrooke, Quebec, Canada

Cyclotron production of  $^{68}\text{Ga}$  is a promising approach to supply  $^{68}\text{Ga}$  radiopharmaceuticals. To validate this capability, an integrated solution for a robust synthesis of  $^{68}\text{Ga}$ -DOTATATE prepared from cyclotron-produced  $^{68}\text{Ga}$  was achieved. A retrospective comparison analysis was performed on patients who underwent PET/CT imaging after injection of DOTATATE labeled with  $^{68}\text{Ga}$  produced by a cyclotron or eluted from a generator to demonstrate the clinical safety and diagnostic efficacy of the radiopharmaceutical as a routine standard-of-care diagnostic tool in the clinic. **Methods:** An enriched pressed  $^{68}\text{Zn}$  target was irradiated by a cyclotron with a proton beam set at 12.7 MeV for 100 min. The fully automated process uses an in-vault dissolution system in which a liquid distribution system transfers the dissolved target to a dedicated hot cell for the purification of  $^{68}\text{GaCl}_3$  and radiolabeling of DOTATATE using a cassette-based automated module. Quality control tests were performed on the resulting tracer solution. The internal radiation dose for  $^{68}\text{Ga}$ -DOTATATE was based on extrapolation from rat biodistribution experiments. A retrospective comparison analysis was performed on patients who underwent PET/CT imaging after injection of DOTATATE labeled with cyclotron- or generator-produced  $^{68}\text{Ga}$ . **Results:** The synthesis of  $^{68}\text{Ga}$ -DOTATATE ( $20.7 \pm 1.3$  GBq) with high apparent molar activity ( $518 \pm 32$  GBq/ $\mu\text{mol}$  at the end of synthesis) was completed in 65 min, and the radiopharmaceutical met the requirements specified in the *European Pharmacopoeia* monograph on  $^{68}\text{Ga}$ -chloride (accelerator-produced) solution for radiolabeling.  $^{68}\text{Ga}$ -DOTATATE was stable for at least 5 h after formulation. The dosimetry calculated with OLINDA for cyclotron- and generator-produced  $^{68}\text{Ga}$ -DOTATATE was roughly equivalent. The  $\text{SUV}_{\text{mean}}$  or  $\text{SUV}_{\text{max}}$  of tumoral lesions with cyclotron-produced  $^{68}\text{Ga}$ -DOTATATE was equivalent to that with generator-produced  $^{68}\text{Ga}$ . Among physiologic uptake levels, a significant difference was found in kidneys, spleen, and stomach wall, with lower values in cyclotron-produced  $^{68}\text{Ga}$ -DOTATATE in all cases. **Conclusion:** Integrated cyclotron production achieves reliable high yields of clinical-grade  $^{68}\text{Ga}$ -DOTATATE. The clinical safety and imaging efficacy of cyclotron-produced  $^{68}\text{Ga}$ -DOTATATE in humans provide supporting evidence for its use in routine clinical practice.

**Key Words:** cyclotron  $^{68}\text{Ga}$ ; in-vault dissolution system;  $^{68}\text{Ga}$ -DOTATATE; PET imaging; cancer patients

**J Nucl Med** 2023; 64:232–238

DOI: 10.2967/jnumed.121.263768

Commercial production of the  $^{68}\text{Ge}/^{68}\text{Ga}$  generator increased accessibility and kick-started metal radiolabeling of peptides for medical diagnosis. The demand for  $^{68}\text{Ga}$  now greatly exceeds the production capacity of generators (1), and the use of cyclotrons for production of  $^{68}\text{Ga}$  by a  $^{68}\text{Zn}(p,n)^{68}\text{Ga}$  reaction at energies of 12–14 MeV on a larger scale is becoming a necessity.

Use of cyclotrons for the production of  $^{68}\text{Ga}$  first expanded with liquid targets for a yield increase of 10 times generator production, with the convenience of enriched  $^{68}\text{Zn}$  recycling and compatibility with existing distribution systems for the liquid targets (2–4). However, problems of target density, high pressure, and metal contamination by the targets limit the maximum production quantity and labeling efficiency (2–4). The use of solid targets allows much higher yields from 50 to 100 times generator capacity. However, its spread to different sites is limited by the complexity of target production, the recovery of the solid target while avoiding a high dose for handling, and the complex, expensive systems required for transfers from the cyclotron vault to the units of synthesis (5–11).

The aim of this study was to give a complete high-yield integrated solution, from simple target preparation, irradiation, and dissolution to production of good-manufacturing-practice-compliant  $^{68}\text{Ga}$ -DOTATATE. To take advantage of the higher production capacity of cyclotrons with solid targets, we first investigated the quality of  $^{68}\text{Ga}$  produced at 12.7 MeV to demonstrate robustness in the production of multiple doses of  $^{68}\text{Ga}$ -DOTATATE. The chemical and radiochemical purity and the dosimetry of this radiopharmaceutical were examined for human use. A phase 3 study aiming to evaluate the innocuity and safety profile of  $^{68}\text{Ga}$ -DOTATATE prepared from  $^{68}\text{Ga}$  produced by a cyclotron was initiated to establish the procedure as a routine standard-of-care diagnostic tool for all neuroendocrine cancer patients. This was a single-center study but with recruitment across all of Canada. The trial was prospective, nonrandomized, and open-label and had no control group (ClinicalTrials.gov identifier NCT04847505, approved by Health Canada). From this study, a retrospective comparison analysis was performed

Received Jan. 13, 2022; revision accepted Jul. 18, 2022.

For correspondence or reprints, contact Brigitte Guérin (brigitte.guerin2@usherbrooke.ca).

Published online Jul. 29, 2022.

Immediate Open Access: Creative Commons Attribution 4.0 International License (CC BY) allows users to share and adapt with attribution, excluding materials credited to previous publications. License: <https://creativecommons.org/licenses/by/4.0/>. Details: <http://jnm.snmjournals.org/site/misc/permission.xhtml>.

Copyright © 2023 by the Society of Nuclear Medicine and Molecular Imaging.

on patients who underwent PET/CT imaging after injection of DOTATATE labeled with  $^{68}\text{Ga}$  produced by a cyclotron or eluted from a generator (ClinicalTrials.gov identifier NCT02810600, a completed phase 2 study with 2,120 participants).

## MATERIALS AND METHODS

$^{68}\text{Zn}$  metal powder ( $\geq 98.1\%$  enriched) was purchased from ISO-FLEX USA and Neonest AB. Nitric acid, 70% ( $\geq 99.999\%$  trace metals basis); hydrochloric acid, 37% ( $\geq 99.999\%$  trace metals basis); ammonium formate ( $\geq 99.995\%$  trace metals basis); sodium phosphate dibasic ( $\geq 99.99\%$  trace metals basis); potassium phosphate monobasic (99.99% trace metals basis); acetonitrile; hydroxylamine hydrochloride, 99% (ReagentPlus); 2,3,5,6-tetrafluorophenol; and sodium hydroxide, 98% (of American Chemical Society grade) were purchased from Aldrich Chemical. Ascorbic acid ( $\geq 99.99998\%$  trace select) was obtained from Honeywell. All solutions and dilutions were prepared with Optima (Sorbent Technologies) ultra-performance liquid chromatography/high-performance liquid chromatography water. Methanol of high-performance liquid chromatography grade and NaCl were purchased from Fisher Scientific. The reverse-phase cartridge and Accell Plus CM cationic exchange resin were purchased from Waters. Empty cartridges were purchased from UCT, and *N*-(3-dimethylamino-propyl)-*N'*-ethylcarbodiimide hydrochloride was from Matrix Innovation. DOTATATE was obtained from AUSPEP. The radio thin-layer chromatography (TLC) was performed using instant-TLC silica gel paper from Agilent and a radio-TLC scanner (Bioscan AR-2000).  $\gamma$ -ray spectrometry was conducted on a high-purity germanium detector (GMX; Ortec) calibrated with a National Institute of Standards and Technology–traceable  $\gamma$ -set ( $^{133}\text{Ba}$ ,  $^{109}\text{Cd}$ ,  $^{57}\text{Co}$ ,  $^{60}\text{Co}$ ,  $^{137}\text{Cs}$ ,  $^{54}\text{Mn}$ , and  $^{22}\text{Na}$ ) from Eckert and Ziegler Isotope Products. The pH strips (range, 2–10) were purchased from Millipore-Sigma, and Quantofix (Macherey-Nagel) iron and zinc test strips were from Aldrich. Hydroxamate resin was prepared from the modified Accell Plus CM cationic exchange resin using the procedure developed by Verel et al. (12) and was packed in a 1-mL cartridge (United Chemical Technologies). Benzene sulfonic resin (CUBCX123 and CUBCX111) was bought from UCT. A IGG100  $^{68}\text{Ge}/^{68}\text{Ga}$  generator was obtained from Eckert and Ziegler EUROTOPE.

### Target Preparation

The target preparation was already described by Alnahwi et al. (6). Briefly, isotopically enriched  $^{68}\text{Zn}$  powder was pressed in a die of 8 mm (155 mg) by a hydraulic press (module 3912; Carver) and deposited in the appropriate cavity diameter of the magnetic target carrier (6).

### Irradiation Procedure

Targets were irradiated facing a perpendicular proton beam in a solid target holder, TA-1186D (ACSI), mounted to a target selector installed directly on a TR-19 or TR-24 cyclotron (Advanced Cyclotron Systems) in conjunction with our customized magnetic target carrier (6). Beam degradation was achieved by the combined density of a tantalum foil (125–150  $\mu\text{m}$ ; Goodfellow) and the target carrier. The resulting energy was determined using the SRIM 2013 simulator (13). For irradiation, the incident energy beam was set to 18.2 MeV and degraded to 12.7 MeV with the aluminum degrader of 0.4 mm to minimize formation of  $^{67}\text{Ga}$  by the nuclear reaction  $^{68}\text{Zn}(p,n)^{67}\text{Ga}$  (14), with a target current of 20  $\mu\text{A}$  applied during approximately 100-min irradiations on both cyclotrons.

### In-Vault Dissolution System

After the irradiation in the cyclotron target holder, the target carrier was released down a tube line into a dissolution system (Fig. 1). This custom-built system is located in the cyclotron vault and remotely automated by an industrial programmable logic controller. The top

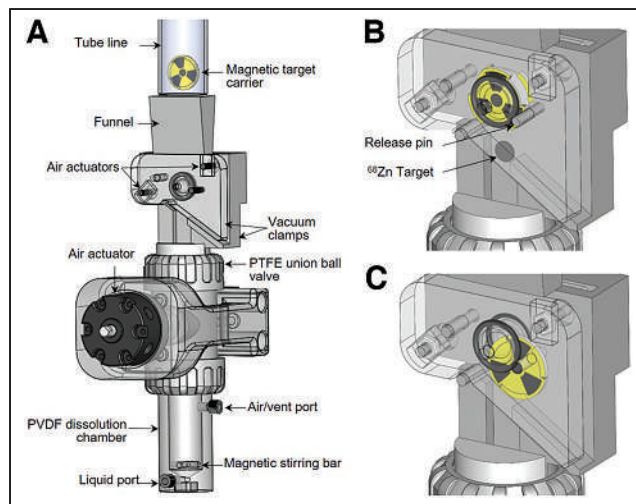


**FIGURE 1.** In-vault dissolution system: component assembly (A),  $^{68}\text{Zn}$ -enriched target release (B), and magnetic target carrier release (C). PTFE = polytetrafluoroethylene; PVDF = polyvinylidene fluoride.

portion of the system funnels the target carrier into an air-activated vacuum clamp that opens and closes the magnetic target carrier to release the  $^{68}\text{Zn}$  target payload into the polyvinylidene fluoride dissolution chamber. The middle section gates the passage of the target to the dissolution chamber with an air-activated union ball valve (19-mm opening) that seals off the chamber during the target dissolution process. The final portion of the system is the dissolution chamber, where an air/vent port (Fig. 1A) and an air-activated distribution valve (VICI) govern the incoming injections of 1.5 mL of 7 M nitric acid, 3 mL of water, and 2.75 mL of 2.5 M ammonium formate buffering solution through the liquid port (Fig. 1A) during the dissolution sequence and selects the destination line of the dissolved target to the proper synthesis unit. Inside the chamber, a magnetic stirring bar is activated for 2 min for complete dissolution (6), after which water and ammonium formate were added. The dissolved target solution arrives about 7 min after the cyclotron irradiation in the destination hot cell. With the process completed, the vacuum clamp and air-actuated release pin (Fig. 1B) allow the magnetic target carrier to exit the system via the ejection slide (Fig. 1C). At this point, all valves are reset, and the system is ready for another combined synthesis–dissolution process to target water flushing; the overall step is accomplished in 20 min after the end of bombardment.

### Peptide Radiolabeling

The  $^{68}\text{GaCl}_3$  purification (6) and peptide radiolabeling steps were both performed on an AllInOne automated module (TRASIS), as shown in Figure 2. The  $^{68}\text{GaCl}_3$  purification was performed using the optimized procedure described by Alnahwi et al. (6). After the transfer of  $^{68}\text{Ga}$ , the line was rinsed with 0.01 M HCl (0.5 mL) for maximum recovery. The pH was adjusted to 3.5 with 1.2 mL of a 0.2 M ammonium formate metal trace buffer solution. The buffered solution was transferred to the reactor prefilled with a 1-mL solution of 60  $\mu\text{g}$  of DOTATATE and 25 mg of ascorbic acid of traceSELECT (Sigma-Aldrich) grade. After mixing with nitrogen, the pH was 3.4–3.8 and the reaction mixture was raised to 100°C during 13 min. The radiolabeling yield was greater than 98%. After the labeling step, the reactor was cooled to 50°C, and the solution was then drawn into a syringe prefilled with 5 mL of water at room temperature. The peptide solution was passed through 500-mg C18 reversed-phase resin, and the reactor was rinsed with an extra 4 mL of water. The column was then washed twice with 10 mL of water. The  $^{68}\text{Ga}$ -DOTATATE was recovered

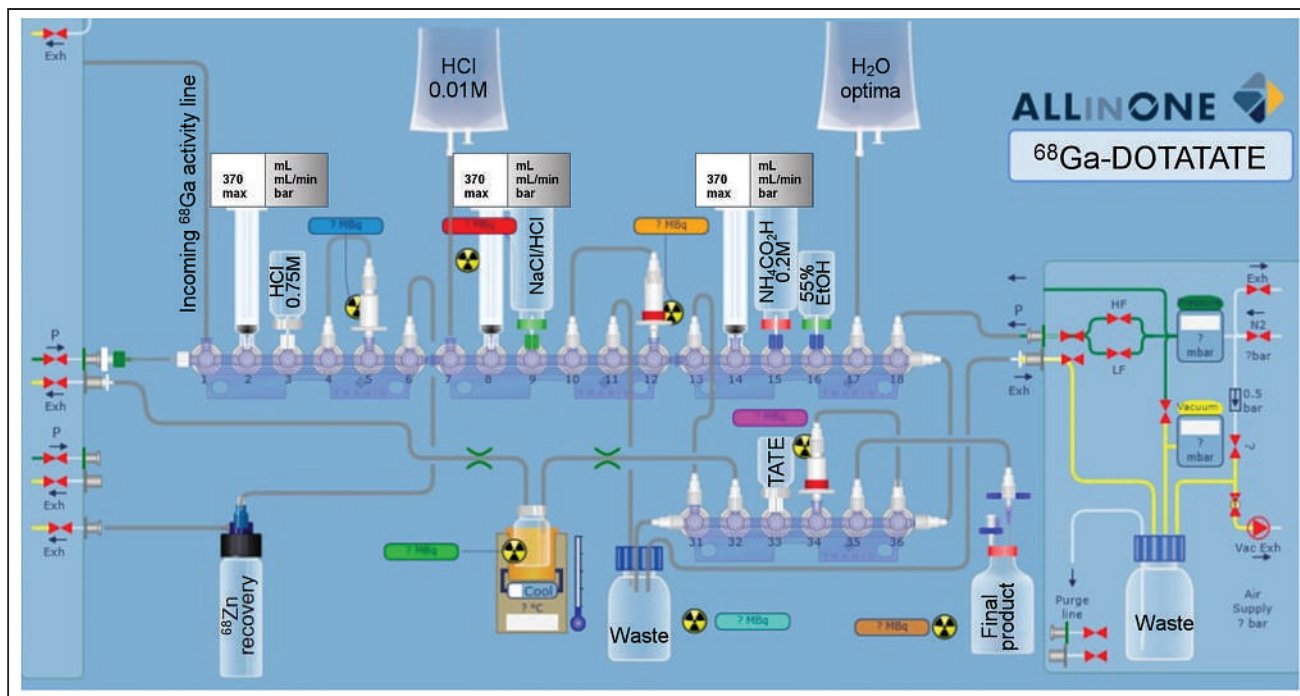


**FIGURE 2.** AllinOne schematic of  $^{68}\text{Ga}$ -DOTATATE synthesis, including  $^{68}\text{GaCl}_3$  purification. Exh = exhaust; mbar = millibar; vac = vacuum.

with 3.5 mL of 55% (v/v) ethanol/water solution through the C18 column to the product vial for final formulation. The formulation was achieved by adding 17.5 mL of solution containing 0.14 g of  $\text{Na}_2\text{HPO}_4$ , 0.024 g of  $\text{KH}_2\text{PO}_4$ , 0.1 g of NaCl, and 100 mg of ascorbic acid to the product vial for a total volume of 21 mL and 9.4% ethanol. This solution was filtered through a sterile 0.22- $\mu\text{m}$  polyvinylidene fluoride membrane filter (Millipore) and fractionized with the Eckert and Ziegler module in the clean room.

#### Quality Control Tests

Quality control tests were performed on formulated  $^{68}\text{Ga}$ -DOTATATE. The pH was measured with pH strips. The radiochemical identity and purity were determined by ultra-high-performance liquid chromatography (Acquity; Waters) with an evaporative light-scattering detector, a flow-count radiodetector (Bioscan), and instant TLC. Samples (1  $\mu\text{L}$ ) were injected and analyzed on an Acquity BEH C18 column (1.7  $\mu\text{m}$ , 2.1  $\times$  50 mm) and compared with a home-made

**TABLE 1**  
Quality Control Results for  $^{68}\text{Ga}$ -DOTATATE

Analysis	Method	Specifications EOS	Results ( $n = 14$ )
Appearance	Visual	Clear, no color	Pass
pH	pH strip	4.0–8.0*	5.4 $\pm$ 0.2
Peptide DOTATATE	Calculation	$\leq 60 \mu\text{g}^*$	57.3 $\pm$ 0.5 $\mu\text{g}$
Radiochemical identity	Ultra-performance liquid chromatography retention time	$\pm 10\%$	0.90% $\pm$ 0.05%
Radiochemical purity	$(100-A) \times T = \%$	$\geq 91\%$	98.4% $\pm$ 0.9%
Radionuclidic purity	$\gamma$ -511 and 1,077 keV	$\geq 98\%$	99.7% $\pm$ 0.3%
Radionuclide identification	Half-life	62–74 min*	67.5 $\pm$ 0.5 min
Pyrogenicity	Inoculation	$\leq 8.3 \text{ IU/mL}^*$	Pass
Filter integrity	Bubble point	$\geq 345 \text{ kPa}$ (50 psi)	Pass
Zinc/iron	Strips	$\leq 10 \mu\text{g/GBq}$	$< 1 \mu\text{g/GBq}$
$^{67}\text{Ga}$ and $^{66}\text{Ga}$ contents	$\gamma$ -ray analysis	$\leq 2\%$	$^{67}\text{Ga} \leq 0.052\% \pm 0.004\%^\dagger$ $^{66}\text{Ga} \leq 0.017\% \pm 0.006\%^\dagger$

\*Our release criteria.

$^\dagger$ Values recalculated to moment of EOS from results obtained 16–24 h after EOS.

A = percentage of radioactivity due to  $^{68}\text{Ga}$  impurity (retardation factor = 0–0.1) determined by instant TLC; T = proportion of the radioactivity in the area of the peak due to  $^{68}\text{Ga}$ -DOTATATE relative to the total areas of the peaks in the chromatogram obtained from ultra-high-performance liquid chromatography analysis.

nonradioactive gallium-DOTATATE standard. The instant-TLC silica gel paper was eluted with a 77 g/L solution of ammonium acetate: MeOH (1:1). The radionuclidic purity was verified by  $\gamma$ -ray spectrometry on a calibrated high-purity germanium detector with a zoom energy window of 1–2,000 keV. Samples were counted for 2 min after the end of synthesis (EOS). In addition, the tests were repeated at 16–24 h after EOS to quantify radionuclidic impurities ( $^{67}\text{Ga}$  [half-life, 3.26 d] and  $^{66}\text{Ga}$  [half-life, 9.49 h]). Chemical purity was evaluated using commercially available indicator strips to measure iron and zinc in the formulated  $^{68}\text{Ga}$ -DOTATATE. The endotoxin levels were assayed by the *Limulus* amoebocyte lysate method with an Endosafe-PTS test system (Charles River Laboratories International). Sterility tests were performed by a licensed laboratory (Nucro-Technics).

### Animals

All animal studies were conducted in compliance with the Canadian Council on Animal Care guidelines and with the approval of the Animal Care Committee of the Université de Sherbrooke.

### Biodistribution Studies

Biodistribution studies were conducted on 12-wk-old Fisher female rats weighing 150–175 g (Charles River) to determine the uptake of  $^{68}\text{Ga}$ -DOTATATE in various organs. A 7- to 14-MBq dose of cyclotron- or generator-produced  $^{68}\text{Ga}$ -DOTATATE was injected into the tail vein of the isoflurane-anesthetized rats. At 15, 30, 45, 60, or 120 min after injection, while anesthesia was maintained, blood was taken by cutting the femoral artery. The animals were then killed by  $\text{CO}_2$  inhalation and the organs of interest were removed, rinsed, and blotted dry before the radioactivity was counted in a Hidex  $\gamma$ -counter. The results were expressed as percentage injected dose per gram of tissue.

### Clinical PET Imaging

A retrospective comparison analysis was performed on patients who underwent PET/CT imaging after injection of DOTATATE labeled with cyclotron- or generator-produced  $^{68}\text{Ga}$ . The institutional ethic board approved the study, and all subjects gave written informed consent.

Patients with progressive disease between the 2 examinations (defined by at least one new lesion) or examinations performed with different cameras were excluded.

PET/CT imaging was performed from head to mid thigh, on a Gemini TF or Gemini GXL PET/CT scanner (Philips). An unenhanced CT scan was obtained using the following parameters: slice thickness, 3 mm; increment, 3 mm; 120 kVp, and 55–83 mAs, depending on the patient's weight. Immediately after CT scanning, whole-body PET was performed in 3-dimensional mode (matrix,  $144 \times 144$ ). For each bed position (15 cm; overlapping scale, 5 cm), a 2-min acquisition with a 57.6-cm field of view was used.

The emission data were corrected for decay and for random and scatter events. Reconstruction used the 3-dimensional row-action maximum-likelihood algorithm with 2 iterations, a relaxation parameter of 0.5, and a 2-mm-radius spherically symmetric basis function (blobs). Attenuation was corrected using the low-dose unenhanced CT data. Image analysis was performed using OASIS software (Segami).

To compare both cyclotron- and generator-produced  $^{68}\text{Ga}$ -DOTATATE, regions of interest were drawn on transaxial slices around areas of focal uptake in the pituitary gland; lacrimal, parotid, submandibular, and sublingual salivary glands; nasal mucosa; thyroid gland; mediastinal blood pool (aortic arch); adrenals; liver; spleen; stomach wall; bowel; kidney cortex; uncinat process; and gluteal musculature (as background). Isocontour volumes at 70% of the maximum pixel value were drawn automatically, and the  $\text{SUV}_{\text{mean}}$  and  $\text{SUV}_{\text{max}}$  were measured in all these volumes. The  $\text{SUV}_{\text{mean}}$  and  $\text{SUV}_{\text{max}}$  of neuroendocrine lesions were also recorded for up to 10 lesions per patient.

Cyclotron- and generator-produced  $^{68}\text{Ga}$ -DOTATATE values were compared using Wilcoxon matched-pairs rank tests for each patient. A *P* value of less than 0.05 was considered statistically significant.

## RESULTS

### Target Preparation and Irradiation

The  $^{68}\text{Zn}$ -pressed target irradiation challenge was to manage the low melting point of the zinc (419.5°C) and the focused beam on the solid target. To avoid target overheating at low current, a 125- $\mu\text{m}$  tantalum foil was efficiently used to diffuse the beam and reduce the proton energy to 12.7 MeV on the target.

### $^{68}\text{Ga}$ -DOTATATE Preparation

A fully automated dissolution system was developed to facilitate the radiosynthesis of  $^{68}\text{Ga}$  for large-scale and routine production using a pressed  $^{68}\text{Zn}$  target. The activity of the transferred  $^{68}\text{GaCl}_3$  solution from the vault to the hot cell was  $46.2 \pm 2.2$  GBq (56.6 GBq at the end of bombardment), with a saturated yield of  $4.4 \pm 0.1$  GBq/ $\mu\text{A}$  when using the 8-mm-diameter  $^{68}\text{Zn}$  target irradiated at 12.7 MeV for  $100.3 \pm 2.4$  min at  $20 \pm 0.4$   $\mu\text{A}$ . The  $^{68}\text{GaCl}_3$  was purified using the optimized procedure described by Alnahwi et al. (6).

DOTATATE aliquots (60  $\mu\text{g}$ ) formulated in water (300  $\mu\text{L}$ ) were stable for up to 30 d when the solution was kept frozen at  $-20^\circ\text{C}$ . To avoid radiolysis at high activity levels, the peptide

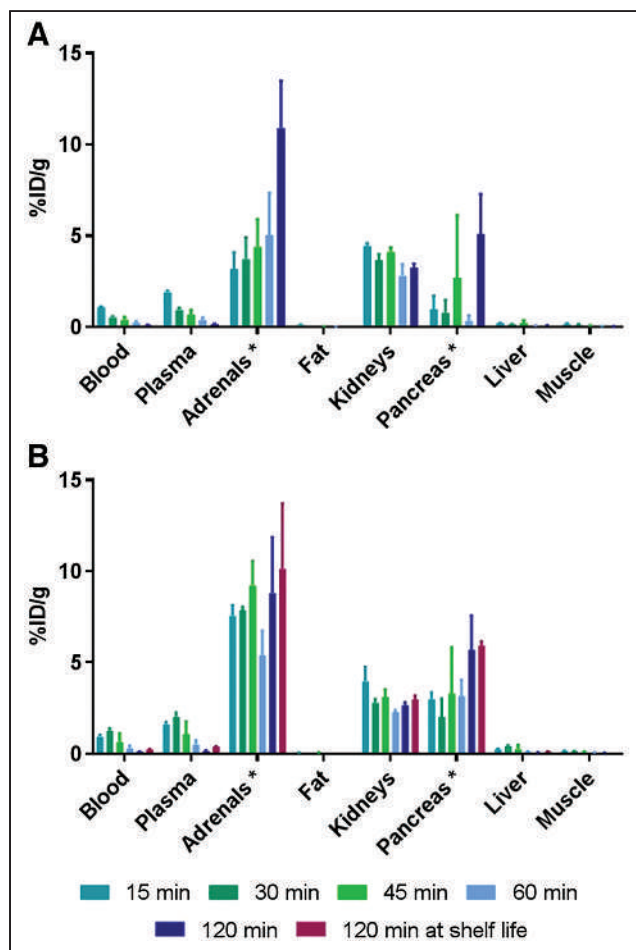


**FIGURE 3.** Biodistribution in rats of DOTATATE labeled with generator-produced (A) and cyclotron-produced (B)  $^{68}\text{Ga}$  at various time points. %ID = percentage injected dose.

precursor was loaded in the reaction vessel in the presence of ascorbic acid, and the pH was adjusted before transfer of the purified  $^{68}\text{GaCl}_3$  solution. A mean of  $20.7 \pm 1.3$  GBq ( $n = 14$ ) of  $^{68}\text{Ga}$ -DOTATATE at EOS was produced in less than 35 min, for a global decay-corrected yield of  $66\% \pm 5\%$  ( $n = 14$ ). The final formulation, filtration, and distribution process was performed within 10–15 min.

The estimated apparent molar activity at EOS was  $518 \pm 32$  GBq/ $\mu\text{mol}$  ( $n = 14$ ), which is 20-fold higher than the 25 GBq/ $\mu\text{mol}$  reported by Thisgaard et al. (11) for cyclotron-produced  $^{68}\text{Ga}$ -DOTATATE. From our previous studies, new generators produce  $0.665 \pm 0.043$  GBq ( $n = 10$ ) of  $^{68}\text{Ga}$ -DOTATATE that has an apparent molar activity of  $63 \pm 13$  GBq/ $\mu\text{mol}$  with a performance that decays over time.

#### Quality Control Results

Samples of all productions ( $n = 14$ , Table 1) complied with all specifications.  $^{67}\text{Ga}$  and  $^{66}\text{Ga}$  contents were, respectively, 0.052%  $\pm$  0.004% and 0.017%  $\pm$  0.006% at EOS ( $n = 14$ ).

#### Assessment of Internal Radiation Dose

To estimate the dosimetry of the  $^{68}\text{Ga}$ -DOTATATE, biodistribution experiments were conducted on female Fischer rats at different time points after injection (Fig. 3). Cyclotron-produced  $^{68}\text{Ga}$ -DOTATATE showed significantly higher uptake in the adrenals and

**TABLE 2**

Dosimetry Extrapolated to Humans for  $^{68}\text{Ga}$ -DOTATATE

Tissue	Absorbed dose (mGy/MBq)	
	Generator $^{68}\text{Ga}$	Cyclotron $^{68}\text{Ga}$
Adrenals	1.33e-01	1.52e-01
Brain	5.45e-04	7.41e-04
Breasts	8.99e-04	9.52e-04
Gallbladder wall	1.66e-03	1.85e-03
Lower large intestine wall	9.41e-04	9.78e-04
Small intestine	1.21e-03	1.20e-03
Stomach wall	1.42e-03	1.79e-03
Upper large intestine wall	1.14e-03	1.14e-03
Heart wall	2.52e-02	2.69e-02
Kidneys	9.01e-02	6.29e-02
Liver	4.42e-03	5.30e-03
Lungs	1.12e-02	1.17e-02
Muscle	3.23e-03	3.41e-03
Ovaries	7.95e-03	4.94e-03
Pancreas	1.36e-02	7.28e-02
Red marrow	6.46e-03	6.68e-03
Osteogenic cells	7.25e-03	8.96e-03
Skin	6.10e-04	6.35e-04
Spleen	5.42e-03	5.79e-03
Thymus	1.61e-03	1.70e-03
Thyroid	7.12e-04	7.60e-04
Bladder wall	7.51e-04	7.83e-04
Uterus	5.28e-03	6.67e-03
Total body	2.83e-03	3.00e-03

**TABLE 3**

Comparison of  $\text{SUV}_{\text{max}}$  of Physiologic and Tumoral Uptake Between Cyclotron- and Generator-Produced  $^{68}\text{Ga}$ -DOTATATE

Tissue	$\text{SUV}_{\text{max}}$		<i>P</i>
	Cyclotron $^{68}\text{Ga}$	Generator $^{68}\text{Ga}$	
Pituitary	4.56 $\pm$ 1.57	5.13 $\pm$ 1.54	0.3291
Liver	8.33 $\pm$ 2.19	8.95 $\pm$ 2.47	0.3804
Thyroid	4.25 $\pm$ 2.03	4.25 $\pm$ 2.11	>0.9999
Parotid	2.37 $\pm$ 1.01	2.41 $\pm$ 1.04	0.8657
Submandibular	2.77 $\pm$ 1.21	2.87 $\pm$ 1.17	0.6079
Nasal mucosa	2.16 $\pm$ 0.54	2.34 $\pm$ 0.45	0.9463
Aortic arch	0.95 $\pm$ 0.36	0.97 $\pm$ 0.20	0.6221
Kidneys	14.30 $\pm$ 5.23	16.76 $\pm$ 4.12	0.0024*
Spleen	22.79 $\pm$ 5.29	26.44 $\pm$ 5.33	0.0015*
Uncinate process	5.31 $\pm$ 2.45	5.96 $\pm$ 2.88	0.1475
Stomach wall	6.30 $\pm$ 3.36	8.69 $\pm$ 2.37	0.0093*
Bowel	6.91 $\pm$ 1.94	7.96 $\pm$ 1.92	0.1294
Adrenal	11.09 $\pm$ 4.41	12.44 $\pm$ 4.39	0.0923
Gluteal musculature	1.19 $\pm$ 0.49	1.31 $\pm$ 0.33	0.292
Tumors	9.13 $\pm$ 6.18	7.94 $\pm$ 5.61	0.346

\**P* value  $\leq$  0.05.

Data are mean  $\pm$  SD.

**TABLE 4**

Comparison of  $\text{SUV}_{\text{mean}}$  of Physiologic and Tumoral Uptake Between Cyclotron- and Generator-Produced  $^{68}\text{Ga}$ -DOTATATE

Tissue	$\text{SUV}_{\text{mean}}$		<i>P</i>
	Cyclotron $^{68}\text{Ga}$	Generator $^{68}\text{Ga}$	
Pituitary	3.82 $\pm$ 1.34	4.32 $\pm$ 1.31	0.457
Liver	6.56 $\pm$ 1.67	6.95 $\pm$ 1.81	0.4131
Thyroid	3.43 $\pm$ 1.65	3.42 $\pm$ 1.72	>0.9999
Parotid	1.89 $\pm$ 0.83	1.91 $\pm$ 0.82	0.8657
Submandibular	2.22 $\pm$ 0.96	2.31 $\pm$ 0.95	0.6377
Nasal mucosa	1.75 $\pm$ 0.45	1.85 $\pm$ 0.33	0.8945
Aortic arch	0.76 $\pm$ 0.29	0.79 $\pm$ 0.19	0.5879
Kidneys	11.09 $\pm$ 4.07	13.00 $\pm$ 3.36	0.0049*
Spleen	18.72 $\pm$ 4.24	21.41 $\pm$ 4.14	0.002*
Uncinate process	4.25 $\pm$ 1.56	4.80 $\pm$ 2.29	0.083
Stomach wall	5.04 $\pm$ 2.74	6.96 $\pm$ 1.87	0.0093*
Bowel	5.49 $\pm$ 1.56	6.33 $\pm$ 1.48	0.1099
Adrenal	9.01 $\pm$ 3.59	10.05 $\pm$ 3.55	0.1133
Gluteal musculature	0.97 $\pm$ 0.39	1.09 $\pm$ 0.28	0.207
Tumors	5.14 $\pm$ 5.42	6.52 $\pm$ 4.59	0.583

\**P* value  $\leq$  0.05.

Data are mean  $\pm$  SD.



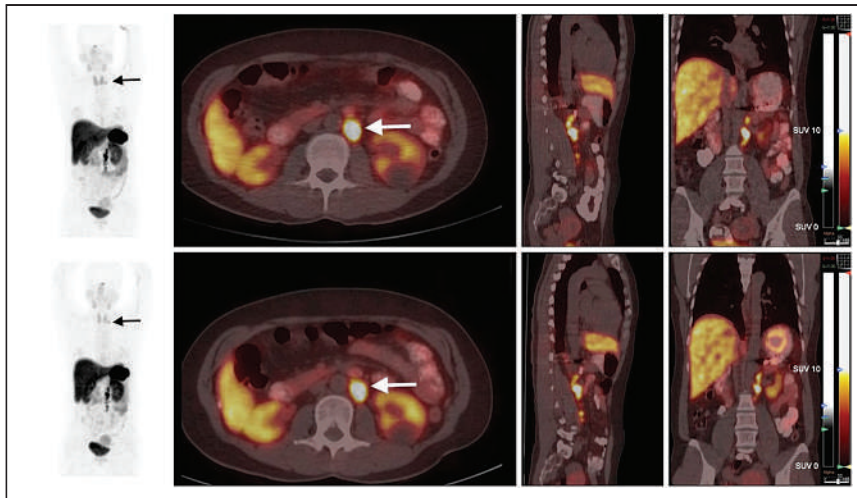


**FIGURE 4.** Example of 2 examinations, with cyclotron-produced (top row) and generator-produced (bottom row)  $^{68}\text{Ga}$ -DOTATATE PET/CT. From left to right in each row maximum-intensity projection (MIP), axial, sagittal and coronal planes. Examinations were performed 16 mo apart on same patient, who was being followed after removal of left pheochromocytoma but had secondary supraclavicular (black arrows) and retroperitoneal (white arrows) node metastasis.

pancreas, organs of interest rich in somatostatin receptors, at early time points (15 and 30 min,  $P < 0.005$ ) after injection. A potential explanation is that the cyclotron-produced  $^{68}\text{Ga}$ -DOTATATE has the larger apparent molar activity. Cyclotron-produced  $^{68}\text{Ga}$ -DOTATATE and generator-produced  $^{68}\text{Ga}$ -DOTATATE were biologically equivalent at late time points, giving identical kinetic and biodistribution patterns in animals.

Dosimetry extrapolated to humans was computed using OLINDA/EXM (Vanderbilt University, 2003) from the residence times scaled to humans. Since female rats were used for the biodistribution experiments, the adult female model provided by the software was applied for computations. Extrapolated dosimetry is detailed in Table 2 as absorbed dose.

Estimated  $^{68}\text{Ga}$ -DOTATATE dosimetry is acceptable when compared with other PET tracers in use in humans and shows that dosimetry for  $^{68}\text{Ga}$ -DOTATATE synthesized from cyclotron-produced  $^{68}\text{Ga}$  and generator-produced  $^{68}\text{Ga}$  is roughly equivalent. The main difference in calculated dosimetry between the 2 tracers is in the pancreas, kidneys, and adrenals.

#### Clinical Studies

PET/CT examinations after injection of cyclotron- and generator-produced  $^{68}\text{Ga}$ -DOTATATE were compared for 12 patients (14 lesions): 4 using the Gemini GXL scanner and 8 the Gemini TF PET/CT scanner. The mean interval between the examinations was  $373.5 \pm 315.8$  d.

Cyclotron production allowed injection of a higher radiotracer activity than did generator production ( $3.9 \pm 1.0$  MBq/kg and  $1.9 \pm 0.6$  MBq/kg, respectively;  $P = 0.01$ ). There was no difference in injection-to-acquisition interval between the examinations ( $69.5 \pm 11.9$  and  $65.4 \pm 11.6$  min, respectively;  $P = 0.34$ ).

$\text{SUV}_{\text{max}}$  and  $\text{SUV}_{\text{mean}}$  are compared in Tables 3 and 4, respectively. The  $\text{SUV}_{\text{mean}}$  and  $\text{SUV}_{\text{max}}$  of tumoral lesions did not differ between cyclotron and generator production. Regarding physiologic uptake, a significant difference was found in the kidneys, spleen, and stomach wall, with lower values in cyclotron-produced  $^{68}\text{Ga}$ -DOTATATE in all cases (Fig. 4). All these organs are large and highly

somatostatin receptor-expressing (15), but to our knowledge, the effect of injected activity or apparent molar activity on physiologic uptake in somatostatin receptor PET imaging has not been described.

#### DISCUSSION

In recent years, several groups, including ours, have developed new liquid and solid targets and robust separation procedures to manufacture high-purity  $^{68}\text{Ga}$  with cyclotrons (2–11). As previously described by Alnawhi et al. (6), the preparation and assembly of  $^{68}\text{Zn}$ -pressed target was easy, time-effective for serial production, and inexpensive. There is clear and convincing evidence that the quality of cyclotron-produced  $^{68}\text{Ga}$  is comparable to that of generator-produced  $^{68}\text{Ga}$  (2–11) and that large quantities can be prepared (5,6,10,11), which enable transportation of  $^{68}\text{Ga}$  tracer.  $^{68}\text{Ga}$ -DOTATATE can safely be used up to 5 h after EOS, when the combined value for  $^{66}\text{Ga}$  and  $^{67}\text{Ga}$  content

reaches 1.25% of the activity of  $^{68}\text{Ga}$  as compared with the 2% limit prescribed in the *European Pharmacopoeia* monograph (16).

The lower physiologic uptake and similar tumor uptake obtained with  $^{68}\text{Ga}$ -DOTATATE produced by cyclotron could result in only a better tumor-to-background ratio in these areas. For the last 18 mos, a weekly production of  $^{68}\text{Ga}$ -DOTATATE was successfully performed and more than 1,075 clinical scans were done. One should note that a single cyclotron production of  $^{68}\text{Ga}$ -DOTATATE allowed for scheduling of 10 patients on 2 simultaneously running PET scanners, compared with 2 patients for generator-produced  $^{68}\text{Ga}$ -DOTATATE.

The present clinical trial confirmed that  $^{68}\text{Ga}$ -DOTATATE prepared from cyclotron-produced  $^{68}\text{Ga}$  is safe and provides diagnostic efficacy equivalent to that of the radiopharmaceutical prepared from generator-produced  $^{68}\text{Ga}$ .

#### CONCLUSION

We propose a complete high-yield integrated solution for cyclotron-produced and good-manufacturing-practice-compliant  $^{68}\text{Ga}$ -DOTATATE. Use of the in-vault dissolution system combines the high-yield production of the solid target with the versatility of the liquid-target distribution to multiple synthesis units. The results of the present study further support adoption of cyclotron-produced  $^{68}\text{Ga}$ -DOTATATE in clinical practice.

#### DISCLOSURE

Étienne Rousseau, Éric Turcotte, and Brigitte Guérin are members of the Centre de recherche du CHUS, funded by the Fonds de recherche du Québec-Santé. Brigitte Guérin is the holder of the Jeanne and J.-Louis Lévesque Chair in Radiobiology at the Université de Sherbrooke. This work was partially financed by Oncopole, which receives funding from Merck Canada Inc. and from Fonds de recherche du Québec-Santé, as well as from the Cancer Research Society. One Patent Cooperation Treaty patent was filed for some of the material presented in this article. No other potential conflict of interest relevant to this article was reported.

## ACKNOWLEDGMENTS

We thank the cyclotron PET operators and Chantale Pouliot for technical support with tracer preparation. We also thank Jean-François Rousseau and Annick Landry for support with quality assurance and quality control, as well as Amélie Tétu and the Unité de Recherche Clinique et Epidémiologique (URCE) for their contribution to the funding application.

## KEY POINTS

**QUESTION:** How does the development of cyclotron-produced  $^{68}\text{Ga}$ -DOTATATE facilitate PET imaging of neuroendocrine cancer patients?

**PERTINENT FINDINGS:** A robust and good-manufacturing-practice-compliant synthesis of  $^{68}\text{Ga}$ -DOTATATE from cyclotron-produced  $^{68}\text{Ga}$  was achieved, expanding the imaging time window and the number of patients per production compared with generator-based  $^{68}\text{Ga}$ -DOTATATE. We also showed that cyclotron-produced  $^{68}\text{Ga}$ -DOTATATE is safe for clinical use.

**IMPLICATIONS FOR PATIENT CARE:** Cyclotron-produced  $^{68}\text{Ga}$ -DOTATATE can provide high-contrast detection of neuroendocrine tumors with reduced physiologic uptake in highly somatostatin receptor-expressing organs.

## REFERENCES

1. Mueller D, Fuchs A, Leshch Y, Proehl M. The shortage of approved  $^{68}\text{Ge}/^{68}\text{Ga}$  generators: incoming material inspection and GMP compliant use of non-approved generators [abstract]. *J Nucl Med*. 2019;60(suppl 1):1059.
2. Pandey MK, Byrne JF, Schlasner KN, Schmit NR, DeGrado TR. Cyclotron production of  $^{68}\text{Ga}$  in a liquid target: effects of solution composition and irradiation parameters. *Nucl Med Biol*. 2019;74–75:49–55.
3. Alves F, Alves VH, Neves ACB, et al. Cyclotron production of Ga-68 for human use from liquid targets: from theory to practice. *AIP Conf Proc*. 2017;1845:10.1063/1.4983532.
4. Rodnick ME, Sollert C, Stark D, et al. Cyclotron-based production of  $^{68}\text{Ga}$ , [ $^{68}\text{Ga}$ ]GaCl<sub>3</sub>, and [ $^{68}\text{Ga}$ ]Ga-PSMA-11 from a liquid target. *EJNMMI Radiopharm Chem*. 2020;5:25.
5. Lin M, Waligorski GJ, Lepera CG. Production of curie quantities of  $^{68}\text{Ga}$  with a medical cyclotron via the  $^{68}\text{Zn}(p,n)^{68}\text{Ga}$  reaction. *Appl Radiat Isot*. 2018;133:1–3.
6. Alnahwi AH, Tremblay S, Ait-Mohand S, Beaudoin JF, Guérin B. Automated radiosynthesis of  $^{68}\text{Ga}$  for large-scale routine production using  $^{68}\text{Zn}$  pressed target. *Appl Radiat Isot*. 2020;156:109014.
7. Sadeghi M, Kakavand T, Rajabifar S, Mokhtari L, Rahimi-Nezhad A. Cyclotron production of  $^{68}\text{Ga}$  via proton-induced reaction on  $^{68}\text{Zn}$  target. *Nukleonika*. 2009;54:25–28.
8. International Atomic Energy Agency. *Gallium-68 Cyclotron Production*. IAEA; 2019. TECDOC-1863.
9. Tieu W, Hollis CA, Kuan KKW, et al. Rapid and automated production of [ $^{68}\text{Ga}$ ]gallium chloride and [ $^{68}\text{Ga}$ ]Ga-DOTA-TATE on a medical cyclotron. *Nucl Med Biol*. 2019;74–75:12–18.
10. Nelson BJB, Wilson J, Richter S, Duke MJM, Wuest M, Wuest F. Taking cyclotron  $^{68}\text{Ga}$  production to the next level: expeditious solid target production of  $^{68}\text{Ga}$  for preparation of radiotracers. *Nucl Med Biol*. 2020;80–81:24–31.
11. Thisgaard H, Kumlin J, Langkjær N, et al. Multi-curie production of gallium-68 on a biomedical cyclotron and automated radiolabelling of PSMA-11 and DOTA-TATE. *EJNMMI Radiopharm Chem*. 2021;6:1.
12. Verel I, Visser GWM, Boellaard R, Stigter-van Walsum M, Snow GB, van Dongen GAMS.  $^{89}\text{Zr}$  immuno-PET: comprehensive procedures for the production of  $^{89}\text{Zr}$ -labeled monoclonal antibodies. *J Nucl Med*. 2003;44:1271–1281.
13. Ziegler JF, Ziegler MD, Biersack JP. The stopping and range of ions in matter (2010). *Nucl Instrum Methods Phys Res B*. 2010;268:1818–1823.
14. Szelecsényi F, Boothe TE, Takács S, Tárkányi F, Tavano E. Evaluated cross section and thick target yield data of Zn+P processes for practical applications Private communication. *Appl Radiat Isot*. 1997;49:1005–1032.
15. Reubi JC, Waser B, Schaer JC, Laissue JA. Somatostatin receptor sst1-sst5 expression in normal and neoplastic human tissues using receptor autoradiography with subtype-selective ligands. *Eur J Nucl Med*. 2001;28:836–846.
16. Gallium ( $^{68}\text{Ga}$ ) chloride (accelerator produced) solution for radiolabelling. In: *European Pharmacopoeia*. Council of Europe; 2020:4864–4865.

---

---

# Application of the Lugano Classification for Initial Evaluation, Staging, and Response Assessment of Hodgkin and Non-Hodgkin Lymphoma: The PRoLoG Consensus Initiative (Part 2—Technical)

Fabien Ricard\*<sup>1</sup>, Sally Barrington\*<sup>2</sup>, Ron Korn<sup>3</sup>, Guenther Brueggenwerth<sup>4</sup>, Judith Trotman<sup>5</sup>, Bruce Cheson<sup>6</sup>, Gilles Salles<sup>7</sup>, Larry Schwartz<sup>8</sup>, Greg Goldmacher<sup>9</sup>, Rudresh Jarecha<sup>10</sup>, Jayant Narang<sup>11</sup>, Florence Broussais<sup>12</sup>, Paul Galette<sup>13</sup>, Min Liu<sup>14</sup>, Surabhi Bajpai<sup>15</sup>, Eric Perlman<sup>16</sup>, Julie Gillis<sup>17</sup>, Ira Smalberg<sup>18</sup>, Pierre Terve<sup>19</sup>, Gudrun Zahlmann<sup>20</sup>, and Annette Schmid<sup>11</sup>

<sup>1</sup>Relay Therapeutics, Cambridge, Massachusetts; <sup>2</sup>King's College London and Guy's and St. Thomas' PET Centre, School of Biomedical Engineering and Imaging Sciences, King's College London, King's Health Partners, London, United Kingdom; <sup>3</sup>Adjunct Faculty TGEN/City of Hope and Imaging Endpoints Core Lab, Scottsdale, Arizona; <sup>4</sup>Bayer AG, Berlin, Germany; <sup>5</sup>Concord Repatriation General Hospital, University of Sydney, Concord, Australia; <sup>6</sup>Lymphoma Research Foundation, New York, New York; <sup>7</sup>Department of Medicine, Memorial Sloan Kettering Cancer Center and Weil Cornell Medicine, New York, New York; <sup>8</sup>Department of Radiology, Columbia University College of Physicians and Surgeons and Radiologist-in-Chief, The New York Presbyterian Hospital, Columbia, New York; <sup>9</sup>Merck & Co, Inc., Kenilworth, New Jersey; <sup>10</sup>Deciphera Pharmaceuticals LLC, Waltham, Massachusetts; <sup>11</sup>Takeda Pharmaceutical Company Ltd, Cambridge, Massachusetts; <sup>12</sup>Lymphoma Study Association Research Center LYSARC, Pierre Benite, France Calyx International, Billerica, Massachusetts; <sup>13</sup>GSK, Colleagueville, Pennsylvania; <sup>14</sup>Autolus Therapeutics, London, United Kingdom; <sup>15</sup>Calyx International, Billerica, Massachusetts; <sup>16</sup>Perlman Advisory Group LLC, Boynton Beach, Florida; <sup>17</sup>Merigold LLC, Branford, Connecticut; <sup>18</sup>Saint John's Cancer Institute and Tower Imaging Medical Group, Sherman Oaks, California; <sup>19</sup>KEOSYS Medical Imaging, Saint Herblain, France; and <sup>20</sup>QIBA/RSNA, Radiological Society of North America, Oak Brook, Illinois

---

The aim of this initiative was to provide consensus recommendations from a consortium of academic and industry experts in the field of lymphoma and imaging for the consistent application of imaging assessment with the Lugano classification. **Methods:** Consensus was obtained through a series of meetings from July 2019 to October 2021 sponsored by the PINTaD (Pharma Imaging Network for Therapeutics and Diagnostics) as part of the ProLoG (PINTaD RespOnse criteria in Lymphoma wOrking Group) consensus initiative. **Results:** Consensus recommendations encompass all technical imaging aspects of the Lugano classification. Some technical considerations for PET/CT and diagnostic CT are clarified with regards to required imaging series and scan visits, as well as acquisition and reconstruction of PET images and influence of lesion size and background activity. Recommendations are given on the role of imaging and clinical reviewers as well as on training and monitoring. Finally, an example template of an imaging case report form is provided to support efficient collection of data with Lugano Classification. **Conclusion:** Consensus recommendations are made to comprehensively address technical and imaging areas of inconsistency and ambiguity in the classification encountered by end users. Such guidance should be used to support standardized acquisition and evaluation with the Lugano 2014.

**Key Words:** Lugano classification; technical recommendations; consensus; standardization

**J Nucl Med 2023; 64:239–243**  
DOI: 10.2967/jnumed.122.264124

---

**I**n 2014, the Lugano classification (1) together with an imaging-focused companion report (2) (referred together as Lugano 2014) provided a standardized approach to classifying response based on <sup>18</sup>F-FDG PET/CT in <sup>18</sup>F-FDG-avid lymphomas. The Lugano 2014 was an update to the Revised Response Criteria for Malignant Lymphoma published in 2007 (referred to as Cheson 2007) (3).

The Lugano 2014 has since been used by regulatory agencies for recent drug approval and widely adopted both by the pharmaceutical industry and also by clinicians for evaluation of Hodgkin lymphoma (HL) and non-Hodgkin lymphoma (NHL). Currently, hundreds of actively recruiting and ongoing investigational trials are using the Lugano classification (<https://clinicaltrials.gov>).

The PRoLoG committee (PINTaD RespOnse criteria in Lymphoma wOrking Group), sponsored by the PINTaD (Pharma Imaging Network for Therapeutics and Diagnostics) (<https://www.pintad.net>), is a cross-functional group of volunteers from the industry and academy who engaged in discussions to provide expert end-users consensus recommendations for the consistent application of the Lugano classification.

This article, focusing on the technical imaging recommendations, is not intended to replace the classification. It may also be applied to some extent to the newer lymphoma response assessment criteria (e.g., Lymphoma Response to Immunomodulatory Therapy Criteria 2016 (4) and Response Evaluation Criteria in Lymphoma 2017 (5)).

---

Received Mar. 11, 2022; revision accepted Jul. 7, 2022.  
For correspondence or reprints, contact Fabien Ricard ([fabienricardmd@gmail.com](mailto:fabienricardmd@gmail.com)).

\*Contributed equally to this work.

Published online Jul. 14, 2022.

COPYRIGHT © 2023 by the Society of Nuclear Medicine and Molecular Imaging.

Although these recommendations are primarily given for clinical trial end-users, it may be valuable information for health-care providers as well.

## MATERIALS AND METHODS

Task forces (TFs) were created to evaluate technical imaging and clinical considerations of the Lugano classification that could affect its uniformity in evaluating lymphoma response.

The TF members included representatives from academic or scientific organizations ( $n = 3$ ), pharmaceutical industry ( $n = 9$ ), clinical research organizations ( $n = 13$ ), and other clinical trial specialists ( $n = 4$ ), as well as independent research leaders. A steering committee oversaw the activities of each TF. All meetings were held virtually, from July 2019 to October 2021, recorded and transcribed into minutes that were approved by the TF members. In instances for which there was lack of evidence-based data, or consensus, a call for future research on that topic was suggested. Additional recommendations from the TF, primarily for clinical imaging considerations, have been previously published (6).

Any individual involved in the implementation of the Lugano classification is considered an end-user. Any physician responsible for assessing response in lymphoma is considered a reviewer.

## TECHNICAL CONSIDERATIONS FOR IMAGE ACQUISITION, RECONSTRUCTION, AND EVALUATION

### Required Images and Viewing Stations

The assessment of the Lugano classification is informed by both anatomic imaging (diagnostic CT preferred; however, it can be interchangeable with MRI; ultrasound should not be used because of the operator-dependency of the method) and metabolic ( $^{18}\text{F}$ -FDG PET/CT) imaging, for  $^{18}\text{F}$ -FDG-avid lymphomas.

The following images should be provided to the reviewers, when available:  $^{18}\text{F}$ -FDG PET/CT images and diagnostic CT images.  $^{18}\text{F}$ -FDG PET/CT images include PET attenuation-corrected (AC) images; PET non-attenuation-corrected images; low-dose CT for attenuation correction (CTAC) and for localization purposes; and reconstructed images—AC MIP (maximum-intensity-projection) and PET/CT fusion images, unless the viewing software enables creation from AC images, and care should be taken that no patient identifiers are embedded on reconstructed images.

Diagnostic CT images should include CT images with anatomic coverage to encompass all areas of known or suspected disease with appropriate acquisition settings for kVp, mAs, slice thickness of  $\leq 5$  mm, intravenous contrast, and patient positioning and breathing instructions (e.g., deep inspiration breath-hold); and standard soft-tissue and lung reconstruction images.

Viewing stations for image review and interpretation should provide adequate functionality to allow multiplanar display (i.e., axial, coronal and sagittal views) of PET, diagnostic CT and fused PET/CT images for image interpretation and lesion cross-referencing purposes. PET images should be scaled to a set SUV range and color table.

PET software should allow creation of maximum-intensity-projection images (of special importance for providing visual scoring assessments of distant lesions to mediastinum and liver reference tissues). Reading software should allow for vendor-neutral evaluation of PET images, including semiquantitative uptake measurements, and of CT images, including size measurements, and may ideally allow for volumetric assessments (which are interesting exploratory measurements but not included in the Lugano classification). The Quantitative Imaging Biomarkers Alliance (QIBA [<https://rsna.org/QIBA/>]) has provided guidance on system's

technical performance standards (7,8) when the aim is to use  $^{18}\text{F}$ -FDG PET as a quantitative imaging biomarker.

### $^{18}\text{F}$ -FDG PET/CT and Diagnostic CT Scan Visits

PET/CT should provide sufficient anatomic coverage to accurately assess whole-body tumor burden. As a minimum for all patients, PET/CT should include common areas of disease involvement including the neck, chest, abdomen, and pelvis (including groin). Coverage should be adjusted to include additional areas of known or suspected disease (e.g., extremities). Inclusion of the brain is dependent on the lymphoma disease status and imaging center standard protocol. It is highly recommended that  $^{18}\text{F}$ -FDG PET emission scanning commences in the pelvis or thigh region and extend to the upper body, to avoid reconstruction artifacts due to high bladder uptake. The same PET/CT scanner and scanning direction should be used on follow-up time points, and consistent patient positioning and breathing instructions should be ensured across all imaging visits. Time from injection of  $^{18}\text{F}$ -FDG to acquisition of PET images should be kept rigorously constant across successive scans in a patient to allow for comparability of metabolic images (ideally  $\pm 5$  min, up to  $\pm 10$  min, compared with time used at baseline), and acquisition should always be timed to close to 60 min after injection (55–75 min is acceptable) (7–10). Factors affecting SUV calculation (e.g., injection time, but also administered activity, weight) that are entered manually onto the scanner should be carefully checked and documented for quality control purposes.

Whenever possible,  $^{18}\text{F}$ -FDG PET/CT and diagnostic CT scans, if both are required at the same time point, should be acquired on the same scanner during the scheduled imaging visit for patient convenience. CTAC scans should be obtained without intravenous or positive oral bowel contrast. Diagnostic CT with intravenous contrast should be performed after the PET CTAC acquisition in order to avoid overattenuation of the PET images from the CT contrast medium.

A CT should be considered of diagnostic quality (so-called diagnostic CT) if it has adequate resolution to detect and accurately measure lesions and spleen size and should contain intravenous contrast, unless contraindicated, ideally in the portal venous phase for clinical trials. Oral contrast is recommended per site standard of care, especially in patients with known or suspected hollow viscus involvement or mesenteric lymphadenopathy. Technical acquisition parameters, use of intravenous contrast unless medically contraindicated, breath-hold techniques, and arm positioning should be specified beforehand in study documents and kept as consistent as possible for a given subject across time points, and as much as possible for the trial. The CT portion of a PET/CT can be used for lesion and spleen measurements if it is considered of acceptable diagnostic quality.

For situations in which a patient is diagnosed at a center different from the treating institution, it is of utmost importance that the baseline scan (images and image acquisition fields) be made available in DICOM format to enable comparison to subsequent imaging. Ideally, all scans for a same patient should be conducted with the same scanner and at same institution throughout the trial.

Further recommendations are provided in Supplemental Table 1 (available at <http://jnm.snmjournals.org>).

### PET Acquisition and Image Reconstruction

Phantom-based quantitative calibration validation is strongly recommended before a clinical trial is started, and is even critical in trials in which main endpoints require SUV/activity concentration-based quantitative measurements. However, for trials with no

quantitative measurements, the regular quality control that is used for clinical care recommended by the imaging facilities, manufacturer, and institution may be sufficient.

Semiquantitative SUV read-outs can be of interest in trials using the Lugano classification (2), and it is highly recommended that the comprehensive QIBA  $^{18}\text{F}$ -FDG profile (7,8) be implemented at each site as a guideline for standardization of the  $^{18}\text{F}$ -FDG PET workflow. Other guidance exists, such as the European Association of Nuclear Medicine procedure guidelines for tumor imaging with  $^{18}\text{F}$ -FDG PET/CT (10). The scanning sites and study sponsor should agree on key PET reconstruction parameters in order to harmonize image quality and quantification.

Change in  $\text{SUV}_{\text{max}}$  ( $\Delta\text{SUV}$ ) and metabolic tumor volume may be promising tools for response evaluation and prognosis in lymphoma (11,12), including for clinical trials, further emphasizing the need for standardization of PET acquisition (13). A change in SUV measurement (e.g.,  $\Delta\text{SUV}_{\text{max}}$  of less than or equal to 66% in  $^{18}\text{F}$ -FDG PET/CT after 2 cycles of chemotherapy for diffuse large B-cell lymphoma as a correlate to an unfavorable outcome (14–17)) has been suggested for response and prognosis evaluation at interim PET as well as for assessment in PET-guided therapy (18). This promising measurement is undergoing further validation (19–21).

Acquisition and reconstruction methods should be kept consistent throughout the trial and between patient visits. PET 3-dimensional mode acquisition with time-of-flight is preferred when available. In the interest of harmonizing image acquisition across sites, newer reconstruction methods that may not be widely available (e.g., point spread function corrections, regularized reconstructions, artificial intelligence-based acquisition and reconstruction algorithms) and for which the effect on the 5-point scale (5-PS) is not yet known should be used cautiously to assess study outcomes for PET-guided therapy decisions until the impact of these newer methods on the 5-PS is better understood.

However, the TF acknowledges that phantom harmonization programs that align scanner performances across institutions may help to mitigate such differences between newer reconstruction methods, especially for semiquantitative assessments (e.g., SUV and metabolic tumor volume). Although prospective harmonization of PET scanners in a multiinstitutional clinical trial setting is desirable, it may not always be entirely practical or feasible due to variety of reasons (including the use of different reconstruction algorithms, such as Bayesian penalized likelihood and point spread function, compared with older methods, such as traditional ordered-subset expectation maximization).

#### Technical Influence of Lesion Size and Background Activity

The influence of lesion size and activity concentration on partial volume is difficult to correct for in smaller lesions. This is particularly relevant when using the 5-PS to assess small residual lesions in lymphoma response assessment. In phantom studies using different sized spheres filled with identical concentrations of  $^{18}\text{F}$  to mimic tumor sizes, smaller lesions (<2 cm) appeared to have less  $^{18}\text{F}$ -FDG activity than larger lesions ( $\geq 2$  cm) (22–24). This is due to the inability of PET scanners to fully recover all the counts (i.e., partial-volume effects) from smaller compared with larger spheres (or lesions) (22).

Although newer scanners may have advanced reconstruction algorithms to account for the loss of signal (point-response function or regularized reconstructions), there have been no well-controlled studies addressing this issue or its influence on the application of the 5-PS.

Therefore, a uniform recommendation by the TF on how to integrate lesion size information into Lugano evaluation is not possible at this time, and further investigation is encouraged.

Signal-to-noise ratio plays an important role in lesion detection. Image reconstruction and postprocessing of images with available reconstruction algorithms and filtering help to control for and remove noise, which should be optimized for individual scanners based on either phantom testing or according to the suggested recommendations of manufacturers' specifications. However, the conspicuity of lesions is not only dependent on lesion signal but also on the uptake or signal in surrounding tissue and organs. Therefore, the reader should be aware of this phenomenon when interpreting scans.

#### SUV Measurements

Some semiquantitative measurements are routinely recorded (e.g., most hypermetabolic lesion, reference regions), and such measurement may be used to confirm visual assessment, for example, to assign a score of 5 on the 5-PS (2,11).

SUVs that are captured (e.g., most hypermetabolic lesion, reference regions) usually represent the  $\text{SUV}_{\text{max}}$ , in alignment with the Lugano classification. However, other types of measurements (e.g., lesion  $\text{SUV}_{\text{peak}}$ , reference region  $\text{SUV}_{\text{mean}}$ ) are frequently recorded in clinical trials (11).

$\text{SUV}_{\text{max}}$  represents the uptake in the single voxel exhibiting the highest tracer uptake in the region of interest. It is easily available on read stations, has good interreader reproducibility, and is relatively unaffected by partial-volume effects. However,  $\text{SUV}_{\text{max}}$  is influenced by noise.

$\text{SUV}_{\text{peak}}$  is the average of the SUV in the  $1\text{ cm}^3$  of voxels with the highest activity in a volume of interest.  $\text{SUV}_{\text{peak}}$  (corrected for lean body mass) is used in PERCIST (25). PERCIST was proposed in 2009 to better standardize PET response criteria in solid tumors and to combine good interreader reproducibility, reduce the influence of partial volume with  $\text{SUV}_{\text{max}}$ , and improve count rate stability.

$\text{SUV}_{\text{mean}}$  represents the mean tracer uptake in the region of interest. Usually, the most metabolically active portion within the area of interest should be used within the region of interest in which  $\text{SUV}_{\text{mean}}$  is calculated. Measurement of the mean is dependent on the size of the region or volume of interest, which should be standardized.

Further work is warranted in this field to identify the optimal measure for lymphomas. Besides, metabolic assessments (e.g., metabolic tumor volumes) and other radiomic features may become more important in the future.

#### Terminology for Image Evaluation and Reporting

Lugano 2014 considers both metabolic and anatomic assessments when evaluating  $^{18}\text{F}$ -FDG-avid lymphomas. With regard to response assessed on diagnostic CT, both radiographic and anatomic terminology have been used. The TF recommends using the term “anatomic” to describe response.

When response to therapy is evaluated, it is recommended that the metabolic, anatomic, imaging (metabolic response, anatomic response, or combination of both when both available), and overall (used to determine endpoints, integrating clinical data when available) responses be assessed and recorded. In order to differentiate anatomic and overall responses—which currently are using the same terminology—it was suggested to incorporate “anatomic” when recording the anatomic response. Thus, the anatomic response is now referred to as complete anatomic response (CAR), partial anatomic response (PAR), stable anatomic disease (SAD), and

progressive anatomic disease (PAD). Metabolic response remains defined as complete metabolic response or partial metabolic response (CMR or PMR, respectively), no metabolic response (NMR, preferred term, because “stable disease” usually refers to radiographic stability) or stable metabolic disease (SMD), and progressive metabolic disease (PMD). The overall response remains defined as complete response, partial response, stable disease, and progressive disease. Thus, it is clear what each component of the response is, and how each component complementarily results in the overall response.

## **ROLE OF THE REVIEWERS: EXPERIENCE AND QUALIFICATIONS, TRAINING, AND MONITORING**

### **Imaging Reviewers Qualifications and Experience**

Dependent on the read requirements of a clinical protocol, the imaging reviewers should meet certain qualifications, including documentation of competency in diagnostic CT or PET/CT.

Reviewers should be board-eligible (BE) or board-certified (BC) nuclear medicine physicians (or the regional/national equivalent) with experience or certification in CT/MRI, or BE/BC radiologist physicians with experience or training in PET/CT imaging.

### **Clinical Reviewers Qualifications and Experience**

Although Lugano classification does not specifically recommend separate imaging and clinical reviews, if a hematology–oncology review is requested, then the selection of clinical reviewers should meet prespecified qualifications including the credentials as a BE or BC physician in hematology or oncology (or the regional/national equivalent).

Additional experience in clinical care of hematologic malignancies—either through clinical practice or in clinical trials—is required.

In addition, all reviewers, both imaging and clinical, should provide documented evidence of prior clinical experience with lymphomas and clinical trial participation in lymphoma studies on their CV or through attestations of participation. In cases where a reviewer may have no prior experience in clinical trial reads, a program of appropriate training about the application of the Lugano classification in the context of clinical trials and including test cases is required.

Close monitoring of on-trial performance is recommended for all reviewers, both imaging and clinical, regardless of training or experience.

### **Role of the Imaging Reviewer**

The role of a blinded independent central reviewer (BICR) is to provide independent review of cases without bias or unblinding to treatment. It is recommended, when possible, that the reviewer remains the same throughout the reads of all time points for a patient. Where feasible, it is ideal to have the same reviewer provide assessment of both the  $^{18}\text{F}$ -FDG PET/CT and the diagnostic CT throughout the entire study for an individual patient basis. If separate reads of diagnostic CT and  $^{18}\text{F}$ -FDG PET/CT occur, it is recommended that both readers meet for an integration read of anatomic and metabolic assessments that should be conducted to provide 1 patient-level imaging time-point assessment.

Whenever there are 2 BICRs evaluating scans from the same patient and modality, a third independent reviewer (adjudicator) should be assigned to review the scans in cases of time-point assessment discrepancies to resolve any disagreements that would impact the overall time-point responses.

During an adjudication event, the adjudicator should select which reader he or she most closely agrees with, rather than providing a third independent assessment, and a rationale for the selection should be provided. Alternative adjudication workflows exist, which are beyond the scope of this article.

### **Reviewers Training and Monitoring**

Recommended activities that both imaging and clinical reviewers should complete before the start of on-study reads include training on Lugano classification (and any protocol-specified modifications or clarifications) and on completion of imaging case report forms as well as familiarization with workstation usage and group review of clinical cases for formulating consensus on scan interpretation and time-point responses.

Borderline and challenging cases should be involved in the training; the number of cases to be included should be dependent on the study design and experience of reviewers with the response criteria (best practice is to consider 3 cases as a minimum and it should be more especially in the case of less-experienced readers or more complex studies), being mindful that statistics on such small sample of training may not be significant.

Monitoring (e.g., intra- and interreader variability, adjudication rates) is recommended per guidance documents of the Food and Drug Administration (26) and should be performed for all reviewers regardless of training or experience. Members from the PINTaD recently published additional information on reader variability and monitoring of performance (27,28). Reader monitoring should start early in the course of the trial to allow for timely retraining when necessary. Group retraining is recommended on the basis of monitoring results or as periodic follow-up group retraining or reviews to ensure that all readers are provided with identical information to ensure systematic discordance is not introduced.

An example of an imaging case report form and a summary of recommendations can be found in the supplemental materials and Supplemental Table 1, respectively.

## **CONCLUSION**

The PRoLoG initiative has created a platform to gather recommendations from an international group of recognized imaging and clinical expert end-users from academia and industry in the field of lymphoma response assessment to standardize application of the Lugano classification in clinical trials and beyond.

These recommendations are intended for clinical users, at local sites and central facilities, in academic and pharmaceutical clinical trials to enhance standardized acquisition and evaluation with the Lugano classification, facilitating conduction of clinical trials and regulatory review, ultimately leading to improved lymphoma patient outcome.

## **DISCLOSURE**

Sally Barrington acknowledges support from the National Institute for Health and Care Research (NIHR) (RP-2-16-07-001) and by core funding from the Wellcome/EPSCRC Centre for Medical Engineering at King's College London (WT203148/Z/16/Z) and the NIHR Biomedical Research Centre based at Guy's and St. Thomas' NHS Foundation Trust and King's College London and the NIHR Clinical Research Facility. The views expressed by Professor Barrington are not necessarily those of the NHS, the NIHR or the Department of Health and Social Care. This project was sponsored by PINTaD, and the views expressed are those of the authors, not necessarily of their institution. Fabien Ricard,

employed by Bayer at the time of first submitting the manuscript for this article, is now an employee and has shares of Relay Tx. Paul Galette is employed by and a shareholder of GSK. Greg Goldmacher is employed by Merck and has stocks in Merck, ImmunoGen, and Aveo. Julie Gillis, formerly employed by Imaging Endpoints, is at Merigold LLC. Pierre Terve is with Keosys Medical Imaging. Min Liu has shares at Autolus. Larry Schwartz reports to BMS, Regeneron, and Merck as a member of an independent review panel and data safety monitoring board for clinical trials. Jayant Narang and Rudresh Jarecha, formerly employed by Calyx, are with Takeda Pharmaceuticals and Deciphera Pharmaceuticals, respectively. Ron Korn is owner and CMO at Imaging Endpoints Core Lab, a consultant for the Virginia G. Piper Cancer Center and ImaginAB Technologies, and a shareholder of Verve Medical, Telelite Health, Globavir, and Renibus. No other potential conflict of interest relevant to this article was reported.

## ACKNOWLEDGMENTS

We thank all the members from the PINTaD who participated to the PROLoG initiative, especially Klaus Noever, Melissa Burkett, Anand Devasthanam, Nick Enus, Andres Forero Torres, Nick Galante, Sayali Karve, Katarina Ludajic, Michael O'Neal, Ravikanth Mankala, Daniel Mollura, and Jason Vilardi. In addition, we thank Tina Nielsen and John Sunderland for their review of the manuscript, as well as the original authors of the classification and companion paper. Finally, we thank Deming Litner for her administrative support and the CDISC group for discussion on terminology for anatomic and metabolic responses.

## KEY POINTS

**QUESTION:** How can the Lugano classification be consistently applied among imaging end-users?

**PERTINENT FINDINGS:** These consensus recommendations should be used as a companion to the Lugano classification with regards to required imaging series and scan visits and acquisition and reconstruction of PET images. The roles of imaging and clinical reviewers as well as of training and monitoring are clarified.

**IMPLICATIONS FOR PATIENT CARE:** This guidance will enhance usage of the Lugano classification, facilitating the conduction of clinical trials and regulatory review, ultimately leading to improved lymphoma patient outcome.

## REFERENCES

- Cheson BD, Fisher RI, Barrington SF, et al. Recommendations for initial evaluation, staging, and response assessment of Hodgkin and non-Hodgkin lymphoma: the Lugano classification. *J Clin Oncol*. 2014;32:3059–3068.
- Barrington SF, Mikhael NG, Kostakoglu L, et al. Role of imaging in the staging and response assessment of lymphoma: consensus of the international conference on malignant lymphomas imaging working group. *J Clin Oncol*. 2014;32:3048–3058.
- Cheson BD, Pfistner B, Juweid ME, et al. Revised response criteria for malignant lymphoma. *J Clin Oncol*. 2007;25:579–586.
- Cheson BD, Ansell S, Schwartz L, et al. Refinement of the Lugano classification lymphoma response criteria in the era of immunomodulatory therapy. *Blood*. 2016;128:2489–2496.
- Younes A, Hilden P, Coiffier B, et al. International working group consensus response evaluation criteria in lymphoma (RECIL 2017). *Ann Oncol*. 2017;28:1436–1447.
- Ricard F, Cheson B, Barrington S, et al. Application of the Lugano classification for initial evaluation, staging, and response assessment of Hodgkin and non-Hodgkin lymphoma: the ProLog consensus initiative (part 1—clinical). *J Nucl Med*. 2023;64:102–108.
- Kinahan PE, Perlman E, Sunderland J, et al. The QIBA profile for FDG PET/CT as an imaging biomarker measuring response to cancer therapy. *Radiology*. 2020;294:647–657.
- FDG PET-CT Technical Committee. FDG PET-CT as an imaging biomarker measuring response to cancer therapy, quantitative imaging biomarkers alliance, version 1.13, technically confirmed version. QIBA, November 18, 2016. RSNA website. [http://qibawiki.rsna.org/images/1/1f/QIBA\\_FDG-PET\\_Profile\\_v113.pdf](http://qibawiki.rsna.org/images/1/1f/QIBA_FDG-PET_Profile_v113.pdf). Accessed November 21, 2022.
- FDG PET-CT UPICT V 2.0 Full document, publicly reviewed version (December 2014). RSNA website. [http://qibawiki.rsna.org/images/7/71/UPICT\\_Oncologic\\_FDG-PETCTProtocol\\_Dec-2014a.pdf](http://qibawiki.rsna.org/images/7/71/UPICT_Oncologic_FDG-PETCTProtocol_Dec-2014a.pdf). Accessed November 21, 2022.
- Boellaard R, Delgado-Bolton R, Oyen WJG, et al. FDG PET/CT: EANM procedure guidelines for tumour imaging: version 2.0. *Eur J Nucl Med Mol Imaging*. 2015;42:328–354.
- Barrington SF, Kluge R. FDG PET for therapy monitoring in Hodgkin and non-Hodgkin lymphomas. *Eur J Nucl Med Mol Imaging*. 2017;44(suppl 1):97–110.
- Schöder H, Moskowitz CH. Metabolic tumor volume in lymphoma: hype or hope? *J Clin Oncol*. 2016;34:3591–3594.
- Kostakoglu L, Chauvie S. Metabolic tumor volume metrics in lymphoma. *Semin Nucl Med*. 2018;48:50–66.
- Lin C, Itti E, Haioun C, et al. Early <sup>18</sup>F-FDG PET for prediction of prognosis in patients with diffuse large B-cell lymphoma: SUV-based assessment versus visual analysis. *J Nucl Med*. 2007;48:1626–1632.
- Itti E, Meignan M, Berriolo-Riedinger A, et al. An international confirmatory study of the prognostic value of early PET/CT in diffuse large B-cell lymphoma: comparison between Deauville criteria and  $\Delta$ SUVmax. *Eur J Nucl Med Mol Imaging*. 2013;40:1312–1320.
- Casasnovas RO, Meignan M, Berriolo-Riedinger A, et al. SUVmax reduction improves early prognosis value of interim positron emission tomography scans in diffuse large B-cell lymphoma. *Blood*. 2011;118:37–43.
- Eertink JJ, Burggraaff C, Heymans M, et al. Optimal timing and criteria of interim PET in DLBCL: a comparative study of 1692 patients. *Blood Adv*. 2021;5:2375–2384.
- Le Gouill S, Ghesquieres H, Oberic L, et al. Obinutuzumab vs rituximab for advanced DLBCL: a PET-guided and randomized phase 3 study by LYSA. *Blood*. 2021;137:2307–2320.
- Rekowski J, Hüttmann A, Schmitz C, et al. Interim PET evaluation in diffuse large B-cell lymphoma using published recommendations: comparison of the Deauville 5-Point scale and the  $\Delta$ SUV max method. *J Nucl Med*. 2021;62:37–42.
- Kurch L, Andreas H, Georgi TM, et al. Interim positron emission tomography in diffuse large B-cell lymphoma. *J Nucl Med*. 2021;62:1068–1074.
- Schöder H, Polley MYC, Knopp MV, et al. Prognostic value of interim FDG PET in diffuse large cell lymphoma: results from the CALGB 50303 Clinical Trial. *Blood*. 2020;135:2224–2234.
- Raylman RR, Kison P, Wahl R. Capabilities of two- and three-dimensional FDG-PET for detecting small lesions and lymph nodes in the upper torso: a dynamic phantom study. *Eur J Nucl Med*. 1999;26:39–45.
- de Langen AJ, Vincent A, Velasquez LM, et al. Repeatability of <sup>18</sup>F-FDG uptake measurements in tumors: a metaanalysis. *J Nucl Med*. 2012;53:701–708.
- Itti E, Juweid ME, Haioun C, et al. Improvement of early <sup>18</sup>F-FDG PET interpretation in diffuse large B-cell lymphoma: importance of the reference background. *J Nucl Med*. 2010;51:1857–1862.
- Wahl RL, Jacene H, Kasamaon Y, et al. From RECIST to PERCIST: evolving considerations for PET response criteria in solid tumors. *J Nucl Med*. 2009;50(suppl 1):122S–150S.
- Clinical Trial Imaging Endpoint Process Standards. Guidance for Industry. U.S. Department of Health and Human Services. Food and Drug Administration Center for Drug Evaluation and Research (CDER). Center for Biologics Evaluation and Research (CBER). April 2018, Clinical/Medical. FDA website. <https://www.fda.gov/files/drugs/published/Clinical-Trial-Imaging-Endpoint-Process-Standards-Guidance-for-Industry.pdf>. Accessed November 21, 2022.
- Schmid AM, Raunig DL, Miller CG, et al. Radiologists and clinical trials: part 1—the truth about reader disagreements. *Ther Innov Regul Sci*. 2021;55:1111–1121.
- Raunig DL, Schmid AM, Miller CG, et al. Radiologists and clinical trials: part 2—practical statistical methods for understanding and monitoring independent reader performance. *Ther Innov Regul Sci*. 2021;55:1122–1138.

---

---

# Static and Dynamic $^{68}\text{Ga}$ -FAPI PET/CT for the Detection of Malignant Transformation of Intraductal Papillary Mucinous Neoplasia of the Pancreas

Matthias Lang<sup>1</sup>, Anna-Maria Spektor<sup>2</sup>, Thomas Hielscher<sup>3</sup>, Jorge Hoppner<sup>2</sup>, Frederik M. Glatting<sup>2,4,5</sup>, Felix Bicu<sup>2</sup>, Thilo Hackert<sup>1</sup>, Ulrike Heger<sup>1</sup>, Thomas Pausch<sup>1</sup>, Ewgenija Gutjahr<sup>6</sup>, Hendrik Rathke<sup>2,7</sup>, Frederik L. Giesel<sup>2,8</sup>, Clemens Kratochwil<sup>2</sup>, Christine Tjaden<sup>1</sup>, Uwe Haberkorn<sup>2,9,10</sup>, and Manuel Röhrich<sup>2</sup>

<sup>1</sup>Department of General, Visceral, and Transplantation Surgery, University Hospital Heidelberg, Heidelberg, Germany; <sup>2</sup>Department of Nuclear Medicine, University Hospital Heidelberg, Heidelberg, Germany; <sup>3</sup>Department of Biostatistics, German Cancer Research Center, Heidelberg, Germany; <sup>4</sup>Clinical Cooperation Unit Molecular and Radiation Oncology, German Cancer Research Center (DKFZ), Heidelberg, Germany; <sup>5</sup>Department of Radiation Oncology, University Hospital Heidelberg, Heidelberg, Germany; <sup>6</sup>Department of Pathology, University Hospital Heidelberg, Heidelberg, Germany; <sup>7</sup>Department of Nuclear Medicine, The Inselspital, Bern University Hospital, University of Bern, Bern, Switzerland; <sup>8</sup>Department of Nuclear Medicine, University Hospital Düsseldorf, Düsseldorf, Germany; <sup>9</sup>Translational Lung Research Center Heidelberg (TLRC), Member of the German Center for Lung Research DZL, Heidelberg, Germany; and <sup>10</sup>Clinical Cooperation Unit Nuclear Medicine, German Cancer Research Center (DKFZ), Heidelberg, Germany

---

Pancreatic ductal adenocarcinoma (PDAC) may arise from intraductal papillary mucinous neoplasms (IPMN) with malignant transformation, but a significant portion of IPMN remains to show benign behavior. Therefore, it is important to differentiate between benign IPMN and IPMN lesions undergoing malignant transformation. However, nonoperative differentiation by ultrasound, CT, MRI, and carbohydrate antigen 19-9 (CA19-9) is still unsatisfactory. Here, we assessed the clinical feasibility of additional assessment of malignancy by PET using  $^{68}\text{Ga}$ -labeled fibroblast activation protein inhibitors ( $^{68}\text{Ga}$ -FAPI PET) in 25 patients with MRI- or CT-proven cystic pancreatic lesions. **Methods:** Twenty-five patients with cystic pancreatic lesions who were followed up in the European Pancreas Center of Heidelberg University hospital and who were led to surgical resection or fine-needle aspiration due to suspicious clinical, laboratory chemistry, or radiologic findings were examined by static (all patients) and dynamic (20 patients)  $^{68}\text{Ga}$ -FAPI PET. Cystic pancreatic lesions were delineated and  $\text{SUV}_{\text{max}}$  and  $\text{SUV}_{\text{mean}}$  were determined. Time-activity curves and dynamic parameters (time to peak,  $K_1$ ,  $k_2$ ,  $K_3$ ,  $k_4$ ) were extracted from dynamic PET data. Receiver-operating curves of static and dynamic PET parameters were calculated. **Results:** Eleven of the patients had menacing IPMN (high-grade IPMN with [6 cases] or without [5 cases] progression into PDAC) and 11 low-grade IPMN; 3 patients had other benign entities. Menacing IPMN showed significantly elevated  $^{68}\text{Ga}$ -FAPI uptake compared with low-grade IPMN and other benign cystic lesions. In dynamic imaging, menacing IPMN showed increasing time-activity curves followed by slow decrease afterward; time-activity curves of low-grade IPMN showed an immediate peak followed by rapid decrease for about 10 min and slower decrease for the rest of the time. Receiver-operating curves showed high sensitivity and specificity (area under the curve greater than 80%) of static and dynamic PET parameters for the differentiation of IPMN subtypes. **Conclusion:**  $^{68}\text{Ga}$ -FAPI PET is a helpful new tool for the differentiation

of menacing and low-grade IPMN and shows the potential to avoid unnecessary surgery for nonmalignant pancreatic IPMN.

**Key Words:** fibroblast activation protein; FAPI; PET; dynamic PET; cancer; PDAC; IPMN

**J Nucl Med 2023; 64:244–251**  
DOI: 10.2967/jnumed.122.264361

---

**T**he pancreatic ductal adenocarcinoma (PDAC) belongs to the most lethal cancers, with a poor 5-y survival rate of less than 10% despite surgical resection, radiotherapy, and chemotherapy (1). Intraductal papillary mucinous neoplasms (IPMN) with high-grade dysplasia (hg-IPMN) are precursors for malignant transformation into PDAC (2). Therefore, resection of hg-IPMN before the development of invasive PDAC is mandatory (3,4). hg-IPMN with and without development into PDAC are grouped together in this article as menacing IPMN (men-IPMN). In contrast, IPMN with low-grade dysplasia (lg-IPMN) are regarded as benign lesions that should be controlled regularly but not resected (3,4). Regarding the significant risk of complications in pancreatic surgery (morbidity rates of 35%–50% and mortality rates up to 1% (5,6)), the selective resection of men-IPMN is an important goal.

Currently, evaluation of IPMN regarding malignant potential is controversial and mostly based on the Fukuoka consensus criteria of 2017 or the European guidelines for pancreatic cystic neoplasms. Both rely on multiple clinical and morphologic parameters (3,4). However, several publications have shown the shortcomings of these guidelines due to their limited specificity and sensitivity (7–9). Recent studies revealed that only 35% of IPMN were resected in a timely fashion (10). Therefore, the decision for surgical treatment remains challenging, and clinical tools to distinguish between lg-IPMN and men-IPMN are urgently needed.

PET using  $^{68}\text{Ga}$ -labeled fibroblast activation protein inhibitors combined with CT ( $^{68}\text{Ga}$ -FAPI PET/CT) has shown excellent

---

Received May 2, 2022; revision accepted Jul. 16, 2022.  
For correspondence or reprints, contact Manuel Röhrich (manuel.roehrich@med.uni-heidelberg.de).  
Published online Jul. 29, 2022.  
COPYRIGHT © 2023 by the Society of Nuclear Medicine and Molecular Imaging.



imaging properties and high clinical potential for PDAC. The intense FAPI tracer accumulation in PDAC is based on the strong stromal portion of PDAC including fibroblast activation protein (FAP)-positive cancer-associated fibroblasts (11). We hypothesized that FAP-positive stroma could be a common feature of PDAC and men-IPMN, but not of lg-IPMN, as the desmoplastic stromal reaction is a prominent hallmark of malignancy but not of benign lesions (12). Here, we retrospectively analyzed preoperative static and dynamic <sup>68</sup>Ga-FAPI PET data of 25 patients with suspected IPMN and compared imaging features with histologic diagnoses to evaluate the potential value of <sup>68</sup>Ga-FAPI PET for the differentiation of lg- and men-IPMN.

## MATERIALS AND METHODS

### Patient Characteristics

Patients were selected for <sup>68</sup>Ga-FAPI PET according to the following criteria: age, 18 y or older; MRI- or CT-proven pancreatic cyst leading to the clinical diagnosis of IPMN; absolute or relative indication for surgery; and sufficient compliance for and consent to the <sup>68</sup>Ga-FAPI PET procedure. All patients conforming to these selection

criteria who presented in the European Pancreas Center Heidelberg during the examination period (June 2020 to December 2021) were included in our analysis. Twenty-five patients (mean age, 63.8 y; maximum age, 83 y; minimum age, 38 y; 13 men) with contrast-enhanced MRI- (24 patients) or CT- (2 patients) proven cystic pancreatic lesions planned for surgery underwent <sup>68</sup>Ga-FAPI PET imaging. All patients were referred by their treating physicians to exclude metastatic disease. Additionally, in 8 patients an endoscopic ultrasound (EUS)-guided fine-needle aspiration (FNA) cytology was obtained. No malignant results were found. Clinical diagnosis of IPMN was based on the identification of a cystic lesion larger than 10 mm, related to the pancreatic main duct, or a main duct dilatation of more than 5 mm without signs of chronic pancreatitis using MRI or CT. All patients had a relative or absolute indication for pancreatic surgery according to recent European guidelines (4). In 7 patients the diameter of the pancreatic main duct exceeded 10 mm, in 1 patient diameter was more than 5 mm, and 1 patient presented with jaundice. Four patients showed an elevated carbohydrate antigen 19-9 (CA 19-9) level and 9 a branch duct dilatation greater than 40 mm; in 1 patient an enhancing mural nodule less than 5 mm was detected. One female presented symptomatic with recurrent IPMN-related acute pancreatitis. Tumor marker

**TABLE 1**  
Clinical Characteristics and Histologic Diagnoses of 25 Patients with Suspected IPMN and <sup>68</sup>Ga-FAPI-74 PET/CT

Patient	Sex	Age (y)	Cyst size (mm)	IPMN type	Additional information	Surgery/histology	Histologic diagnosis
1	M	52	29	BD		Whipple	lg-IPMN
2	F	52	57	BD		Excision	lg-IPMN
3	M	76	40	BD		Cytology	lg-IPMN
4	F	42	30	BD		Whipple	lg-IPMN
5	M	71	60	BD		Whipple	lg-IPMN
6	F	67	44	BD		Distal pancreatectomy	lg-IPMN
7	M	56	18*	MD	Mural nodule	Enucleation	hg-IPMN
8	M	79	10*	MD		Whipple	hg-IPMN
9	M	53	20*	MD		Distal pancreatectomy	PDAC
10	F	64	11*	MD		Whipple	PDAC
11	M	68	32	BD	MD with dilatation to 4.8 mm, jaundice	Whipple	PDAC
12	F	44	10*	Mixed type		Distal pancreatectomy	hg-IPMN
13	F	57	50*	MD		Pancreatectomy	PDAC
14	M	78	90	Mixed type	Solid components	Therapy refused	None
15	F	74	25	BD	Size progressing	Distal pancreatectomy	hg-IPMN
16	F	80	42	BD		Distal pancreatectomy	PDAC
17	F	83	45	BD		Distal pancreatectomy	PDAC
18	M	63	30	BD		Cytology (nonconclusive)	None
19	M	77	60	BD		Cytology	None
20	F	64	30	BD		Cytology (nonconclusive)	None
21	F	57	23	BD	Size progressing	None	None
22	M	74	10	BD		None	None
23	F	54	38			Cytology	SCN
24	F	38	38			Distal pancreatectomy	SCN
25	M	62	21			Distal pancreatectomy	PanIN

\*Main duct diameter.

BD = branch duct; MD = main duct; SCN = serous cystic neoplasia; PanIN = pancreatic intraepithelial neoplasia.

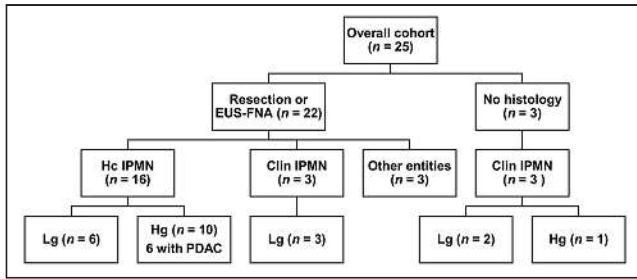


**FIGURE 1.** Histologic diagnoses and clinical classification of 25 patients with suspected IPMN who underwent  $^{68}\text{Ga}$ -FAPI PET/CT. Clin IPMN = clinical IPMN; EUS-FNA = endoscopic ultrasound-guided fine-needle aspiration; hc IPMN = histologically confirmed IPMN; hg = high grade; lg = low grade; PDAC = pancreatic ductal adenocarcinoma.

carcinoembryonic antigen was moderately elevated in 1 individual (3.4  $\mu\text{g/L}$ , upper limit of normal [ULN] 2.5), who had a highly elevated CA 19-9 (476 U/mL, ULN 37) too. The following absolute or relative criteria for resection according to the European guidelines (4) were not observed: EUS-guided malignant cytology/histology, growth rate of branch duct IPMN (BD-IPMN) greater than 5 mm per year, and new onset of diabetes mellitus. Table 1 provides a detailed patient-wise overview of clinical characteristics and histologic diagnoses.

#### $^{68}\text{Ga}$ -FAPI PET/CT Imaging

Synthesis and labeling of  $^{68}\text{Ga}$ -FAPI-74 were conducted as previously described (13–15). For PET imaging, a Biograph mCT Flow scanner (Siemens) was used, according to previously published protocols (16). In short, after a low-dose CT without contrast, 3-dimensional PET scans were acquired (matrix,  $200 \times 200$ ), reconstructions performed, and emission data corrected for attenuation. For all patients, static PET scans were acquired at 60 min after administration of 180–329 MBq of  $^{68}\text{Ga}$ -labeled FAPI-74. To characterize early  $^{68}\text{Ga}$ -FAPI-74 uptake kinetics, additional dynamic PET scanning was performed in 20 patients as previously described (16).

#### Image Evaluation

For static PET scans,  $\text{SUV}_{\text{max}}$  and  $\text{SUV}_{\text{mean}}$  of cystic pancreatic lesions and healthy organs were analyzed using a volume of interest (VOI) technique. VOIs were defined by an automatic isocontour with a cutoff at 50% of  $\text{SUV}_{\text{max}}$ . For dynamic PET imaging analysis, VOIs of cystic lesions and aortal blood were drawn and applied to the entire dynamic dataset. Time-activity curves of  $^{68}\text{Ga}$ -FAPI-74 uptake were obtained, and time to peak (TTP) values (minutes from the beginning of the dynamic acquisition to the  $\text{SUV}_{\text{max}}$  of the lesion) were derived from these. Kinetic modeling using a 2-compartment model was performed to generate  $K_1$  and  $k_2$  values. Dynamic data analysis was performed using PMOD software (PMOD Technologies Ltd.).

#### Statistical Analysis

Receiver-operating curve (ROC) analysis was used to assess discriminative ability of PET parameters. Area under the ROC curve with corresponding 95% CI using Delong's method (17) was computed using R package pROC (18).

## RESULTS

### Histologic Results and Surgical Management of the Patients

Twenty-two of 25 patients examined by  $^{68}\text{Ga}$ -FAPI PET/CT underwent resection or EUS-FNA. Six of these 22 patients had a histologically confirmed (hc) lg-IPMN. Ten of 22 patients had a hc men-IPMN (6 of them with transition into PDAC). In 3 of 22 patients, EUS-guided fluid aspiration strongly indicated a mucinous lesion without signs of malignancy; thus, we considered these cases as clinical lg-IPMN. Three of 22 patient had a histologic confirmation of entities other than IPMN (2 serous cystic neoplasia, 1 pancreatic intraepithelial neoplasia). Three of 25 patients had no histologic confirmation. Because of radiologic appearance and clinical course, 2 patients were considered as clinical lg-IPMN and 1 as clinical hg-IPMN (Fig. 1). Of the 10 patients with hc men-IPMN, 5 underwent distal pancreatectomy, 3 pancreatoduodenectomy, 1 complete pancreatectomy, and 1 enucleation. Of 6 patients with hc lg-IPMN, 2 underwent pancreaticoduodenectomy, 1 distal pancreatectomy, and 1 enucleation. Two patients underwent EUS-FNA only and are still under surveillance without any complications. As  $^{68}\text{Ga}$ -FAPI-74 PET imaging did not reveal any metastatic diseases, it did not influence the surgical management of the patients analyzed.

### $^{68}\text{Ga}$ -FAPI-74 Biodistribution and Uptake of Men-IPMN and Low-Grade IPMN

On the basis of static PET images acquired at 1 h after injection, normal tissues including the healthy part of the pancreas all showed low  $\text{SUV}_{\text{max}}$  and  $\text{SUV}_{\text{mean}}$  resulting in low background signal for the analysis of pathologies (Fig. 2A). Clinical and hc men-IPMN showed markedly higher  $^{68}\text{Ga}$ -FAPI-74 uptake than clinical and hc lg-IPMN and other pathologies (Figs. 3A and 3B). Of note, hg-IPMN, which had already undergone malignant progression into PDAC, showed higher  $\text{SUV}_{\text{max}}$  and  $\text{SUV}_{\text{mean}}$  than those without (Supplemental Fig. 1; supplemental materials are available at <http://jnm.snmjournals.org>). Grouped according to surgical management,  $^{68}\text{Ga}$ -FAPI-74 uptake of lesions with an indication for surgery (hc and clinical men-IPMN) was significantly higher than that of lesions without (hc and clinical lg-IPMN and other pathologies) (Figs. 3C and 3D).

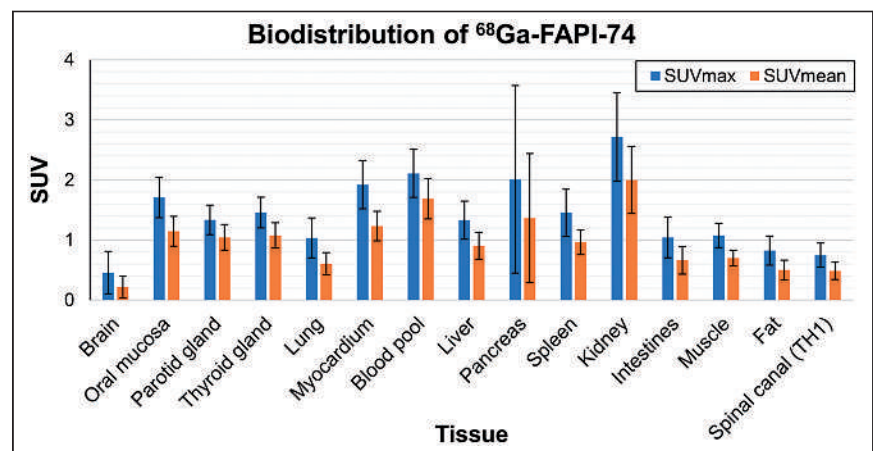


**FIGURE 2.** Biodistribution analysis ( $\text{SUV}_{\text{max}}$  and  $\text{SUV}_{\text{mean}} \pm \text{SD}$ ) of 25 patients with suspected IPMN based on static PET imaging at 1 h after injection of  $^{68}\text{Ga}$ -labeled FAPI-74.

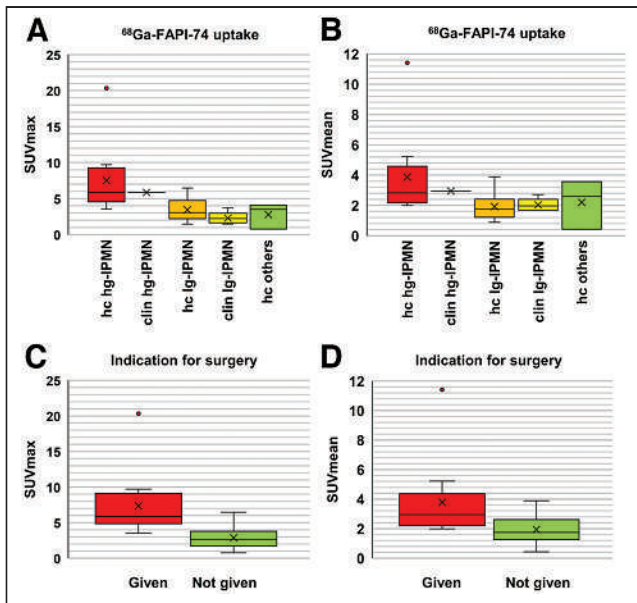


**FIGURE 3.** (A and B) Boxplots of  $SUV_{max}$  (A) and  $SUV_{mean}$  (B) of different types of cystic pancreatic lesions. (C and D) Boxplots of  $SUV_{max}$  (C) and  $SUV_{mean}$  (D) sorted by given or not given indication for surgery. Boxes represent the interquartile range (IQR) and whiskers the range of 1.5 IQR; horizontal line within box indicates the median and cross the mean. Data outliers are shown separately within graph. clin hg-IPMN = clinical high-grade IPMN; clin lg-IPMN = clinical low-grade IPMN; hc hg-IPMN = histologically confirmed high-grade IPMN; hc lg-IPMN = histologically confirmed low-grade IPMN; hc others = histologically confirmed other entities.

### Dynamic Imaging

Dynamic  $^{68}\text{Ga}$ -FAPI-74 PET was performed in 20 patients (9 with hc men-IPMN, 4 with hc lg-IPMN, 5 with clinical lg-IPMN and 2 with other pathologies [not evaluated]). Time-activity curves of hc men-IPMN differed markedly from those of hc and clinical lg-IPMN. Whereas hc men-IPMN showed an increasing time-activity curve for about 6 min and slowly decreasing time-activity curves afterward, hc and clinical lg-IPMN showed an immediate peak followed by rapid decrease for about 10 min and slower decrease for the rest of the time (Figs. 4A–4C). The delayed increase and prolonged washout of the tracer in men-IPMN compared with lg-IPMN are also reflected by increased TTP (Fig. 4D). Kinetic modeling using a 2-tissue-compartment model revealed decreased  $K_1$  and  $k_2$  values (Figs. 4E and 4F) as well as decreased  $K_3$  and  $k_4$  values (Supplemental Fig. 2) of men-IPMN compared with lg-IPMN.

### Sensitivity and Specificity

Figure 5 shows ROCs displaying the sensitivity and specificity of  $SUV_{max}$ ,  $SUV_{mean}$ , and TTP for the distinction between hc lg-IPMN and hc men-IPMN (Fig. 5A) and between entities requiring surgery or not (Fig. 5B). For all parameters, the area under the curve (AUC) was greater than 80%, suggesting a high discriminatory power of static and dynamic  $^{68}\text{Ga}$ -FAPI PET for both distinctions, whereas TTP showed slightly higher AUC values than static parameters for both distinctions (for men-IPMN vs. lg-IPMN: 97.2% vs. 86.7% [ $SUV_{max}$ ] and 88.3% [ $SUV_{mean}$ ], for indication for surgery 92.6% vs. 91.6% [ $SUV_{max}$ ] and 81.8% [ $SUV_{mean}$ ]). Table 2 provides thresholds and specificities at fixed sensitivities of 90% and 80%, including 95% CIs for  $SUV_{max}$ ,  $SUV_{mean}$ , and TTP with respect to the discrimination of hc men-IPMN and hc lg-IPMN and given or not given indication for surgery.

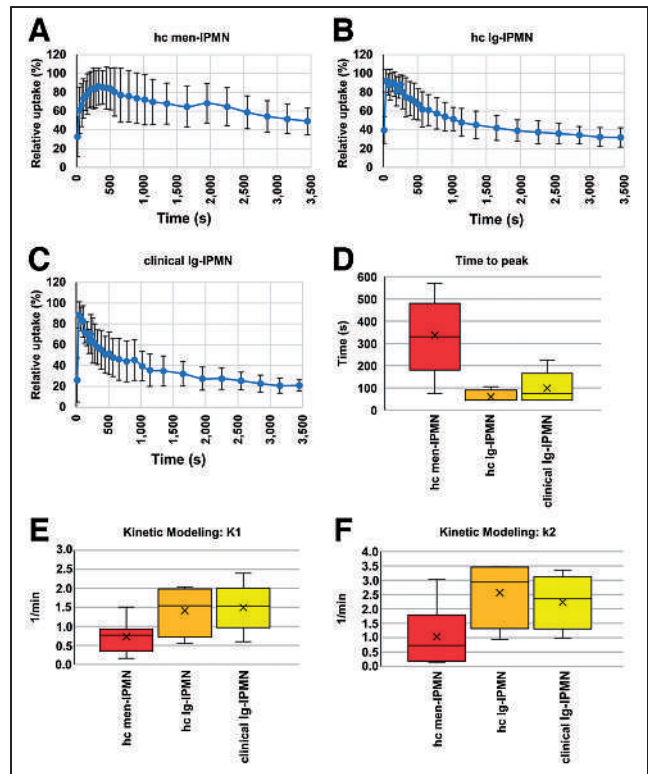


**FIGURE 4.** (A–C) Time-activity curves displaying averaged  $^{68}\text{Ga}$ -FAPI-74 uptake (relative to peak) kinetics of histologically confirmed menacing IPMN (hc men-IPMN) (A), histologically confirmed low-grade IPMN (hc lg-IPMN) (B), and clinical low-grade IPMN (clin lg-IPMN) (C). (D) Box plot displaying time to peak values of histologically confirmed menacing IPMN, histologically confirmed low-grade IPMN, and clinical low-grade IPMN as measured by dynamic  $^{68}\text{Ga}$ -FAPI-74 PET imaging. (E and F) Box plots displaying  $K_1$  (E) and  $k_2$  (F) values of histologically confirmed menacing IPMN, histologically confirmed low grade IPMN, and clinical low-grade IPMN as calculated by kinetic modeling of dynamic  $^{68}\text{Ga}$ -FAPI-74 PET imaging data. Boxes represent the interquartile range (IQR) and whiskers the range of 1.5 IQR; horizontal line within box indicates the median and cross the mean. Data outliers are shown separately within graph.

### Case Vignette

In Figure 6, 3 representative cases are highlighted. The patient with PDAC based on an IPMN is a 68-y-old male, who presented in our department with slight jaundice and brown urine. A weight loss of 6 kg in 3 wk had occurred. Otherwise, the patient was completely asymptomatic. Laboratory results revealed a bilirubin of 8.1 mg/dL (ULN 1.0) and a CA 19-9 of 341.9 U/mL (ULN 37). In contrast-enhanced (ce) MRI, a double duct sign and several cystic lesions of the pancreatic head were apparent. There was no visible solid mass in the pancreas. A malignant transformation of a mixed-type IPMN was diagnosed. To exclude extrapancreatic manifestation, a  $^{68}\text{Ga}$ -FAPI PET/CT image was obtained. The pancreatic head showed intense  $^{68}\text{Ga}$ -FAPI uptake, indicating pancreatic tumor. As no metastatic lesions were apparent, a Whipple procedure was performed. Histologically an adenocarcinoma of the pancreatic head (35 mm), based on a mixed-type IPMN with high-grade dysplasia, was confirmed (pT2, pN2 [19/26], L1, V1, Pn1, G3, R0, CRM+). For the patient with hg-IPMN without progression into PDAC, a woman aged 44 y, randomly determined elevated pancreatic enzymes led to an MRI examination. The examination showed dilation of the main pancreatic duct by 10 mm

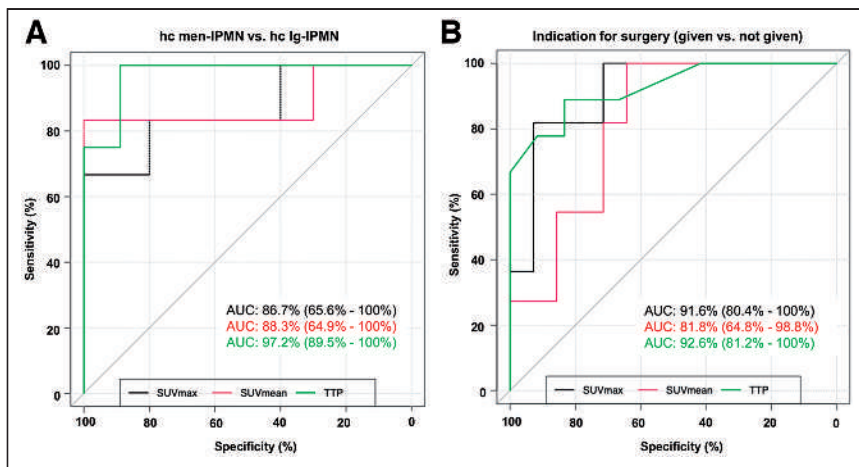


**FIGURE 5.** (A and B) Receiver-operating-characteristic (ROC) curves depicting sensitivity and specificity of quantitative static ( $SUV_{max}$  and  $SUV_{mean}$ ) and dynamic (TTP)  $^{68}\text{Ga}$ -FAPI-74 PET parameters for differentiation of histologically confirmed menacing IPMN and low-grade IPMN (A) and of lesions with and without indication for surgery (B). AUC = area under the curve.

and dilation of the branch duct by 16 mm. There were no symptoms of weight loss, abdominal pain, or pancreatitis. Laboratory results for CA 19-9, bilirubin, or inflammation were unremarkable; only lipase was slightly elevated (92 U/L, ULN 63 U/L). A diagnosis of mixed-type IPMN was made.  $^{68}\text{Ga}$ -FAPI PET/CT showed a markedly increased  $SUV_{max}$  of 4.9. Via robotic assisted distal pancreatectomy, a mixed-type IPMN with high-grade dysplasia (pTis, N0) was successfully removed.

The patient with lg-IPMN was a 52-y-old woman who complained about abdominal pain. An abdominal ultrasound revealed a 60-mm cystic lesion in the pancreatic head without nodules or suspect perfusion on contrast-enhanced ultrasound. This lesion was confirmed on ceMRI and classified as a 60-mm side branch IPMN. The laboratory results were unremarkable. The medical history included a type 1 diabetes diagnosis with an onset at 2 y of age,

complicated by neuropathy, retinopathy, and terminal nephropathy. In  $^{68}\text{Ga}$ -FAPI PET/CT only a low accumulation was observed. As the size exceeded by far the guideline's limits, the cystic lesion was removed by laparoscopic robotic enucleation. Histologically a large branch duct IPMN with low-grade dysplasia was diagnosed.

## DISCUSSION

### Summary of Results

In this retrospective analysis of  $^{68}\text{Ga}$ -FAPI-74 PET imaging in 25 patients with cystic pancreatic lesions, we observed significantly higher  $^{68}\text{Ga}$ -FAPI-74 uptake measured as  $SUV_{max}$  and  $SUV_{mean}$  in men-IPMN than in lg-IPMN and other benign lesions. In dynamic  $^{68}\text{Ga}$ -FAPI PET imaging, men-IPMN and lg-IPMN showed dif-

ferential kinetic behavior, reflected by differences in TTP,  $K_1$ , and  $k_2$  as well as  $K_3$  and  $k_4$  values. The high diagnostic accuracy of static and dynamic  $^{68}\text{Ga}$ -FAPI-74 PET for the differentiation of men-IPMN and lg-IPMN was reflected by high AUC values in all ROC curves analyzed. These results suggest that  $^{68}\text{Ga}$ -FAPI-74 PET is a promising new imaging technique for the clinical evaluation of pancreatic cystic lesions.

### Static and Dynamic $^{68}\text{Ga}$ -FAPI-74 PET Imaging

We observed a high  $^{68}\text{Ga}$ -FAPI-74 uptake in men-IPMN (with and without PDAC) and significantly lower  $^{68}\text{Ga}$ -FAPI uptake in lg-IPMN, whereas healthy tissues had negligible background activity, leading to excellent contrast for suspicious lesions, similar to those shown by previous studies on  $^{68}\text{Ga}$ -FAPI PET/CT in PDAC and other tumors (19,20). Next to static imaging results, we could

**TABLE 2**

Threshold and Specificity at Fixed Sensitivities of 90% and 80% for Differentiation Between Histologically Confirmed Low-Grade IPMN and Histologically Confirmed Menacing IPMN and Given Versus Not Given Indication for Surgery

Endpoint	Parameter	Threshold	Sensitivity (%)	95% CI	Specificity (%)	95% CI	TN	TP	FN	FP
lg/men	$SUV_{max}$	3.62	90.0	55.5–99.7	66.7	22.3–95.7	4	9	1	2
		4.85	80.0	44.4–97.5	83.3	35.9–99.6	5	8	2	1
lg/men	$SUV_{mean}$	2.07	90.0	55.5–99.7	83.3	35.9–99.6	5	9	1	1
		2.19	80.0	44.4–97.5	83.3	35.9–99.6	5	8	2	1
lg/men	TTP	135.00	88.9	51.8–99.7	100.0	39.8–100.0	4	8	1	0
		225.00	77.8	40.0–97.2	100.0	39.8–100.0	4	7	2	0
Surgery	$SUV_{max}$	3.62	90.9	58.7–99.8	71.4	41.9–91.6	10	10	1	4
		4.85	81.8	48.2–97.7	92.9	66.1–99.8	13	9	2	1
Surgery	$SUV_{mean}$	2.07	90.9	58.7–99.8	64.3	35.1–87.2	9	10	1	5
		2.19	81.8	48.2–97.7	71.4	41.9–91.6	10	9	2	4
Surgery	TTP	135	88.9	51.8–99.7	83.3	51.6–97.9	10	8	1	2
		225	77.8	40.0–97.2	91.7	61.5–99.8	11	7	2	1

FN = false negative; FP = false positive; lg/men = histologically confirmed low-grade IPMN vs. histologically confirmed menacing IPMN; TN = true negative; TP = true positive; TTP = time to peak. For some settings only approximate sensitivities could be selected due to sparsity of data.

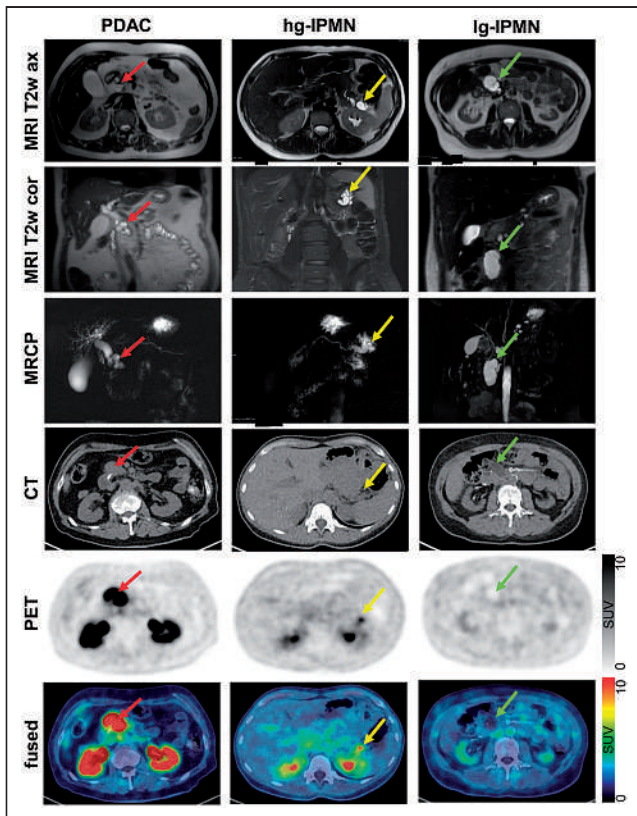


**FIGURE 6.** Representative axial and coronal T2-weighted MRI (MRI T2w ax and MRI T2w cor, respectively), MR cholangiopancreatography (MRCP), axial CT (CT ax), axial PET (PET ax), and fused images of a patient with hc hg-IPMN with progression into PDAC, a patient with hg-IPMN without PDAC, and patient with lg-IPMN. Red, yellow, and green arrows indicate pathologies.

demonstrate that dynamic imaging delivers additional diagnostic information and may improve the clinical classification of lg-IPMN and men-IPMN due to delayed binding and delayed washout of men-IPMN compared with lg-IPMN. These findings are in line with our previously published data on dynamic  $^{68}\text{Ga}$ -FAPI PET imaging in patients with lung cancer and fibrosing interstitial lung diseases, for which we observed delayed washout of tumors compared with fibrotic lesions (16). Similarly, we could show in a previous project on  $^{68}\text{Ga}$ -FAPI PET in PDAC that PDAC had a delayed washout compared with pancreatitis (19). Although the overall experience with dynamic behavior of  $^{68}\text{Ga}$ -FAPI tracers is limited to few publications to date (16,21,22), delayed  $^{68}\text{Ga}$ -FAPI washout appears to be sign of malignancy in this imaging method.

#### Risk Stratification of IPMN

To date, a compound of imaging, clinical, and laboratory criteria has been used to estimate the risk of malignant progression of IPMN. Most data exist on results of imaging techniques. Recent studies, mostly postoperative with a retrospective design, concluded that jaundice, a contrast-enhancing solid component or mural nodule, or a  $\geq 10$  mm main duct dilatation have a positive predictive value for malignancy of between 56% and 89% (23–25). A cyst size  $\geq 30$  mm without other clinical or radiologic risk factors has a low positive predictive value for malignant transformation of an IPMN ranging from 27% to 33% (26–30). Several studies regarding mostly surgically resected IPMN reported a wide

risk range of 37%–91% for high-grade dysplasia or cancer for main duct dilatations of 5–9.9 mm (31–33). In patients after surgical resection of BD-IPMN, it was found that mural nodules  $\geq 5$  mm on EUS have a sensitivity of 73%–85% and specificity of 71%–100% for the presence of men-IPMN. Imaging detectability of mural nodes  $\geq 10$  mm on CT, MRI, ultrasound, and EUS were 64%, 68%, 89%, and 97%, respectively. Detectability of mural nodes  $\geq 10$  mm is excellent in abdominal and endoscopic ultrasound (34–36). In summary, main duct dilatation  $\geq 10$  mm and mural nodules on ultrasound examination are the most reliable factors. It must be considered that mural nodules are a rare condition. Next to morphologic imaging, PET/CT using  $^{18}\text{F}$ -FDG has been applied in IPMN to detect malignancy based on increased glucose metabolism. For this approach, several older meta-analyses had calculated sensitivity and specificity rates of 80%–95% and 60%–95%, respectively (37–40), but more recent studies could not prove a benefit of  $^{18}\text{F}$ -FDG PET/CT in IPMN (41,42). Given the low background activity of  $^{68}\text{Ga}$ -FAPI radiotracers compared with  $^{18}\text{F}$ -FDG in the pancreas and given the promising preliminary results of our study, one would expect that  $^{68}\text{Ga}$ -FAPI PET may be superior to  $^{18}\text{F}$ -FDG for the detection of malignancy in IPMN. On the basis of our data it appears that  $^{68}\text{Ga}$ -FAPI-74 PET signal intensity and uptake kinetics offer high specificity and sensitivity for the detection of subtypes and may complement established predictors of malignancy.

Despite promising results, several limitations of our analysis must be considered. The major limitation of our study is the relatively small number of patients with IPMN included, especially with respect to dynamic imaging, which was performed in just 9 subjects. According to this, no definite conclusions should be drawn from our data, and further studies with more patients—including intraindividual comparisons of the diagnostic value for IPMN of  $^{68}\text{Ga}$ -FAPI-74 PET and other imaging modalities such as CT, MRI, and ultrasound—are necessary to validate our findings. Another limitation arising from the sparsity of dynamic PET data is that our dataset does not allow a comparison between the discriminatory power of static alone versus dynamic alone versus combined static and dynamic imaging. An additional limitation is that not all patients included had undergone biopsy or surgery for definitive confirmation of their diagnoses. Although we considered the appearance of these lesions in MRI and ultrasound and the clinical course of the patients to gain valid clinical classifications, uncertainty remains for these cases, especially as our information available only reflects the status of the patients during a limited period of follow-up. Additionally, a certain selection bias may arise from the fact that all patients included into this analysis were referred by a highly specialized outpatient clinic. Thus, the dataset may not fully reflect the epidemiology of IPMN subtypes. However, a recently published study on the frequency of IPMN subtypes found a similar distribution of hg-IPMN and lg-IPMN (10). Taken together, our findings should be interpreted with caution and need confirmation in larger cohorts, optimally in prospective studies.

#### CONCLUSION

Static and dynamic  $^{68}\text{Ga}$ -FAPI-74 PET/CT showed promising imaging properties for IPMN and predicted the grade of dysplasia of IPMN with high accuracy. We recommend further clinical evaluation of  $^{68}\text{Ga}$ -FAPI-74 PET in combination with and comparison to MRI or EUS for the detection of malignant IPMN of the pancreas.

## DISCLOSURE

This work was funded by the Federal Ministry of Education and Research (grant no. 13N 13341). Ulrike Heger, Clemens Kratochwil, and Frederik L. Giesel have filed a patent application for quinoline-based FAP-targeting agents for imaging and therapy in nuclear medicine. Ulrike Heger, Clemens Kratochwil, and Frederik L. Giesel also have shares of a consultancy group for iTheranostics. All procedures performed in studies involving human participants were in accordance with the ethical standards of the institutional or national research committee and with the 1964 Helsinki declaration and its later amendments or comparable ethical standards. This retrospective study was approved by the local institutional review board (study number S-115/2020). No other potential conflict of interest relevant to this article was reported.

## KEY POINTS

**QUESTION:** Are static and dynamic  $^{68}\text{Ga}$ -FAPI PET helpful for the discrimination of menacing (high-grade with and without progression into PDAC) and low-grade IPMN of the pancreas?

**PERTINENT FINDINGS:** Menacing IPMN with and without transformation into PDAC showed significantly higher  $^{68}\text{Ga}$ -FAPI uptake than low-grade IPMN. Dynamic PET parameters (time to peak,  $K_1$ ,  $k_2$ ,  $K_3$ ,  $k_4$ ) differed markedly between menacing and low-grade IPMN.

**IMPLICATIONS FOR PATIENT CARE:**  $^{68}\text{Ga}$ -FAPI PET showed promising results with respect to the differentiation of menacing and low-grade IPMN and should be further evaluated in patients with IPMN or PDAC.

## REFERENCES

- Park W, Chawla A, O'Reilly EM. Pancreatic cancer: a review. *JAMA*. 2021;326:851–862.
- Rezaee N, Barbon C, Zaki A, et al. Intraductal papillary mucinous neoplasm (IPMN) with high-grade dysplasia is a risk factor for the subsequent development of pancreatic ductal adenocarcinoma. *HPB (Oxford)*. 2016;18:236–246.
- Tanaka M, Fernandez-Del Castillo C, Kamisawa T, et al. Revisions of international consensus Fukuoka guidelines for the management of IPMN of the pancreas. *Pancreatol*. 2017;17:738–753.
- European Study Group on Cystic Tumours of the Pancreas. European evidence-based guidelines on pancreatic cystic neoplasms. *Gut*. 2018;67:789–804.
- Fritz S, Buchler MW, Werner J. Surgical therapy of intraductal papillary mucinous neoplasms of the pancreas [in German]. *Chirurg*. 2012;83:130–135.
- Schnelldorfer T, Sarr MG, Nagorney DM, et al. Experience with 208 resections for intraductal papillary mucinous neoplasm of the pancreas. *Arch Surg*. 2008;143:639–646, discussion 646.
- de Jong K, van Hooft JE, Nio CY, et al. Accuracy of preoperative workup in a prospective series of surgically resected cystic pancreatic lesions. *Scand J Gastroenterol*. 2012;47:1056–1063.
- Morris-Stiff G, Lentz G, Chalikhonda S, et al. Pancreatic cyst aspiration analysis for cystic neoplasms: mucin or carcinoembryonic antigen—which is better? *Surgery*. 2010;148:638–644, discussion 644–635.
- Heckler M, Brieger L, Heger U, et al. Predictive performance of factors associated with malignancy in intraductal papillary mucinous neoplasia of the pancreas. *BJS Open*. 2018;2:13–24.
- Tjaden C, Sandini M, Mihaljevic AL, et al. Risk of the watch-and-wait concept in surgical treatment of intraductal papillary mucinous neoplasm. *JAMA Surg*. 2021;156:818–825.
- von Ahrens D, Bhagat TD, Nagrath D, Maitra A, Verma A. The role of stromal cancer-associated fibroblasts in pancreatic cancer. *J Hematol Oncol*. 2017;10:76.
- Hanahan D, Weinberg RA. Hallmarks of cancer: the next generation. *Cell*. 2011;144:646–674.
- Lindner T, Loktev A, Altmann A, et al. Development of quinoline-based theranostic ligands for the targeting of fibroblast activation protein. *J Nucl Med*. 2018;59:1415–1422.
- Lindner T, Altmann A, Giesel F, et al.  $^{18}\text{F}$ -labeled tracers targeting fibroblast activation protein. *EJNMMI Radiopharm Chem*. 2021;6:26.
- Loktev A, Lindner T, Mier W, et al. A tumor-imaging method targeting cancer-associated fibroblasts. *J Nucl Med*. 2018;59:1423–1429.
- Röhrich M, Leitz D, Glatting FM, et al. Fibroblast activation protein-specific PET/CT imaging in fibrotic interstitial lung diseases and lung cancer: a translational exploratory study. *J Nucl Med*. 2022;63:127–133.
- DeLong ER, DeLong DM, Clarke-Pearson DL. Comparing the areas under two or more correlated receiver operating characteristic curves: a nonparametric approach. *Biometrics*. 1988;44:837–845.
- Robin X, Turck N, Hainard A, et al. pROC: an open-source package for R and S+ to analyze and compare ROC curves. *BMC Bioinformatics*. 2011;12:77.
- Röhrich M, Naumann P, Giesel FL, et al. Impact of  $^{68}\text{Ga}$ -FAPI-PET/CT imaging on the therapeutic management of primary and recurrent pancreatic ductal adenocarcinomas. *J Nucl Med*. 2021;62:779–786.
- Kratochwil C, Flechsig P, Lindner T, et al.  $^{68}\text{Ga}$ -FAPI PET/CT: tracer uptake in 28 different kinds of cancer. *J Nucl Med*. 2019;60:801–805.
- Wang S, Zhou X, Xu X, et al. Dynamic PET/CT imaging of  $^{68}\text{Ga}$ -FAPI-04 in Chinese subjects. *Front Oncol*. 2021;11:651005.
- Geist BK, Xing H, Wang J, et al. A methodological investigation of healthy tissue, hepatocellular carcinoma, and other lesions with dynamic  $^{68}\text{Ga}$ -FAPI-04 PET/CT imaging. *EJNMMI Phys*. 2021;8:8.
- Fritz S, Klaus M, Bergmann F, et al. Pancreatic main-duct involvement in branch-duct IPMNs: an underestimated risk. *Ann Surg*. 2014;260:848–855, discussion 855–846.
- Roch AM, Ceppa EP, DeWitt JM, et al. International consensus guidelines parameters for the prediction of malignancy in intraductal papillary mucinous neoplasm are not properly weighted and are not cumulative. *HPB (Oxford)*. 2014;16:929–935.
- Goh BK, Thng CH, Tan DM, et al. Evaluation of the Sendai and 2012 international consensus guidelines based on cross-sectional imaging findings performed for the initial triage of mucinous cystic lesions of the pancreas: a single institution experience with 114 surgically treated patients. *Am J Surg*. 2014;208:202–209.
- Sahora K, Mino-Kenudson M, Brugge W, et al. Branch duct intraductal papillary mucinous neoplasms: does cyst size change the tip of the scale? A critical analysis of the revised international consensus guidelines in a large single-institutional series. *Ann Surg*. 2013;258:466–475.
- Aso T, Ohtsuka T, Matsunaga T, et al. “High-risk stigmata” of the 2012 international consensus guidelines correlate with the malignant grade of branch duct intraductal papillary mucinous neoplasms of the pancreas. *Pancreas*. 2014;43:1239–1243.
- Nguyen AH, Toste PA, Farrell JJ, et al. Current recommendations for surveillance and surgery of intraductal papillary mucinous neoplasms may overlook some patients with cancer. *J Gastrointest Surg*. 2015;19:258–265.
- Dortch JD, Stauffer JA, Asbun HJ. Pancreatic resection for side-branch intraductal papillary mucinous neoplasm (SB-IPMN): a contemporary single-institution experience. *J Gastrointest Surg*. 2015;19:1603–1609.
- Robles EP, Maire F, Cros J, et al. Accuracy of 2012 international consensus guidelines for the prediction of malignancy of branch-duct intraductal papillary mucinous neoplasms of the pancreas. *United European Gastroenterol J*. 2016;4:580–586.
- Seo N, Byun JH, Kim JH, et al. Validation of the 2012 international consensus guidelines using computed tomography and magnetic resonance imaging: branch duct and main duct intraductal papillary mucinous neoplasms of the pancreas. *Ann Surg*. 2016;263:557–564.
- Hackert T, Fritz S, Klaus M, et al. Main-duct intraductal papillary mucinous neoplasm: high cancer risk in duct diameter of 5 to 9 mm. *Ann Surg*. 2015;262:875–880, discussion 880–871.
- Abdeljawad K, Vemulapalli KC, Schmidt CM, et al. Prevalence of malignancy in patients with pure main duct intraductal papillary mucinous neoplasms. *Gastrointest Endosc*. 2014;79:623–629.
- Kawada N, Uehara H, Nagata S, Tsuchishima M, Tsutsumi M, Tomita Y. Mural nodule of 10 mm or larger as predictor of malignancy for intraductal papillary mucinous neoplasm of the pancreas: pathological and radiological evaluations. *Pancreatol*. 2016;16:441–448.
- Kobayashi N, Sugimori K, Shimamura T, et al. Endoscopic ultrasonographic findings predict the risk of carcinoma in branch duct intraductal papillary mucinous neoplasms of the pancreas. *Pancreatol*. 2012;12:141–145.
- Shimizu Y, Yamaue H, Maguchi H, et al. Predictors of malignancy in intraductal papillary mucinous neoplasm of the pancreas: analysis of 310 pancreatic resection patients at multiple high-volume centers. *Pancreas*. 2013;42:883–888.

37. Best LM, Rawji V, Pereira SP, Davidson BR, Gurusamy KS. Imaging modalities for characterising focal pancreatic lesions. *Cochrane Database Syst Rev.* 2017;4: CD010213.
38. Xu MM, Yin S, Siddiqui AA, et al. Comparison of the diagnostic accuracy of three current guidelines for the evaluation of asymptomatic pancreatic cystic neoplasms. *Medicine (Baltimore).* 2017;96:e7900.
39. Sultana A, Jackson R, Tim G, et al. What is the best way to identify malignant transformation within pancreatic IPMN: a systematic review and meta-analyses. *Clin Transl Gastroenterol.* 2015;6:e130.
40. Bertagna F, Treglia G, Baiocchi GL, Giubbini R. F18-FDG-PET/CT for evaluation of intraductal papillary mucinous neoplasms (IPMN): a review of the literature. *Jpn J Radiol.* 2013;31:229–236.
41. Regenet N, Sauvanet A, Muscari F, et al. The value of <sup>18</sup>F-FDG positron emission tomography to differentiate benign from malignant intraductal papillary mucinous neoplasms: a prospective multicenter study. *J Visc Surg.* 2020;157:387–394.
42. Liu H, Cui Y, Shao J, Shao Z, Su F, Li Y. The diagnostic role of CT, MRI/MRCP, PET/CT, EUS and DWI in the differentiation of benign and malignant IPMN: A meta-analysis. *Clin Imaging.* 2021;72:183–193.

---

---

# Prospective Phase II Trial of [<sup>68</sup>Ga]Ga-NODAGA-E[c(RGDyK)]<sub>2</sub> PET/CT Imaging of Integrin α<sub>v</sub>β<sub>3</sub> for Prognostication in Patients with Neuroendocrine Neoplasms

Esben Andreas Carlsen<sup>1,2</sup>, Mathias Loft<sup>1,2</sup>, Annika Loft<sup>1,2</sup>, Dorota Czyzewska<sup>1,2</sup>, Mikkel Andreassen<sup>2,3</sup>, Seppo W. Langer<sup>2,4,5</sup>, Ulrich Knigge<sup>2,3,6</sup>, and Andreas Kjaer<sup>1,2</sup>

<sup>1</sup>Department of Clinical Physiology and Nuclear Medicine & Cluster for Molecular Imaging, Copenhagen University Hospital, Rigshospitalet & Department of Biomedical Sciences, University of Copenhagen, Copenhagen, Denmark; <sup>2</sup>ENETS Neuroendocrine Tumor Center of Excellence, Copenhagen University Hospital, Rigshospitalet, Copenhagen, Denmark; <sup>3</sup>Department of Clinical Endocrinology, Copenhagen University Hospital, Rigshospitalet, Copenhagen, Denmark; <sup>4</sup>Department of Oncology, Copenhagen University Hospital, Rigshospitalet, Copenhagen, Denmark; <sup>5</sup>Department of Clinical Medicine, University of Copenhagen, Copenhagen, Denmark; and <sup>6</sup>Department of Surgical Gastroenterology, Copenhagen University Hospital, Rigshospitalet, Copenhagen, Denmark

Integrin α<sub>v</sub>β<sub>3</sub>, a subtype of the arginine-glycine-aspartate (RGD)-recognizing cell surface integrins, is upregulated on endothelial cells during angiogenesis and on tumor cells. Because of involvement in tumor growth, invasiveness and metastases, and angiogenesis, integrin α<sub>v</sub>β<sub>3</sub> is an attractive target in cancers. In this study, we applied <sup>68</sup>Ga-NODAGA-E[c(RGDyK)]<sub>2</sub> for imaging of integrin α<sub>v</sub>β<sub>3</sub> in patients with neuroendocrine neoplasms (NENs) and its potential use for prognostication. We hypothesized that <sup>68</sup>Ga-NODAGA-E[c(RGDyK)]<sub>2</sub> PET/CT would show tumor lesion uptake and that higher tumor lesion uptake was associated with a poorer prognosis. **Methods:** Between December 2017 and November 2020 we prospectively enrolled 113 patients with NEN of all grades (2019 World Health Organization classification) for <sup>68</sup>Ga-NODAGA-E[c(RGDyK)]<sub>2</sub> PET/CT. The scan was acquired 45 min after injection of 200 MBq of <sup>68</sup>Ga-NODAGA-E[c(RGDyK)]<sub>2</sub>. Board-certified specialists in nuclear medicine and radiology analyzed the PET/CT measuring SUV<sub>max</sub> in tumor lesions. Positive tumor lesions were defined as those with tumor-to-liver background ≥ 2. Maximal tumor SUV<sub>max</sub> for each patient was used as a predictor of outcome. Patients were followed for at least 1 y to assess progression-free survival and overall survival. **Results:** Of 113 patients enrolled in the trial, 99 underwent <sup>68</sup>Ga-NODAGA-E[c(RGDyK)]<sub>2</sub> PET/CT, with 97 patients having evaluable lesions. The patients predominantly had small intestinal (64%) or pancreatic (20%) NEN and most had metastatic disease (93%). Most patients had low-grade tumors (78%), whereas 22% had high-grade tumors. During a median follow-up of 31 mo (interquartile range, 26–38 mo), 62 patients (64%) experienced disease progression and 25 (26%) patients died. In total, 76% of patients had positive tumor lesions, and of the patients with high-grade tumors 91% had positive tumor lesions. High integrin α<sub>v</sub>β<sub>3</sub> expression, defined as an SUV<sub>max</sub> of at least 5.25, had a hazard ratio of 2.11 (95% CI, 1.18–3.78) and 6.95 (95% CI, 1.64–29.51) for progression-free survival and overall survival, respectively (*P* = 0.01 for both). **Conclusion:** Tumor lesion uptake of <sup>68</sup>Ga-NODAGA-E[c(RGDyK)]<sub>2</sub> was evident in patients with all grades of NEN. High uptake was associated with a poorer prognosis. Further studies are warranted to establish whether <sup>68</sup>Ga-NODAGA-E[c(RGDyK)]<sub>2</sub> PET/CT may become a prediction tool for identification of patients eligible for treatments targeting integrin α<sub>v</sub>β<sub>3</sub>.

**Key Words:** integrin α<sub>v</sub>β<sub>3</sub>; neuroendocrine neoplasms; PET; prognosis; molecular imaging

**J Nucl Med 2023; 64:252–259**  
DOI: 10.2967/jnumed.122.264383

**N**euroendocrine neoplasms (NENs) represent a heterogeneous group of tumors originating from the neuroendocrine cells. NEN are primarily found in the gastrointestinal tract, pancreas, and lungs. Patients with NEN are often diagnosed when the disease has metastasized, yet the clinical course for these patients varies greatly. Origin of primary tumor, presence of metastases as well as tumor morphology and proliferation activity (i.e., Ki-67) are known prognostic factors (1). The 2019 World Health Organization (WHO) classification stratifies NEN into neuroendocrine tumor (NET) G1 (Ki-67 < 3%), NET G2 (Ki-67 3%–20%), NET G3 (Ki-67 > 20% and well-differentiated), and neuroendocrine carcinoma (NEC) (Ki-67 > 20% and poorly differentiated) (2). Furthermore, imaging modalities aid in diagnosis, staging, treatment selection, and follow-up for patients with NEN. In particular, PET radiotracers reflecting somatostatin receptor expression (e.g., <sup>64</sup>Cu-DOTATATE or <sup>68</sup>Ga-DOTATATE) and glucose metabolism (<sup>18</sup>F-FDG) are used for these purposes in addition to providing prognostic information (3,4). Finally, targeting the somatostatin receptors with peptide receptor radionuclide therapy (PRRT), for example, <sup>177</sup>Lu-DOTATATE, has been approved for patients with NEN.

Additional tumor markers may be useful for further improvement in prognostication and ultimately identifying novel treatment targets in patients with NEN. Cell surface adhesion receptors of the integrin superfamily have been extensively investigated because their role in physiologic as well as in pathophysiologic processes, and especially in cancers (5). The subfamily of arginine-glycine-aspartate (RGD)-recognizing integrins has implications on several of hallmarks of cancer: tumor growth, invasiveness, and metastases and angiogenesis. Integrin α<sub>v</sub>β<sub>3</sub> is significantly upregulated on activated endothelial cells during angiogenesis but absent on quiescent endothelial cells as well as overexpressed on tumor cells in several cancers (6). NENs are generally characterized as highly vascularized tumors with overexpression of various proangiogenic factors such as vascular endothelial growth factor (7). Previously we found, using quantitative gene expression,

---

Received May 20, 2022; revision accepted Aug. 13, 2022.  
For correspondence or reprints, contact Andreas Kjaer (akjaer@sund.ku.dk).  
Published online Aug. 18, 2022.  
COPYRIGHT © 2023 by the Society of Nuclear Medicine and Molecular Imaging.



that the expression of integrin  $\alpha_v\beta_3$  shows high variability between NENs (8). Because of its integral role in cancer, our group therefore developed and clinically translated the PET radiotracer  $^{68}\text{Ga}$ -NODAGA-E[c(RGDyK)]<sub>2</sub> targeting integrin  $\alpha_v\beta_3$  with high affinity (9,10).

The aim of this phase II clinical trial of  $^{68}\text{Ga}$ -NODAGA-E[c(RGDyK)]<sub>2</sub> PET/CT in patients with NEN of all grades was to further assess tumor uptake and prognostic value. We hypothesized that PET/CT with  $^{68}\text{Ga}$ -NODAGA-E[c(RGDyK)]<sub>2</sub> would show accumulation in tumor lesions in patients with NEN of all grades and that the uptake of the radiotracer would be associated with progression-free survival (PFS) and overall survival (OS).

## MATERIALS AND METHODS

### Patients

Patients with histologically confirmed NEN were included from the Department of Endocrinology (managing low-grade NEN, Ki-67  $\leq$  20%) and Department of Oncology (managing high-grade NEN, Ki-67  $>$  20%), Copenhagen University Hospital–Rigshospitalet, Denmark, between December 4, 2017, and November 26, 2020. Rigshospitalet is a Neuroendocrine Tumor Center of Excellence accredited by the European Neuroendocrine Tumor Society. The study was conducted in accordance with the Helsinki Declaration and Good Clinical Practice. The study was approved by the Danish Medicines Agency (EudraCT 2017-002512-14), Scientific Ethics Committee (H-17019542), and Danish Data Protection Agency (2012-58-0004), and registered on clinicaltrials.gov (NCT03271281).

Eligible patients were 18 y or older, capable of reading and understanding the patient information in Danish and giving informed consent, diagnosed with gastroenteropancreatic NEN of all grades or bronchopulmonary NEN, and had a WHO performance status of 0–2. Patients were excluded if they were pregnant or breastfeeding, had a body mass more than 140 kg, or had a history of allergic reaction attributable to compounds of chemical or biologic composition similar to  $^{68}\text{Ga}$ -NODAGA-E[c(RGDyK)]<sub>2</sub> or in the case of bronchopulmonary NEN if the subtype was small cell lung cancer. After written informed consent was obtained, the patients were referred for a  $^{68}\text{Ga}$ -NODAGA-E[c(RGDyK)]<sub>2</sub> PET/CT at the first opportunity.

### Image Acquisition

Data were acquired using a Biograph 128 mCT PET/CT scanner (Siemens Medical Solutions) with an axial field of view of 216 mm. On the basis of the previous phase I trial, the scans were acquired 45 min after intravenous administration of approximately 200 MBq of  $^{68}\text{Ga}$ -NODAGA-E[c(RGDyK)]<sub>2</sub> ( $^{68}\text{Ga}$ )-NODAGA-Glu[cyclo(-Arg-Gly-Asp-D-Tyr-Lys-)]<sub>2</sub> equaling 4.4 mSv. Radiotracer were produced as previously described (9). Whole-body PET scans (mid orbita to mid thigh) were obtained with an acquisition time of 4 min per bed position. Attenuation- and scatter-corrected PET data were reconstructed iteratively using a 3-dimensional ordinary Poisson ordered-subset expectation maximization algorithm including point-spread function and time-of-flight information using the TrueX algorithm (Siemens Medical Solutions); the settings were 2 iterations, 21 subsets, 2-mm gaussian filter. A diagnostic CT scan was obtained before the PET scan with a 2-mm slice thickness, 120 kV, and a quality reference of 225 mAs modulated by the Care Dose 4D automatic exposure control system (Siemens Medical Solutions). An automatic injection system was used to administer 75 mL of an iodine-containing contrast agent (Optiray 300; Covidien) for arterial and venous phase CT.

Patients were observed for adverse events after injection of  $^{68}\text{Ga}$ -NODAGA-E[c(RGDyK)]<sub>2</sub>, and after discharge patients were asked to

**TABLE 1**  
Baseline Characteristics of 97 Patients with NENs

Baseline characteristic	Data
Median age (y)	67 (range, 44–83)
Sex	
Female	43 (44%)
Male	54 (56%)
Site of primary tumor	
Small intestine	62 (64%)
Pancreas	19 (20%)
Lung	6 (6%)
Colon	6 (6%)
Stomach	2 (2%)
Esophagus	1 (1%)
Rectum	1 (1%)
Metastatic disease	90 (93%)
Liver metastases	76 (79%)
Median Ki-67 (%)	6 (range, 1–100)
2019 World Health Organization grade	
NET G1	21 (22%)
NET G2	55 (57%)
NET G3	14 (14%)
NEC	7 (7%)
Median time from diagnosis to PET/CT (mo)	27 (range, 2–265)
Primary tumor resected	37 (38%)
Ongoing treatment at PET/CT scan time	
Somatostatin analog	75 (77%)
Interferon	8 (8%)
Capecitabine/5-fluorouracil	5 (5%)
Etoposide $\pm$ carboplatin	4 (4%)
Streptozotocin	4 (4%)
Everolimus	3 (3%)
Temozolomide	2 (2%)
Completed treatment before PET/CT	
On first line of therapy	45 (46%)
Peptide receptor radionuclide therapy	30 (31%)
Etoposide $\pm$ carboplatin	16 (16%)
Capecitabine/5-fluorouracil	12 (12%)
Temozolomide	7 (7%)
Streptozotocin	7 (7%)
Interferon	6 (6%)
External radiation therapy	5 (5%)
Liver radiofrequency ablation or embolization	5 (5%)
Resection of liver metastases	4 (4%)
Everolimus or sunitinib	2 (2%)

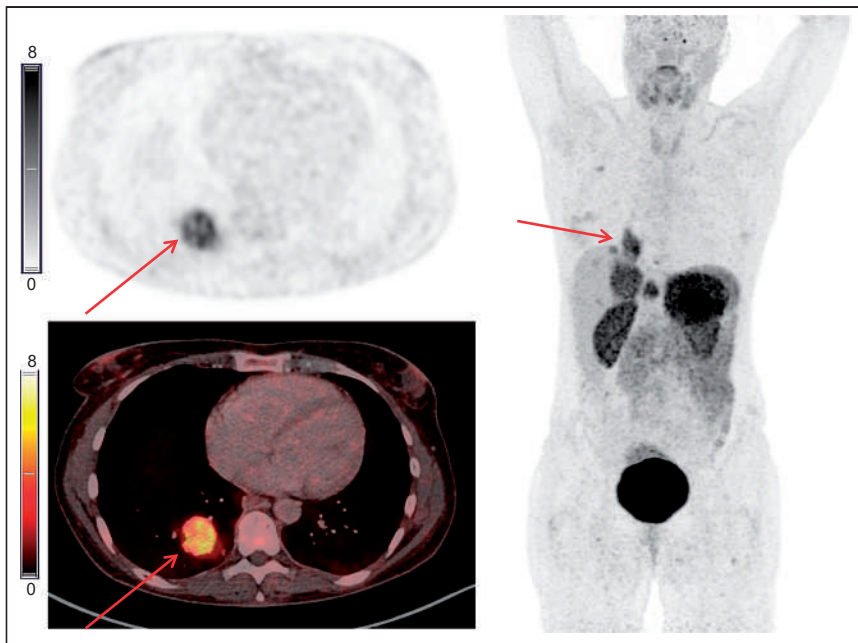


**FIGURE 1.** Example of  $^{68}\text{Ga}$ -NODAGA-E[c(RGDyK)]<sub>2</sub> PET/CT. Transaxial PET and fused PET/CT and maximum-intensity projection with color bars (unit: SUV). Patient with lung NET grade 2 (Ki-67 15%) with liver and bone metastases. Arrows point to primary tumor.

record any adverse events occurring within the first 24 h of injection. Adverse events were categorized according to Common Terminology Criteria for Adverse Events (version 5.0).

#### Image Analysis

Together, an experienced board-certified nuclear medicine physician and an experienced board-certified radiologist analyzed the

crine Tumor Society guidelines, typically every 3–6 mo (11). The  $^{68}\text{Ga}$ -NODAGA-E[c(RGDyK)]<sub>2</sub> PET/CT was not made available for the treating physicians and thus not used to guide clinical decisions regarding treatment or follow-up. The end of follow-up was December 31, 2021, for the current study. Routine CT and or MRI were used for evaluation of PFS in accordance with RECIST (version 1.1) (12). PFS was defined as time from  $^{68}\text{Ga}$ -NODAGA-E[c(RGDyK)]<sub>2</sub> PET/CT to, if any, progression or death from any cause. If no progression or death from any cause occurred within the follow-up time period, the patient was censored at the time of last available diagnostic imaging. OS was defined as time from  $^{68}\text{Ga}$ -NODAGA-E[c(RGDyK)]<sub>2</sub> PET/CT to death by any cause. As all deaths but 2 were directly related to NEN, we refrained from analyzing disease-specific survival. Patients alive at follow-up were censored to the day of the end of follow-up (December 31, 2021).

#### Statistics

Continuous variables are reported as mean  $\pm$  SD or median with range unless otherwise noted. Kaplan–Meier analyses were used for estimation of time to outcome (PFS and OS) and reverse Kaplan–Meier analysis was used to estimate median follow-up time. Univariate and multivariate Cox regression analyses for OS and PFS, with predictor variables being  $\text{SUV}_{\text{max}}$  and WHO grade, were performed to determine hazard ratio (HR) and 95% CI. We used the Cutoff Finder application to determine the optimal cutoff for  $\text{SUV}_{\text{max}}$  (13). A *P* value of less than 0.05 was considered statistically significant. R version 3.6.0 (R Foundation for Statistical Computing) was used for the analyses.

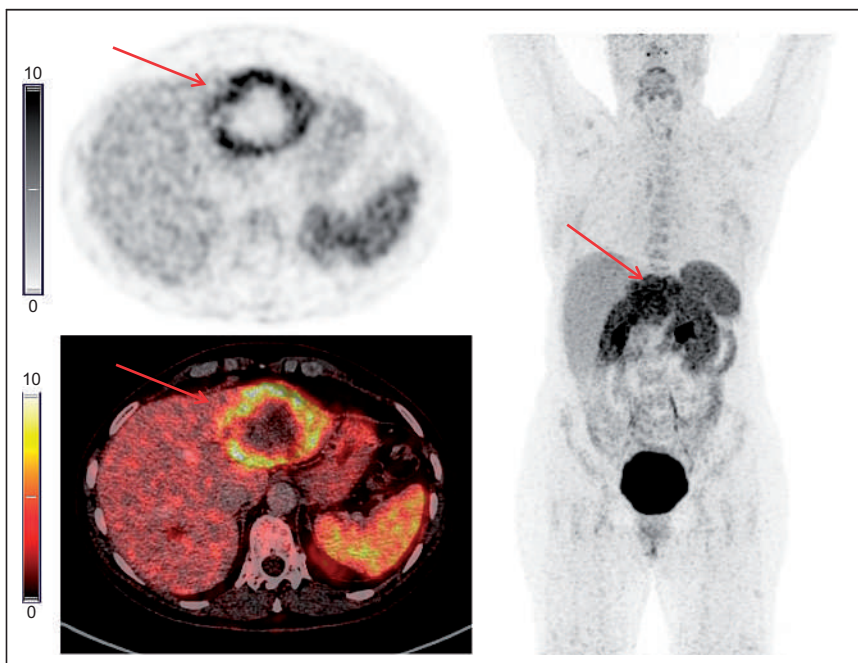


**FIGURE 2.** Example of  $^{68}\text{Ga}$ -NODAGA-E[c(RGDyK)]<sub>2</sub> PET/CT. Transaxial PET and fused PET/CT and maximum-intensity projection with color bars (unit: SUV). Patient with gastric NET grade 2 (Ki-67 8%) with liver metastases. Arrows point to liver metastasis.

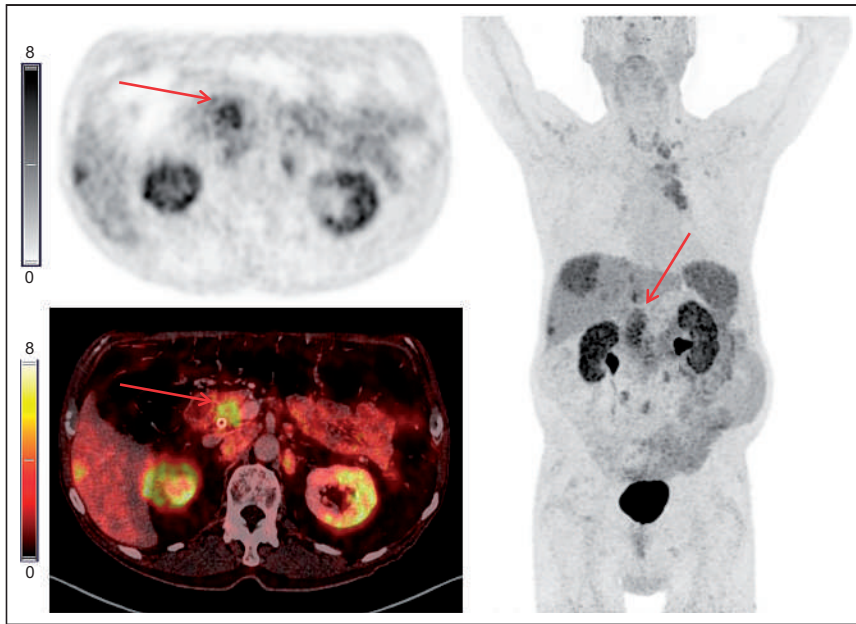


**FIGURE 3.** Example of  $^{68}\text{Ga}$ -NODAGA-E[c(RGDyK)]<sub>2</sub> PET/CT. Transaxial PET and fused PET/CT and maximum-intensity projection with color bars (unit: SUV). Patient with pancreatic NET grade 2 (Ki-67 11%) with liver and lymph node metastases. Arrows point to primary tumor.

## RESULTS

### Patients and Image Acquisition

We prospectively included 113 patients, 14 of whom did not undergo  $^{68}\text{Ga}$ -NODAGA-E[c(RGDyK)]<sub>2</sub> PET/CT because of disease worsening ( $n = 4$ ), consent withdrawal ( $n = 2$ ), death before PET/CT ( $n = 3$ ), logistical impossibility for PET/CT to be performed ( $n = 2$ ), and infeasibility for PET/CT scanning due to COVID-19 restrictions ( $n = 3$ ). Of the 99 patients scanned with PET/CT, 97 patients had evaluable lesions. The patients predominately had small intestinal ( $n = 62$ , 64%) or pancreatic ( $n = 19$ , 20%) NEN and metastatic disease ( $n = 90$ , 93%) (Table 1). Most patients had low-grade tumors (Ki-67  $\leq 20\%$ ) ( $n = 76$ , 78%), whereas 21 (22%) had high-grade tumors (Ki-67  $> 20\%$ ). No patients were treatment-naïve before the PET/CT scan.

Patients undergoing  $^{68}\text{Ga}$ -NODAGA-E[c(RGDyK)]<sub>2</sub> PET/CT ( $n = 99$ ) received a median mass dose of 18.9 (range, 7.7–49.3)  $\mu\text{g}$  of  $^{68}\text{Ga}$ -NODAGA-E[c(RGDyK)]<sub>2</sub> and the

**TABLE 2**

Patients with  $^{68}\text{Ga}$ -NODAGA-E[c(RGDyK)]<sub>2</sub> PET-Positive Lesions (TLR  $\geq 2$ ) According to WHO Classification of NENs

Uptake ratio	NET G1 ( $n = 21$ )	NET G2 ( $n = 55$ )	NET G3/NEC ( $n = 21$ )	All ( $n = 97$ )
TLR $\geq 2$	13 (62%)	42 (76%)	19 (91%)	74 (76%)
TLR $< 2$	8 (38%)	13 (24%)	2 (10%)	23 (24%)

A tumor was defined as positive when the TLR, measured as lesion  $\text{SUV}_{\text{max}}$ -to-normal liver  $\text{SUV}_{\text{mean}}$ , was  $\geq 2$ . Of the patients with NET G3/NEC tumors, 13 of 14 (93%) patients with NET G3 were positive and 6 of 7 (86%) patients with NEC were positive.

**TABLE 3**

Treatments Given to Patients with NENs ( $n = 97$ ) During Follow-up

Treatment after PET/CT	$n$ (%)
Somatostatin analog	78 (80%)
Peptide receptor radionuclide therapy	31 (32%)
Capecitabine/5-fluorouracil	13 (13%)
Everolimus or sunitinib	12 (12%)
Surgery	11 (11%)
Temozolomide	9 (9%)
Liver radiofrequency ablation or embolization	9 (9%)
External radiation therapy	7 (7%)
Etoposide $\pm$ carboplatin	5 (5%)
Interferon	5 (5%)
Streptozotocin	3 (3%)
Docetaxel	3 (3%)

activity dose was 193 (range, 104–226) MBq. Median time from injection to the start of PET scanning was 47 min (range, 35–86 min). Three patients experienced an adverse event: dizziness (grade 1), fall (grade 1), and infusion-related reaction to injection of CT contrast (grade 2) within 24 h of injection of  $^{68}\text{Ga}$ -NODAGA-E[c(RGDyK)]<sub>2</sub>. All were deemed unrelated to  $^{68}\text{Ga}$ -NODAGA-E[c(RGDyK)]<sub>2</sub> injection. No grade 3–5 adverse events occurred.

### Image Analysis

The median maximal tumor lesion  $\text{SUV}_{\text{max}}$  was 6.1 (range, 1.4–14.1). The mean  $\pm$  SD of tumor lesion  $\text{SUV}_{\text{max}}$  was  $6.36 \pm 2.49$  and the mean  $\pm$  SD normal liver  $\text{SUV}_{\text{mean}}$  was  $2.41 \pm 0.55$ . Examples of  $^{68}\text{Ga}$ -NODAGA-E[c(RGDyK)]<sub>2</sub> PET/CT are shown in Figures 1–3. When the cutoff of TLR  $\geq 2$  to determine positive lesions was applied, approximately two thirds of patients with NET G1 had positive lesions, which gradually increased to nearly all patients with NET G3/NEC (91%) having positive lesions (Table 2). In total, 76% of patients had positive tumor lesions.

### Follow-up

During a median follow-up of 31 mo (interquartile range, 26–38 mo), 62 patients (64%) experienced disease progression and 25 (26%)

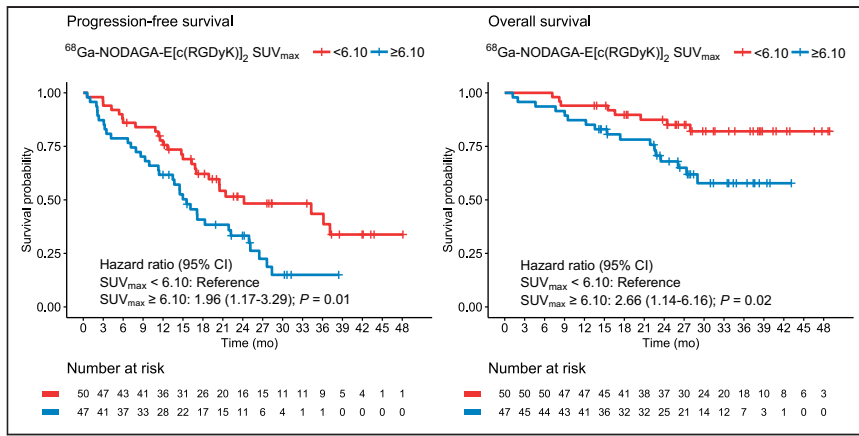


**FIGURE 4.** Kaplan-Meier plots of  $^{68}\text{Ga}$ -NODAGA-E[c(RGDyK)]<sub>2</sub> PET SUV<sub>max</sub> dichotomized at 6.10 (median) for prediction of PFS and OS.

in Table 3. Treatment with somatostatin analog was the most frequent (80%, 78/97), and 32% (31/97) of all patients underwent PRRT during the follow-up period.

### PFS and OS

In univariate analyses, the maximal tumor SUV<sub>max</sub> as a continuous variable was significantly associated with PFS and OS, with an HR of 1.17 (95% CI, 1.07–1.28),  $P < 0.001$ , and 1.19 (95% CI, 1.03–1.38),  $P = 0.02$ , per 1 unit increase, respectively. High integrin  $\alpha_v\beta_3$  expression, defined as maximal tumor SUV<sub>max</sub> above median (SUV<sub>max</sub> 6.10) had an HR of 1.96 (95% CI, 1.17–3.29) and 2.66 (95% CI, 1.14–6.16) for PFS and OS, respectively ( $P < 0.05$  for

**TABLE 4**  
Uni- and Multivariate Cox Regression Analyses for PFS (SUV<sub>max</sub> Cutoff at 6.10)

PFS	Univariate Cox		Multivariate Cox	
	HR	<i>P</i>	HR	<i>P</i>
<b>SUV<sub>max</sub></b>				
<6.10	Reference	—	Reference	—
≥6.10	1.96 (1.17–3.29)	0.01	1.82 (1.07–3.08)	0.03
<b>WHO grades</b>				
NET G1	Reference		Reference	
NET G2	1.25 (0.63–2.49)	0.52	1.25 (0.63–2.49)	0.52
NET G3	4.01 (1.68–9.54)	<0.01	4.08 (1.70–9.77)	<0.01
NEC	7.01 (2.65–18.50)	<0.001	5.87 (2.21–15.61)	<0.001

The median SUV<sub>max</sub> was 6.10. Data in parentheses are 95% CIs.

patients died. Overall median PFS was 18.9 mo (interquartile range, 15.5–25.1 mo). No patients were lost to follow-up. The patients' treatments after  $^{68}\text{Ga}$ -NODAGA-E[c(RGDyK)]<sub>2</sub> PET/CT are given

both (Fig. 4; Tables 4 and 5). Optimal cutoffs for dichotomizing maximal tumor SUV<sub>max</sub> were assessed by Cutoff Finder for either PFS or OS as outcome (Supplemental Fig. 1; supplemental materials

**TABLE 5**  
Uni- and Multivariate Cox Regression Analyses for OS (SUV<sub>max</sub> Cutoff at 6.10)

OS	Univariate Cox		Multivariate Cox	
	HR	<i>P</i>	HR	<i>P</i>
<b>SUV<sub>max</sub></b>				
<6.10	Reference	—	Reference	—
≥6.10	2.66 (1.14–6.16)	0.02	2.59 (1.08–6.24)	0.03
<b>WHO grades</b>				
NET G1	Reference		Reference	
NET G2	1.84 (0.40–8.50)	0.44	1.80 (0.39–8.35)	0.45
NET G3	15.99 (3.26–78.50)	<0.01	18.04 (3.59–90.63)	<0.001
NEC	28.46 (5.62–144.24)	<0.001	22.55 (4.45–114.27)	<0.001

The median SUV<sub>max</sub> was 6.10. Data in parentheses are 95% CIs.

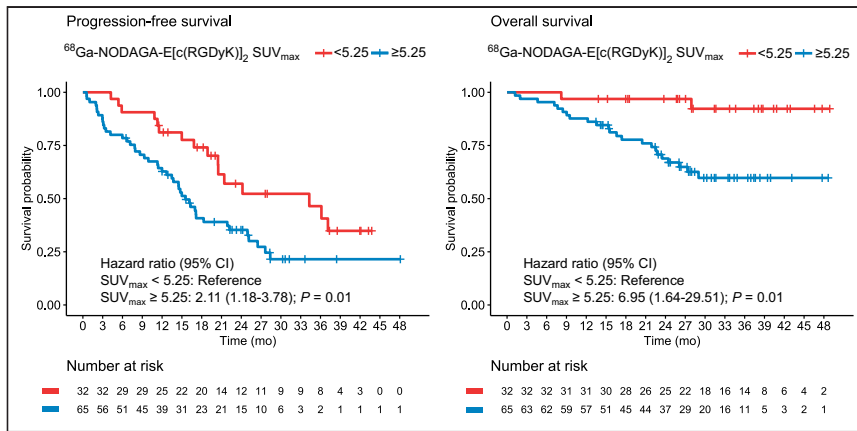


**FIGURE 5.** Kaplan-Meier plots of  $^{68}\text{Ga-NODAGA-E[c(RGDyK)}_2\text{] PET SUV}_{\text{max}}$  dichotomized at 5.25 for prediction of PFS and OS.

are available at <http://jnm.snmjournals.org>). When a lower cutoff of  $\text{SUV}_{\text{max}}$  (5.25) was used, a smaller group of patients ( $n = 32$ ) with a very low risk of death could be identified (Fig. 5; Tables 6 and 7). Patients with an  $\text{SUV}_{\text{max}}$  above 5.25 had an HR of 2.11 (95% CI, 1.18–3.78) and 6.95 (95% CI, 1.64–29.51) for PFS and OS, respectively ( $P = 0.01$  for both). With the cutoff of 5.25, median OS was not reached in either groups with low or groups with high  $\text{SUV}_{\text{max}}$ , and median PFS was 34.3 mo (20.5; upper limit not reached) for patients with low  $\text{SUV}_{\text{max}}$  versus 15.5 mo (13.5–22.2) for patients with high  $\text{SUV}_{\text{max}}$ . Furthermore, when a higher cutoff of  $\text{SUV}_{\text{max}}$  of 7.45 was used, the dichotomization was optimized for prediction of disease progression with an HR of 2.57 (95% CI, 1.52–4.34),  $P < 0.001$  (Supplemental Fig. 2; Supplemental Tables 1 and 2). Patients with NET G3 and NEC had significantly worse PFS and OS as compared with patients with NET G1, whereas no difference was seen between NET G2 and NET G1 (Tables 4 and 5). In multivariate analyses including  $\text{SUV}_{\text{max}}$  and WHO classification (NET G3 and NEC vs. NET G1), both remained significantly associated with PFS and OS (Tables 4–7).

## DISCUSSION

The major finding of our phase II prospective study of  $^{68}\text{Ga-NODAGA-E[c(RGDyK)}_2\text{] PET/CT$  for integrin  $\alpha_v\beta_3$  imaging in

patients with NEN was that integrin  $\alpha_v\beta_3$  expression was seen in both low- and high-grade NEN. Furthermore, we found a significant association between radiotracer uptake and both PFS and OS. When dichotomized at  $\text{SUV}_{\text{max}}$  5.25, patients with higher radiotracer uptake in tumor lesion had a 2-fold higher risk of progressive disease and a 7-fold higher risk of death. These findings highlight integrin  $\alpha_v\beta_3$  as an important prognostic marker in patients with NEN.

Many radiotracers using the RGD motif have been tested preclinically, with only some being further translated into clinical trials (14). In our phase I trial on  $^{68}\text{Ga-NODAGA-E[c(RGDyK)}_2\text{] PET/CT$  imaging, we included patients with NEN or breast cancer and demonstrated that administration of

the radiotracer was safe and had low radiation burden and high tumor lesion uptake (9). Besides our phase I trial, no specific PET imaging studies with an RGD-based radiotracer in patients with NEN have been conducted, although combined integrin  $\alpha_v\beta_3$  and somatostatin receptor targeting has been examined with  $^{68}\text{Ga-NOTA-3P-TATE-RGD PET/CT}$  (15). To our knowledge, the current study is the largest to be conducted with an RGD-based PET radiotracer. Other clinical trials have used RGD-based radiotracers to examine patients with, for example, breast cancer and head and neck cancers, as well as several other nononcologic applications, for example, atherosclerosis and rheumatoid arthritis (16–19).

Integrin  $\alpha_v\beta_3$  is a cell surface adhesion receptor and a member of the integrin superfamily. The subfamily of integrins recognized by RGD also includes  $\alpha_v\beta_1$ ,  $\alpha_v\beta_5$ ,  $\alpha_v\beta_6$ ,  $\alpha_v\beta_8$ ,  $\alpha_5\beta_1$ ,  $\alpha_8\beta_1$ , and  $\alpha_{\text{IIb}}\beta_3$  (20). Integrins are involved in several physiologic and pathophysiologic pathways, for example, embryogenesis, wound healing, and angiogenesis as well as tumor growth, invasion or metastasis, and angiogenesis related to cancer. The natural ligands of integrin  $\alpha_v\beta_3$  are extracellular matrix proteins such as fibronectin and vitronectin. Additionally, integrins interact with several other factors also involved in angiogenesis and invasive growth, for example, vascular endothelial growth factor and urokinase plasminogen activator receptor (5,21). An indication that integrin expression is involved in promoting the metastatic process in patients with NEN is supported by

**TABLE 6**  
Uni- and Multivariate Cox Regression Analyses for PFS ( $\text{SUV}_{\text{max}}$  Cutoff at 5.25)

PFS	Univariate Cox		Multivariate Cox	
	HR	P	HR	P
$\text{SUV}_{\text{max}}$				
<5.25	Reference	—	Reference	—
≥5.25	2.11 (1.18–3.78)	0.01	1.92 (1.06–3.47)	0.03
WHO grades				
NET G1	Reference		Reference	
NET G2	1.25 (0.63–2.49)	0.52	1.22 (0.62–2.44)	0.56
NET G3	4.01 (1.68–9.54)	<0.01	3.94 (1.65–9.44)	<0.01
NEC	7.01 (2.65–18.50)	<0.001	5.84 (2.20–15.55)	<0.001

$\text{SUV}_{\text{max}}$  cutoff optimized for prediction of OS was 5.25. Data in parentheses are 95% CIs.

**TABLE 7**  
Uni- and Multivariate Cox Regression Analyses for OS (SUV<sub>max</sub> Cutoff at 5.25)

OS	Univariate Cox		Multivariate Cox	
	HR	P	HR	P
<b>SUV<sub>max</sub></b>				
<5.25	Reference	—	Reference	—
≥5.25	6.95 (1.64–29.51)	0.01	5.45 (1.26–23.60)	0.02
<b>WHO grades</b>				
NET G1	Reference		Reference	
NET G2	1.84 (0.40–8.50)	0.44	1.78 (0.38–8.26)	0.46
NET G3	15.99 (3.26–78.50)	<0.01	15.67 (3.13–78.47)	<0.001
NEC	28.46 (5.62–144.24)	<0.001	20.23 (3.98–102.87)	<0.001

SUV<sub>max</sub> cutoff optimized for prediction of OS was 5.25. Data in parentheses are 95% CIs.

gene expression analysis in patients with pulmonary NEN. Upregulation of fibrogenic genes, including ITGAV (the gene encoding integrin  $\alpha_v$ ), was related to poor differentiation and increased risk of metastases (22). However, conflicting data regarding the relation between poorer prognosis and integrin  $\alpha_v\beta_3$  expression have been reported for immunohistochemical staining of gastric cancer (23) and non-small cell lung cancer (24).

Spurred by the upregulation of  $\alpha_v\beta_3$  during angiogenesis, early phase clinical trials with the  $\alpha_v\beta_3/\alpha_v\beta_5$ -targeting ligand cilengitide were performed, showing modest effect on tumor growth (25,26). However, later phase II and phase III trials failed to meet expectations because of an unintended proangiogenic effect at lower concentrations while an antiangiogenic effect was seen only at higher concentration (27). Recently, new promising pure  $\alpha_v\beta_3$  ligands (TDI-4161 and TDI-3761) have been shown to circumvent the proangiogenic effect previously seen with cilengitide (28), hence reinforcing the need for development of methods as companion diagnostics to assess in vivo the level of integrin  $\alpha_v\beta_3$  expression for selection of patients for such targeted therapies.

Another possible avenue for integrin  $\alpha_v\beta_3$ -targeted treatments is PRRT. In patients with NEN, PRRT with <sup>177</sup>Lu-DOTATATE, exploiting somatostatin receptor overexpression, has become an integrated part of treatment (29,30). In 2 preclinical studies, the potential of extending the use of the RGD sequence by coupling it with a radionuclide for therapy has been examined. One combined  $\alpha_v\beta_3$ -targeting PRRT with immune checkpoint inhibitor programmed death ligand 1 (31) and the other  $\alpha_v\beta_3$ -targeting PRRT with temozolomide (32). Both demonstrated additional effect of the combined therapy. Further studies of coupling imaging and PRRT in the setting of integrin  $\alpha_v\beta_3$  are needed. Concerns over physiologic uptake reported in RGD-based imaging have been raised regarding PRRT (20). However, compared with dosimetry data from somatostatin-based PET radiotracers <sup>68</sup>Ga-DOTATATE and <sup>68</sup>Ga-DOTATOC (33), we found similar kidney, liver, spleen, and intestinal absorbed doses in our phase I trial study assessing the dosimetry of <sup>68</sup>Ga-NODAGA-E[c(RGDyK)]<sub>2</sub> (9). Finally, a potential advantage of  $\alpha_v\beta_3$ -targeting PRRT over somatostatin receptor-targeting PRRT in NEN is that in particular in high-grade tumors, somatostatin receptor expression is low or absent and therefore somatostatin receptor PRRT cannot be used. In contrast, we found a

high uptake of <sup>68</sup>Ga-NODAGA-E[c(RGDyK)]<sub>2</sub> also in high-grade tumors (91% of patients with NET G3/NEC).

In our study, included patients predominately had small intestinal or pancreatic primary tumors and nearly all had metastatic disease with liver involvement. Hence use of <sup>68</sup>Ga-NODAGA-E[c(RGDyK)]<sub>2</sub> PET/CT in other settings, for example, for assessment of newly diagnosed patients with localized disease, remains to be elucidated.

## CONCLUSION

Tumor uptake of <sup>68</sup>Ga-NODAGA-E[c(RGDyK)]<sub>2</sub> was evident in patients both with low- and with high-grade NEN, although tumor uptake was more pronounced with increasing grade. High tumor uptake of <sup>68</sup>Ga-NODAGA-E[c(RGDyK)]<sub>2</sub> was associated with a poorer prognosis in patients with NEN, with a 2-fold higher risk of progression and 7-fold higher risk of death. Further studies are warranted to establish whether <sup>68</sup>Ga-NODAGA-E[c(RGDyK)]<sub>2</sub> PET/CT may become a tool for risk stratification and for identification of patients eligible for treatments targeting integrin  $\alpha_v\beta_3$ .

## DISCLOSURE

This project received funding from the European Union's Horizon 2020 research and innovation program under grant agreements no. 670261 (ERC Advanced Grant) and 668532 (Click-It), the Lundbeck Foundation, the Novo Nordisk Foundation, the Innovation Fund Denmark, IPSEN Nordic, the Danish Cancer Society, Arvid Nilsson Foundation, the Neye Foundation, Novartis Health Care, the Research Foundation of Rigshospitalet, the Danish National Research Foundation (grant 126), the Research Council of the Capital Region of Denmark, the Danish Health Authority, the John and Birthe Meyer Foundation, the Research Council for Independent Research, and the Neuroendocrine Tumor Research Foundation. Andreas Kjaer is a Lundbeck Foundation Professor and is an inventor/holds intellectual property rights on a patent application: “<sup>68</sup>Ga- and <sup>64</sup>Cu -NODAGA-E[c(RGDyK)]<sub>2</sub> for use as pet tracers in the imaging of angiogenesis in humans” (WO2019091534A1). No other potential conflicts of interest relevant to this article exist.

## ACKNOWLEDGEMENT

We are grateful to our dedicated colleagues at the Department of Clinical Physiology and Nuclear Medicine, Department of Endocrinology, and Department of Oncology at Rigshospitalet for assistance with patient recruitment, radiotracer production, and acquisition of PET/CT scans. We express our sincere gratitude to all the patients who participated in the study.

## KEY POINTS

**QUESTION:** Is integrin  $\alpha_v\beta_3$  expression assessed by PET evident in tumor lesions of patients with NENs and associated with prognosis?

**PERTINENT FINDINGS:** When  $^{68}\text{Ga}$ -NODAGA-E[c(RGDyK)]<sub>2</sub> for integrin  $\alpha_v\beta_3$  PET imaging was used, integrin  $\alpha_v\beta_3$  was evident in tumor lesions of patients with both low- and high-grade tumors. High tumor uptake of  $^{68}\text{Ga}$ -NODAGA-E[c(RGDyK)]<sub>2</sub> was associated with a poorer prognosis for both disease progression and death.

**IMPLICATIONS FOR PATIENT CARE:** Integrin  $\alpha_v\beta_3$  is a prognostic marker and a potential treatment target in patients with NENs.

$^{68}\text{Ga}$ -NODAGA-E[c(RGDyK)]<sub>2</sub> PET/CT may become a tool for risk stratification and for identification of patients eligible for treatments targeting integrin  $\alpha_v\beta_3$ .

## REFERENCES

1. Dasari A, Shen C, Halperin D, et al. Trends in the incidence, prevalence, and survival outcomes in patients with neuroendocrine tumors in the United States. *JAMA Oncol.* 2017;3:1335–1342.
2. Digestive System Tumours. *WHO Classification of Tumours*. 5th ed. International Agency for Research on Cancer; 2019:16–19.
3. Carlsen EA, Johnbeck CB, Loft M, et al. Semiautomatic tumor delineation for evaluation of  $^{64}\text{Cu}$ -DOTATATE PET/CT in patients with neuroendocrine neoplasms: prognostication based on lowest lesion uptake and total tumor volume. *J Nucl Med.* 2021;62:1564–1570.
4. Binderup T, Knigge U, Johnbeck CB, et al.  $^{18}\text{F}$ -FDG PET is superior to WHO grading as a prognostic tool in neuroendocrine neoplasms and useful in guiding PRRT: a prospective 10-year follow-up study. *J Nucl Med.* 2021;62:808–815.
5. Ludwig BS, Kessler H, Kossatz S, Reuning U. RGD-binding integrins revisited: how recently discovered functions and novel synthetic ligands (re-)shape an ever-evolving field. *Cancers (Basel).* 2021;13:1711.
6. Nieberler M, Reuning U, Reichart F, et al. Exploring the role of RGD-recognizing integrins in cancer. *Cancers (Basel).* 2017;9:116.
7. Cives M, Pelle E, Quaresmini D, Rizzo FM, Tucci M, Silvestris F. The tumor microenvironment in neuroendocrine tumors: biology and therapeutic implications. *Neuroendocrinology.* 2019;109:83–99.
8. Oxboel J, Binderup T, Knigge U, Kjaer A. Quantitative gene-expression of the tumor angiogenesis markers vascular endothelial growth factor, integrin  $\alpha_v$  and integrin  $\beta_3$  in human neuroendocrine tumors. *Oncol Rep.* 2009;21:769–775.
9. Clausen MM, Carlsen EA, Christensen C, et al. First-in-human study of [ $^{68}\text{Ga}$ ]Ga-NODAGA-E[c(RGDyK)]<sub>2</sub> PET for integrin alphavbeta3 imaging in patients with breast cancer and neuroendocrine neoplasms: safety, dosimetry and tumor imaging ability. *Diagnostics (Basel).* 2022;12:851.
10. Oxboel J, Brandt-Larsen M, Schjoeth-Eskesen C, et al. Comparison of two new angiogenesis PET tracers  $^{68}\text{Ga}$ -NODAGA-E[c(RGDyK)]<sub>2</sub> and  $^{64}\text{Cu}$ -NODAGA-E[c(RGDyK)]<sub>2</sub>: in vivo imaging studies in human xenograft tumors. *Nucl Med Biol.* 2014;41:259–267.
11. Knigge U, Capdevila J, Bartsch DK, et al. ENETS consensus recommendations for the standards of care in neuroendocrine neoplasms: follow-up and documentation. *Neuroendocrinology.* 2017;105:310–319.
12. Eisenhauer EA, Therasse P, Bogaerts J, et al. New response evaluation criteria in solid tumours: revised RECIST guideline (version 1.1). *Eur J Cancer.* 2009;45:228–247.
13. Budczies J, Klauschen F, Sinn BV, et al. Cutoff Finder: a comprehensive and straightforward web application enabling rapid biomarker cutoff optimization. *PLoS One.* 2012;7:e51862.
14. Liolios C, Sachpekidis C, Kolocouris A, Dimitrakopoulou-Strauss A, Bouziotis P. PET diagnostic molecules utilizing multimeric cyclic RGD peptide analogs for imaging integrin alphavbeta3 receptors. *Molecules.* 2021;26:1792.
15. Zheng Y, Wang H, Tan H, et al. Evaluation of lung cancer and neuroendocrine neoplasm in a single scan by targeting both somatostatin receptor and integrin  $\alpha_v\beta_3$ . *Clin Nucl Med.* 2019;44:687–694.
16. Dietz M, Kamani CH, Deshayes E, et al. Imaging angiogenesis in atherosclerosis in large arteries with  $^{68}\text{Ga}$ -NODAGA-RGD PET/CT: relationship with clinical atherosclerotic cardiovascular disease. *EJNMMI Res.* 2021;11:71.
17. Wu J, Wang S, Zhang X, et al.  $^{18}\text{F}$ -Alfatide II PET/CT for identification of breast cancer: a preliminary clinical study. *J Nucl Med.* 2018;59:1809–1816.
18. Zhu Z, Yin Y, Zheng K, et al. Evaluation of synovial angiogenesis in patients with rheumatoid arthritis using  $^{68}\text{Ga}$ -PRGD2 PET/CT: a prospective proof-of-concept cohort study. *Ann Rheum Dis.* 2014;73:1269–1272.
19. Durante S, Dunet V, Gorostidi F, et al. Head and neck tumors angiogenesis imaging with  $^{68}\text{Ga}$ -NODAGA-RGD in comparison to  $^{18}\text{F}$ -FDG PET/CT: a pilot study. *EJNMMI Res.* 2020;10:47.
20. Steiger K, Quigley NG, Groll T, et al. There is a world beyond alphavbeta3-integrin: multimeric ligands for imaging of the integrin subtypes alphavbeta6, alphavbeta8, alphavbeta3, and alpha5beta1 by positron emission tomography. *EJNMMI Res.* 2021;11:106.
21. Mahmood N, Mihalciou C, Rabbani SA. Multifaceted role of the urokinase-type plasminogen activator (uPA) and its receptor (uPAR): diagnostic, prognostic, and therapeutic applications. *Front Oncol.* 2018;8:24.
22. Prieto TG, Machado-Rugolo J, Baldavira CM, et al. The fibrosis-targeted collagen/integrins gene profile predicts risk of metastasis in pulmonary neuroendocrine neoplasms. *Front Oncol.* 2021;11:706141.
23. Böger C, Warneke VS, Behrens HM, et al. Integrins alphavbeta3 and alphavbeta5 as prognostic, diagnostic, and therapeutic targets in gastric cancer. *Gastric Cancer.* 2015;18:784–795.
24. Böger C, Kalthoff H, Goodman SL, Behrens H-M, Röcken C. Integrins and their ligands are expressed in non-small cell lung cancer but not correlated with parameters of disease progression. *Virchows Arch.* 2014;464:69–78.
25. Nabors LB, Mikkelsen T, Hegi ME, et al. A safety run-in and randomized phase 2 study of cilengitide combined with chemoradiation for newly diagnosed glioblastoma (NABTT 0306). *Cancer.* 2012;118:5601–5607.
26. Reardon DA, Fink KL, Mikkelsen T, et al. Randomized phase II study of cilengitide, an integrin-targeting arginine-glycine-aspartic acid peptide, in recurrent glioblastoma multiforme. *J Clin Oncol.* 2008;26:5610–5617.
27. Stupp R, Hegi ME, Gorlia T, et al. Cilengitide combined with standard treatment for patients with newly diagnosed glioblastoma with methylated MGMT promoter (CENTRIC EORTC 26071-22072 study): a multicentre, randomised, open-label, phase 3 trial. *Lancet Oncol.* 2014;15:1100–1108.
28. Li J, Fukase Y, Shang Y, et al. Novel pure alphaVbeta3 integrin antagonists that do not induce receptor extension, prime the receptor, or enhance angiogenesis at low concentrations. *ACS Pharmacol Transl Sci.* 2019;2:387–401.
29. Janson ET, Knigge U, Dam G, et al. Nordic guidelines 2021 for diagnosis and treatment of gastroenteropancreatic neuroendocrine neoplasms. *Acta Oncol.* 2021;60:931–941.
30. Hope TA, Bodei L, Chan JA, et al. NANETS/SNMMI consensus statement on patient selection and appropriate use of  $^{177}\text{Lu}$ -DOTATATE peptide receptor radionuclide therapy. *J Nucl Med.* 2020;61:222–227.
31. Chen H, Zhao L, Fu K, et al. Integrin alphavbeta3-targeted radionuclide therapy combined with immune checkpoint blockade immunotherapy synergistically enhances anti-tumor efficacy. *Theranostics.* 2019;9:7948–7960.
32. Lee SH, Choi JY, Jung JH, et al. Effect of peptide receptor radionuclide therapy in combination with temozolomide against tumor angiogenesis in a glioblastoma model. *Cancers (Basel).* 2021;13:5029.
33. Sandström M, Velikyan I, Garske-Román U, et al. Comparative biodistribution and radiation dosimetry of  $^{68}\text{Ga}$ -DOTATOC and  $^{68}\text{Ga}$ -DOTATATE in patients with neuroendocrine tumors. *J Nucl Med.* 2013;54:1755–1759.

---

---

# Precision of Myocardial Blood Flow and Flow Reserve Measurement During CZT SPECT Perfusion Imaging Processing: Intra- and Interobserver Variability

Matthieu Bailly<sup>1,2</sup>, Frédérique Thibault<sup>1</sup>, Gilles Metrard<sup>1</sup>, Maxime Courtehoux<sup>3</sup>, Denis Angoulvant<sup>\*4,5</sup>, and Maria Joao Ribeiro<sup>\*2,3</sup>

<sup>1</sup>Nuclear Medicine Department, CHR Orleans, Orleans, France; <sup>2</sup>UMR 1253, iBrain, Université de Tours, INSERM, Tours, France;

<sup>3</sup>Nuclear Medicine Department, CHRU Tours, Tours, France; <sup>4</sup>Cardiology Department, CHRU Tours, Tours, France; and

<sup>5</sup>EA4245 T2i, Tours University, Tours, France

The aim of this study was to evaluate the reproducibility of myocardial blood flow (MBF) and myocardial flow reserve (MFR) measurement in patients referred for dynamic SPECT. **Methods:** We retrospectively analyzed patients referred for myocardial perfusion imaging. SPECT data were acquired on a cadmium zinc telluride-based pinhole cardiac camera in list mode using a stress ( $251 \pm 15$  MBq)/rest ( $512 \pm 26$  MBq) 1-d <sup>99m</sup>Tc-tetrofosmin protocol. Kinetic analyses were done with software using a 1-tissue-compartment model and converted to MBF using a previously determined extraction fraction correction. MFR was analyzed and compared globally and regionally. Motion detection was applied, but not attenuation correction. **Results:** In total, 124 patients (64 male, 60 female) were included, and SPECT acquisitions were twice reconstructed by the same nuclear medicine board-certified physician for 50 patients and by 2 different physicians for 74. Both intra- and interobserver measurements of global MFR had no significant bias ( $-0.01$  [ $P = 0.94$ ] and  $0.01$  [ $P = 0.67$ ], respectively). However, rest MBF and stress MBF were significantly different in global left ventricular evaluation ( $P = 0.001$  and  $P = 0.002$ , respectively) and in the anterior territory ( $P < 0.0001$ ) on interuser analysis. The average coefficient of variation was 15%–30% of the mean stress MBF if the analysis was performed by the same physician or 2 different physicians and was around 20% of the mean MFR independently of the processing physician. Using the MFR threshold of 2, we noticed good intrauser agreement, whereas it was moderate when the users were different ( $\kappa = 0.75$  [95% CI, 0.56–0.94] vs. 0.56 [95% CI, 0.36–0.75], respectively). **Conclusion:** Repeated measurements of global MFR by the same physician or 2 different physicians were similar, with an average coefficient of variation of 20%. Better reproducibility was achieved for intrauser MBF evaluation. Automation of processing is needed to improve reproducibility.

**Key Words:** myocardial blood flow; myocardial flow reserve; CZT SPECT; variability

J Nucl Med 2023; 64:260–265

DOI: 10.2967/jnumed.122.264454

---

Received May 27, 2022; revision accepted Sep. 8, 2022.

For correspondence or reprints, contact Matthieu Bailly (matthieu.bailly@chr-orleans.fr).

\*Contributed equally to this work.

Published online Sep. 15, 2022.

Immediate Open Access: Creative Commons Attribution 4.0 International License (CC BY) allows users to share and adapt with attribution, excluding materials credited to previous publications. License: <https://creativecommons.org/licenses/by/4.0/>. Details: <http://jnm.snmjournals.org/site/misc/permission.xhtml>.

COPYRIGHT © 2023 by the Society of Nuclear Medicine and Molecular Imaging.

Myocardial blood flow (MBF) at stress (sMBF) and at rest (rMBF) and myocardial flow reserve (MFR) derived from PET perfusion imaging have been shown to provide diagnostic (1,2) and prognostic (3) information in addition to that provided by relative perfusion analysis alone. Several studies have shown that clinical measurement of MBF and MFR using dynamic cadmium zinc telluride (CZT) SPECT myocardial perfusion imaging with <sup>99m</sup>Tc-radiopharmaceuticals is technically possible, resulting in an MFR similar to that of PET (4–9).

However, with the idea of greater clinical use, there is a need to evaluate the precision and reproducibility of this measurement. A day-to-day test–retest precision study using a dedicated cardiac camera on a group of 30 patients found that the SD for the difference in measured MBFs was around 30%, including physiologic and processing variability (10). A recent simulation study evaluated the impact of SPECT MFR imprecision on confidence in clinically relevant categorization. The authors concluded that current SPECT MFR precision as categorization with high confidence (>80%) was achieved only for extreme MFRs (<1.0 or > 2.5), with correct classification in only 15% of patients in a typical lab with an MFR of  $1.8 \pm 0.5$  (11). A third paper evaluated the intra- and interobserver repeatability of MBF and MFR values obtained by the same operator and 2 independent operators for 57 patients. This study showed reproducibility that was quite good in the whole-myocardium, left-anterior-descending-artery (LAD), and left-circumflex vascular territories but poor in the right-coronary-artery (RCA) territory (12).

In this study, we evaluated the intra- and interuser processing repeatability of global and regional SPECT MBF and MFR in a larger cohort of patients.

## MATERIALS AND METHODS

### Patient Population

From October 2018 to January 2021, 128 patients referred to 2 nuclear medicine departments for SPECT myocardial perfusion imaging with MBF and MFR quantification were initially enrolled in the CFR-OR trial for coronary artery disease screening (13) (clinicaltrials.gov identifier NCT03586492), and their images were retrospectively reconstructed and analyzed. The study protocol was approved by the institutional review board, and the procedures were in accordance with the Declaration of Helsinki. Every patient gave written informed consent.

The inclusion criterion was dynamic SPECT myocardial perfusion imaging. Exclusion criteria included missing files for new processing



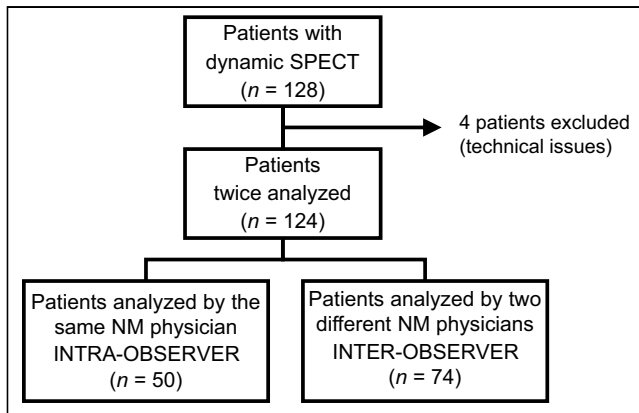


**FIGURE 1.** Study flowchart.

or technical issues. Technical issues were reported for MBF and MFR measurement in 4 patients (late acquisition after injection). A flowchart of the study is displayed in Figure 1.

### SPECT Acquisition

List-mode acquisitions were performed on 2 Discovery NM530c cardiac CZT cameras (GE Healthcare) (1 scanner for each department). An initial injection of 37 MBq of  $^{99m}\text{Tc}$ -tetrofosmin was used to center the patient's heart in the field of view. Pharmacologic stress was then performed using either a regadenoson (400  $\mu\text{g}$ ) injection or a dipyridamole perfusion (0.56 mg/kg), immediately followed by a 250-MBq injection of  $^{99m}\text{Tc}$ -tetrofosmin at the hyperemia peak and flushing with 50 mL of saline to ensure consistent delivery of a tight bolus. The rest dynamic acquisition was realized 3 h later, with a 500-MBq injection of  $^{99m}\text{Tc}$ -tetrofosmin.

### SPECT MBF and MFR Quantification

Dynamic SPECT images were reconstructed using Corridor 4DM software (INVIA) on a Xeleris workstation (GE Healthcare). The SPECT initial list-mode data were resampled into frames of  $12 \times 10$  s and  $8 \times 30$  s. The partial-volume value was set to 0.6; the correction factor for myocardial density was set to 1. Spillover of activity from the myocardium to the blood pool was assumed negligible and was set to 0. The uptake rate,  $K_1$ , was related to MBF using the Renkin-Crone equation according to Leppo and Meerdink (14), applying a net retention model in which  $A = 0.874$  and  $B = 0.443$ :

$$K_1 = \text{MBF} \times (1 - A \times e^{-\frac{B}{\text{MBF}}}).$$

Residual activity subtraction on rest-image sets after the stress dose was always applied. Because our previous results (15) showed no difference in MFR whether attenuation correction was applied or not, we did not apply it in this study. All MBF and MFR values are presented without attenuation correction. Motion was detected for each patient, and the operator could choose whether to perform motion correction. However, none of the movement was significant, resulting in no correction of data. Double-product (heart rate  $\times$  blood pressure) correction was used for MBF correction in all studies.

Images of all 124 patients were reconstructed and analyzed by the same expert nuclear medicine physician for the second analysis. The images of 50 patients had initially been reconstructed by the same physician (i.e., intrauser analysis). The images of 74 patients had been analyzed at the first reading by another nuclear medicine physician (i.e., interuser analysis). The mean elapsed time between the 2 analyses was 12.8 mo.

When available, results from invasive coronary angiography were collected. Coronary angiograms were visually assessed by the experienced interventional cardiologist responsible for the procedure. The angiograms were assessed according to the clinical routine, considering available clinical data and patient history. According to the recent guidelines

**TABLE 1**  
Patient Description

Parameter	Total	Intraobserver	Interobserver	<i>P</i>
Number of patients	124	50	74	
Sex				0.72
Male	61 (45%)	26 (52%)	35 (47%)	
Female	63 (55%)	24 (48%)	39 (53%)	
Age (y)	68 $\pm$ 9.3 (41–87)	69 $\pm$ 8.6 (41–87)	67 $\pm$ 10.5 (44–85)	0.99
BMI (kg/m <sup>2</sup> )	28.3 $\pm$ 5.4 (15–44)	28.2 $\pm$ 5.5 (18–40)	29.4 $\pm$ 6.8 (15–44)	0.33
Stress activity (MBq)	261 $\pm$ 14 (240–294)	262 $\pm$ 13 (248–294)	258 $\pm$ 15 (240–287)	0.99
Rest activity (MBq)	519 $\pm$ 18 (468–545)	517 $\pm$ 17 (468–538)	522 $\pm$ 18 (478–545)	0.99
Positioning activity (MBq)	41 $\pm$ 5 (34–55)	41 $\pm$ 3 (38–53)	40 $\pm$ 5 (34–55)	0.99
CVR factors				
Diabetes	44 (35%)	17 (33%)	27 (36%)	0.87
Hypertension	84 (68%)	35 (70%)	49 (66%)	0.75
Smoking	61 (49%)	26 (51%)	35 (47%)	0.88
Dyslipidemia	82 (66%)	32 (64%)	50 (68%)	0.84
Family history of coronary artery disease	18 (15%)	8 (16%)	10 (14%)	0.92
Mean number of CVR factors	2.3 $\pm$ 1 (0–5)	2.4 $\pm$ 1 (0–5)	2.2 $\pm$ 0.8 (0–5)	0.71

CVR = cardiovascular risk.

Qualitative data are number and percentage; continuous data are mean and range.

defining very high-risk patients as in need of secondary prevention intervention, we considered all patients having significant coronary artery plaque  $\geq 50\%$  according to the angiographer conclusion (16). We put into perspective the MFR variability by considering the results of invasive coronary angiography, globally and regionally, for each vessel with a significant lesion.

### Statistical Analysis

Continuous variables are presented as mean  $\pm$  SD. Categorical variables are provided as total number and percentage. Gaussian distribution was assessed using the D'Agostino–Pearson normality test. In analyzing differences between 2 groups, we applied the independent-samples *t* test when comparing continuous variables and the  $\chi^2$  or Fisher exact test, as appropriate, when comparing categorical variables. In analyzing differences between 2 paired groups, the Wilcoxon matched-pairs signed-rank test was applied because of the nonnormally distributed variables. Spearman correlation coefficients were computed between variables. Bland–Altman analysis was used to calculate the bias and the limits of agreement. Precision between the 2 measurements was determined as the coefficient of variation (COV) in the measured difference (COV = SD of the percentage difference). The strength of the agreement between users was evaluated using Fleiss  $\kappa$ . A *P* value of less than 0.05 was considered statistically significant. All analyses were performed using Prism, version 9 (GraphPad).

### RESULTS

The study had 124 patients (61 male, 63 female); both subpopulations were comparable in sex, age, body mass index (BMI), cardiovascular risk factors, and technical parameters (Table 1). Both intra- and interobserver measurements of global MFR had no significant bias ( $-0.01$  [ $P = 0.94$ ] and  $0.01$  [ $P = 0.67$ ], respectively) (Table 2). Regarding regional MFR, no significant difference was found either for intra- or interobserver analysis. On the interuser analysis, sMBF was significantly different in the global left ventricular evaluation ( $P = 0.0002$ ) and in the anterior territory (LAD) ( $P < 0.0001$ ); rMBF was also significantly different. Lower differences were found for intrauser sMBF evaluation; only sMBF LAD was significantly different ( $P = 0.04$ ). Considering rMBF, no significant difference was found for intraobserver analysis ( $P = 0.15$ ). Bland–Altman analysis showed that the variation in the difference between repeated analyses was consistent across the range of sMBF and MFR considered (Fig. 2).

Bland–Altman analysis of the intrauser evaluation also showed better precision in MBF evaluation (Fig. 2B). The COV between MFR measurements was similar both for intrauser and for interuser evaluations: respectively, 20.2% versus 18.9% for global left ventricular MFR. This COV was similar, at around 20% for all regional MFR territories and analyses; however, the COV was

**TABLE 2**  
Differences in MFR and sMBF Between 2 Measurements, with Statistical Results

Parameter	Mean value $\pm$ SD		Mean difference	COV	<i>P</i>	Spearman <i>r</i>	Agreement (Bland–Altman)	
	Measurement 1	Measurement 2					Bias	95% limits of agreement
Intraobserver ( <i>n</i> = 50)								
sMBF LAD	1.72 $\pm$ 0.74	1.79 $\pm$ 0.73	-0.06	15.1%	0.04	0.86	-0.06	-0.52 to 0.39
sMBF LCx	1.44 $\pm$ 0.62	1.48 $\pm$ 0.63	-0.04	16.8%	0.22	0.86	-0.04	-0.47 to 0.39
sMBF RCA	1.29 $\pm$ 0.75	1.31 $\pm$ 0.74	-0.02	13.9%	0.38	0.93	-0.02	-0.38 to 0.34
sMBF global	1.51 $\pm$ 0.68	1.56 $\pm$ 0.68	-0.04	14.8%	0.10	0.87	-0.04	-0.45 to 0.36
rMBF global	0.72 $\pm$ 0.34	0.75 $\pm$ 0.41	-0.04	18.8%	0.15	0.87	-0.04	-0.40 to 0.33
MFR LAD	2.41 $\pm$ 0.84	2.39 $\pm$ 0.98	0.01	20.9%	0.64	0.90	0.01	-0.85 to 0.87
MFR LCx	2.34 $\pm$ 0.92	2.37 $\pm$ 0.97	-0.04	22.0%	0.79	0.84	-0.04	-0.96 to 0.88
MFR RCA	2.11 $\pm$ 0.95	2.10 $\pm$ 0.94	0.00	20.0%	0.94	0.88	0.003	-0.80 to 0.81
MFR global	2.29 $\pm$ 0.81	2.29 $\pm$ 0.89	-0.01	20.2%	0.94	0.88	0.01	-0.80 to 0.81
Interobserver ( <i>n</i> = 74)								
sMBF LAD	1.58 $\pm$ 0.56	1.78 $\pm$ 0.63	-0.21	23.1%	<0.0001	0.72	-0.21	-1.01 to 0.59
sMBF LCx	1.48 $\pm$ 0.49	1.54 $\pm$ 0.56	-0.06	22.2%	0.53	0.79	-0.06	-0.90 to 0.78
sMBF RCA	1.14 $\pm$ 0.48	1.18 $\pm$ 0.48	-0.04	21.8%	0.17	0.83	-0.04	-0.56 to 0.48
sMBF global	1.42 $\pm$ 0.48	1.52 $\pm$ 0.56	-0.11	32.2%	0.002	0.75	-0.11	-0.85 to 0.64
rMBF global	0.62 $\pm$ 0.25	0.68 $\pm$ 0.27	-0.05	25.3%	0.001	0.77	-0.05	-0.46 to 0.35
MFR LAD	2.45 $\pm$ 0.98	2.45 $\pm$ 0.93	0.01	20.7%	0.87	0.82	-0.01	-0.88 to 0.86
MFR LCx	2.68 $\pm$ 1.12	2.65 $\pm$ 1.12	0.03	18.8%	0.40	0.86	0.03	-1.00 to 1.07
MFR RCA	2.33 $\pm$ 1.06	2.28 $\pm$ 0.97	0.05	19.4%	0.51	0.89	0.04	-0.74 to 0.83
MFR global	2.46 $\pm$ 0.94	2.45 $\pm$ 0.90	0.01	18.9%	0.67	0.84	-0.01	-0.84 to 0.82

LCx = left circumflex.  
MBF data are in mL/min/g.

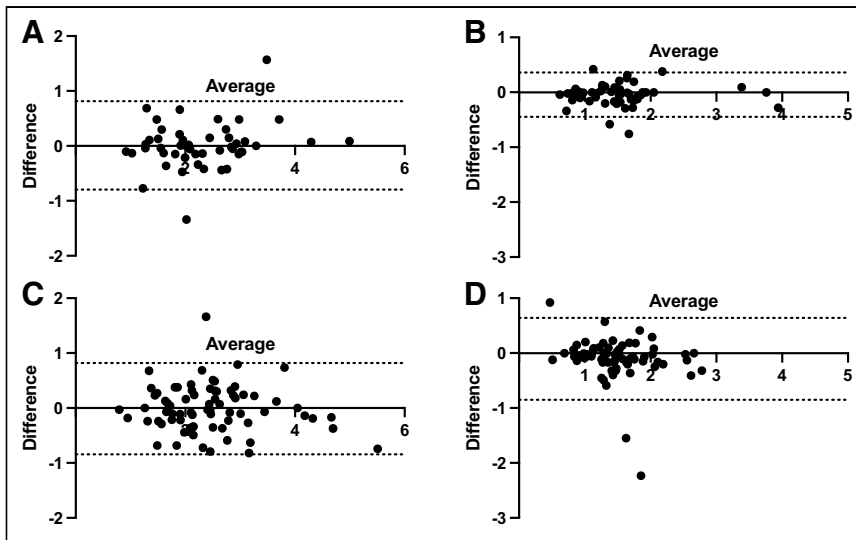


**FIGURE 2.** Differences in repeated measurements of MFR and sMBF for intraobserver analysis (A and B, respectively) and interobserver analysis (C and D, respectively). Dashed lines indicate 95% confidence limits. Results are displayed for global left ventricle; results for regional analysis were similar.

significantly lower for MBF evaluation on the intraobserver analysis than on the interuser analysis: 14.8% versus 32.2% for global sMBF ( $P < 0.001$ ). For the intraobserver subpopulation, 17 patients had a BMI of more than 30, and for the interobserver subpopulation, 27 patients had a BMI of more than 30. Obesity did not impact COV: 21.4% for a BMI of less than 30 and 17.9% for a BMI of more than 30 for intraobserver analysis; 17.3% for a BMI of less than 30 and 22.5% for a BMI of more than 30 for interobserver analysis.

Using an MFR threshold of 2, we noticed good agreement when the 2 measurements were made by the same physician, with consistent classification of 27 patients with an MFR of more than 2 and 17 patients with an MFR of less than 2 (88% of observed agreements;  $\kappa = 0.75$ ; 95% CI, 0.56–0.94). Among the 6 patients differently classified, 4 patients had a very similar result of around 2, with a difference of less than 0.2 (1.89 and 2.01, for example). However, this agreement became moderate when the users were different ( $\kappa = 0.56$ ; 95% CI, 0.36–0.75), with consistent classification of 41 patients with an MFR of more than 2 and 18 patients with an MFR of less than 2 (79.73% of observed agreements). Fifteen patients were classified differently, with only 2 patients having similar MFR results of around 2 and a difference of less than 0.2.

Thirty-four patients underwent invasive coronary angiography within 3 mo. Seven patients had no significant lesion; 4 of them had global and regional MFRs of more than 2 on both analyses. The other 3 had an MFR of less than 2 on both analyses. Among the 27 patients with lesions, 55 significant plaques were found (24 in the LAD coronary artery, 15 in the left circumflex coronary artery, and 16 in the RCA). Seven of these 55 vessel lesions (12.7%) had discrepant MFRs: 1 below 2 and 1 above, with a mean difference of 0.43 (0.34, 0.93, and 0.04 in the LAD coronary artery, left circumflex coronary artery, and RCA territories, respectively).

## DISCUSSION

In this study, SPECT sMBF and MFR remained globally similar between different measurements whether the analysis was performed by the same physician or by 2 different physicians, except

for sMBF (global left ventricular and LAD territory) and rMBF, for which significant differences were found for interuser evaluation. Using the MFR threshold of 2, we found good agreement when the analysis was performed by the same user.

With the development of CZT heart-dedicated SPECT systems, SPECT MBF and MFR have been shown to have a certain diagnostic value for patients with suspected or known CAD and represent a useful supplement to the conventional qualitative diagnostic methods (13,17,18). As in PET, an MFR of more than 2 has been considered a normal value, resulting in a very low rate of cardiac events (3,19). Recent studies have evaluated the day-to-day test–retest precision of sMBF and MFR. Using  $^{82}\text{Rb}$  PET, the test–retest methodologic precision of serial quantitative global myocardial perfusion for minutes apart is  $\pm 10\%$  (mean difference in SD of  $\pm 0.09$  mL/min/g at rest and  $\pm 0.23$  mL/min/g at stress) and for days apart is

$\pm 21\%$  (mean difference in SD of  $\pm 0.2$  mL/min/g at rest and  $\pm 0.46$  mL/min/g at stress), reflecting added biologic variability (20). Recently, Wells et al. determined the day-to-day test–retest precision of SPECT global MBF and MFR to be between 28% and 31% and 33% to 38%, respectively, considering all the processing approaches (use of attenuation correction or not, use of manual motion correction or not) (10). The day-to-day test–retest precision in their study included not only methodologic variability but also physiologic variability in the patient imaged during 2 separate sessions multiple days apart. Though this study reported both methodologic and physiologic variation, the authors noticed a higher variability for SPECT evaluation. Wells et al. advanced the following hypothesis to explain this greater variation: the low extraction fraction of tetrofosmin, the greater statistical noise in the dynamic images, and reduced resolution compared with PET, with the last of these leading to increased partial-volume effects and a need for larger spillover corrections, as well as the additional variability introduced from the manual registration of externally acquired CT images when attenuation correction was applied (because most heart-dedicated CZT SPECT systems are not hybrid).

The impact of attenuation correction and motion correction on MBF accuracy has been evaluated previously by Wells et al. (21). They agreed that attenuation correction had only a small benefit, which may have been offset by the variability due to manual registration of the attenuation map. In our study, we did not apply attenuation correction because it has been our experience, like other investigators, that attenuation correction does not affect MFR (7,15,21) and because attenuation correction may not be routinely achievable in that most CZT SPECT cameras are not equipped with CT. Regarding motion correction, we evaluated on a case-by-case basis the need for manual registration, but no correction was needed.

Our study focused only on processing variability (not on physiologic individual variability). We reported a lower SPECT MFR COV of around 20% than did Wells et al. (33%–38% (10)), who evaluated both physiologic and processing variation. A previous study focusing on analysis only, with the same initial dynamic image series on a conventional dual-head camera with sestamibi SPECT MBF using FlowQuant software (Ottawa Heart Institute), reported the SD of the

differences to be around 0.30 mL/min/g, with an average MBF of 1.5 mL/min/g, giving a COV of 20% (22). However, we noticed a significantly lower COV on rMBF and sMBF measurements when the processing was performed by the same physician (18.8%–14.8% vs. 25.3%–32.2% for intrauser and interuser, respectively). This lower variation was not noticed on MFR, probably because of the ratio, considering that the variability between 2 different users remained the same on sMBF and rMBF reconstructions. Our limits of agreement for global MFR were also very close to the results of a recent simulation study (11).

Regarding regional MFR, unlike Cichocki et al. (12), we did not notice poor repeatability for MBF and MFR in the RCA territory. Indeed, we observed even lower limits of agreement in the RCA territory on Bland–Altman analysis. The COV remained similar. However, we noticed a greater variability in the LAD territory when processing was performed by different physicians. This finding might also be explained by poor automatic orientation of the heart axis during postprocessing. Better automatic heart orientation and introduction of automatic motion correction are likely to drastically improve interobserver repeatability.

There is a need to increase the analytic precision of SPECT MBF and MFR, as integrated assessment of sMBF and MFR helps improve diagnostic performance (23,24). sMBF is 2.7 mL/min/g in young, healthy subjects (25). Considering a precision of 15% and 32% for intra- and interuser processing, the lower 95% confidence limit would be 1.9 mL/min/g and 1.2 mL/min/g, respectively. This remains a major limitation in the identification of patients with a moderate reduction in sMBF. In a previous study with invasive coronary angiography correlation, we identified the best sMBF SPECT threshold to be around 1.28 mL/min/g (13). In their simulation study, Renaud et al. showed correct classification in up to only 34% of patients when true MFR was greater than or equal to 1.5 and less than or equal to 2.0. Categorization with high confidence (>80%) was achieved only for extreme MFRs (<1.0 or >2.5), with correct classification in only 15% of patients with an MFR of  $1.8 \pm 0.5$  (11). Our results showed better agreement when the analysis was performed by the same expert nuclear medicine physician. However, 20% of the patients were classified differently using the MFR threshold of 2 in our interuser analysis of 74 patients. Considering the results of invasive coronary angiography on a smaller scale, only 13% of patients were classified differently on a vessel-based analysis. This result is interesting because it counteracts the 20% variability that we observed in the MFR result. At this time, clinical interpretation should remain cautious for a SPECT global MFR of around 2, and even more for regional MFR.

In fact, MFR variability is higher in SPECT than in PET because many steps of the processing remain manual. SPECT MBF is a promising technique, but further work to improve its precision would enhance its potential clinical value, and there is a need for automation and standardization in the processing and software used. This remains difficult, partly because of the lower SPECT spatial resolution and the artifacts at the edge of the field of view, which make it more difficult for the software to automatically identify the location, size, and orientation of the heart. At this point, automated motion-correction software such as what was recently proposed for PET imaging (26) may reduce variability, as may improvements in image quality provided by more advanced reconstruction approaches (27,28).

Our study had a major limitation: we did not compare our results with MFR calculated in PET, which remains the gold standard. But, as mentioned before, several studies have shown similar quantification of MBF and MFR using dynamic CZT SPECT myocardial perfusion imaging with  $^{99m}\text{Tc}$ -sestamibi compared

with PET (4–7). Moreover, we focused only on a processing variation, with the same initial dynamic data. To our knowledge, this work represents the largest study focusing on the intra- and inter-user variability of dynamic SPECT, with clinical impact.

## CONCLUSION

The precision of sMBF analysis, measured as the SD of the difference in measured sMBF, was between 15% and 30% of the mean sMBF if the analysis was performed by the same nuclear medicine physician or by 2 different nuclear medicine physicians. On the other hand, the precision of MFR analysis was around 20% independently of the processing physician. MFR remained similar between different measurements, both in global left ventricular and in regional artery territories, whether the analysis was performed by the same physician or by 2 different physicians. Regarding the MFR threshold of 2, we noticed good agreement on patient classification when processing was by the same physician, whereas agreement was moderate if this was not the case. However, the limits of agreement seemed to be quite wide regarding the threshold of MFR. Though dynamic SPECT is promising, further work is mandatory to improve its precision and enhance its potential value before it can be widely applied to clinical use. The major key point is a need for automation and standardization in the processing and software used.

## DISCLOSURE

This study was supported by CHR d'Orleans. Matthieu Bailly and Gilles Metrard received honoraria and travel grants from GE Healthcare (from previous and other works). Denis Angoulvant received honoraria and travel grants from Astra Zeneca, MSD, Amgen, Servier, Sanofi, Bayer, BMS, Pfizer, Boehringer, Novartis, and Novo Nordisk (from previous and other works). No other potential conflict of interest relevant to this article was reported.

## ACKNOWLEDGMENTS

We thank the cardiologists and the technical and radiopharmaceutical staff of CHR of Orleans and CHRU of Tours. This study is part of the French network of university hospitals, HUGO (Hôpitaux Universitaires du Grand Ouest).

## KEY POINTS

**QUESTION:** How repeatable are MBF and MFR values measured during dynamic SPECT?

**PERTINENT FINDINGS:** In 124 patients who were twice processed, the precision of MFR analysis was around 20% independently of the processing physician; for sMBF, it was 15%–30% if the analysis was performed by the same physician or by 2 different physicians. Nevertheless, we noticed quite good agreement on patient classification.

**IMPLICATIONS FOR PATIENT CARE:** Clinical interpretation should remain cautious for a SPECT MFR of around 2. To improve the reliability of this promising technique, there is a need for automation and standardization in the processing and software used.

## REFERENCES

1. Camici PG, Rimoldi OE. The clinical value of myocardial blood flow measurement. *J Nucl Med.* 2009;50:1076–1087.

2. Valenta I, Dilsizian V, Quercioli A, Ruddy TD, Schindler TH. Quantitative PET/CT measures of myocardial flow reserve and atherosclerosis for cardiac risk assessment and predicting adverse patient outcomes. *Curr Cardiol Rep.* 2013;15:344.
3. Herzog BA, Husmann L, Valenta I, et al. Long-term prognostic value of  $^{13}\text{N}$ -ammonia myocardial perfusion positron emission tomography added value of coronary flow reserve. *J Am Coll Cardiol.* 2009;54:150–156.
4. Nkoulou R, Fuchs TA, Pazhenkottil AP, et al. Absolute myocardial blood flow and flow reserve assessed by gated SPECT with cadmium-zinc-telluride detectors using  $^{99\text{m}}\text{Tc}$ -tetrofosmin: head-to-head comparison with  $^{13}\text{N}$ -ammonia PET. *J Nucl Med.* 2016;57:1887–1892.
5. Agostini D, Roule V, Nganoa C, et al. First validation of myocardial flow reserve assessed by dynamic  $^{99\text{m}}\text{Tc}$ -sestamibi CZT-SPECT camera: head to head comparison with  $^{15}\text{O}$ -water PET and fractional flow reserve in patients with suspected coronary artery disease. The WATERDAY study. *Eur J Nucl Med Mol Imaging.* 2018;45:1079–1090.
6. Acampa W, Zampella E, Assante R, et al. Quantification of myocardial perfusion reserve by CZT-SPECT: a head to head comparison with  $^{82}\text{Rb}$  rubidium PET imaging. *J Nucl Cardiol.* 2021;28:2827–2839.
7. Giubbini R, Bertoli M, Durmo R, et al. Comparison between  $\text{N}^{13}\text{NH}_3$ -PET and  $^{99\text{m}}\text{Tc}$ -tetrofosmin-CZT SPECT in the evaluation of absolute myocardial blood flow and flow reserve. *J Nucl Cardiol.* 2021;28:1906–1918.
8. Zavadovsky KV, Mochula AV, Maltseva AN, et al. The current status of CZT SPECT myocardial blood flow and reserve assessment: tips and tricks. *J Nucl Cardiol.* April 30, 2021 [Epub ahead of print].
9. Bailly M, Ribeiro MJ, Angoulvant D. Combining flow and reserve measurement during myocardial perfusion imaging: a new era for myocardial perfusion scintigraphy? *Arch Cardiovasc Dis.* 2021;114:818–827.
10. Wells RG, Radonjic I, Clackdoyle D, et al. Test-retest precision of myocardial blood flow measurements with  $^{99\text{m}}\text{Tc}$ -tetrofosmin and solid-state detector single photon emission computed tomography. *Circ Cardiovasc Imaging.* 2020;13:e009769.
11. Renaud JM, Poitras-Riviere A, Hagio T, et al. Myocardial flow reserve estimation with contemporary CZT-SPECT and  $^{99\text{m}}\text{Tc}$ -tracers lacks precision for routine clinical application. *J Nucl Cardiol.* 2022;29:2078–2089.
12. Cichocki P, Blaszczyk M, Cygulska K, et al. Inter- and intraobserver repeatability of myocardial flow reserve values determined with SPECT study using a Discovery NM530c camera and Corridor 4DM software. *J Pers Med.* 2021;11:1164.
13. Bailly M, Thibault F, Courtehoux M, Metrard G, Angoulvant D, Ribeiro MJ. Myocardial flow reserve measurement during CZT-SPECT perfusion imaging for coronary artery disease screening: correlation with clinical findings and invasive coronary angiography—the CFR-OR study. *Front Med (Lausanne).* 2021;8:691893.
14. Leppo JA, Meerdink DJ. Comparison of the myocardial uptake of a technetium-labeled isonitrite analogue and thallium. *Circ Res.* 1989;65:632–639.
15. Bailly M, Thibault F, Courtehoux M, Metrard G, Ribeiro MJ. Impact of attenuation correction for CZT-SPECT measurement of myocardial blood flow. *J Nucl Cardiol.* 2021;28:2560–2568.
16. Mach F, Baigent C, Catapano AL, et al. 2019 ESC/EAS guidelines for the management of dyslipidaemias: lipid modification to reduce cardiovascular risk—the task force for the management of dyslipidaemias of the European Society of Cardiology (ESC) and European Atherosclerosis Society (EAS). *Eur Heart J.* 2020;41:111–188.
17. Ferenczi P, Couffinhal T, Mamou A, et al. Myocardial blood flows and reserves on solid state camera: correlations with coronary history and cardiovascular risk factors. *J Nucl Cardiol.* 2022;29:1671–1678.
18. Pang Z, Wang J, Li S, Chen Y, Wang X, Li J. Diagnostic analysis of new quantitative parameters of low-dose dynamic myocardial perfusion imaging with CZT SPECT in the detection of suspected or known coronary artery disease. *Int J Cardiovasc Imaging.* 2021;37:367–378.
19. Ziadi MC, Dekemp RA, Williams KA, et al. Impaired myocardial flow reserve on rubidium-82 positron emission tomography imaging predicts adverse outcomes in patients assessed for myocardial ischemia. *J Am Coll Cardiol.* 2011;58:740–748.
20. Kitkungvan D, Johnson NP, Roby AE, Patel MB, Kirkeeide R, Gould KL. Routine clinical quantitative rest stress myocardial perfusion for managing coronary artery disease: clinical relevance of test-retest variability. *JACC Cardiovasc Imaging.* 2017;10:565–577.
21. Wells RG, Marvin B, Poirier M, Renaud J, deKemp RA, Ruddy TD. Optimization of SPECT measurement of myocardial blood flow with corrections for attenuation, motion, and blood binding compared with PET. *J Nucl Med.* 2017;58:2013–2019.
22. Klein R, Hung GU, Wu TC, et al. Feasibility and operator variability of myocardial blood flow and reserve measurements with  $^{99\text{m}}\text{Tc}$ -sestamibi quantitative dynamic SPECT/CT imaging. *J Nucl Cardiol.* 2014;21:1075–1088.
23. Cho SG, Lee SJ, Na MH, Choi YY, Bom HH. Comparison of diagnostic accuracy of PET-derived myocardial blood flow parameters: a meta-analysis. *J Nucl Cardiol.* 2020;27:1955–1966.
24. Gupta A, Taqueti VR, van de Hoef TP, et al. Integrated noninvasive physiological assessment of coronary circulatory function and impact on cardiovascular mortality in patients with stable coronary artery disease. *Circulation.* 2017;136:2325–2336.
25. Lortie M, Beanlands RS, Yoshinaga K, Klein R, Dasilva JN, DeKemp RA. Quantification of myocardial blood flow with  $^{82}\text{Rb}$  dynamic PET imaging. *Eur J Nucl Med Mol Imaging.* 2007;34:1765–1774.
26. Lee BC, Moody JB, Poitras-Riviere A, et al. Automated dynamic motion correction using normalized gradient fields for  $^{82}\text{Rb}$  rubidium PET myocardial blood flow quantification. *J Nucl Cardiol.* 2020;27:1982–1998.
27. Shrestha U, Sciammarella M, Alhassen F, et al. Measurement of absolute myocardial blood flow in humans using dynamic cardiac SPECT and  $^{99\text{m}}\text{Tc}$ -tetrofosmin: method and validation. *J Nucl Cardiol.* 2017;24:268–277.
28. Shi L, Lu Y, Wu J, et al. Direct list mode parametric reconstruction for dynamic cardiac SPECT. *IEEE Trans Med Imaging.* 2020;39:119–128.

---

---

# Early-Phase $^{18}\text{F}$ -Florbetapir and $^{18}\text{F}$ -Flutemetamol Images as Proxies of Brain Metabolism in a Memory Clinic Setting

Cecilia Boccalini<sup>1–3</sup>, Débora Elisa Peretti<sup>1</sup>, Federica Ribaldi<sup>4,5</sup>, Max Scheffler<sup>6</sup>, Sara Stampacchia<sup>1</sup>, Szymon Tomczyk<sup>4</sup>, Cristelle Rodriguez<sup>7,8</sup>, Marie-Louise Montandon<sup>8,9</sup>, Sven Haller<sup>10–13</sup>, Panteleimon Giannakopoulos<sup>7,8</sup>, Giovanni B. Frisoni<sup>4,5</sup>, Daniela Perani<sup>2,3,14</sup>, and Valentina Garibotto<sup>1,15,16</sup>

<sup>1</sup>Laboratory of Neuroimaging and Innovative Molecular Tracers (NIMTlab), Geneva University Neurocenter and Faculty of Medicine, University of Geneva, Geneva, Switzerland; <sup>2</sup>Vita-Salute San Raffaele University, Milan, Italy; <sup>3</sup>In Vivo Human Molecular and Structural Neuroimaging Unit, Division of Neuroscience, IRCCS San Raffaele Scientific Institute, Milan, Italy; <sup>4</sup>Laboratory of Neuroimaging of Aging (LANVIE), University of Geneva, Geneva, Switzerland; <sup>5</sup>Memory Clinic, Geneva University Hospitals, Geneva, Switzerland; <sup>6</sup>Division of Radiology, Diagnostic Department, Geneva University Hospitals, Geneva, Switzerland; <sup>7</sup>Division of Institutional Measures, Medical Direction, University Hospitals of Geneva, Geneva, Switzerland; <sup>8</sup>Department of Psychiatry, Faculty of Medicine, University of Geneva, Geneva, Switzerland; <sup>9</sup>Department of Rehabilitation and Geriatrics, Geneva University Hospitals and University of Geneva, Geneva, Switzerland; <sup>10</sup>CIMC–Centre d’Imagerie Médicale de Cornavin, Geneva, Switzerland; <sup>11</sup>Faculty of Medicine of University of Geneva, Geneva, Switzerland; <sup>12</sup>Division of Radiology, Department of Surgical Sciences, Uppsala University, Uppsala, Sweden; <sup>13</sup>Department of Radiology, Beijing Tiantan Hospital, Capital Medical University, Beijing, China; <sup>14</sup>Nuclear Medicine Unit, San Raffaele Hospital, Milan, Italy; <sup>15</sup>Division of Nuclear Medicine and Molecular Imaging, Geneva University Hospitals, Geneva, Switzerland; and <sup>16</sup>CIBM Center for Biomedical Imaging, Geneva, Switzerland

Alzheimer disease (AD) neuropathologic changes are  $\beta$ -amyloid ( $\text{A}\beta$ ) deposition, pathologic tau, and neurodegeneration. Dual-phase amyloid PET might be able to evaluate  $\text{A}\beta$  deposition and neurodegeneration with a single tracer injection. Early-phase amyloid PET scans provide a proxy for cerebral perfusion, which has shown good correlations with neural dysfunction measured through metabolic consumption, whereas the late frames depict amyloid distribution. Our study aimed to assess the comparability between early-phase amyloid PET scans and  $^{18}\text{F}$ -FDG PET brain topography at the individual level and their ability to discriminate patients. **Methods:** One hundred sixty-six subjects evaluated at the Geneva Memory Center, ranging from no cognitive impairment to mild cognitive impairment and dementia, underwent early-phase amyloid PET—using either  $^{18}\text{F}$ -florbetapir (eFBP) ( $n = 94$ ) or  $^{18}\text{F}$ -flutemetamol (eFMM) ( $n = 72$ )—and  $^{18}\text{F}$ -FDG PET.  $\text{A}\beta$  status was assessed. SUV ratios (SUVr) were extracted to evaluate the correlation of eFBP/eFMM and their respective  $^{18}\text{F}$ -FDG PET scans. The single-subject procedure was applied to investigate hypometabolism and hypoperfusion maps and their spatial overlap by the Dice coefficient. Receiver-operating-characteristic analyses were performed to compare the discriminative power of eFBP/eFMM and  $^{18}\text{F}$ -FDG PET SUVr in AD-related meta-regions of interest between  $\text{A}\beta$ -negative healthy controls and cases in the AD continuum. **Results:** Positive correlations were found between eFBP/eFMM and  $^{18}\text{F}$ -FDG PET SUVr independently of  $\text{A}\beta$  status and  $\text{A}\beta$  radiotracer ( $R > 0.72$ ,  $P < 0.001$ ). eFBP/eFMM single-subject analysis revealed clusters of significant hypoperfusion with good correspondence to hypometabolism topographies, independently of the underlying neurodegenerative patterns. Both eFBP/eFMM and  $^{18}\text{F}$ -FDG PET SUVr significantly discriminated AD patients from controls in the AD-related meta-regions of interest (eFBP area under the curve [AUC], 0.888; eFMM AUC, 0.801), with  $^{18}\text{F}$ -FDG PET performing slightly better, although not significantly (all  $P$  values higher than 0.05), than others ( $^{18}\text{F}$ -FDG AUC,

0.915 and 0.832 for subjects evaluated with eFBP and eFMM, respectively). **Conclusion:** The distribution of perfusion was comparable to that of metabolism at the single-subject level by parametric analysis, particularly in the presence of a high neurodegeneration burden. Our findings indicate that eFBP and eFMM imaging can replace  $^{18}\text{F}$ -FDG PET imaging, as they reveal typical neurodegenerative patterns or allow exclusion of the presence of neurodegeneration. The findings show cost-saving capacities of amyloid PET and support routine use of the modality for individual classification in clinical practice.

**Key Words:** neurodegeneration; early-phase amyloid PET;  $^{18}\text{F}$ -FDG PET; individual maps

**J Nucl Med 2023; 64:266–273**

DOI: 10.2967/jnumed.122.264256

**P**ET can provide in vivo evaluation of protein deposition and neuronal injury ( $I$ ), playing a leading role in the diagnosis of Alzheimer disease (AD) and other dementia conditions. Brain  $^{18}\text{F}$ -FDG PET is a well-established tool for investigating neurodegeneration, through the detection of changes in cerebral glucose metabolism. Regional analysis of the  $^{18}\text{F}$ -FDG PET signal can reveal specific brain hypometabolism patterns highly indicative of neurodegeneration along the AD, frontotemporal dementia, and Lewy body spectrum, including subjects from the preclinical phases to clinically overt dementia (2). In longitudinal studies, the absence of disease-specific hypometabolism patterns was a strong predictor of preserved cognition (3–5).

Amyloid PET imaging, initially with  $^{11}\text{C}$ -labeled Pittsburgh compound B and now also with 3  $^{18}\text{F}$ -labeled compounds, namely  $^{18}\text{F}$ -florbetapir,  $^{18}\text{F}$ -florbetaben, and  $^{18}\text{F}$ -flutemetamol, allows the assessment of  $\beta$ -amyloid ( $\text{A}\beta$ ) plaque burden in vivo ( $I$ ). A dual-phase amyloid PET protocol of acquisition has been proposed, adding to the reference late acquisition an acquisition of the tracer distribution immediately after injection (6). These early-phase images can

---

Received Apr. 8, 2022; revision accepted Jul. 15, 2022.  
For correspondence or reprints, contact Cecilia Boccalini (cecilia.boccalini@unige.ch).  
Published online Jul. 21, 2022.  
COPYRIGHT © 2023 by the Society of Nuclear Medicine and Molecular Imaging.

provide a proxy for cerebral perfusion because of the high lipophilicity of the tracers (6,7). In turn, cerebral perfusion is strongly related to neural dysfunction as measured through metabolic consumption (8,9). In AD, the early-phase acquisition of amyloid PET has shown a good correlation to  $^{18}\text{F}$ -FDG PET uptake at the group level, suggesting its potential use as a biomarker of neuronal dysfunction (10–21).

Despite multiple descriptions in the literature of dual-phase amyloid PET, the use of early-phase images in clinical and research settings is not yet widely implemented. Our study explored the utility of early-phase images of amyloid PET scans, using either  $^{18}\text{F}$ -florbetapir or  $^{18}\text{F}$ -flutemetamol, for individual classification and their comparability with the respective  $^{18}\text{F}$ -FDG PET brain hypometabolic voxel-wise maps in a memory clinic cohort.

## MATERIALS AND METHODS

### Participants

The study included subjects assessed at the Geneva University Hospitals, ranging from cognitively unimpaired (CU) to mild cognitive impairment (MCI) and dementia, in 2 ongoing studies as described previously (22–26). The local ethics committee approved the different imaging studies, which were conducted under the principles of the Declaration of Helsinki and the International Conference on Harmonization good clinical practice. The requirement to obtain informed consent was waived.

We included a total of 166 subjects classified as  $\text{A}\beta$ -negative ( $\text{A}\beta^-$ ) CU ( $n = 42$ ),  $\text{A}\beta$ -positive ( $\text{A}\beta^+$ ) CU ( $n = 30$ ), MCI ( $n = 73$ ) (27), and dementia ( $n = 21$ ) (28) subjects, following standardized criteria for clinical staging. Specifically, the  $\text{A}\beta^-$  CU group, including healthy volunteers and individuals with subjective cognitive decline (29), all with  $^{18}\text{F}$ -FDG PET-negative scans, was used as a healthy control (HC) reference for comparisons. The  $\text{A}\beta^+$  CU group was considered a group of interest, given the higher risk of progression in this population (30). Inclusion criteria were at least one 3-dimensional T1-weighted MRI scan, dual-phase amyloid PET using either  $^{18}\text{F}$ -florbetapir or  $^{18}\text{F}$ -flutemetamol, an  $^{18}\text{F}$ -FDG PET scan, and an interval of less than 1 year between imaging measures.

### MRI Acquisition

MRI was performed at Geneva University Hospitals' Division of Radiology using a 3-T scanner (Magnetom Skyra; Siemens Healthineers) equipped with a 20- or 64-channel head coil. The supplemental materials, section 1, detail the acquisition parameters (supplemental materials are available at <http://jnm.snmjournals.org>). The lesion prediction algorithm (31), implemented in the lesion segmentation toolbox, was used to segment fluid-attenuated inversion recovery images, allowing us to extract the total lesion volume. White matter lesions were also quantified visually according to the age-related white matter change scale (32).

### PET Acquisition

$^{18}\text{F}$ -FDG PET and amyloid PET were performed at the Division of Nuclear Medicine and Molecular Imaging at Geneva University Hospitals using a Biograph 128 mCT, Biograph 128 Vision 600 Edge, Biograph 40 mCT, or Biograph 64 TruePoint PET scanner (Siemens Medical Solutions). All scanners were comparable.  $^{18}\text{F}$ -FDG PET was performed according to the European Association of Nuclear Medicine guidelines (33,34). Amyloid PET images were acquired using  $^{18}\text{F}$ -florbetapir (FBP) ( $n = 94$ ) or  $^{18}\text{F}$ -flutemetamol (FMM) ( $n = 72$ ). Amyloid status ( $\text{A}\beta^+/\text{A}\beta^-$ ) was determined for each late image by an expert in nuclear medicine, applying the standard operating procedures approved by the European Medicines Agency.

Regarding the early phase of amyloid PET (eFBP and eFMM), the image acquisition was started immediately after tracer injection, and

a static image was acquired for 5 min (eFBP) or 10 min (eFMM) (20,35).

The supplemental materials, section 2, provide full details on the PET acquisition.

### MRI and PET Normalization Processing

Processing was performed as previously described (25) using Statistical Parametric Mapping (SPM 12; Wellcome Trust Centre for Neuroimaging), running in MATLAB R2018b, version 9.5 (MathWorks Inc.). All details are reported in the supplemental materials, section 3.

### SUV Ratio (SUVR) Extraction in Automated Anatomic Labeling (AAL) ROIs and AD Meta-Region of Interest (Meta-ROI)

Uptake values were extracted within regions from AAL atlas 3 (36) and key regions sensitive to AD according to a predefined meta-ROI approach (37). SUVRs were calculated by normalizing the uptake to the mean value of the pons and cerebellar vermis together as the reference region. Intensity-normalized PET images were saved for further voxelwise analyses.

### Single-Subject Voxel-wise Analyses

According to a validated SPM single-subject procedure (38), each PET image was tested for relative hypometabolism/hypoperfusion by means of a 2-sample  $t$  test in comparison with PET images of controls. HC groups included 28 and 14 subjects with  $\text{A}\beta^-$  and  $^{18}\text{F}$ -FDG PET-negative scans, for eFBP and eFMM samples, respectively. We used the same HC subjects also for the  $^{18}\text{F}$ -FDG PET analyses. The statistical threshold for the resulting hypometabolic and hypoperfusion SPM maps was set at a  $P$  value of 0.05, uncorrected for multiple comparisons, considering significant clusters containing more than 100 voxels. SPM maps were then binarized for further Dice analyses. The resulting single-subject SPM hypometabolic maps were visually inspected by nuclear medicine experts blinded to clinical diagnoses and classified into hypometabolism patterns suggestive of neurodegenerative conditions (3,39–41) or excluding the presence of neurodegeneration. Hypometabolic and hypoperfusion maps were visually inspected at the single-subject level to define the visual match between maps. The same assessment was applied also to  $^{18}\text{F}$ -FDG PET and eFBP/eFMM uptake distribution images.

### Statistical Analysis

Dice coefficients were calculated, using FSL software (42), to quantify the whole-brain spatial overlap between hypometabolic and hypoperfusion binary maps at the single-subject level (supplemental materials, section 4) (43). Moreover, we calculated  $\Delta$  scores between the hypometabolic and hypoperfusion maps' extents (number of voxels) to quantify discrepancies between the 2 patterns.

General linear models were performed to assess the correlation between eFBP/eFMM SUVR in the AAL ROIs and their respective  $^{18}\text{F}$ -FDG SUVR in the whole sample. We assessed the correlations also in  $\text{A}\beta^+$  and  $\text{A}\beta^-$  subjects separately. We tested the correlation of eFBP, eFMM, and  $^{18}\text{F}$ -FDG SUVR in the AD composite meta-ROI with Mini-Mental State Examination scores.

Finally, we identified patients in the AD continuum, including specifically MCI and AD dementia cases according to the  $\text{A}\beta^+$  status and AD-like hypometabolism patterns. We performed receiver-operating-characteristic (ROC) analyses to compare the discriminative power of eFBP, eFMM, and  $^{18}\text{F}$ -FDG meta-ROI SUVRs between HC and AD patients. The resulting areas under the curve (AUCs) from different tracers were compared using a De Long test (44) for 2 correlated ROC curves, setting the threshold for significance at a  $P$  value of 0.05. All statistical analyses were performed with R, version 4.0.2 (R Foundation for statistical computing, <https://www.r-project.org/>).

**TABLE 1**  
Demographic Characteristics of Subjects

Characteristic	Whole sample	FBP group	FMM group	<i>P</i> *
<i>n</i>	166	94	72	
Age	73.18 ± 6.35	74.27 ± 5.548	71.76 ± 7.068	0.012
Sex				0.425
Female	98	58	40	
Male	68	36	32	
MMSE	25.92 ± 4.00	26.12 ± 3.857	25.66 ± 4.202	0.471
Aβ status				0.980
Negative	70	39	31	
Positive	93	52	41	
Clinical groups according to Aβ status				
Aβ+ AD dementia	18	13	5	
Aβ- dementia	3	2	1	
Aβ+ MCI	52	31	22	
Aβ- MCI	21	9	11	
Aβ+ CU	30	11	19	
Aβ- CU (HC)	42	28	14	

\*From *t* test comparing data from eFBP and eFMM subgroups.

MMSE = Mini-Mental State Examination; FBP = florbetapir; FMM = flutemetamol; *n* = number; Aβ- = amyloid negative; Aβ+ = amyloid positive; AD = Alzheimer disease; MCI = mild cognitive impairment; CU = cognitively unimpaired; HC = healthy controls. Qualitative data are number; continuous data are mean ± SD.

## RESULTS

Demographic and clinical data for our cohort are displayed in Table 1. The average intervals between amyloid PET and <sup>18</sup>F-FDG PET, between MRI and <sup>18</sup>F-FDG PET, and between MRI and amyloid PET were 2.15 months (SD, 3.06), 1.89 months (SD, 4.15), and 2.76 months (SD, 3.40), respectively.

### Correlations Between eFBP/eFMM and <sup>18</sup>F-FDG SUVR

Both eFBP and eFMM SUVR in the AAL ROIs presented a strong correlation with <sup>18</sup>F-FDG SUVR in the whole group (eFBP *r* = 0.786, *P* < 0.001; eFMM *r* = 0.806, *P* < 0.001). Good correlations between eFBP/eFMM and <sup>18</sup>F-FDG SUVR were also found separately in Aβ+ (eFBP *r* = 0.843, *P* < 0.001; eFMM *r* = 0.827, *P* < 0.001) and Aβ- (eFBP *r* = 0.72, *P* < 0.001; eFMM *r* = 0.791, *P* < 0.001) subjects. Figure 1 shows scatterplots for the whole sample and subgroups according to Aβ status.

The composite meta-ROI SUVRs for eFBP/eFMM uptake and those for <sup>18</sup>F-FDG uptake correlated significantly with Mini-Mental State Examination scores (<sup>18</sup>F-FDG *r* = 0.536, *P* < 0.001; eFBP *r* = 0.413, *P* < 0.001; eFMM *r* = 0.482, *P* < 0.001).

### Single-Subject eFBP/eFMM and <sup>18</sup>F-FDG Patterns

The SPM single-subject analysis revealed disease-specific hypometabolism and hypoperfusion maps (Fig. 2; Tables 2 and 3). The supplemental materials, section 5, and Supplemental Tables 1–3

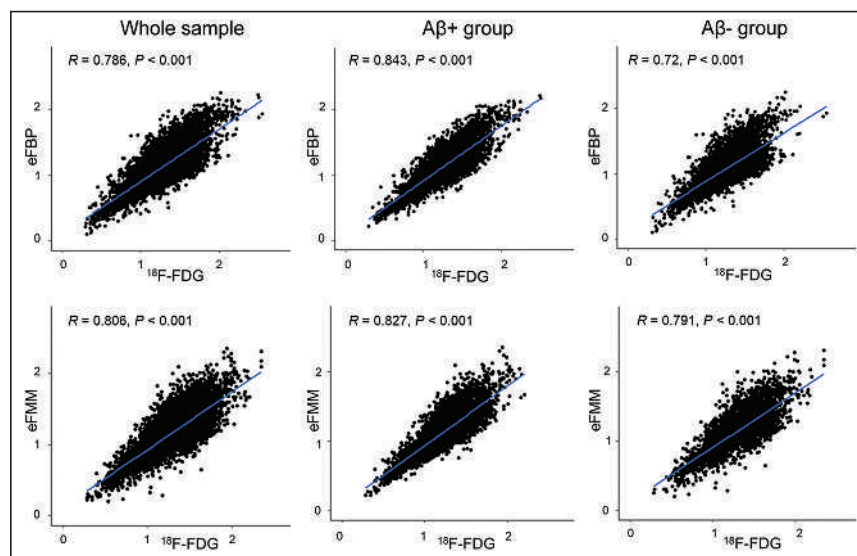


**FIGURE 1.** Correlation between eFBP/eFMM and <sup>18</sup>F-FDG PET SUVR. Scatterplots showing association between eFBP/eFMM SUVR (*y*-axis) in AAL regions and their respective <sup>18</sup>F-FDG SUVR (*x*-axis). Results are presented for whole sample and separately for subgroups divided according to Aβ status. Lines resulting from linear regression are shown in blue. *R* and *P* values are given in the upper left corner. FBP = florbetapir; FMM = flutemetamol; eFBP = early FBP; eFMM = early FMM; Aβ- = amyloid negative; Aβ+ = amyloid positive.



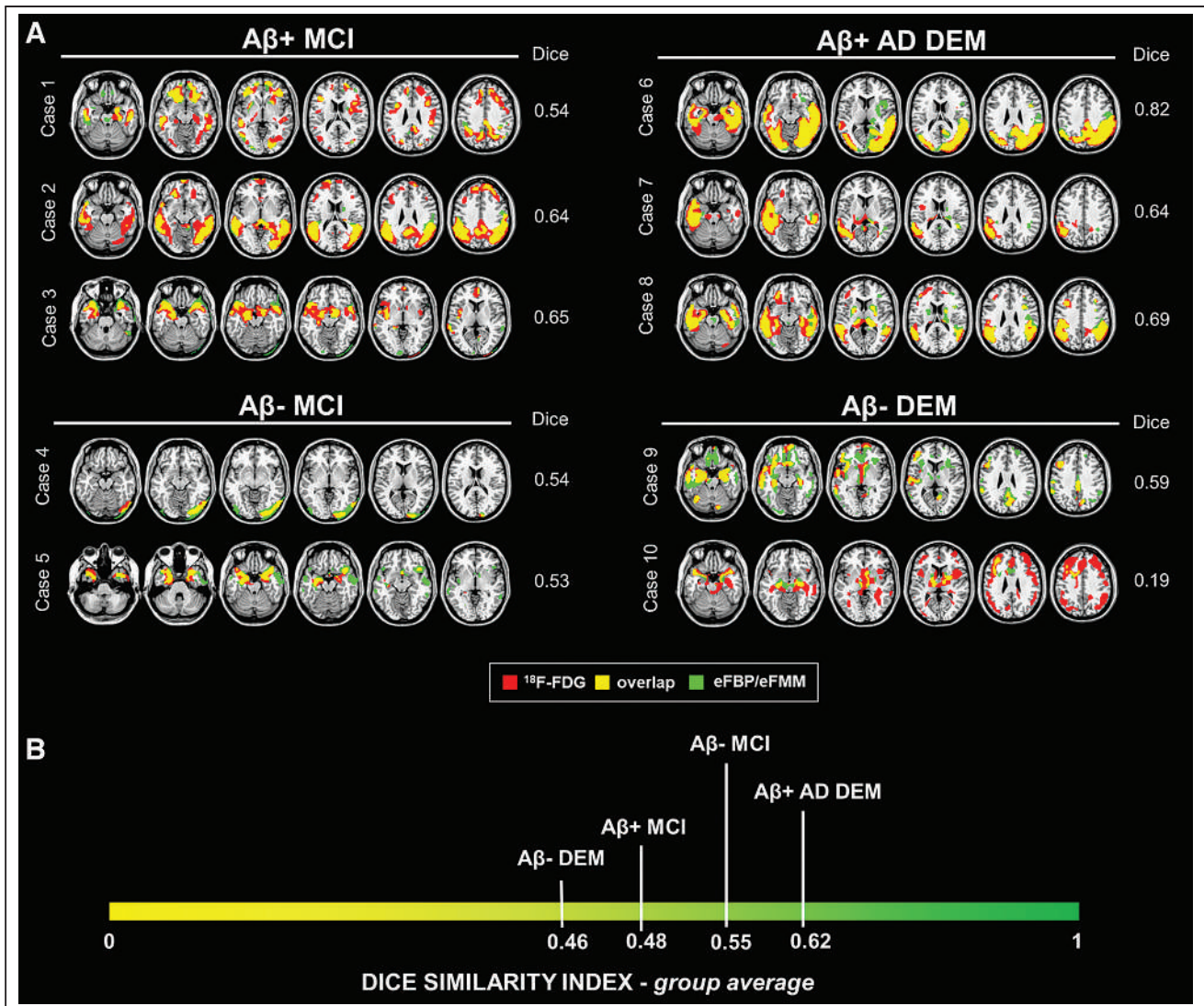


**FIGURE 2.** Hypometabolic and hypoperfusion patterns at the single-subject level. (A) Patterns of <sup>18</sup>F-FDG PET hypometabolism and eFBP/eFMM hypoperfusion in single individuals. Hypometabolism maps, hypoperfusion maps, and their overlap were imposed on standard Montreal Neurological Institute template. These maps were obtained from binarization of single-subject <sup>18</sup>F-FDG PET SPM T-maps and eFBP/eFMM SPM T-maps ( $P < 0.05$  uncorrected,  $k > 100$ ). The Dice similarity index is reported to the right of the brain template of each subject. (B) Clinical groups ordered according to degree of similarity between brain hypometabolism and hypoperfusion, as measured by Dice similarity index average. Lower-to-higher values of Dice indicate increasing degree of overlap. DEM = dementia; eFBP = early florbetapir; eFMM = early flutemetamol; Aβ+ = amyloid positive; Aβ- = amyloid negative; AD = Alzheimer disease; MCI = mild cognitive impairment.

**TABLE 2**  
Contingency Table Reporting Frequency of Different Hypometabolism and Hypoperfusion Patterns in Whole Sample

Hypometabolism pattern	Hypoperfusion pattern					Normal	Total
	AD-like	FTD-like	DLB-like	Limbic-like	Unclassified		
AD-like	30	1	0	4	2	2	39
FTD-like	0	9	0	1	0	0	10
DLB-like	0	0	3	0	0	0	3
Limbic-like	0	0	0	14	0	0	14
Unclassified	0	0	0	1	24	1	26
Normal	2	0	0	0	1	29	32
Total	32	11	2	19	28	32	124

AD = Alzheimer disease; FTD = frontotemporal dementia; DLB = dementia with Lewy bodies.

**TABLE 3**  
Distribution of Hypometabolism Patterns and Their Voxel-by-Voxel Concordance with Hypoperfusion Maps in Clinical Groups

<sup>18</sup> F-FDG hypometabolism pattern	Dementia			MCI			CU			Whole group		
	Sample (n = 21)	Dice*	% visual match	Sample (n = 73)	Dice*	% visual match	Sample (n = 30)	Dice*	% visual match	Sample (n = 124)	Dice	% visual match
AD-like	10 (all Aβ+)	0.632 ± 0.159	90	25 (all Aβ+)	0.459 ± 0.178	68	4 (all Aβ+)	0.611 ± 0.135	100	39 (all Aβ+)	0.516 ± 0.185	77
FTD-like	5 (3 Aβ+, 2 Aβ-)	0.483 ± 0.201	80	5 (3 Aβ+, 2 Aβ-)	0.531 ± 0.128	100	0		100	10 (6 Aβ+, 4 Aβ-)	0.507 ± 0.161	90
DLB-like	0			3 (2 Aβ+, 1 Aβ-)	0.467 ± 0.236	100	0		100	3 (2 Aβ+, 1 Aβ-)	0.467 ± 0.236	100
Limbic-like	0			13 (9 Aβ+, 4 Aβ-)	0.504 ± 0.078	100	1 (all Aβ+)	0.521	100	14 (10 Aβ+, 4 Aβ-)	0.504 ± 0.075	100
Unclassified	6 (5 Aβ+, 1 Aβ-)	0.621 ± 0.071	83	13 (8 Aβ+, 5 Aβ-)	0.498 ± 0.205	100	7 (all Aβ+)	0.381 ± 0.293	86	26 (20 Aβ+, 6 Aβ-)	0.499 ± 0.217	92
Normal	0			14 (6 Aβ+, 8 Aβ-)		86†	18 (all Aβ+)		94†	32 (24 Aβ+, 8 Aβ-)		90†

\*Average ± SD.

†Percentage of patients consistently negative on <sup>18</sup>F-FDG and early-phase scans.

FTD = frontotemporal dementia; DLB = dementia with Lewy bodies; MCI = mild cognitive impairment; CU = cognitively unimpaired; AD = Alzheimer disease.

present the results of visual analyses for the uptake distribution images. The visual rating of SPM maps allowed identification of 4 neurodegenerative patterns: temporoparietal hypometabolism (AD-like pattern,  $n = 39$ ), temporoparietal and occipital hypometabolism (Lewy body (DLB)-like pattern,  $n = 3$ ), frontotemporal hypometabolism (FTD-like pattern,  $n = 10$ ), and limbic-like or medial-temporal pattern ( $n = 14$ ). Thirty-two of 124 subjects showed negative <sup>18</sup>F-FDG scans for neurodegenerative patterns. Some subjects revealed severe atrophy on T1-weighted MRI and unclassifiable SPM patterns for neurodegenerative disease ( $n = 26$ ). Despite this heterogeneity, for 86% of subjects the patterns identified by <sup>18</sup>F-FDG PET were consistently found in early-phase maps at visual assessment. The frequency of the different hypometabolism and hypoperfusion patterns classified on the basis of SPM map interpretation is reported in Table 2. Table 3 shows the frequency of hypometabolism patterns and their spatial overlaps with hypoperfusion maps as measured by Dice and visual assessment, in the whole sample and separately in the 3 clinical subgroups (CU, MCI, and dementia). The hypometabolic/hypoperfusion maps resulting in the 3 clinical subgroups are fully detailed in the supplemental materials.

Only 16 of 124 subjects (13%) showed a mismatch between <sup>18</sup>F-FDG and eFBP/eFMM scans. When we compared MRI total lesion volume and age-related white matter change scale scores between the matched and mismatched subgroups, we found a more severe cerebrovascular pathology in cases with mismatch than in matched cases (Mann-Whitney  $U = 384$ ,  $P = 0.021$ , for total lesion volume; Mann-Whitney  $U = 431$ ,  $P = 0.041$ , for age-related white matter change scale).

When we calculated  $\Delta$  scores to explore discrepancies between the eFBP/eFMM and <sup>18</sup>F-FDG PET maps, the main difference was in the extent of the abnormalities. Sixty-five of 92 subjects showed positive  $\Delta$  scores indicating that the hypometabolism patterns were more extended than the hypoperfusion ones ( $\Delta$  scores,  $13,012 \pm 12,996$  voxels), regardless of the clinical category. Only 27 of 92 subjects presented negative  $\Delta$  scores, indicating hypoperfusion patterns slightly more extended than the hypometabolic ones ( $\Delta$  scores,  $-6,606 \pm 6,943$  voxels).

#### Discriminative Performance of AD Meta-ROI Approach

When testing the performance of the eFBP/eFMM SUVR in the AD composite meta-ROI in distinguishing AD patients from HC subjects, we found good AUC discriminative values (eFBP AUC, 0.888, eFMM AUC, 0.801), like those of the <sup>18</sup>F-FDG SUVR (<sup>18</sup>F-FDG AUC, 0.915 and 0.832, respectively). The DeLong test confirmed no significant differences in the discriminatory performance of different tracers (<sup>18</sup>F-FDG vs. eFBP  $P = 0.396$ ; <sup>18</sup>F-FDG vs. eFMM  $P = 0.665$ ). Figure 3 compares the diagnostic performance of <sup>18</sup>F-FDG PET SUVR and eFBP/eFMM SUVR in the AD composite meta-ROI in terms of ROC curves for the whole AD-continuum group.

As for the other AD-related meta-ROIs (37), none presented significant differences in the discriminatory power of <sup>18</sup>F-FDG PET and eFBP/eFMM SUVR between AD patients and HC subjects (Supplemental Table 4).

#### DISCUSSION

This study compared early-phase amyloid PET with <sup>18</sup>F-FDG PET patterns and the power to discriminate subjects in the AD continuum and subjects with other neurodegenerative conditions from HC. The correlation between cerebral perfusion and metabolism

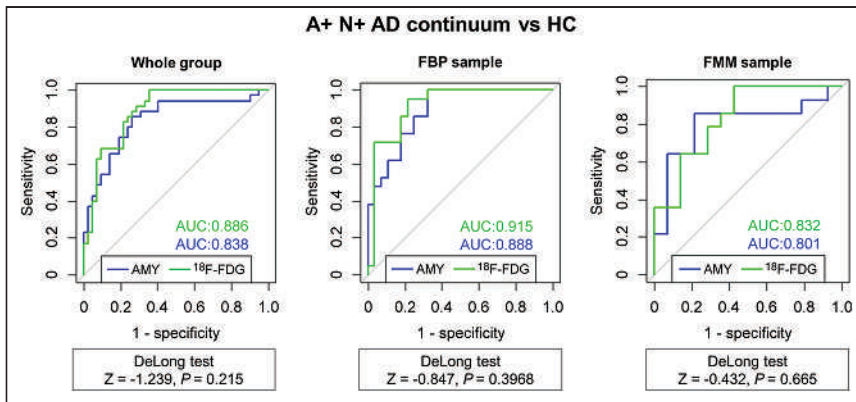


**FIGURE 3.** Discriminative performance of eFBP/eFMM and  $^{18}\text{F}$ -FDG PET SUVR. ROC curves showing diagnostic performance of  $^{18}\text{F}$ -FDG PET and eFBP/eFMM SUVR in AD composite meta-ROI for distinguishing AD patients from HC. AUCs for eFBP/eFMM and  $^{18}\text{F}$ -FDG PET are shown in blue and green, respectively. Results of De Long test comparing 2 AUCs (eFBP/eFMM vs.  $^{18}\text{F}$ -FDG PET) are given in bottom box. A+ = A $\beta$ -positive; N+ = neurodegeneration-positive; AUC = area under the curve; FBP = florbetapir; FMM = flutemetamol; AD = Alzheimer disease; HC = healthy controls.

has long been established in aging and dementia conditions based on neurovascular coupling (8). At the same time, early-acquisition images of amyloid PET have been proposed as a topographic or functional biomarker reflecting cerebral perfusion (6).

Dual-phase amyloid PET may thus offer the advantage of—in a single procedure—acquiring information about amyloidosis and brain perfusion deficits reflecting neurodegeneration (6). Published work has focused on the relationship between brain perfusion and metabolism at a group level, but to our knowledge no studies have yet evaluated whether early-phase images might replace  $^{18}\text{F}$ -FDG PET images in single individuals. This study evaluated brain hypoperfusion at the single-subject level and its comparability to respective brain hypometabolism, demonstrating a good correlation and a similar capacity in distinguishing patients from controls. In the presence of neurodegeneration assessed by  $^{18}\text{F}$ -FDG PET, eFBP/eFMM single-subject analysis showed clusters of significant hypoperfusion, compared with controls, with good correspondence to the brain hypometabolism topography. The spatial overlap showed independence from underlying neurodegeneration topography, but with a more clear-cut correspondence in the dementia stages (Fig. 2).

In line with previous studies (10–18), our study confirmed strong positive correlations between eFBP/eFMM and  $^{18}\text{F}$ -FDG SUVR ( $R > 0.72$ ,  $P < 0.001$ ) in a memory clinic cohort (Fig. 1). The correlation was independent of the used A $\beta$  radiotracers and A $\beta$  status, in agreement with other studies (10,11,13,15). Further supporting the comparability between the eFBP/eFMM and  $^{18}\text{F}$ -FDG PET images, we found that lower Mini-Mental State Examination scores correlated significantly with decreases in both perfusion and metabolism measures (10,12,13,16).

When we applied the SPM single-subject analysis on eFBP/eFMM images, clusters of significant hypoperfusion were present in patients compared with controls, with good correspondence to the hypometabolism maps (Fig. 2; Table 2). As for negative scans, characterizing mostly the CU and MCI subgroups, the perfusion maps' ability was comparable to that of metabolism maps in excluding the presence of neurodegeneration for 90% of the negative scans. In the sample of CU subjects, we found 60%  $^{18}\text{F}$ -FDG PET-negative scans, and for 94% of these, eFBP/eFMM images agreed on ruling out neurodegenerative patterns.

In MCI, eFBP/eFMM maps were able to identify patterns specific to neurodegenerative conditions for most cases, showing a moderate-to-good degree of overlap with hypometabolism patterns (Table 3). In most cases, hypometabolism SPM maps showed a greater extent than the hypoperfusion ones, although the disease-specific hallmark was detectable in both (Fig. 2). The lack of a full overlap here between perfusion and metabolism maps is likely because they measure different brain biological processes (8,17). Other reasonable explanations are the noisy feature of the initial frames and the nonuniform delivery of the tracer (13). However, although the early-phase image may be noisier, the similarity between the patterns is also striking in MCI conditions, supporting its use (Fig. 2). A negative  $^{18}\text{F}$ -FDG PET scan in MCI was confirmed in 86% of eFBP/eFMM images. This is compatible with the absence of neurodegeneration in MCI, followed by a stable condition at follow-up (45,46).

In dementia conditions, the high comparability of hypoperfusion and hypometabolism maps suggests an increase in concordance with the advance of disease stages (Fig. 2B). Since hypoperfusion usually showed less extension than hypometabolism maps, a more severe underlying neurodegeneration may be necessary to reveal specific patterns that are instead detectable with  $^{18}\text{F}$ -FDG PET. This finding suggests that  $^{18}\text{F}$ -FDG PET might be more suitable for preclinical and prodromal stages. Further studies are needed to specifically address preclinical phases, such as subjective cognitive decline, based on larger samples and follow-up data.

We found only 13% of subjects with a mismatch between hypometabolism and hypoperfusion maps in the whole sample, mostly in the CU and MCI groups. In these cases, the eFBP/eFMM images were less sensitive in detecting the underlying neurodegeneration than  $^{18}\text{F}$ -FDG PET. The risk of having false-negative findings with early-phase imaging warrants an additional  $^{18}\text{F}$ -FDG PET exam when clinical suspicion of neurodegenerative conditions is high. The group of mismatch cases showed greater cerebrovascular lesion volumes on MRI than the match group. This result is consistent with the fact that both  $^{18}\text{F}$ -FDG PET and eFBP/eFMM images can suffer from biases in the presence of severe atrophy or cerebral vascular disease (8). Thus, this limitation needs to be considered in the application and interpretation of SPM analysis both with  $^{18}\text{F}$ -FDG PET and with early-phase imaging.

Finally, we found good diagnostic performance for the meta-ROI approach using perfusion measures (Fig. 3). Both eFBP and eFMM SUVR in the AD composite meta-ROI significantly discriminated AD patients from HC subjects. At ROC analyses,  $^{18}\text{F}$ -FDG SUVR was slightly superior to perfusion measures in discriminating these subjects from controls, but without reaching the significance threshold for differences ( $P > 0.05$ ) (Fig. 3).

As a limitation of our study, we acquired the early-phase images using published protocols (20); however, different early time frames for eFBP have also been proposed in the literature to achieve the best association with  $^{18}\text{F}$ -FDG PET (16,18). We are aware of the relatively limited sample size of HC subjects included for comparisons; further studies will help to confirm the findings.

An appropriate normalization procedure and HC dataset are mandatory to achieve good performances in voxel-wise analyses, and methods for early-phase images are, in this respect, less mature than for  $^{18}\text{F}$ -FDG PET (47).

## CONCLUSION

To our knowledge, this was the first study to evaluate, at the single-subject level by applying voxel-based analysis, the classification performance of early-phase amyloid PET images. eFBP and eFMM imaging is able to identify different and typical neurodegenerative patterns or to exclude the presence of neurodegeneration. Dual-phase amyloid PET permits assessment of neurodegeneration and A $\beta$  pathology with a single tracer injection and should be systematically implemented in routine clinical practice. In our opinion, when there is discrepancy between clinical and imaging results, mainly in the early phase of the disease, an additional  $^{18}\text{F}$ -FDG PET exam is recommended.

## DISCLOSURE

PET scans were performed within research projects funded by the Swiss National Science Foundation (SNSF, projects 320030\_169876, 320030\_185028, and 320030\_182772), Horizon 2020 (project 667375), Human Brain Project, and the EU-EFPIA Innovative Medicines Initiatives 2 Joint Undertaking (IMI 2 JU; grants 115952 and 115736). This project was funded in part by grants from the Swiss National Science Foundation (SNF 3200B0-1161193 and SPUM 33CM30-124111) and an unrestricted grant from the Association pour la Recherche sur l'Alzheimer, Geneva, Switzerland. The Centre de la mémoire at Geneva University Hospital, collecting data with contributions from the Clinical Research Center (University Hospital and Faculty of Medicine, Geneva), is funded by private donors: Association Suisse pour la Recherche sur l'Alzheimer, Genève; Fondation Segré, Genève; Fondazione Agusta, Lugano; Race Against Dementia Foundation, London, UK; Fondation Child Care, Genève; Fondation Edmond J. Safra, Genève; Fondation Minkoff, Genève; McCall Macbain Foundation, Canada; Nicole et Renè Keller, Genève; Fondation AETAS, Genève; VELUX Foundation. Cecilia Boccalini was supported by an IBRO Exchange Fellowship. No other potential conflict of interest relevant to this article was reported.

## KEY POINTS

**QUESTION:** Can we use early-phase amyloid PET scans instead of  $^{18}\text{F}$ -FDG PET for individual classification?

**PERTINENT FINDINGS:** The single-subject procedure applied to early-phase amyloid PET provided typical neurodegenerative patterns in patients as compared with controls, especially in the advanced stage of the diseases. The topographic similarity between the hypoperfusion and hypometabolic patterns was striking, supporting their use for individual classification. Early-phase amyloid PET imaging can exclude the presence of neurodegeneration.

**IMPLICATIONS FOR PATIENT CARE:** Dual-phase amyloid PET permits assessment of neurodegeneration and A $\beta$  pathology with a single tracer injection in 1 exam, and its implementation will be optimal in terms of costs, patient comfort, and radiation exposure.

## REFERENCES

1. Villemagne VL, Barkhof F, Garibotto V, Landau SM, Nordberg A, van Berckel BNM. Molecular imaging approaches in dementia. *Radiology*. 2021;298:517–530.
2. Perani D, Caminiti SP, Carli G, Tondo G. PET neuroimaging in dementia conditions. In: Dierckx RAJO, Otte A, de Vries EFJ, van Waarde A, Leenders KL, eds. *PET and SPECT in Neurology*. Springer; 2020:211–282.
3. Cerami C, Della Rosa PA, Magnani G, et al. Brain metabolic maps in mild cognitive impairment predict heterogeneity of progression to dementia. *Neuroimage Clin*. 2014;7:187–194.
4. Ossenkoppele R, Prins ND, Pijnenburg YAL, et al. Impact of molecular imaging on the diagnostic process in a memory clinic. *Alzheimers Dement*. 2013;9:414–421.
5. Silverman DHS, Mosconi L, Ercoli L, Chen W, Small GW. Positron emission tomography scans obtained for the evaluation of cognitive dysfunction. *Semin Nucl Med*. 2008;38:251–261.
6. Valentina G, Silvia M, Marco P. Dual-phase amyloid PET: hitting two birds with one stone. *Eur J Nucl Med Mol Imaging*. 2016;43:1300–1303.
7. Gjedde A, Aanerud J, Braendgaard H, Rodell AB. Blood-brain transfer of Pittsburgh compound B in humans. *Front Aging Neurosci*. 2013;5:70.
8. Silverman DHS. Brain  $^{18}\text{F}$ -FDG PET in the diagnosis of neurodegenerative dementias: comparison with perfusion SPECT and with clinical evaluations lacking nuclear imaging. *J Nucl Med*. 2004;45:594–607.
9. Jueptner M, Weiller C. Does measurement of regional cerebral blood flow reflect synaptic activity?—Implications for PET and fMRI. *Neuroimage*. 1995;2:148–156.
10. Tiepolt S, Hesse S, Patt M, et al. Early [ $^{18}\text{F}$ ]florbetaben and [ $^{11}\text{C}$ ]PiB PET images are a surrogate biomarker of neuronal injury in Alzheimer's disease. *Eur J Nucl Med Mol Imaging*. 2016;43:1700–1709.
11. Seiffert AP, Gómez-Grande A, Villarejo-Galende A, et al. High correlation of static first-minute-frame (FMF) PET imaging after  $^{18}\text{F}$ -labeled amyloid tracer injection with [ $^{18}\text{F}$ ]FDG pet imaging. *Sensors (Basel)*. 2021;21:1–14.
12. Meyer PT, Hellwig S, Amtage F, et al. Dual-biomarker imaging of regional cerebral amyloid load and neuronal activity in dementia with PET and  $^{11}\text{C}$ -labeled Pittsburgh compound B. *J Nucl Med*. 2011;52:393–400.
13. Rostomian AH, Madison C, Rabinovici GD, Jagust WJ. Early  $^{11}\text{C}$ -PiB frames and  $^{18}\text{F}$ -FDG PET measures are comparable: a study validated in a cohort of AD and FTLN patients. *J Nucl Med*. 2011;52:173–179.
14. Rodríguez-Vieitez E, Leuz A, Chiotis K, Saint-Aubert L, Wall A, Nordberg A. Comparability of [ $^{18}\text{F}$ ]THK5317 and [ $^{11}\text{C}$ ]PiB blood flow proxy images with [ $^{18}\text{F}$ ]FDG positron emission tomography in Alzheimer's disease. *J Cereb Blood Flow Metab*. 2017;37:740–749.
15. Daerr S, Brendel M, Zach C, et al. Evaluation of early-phase [ $^{18}\text{F}$ ]florbetaben PET acquisition in clinical routine cases. *Neuroimage Clin*. 2016;14:77–86.
16. Ottoy J, Verhaeghe J, Niemantsverdriet E, et al.  $^{18}\text{F}$ -FDG PET, the early phases and the delivery rate of  $^{18}\text{F}$ -AV45 PET as proxies of cerebral blood flow in Alzheimer's disease: validation against  $^{15}\text{O}$ -H $_2$ O PET. *Alzheimers Dement*. 2019;15:1172–1182.
17. Peretti DE, García DV, Reesink FE, et al. Relative cerebral flow from dynamic PiB scans as an alternative for FDG scans in Alzheimer's disease PET studies. *PLoS One*. 2019;14:e0211000.
18. Vanhoutte M, Landeau B, Sherif S, et al. Evaluation of the early-phase [ $^{18}\text{F}$ ]AV45 PET as an optimal surrogate of [ $^{18}\text{F}$ ]FDG PET in ageing and Alzheimer's clinical syndrome. *Neuroimage Clin*. 2021;31:102750.
19. Forsberg A, Engler H, Blomquist G, Långström B, Nordberg A. The use of PiB-PET as a dual pathological and functional biomarker in AD. *Biochim Biophys Acta*. 2012;1822:380–385.
20. Hsiao IT, Huang CC, Hsieh CJ, et al. Correlation of early-phase  $^{18}\text{F}$ -florbetapir (AV-45/Amyvid) PET images to FDG images: preliminary studies. *Eur J Nucl Med Mol Imaging*. 2012;39:613–620.
21. Rodríguez-Vieitez E, Carter SF, Chiotis K, et al. Comparison of early-phase  $^{11}\text{C}$ -deuterium-L-deprenyl and  $^{11}\text{C}$ -Pittsburgh compound B PET for assessing brain perfusion in Alzheimer disease. *J Nucl Med*. 2016;57:1071–1077.
22. Montandon ML, Herrmann FR, Garibotto V, Rodriguez C, Haller S, Giannakopoulos P. Determinants of mesial temporal lobe volume loss in older individuals with preserved cognition: a longitudinal PET amyloid study. *Neurobiol Aging*. 2020;87:108–114.
23. Giannakopoulos P, Rodriguez C, Montandon ML, Garibotto V, Haller S, Herrmann FR. Less agreeable, better preserved? A PET amyloid and MRI study in a community-based cohort. *Neurobiol Aging*. 2020;89:24–31.
24. Zanchi D, Montandon ML, Sinanaj I, et al. Decreased fronto-parietal and increased default mode network activation is associated with subtle cognitive deficits in elderly controls. *Neurosignals*. 2017;25:127–138.
25. Dodich A, Mendes A, Assal F, et al. The A/T/N model applied through imaging biomarkers in a memory clinic. *Eur J Nucl Med Mol Imaging*. 2020;47:247–255.

26. Frisoni GB, Barkhof F, Altomare D, et al. AMYPAD diagnostic and patient management study: rationale and design. *Alzheimers Dement*. 2019;15:388–399.
27. Albert MS, DeKosky ST, Dickson D, et al. The diagnosis of mild cognitive impairment due to Alzheimer's disease: recommendations from the National Institute on Aging–Alzheimer's Association workgroups on diagnostic guidelines for Alzheimer's disease. *Alzheimers Dement*. 2011;7:270–279.
28. McKhann GM, Knopman DS, Chertkow H, et al. The diagnosis of dementia due to Alzheimer's disease: recommendations from the National Institute on Aging–Alzheimer's Association workgroups on diagnostic guidelines for Alzheimer's disease. *Alzheimers Dement*. 2011;7:263–269.
29. Ribaldi F, Chicherio C, Altomare D, et al. Brain connectivity and metacognition in persons with subjective cognitive decline (COSCODE): rationale and study design. *Alzheimers Res Ther*. 2021;13:105.
30. Jessen F, Amariglio RE, Buckley RF, et al. The characterisation of subjective cognitive decline. *Lancet Neurol*. 2020;19:271–278.
31. Schmidt P. *Bayesian Inference for Structured Additive Regression Models for Large-Scale Problems with Applications to Medical Imaging*. Dissertation [chapter 6.1]. LMU München; 2016.
32. Wahlund LO, Barkhof F, Fazekas F, et al. A new rating scale for age-related white matter changes applicable to MRI and CT. *Stroke*. 2001;32:1318–1322.
33. Guedj E, Varrone A, Boellaard R, et al. EANM procedure guidelines for brain PET imaging using [<sup>18</sup>F]FDG, version 3. *Eur J Nucl Med Mol Imaging*. 2022;49:632–651.
34. Boellaard R, Delgado-Bolton R, Oyen WJG, et al. FDG PET/CT: EANM procedure guidelines for tumour imaging: version 2.0. *Eur J Nucl Med Mol Imaging*. 2015;42:328–354.
35. Schmitt J, Palleis C, Sauerbeck J, et al. Dual-phase  $\beta$ -amyloid PET captures neuronal injury and amyloidosis in corticobasal syndrome. *Front Aging Neurosci*. 2021;13:661284.
36. Rolls ET, Huang CC, Lin CP, Feng J, Joliot M. Automated anatomical labelling atlas 3. *Neuroimage*. 2020;206:116189.
37. Landau SM, Harvey D, Madison CM, et al. Associations between cognitive, functional, and FDG-PET measures of decline in AD and MCI. *Neurobiol Aging*. 2011;32:1207–1218.
38. Perani D, Anthony P, Rosa D, et al. Validation of an optimized SPM procedure for FDG-PET in dementia diagnosis in a clinical setting. *Neuroimage Clin*. 2014;6:445–454.
39. Caminiti SP, Ballarini T, Sala A, et al. FDG-PET and CSF biomarker accuracy in prediction of conversion to different dementias in a large multicentre MCI cohort. *Neuroimage Clin*. 2018;18:167–177.
40. Tondo G, Carli G, Santangelo R, et al. Biomarker-based stability in limbic-predominant amnesic mild cognitive impairment. *Eur J Neurol*. 2021;28:1123–1133.
41. Teune LK, Bartels AL, De Jong BM, et al. Typical cerebral metabolic patterns in neurodegenerative brain diseases. *Mov Disord*. 2010;25:2395–2404.
42. Jenkinson M, Beckmann CF, Behrens TEJ, Woolrich MW, Smith SM. FSL. *Neuroimage*. 2012;62:782–790.
43. Savio A, Fänger S, Tahmasian M, et al. Resting-state networks as simultaneously measured with functional MRI and PET. *J Nucl Med*. 2017;58:1314–1317.
44. DeLong ER, DeLong DM, Clarke-Pearson DL. Comparing the areas under two or more correlated receiver operating characteristic curves: a nonparametric approach. *Biometrics*. 1988;44:837–845.
45. Pandya SY, Clem MA, Silva LM, Woon FL. Does mild cognitive impairment always lead to dementia? A review. *J Neurol Sci*. 2016;369:57–62.
46. Petersen RC, Lopez O, Armstrong MJ, et al. Practice guideline update summary: mild cognitive impairment—report of the Guideline Development, Dissemination, and Implementation Subcommittee of the American Academy of Neurology. *Neurology*. 2018;90:126–135.
47. Della Rosa PA, Cerami C, Gallivanone F, et al. A standardized [<sup>18</sup>F]-FDG-PET template for spatial normalization in statistical parametric mapping of dementia. *Neuroinformatics*. 2014;12:575–593.

---

---

# Differential Effects of Tau Stage, Lewy Body Pathology, and Substantia Nigra Degeneration on <sup>18</sup>F-FDG PET Patterns in Clinical Alzheimer Disease

Jesús Silva-Rodríguez<sup>1</sup>, Miguel A. Labrador-Espinosa<sup>1-3</sup>, Alexis Moscoso<sup>4</sup>, Michael Schöll<sup>4,5</sup>, Pablo Mir<sup>1-3</sup>, and Michel J. Grothe<sup>1,2,4</sup>; for the Alzheimer's Disease Neuroimaging Initiative

<sup>1</sup>Unidad de Trastornos del Movimiento, Servicio de Neurología y Neurofisiología Clínica, Instituto de Biomedicina de Sevilla, Hospital Universitario Virgen del Rocío/CSIC/Universidad de Sevilla, Sevilla, Spain; <sup>2</sup>Centro de Investigación Biomédica en Red sobre Enfermedades Neurodegenerativas (CIBERNED), Madrid, Spain; <sup>3</sup>Departamento de Medicina, Facultad de Medicina, Universidad de Sevilla, Sevilla, Spain; <sup>4</sup>Wallenberg Center for Molecular and Translational Medicine and Department of Psychiatry and Neurochemistry, University of Gothenburg, Gothenburg, Sweden; and <sup>5</sup>Dementia Research Centre, Queen Square Institute of Neurology, University College London, London, United Kingdom

Comorbid Lewy body (LB) pathology is common in Alzheimer disease (AD). The effect of LB copathology on <sup>18</sup>F-FDG PET patterns in AD is yet to be studied. We analyzed associations of neuropathologically assessed tau pathology, LB pathology, and substantia nigra neuronal loss (SNnl) with antemortem <sup>18</sup>F-FDG PET hypometabolism in patients with a clinical AD presentation. **Methods:** Twenty-one patients with autopsy-confirmed AD without LB neuropathologic changes (LBNC) (pure-AD), 24 with AD and LBNC copathology (AD-LB), and 7 with LBNC without fulfilling neuropathologic criteria for AD (pure-LB) were studied. Pathologic groups were compared regarding regional and voxelwise <sup>18</sup>F-FDG PET patterns, the cingulate island sign ratio (CISr), and neuropathologic ratings of SNnl. Additional analyses assessed continuous associations of Braak tangle stage and SNnl with <sup>18</sup>F-FDG PET patterns. **Results:** Pure-AD and AD-LB showed highly similar patterns of AD-typical temporoparietal hypometabolism and did not differ in CISr, regional <sup>18</sup>F-FDG SUVR, or SNnl. By contrast, pure-LB showed the expected pattern of pronounced posterior-occipital hypometabolism typical for dementia with LB (DLB), and both CISr and SNnl were significantly higher compared with the AD groups. In continuous analyses, Braak tangle stage correlated significantly with more AD-like, and SNnl with more DLB-like, <sup>18</sup>F-FDG PET patterns. **Conclusion:** In autopsy-confirmed AD dementia patients, comorbid LB pathology did not have a notable effect on the regional <sup>18</sup>F-FDG PET pattern. A more DLB-like <sup>18</sup>F-FDG PET pattern was observed in relation to SNnl, but advanced SNnl was mostly limited to relatively pure LB cases. AD pathology may have a dominant effect over LB pathology in determining the regional neurodegeneration phenotype.

**Key Words:** <sup>18</sup>F-FDG; LBD; AD; autopsy

**J Nucl Med 2023; 64:274–280**

DOI: 10.2967/jnumed.122.264213

---

**A**lzheimer disease (AD) and dementia with Lewy bodies (DLB) are 2 distinct neurodegenerative conditions defined by the cerebral accumulation of amyloid- $\beta$  plaques and tau neurofibrillary

tangles (NFTs) and of  $\alpha$ -synuclein containing Lewy bodies (LB), respectively (1,2). In contrast to AD, DLB typically presents with denervation of the nigrostriatal dopaminergic pathway caused by degeneration of dopaminergic substantia nigra neurons (3), as well as more predominant executive and visuospatial deficits accompanied by visual hallucinations, cognitive fluctuations, parkinsonism, and rapid-eye-movement sleep behavioral disorder (4). Although AD and DLB have unique neuropathologic profiles, up to 60% of clinical AD and DLB patients present with neuropathologic findings of both diseases (5,6). Concomitant LB pathology in clinical AD has been associated with faster cognitive decline (7–9), younger age at death (8), and usually more DLB-like clinical features (9–12), although this could not be confirmed by others (7,13,14). In the era of disease-modifying therapies, these patients may benefit less from amyloid-lowering therapies (15) and may potentially show a better response to cholinesterase inhibitors (16). Biomarkers identifying these patients may thus allow for a more targeted treatment of AD (11,17).

PET with the glucose analog <sup>18</sup>F-FDG is a well-established modality for imaging neurodegeneration, and differentiated hypometabolism patterns have been established for different conditions (18). Particularly, in contrast to the characteristic temporoparietal pattern of hypometabolism in AD, patients with DLB are characterized by a more pronounced posterior-occipital pattern of hypometabolism with relatively preserved metabolism in the medial temporal lobe (MTL) and in the posterior cingulate, with the latter being known as the cingulate island sign (19,20). The cingulate island sign is a well-established biomarker for distinguishing patients with DLB and AD (19,21), even at prodromal stages (22).

Previous imaging-pathologic association studies have demonstrated that AD copathology in DLB associates with a less DLB-typical hypometabolic pattern (20,23), but the potential contributions of <sup>18</sup>F-FDG PET to the identification of mixed pathology in AD-like presentations are yet to be explored. Here, we assessed antemortem <sup>18</sup>F-FDG PET patterns of clinically diagnosed AD patients in relation to AD and LB neuropathology at autopsy.

## MATERIALS AND METHODS

### Study Participants

Our cohort included 59 participants enrolled in the Alzheimer's Disease Neuroimaging Initiative (ADNI, <https://adni.loni.usc.edu/>) who

---

Received Apr. 5, 2022; revision accepted Aug. 3, 2022.  
For correspondence or reprints, contact Pablo Mir (pmir@us.es) or Michel Grothe (mgrothe@us.es).  
Published online Aug. 25, 2022.  
COPYRIGHT © 2023 by the Society of Nuclear Medicine and Molecular Imaging.

had neuropathologic examinations at autopsy, a clinical diagnosis of AD dementia or amnesic mild cognitive impairment at the last clinical evaluation, and available antemortem  $^{18}\text{F}$ -FDG PET scans. The average interval between the last available  $^{18}\text{F}$ -FDG PET acquisition and death was  $3.0 \pm 2.6$  y.

### Neuropathologic Assessments

Neuropathologic assessments were performed by the ADNI Neuropathology Core following the National Institute on Aging–Alzheimer’s Association guidelines (24–26). Standard rating scales for AD pathology (amyloid, tau, neuritic plaques) were further merged into the AD neuropathologic change (ADNC) composite, whereas LB pathology assessment followed the criteria of McKeith et al. (4). Patients were considered to have autopsy-confirmed AD when presenting with intermediate or high ADNC (24), and the presence of LB neuropathologic changes (LBNC) was denoted when LBs were present in limbic or neocortical regions or the amygdala (4). Amygdala-predominant LBs, which have been suggested to be characteristic of advanced AD and less likely related to DLB (27), were considered as positive for LBNC. Patients with LBNC restricted to the brain stem were excluded. Patients were stratified as having autopsy-confirmed AD without LBNC (pure-AD), autopsy-confirmed AD with comorbid LBNC (AD-LB), LBNC without fulfilling neuropathologic criteria for AD (pure-LB), or none of these (negative). We also studied semiquantitative ratings (assessed on a scale from 0 to 3) of substantia nigra neuronal loss (SNnl) as a marker of DLB-specific neurodegeneration (4,28). For a subset of patients ( $n = 45/59$ ), semiquantitative ratings of the regional loads of tau NFTs and LBs were available (Supplemental Table 1; supplemental materials are available at <http://jnm.snmjournals.org>).

### Genetics

*APOE* genotype was determined by Cogenics using standard methods to genotype the 2 *APOE*- $\epsilon 4$ -defining single-nucleotide polymorphisms (rs429358 and rs7412). Patients were labeled as having 0, 1 or 2  $\epsilon 4$  copies.

### Neuropsychologic Evaluation

The Mini-Mental State Examination was used to characterize global cognitive performance (29). Domain-specific composite scores were used to assess memory (MEM) (30) and executive function (EXEC) (31). In addition, we calculated a cognitive profile variable,  $\Delta$  (MEM – EXEC), to characterize relative impairments between these 2 domains (32). The average interval between neuropsychologic evaluation and death was  $1.9 \pm 2.0$  y.

### $^{18}\text{F}$ -FDG PET Acquisition and Processing

We used  $^{18}\text{F}$ -FDG PET images in fully preprocessed format (level 4) as provided by ADNI. The acquisition and preprocessing are detailed elsewhere (33). Blood glucose levels, previously associated with changes in posterior–occipital hypometabolism (34), are reported.  $^{18}\text{F}$ -FDG PET images were spatially normalized using SPM, version 12 (<https://www.fil.ion.ucl.ac.uk/spm/>), and intensity normalized using a previously validated data-driven method (35) and  $^{18}\text{F}$ -FDG PET data from 179 cognitively normal ADNI subjects (the control group). Region-of-interest (ROI) analysis was performed to calculate the average  $^{18}\text{F}$ -FDG uptake in the occipital cortex and the MTL (21), as well as the cingulate island sign ratio (CISr) (20,22) between the posterior cingulate cortex and the precuneus and cuneus uptake. To this end, we used the corresponding ROIs from the Harvard–Oxford neuroanatomic atlas.

### Statistical Analysis

Two-sample *t* tests and Mann–Whitney *U* tests were used for comparing normally distributed continuous variables and nonnormally distributed and ordinal variables, respectively. Effect sizes were reported as Cohen’s *d*.

Hypometabolism patterns were determined by voxel-wise 2-sample *t* tests between each pathologic group and the control group using SPM. Age, sex, and blood glucose levels were used as confounding nuisance covariates (34,36). *T*-score maps were transformed to Cohen’s *d* maps, and a threshold was applied using a *P* value of less than 0.05 (corrected using the false discovery rate [FDR]) and a cluster size of more than 250 voxels. For secondary analysis, the AD-LB group was separated into AD with amygdala-predominant LBs and AD with limbic or neocortical LBs. The different pathologic groups were also directly compared. Spatial similarities between hypometabolism patterns were assessed using spatial Spearman correlation analysis across the 52 ROIs defined in the Harvard–Oxford atlas (37).

In addition, we performed regional and voxel-wise Spearman correlation analyses of the association of AD-specific (Braak tau stage) and DLB-specific (SNnl) neuropathologic markers with  $^{18}\text{F}$ -FDG PET patterns. In complementary analyses, we also assessed associations between  $^{18}\text{F}$ -FDG PET and semiquantitative ratings of regional LB and NFT load (supplemental materials).

## RESULTS

### Demographics and Neuropathology

Seven subjects (11.9%) did not fulfil the criteria for either ADNC or LBNC, including 2 cases that had LBs restricted to the brain stem (and ADNC  $\leq 1$ ). Of the remaining 52 subjects, 21 (35.6%) had autopsy-confirmed AD without LBNC (pure-AD), 24 (40.7%) had autopsy-confirmed AD with LBNC copathology (AD-LB), and 7 (11.9%) had LBNC without fulfilling pathologic criteria for AD (ADNC  $\leq 1$ ) (pure-LB). Among AD-LB, 16 patients presented limbic/transitional or neocortical LBNC (67%), whereas 8 patients presented amygdala-predominant LBNC (33%).

Patients in the pure-AD and AD-LB groups did not differ with respect to age, sex, *APOE*  $\epsilon 4$  positivity, or blood glucose levels, but pure-LB patients were significantly older ( $P = 0.039$ ) and less often carriers of the *APOE*  $\epsilon 4$  allele ( $P = 0.018$ ) than the other groups (Table 1). Regarding neuropathology, the pure-AD and the AD-LB groups did not differ in severity of Braak stages ( $P = 0.695$ ) or regional NFT burden (Supplemental Fig. 1). Amygdala-predominant LBs were significantly more frequent in the AD-LB group than in the pure-LB group ( $P = 0.047$ ), but semiquantitative ratings of regional LB burden did not differ between these groups (Supplemental Fig. 1). Finally, SNnl was significantly higher for pure-LB than for pure-AD ( $P = 0.005$ ) and AD-LB ( $P = 0.020$ ) but similar between pure-AD and AD-LB ( $P = 0.210$ ).

In terms of cognition, there were no significant differences in Mini-Mental State Examination between groups, but patients in the AD-LB group showed significantly worse memory performance than the pure-AD ( $P = 0.012$ ) and pure-LB ( $P = 0.004$ ) groups, whereas executive function was similar among groups. Accordingly, AD-LB subjects showed a memory-predominant cognitive profile in  $\Delta$  (MEM – EXEC) (1-sample *t* test,  $P = 0.045$ ), whereas pure-LB subjects showed a disproportionate executive impairment ( $P = 0.057$ ), and pure-AD cases showed balanced deficits in both domains ( $P = 0.161$ ). Limbic LB load correlated negatively with MEM (after correcting for the effect of tau NFT burden) across the whole cohort but not in the AD-LB group alone (Supplemental Table 2).

### $^{18}\text{F}$ -FDG Patterns of Pathologically Defined Groups

Compared with healthy controls, the pure-AD group showed the classic AD hypometabolism pattern, with pronounced medial and lateral temporal effects extending to the lateral parietal cortex,

**TABLE 1**  
Demographic Characteristics of the Different Pathologic Subgroups

Characteristic	Pure-AD (n = 21)	AD-LB (n = 24)	Pure-LB (n = 7)
Age at death (y)	81.8 ± 7.7	81.0 ± 8.4	88.6 ± 4.9
Imaging to death (y)	2.3 ± 3.5	3.3 ± 3.0	3.1 ± 2.7
MCI (at death)	3	1	2
Dementia (at death)	18	23	5
Sex			
Male	12	19	6
Female	8	5	1
APOE ε4			
--	9	7	6
±	11	11	0
++	1	6	0
Braak stage			
I–IV	3	1	7
V	14	18	0
VI	5	5	0
LB			
Limbic	0	2	1
Neocortical	0	14	6
Amygdala	0	8	0
SNnl	0.86 ± 0.47	1.04 ± 0.46	1.57 ± 0.49
<sup>18</sup> F-FDG PET blood glucose levels (mg/dL)	101.7 ± 11.7	97.8 ± 19.9	94.4 ± 8.2
Mini-Mental State Examination score	22.4 ± 6.6	21.5 ± 5.7	24.7 ± 3.9
MEM	−1.06 ± 0.94	−1.61 ± 0.66	−0.69 ± 0.67
EXEC	−1.36 ± 1.21	−1.48 ± 0.95	−1.50 ± 0.95
Δ (MEM – EXEC)	0.16 ± 0.50	−0.33 ± 0.71	0.53 ± 0.55

posterior cingulate, and precuneus; mild frontal hypometabolism; and well-preserved occipital metabolism (Fig. 1A). The mixed-pathology AD-LB group was characterized by a spatial pattern remarkably similar to the pure-AD group (spatial correlation,  $\rho = 0.82$ ). Interestingly, the same pattern was also observed when analyzing AD-LB cases with limbic/neocortical or amygdala-predominant LB separately (Fig. 1B). By contrast, the pure-LB group showed the typical DLB pattern of pronounced posterior–occipital hypometabolism with relative sparing of the MTL and the posterior cingulate, which as expected did not spatially correlate with the pure-AD pattern ( $\rho = 0.09$ ). In direct comparisons, only non-significant differences were observed between the pure-AD and AD-LB groups, whereas the pure-LB group showed significant posterior–occipital hypometabolism and a relative sparing of frontal and temporal regions in comparison to both the pure-AD and the AD-LB groups (Fig. 1C).

ROI-based analyses fully reproduced and quantified the voxel-wise observations, revealing significant MTL hypometabolism in the pure-AD and AD-LB groups, and occipital hypometabolism in the pure-LB group (Fig. 2).

Additionally, patients in the pure-LB group exhibited significantly higher CISr than those in the pure-AD ( $d = 0.78$ ,  $P = 0.010$ ) and the AD-LB ( $d = 0.95$ ,  $P = 0.002$ ) groups, but the CISr did not differ between the pure-AD and AD-LB groups ( $d = 0.15$ ,  $P = 0.375$ ) (Fig. 3A). CISr was also similar for limbic/neocortical

and amygdala-predominant AD-LB patients ( $d = 0.18$ ,  $P = 0.516$ ). By contrast, patients with an elevated SNnl ( $\geq 2$ ) showed a significantly higher CISr ( $d = 1.49$ ,  $P < 0.001$ ), even when considering only the pure-AD and AD-LB groups ( $d = 1.31$ ,  $P = 0.016$ ). Moreover, individual  $z$  score maps of the 3 AD-LB patients with elevated SNnl revealed a more prominent DLB-like or mixed hypometabolism pattern (Fig. 3B; spatial correlations: case 1,  $\rho = 0.82$  and  $0.26$ ; case 2,  $\rho = 0.57$  and  $0.17$ ; case 3,  $\rho = 0.57$  and  $0.41$ , for the pure-LB and pure-AD patterns, respectively).

#### Continuous Associations of Braak Tau Stage and SNnl with <sup>18</sup>F-FDG PET Patterns

To better understand the role of AD- and DLB-specific neuropathologic markers in shaping the observed <sup>18</sup>F-FDG PET patterns, we studied the continuous associations of Braak tau stage and SNnl with <sup>18</sup>F-FDG PET ROI values across the full sample (Fig. 4). Braak stage correlated negatively with CISr and MTL metabolism, whereas SNnl correlated positively with CISr and negatively with occipital metabolism. In complementary analyses, similar associations with regional <sup>18</sup>F-FDG PET markers were observed when using regional tau NFT loads instead of Braak tau stage (Supplemental Fig. 2), but regional LB burden did not significantly correlate with <sup>18</sup>F-FDG PET features (Supplemental Fig. 3).

In additional voxel-wise analyses, higher Braak tau stages correlated with more hypometabolism in the posterior cingulate, MTL,



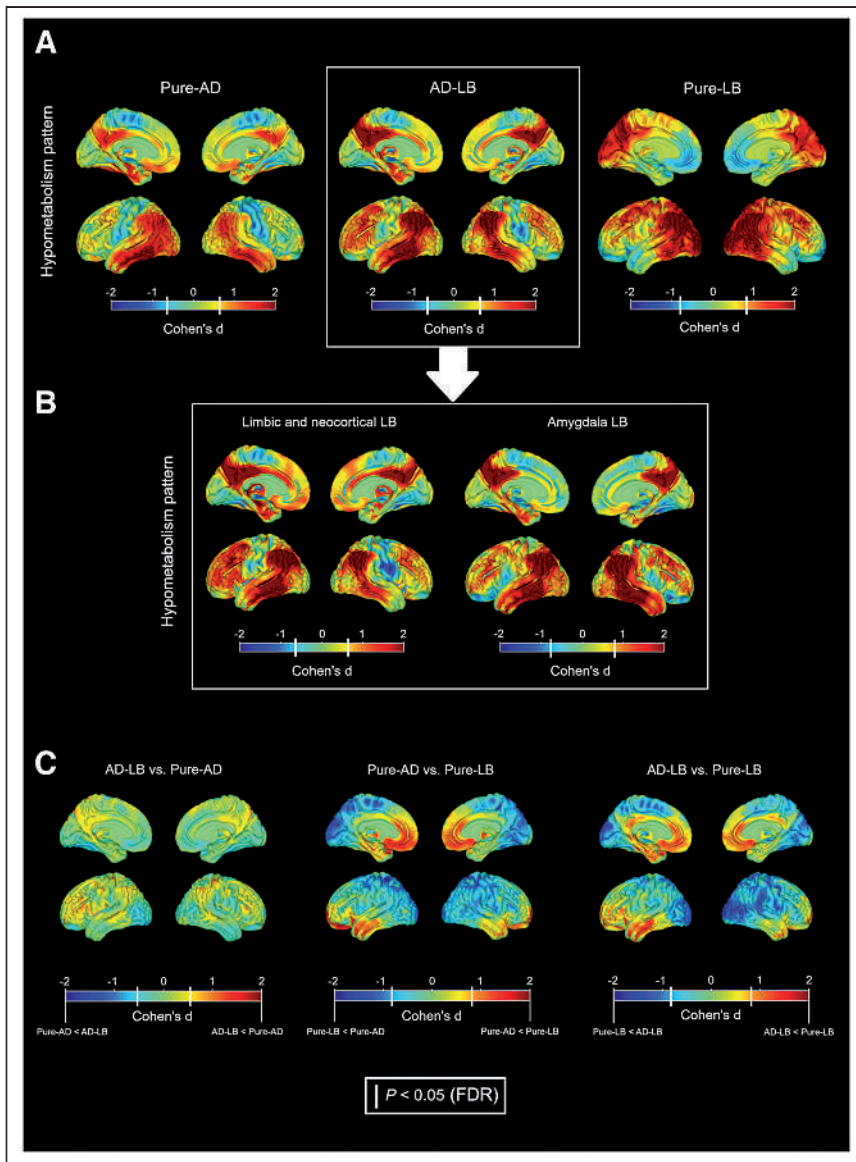


**FIGURE 1.** (A) Hypometabolism patterns of pathologic groups compared with controls. (B) Patterns of limbic/neocortical and amygdala-predominant LB subgroups in AD-LB. (C) Direct comparisons between pathologic groups. Color represents effect size. White bars in color bars:  $P < 0.05$  (FDR-corrected).

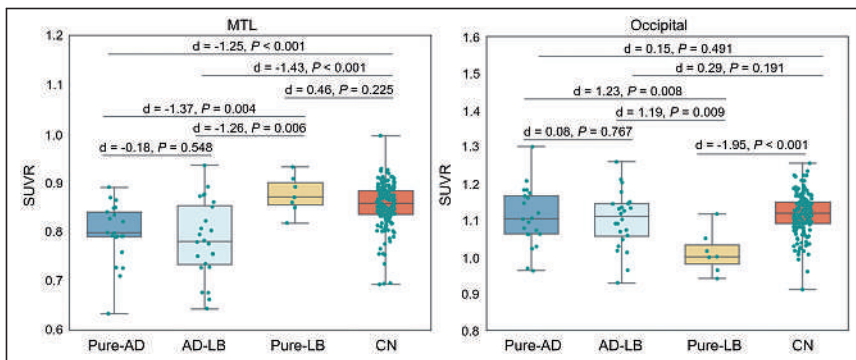


**FIGURE 2.** Comparison of MTL and occipital cortex  $^{18}\text{F}$ -FDG SUV ratios (SUVr) between different neuropathologic groups and the control group (CN).

and temporoparietal cortex, as well as with less hypometabolism in the occipital and the paracentral cortex (Fig. 5, top). SNnl was correlated with more hypometabolism in occipital and parietotemporal regions and less hypometabolism in the orbitofrontal cortex and the posterior cingulate (Fig. 5, bottom).

## DISCUSSION

In the present work, we analyzed ante-mortem  $^{18}\text{F}$ -FDG PET patterns in relation to AD and LB pathology in a cohort of clinical AD patients. Concomitant AD-LB patients did not show more DLB-like  $^{18}\text{F}$ -FDG PET features but, rather, a pattern regionally very similar to the pure-AD pattern (Figs. 1 and 2). Accordingly, the CISr (20–22) did not differ between the pure-AD and AD-LB groups (Fig. 3). In contrast to our results, in a previous work comparing pathologically verified DLB ( $n = 3$ ) and AD-LB ( $n = 3$ ) patients (38), the authors reported similar occipital hypometabolism in both groups. These differences may be explained by different definitions of the AD-LB group, since AD-LB patients in this previous work presented DLB symptomatology whereas those in our study exhibited a relatively pure AD phenotype. Interestingly, the amygdala-predominant LB type, which has been previously linked to AD (27), was indeed higher in the AD-LB group than in the pure-LB group (from which it was completely absent), but this did not seem to affect the neurodegeneration phenotype (Fig. 1B). Although the little effect of comorbid LB pathology on the regional  $^{18}\text{F}$ -FDG PET pattern may come as a surprise, it is in line with the lack of elevated SNnl, a pathologic hallmark of LB-typical neurodegeneration, in these comorbid AD-LB cases (28,39).

Although AD-LB patients showed an even more amnesic-predominant cognitive profile than the pure-AD patients, rather than a more dysexecutive phenotype typical of DLB (4), this difference is unlikely to result from a more advanced AD pathology in the AD-LB group, as severity of both Braak tau stage (Table 1) and regional NFT burden (Supplemental Fig. 1) were comparable between pure-AD and AD-LB. Previous studies have similarly suggested that comorbid LB pathology exacerbates AD-typical cognitive deficits but does not necessarily produce a mixed clinical phenotype (7,13,14), whereas others did observe more DLB symptomatology in AD-LB cases (8–12,40). These differences may be explained by different clinicopathologic definitions of the AD-LB groups, as some autopsy

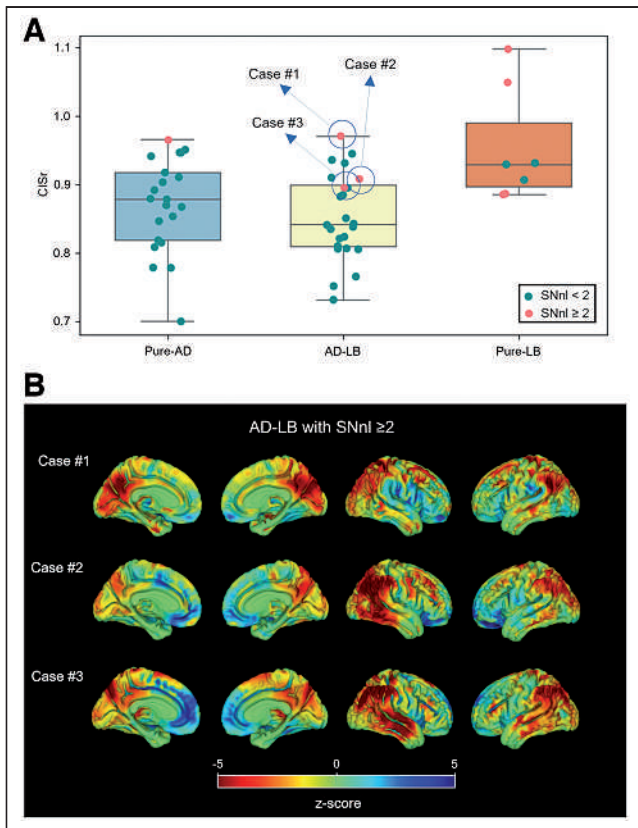


**FIGURE 3.** (A) CISr comparisons between pathologic groups. Cases with high SNnl ( $\geq 2$ ) are highlighted in orange. (B) Individual z score maps of 3 AD-LB cases with high SNnl.

studies define the different pathology groups based solely on neuropathologic criteria (8,40), whereas others also restrict their samples to a particular clinical phenotype as in our study (6,13,20,23).

Interestingly, a smaller group of patients (12%) who had relatively pure LBNC with no or low ADNC did indeed show the expected DLB-like posterior-occipital hypometabolism pattern (20), which was accompanied by significantly elevated SNnl. Moreover, quantitative neuropsychologic analysis showed these patients to have a more dysexecutive rather than amnesic-predominant profile. Thus, it is likely that these cases may reflect misdiagnosed DLB patients with no DLB-specific symptomatology and a clinical profile more similar to AD (4,41). Our findings indicate that  $^{18}\text{F}$ -FDG PET may serve as a useful imaging marker to identify this nonnegligible and clinically highly relevant portion of misdiagnosed AD patients in vivo. Interestingly, despite having similar regional loads of LB pathology (Supplemental Fig. 1), the comorbid AD-LB group did not exhibit a DLB-like  $^{18}\text{F}$ -FDG PET pattern or elevated SNnl, suggesting that AD pathology may have a dominant effect over LB pathology in determining the regional neurodegeneration phenotype in these patients. Altogether, these results suggest that the role of LBs in AD-LB may be different from that of pure-LBs. Although recent studies have provided evidence of in vivo interactions between tau and  $\alpha$ -synuclein (42), more work is needed to better understand how these interactions may modify the effect of LB pathology on the neurodegeneration phenotype in AD-LB.

In continuous association analyses, we observed that Braak tau stage (Figs. 4 and 5) and tau NFT load (Supplemental Fig. 2) correlated significantly with more AD-like  $^{18}\text{F}$ -FDG PET features,

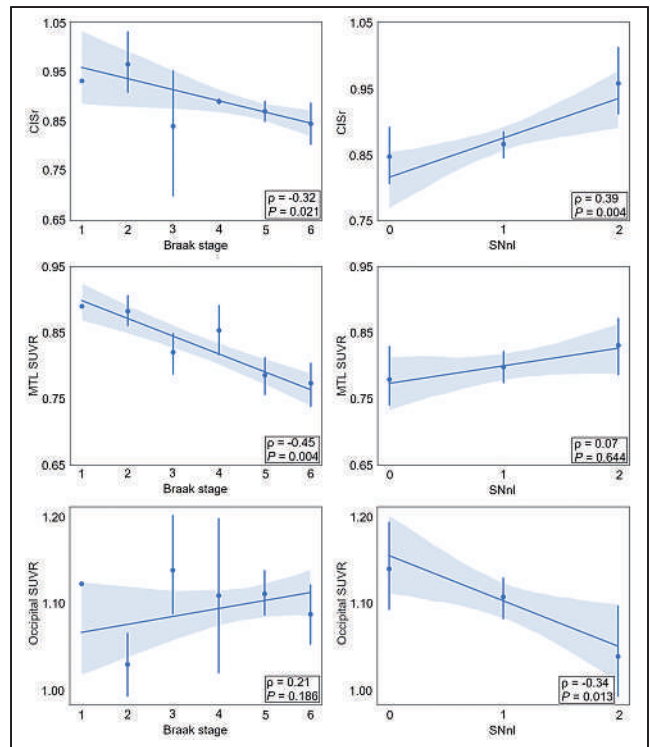


**FIGURE 4.** Correlations of Braak tau stage and SNnl with regional  $^{18}\text{F}$ -FDG PET markers.

confirming and expanding recent findings obtained in a smaller subsample of the ADNI autopsy cohort (43) as well as similar observations previously reported in clinical DLB (20,23). Interestingly, SNnl showed the opposite pattern of associations, being associated with a higher CISr, lower occipital SUVR, and a more DLB-like hypometabolism pattern in voxelwise analysis (Figs. 4 and 5). Most interestingly, this association was even observed on an individual basis in a small subset of AD-LB patients who did have advanced SNnl (Fig. 3B). Nevertheless, this applied only to 3 AD-LB cases (12.5%), suggesting that comorbid LB rarely affects the neurodegeneration phenotype in cases with fully developed AD pathology. More research is necessary to better understand the

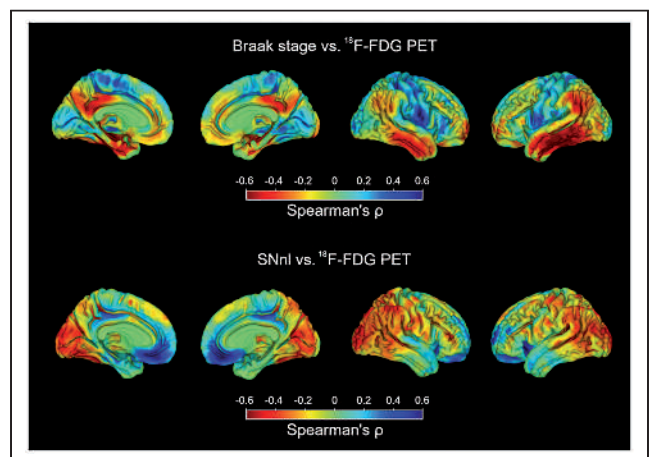


**FIGURE 5.** Voxel-wise correlations of Braak tau stage and SNnl with  $^{18}\text{F}$ -FDG uptake.

neurobiologic factors that determine why comorbid LB pathology leads to SNnl and a DLB-typical neurodegeneration pattern in some patients but not in others (44).

Altogether, our results suggest that it may not be the presence of LB pathology by itself, but rather the associated SNnl, that links with a more DLB-like hypometabolic pattern in these clinical AD patients. This notion was further corroborated by the fact that semi-quantitative ratings of regional LB burden were not significantly associated with  $^{18}\text{F}$ -FDG PET markers (Supplemental Fig. 3). To the best of our knowledge, our study is the first report demonstrating these associations. A very recent multimodal neuroimaging study ( $n = 55$ ) has pointed to an association between nigrostriatal degeneration (as assessed by dopamine transporter SPECT) and cortical hypometabolism in clinical DLB (45). However, such associations had not yet been assessed using neuropathologic evaluations or in the context of clinical AD. Additional studies combining  $^{18}\text{F}$ -FDG PET with imaging modalities aimed to evaluate SN degeneration in vivo (45–48) would be of great interest for replicating and studying these associations in larger observational cohorts.

Regarding the clinical implications of our work, our novel finding of comparable  $^{18}\text{F}$ -FDG PET patterns in AD-LB and pure-AD suggests that  $^{18}\text{F}$ -FDG PET may not be able to readily detect comorbid LB pathology in AD patients, which may be a disappointing finding that is nevertheless of the utmost clinical relevance. Although larger studies might be useful to corroborate these findings, the comparably large sample used here ( $n = 21$  for pure-AD vs.  $n = 23$  for AD-LB) and the low effect size estimates indicate that this finding would be unlikely to change with higher sample sizes. However, according to our findings,  $^{18}\text{F}$ -FDG PET may be useful for identifying a subset of clinically diagnosed AD patients who have relatively pure LB pathology, as well as those pathologic AD patients for whom the comorbid LB pathology is accompanied by substantia nigra neurodegeneration. Identifying these patients has important clinical implications because these will most likely also show different clinical trajectories (7), including development of more DLB-typical symptomatology (9), and may possibly also exhibit the typical susceptibility to antagonistic dopaminergic neuroleptics known for DLB patients (49).

Our work also presents a series of limitations. First, the restriction to patients with typical AD-like clinical presentations limits the reach of our conclusions to this particular clinical setting, and different effects of comorbid AD-LB pathology may be observed in clinically more diverse dementia cohorts (8). Nevertheless, identifying (comorbid) LB pathology in clinical AD patients poses a distinct diagnostic challenge—which has not been addressed so far using  $^{18}\text{F}$ -FDG PET—that has potentially high relevance for individual patient management and recruitment into AD clinical trials (6). In close relation, neuropsychologic data collected within the ADNI study allow for the assessment of a specific dysexecutive or amnesic-predominant neuropsychologic profile, but DLB core features are not assessed in enough detail (or are not assessed at all). Finally, quantitative assessments of regional pathologic load may represent a closer pathologic correlate of phenotypic differences than the standardized semiquantitative rating scales used here (44).

## CONCLUSION

$^{18}\text{F}$ -FDG PET may not be able to readily detect comorbid LB pathology in clinical AD, but it may be useful for identifying a subset of patients with prominent LB-related neurodegeneration—a capability that may have important implications for patient

management, individualized disease prognostication, and selection for treatment trials.

## DISCLOSURE

This study has been funded by Instituto de Salud Carlos III through the projects “PI20/00613 and PI19/01576” (co-funded by European Regional Development Fund; “A way to make Europe”) and the Junta de Andalucía (CVI-02526, CTS-7685, PE-0186–2019, and PI-0046-2021). Jesús Silva-Rodríguez is a “Sara Borrell” fellow (CD21/00067), and Michel Grothe is a “Miguel Servet” fellow (CP19/00031). Miguel Labrador-Espinosa is supported by VI-PPIT-US (University of Seville, USE-19094-G). Alexis Moscoso is supported by Gamla Tjänarinnor. Michael Schöll is supported by the Knut and Alice Wallenberg Foundation (KAW 2014.0363), the Swedish Research Council (2017-02869), the Swedish state under the ALF-agreement (ALFGBG-813971), and the Swedish Alzheimer Foundation (AF-740191). Data collection and sharing for this project were funded by the ADNI, a public–private partnership program supported by national funding agencies, as well as contributions from several companies (<https://adni-dup.loni.usc.edu/about/funding/>). No other potential conflict of interest relevant to this article was reported.

## ACKNOWLEDGMENT

Data used in preparation of this article were obtained from the ADNI database. A complete listing of ADNI investigators can be found at [http://adni.loni.usc.edu/wp-content/uploads/how\\_to\\_apply/ADNI\\_Acknowledgement\\_List.pdf](http://adni.loni.usc.edu/wp-content/uploads/how_to_apply/ADNI_Acknowledgement_List.pdf).

## KEY POINTS

**QUESTION:** Is the presence of LB pathology, or related SNnl, associated with a differential  $^{18}\text{F}$ -FDG PET pattern in clinical AD?

**PERTINENT FINDINGS:** LB copathology did not affect the  $^{18}\text{F}$ -FDG PET pattern in autopsy-confirmed AD, but a distinct posterior–occipital  $^{18}\text{F}$ -FDG PET pattern was observed in relation to SNnl, most commonly in clinical AD cases with relatively pure LB pathology at autopsy.

**IMPLICATIONS FOR PATIENT CARE:**  $^{18}\text{F}$ -FDG PET can identify clinically diagnosed AD patients who have relatively pure LB pathology and substantia nigra neurodegeneration at autopsy. In vivo identification of these patients has important implications for clinical patient management, individualized disease prognostication, and selection for treatment trials.

## REFERENCES

1. Kövari E, Horvath J, Bouras C. Neuropathology of Lewy body disorders. *Brain Res Bull.* 2009;80:203–210.
2. Perl DP. Neuropathology of Alzheimer’s disease. *Mt Sinai J Med.* 2010;77:32–42.
3. Seidel K, Mahlke J, Siswanto S, et al. The brainstem pathologies of Parkinson’s disease and dementia with Lewy bodies. *Brain Pathol.* 2015;25:121–135.
4. McKeith IG, Boeve BF, Dickson DW, et al. Diagnosis and management of dementia with Lewy bodies: fourth consensus report of the DLB consortium. *Neurology.* 2017;89:88–100.
5. Irwin DJ, Hurtig HI. The contribution of tau, amyloid-beta and alpha-synuclein pathology to dementia in Lewy body disorders. *J Alzheimers Dis Parkinsonism.* 2018;8:444.
6. Robinson JL, Richardson H, Xie SX, et al. The development and convergence of co-pathologies in Alzheimer’s disease. *Brain.* 2021;144:953–962.

7. Malek-Ahmadi M, Beach TG, Zamrini E, et al. Faster cognitive decline in dementia due to Alzheimer disease with clinically undiagnosed Lewy body disease. *PLOS ONE*. 2019;14:e0217566.
8. Chung EJ, Babulal GM, Monsell SE, Cairns NJ, Roe CM, Morris JC. Clinical features of Alzheimer disease with and without Lewy bodies. *JAMA Neurol*. 2015;72:789–796.
9. Chatterjee A, Hirsch-Reinshagen V, Moussavi SA, Ducharme B, Mackenzie IR, Hsiung GR. Clinico-pathological comparison of patients with autopsy-confirmed Alzheimer's disease, dementia with Lewy bodies, and mixed pathology. *Alzheimers Dement (Amst)*. 2021;13:e12189.
10. Savica R, Beach TG, Hentz JG, et al. Lewy body pathology in Alzheimer's disease: a clinicopathological prospective study. *Acta Neurol Scand*. 2019;139:76–81.
11. Thomas AJ, Mahin-Babaei F, Saidi M, et al. Improving the identification of dementia with Lewy bodies in the context of an Alzheimer's-type dementia. *Alzheimers Res Ther*. 2018;10:27.
12. Azar M, Chapman S, Gu Y, Leverenz JB, Stern Y, Cosentino S. Cognitive tests aid in clinical differentiation of Alzheimer's disease versus Alzheimer's disease with Lewy body disease: evidence from a pathological study. *Alzheimers Dement*. 2020;16:1173–1181.
13. Roudil J, Deramecourt V, Dufournet B, et al. Influence of Lewy pathology on Alzheimer's disease phenotype: a retrospective clinico-pathological study. *J Alzheimers Dis*. 2018;63:1317–1323.
14. Ryman SG, Yutsis M, Tian L, et al. Cognition at each stage of Lewy body disease with co-occurring Alzheimer's disease pathology. *J Alzheimers Dis*. 2021;80:1243–1256.
15. Budd Haerlein S, Aisen PS, Barkhof F, et al. Two randomized phase 3 studies of aducanumab in early Alzheimer's disease. *J Prev Alzheimers Dis*. 2022;9:197–210.
16. Liberini P, Valerio A, Memo M, Spano P. Lewy-body dementia and responsiveness to cholinesterase inhibitors: a paradigm for heterogeneity of Alzheimer's disease? *Trends Pharmacol Sci*. 1996;17:155–160.
17. Iturria-Medina Y, Carbonell FM, Evans AC. Multimodal imaging-based therapeutic fingerprints for optimizing personalized interventions: application to neurodegeneration. *Neuroimage*. 2018;179:40–50.
18. Brown RKJ, Bohnen NI, Wong KK, Minoshima S, Frey KA. Brain PET in suspected dementia: patterns of altered FDG metabolism. *Radiographics*. 2014;34:684–701.
19. Lim SM, Katsifis A, Villemagne VL, et al. The <sup>18</sup>F-FDG PET cingulate island sign and comparison to <sup>123</sup>I-β-CIT SPECT for diagnosis of dementia with Lewy bodies. *J Nucl Med*. 2009;50:1638–1645.
20. Graff-Radford J, Murray JE, Lowe VJ, et al. Dementia with Lewy bodies: basis of cingulate island sign. *Neurology*. 2014;83:801–809.
21. Gjerum L, Frederiksen KS, Henriksen OM, et al. Evaluating 2-[<sup>18</sup>F]FDG-PET in differential diagnosis of dementia using a data-driven decision model. *Neuroimage Clin*. 2020;27:102267.
22. Kantarci K, Boeve BF, Przybelski SA, et al. FDG PET metabolic signatures distinguishing prodromal DLB and prodromal AD. *Neuroimage Clin*. 2021;31:102754.
23. Graff-Radford J, Lesnick TG, Savica R, et al. <sup>18</sup>F-fluorodeoxyglucose positron emission tomography in dementia with Lewy bodies. *Brain Commun*. 2020;2:fcaa040.
24. Montine TJ, Phelps CH, Beach TG, et al. National Institute on Aging–Alzheimer's Association guidelines for the neuropathologic assessment of Alzheimer's disease: a practical approach. *Acta Neuropathol (Berl)*. 2012;123:1–11.
25. Hyman BT, Phelps CH, Beach TG, et al. National Institute on Aging–Alzheimer's Association guidelines for the neuropathologic assessment of Alzheimer's disease. *Alzheimers Dement*. 2012;8:1–13.
26. Franklin EE, Perrin RJ, Vincent B, et al. Brain collection, standardized neuropathologic assessment, and comorbidity in Alzheimer's Disease Neuroimaging Initiative 2 participants. *Alzheimers Dement*. 2015;11:815–822.
27. Uchikado H, Lin W-L, DeLucia MW, Dickson DW. Alzheimer disease with amygdala Lewy bodies: a distinct form of α-synucleinopathy. *J Neuropathol Exp Neurol*. 2006;65:685–697.
28. Parkkinen L, O'Sullivan SS, Collins C, et al. Disentangling the relationship between Lewy bodies and nigral neuronal loss in Parkinson's disease. *J Parkinsons Dis*. 2011;1:277–286.
29. Balsis S, Bengtson JF, Lowe DA, Geraci L, Doody RS. How do scores on the ADAS-Cog, MMSE, and CDR-SOB correspond? *Clin Neuropsychol*. 2015;29:1002–1009.
30. Crane PK, Carle A, Gibbons LE, et al. Development and assessment of a composite score for memory in the Alzheimer's Disease Neuroimaging Initiative (ADNI). *Brain Imaging Behav*. 2012;6:502–516.
31. Gibbons LE, Carle AC, Mackin RS, et al. A composite score for executive functioning, validated in Alzheimer's Disease Neuroimaging Initiative (ADNI) participants with baseline mild cognitive impairment. *Brain Imaging Behav*. 2012;6:517–527.
32. Levin F, Ferreira D, Lange C, et al. Data-driven FDG-PET subtypes of Alzheimer's disease-related neurodegeneration. *Alzheimers Res Ther*. 2021;13:49.
33. PET acquisition. ADNI website. <http://adni.loni.usc.edu/methods/pet-analysis-method/pet-analysis/>. Accessed November 18, 2022.
34. Apostolova I, Lange C, Suppa P, et al. Impact of plasma glucose level on the pattern of brain FDG uptake and the predictive power of FDG PET in mild cognitive impairment. *Eur J Nucl Med Mol Imaging*. 2018;45:1417–1422.
35. López-González FJ, Silva-Rodríguez J, Paredes-Pacheco J, et al. Intensity normalization methods in brain FDG-PET quantification. *Neuroimage*. 2020;222:117229.
36. Hsieh T-C, Lin W-Y, Ding H-J, et al. Sex- and age-related differences in brain FDG metabolism of healthy adults: an SPM analysis. *J Neuroimaging*. 2012;22:21–27.
37. Grothe MJ, Sepulcre J, Gonzalez-Escamilla G, et al. Molecular properties underlying regional vulnerability to Alzheimer's disease pathology. *Brain*. 2018;141:2755–2771.
38. Albin RL, Minoshima S, D'Amato CJ, Frey KA, Kuhl DA, Sima AAF. Fluorodeoxyglucose positron emission tomography in diffuse Lewy body disease. *Neurology*. 1996;47:462–466.
39. Wakabayashi K, Mori F, Takahashi H. Progression patterns of neuronal loss and Lewy body pathology in the substantia nigra in Parkinson's disease. *Parkinsonism Relat Disord*. 2006;12(suppl 2):S92–S98.
40. Brenowitz WD, Hubbard RA, Keene CD, et al. Mixed neuropathologies and associations with domain-specific cognitive decline. *Neurology*. 2017;89:1773–1781.
41. Janvin CC, Larsen JP, Aarsland D, Hugdahl K. Subtypes of mild cognitive impairment in Parkinson's disease: progression to dementia. *Mov Disord*. 2006;21:1343–1349.
42. Torres-García L, Domingues JM, Brandt E, et al. Monitoring the interactions between alpha-synuclein and tau in vitro and in vivo using bimolecular fluorescence complementation. *Sci Rep*. 2022;12:2987.
43. Blazhenets G, Frings L, Sörensen A, Meyer PT. Principal-component analysis-based measures of PET data closely reflect neuropathologic staging schemes. *J Nucl Med*. 2021;62:855–860.
44. Spires-Jones TL, Attems J, Thal DR. Interactions of pathological proteins in neurodegenerative diseases. *Acta Neuropathol (Berl)*. 2017;134:187–205.
45. Yoo HS, Jeong SH, Oh KT, et al. Interrelation of striatal dopamine, brain metabolism and cognition in dementia with Lewy bodies. *Brain*. March 2, 2022 [Epub ahead of print].
46. Oliveira FPM, Walker Z, Walker RWH, et al. <sup>123</sup>I-FP-CIT SPECT in dementia with Lewy bodies, Parkinson's disease and Alzheimer's disease: a new quantitative analysis of autopsy confirmed cases. *J Neurol Neurosurg Psychiatry*. February 4, 2021 [Epub ahead of print].
47. Shim J-H, Baek H-M. Diffusion measure changes of substantia nigra subregions and the ventral tegmental area in newly diagnosed Parkinson's disease. *Exp Neurol*. 2021;30:365–373.
48. Bae YJ, Kim J-M, Sohn C-H, et al. Imaging the substantia nigra in Parkinson disease and other parkinsonian syndromes. *Radiology*. 2021;300:260–278.
49. Ballard C, Grace J, McKeith I, Holmes C. Neuroleptic sensitivity in dementia with Lewy bodies and Alzheimer's disease. *Lancet*. 1998;351:1032–1033.

---

---

# Longitudinal Tau PET Using $^{18}\text{F}$ -Flortaucipir: The Effect of Relative Cerebral Blood Flow on Quantitative and Semiquantitative Parameters

Denise Visser<sup>\*1</sup>, Hayel Tuncel<sup>\*1</sup>, Rik Ossenkoppele<sup>2,3</sup>, Maqsood Yaqub<sup>1</sup>, Emma E. Wolters<sup>1,2</sup>, Tessa Timmers<sup>1,2</sup>, Emma Weltings<sup>1</sup>, Emma M. Coomans<sup>1</sup>, Marijke E. den Hollander<sup>1</sup>, Wiesje M. van der Flier<sup>2,4</sup>, Bart N.M. van Berckel<sup>1</sup>, and Sandeep S.V. Golla<sup>1</sup>

<sup>1</sup>Department of Radiology and Nuclear Medicine, Amsterdam Neuroscience, Vrije Universiteit Amsterdam, Amsterdam UMC, Amsterdam, The Netherlands; <sup>2</sup>Alzheimer Center Amsterdam, Department of Neurology, Amsterdam Neuroscience, Vrije Universiteit Amsterdam, Amsterdam UMC, Amsterdam, The Netherlands; <sup>3</sup>Clinical Memory Research Unit, Lund University, Lund, Sweden; and <sup>4</sup>Department of Epidemiology and Biostatistics, Vrije Universiteit Amsterdam, Amsterdam UMC, Amsterdam, The Netherlands

Semiquantitative PET measures such as SUV ratio (SUVr) have several advantages over quantitative measures, such as practical applicability and relative computational simplicity. However, SUVr may potentially be affected by changes in blood flow, whereas quantitative measures such as nondisplaceable binding potential ( $\text{BP}_{\text{ND}}$ ) are not. For  $^{18}\text{F}$ -flortaucipir PET, the sensitivity of SUVr for changes in blood flow is currently unknown. Therefore, we compared semiquantitative (SUVr) and quantitative ( $\text{BP}_{\text{ND}}$ ) parameters of longitudinal  $^{18}\text{F}$ -flortaucipir PET scans and assessed their vulnerability to changes in blood flow.

**Methods:** Subjects with subjective cognitive decline ( $n = 38$ ) and Alzheimer disease patients ( $n = 24$ ) underwent baseline and 2-y follow-up dynamic  $^{18}\text{F}$ -flortaucipir PET scans.  $\text{BP}_{\text{ND}}$  and relative tracer delivery were estimated using receptor parametric mapping, and SUVr at 80–100 min was calculated. Regional SUVrs were compared with corresponding distribution volume ratio ( $\text{BP}_{\text{ND}} + 1$ ) using paired  $t$  tests. Additionally, simulations were performed to model effects of larger flow changes in different binding categories. **Results:** Results in subjective cognitive decline and Alzheimer disease showed only minor differences between SUVr and  $\text{BP}_{\text{ND}}$  changes over time. Relative tracer delivery changes were small in all groups. Simulations illustrated a variable bias for SUVr depending on the amount of binding. **Conclusion:** SUVr provided an accurate estimate of changes in specific binding for  $^{18}\text{F}$ -flortaucipir over a 2-y follow-up during which changes in flow were small. Notwithstanding, simulations showed that large(r) flow changes may affect  $^{18}\text{F}$ -flortaucipir SUVr. Given that it is currently unknown to what order of magnitude pharmacotherapeutic interventions may induce changes in cerebral blood flow, caution may be warranted when changes in flow are potentially large(r), as in clinical trials.

**Key Words:** Alzheimer disease; dynamic (DVR/ $\text{BP}_{\text{ND}}$ ); longitudinal  $^{18}\text{F}$ -flortaucipir PET; quantification; static (SUVr)

J Nucl Med 2023; 64:281–286  
DOI: 10.2967/jnumed.122.263926

In vivo tau imaging allows for quantification of longitudinal changes in tau accumulation during the course of Alzheimer disease (AD) and can serve as a surrogate outcome measure in clinical trials. Several tau PET tracers are available for this purpose, of which  $^{18}\text{F}$ -flortaucipir is the only one approved by the Food and Drug Administration (1–5).  $^{18}\text{F}$ -flortaucipir PET images can be acquired using static or dynamic scanning protocols. Semiquantitative parameters such as SUV ratio (SUVr) can be derived from such a static PET scan. However, parameters derived from a dynamic PET scan, such as distribution volume ratio (DVR) or nondisplaceable binding potential ( $\text{BP}_{\text{ND}}$ ), are fully quantitative and overall more accurate (6,7). Notwithstanding, dynamic protocols—because of the long scan duration—result in patient movement, lower patient comfort, and lower scanning efficiency. A compromise can be achieved by implementing a dual-time-window protocol in which overall scanning time is reduced by introducing a resting period during the scan while maintaining high quantitative accuracy (8–10).

SUVr has the advantage of practical applicability and relative computational simplicity (2–5), while dynamic imaging studies provide more accurate measurements of specific binding and measure the relative tracer delivery ( $R_1$ ), a proxy for relative cerebral blood flow (“ $^{18}\text{F}$ -flortaucipir  $R_1$ ” section in the supplemental materials available at <http://jnm.snmjournals.org>) (7,11–15).  $R_1$  is important because blood flow changes can occur over time in AD because of disease progression or drug intervention. Longitudinal changes using SUVr may be biased by blood flow changes, whereas quantitative measures ( $\text{BP}_{\text{ND}}$ ) are not (6,16). Currently, for  $^{18}\text{F}$ -flortaucipir the sensitivity of SUVr for changes in blood flow has not been investigated. Therefore, with this study we compared SUVr and DVR/ $\text{BP}_{\text{ND}}$  for  $^{18}\text{F}$ -flortaucipir PET in a 2-y follow-up observational study. Second, we used simulations to investigate how larger changes in  $R_1$  affect SUVr and DVR/ $\text{BP}_{\text{ND}}$ .

## MATERIALS AND METHODS

### Participants

We included 62 subjects from the Amsterdam Dementia Cohort (17,18), of whom 38 were cognitively normal with subjective cognitive decline (SCD) and 24 cognitively impaired (i.e., mild cognitive impairment (MCI) due to AD (19) [ $n = 4$ ] or probable AD dementia (20) [ $n = 20$ ], grouped into 1 MCI/AD group).

Received Jan. 28, 2022; revision accepted Aug. 11, 2022.

For correspondence or reprints, contact Denise Visser ([d.visser2@amsterdamumc.nl](mailto:d.visser2@amsterdamumc.nl)).

\*Contributed equally to this work.

Published online Oct. 20, 2022.

Immediate Open Access: Creative Commons Attribution 4.0 International License (CC BY) allows users to share and adapt with attribution, excluding materials credited to previous publications. License: <https://creativecommons.org/licenses/by/4.0/>. Details: <http://jnm.snmjournals.org/site/misc/permission.xhtml>.

COPYRIGHT © 2023 by the Society of Nuclear Medicine and Molecular Imaging.

**TABLE 1**  
Demographics of Study Population

Demographic	SCD (n = 38)	AD (n = 24)
Sex (n)		
Female	16	11
Male	22	13
Age at baseline (y)	65 ± 7	66 ± 7
Age at follow-up (y)	67 ± 7	68 ± 7
Time between PET scans (y)	2.1 ± 0.3*	2.2 ± 0.3*
MMSE at baseline	29 ± 1*	24 ± 3*
Aβ-positive <sup>†</sup> at baseline (n)	12/38*	24/24*
Aβ-positive <sup>†</sup> at follow-up (n)	16/38*	NA
APOE4 allele carriers (n)	12/38*	17/22 (2 unknown)*

\*Significant differences ( $P < 0.05$ ) between diagnostic groups.

<sup>†</sup>SCD subjects were classified as Aβ-positive as evidenced by substantial Aβ pathology after 50- to 70-min SUVR <sup>18</sup>F-florbetapir Aβ PET scan visual assessment, and mild cognitive impairment/AD patients were classified as Aβ-positive as evidenced by cerebrospinal fluid biomarkers for AD (i.e., cerebrospinal fluid Aβ1-42 < 813 ng/L) or positive Aβ PET (<sup>18</sup>F-PiB or <sup>18</sup>F-florbetaben) findings by visual assessment.

MMSE = mini mental state examination; NA = not available.

Mean ± SD are provided, unless otherwise indicated.

Twelve of 38 SCD subjects were classified as amyloid-β (Aβ) PET-positive (<sup>18</sup>F-florbetapir visual assessment (21)). All MCI/AD patients were classified as Aβ-positive by cerebrospinal fluid biomarkers (i.e., cerebrospinal fluid Aβ1-42 < 813 ng/L (22)) or a Aβ PET scan (<sup>11</sup>C-PiB or <sup>18</sup>F-florbetaben) by visual assessment (23,24).

The study protocol was approved by the Medical Ethics Review Committee of the Amsterdam UMC VU Medical center. All patients provided written informed consent before study participation.

### Imaging

All subjects underwent 2 dynamic <sup>18</sup>F-florbetapir PET scans, acquired on a Philips Ingenuity TF-64 PET/CT scanner, with a time period of 2.1 ± 0.3 y (SCD) or 2.2 ± 0.3 y (AD) between both scanning sessions. For SCD subjects, each scanning session consisted of 2 dynamic PET scans of 60 and 50 min, respectively, with a 20-min break in between (14,25). For AD patients, each scanning session consisted of 2 dynamic PET scans of 30 min and 20 min, respectively, with a 50-min break in between (9).

BP<sub>ND</sub>, R<sub>1</sub>, and SUVR at 80–100 min were extracted in a priori-defined regions of interest (ROIs) in subject space using the Hammers and Svarer templates: Braak I/II (entorhinal), Braak III/IV (limbic), and Braak V/VI (neocortical). These ROIs align with neuropathologically defined regions (26) and are informative for tau PET in AD (27–30).

For each parameter and ROI, we calculated percentage change using the following formula (DVR [BP<sub>ND</sub> + 1] or SUVR associated with the follow-up and baseline scans, respectively):

$$\text{Percentage change} = (\text{follow-up/baseline} - 1) \times 100\%$$

We repeated all analyses with partial-volume-corrected data using the iterative deconvolution method, as described previously (31–33).

**TABLE 2**  
<sup>18</sup>F-Flortaucipir DVR, SUVR and R<sub>1</sub> Values for SCD Subjects and AD Patients

	DVR			SUVR at 80–100 min			R <sub>1</sub>		
	BL	FU	%change	BL	FU	%change	BL	FU	%change
SCD (n = 38)									
Braak I/II	1.039 (0.121)	1.066* (0.133)	2.56 <sup>†</sup> (2.85)	1.134 <sup>‡</sup> (0.159)	1.154 <sup>‡  </sup> (0.158)	1.85 (3.27)	0.708 (0.041)	0.714 (0.049)	0.74 (3.96)
Braak III/IV	1.045 (0.075)	1.075* (0.098)	2.82 (2.54)	1.102 <sup>‡</sup> (0.103)	1.130* <sup>‡</sup> (0.118)	2.47 (2.64)	0.836 (0.036)	0.842 (0.043)	0.79 (2.75)
Braak V/VI	1.042 (0.057)	1.067* (0.076)	2.33 (2.77)	1.076 <sup>‡</sup> (0.077)	1.096* <sup>‡</sup> (0.093)	2.17 (3.29)	0.926 (0.043)	0.930 (0.049)	0.47 (2.67)
AD (n = 24)									
Braak I/II	1.277 (0.146)	1.321* (0.157)	3.48 (4.16)	1.426 <sup>‡</sup> (0.192)	1.470 <sup>‡  </sup> (0.194)	3.25 (5.26)	0.713 (0.047)	0.706 (0.053)	−0.87 (5.26)
Braak III/IV	1.256 (0.147)	1.341* (0.185)	6.61 <sup>†</sup> (5.63)	1.367 <sup>‡</sup> (0.190)	1.471* <sup>‡</sup> (0.229)	7.52 (6.66)	0.835 (0.045)	0.821 <sup>§</sup> (0.040)	−1.62 (3.71)
Braak V/VI	1.284 (0.222)	1.379* (0.260)	7.25 (6.85)	1.382 <sup>‡</sup> (0.281)	1.495* <sup>‡</sup> (0.316)	8.21 (8.03)	0.904 (0.051)	0.883 <sup>  </sup> (0.055)	−2.28 (3.67)

\* $P < 0.001$ , baseline vs. follow-up.

<sup>†</sup> $P < 0.05$ , percentage change in DVR vs. percentage change in SUVR.

<sup>‡</sup> $P < 0.001$ , DVR vs. SUVR.

<sup>§</sup> $P < 0.05$ , baseline vs. follow-up.

<sup>||</sup> $P < 0.01$ , baseline vs. follow-up.

BL = baseline; FU = follow-up.

Mean ± SD are provided.

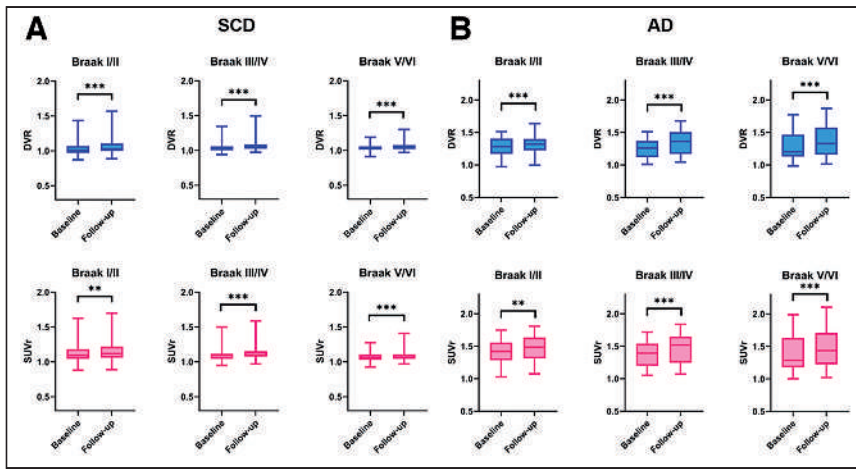


**FIGURE 1.** Box plots of regional DVR (upper row) and SUVR at 80–100 min (lower row) in SCD (A) and AD (B). \*\* $P < 0.01$ . \*\*\* $P < 0.001$ .

### Statistical Analyses

To allow for direct comparison with SUVRs, DVR was used for all analyses. Paired  $t$  tests were performed to assess differences between parameters and time points. Pearson correlation coefficients were computed to assess the correlation between percentage change in SUVR and DVR (all ROIs combined). Bland–Altman analyses were performed to assess bias and agreement between percentage change in SUVR and DVR (all ROIs combined). Analyses were performed in R software, version 4.0.2, and GraphPad Prism, version 9.1.0.

To explore whether the required sample size for (theoretic) future trials would differ when either quantitative or semiquantitative methods are used, sample sizes were calculated using GPower, version 3.1.9.7. For these analyses, we used a range of 0.5%–10% expected change in tracer retention over time, to inform on longitudinal study designs in the context of  $^{18}\text{F}$ -flortaucipir. Sample sizes were calculated for SUVR and DVR, for all 3 ROIs (Braak I/II, III/IV, and V/VI). The differences between 2 dependent means (matched pairs) was calculated, with an  $\alpha$  (error probability) of 0.05 and a power ( $1 - \beta$  error probability) of 0.80. To adhere to the typical duration of clinical trials in AD, we calculated percentage change over an 18-mo period and used those SDs as input for the sample size calculations.

### Simulations

Details on the methods used for simulations can be found in the Methods section of the supplemental materials.

### RESULTS

Patient characteristics are shown in Table 1. In both AD and SCD,  $^{18}\text{F}$ -flortaucipir SUVR were higher than DVR for all regions and at both time points (baseline and follow-up, all  $P < 0.001$ ). Respective DVR, SUVR, and  $R_1$  values are shown in Table 2 (SCD subjects and AD patients) and Supplemental Tables 2 and 3 ( $\text{A}\beta$ -negative and -positive SCD subjects, respectively). The percentage overestimation of SUVR relative to DVR, for all regions and at both time points, is presented in Supplemental Table 4. Annualized percentage change in DVR and SUVR is presented in Supplemental Tables 5 and 6. No significant correlations between DVR or SUVR and  $R_1$  were observed in either SCD or AD patients (Supplemental Fig. 1). Partial-volume-corrected data yielded essentially similar results; therefore, only noncorrected data will be presented further in the article.

#### Differences in $^{18}\text{F}$ -Flortaucipir DVR, SUVR, and $R_1$

**SCD Subjects.** DVR increased at follow-up in all regions (all  $P < 0.001$ ), with the largest increase found in Braak III/IV

(1.045–1.075,  $2.82\% \pm 2.54\%$ ) (Table 2; Fig. 1A; Supplemental Fig. 2A). SUVR also significantly increased at follow-up in all regions (all  $P < 0.003$ ). The largest increase was found in Braak III/IV (1.102–1.130,  $2.47\% \pm 2.64\%$ ) (Table 2; Figs. 1C and 2C). Percentage change was significantly lower for SUVR than for DVR in Braak I/II (SUVR,  $1.85\% \pm 3.27\%$ , vs. DVR,  $2.56\% \pm 2.85\%$ ;  $P = 0.048$ ). Braak III/IV and V/VI did not show any statistically significant differences between percentage change in DVR and SUVR (Table 2; Fig. 2). Taking all regions together, the correlation coefficient between percentage change in SUVR and DVR was 0.83 ( $P < 0.001$ ), and the bias as provided by Bland–Altman analysis was  $0.41 \pm 1.72$  (Figs. 3A and 3C). For  $R_1$ , no significant decreases at follow-up were found in any region (Table 2).

**AD Patients.** DVR increased at follow-up in all regions (all  $P < 0.001$ ), with the largest increase found in Braak V/VI (1.284–1.379,  $7.25\% \pm 6.85\%$ ) (Table 2; Fig. 1B; Supplemental Fig. 2B). SUVR also increased at follow-up in all regions (all  $P < 0.009$ ). Like DVR, the largest increase was found in Braak V/VI (1.382–1.495,  $8.21\% \pm 8.03\%$ ) (Supplemental Table 3; Fig. 1D; Supplemental Fig. 2D). Percentage change was higher for SUVR than for DVR in Braak III/IV (SUVR,  $7.52\% \pm 6.66\%$ , vs. DVR,  $6.61\% \pm 5.63\%$ ;  $P = 0.047$ ). No statistically significant differences between percentage change in SUVR and DVR were found for any other region (Table 2; Fig. 2). Taking all regions together, the correlation coefficient between percentage change in SUVR and DVR was 0.94 ( $P < 0.001$ ), and the bias as provided by Bland–Altman analysis was  $-0.55 \pm 2.56$  (Figs. 3B and 3D). For  $R_1$ , significant decreases at follow-up were found in Braak III/IV (0.835–0.821,  $-1.62\% \pm 3.71\%$ ,  $P = 0.040$ ) and V/VI (0.904–0.883,  $-2.28\% \pm 3.67\%$ ,  $P = 0.003$ ) (Table 2).

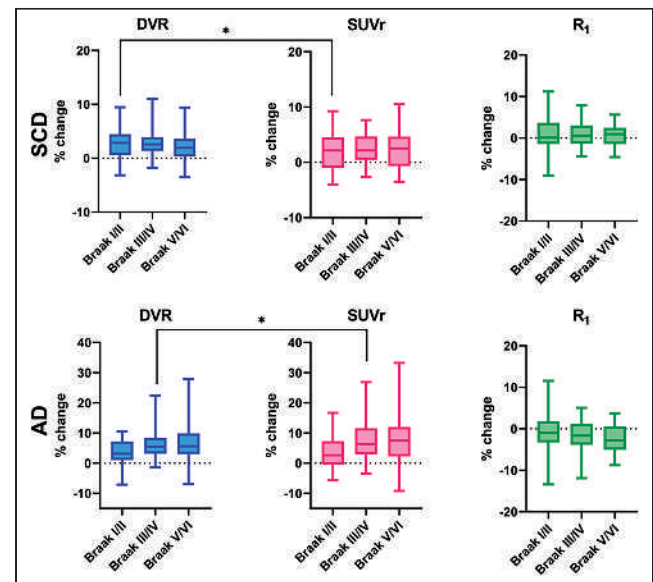


**FIGURE 2.** Regional percentage changes in DVR, SUVR at 80–100 min and  $R_1$  for SCD subjects and AD patients. \* $P < 0.05$ .

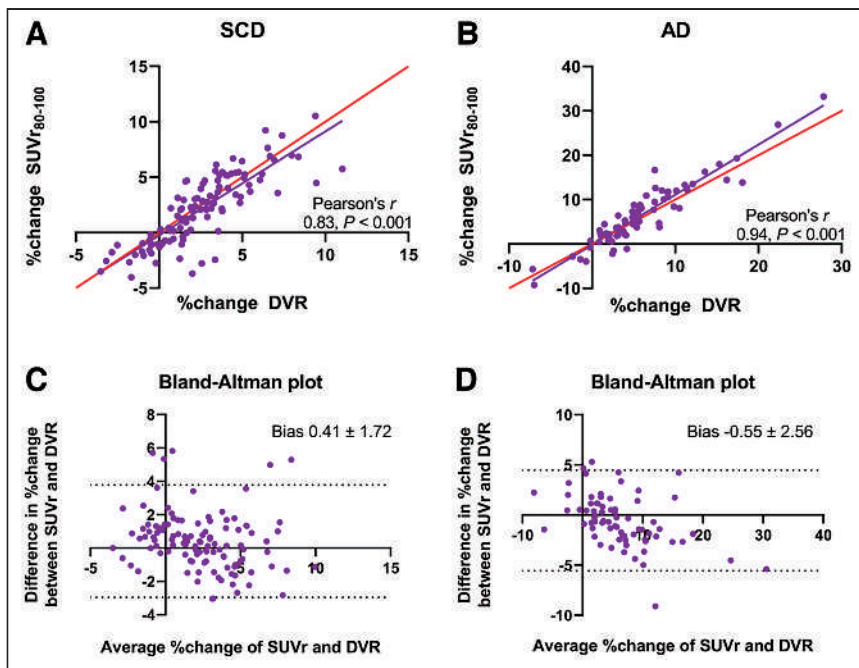


**FIGURE 3.** (A and B) Correlation plot of percentage change in DVR vs. SUVr at 80–100 min ( $SUV_{80-100}$ ) in SCD (A) and AD (B), in which red line represents line of identity. (C and D) Bland-Altman plot of percentage change in DVR vs. SUVr at 80–100 min in SCD (C) and AD (D).

### Sample Size Calculations

Large differences in required sample sizes were observed for small effect sizes, with the largest differences being between methods in the AD group (Supplemental Table 7). However, with larger effect sizes (in line with expectations in clinical trials), differences in required sample size between the 2 methods became negligible for both SCD and AD (Supplemental Table 7).

### Simulations

Simulations with 5% coefficient of variance showed results similar to those for the simulated time–activity curves obtained with almost no noise (0.05% coefficient of variance). Therefore, to mimic real cohort data, only the results from time–activity curves with a 5% coefficient of variance were reported.

Simulations revealed that under the SCD (almost no binding) and low-binding AD patient conditions, an inverse relation was observed; that is, with increasing flow, a decreasing bias for SUVr (with respect to true DVR) was observed (Fig. 4). A similar behavior was also observed under the medium-binding AD patient condition, but to a

lesser extent. In the high-binding condition for AD patients, however, a relatively smaller effect of flow was observed on SUVr, implying that SUVrs remained relatively constant irrespective of the change in flow. In the case of DVR, no effect of flow was observed with any of the conditions (Fig. 4).

### DISCUSSION

We compared changes in  $^{18}\text{F}$ -flortaucipir specific binding using SUVr and DVR. In a 2-y longitudinal study, changes in  $^{18}\text{F}$ -flortaucipir DVR and SUVr were comparable in all patient groups. Only small changes in  $R_1$  occurred during this period, but these most likely contributed to the lack of difference between DVR and SUVr. However,

simulations demonstrated marked differences between DVR and SUVr when large( $r$ ) changes in  $R_1$  were introduced. In addition, these differences between DVR and SUVr were shown to be dependent on the underlying level of tau pathology.

The most important finding in this study was the lack of major differences in the percentage change between  $^{18}\text{F}$ -flortaucipir DVR and SUVr in a 2-y observational study. Congruently, sample size calculations based on these data to inform future trials showed negligible differences between methods. Unlike a previous study using  $^{11}\text{C}$ -PiB (6), this finding indicates that  $^{18}\text{F}$ -flortaucipir SUVr provides an accurate estimate of change in specific binding in both patient groups. There are several possible reasons for the differences in findings between the 2 studies. First, an important factor contributing to our findings could be the relatively small or nonexistent  $R_1$  differences in this cohort. Previously, using  $^{11}\text{C}$ -PiB (6), we reported larger  $R_1$  changes in AD patients, which induced a large difference between SUVr and  $BP_{ND}$ . This effect might perhaps indicate that  $^{11}\text{C}$ -PiB is more sensitive to changes in  $R_1$  than is  $^{18}\text{F}$ -flortaucipir. However, flow sensitivity may also depend on the scanning interval relative

to tracer kinetics, as was seen previously for  $^{11}\text{C}$ -PiB (6). Similarly, this is the scenario for  $^{18}\text{F}$ -flortaucipir, and we therefore cannot directly compare the 2 tracers in this respect. Second, it has been reported that accumulation of tau pathology is a slowly developing process, with annual percentage changes of about 0.5%–3% in  $A\beta$ -positive cognitively unimpaired subjects and up to 3%–10% in  $A\beta$ -positive cognitively impaired subjects (34–37). The annual percentages change in the present study was generally comparable in SCD subjects (on average, 1.08% SUVr and 1.28% DVR) and slightly lower in AD

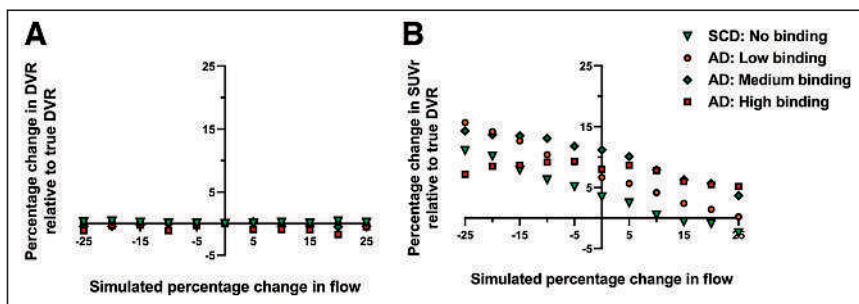


**FIGURE 4.** Percentage change in DVR (A) and SUVr (B) at 80–100 min relative to true DVR values as function of simulated flow changes for each binding condition.



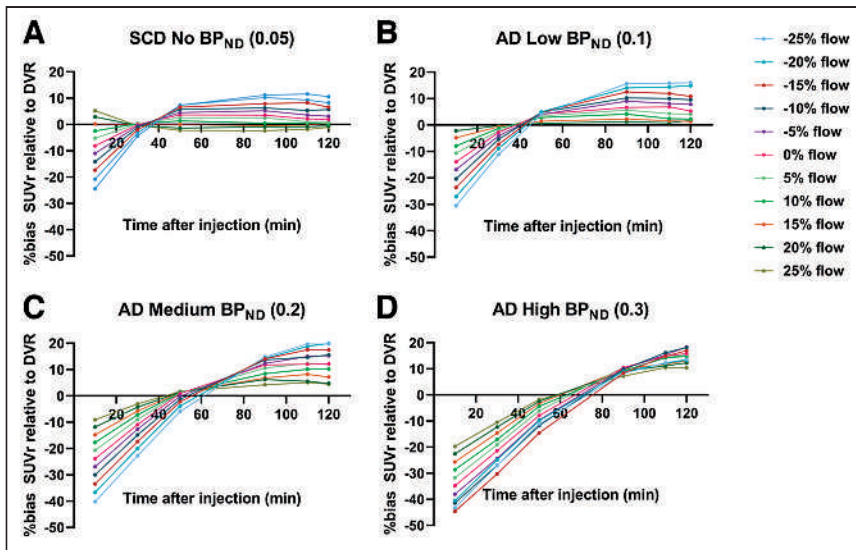


**FIGURE 5.** Percentage bias in SUVr relative to true DVRs as function of SUVr time intervals for simulated flow condition for SCD (almost no binding condition) (A), AD with low binding condition (B), AD with medium binding condition (C), and AD with high binding condition (D). Key illustrates different increases or decreases in flow.

subject (2.73% SUVr and 2.52% DVR). The test–retest repeatability of  $^{18}\text{F}$ -flortaucipir, as reported previously (38), lies at around 1.98% (0.78–3.58) for DVR and 3.05% (1.28–5.52) for SUVr at 80–100 min. Although the test–retest repeatability was significantly better for DVR (38), annual percentage changes as found in the present study still fall within 1 SD of the test–retest repeatability for both DVR and SUVr, suggesting that observed changes might be too small to detect differences between analytic methods. Finally, differences with respect to tracer target affinity, isotope ( $^{11}\text{C}$  vs.  $^{18}\text{F}$ ), and pharmacokinetic behavior might have introduced differences that caused the differences in results.

Currently, the effects of pharmacotherapeutic interventions on cerebral blood flow are unclear. Therefore, we performed simulations to investigate the impact of large(r) changes in relative cerebral blood flow/ $R_1$  on the accuracy of SUVr and DVR. The bias with SUVr relative to DVR was different for each flow condition, and this bias was additionally influenced by the underlying tau load, with decreasing bias in cases of low tau load/binding or constant bias for high tau load/binding. Depending on the underlying tau load, regional changes in flow resulted in variable changes in SUVr, which was not the scenario with DVR. Similar findings were previously observed using  $^{18}\text{F}$ -cyclofoxy (39).

On top of flow condition and the underlying tau load, the choice of SUVr time interval also effected the accuracy, which was again different for different binding conditions. A previous study found large positive biases for SUVr using different time intervals when compared with dynamic methods (8). Furthermore, Golla et al. (8) observed that the bias in SUVr for a specific scanning interval is not constant but is dependent on the underlying tau load and the choice of SUVr scanning interval. This has important implications, since scanning intervals for static protocols are often not strictly enforced; thus, deviations in scanning intervals between static and longitudinal scans are common. These discrepancies will increase variability and uncertainty, which will increase required sample sizes for SUVr. Differing underlying tau load in the sample studied will only increase the bias in SUVr further. It is worth noting that,

in the current study, SUVr was extracted from the dynamically acquired data. In addition, scanning interval was strictly enforced in the context of the 2 scanning sessions within the dynamic protocol. For both these reasons, SUVr in this study was not affected by deviations in scanning, and the results may therefore be too optimistic in this respect.

The discrepancies between methods using simulations may have important implications for longitudinal  $^{18}\text{F}$ -flortaucipir studies and intervention studies. Our findings imply that SUVr is not the parameter of preference when large variations in blood flow are expected, although to what order of magnitude remains to be elucidated. A consideration to address when using repeated dynamic scans is potential selection bias, because severely affected patients might not be able to undergo such a demanding procedure. In patients with moderate to severe AD, this is indeed debatable. However, pharmacotherapeutic trials currently show a shift in target population, primarily including patients with mild, prodromal, or preclinical autosomal-dominant AD. Those patients can tolerate the longer dynamic scan procedures.

$^{18}\text{F}$ -flortaucipir is useful for investigating pathologic tau load differences between SCD subjects and AD patients. However, in an early-dementia cohort for which we do not expect specific binding in the neocortex, measurement of tau deposition shows large variability. Indeed, in such a sample, 64% of the cortical signal variability can be explained by off-target binding (40). Partial-volume correction does not completely explain the variability in the cortical signal. Therefore, the variability in the signal in cohorts with low tau deposition related to off-target binding should be considered when examining early tau deposition using  $^{18}\text{F}$ -flortaucipir.

## CONCLUSION

Static scanning protocols provide accurate estimates of specific  $^{18}\text{F}$ -flortaucipir binding in observational studies. Dynamic scanning protocols and fully quantitative data analysis methods are preferred when large(r) flow changes in the brain are expected (such as in later disease stages or pharmacotherapeutic interventions). Use of semiquantitative methods in such conditions carries the inherent risk that potential effective therapeutic interventions are discarded, especially when expected effect sizes are small.

## DISCLOSURE

Research at the Amsterdam Alzheimer Center is part of the neurodegeneration program of Amsterdam Neuroscience; the Amsterdam Alzheimer Center is supported by Alzheimer Nederland and Stichting VUmc funds.  $^{18}\text{F}$ -flortaucipir PET scans were made possible by Avid Radiopharmaceuticals Inc. This study was funded by a ZonMW Memorabel grant. Wiesje Van der Flier holds the Pasmann chair and received grant support from ZonMW, NWO, EU-FP7, Alzheimer Nederland, CardioVascular Onderzoek Nederland, Stichting Dioraphte, Gieskes-Strijbis Fonds, Boehringer Ingelheim, Piramal Neuroimaging, Roche BV, Janssen Stellar, and Combinostics. All funding is paid to the institution. Bart van Berckel has received research support from EU-FP7, CTMM, ZonMw, NOW,

and Alzheimer Nederland. Bart van Berckel has performed contract research for Rodin, IONIS, AVID, Eli Lilly, UCB, DIAN-TUI, and Janssen; was a speaker at a symposium organized by Springer Healthcare; has a consultancy agreement with IXICO for the reading of PET scans; is a trainer for GE; and receives financial compensation only from Amsterdam UMC. No other potential conflict of interest relevant to this article was reported.

## ACKNOWLEDGMENTS

We kindly thank all participants for their contribution. We thank Ronald Boellaard for sharing his knowledge and thoughts about the project.

## KEY POINTS

**QUESTION:** How do the semiquantitative (SUVr) and quantitative ( $R_1$ ,  $BP_{ND}$ ) parameters of longitudinal  $^{18}\text{F}$ -flortaucipir PET scans, and their vulnerability to changes in blood flow, compare in subjects along the AD continuum?

**PERTINENT FINDINGS:** In a 2-y longitudinal  $^{18}\text{F}$ -flortaucipir PET study including 38 subjects with SCD and 24 patients with AD, relative cerebral blood flow changes ( $R_1$ ) were small, and semiquantitative (SUVr) and quantitative ( $BP_{ND}$ ) parameters yielded highly similar estimates of specific binding. However, simulations showed that large(r) flow changes may potentially affect  $^{18}\text{F}$ -flortaucipir SUVr.

**IMPLICATIONS FOR PATIENT CARE:** Given that it is currently unknown to what order of magnitude pharmacotherapeutic interventions may induce changes in cerebral blood flow, caution may be warranted when changes in flow are large(r), and DVR/ $BP_{ND}$  may be preferred under such conditions to ensure representative quantification of  $^{18}\text{F}$ -flortaucipir PET images.

## REFERENCES

- Jie CV, Treyer V, Schibli R, Mu L. Tauvid<sup>TM</sup>: the first FDA-approved PET tracer for imaging tau pathology in Alzheimer's disease. *Pharmaceuticals (Basel)*. 2021;14:110.
- Chien DT, Bahri S, Szardenings AK, et al. Early clinical PET imaging results with the novel PHF-tau radioligand [ $^{18}\text{F}$ ]-T807. *J Alzheimers Dis*. 2013;34:457–468.
- Leuzy A, Chiotis K, Lemoine L, et al. Tau PET imaging in neurodegenerative tauopathies: still a challenge. *Mol Psychiatry*. 2019;24:1112–1134.
- Johnson KA, Schultz A, Betensky RA, et al. Tau positron emission tomographic imaging in aging and early Alzheimer disease. *Ann Neurol*. 2016;79:110–119.
- Xia CF, Arteaga J, Chen G, et al. [ $^{18}\text{F}$ ] T807, a novel tau positron emission tomography imaging agent for Alzheimer's disease. *Alzheimers Dement*. 2013;9:666–676.
- van Berckel AGN, Ossenkuppele R, Tolboom N, et al. Longitudinal amyloid imaging using  $^{11}\text{C}$ -PiB: methodologic considerations. *J Nucl Med*. 2013;54:1570–1576.
- Ossenkuppele R, Prins ND, Van Berckel BN. Amyloid imaging in clinical trials. *Alzheimers Res Ther*. 2013;5:36.
- Golla SS, Wolters EE, Timmers T, et al. Parametric methods for [ $^{18}\text{F}$ ] flortaucipir PET. *J Cereb Blood Flow Metab*. 2020;40:365–373.
- Tuncel H, Visser D, Yaqub M, et al. Effect of shortening the scan duration on quantitative accuracy of [ $^{18}\text{F}$ ] flortaucipir studies. *Mol Imaging Biol*. 2021;23:604–613.
- Heeman F, Yaqub M, Lopes Alves I, et al. Optimized dual-time-window protocols for quantitative [ $^{18}\text{F}$ ]flutemetamol and [ $^{18}\text{F}$ ]florbetaben PET studies. *EJNMMI Res*. 2019;9:32.
- Rodríguez-Vieitez E, Leuzy A, Chiotis K, Saint-Aubert L, Wall A, Nordberg A. Comparability of [ $^{18}\text{F}$ ] THK5317 and [ $^{11}\text{C}$ ] PIB blood flow proxy images with [ $^{18}\text{F}$ ] FDG positron emission tomography in Alzheimer's disease. *J Cereb Blood Flow Metab*. 2017;37:740–749.
- Peretti DE, García DV, Reesink FE, et al. Diagnostic performance of regional cerebral blood flow images derived from dynamic PIB scans in Alzheimer's disease. *EJNMMI Res*. 2019;9:59.
- Chen YJ, Rosario BL, Mowrey W, et al. Relative  $^{11}\text{C}$ -PiB delivery as a proxy of relative CBF: quantitative evaluation using single-session  $^{15}\text{O}$ -water and  $^{11}\text{C}$ -PiB PET. *J Nucl Med*. 2015;56:1199–1205.
- Visser D, Wolters EE, Verfaillie SC, et al. Tau pathology and relative cerebral blood flow are independently associated with cognition in Alzheimer's disease. *Eur J Nucl Med Mol Imaging*. 2020;47:3165–3175.
- Ottoy J, Verhaeghe J, Niemantsverdriet E, et al.  $^{18}\text{F}$ -FDG PET, the early phases and the delivery rate of  $^{18}\text{F}$ -AV45 PET as proxies of cerebral blood flow in Alzheimer's disease: validation against  $^{15}\text{O}$ -H<sub>2</sub>O PET. *Alzheimers Dement*. 2019;15:1172–1182.
- Ottoy J, Verhaeghe J, Niemantsverdriet E, Engelborghs S, Stroobants S, Staelens S. A simulation study on the impact of the blood flow-dependent component in [ $^{18}\text{F}$ ] AV45 SUVR in Alzheimer's disease. *PLoS One*. 2017;12:e0189155.
- van der Flier WM, Scheltens P. Amsterdam dementia cohort: performing research to optimize care. *J Alzheimers Dis*. 2018;62:1091–1111.
- van der Flier WM, Pijnenburg YA, Prins N, et al. Optimizing patient care and research: the Amsterdam Dementia Cohort. *J Alzheimers Dis*. 2014;41:313–327.
- Albert MS, DeKosky ST, Dickson D, et al. The diagnosis of mild cognitive impairment due to Alzheimer's disease: recommendations from the National Institute on Aging-Alzheimer's Association workgroups on diagnostic guidelines for Alzheimer's disease. *Alzheimers Dement*. 2011;7:270–279.
- McKhann GM, Knopman DS, Chertkow H, et al. The diagnosis of dementia due to Alzheimer's disease: recommendations from the National Institute on Aging-Alzheimer's Association workgroups on diagnostic guidelines for Alzheimer's disease. *Alzheimers Dement*. 2011;7:263–269.
- Golla SS, Verfaillie SC, Boellaard R, et al. Quantification of [ $^{18}\text{F}$ ] florbetapir: a test–retest tracer kinetic modelling study. *J Cereb Blood Flow Metab*. 2019;39:2172–2180.
- Tijms BM, Willems EA, Zwan MD, et al. Unbiased approach to counteract upward drift in cerebrospinal fluid amyloid- $\beta$  1-42 analysis results. *Clin Chem*. 2018;64:576–585.
- Seibyl J, Catafau AM, Barthelemy H, et al. Impact of training method on the robustness of the visual assessment of  $^{18}\text{F}$ -florbetaben PET scans: results from a phase-3 study. *J Nucl Med*. 2016;57:900–906.
- Zwan M, van Harten A, Ossenkuppele R, et al. Concordance between cerebrospinal fluid biomarkers and [ $^{11}\text{C}$ ] PIB PET in a memory clinic cohort. *J Alzheimers Dis*. 2014;41:801–807.
- Golla SS, Timmers T, Ossenkuppele R, et al. Quantification of tau load using [ $^{18}\text{F}$ ] AV1451 PET. *Mol Imaging Biol*. 2017;19:963–971.
- Braak H, Braak E. Staging of Alzheimer's disease-related neurofibrillary changes. *Neurobiol Aging*. 1995;16:271–278.
- Schwarz AJ, Yu P, Miller BB, et al. Regional profiles of the candidate tau PET ligand  $^{18}\text{F}$ -AV-1451 recapitulate key features of Braak histopathological stages. *Brain*. 2016;139:1539–1550.
- Timmers T, Ossenkuppele R, Wolters EE, et al. Associations between quantitative [ $^{18}\text{F}$ ] flortaucipir tau PET and atrophy across the Alzheimer's disease spectrum. *Alzheimers Res Ther*. 2019;11:60.
- Wolters EE, Ossenkuppele R, Verfaillie SC, et al. Regional [ $^{18}\text{F}$ ] flortaucipir PET is more closely associated with disease severity than CSF p-tau in Alzheimer's disease. *Eur J Nucl Med Mol Imaging*. 2020;47:2866–2878.
- Schöll M, Lockhart SN, Schonhaut DR, et al. PET imaging of tau deposition in the aging human brain. *Neuron*. 2016;89:971–982.
- Teo B-K, Seo Y, Bacharach SL, et al. Partial-volume correction in PET: validation of an iterative postreconstruction method with phantom and patient data. *J Nucl Med*. 2007;48:802–810.
- Christian BT, Vandehey NT, Floberg JM, Mistretta CA. Dynamic PET denoising with HYPR processing. *J Nucl Med*. 2010;51:1147–1154.
- Golla SS, Lubberink M, van Berckel BN, Lammertsma AA, Boellaard R. Partial volume correction of brain PET studies using iterative deconvolution in combination with HYPR denoising. *EJNMMI Res*. 2017;7:36.
- Pontecorvo MJ, Devous MD, Kennedy I, et al. A multicentre longitudinal study of flortaucipir ( $^{18}\text{F}$ ) in normal ageing, mild cognitive impairment and Alzheimer's disease dementia. *Brain*. 2019;142:1723–1735.
- Jack CR Jr, Wiste HJ, Schwarz CG, et al. Longitudinal tau PET in ageing and Alzheimer's disease. *Brain*. 2018;141:1517–1528.
- Harrison TM, La Joie R, Maass A, et al. Longitudinal tau accumulation and atrophy in aging and Alzheimer disease. *Ann Neurol*. 2019;85:229–240.
- Cho H, Baek MS, Lee HS, Lee JH, Ryu YH, Lyoo CH. Principal components of tau positron emission tomography and longitudinal tau accumulation in Alzheimer's disease. *Alzheimers Res Ther*. 2020;12:114.
- Timmers T, Ossenkuppele R, Visser D, et al. Test–retest repeatability of [ $^{18}\text{F}$ ] flortaucipir PET in Alzheimer's disease and cognitively normal individuals. *J Cereb Blood Flow Metab*. 2020;40:2464–2474.
- Carson RE, Channing MA, Blasberg RG, et al. Comparison of bolus and infusion methods for receptor quantitation: application to [ $^{18}\text{F}$ ] cyclofoxy and positron emission tomography. *J Cereb Blood Flow Metab*. 1993;13:24–42.
- Baker SL, Harrison TM, Maass A, La Joie R, Jagust WJ. Effect of off-target binding on  $^{18}\text{F}$ -flortaucipir variability in healthy controls across the life span. *J Nucl Med*. 2019;60:1444–1451.

---

---

# Investigating Tau and Amyloid Tracer Skull Binding in Studies of Alzheimer Disease

Shaney Flores<sup>1</sup>, Charles D. Chen<sup>1</sup>, Yi Su<sup>2</sup>, Aylin Dincer<sup>1</sup>, Sarah J. Keefe<sup>1</sup>, Nicole S. McKay<sup>1</sup>, Angela M. Paulick<sup>1</sup>, Gloria Guzman Perez-Carrillo<sup>1</sup>, Liang Wang<sup>1</sup>, Russ C. Hornbeck<sup>1</sup>, Manu Goyal<sup>1,3,4</sup>, Andrei Vlassenko<sup>1,3</sup>, Sally Schwarz<sup>1</sup>, Michael L. Nickels<sup>1</sup>, Dean F. Wong<sup>1</sup>, Zhude Tu<sup>1</sup>, Jonathan E. McConathy<sup>5</sup>, John C. Morris<sup>3,4</sup>, Tammie L.S. Benzinger<sup>1,4</sup>, and Brian A. Gordon<sup>1,4</sup>

<sup>1</sup>Department of Radiology, Washington University School of Medicine, St. Louis, Missouri; <sup>2</sup>Banner Alzheimer's Institute, Phoenix, Arizona; <sup>3</sup>Department of Neurology, Washington University School of Medicine, St. Louis, Missouri; <sup>4</sup>Charles F. and Joanne Knight Alzheimer Disease Research Center, Washington University School of Medicine, St. Louis, Missouri; and <sup>5</sup>University of Alabama at Birmingham, Birmingham, Alabama

Off-target binding of [<sup>18</sup>F]flortaucipir (FTP) can complicate quantitative PET analyses. An underdiscussed off-target region is the skull. Here, we characterize how often FTP skull binding occurs, its influence on estimates of Alzheimer disease pathology, its potential drivers, and whether skull uptake is a stable feature across time and tracers. **Methods:** In 313 cognitively normal and mildly impaired participants, CT scans were used to define a skull mask. This mask was used to quantify FTP skull uptake. Skull uptake of the amyloid- $\beta$  PET tracers [<sup>18</sup>F]florbetapir and [<sup>11</sup>C]Pittsburgh compound B ( $n = 152$ ) was also assessed. Gaussian mixture modeling defined abnormal levels of skull binding for each tracer. We examined the relationship of continuous bone uptake to known off-target binding in the basal ganglia and choroid plexus as well as skull density measured from the CT. Finally, we examined the confounding effect of skull binding on pathologic quantification. **Results:** We found that 50 of 313 (~16%) FTP scans had high levels of skull signal. Most were female ( $n = 41$ , 82%), and in women, lower skull density was related to higher FTP skull signal. Visual reads by a neuroradiologist revealed a significant relationship with hyperostosis; however, only 21% of women with high skull binding were diagnosed with hyperostosis. FTP skull signal did not substantially correlate with other known off-target regions. Skull uptake was consistent over longitudinal FTP scans and across tracers. In amyloid- $\beta$ -negative, but not -positive, individuals, FTP skull binding impacted quantitative estimates in temporal regions. **Conclusion:** FTP skull binding is a stable, participant-specific phenomenon and is unrelated to known off-target regions. Effects were found primarily in women and were partially related to lower bone density. The presence of [<sup>11</sup>C]Pittsburgh compound B skull binding suggests that defluorination does not fully explain FTP skull signal. As signal in skull bone can impact quantitative analyses and differs across sex, it should be explicitly addressed in studies of aging and Alzheimer disease.

**Key Words:** off-target binding; human; tau PET; amyloid PET

**J Nucl Med 2023; 64:287–293**  
DOI: 10.2967/jnumed.122.263948

---

**A**ccrual of hyperphosphorylated tau protein into neurofibrillary tangles is a key pathologic feature of Alzheimer disease (AD)

Received Feb. 22, 2022; revision accepted Aug. 11, 2022.  
For correspondence or reprints, contact Brian A. Gordon (bagordon@wustl.edu).  
Published online Aug. 11, 2022.  
COPYRIGHT © 2023 by the Society of Nuclear Medicine and Molecular Imaging.

and is significantly predictive of clinical symptomatology, cognitive impairment, and neuronal loss (1). The most prominent in-human tau PET radiotracer in use is the 5H-pyrido[4,3-b]indole derivative [<sup>18</sup>F]flortaucipir (FTP, also known as [<sup>18</sup>F]AV-1451). In vivo use has identified notable off-target FTP binding in the choroid plexus (2), basal ganglia, and brain stem (3), none of which are believed to have prominent AD-related tauopathy. Possible explanations for this off-target signal include FTP binding to neuromelanin-containing cells (3), monoamine oxidase enzymes (4), or iron (2).

Another off-target region seldom discussed, but nonetheless identified, is skull bone (5). The first-in-humans FTP study showed skull uptake in 2 participants (a healthy control and a mild cognitive impairment patient), though this observation was not directly referenced (6). Since then, skull signal has been observed anecdotally but minimally noted in the literature. Smith et al. (7) recently reported off-target binding in a mask that extended omnidirectionally from the cerebral surface that included meninges, skull bone, and mid-brain structures. Although informative, the analyses were limited by the lack of mask specificity and restriction to only amyloid-negative individuals instead of individuals across the AD spectrum. Additionally, whereas they examined data across 3 different tau PET radiotracers, data from only 1 tracer were available for each participant.

High skull binding could adversely impact quantification of AD tauopathy. In the current study, we determined the existence and characteristics of off-target FTP skull binding in cognitively normal adults and those with mild dementia using a subject-specific CT-derived skull region of interest (ROI). We then investigated its impact on quantitative PET analyses and examined its stability using longitudinal FTP scans as well as comparisons with [<sup>18</sup>F]florbetapir (FBP, also known as [<sup>18</sup>F]AV-45) and [<sup>11</sup>C]Pittsburgh compound B (PiB).

## MATERIALS AND METHODS

### Participants

Data from 313 (177 women/196 men; median age, 69.9 y; age range, 46.2–91.9 y) cognitively normal ( $n = 273$ , Clinical Dementia Rating = 0) and impaired individuals ( $n = 40$ , Clinical Dementia Rating > 0 and clinical diagnosis of AD dementia or dementia of unknown etiology) enrolled in studies of memory and aging at the Charles F. and Joanne Knight Alzheimer Disease Research Center at Washington University were included in the present study. All participants received FTP and FBP scans within a 1-y period ( $51.25 \pm 63.32$  d [mean  $\pm$  SD]). A subset

( $n = 14$ ) received longitudinal FTP scans and another subset ( $n = 152$ ) received a PiB scan in the years before or after the FTP ( $1,222.74 \pm 562.79$  d). Clinical and demographic data collected within 1 y from the FTP were also used. The Washington University Institutional Review Board approved all procedures. Written informed consent was obtained from all participants or their designated representatives.

## MRI

T1-weighted magnetization-prepared rapid gradient-echo MR images were acquired in sagittal orientation for 176 slices on either a 3-T Biograph PET/MR, Trio, or Vida scanner (Siemens Healthcare). The PET/MRI and Vida scanners used similar parameters (repetition time, 2,300 ms; echo time, 2.95 ms; flip angle,  $9^\circ$ ; voxel resolution,  $1.05 \times 1.05 \times 1.19$  mm); however, the Trio was slightly modified (repetition time, 2,400 ms; echo time, 3.16 ms; flip angle,  $8^\circ$ ; voxel resolution,  $1.0 \times 1.0 \times 1.0$  mm). MR images were segmented into ROIs using FreeSurfer (version 5.3-HCP; Martinos Center of Biomedical Imaging).

## PET Imaging

Radiotracers were synthesized under current good manufacturing practices and underwent quality assessment and acceptance testing for in-human use before injection. FTP radiochemical purity was reported at  $99.9\% \pm 0.07\%$  over 224 synthesized batches used in the study. As FTP purity was at the ceiling, it was not included in any analyses. For tau PET, participants received a single  $339.29 \pm 32.93$  MBq intravenous bolus of FTP. Emission data were collected for the 0- to 110-min ( $n = 117$ ) or 80- to 100-min ( $n = 196$ ) postinjection time interval (p.t.i.) on a Siemens Biograph PET/CT scanner. List-mode data were reconstructed using ordered-subset expectation maximization with no postreconstruction filtering and standard normalization, decay and scatter correction, and dead time. CT transmission scans detailing bone structure and tissue were also obtained.

Amyloid PET was performed with either FBP or PiB on a Siemens Biograph PET/MR scanner or a Biograph PET/CT scanner. After a single bolus injection of  $370 \pm 22.2$  MBq of FBP, emission data covered the p.t.i. of 0–70 ( $n = 210$ ) or 50–70 min ( $n = 103$ ); for PiB,  $513.56 \pm 128.02$  MBq were administered, with data covering the p.t.i. of 0–60 ( $n = 150$ ) or 30–60 min ( $n = 2$ ). For data collected on the PET/MRI scanner, separate CT images were obtained to generate a CT-based  $\mu$ map for attenuation correction (8). Reconstruction procedures were similar to those for tau PET.

PET data were analyzed using the FreeSurfer-based PET Unified Pipeline (<https://github.com/ysu001/PUP>), which includes scanner resolution harmonization (9), interframe motion correction, PET-to-MRI registration, ROI-based time–activity curve extraction, SUV ratio (SUVr) analyses, geometric transfer matrix–based partial-volume correction (PVC) (10), and a non-PVC voxelwise SUVr image coregistered to the structural MRI. SUVrs were calculated for the 80- to 100-, 50- to 70-, and 30- to 60-min p.t.i. for FTP, FBP, and PiB, respectively. Cerebellar gray matter served as the reference region regardless of tracer. Global amyloid burden was calculated as the average of PVC SUVrs for the prefrontal, inferior temporal, precuneal, and gyrus rectus regions. Positivity was based on published values of 1.42 for PiB (11) and 1.19 in FBP (12). Regional PVC FTP SUVrs for the amygdala, entorhinal, inferior temporal, and lateral occipital were averaged into a tauopathy summary measure (13).

## Skull ROI

To create an individual-specific skull ROI, each CT image was linearly aligned using the FMRIB Linear Image Registration Tool with its respective T1 image, which in turn was coregistered to the Montreal Neurological Institute (MNI)–152 stereotactic atlas. The MNI-aligned CT images were then averaged across the cohort. On this population average, a mask of nonskull structures (e.g., vertebra and muscles)

was generated using the `fslmaths` and `FSLeyes` utilities and then removed from the averaged CT image. Voxels below 1,400 Hounsfield units were also removed so that only dense cranial bone remained. The image was then inflated twice using a 2-mm gaussian kernel to capture the largest possible skull size and then nonzero voxels binarized at a threshold of 0.1 Hounsfield units. This mask was then placed back into subject space and applied to the participant's original binarized CT image to generate an individual skull ROI with nonskull structures removed (Fig. 1). The skull ROI was then applied to each voxelwise non-PVC SUVr image, and skull uptake was calculated as the average SUVr within the ROI.

## Visual Reads

All CT images were visually inspected by 1 of 2 neuroradiologists who had a combined 17 y of experience and did not know our hypotheses. The assessment included identifying hyperostosis cranialis interna (a hereditary disease of the skull and sphenoid bone) and sinusitis, as well as an open-ended identification of other bone or skull abnormalities deemed significant. No participants were excluded because of incidental findings.

## Statistical Analysis

Analyses were performed using R software (version 3.3.2, R Core Team). After the skull SUVr had been computed, participants were classified as either having low (S–) or high (S+) skull binding using a gaussian mixture model with 2 components from the `mclust` package (version 5.3) (14). Participants were further subdivided by amyloid positivity (A+/-) based on global amyloid burden. Demographic differences were assessed using Welch *t* tests for continuous variables and Fisher exact tests for categorical variables because of the small size of some groups. Skull SUVr from doses split between individuals scanned on the same day were evaluated using a Pearson correlation. To investigate the possibility of asymmetric FTP binding in the skull, we divided the skull ROI across its midline, obtained SUVrs for both left and right portions, and then assessed the relationship between left and right skull using a Pearson correlation.

We first tested whether skull SUVr shared variance with known FTP off-target regions using partial correlations controlling for age, as well as linear models with main effects of skull SUVr, age, sex, and a sex-by-skull SUVr interaction. Sex was selected as a factor because of previously identified sex differences in FTP skull binding (7). We then examined whether bone density, calculated as the average Hounsfield units in the acquired CT scan, influenced skull SUVr using a linear model with a main effect of sex and a sex-by-cranial-bone density interaction. Results from the CT image visual reads were evaluated using Fisher exact tests.

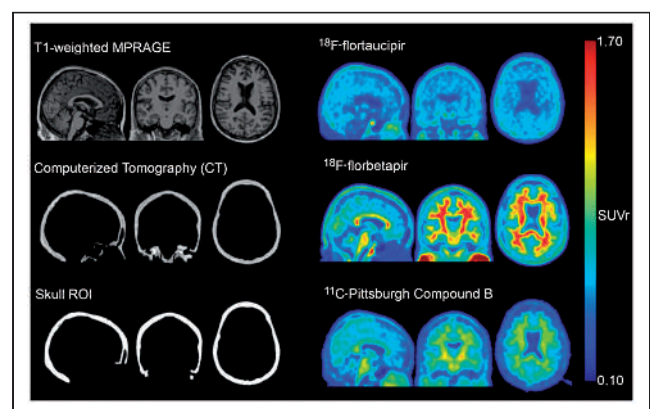


**FIGURE 1.** MR, CT, and SUVr images from amyloid-negative participant with high skull binding in all 3 radiotracers. Images are in MNI-152 space. MPRAGE = magnetization-prepared rapid acquisition with gradient echo.

To determine FTP skull signal's impact on quantitative PET, linear regression and partial correlations controlling for age assessed whether skull SUVr and the tauopathy summary measure differed as a function of amyloid status. Further analyses used linear models predicting regional SUVr from skull SUVr with  $P$  values adjusted for multiple comparisons using the Benjamini–Hochberg procedure at a false discovery rate of  $q = 0.05$ . Similar models were run that included main effects of age and sex.

Spearman correlations tested the radioisotope specificity of skull SUVr between FTP and the 2 amyloid tracers (FBP and PiB) in the same participants. As with FTP, we examined asymmetric FBP and PiB skull binding using a Pearson correlation. We further plotted the mean time–activity curves for several ROIs, including skull, for each tracer. Finally, longitudinal stability of skull binding was assessed with a Pearson correlation between baseline and a randomly chosen follow-up visit in those with longitudinal data.

## RESULTS

### FTP Skull Binding Characteristics

Group-average FTP SUVr images based on amyloid positivity as well as skull binding levels (A+/-, S+/-) are shown in Figure 2. Exemplar cases of high skull binding are shown in Supplemental Figure 1 (supplemental materials are available at <http://jnm.snmjournals.org>), and demographic information is in Table 1. Women were more likely to be classified S+ than men ( $\chi^2_1 = 18.19$ ,  $P < 0.001$ ) but were equally likely to be classified A+/- ( $\chi^2_1 = 0.08$ ,  $P = 0.77$ ). Women composed the majority of the S+ group, regardless of amyloid status (83.8% for S+/A- and 76.9% for S+/A+). S+ individuals were typically younger ( $t_{67.45} = 3.55$ ,  $P < 0.001$ ) than their S- counterparts. There was no association for skull SUVr between individuals who received injections from the same synthesized FTP batch ( $n = 179$ ,  $r = 0.07$ ,  $P = 0.44$ ). FTP SUVrs between the left and

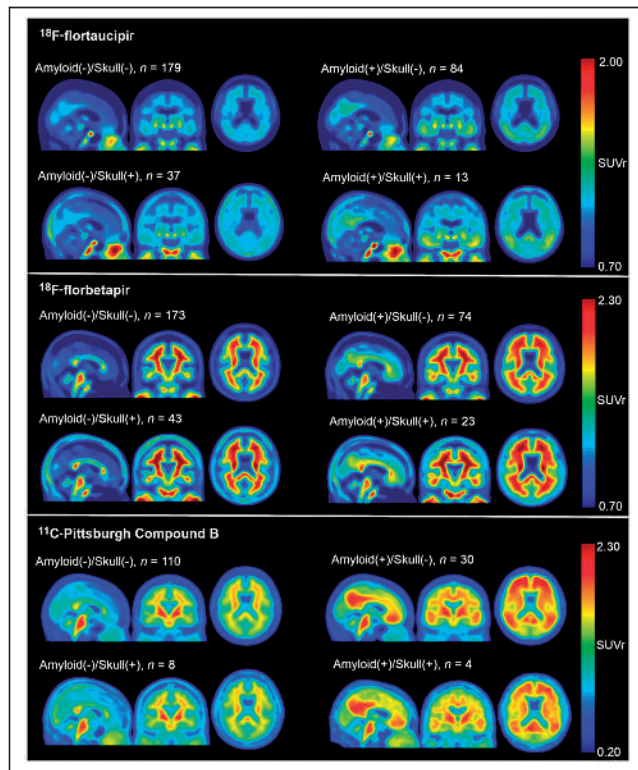


**FIGURE 2.** Group average SUVr images for each tracer. Images are in MNI-152 space.

**TABLE 1**  
Demographics for FTP Groups

Demographic	<i>n</i>	High skull binding	Low skull binding	<i>P</i> *
Sex	313			<0.001
Female		42 (84%)	135 (51%)	
Male		8 (16%)	128 (49%)	
Age (y)	312			<0.001
Mean		66	70	
SD		8	8	
Education (y)	299			0.60
Mean		15.85	16.03	
SD		2.11	2.30	
Clinical dementia rating	313			0.68
0		46 (92%)	227 (86%)	
0.5		3 (6.0%)	29 (11%)	
≥1		1 (2.0%)	7 (2.7%)	
MMSE	311			0.87
Mean		28.92	28.86	
SD		2.51	1.91	
Amyloid status	313			0.51
Negative		37 (74%)	179 (68%)	
Positive		13 (26%)	84 (32%)	

\*Differences assessed using Welch 2-sample  $t$  tests and Fisher exact tests.

MMSE = Mini-Mental State Examination.

right portions of the skull correlated significantly ( $r = 0.98$ ,  $P < 0.001$ ; Supplemental Fig. 2).

### Lack of Relationship Between FTP Skull Binding and Other Off-Target Regions

FTP skull SUVr was not related to choroid plexus binding (partial correlation:  $r = 0.004$ ,  $P = 0.93$ ; Fig. 3A). A linear model predicting choroid plexus SUVr found no effects of skull SUVr ( $t_{308} = 0.03$ ,  $P = 0.98$ ), sex ( $t_{308} = -0.11$ ,  $P = 0.90$ ), or age ( $t_{308} = -0.48$ ,  $P = 0.63$ ). Additionally, the sex-by-skull SUVr interaction was not significant ( $t_{308} = 0.18$ ,  $P = 0.86$ ). Repeating the analysis using PVC SUVr yielded similar results except that increased age showed higher choroid plexus PVC SUVrs ( $t_{308} = 2.90$ ,  $P < 0.01$ ); however, this effect has already been noted (15). Skull SUVr was negatively associated with basal ganglia SUVr (partial correlation:  $r = -0.14$ ,  $P = 0.01$ ; Fig. 3B) such that basal ganglia SUVr decreased with increasing skull SUVr. The linear model evaluating basal ganglia FTP signal found an effect of age ( $t_{308} = 6.05$ ,  $P < 0.001$ ) but no effect of skull SUVr ( $t_{308} = -1.71$ ,  $P = 0.09$ ), sex ( $t_{308} = 0.95$ ,  $P = 0.34$ ), or interaction between sex and skull SUVr ( $t_{308} = -1.32$ ,  $P = 0.19$ ). Repeating the analysis using PVC SUVr produced similar results.

### Relationship Between Decreased Cranial Bone Density and FTP Skull Uptake in Women

A linear model predicting FTP skull SUVr found main effects of sex ( $t_{309} = -3.10$ ,  $P < 0.01$ ) and bone density ( $t_{309} = -6.64$ ,

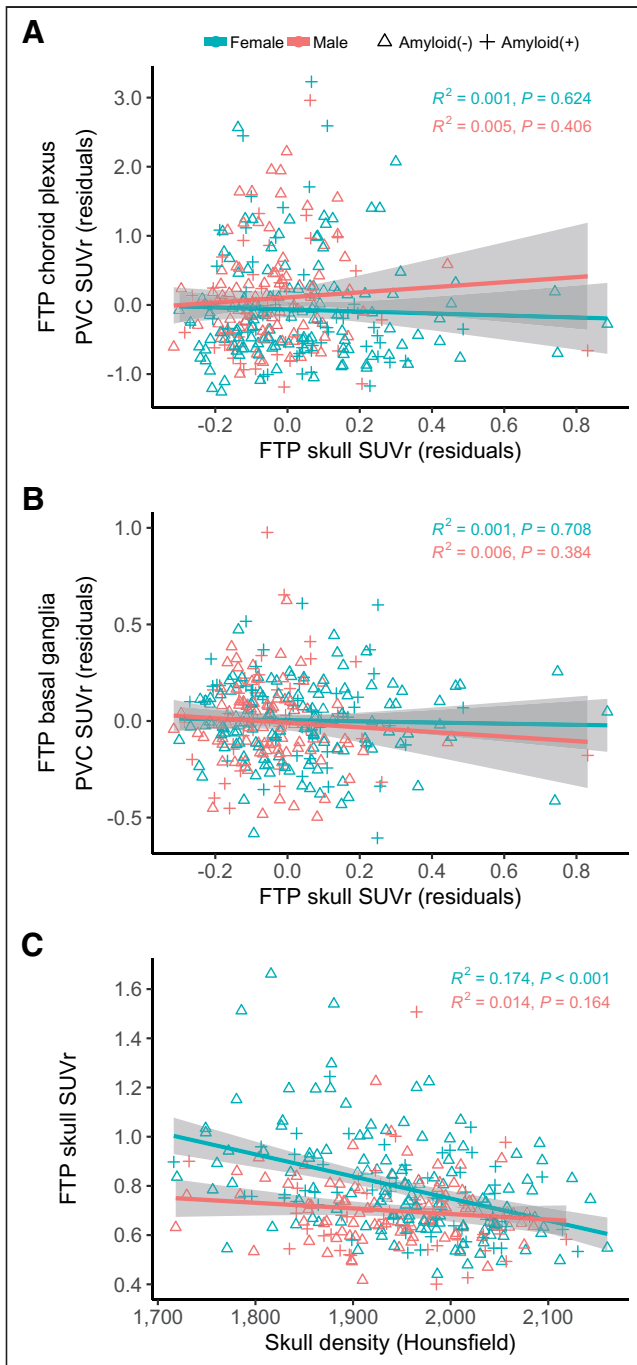


**FIGURE 3.** (A and B) Partial correlations of FTP skull SUVr with FTP choroid plexus partial-volume-corrected (PVC) SUVr (A) and FTP basal ganglia PVC SUVr (B) for men and women. (C) Women with lower bone density displayed higher skull SUVrs, whereas men did not. Shaded regions are 95% CIs.

$P < 0.001$ ), as well as a significant interaction ( $t_{309} = 2.89, P < 0.01$ ; Fig. 3C). When stratified by sex, women had a significant negative association in which those with decreased skull density displayed higher skull SUVr ( $t_{175} = -6.08, P < 0.001$ ) whereas men did not ( $t_{134} = -1.40, P = 0.16$ ). Clinical assessments of CT images revealed 33 participants with hyperostosis (20 S-/13 S+). We found a significant relationship between skull binding and a hyperostosis diagnosis ( $P < 0.001$ ). Approximately 21% (9/42) of

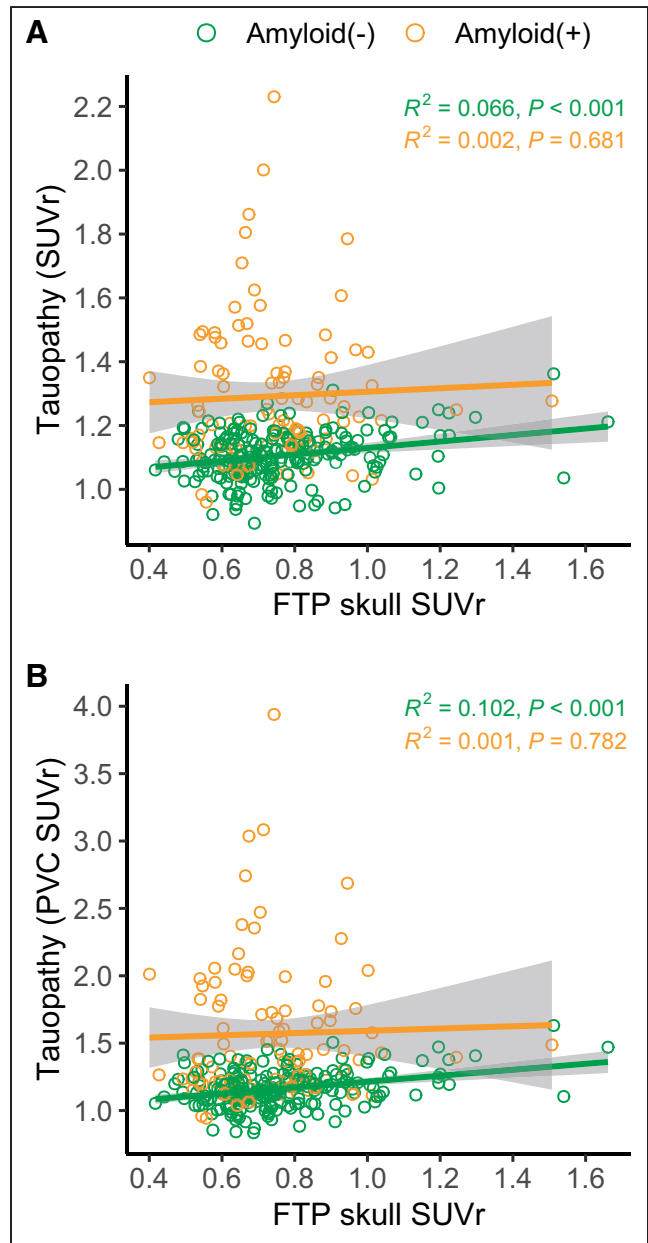


**FIGURE 4.** Relationship between FTP skull SUVr and tauopathy summary measure without (A) and with (B) PVC. Shaded regions are 95% CIs.

S+ women and 50% (4/8) of S+ men were positive for hyperostosis. The visual reads also revealed 20 participants with sinusitis (16 S-/4 S+), although this was unrelated to skull binding ( $P = 0.54$ ). No other significant bone abnormalities were identified.

#### Impact of FTP Skull Binding on Quantitative PET

FTP skull SUVr correlated with the tauopathy summary measure in A- (partial correlation:  $r = 0.32, P < 0.001$ ) but not A+ individuals (partial correlation:  $r = 0.06, P = 0.58$ ; Fig. 4; Supplemental Fig. 3). The correlation observed in A- may be explained by possible bleed-over from proximal skull. Regional impacts of skull binding are shown in Figure 5. In A- individuals, increased skull SUVr produced significantly elevated regional non-PVC SUVrs in the frontal, parietal, and temporal lobes, whereas in A+ individuals, only the postcentral and pars orbitalis non-PVC SUVr

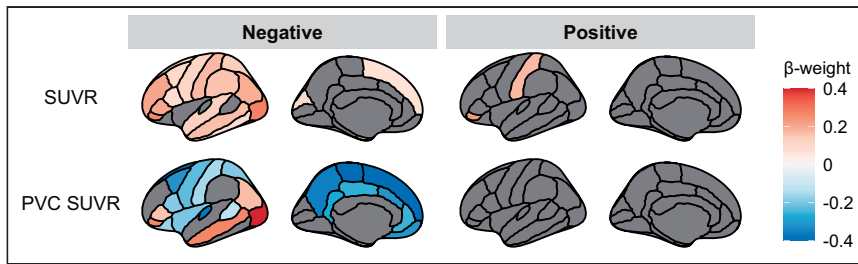


**FIGURE 5.** Cortical regions significantly associated ( $P < 0.05$ ) with FTP skull partial-volume-corrected (PVC) SUVR and non-PVC SUVR for amyloid-negative and -positive individuals.

showed any relationship with skull SUVR. After application of regional PVC, in A− individuals only the middle temporal, inferior parietal, and lateral occipital continued to show elevated regional PVC SUVR. All other previously significant regions either inverted or did not survive multiple-comparisons correction. For A+ individuals, no regions showed a relationship with skull SUVR. Similar analyses controlling for sex and age are in Supplemental Figure 4.

### Skull Binding in Amyloid PET

As with FTP, participants were grouped as S+/- using a gaussian mixture model and further grouped into A+/- on the basis of the respective amyloid tracer. Demographics are in Supplemental Table 1 for FBP and Supplemental Table 2 for PiB, and group-average SUVR images are shown in Figure 2. Sex was related to FBP skull SUVR in both A− ( $\chi^2_1 = 37.64$ ,  $P < 0.001$ ) and A+ individuals ( $\chi^2_1 = 10.44$ ,  $P = 0.001$ ), with women composing 97.6% and 86.9% of the S+ groups, respectively. Although sex was not significant for PiB, few individuals were classified as S+ (8/118, 7%). When examined as a continuous measure, skull SUVR from both tracers significantly correlated with FTP skull SUVR (FBP:  $\rho = 0.48$ ,  $P < 0.001$ ; PiB:  $\rho = 0.34$ ,  $P < 0.001$ ; Figs. 6A and 6B). Mean time-activity curves are presented in Supplemental Figure 5. Generally, skull signal appeared relatively constant, with minimal decay relative to other ROIs in all 3 tracers. SUVRs between left and right skull correlated significantly for both FBP ( $r = 0.98$ ,  $P < 0.001$ ) and PiB ( $r = 0.96$ ,  $P < 0.001$ ; Supplemental Fig. 2).

### Longitudinal Stability of FTP Skull Binding

Using our longitudinal FTP data, skull SUVR at baseline correlated significantly with that at follow-up ( $r = 0.84$ ,  $P < 0.001$ ; Fig. 6C). An exemplar longitudinal case with high skull binding is shown in Supplemental Figure 6.

## DISCUSSION

Previous studies evaluating FTP have noted off-target binding in subcortical regions as well as the skull. Although binding in subcortical regions has been investigated, skull binding has largely been ignored. In a cohort of nondemented older adults and those with mild dementia, we found that 15.9% of individuals scanned with FTP showed elevated skull signal and that this binding influenced estimates of tau pathology in the temporal lobe. Further, skull binding is a stable, individual-specific property tied to sex.

The biologic drivers behind bone uptake are unknown, but the current work reveals important insights. The longitudinal analyses demonstrate that skull binding was consistent across time points, whereas the multitracer analyses suggest that relative levels of skull binding were consistent across FTP, FBP, and PiB. This finding

indicates that individuals with elevated skull binding for 1 tracer and time point are likely to have elevated binding at subsequent visits. In the literature, skull signal is usually attributed to spontaneous defluorination of the  $^{18}\text{F}$ -fluorine radioisotope (16). The significant predicative relationship between clinically diagnosed hyperostosis and skull binding would appear to support this claim. However, we also found that PiB skull SUVR was linearly related to FTP skull SUVR in the same individuals, though the number of PiB individuals classified as S+

was low compared with FTP and FBP. These findings suggest that other factors beyond purely defluorination may be involved in the presence of skull signal. The high FTP radiochemical purity also suggests that skull binding is unlikely to be due to factors involved in radiotracer synthesis.

Elevated binding is driven primarily by the female sex, a finding also observed by Smith et al. (7) in tau PET using FTP,  $^{18}\text{F}$ -MK-6240, and  $^{18}\text{F}$ -RO948. In the present study, women with higher FTP skull binding had low bone density as measured by CT. Women often experience a greater decline in bone density with age than men, including in the cranium (17); our findings support the theory that bone loss is at least partially driving skull binding but is not simply age-related, as overall bone density did not significantly change with increased age for either sex (Supplemental Fig. 7). Recent work with 18-kDa translocator protein tracers in participants with central nervous system disorders found a relationship between decreasing bone density and skull signal in women. These results suggest a role of inflammatory processes and alterations in bone marrow structure (18). Future work should directly compare 18-kDa translocator protein and tau PET skull binding to explore this possibility.

Bone uptake was also distinct from choroid plexus binding, although a negative relationship was present for the basal ganglia. It has been speculated that basal ganglia signal is tied to iron (19), and there are reports of sex-related differences in iron accumulation in the brain (20); such a connection should be explored in future work. The negative association with the basal ganglia may also be tied to age, as FTP in the basal ganglia increases with age, whereas we found that it was a subset of relatively younger, rather than older, women that was driving the observed skull uptake.

The temporal cortex has consistently been shown to have an elevated tau PET signal in both the prodromal (21) and the clinical phases of AD (1). Our analyses demonstrated that in amyloid-negative individuals, bone uptake was positively related to tau PET signal in the inferior temporal cortex and that applying regional PVC partially mitigated these effects. Spillover from bone could spuriously elevate measurements in some individuals and reduce concordance between multiple tauopathy measures. It may also limit the sensitivity of tau PET tracers to increases in true pathology during the early phases of AD. The strong sex effect observed suggests that bone binding should be considered, particularly in investigations of sex on tau PET (22–24).

Our multitracer comparisons indicated that individuals with high bone signal in one tracer are likely to have elevated signal with another tracer. SUVRs were quite high for FTP ( $0.751 \pm 0.187$ ) and FBP ( $0.885 \pm 0.200$ ) but were at a lower range for PiB ( $0.572 \pm 0.087$ ), indicating that this off-target binding is not tied

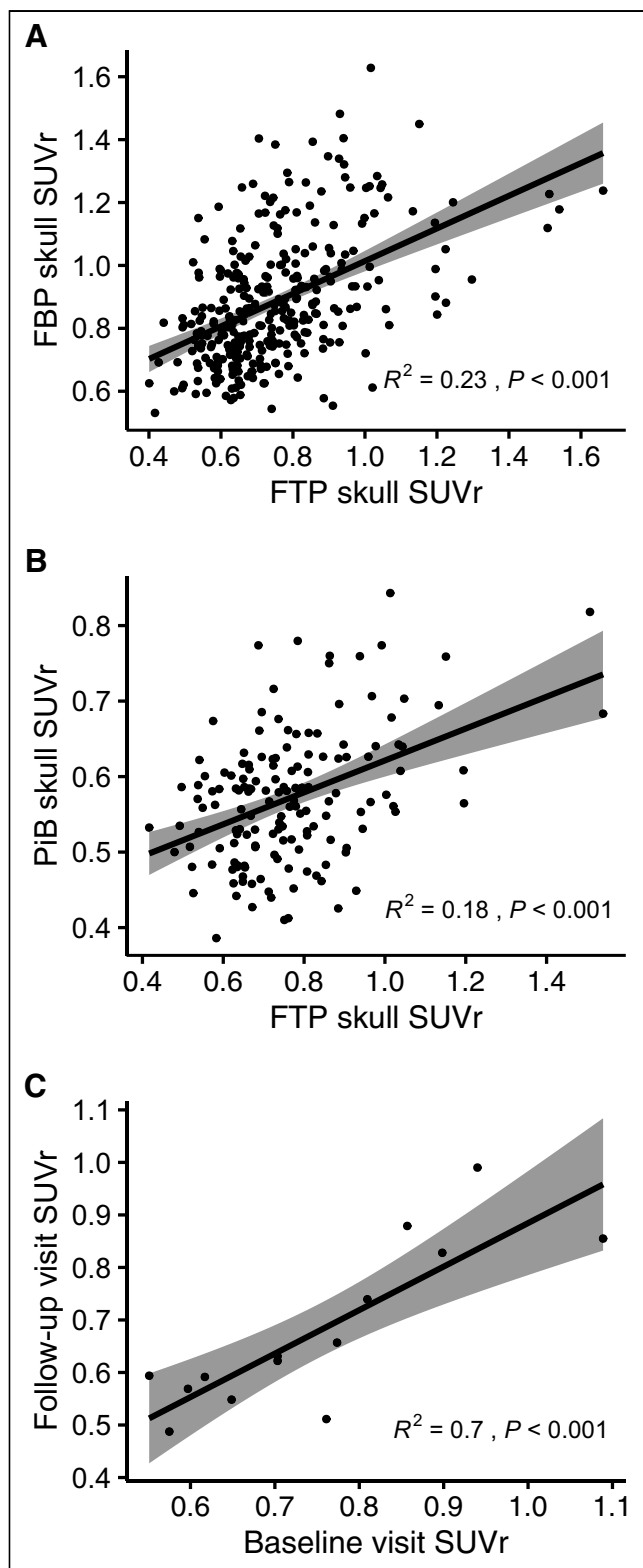


**FIGURE 6.** (A and B) Multitracer comparisons between FTP skull SUVr and FBP (A) or PiB (B) skull SUVr. (C) Longitudinal relationship for skull uptake across FTP visits. Shaded regions are 95% CIs.

to target receptor (e.g., tangles vs. plaques) but that the radioisotope ( $^{18}\text{F}$  vs.  $^{11}\text{C}$ ) determines the degree of bone uptake. Alternatively, the time-activity curves suggest that bone signal appears constant,

whereas counts in brain tissue continue to fall at later time points. Consequently, tracers with a later p.t.i. (i.e., FTP and FBP) are more likely to see problematic contamination. Future work with additional tracers could clarify what factors modulate the degree of skull binding.

There are several limitations to the current study. First, as the PiB scan dates were not constrained to within a certain time frame from FTP, we could not fully investigate age-related factors of skull binding. Additionally, comprehensive participant medical histories were not available, limiting investigations into the role, if any, of medication (e.g., hormone replacement therapy) and medical condition; however, Smith et al. (7) found no relationship with either. Lastly, our analyses were limited to a single cohort. Future work should extend the presented analyses to other cohorts to elucidate the frequency of FTP skull binding across multiple longitudinal studies and the biologic factors that influence its presentation.

## CONCLUSION

FTP skull binding occurred in 15.9% of a sample of cognitively normal adults and those with mild dementia, and this effect was overwhelmingly observed in women. Increased binding was a stable feature across time and multiple tracers. In individuals without amyloid pathology, skull uptake led to elevated tau SUVrs in regions thought to be tied to AD. This could potentially hamper the early detection of emerging tau pathology and merits further investigation.

## DISCLOSURE

This research was supported by NIH grants P30AG66444, P01AG003991, P01AG026276, U01AG042791, R01AG046179, R01AG055444, and R01AG031581. Image acquisition and analysis received additional support from UL1TR000448, P30NS098577, and R01EB009352. Additional support was provided by the Arizona Alzheimer's Research Consortium, the Charles and Joanne Knight Alzheimer Disease Research Center Support Fund, the David and Betty Farrell Medical Research Fund, the Daniel J. Brennan Alzheimer Research Fund, the Fred Simmons and Olga Mohan Alzheimer Research Support Fund, the Barnes-Jewish Hospital Foundation, Eli Lilly & Co., Hoffman La-Roche, Avid Radiopharmaceuticals, the Alzheimer's Association, the GHR Foundation, and an anonymous organization. Avid Radiopharmaceuticals provided the FBP doses, assisted with scanning expenses, and provided precursor and technology transfer for FTP. Manu Goyal reports trip reimbursement and honoraria in 2019 from sponsors of the Linyi Brain PET conference, including Capital Medical University, Tancheng Talent Office, and Shandong Madic Technologies Co., Ltd., and stock equity in IBM, Moderna, and BioNTech. Dean Wong reports investigator-initiated funding from the National Institutes of Health (NIH) and contracts to John Hopkins University and Washington University from LB Pharma, Eisai, Roche Neuroscience, Anavex, Five Eleven Pharma, and Lundbeck (Denmark/US). Tammie Benzinger reports investigator-initiated funding from the NIH, the Alzheimer's Association, the Barnes-Jewish Hospital Foundation, and Avid Radiopharmaceuticals; participates as a site investigator in clinical trials sponsored by Avid Radiopharmaceuticals, Eli Lilly, Biogen, Eisai, Jaansen, and Roche; serves as an unpaid consultant to Eisai and Siemens; and is on the speakers' bureau for Biogen. No other potential conflict of interest relevant to this article was reported.



## KEY POINTS

**QUESTION:** What are the characteristics and quantitative impacts of FTP skull signal?

**PERTINENT FINDINGS:** We examined FTP skull signal in a cohort of cognitively unimpaired adults and those with mild dementia using a skull mask derived from their own CT scan. Skull signal was observed primarily in younger women with decreased skull bone density, was a stable feature across time and tracers, and erroneously elevated quantitative measures of early tau accumulation in AD.

**IMPLICATIONS FOR PATIENT CARE:** FTP skull signal should be considered in examining early increases in tau pathology in neurologic PET studies.

## REFERENCES

1. Brier MR, Gordon B, Friedrichsen K, et al. Tau and Ab imaging, CSF measures, and cognition in Alzheimer's disease. *Sci Transl Med*. 2016;8:338ra66.
2. Choi JY, Cho H, Ahn SJ, et al. Off-target <sup>18</sup>F-AV-1451 binding in the basal ganglia correlates with age-related iron accumulation. *J Nucl Med*. 2018;59:117–120.
3. Lowe VJ, Curran G, Fang P, et al. An autoradiographic evaluation of AV-1451 tau PET in dementia. *Acta Neuropathol Commun*. 2016;4:58.
4. Barrio JR. The irony of PET tau probe specificity. *J Nucl Med*. 2018;59:115–116.
5. Smith R, Schöll M, Leuzy A, et al. Head-to-head comparison of tau positron emission tomography tracers [<sup>18</sup>F]flortaucipir and [<sup>18</sup>F]RO948. *Eur J Nucl Med Mol Imaging*. 2020;47:342–354.
6. Chien DT, Bahri S, Szardenings AK, et al. Early clinical PET imaging results with the novel PHF-tau radioligand [F-18]-T807. *J Alzheimers Dis*. 2013;34:457–468.
7. Smith R, Strandberg O, Leuzy A, et al. Sex differences in off-target binding using tau positron emission tomography. *Neuroimage Clin*. 2021;31:102708.
8. Su Y, Rubin BB, McConathy J, et al. Impact of MR-based attenuation correction on neurologic PET studies. *J Nucl Med*. 2016;57:913–917.
9. Joshi A, Koeppel RA, Fessler JA. Reducing between scanner differences in multi-center PET studies. *Neuroimage*. 2009;46:154–159.
10. Rousset OG, Collins DL, Rahmim A, Wong DF. Design and implementation of an automated partial volume correction in PET: application to dopamine receptor quantification in the normal human striatum. *J Nucl Med*. 2008;49:1097–1106.
11. Su Y, D'Angelo GM, Vlassenko AG, et al. Quantitative analysis of PiB-PET with FreeSurfer ROIs. *PLoS ONE*. 2013;8:e73377.
12. Su Y, Flores S, Wang G, et al. Comparison of Pittsburgh compound B and florbeta-pir in cross-sectional and longitudinal studies. *Alzheimers Dement (Amst)*. 2019;11:180–190.
13. Mishra S, Gordon BA, Su Y, et al. AV-1451 PET imaging of tau pathology in preclinical Alzheimer disease: defining a summary measure. *Neuroimage*. 2017;161:171–178.
14. Scrucca L, Fop M, Murphy TB, Raftery AE. Mclust 5: clustering, classification and density estimation using Gaussian finite mixture models. *R J*. 2016;8:289–317.
15. Wen GY, Wisniewski HM, Kacsak RJ. Biondi ring tangles in the choroid plexus of Alzheimer's disease and normal aging brains: a quantitative study. *Brain Res*. 1999;832:40–46.
16. *Amyvid EU Summary of Product Characteristics*. European Medicines Agency; 2013.
17. Schulte-Geers C, Obert M, Schilling RL, et al. Age and gender-dependent bone density changes of the human skull disclosed by high-resolution flat-panel computed tomography. *Int J Legal Med*. 2011;125:417–425.
18. Kolabas ZI, Kuemmerle LB, Perneczky R, et al. Multi-omics and 3D-imaging reveal bone heterogeneity and unique calvaria cells in neuroinflammation. bioRxiv website. <https://www.biorxiv.org/content/10.1101/2021.12.24.473988v1>. Published December 25, 2021. Accessed November 18, 2022.
19. Spotorno N, Acosta-Cabrero J, Stomrud E, et al. Relationship between cortical iron and tau aggregation in Alzheimer's disease. *Brain*. 2020;143:1341–1349.
20. Persson N, Wu J, Zhang Q, et al. Age and sex related differences in subcortical brain iron concentrations among healthy adults. *Neuroimage*. 2015;122:385–398.
21. Schultz SA, Gordon BA, Mishra S, et al. Widespread distribution of tauopathy in preclinical Alzheimer's disease. *Neurobiol Aging*. 2018;72:177–185.
22. Buckley RF, Scott MR, Jacobs HIL, et al. Sex mediates relationships between regional tau pathology and cognitive decline. *Ann Neurol*. 2020;88:921–932.
23. Wisch JK, Meeker KL, Gordon BA, et al. Sex-related differences in tau positron emission tomography (PET) and the effects of hormone therapy (HT). *Alzheimer Dis Assoc Disord*. 2021;35:164–168.
24. Buckley RF, O'Donnell A, McGrath ER, et al. Menopause status moderates sex differences in tau burden: a Framingham PET study. *Ann Neurol*. 2022;92:11–22.

# The RSNA QIBA Profile for Amyloid PET as an Imaging Biomarker for Cerebral Amyloid Quantification

Anne M. Smith<sup>1</sup>, Nancy A. Obuchowski<sup>2</sup>, Norman L. Foster<sup>3</sup>, Gregory Klein<sup>4</sup>, P. David Mozley<sup>5</sup>, Adriaan A. Lammertsma<sup>6,7</sup>, Richard L. Wahl<sup>8,9</sup>, John J. Sunderland<sup>10</sup>, Jean-Luc Vanderheyden<sup>11</sup>, Tammie L.S. Benzinger<sup>8,9</sup>, Paul E. Kinahan<sup>12</sup>, Dean F. Wong<sup>8</sup>, Eric S. Perlman<sup>13</sup>, Satoshi Minoshima<sup>14</sup>, and Dawn Matthews<sup>15</sup>

<sup>1</sup>Siemens Medical Solutions USA, Inc., Knoxville, Tennessee; <sup>2</sup>Quantitative Health Sciences, Cleveland Clinic, Cleveland, Ohio; <sup>3</sup>Department of Neurology, University of Utah, Salt Lake City, Utah; <sup>4</sup>F. Hoffmann-La Roche Ltd., Basel, Switzerland; <sup>5</sup>Weill Medical College of Cornell University, New York, New York; <sup>6</sup>Amsterdam Department of Radiology and Nuclear Medicine, Amsterdam University Medical Centers, Location VUmc, Amsterdam, The Netherlands; <sup>7</sup>Medical Imaging Center, Department of Nuclear Medicine and Molecular Imaging, University Medical Center Groningen, University of Groningen, Groningen, The Netherlands; <sup>8</sup>Mallinckrodt Institute of Radiology, Washington University School of Medicine, St. Louis, Missouri; <sup>9</sup>Department of Radiation Oncology, Washington University in Saint Louis, St. Louis, Missouri; <sup>10</sup>Division of Nuclear Medicine, Department of Radiology, University of Iowa, Iowa City, Iowa; <sup>11</sup>JLVMI Consulting LLC, Dousman, Wisconsin; <sup>12</sup>Department of Radiology, School of Medicine, University of Washington, Seattle, Washington; <sup>13</sup>Perlman Advisory Group, Hillsdale, New York; <sup>14</sup>Department of Radiology and Imaging Sciences, University of Utah, Salt Lake City, Utah; and <sup>15</sup>ADM Diagnostics, Inc., Northbrook, Illinois

A standardized approach to acquiring amyloid PET images increases their value as disease and drug response biomarkers. Most <sup>18</sup>F PET amyloid brain scans often are assessed only visually (per regulatory labels), with a binary decision indicating the presence or absence of Alzheimer disease amyloid pathology. Minimizing technical variance allows precise, quantitative SUV ratios (SUVRs) for early detection of  $\beta$ -amyloid plaques and allows the effectiveness of anti-amyloid treatments to be assessed with serial studies. **Methods:** The Quantitative Imaging Biomarkers Alliance amyloid PET biomarker committee developed and validated a profile to characterize and reduce the variability of SUVRs, increasing statistical power for these assessments. **Results:** On achieving conformance, sites can justify a claim that brain amyloid burden reflected by the SUVR is measurable to a within-subject coefficient of variation of no more than 1.94% when the same radiopharmaceutical, scanner, acquisition, and analysis protocols are used. **Conclusion:** This overview explains the claim, requirements, barriers, and potential future developments of the profile to achieve precision in clinical and research amyloid PET imaging.

**Key Words:** quantitative imaging biomarkers; amyloid PET; QIBA; guidelines; Alzheimer disease

**J Nucl Med 2023; 64:294–303**  
DOI: 10.2967/jnumed.122.264031

**T**he preponderance of evidence indicates that cerebral  $\beta$ -amyloid plaques are a necessary, but insufficient, precursor of synaptic loss and cognitive impairment in Alzheimer disease (AD). Because of the validation of PET imaging in comparison with postmortem examinations, PET imaging has come to play a central role in definitive

clinical diagnosis and in pharmaceutical clinical trials. It also has become adopted as the gold standard by which to judge cerebrospinal fluid and plasma amyloid biomarkers. Amyloid PET status is incorporated into National Institute on Aging–Alzheimer Association diagnostic criteria for AD and is a critical component of the amyloid/tau/neurodegeneration classification in the Alzheimer’s Association Research Framework (1,2).

Before amyloid PET was available, response to anti-amyloid treatment could be surmised only occasionally and inconclusively from postmortem studies (3). Assessing amyloid load measured as a continuous variable is now used in nearly all anti-amyloid therapies in clinical development or in the regulatory pipeline. There are several large, multicenter AD observational studies and prevention trials in which minimizing within-subject and between-site technical variance is a critical concern. With increasing focus on the benefits of early diagnosis and treatment, the potential impact of more precise tissue ratio quantification is now particularly germane. Notably, a first anti-amyloid immunotherapy (aducanumab) recently received Food and Drug Administration accelerated approval based in part on significant quantitative reduction of amyloid PET pathology as seen on amyloid PET, and additional anti-amyloid agents are progressing in clinical development (e.g., donanemab, lecanemab, and gantenerumab).

Although a visual assessment of amyloid PET images is often used to support patient inclusion or in clinical application, quantification is essential to objectively measure change. The clinical trial of donanemab applied an innovative strategy of using quantitative changes in amyloid PET to decide when individual treatment goals had been achieved and treatment discontinued (4). This approach offers an objective method of knowing when an expensive and burdensome therapy can safely be terminated. Quantification also serves a role in both staging disease and predicting the clinical trajectory; for example, data from the Harvard Aging Brain Study indicated that persons with an amyloid burden greater than a quantitative threshold were more likely to progress clinically (5). As clinical trials move earlier into the disease process, amyloid levels more

Received Feb. 16, 2022; revision accepted Aug. 5, 2022.  
For correspondence or reprints, contact Anne M. Smith (anne.m.smith@siemens-healthineers.com).  
Published online Sep. 22, 2022.  
COPYRIGHT © 2023 by the Society of Nuclear Medicine and Molecular Imaging.

frequently fall into less visually obvious categories. Quantitative, objective methods can decrease the frequency with which diagnostic assessments are ambiguous or indeterminate.

Many factors influence the reliability and repeatability of quantitative amyloid PET measures. Although detection of major reductions to amyloid burden may be robust to technical variability, the detection of slowed rates of accumulation, or of reductions within a short time frame, require minimized technical variance. In a clinical trial, minimizing technical variance in serial measures of amyloid load can have a substantial impact on the number of patients required to adequately power a study and detect an effect. On an individual basis, reproducibility can influence the amount of change that can be interpreted as technically meaningful. Potential sources of variability are numerous and include scanner characteristics; tracer administration parameters; subject positioning and motion; and image reconstruction, processing, and measurement approaches. As a striking example, selection of the reference tissue region for calculation of SUV ratios (SUVr) made a difference in requiring 325 versus 8,076 subjects per arm to measure a 25% reduction in the rate of accumulation over 12 mo (6), consistent with other studies (7–9). Although these and other factors influencing amyloid quantification have been described (9), there had not been a standardized procedural guide that is directly tied to expectations for measurement variability. In addition, the quantitative effects of factors such as subject motion on measured amyloid had not been systematically determined. In 2007, the Radiological Society of North America (RSNA) set up the Quantitative Imaging Biomarkers Alliance (QIBA), whose mission is “... to improve the value and practicality of quantitative imaging biomarkers by reducing variability across devices, sites, patients and time” (10,11). The primary deliverables of the QIBA initiative are standards-based quantitative imaging documents, called profiles, which are derived from a process similar to that of the Integrating the Healthcare Enterprise initiative (12). A profile makes a statistically based performance claim about a quantitative imaging biomarker based on clinical context of use when performance requirements and compliance procedures are met. The amyloid PET profile (11) describes the measurement precision of <sup>18</sup>F-amyloid PET imaging of the brain when meeting defined requirements and quality control specifications. The profile was designed for use both in clinical trials and in the clinic for detecting and monitoring amyloid plaque pathology. It is intended to be a checklist that a site can use to achieve conformance for its <sup>18</sup>F PET amyloid biomarker workflow.

Achieving conformance means that the site’s quantitative precision will be as specified by the profile claim. Consideration has been given to making their implementation reasonable by community sites as well as advanced research sites. Stage 3, the technically confirmed QIBA profile “<sup>18</sup>F-Labeled PET Tracers Targeting Amyloid as an Imaging Biomarker” (provided as a supplement to this paper; supplemental materials are available at <http://jnm.snmjournals.org>) overlaps and builds on imaging protocols already used in observational studies and clinical trials. Although most large, multicenter amyloid imaging studies provide their performance sites with detailed imaging protocol specifications, the QIBA profile includes some potentially important details often not included in study protocols and left to individual sites to implement. The profile proposes a new harmonized reference standard to objectively evaluate acquisition methods and to support regulatory biomarker registration. Although the QIBA profile describes what may be standard operation procedures at many larger, well-equipped imaging centers, these procedures are not universal. The profile will

especially benefit sites that have limited physics and instrumentation support and may lack technical expertise to recognize and address sources of variability.

This overview of the QIBA amyloid profile is intended to provide context for the role of quantitative amyloid PET imaging in clinical trials and patient care, describe the profile scope and claim, summarize profile recommendations for actions and parameters to be followed to achieve the claim, provide the rationale for recommendations, describe the work that was performed to address knowledge gaps, explain the relationship between the profile and other initiatives and governing bodies, identify barriers that were overcome to create the profile, and provide a vision for the future.

The profile is available as a supplemental file (13–57).

## PROFILE STRUCTURE

The overall structure of the profile is shown in Table 1. The context for the profile is described, followed by the claim, which is the central focus of the profile. Examples of clinical applications are provided. The profile then describes and specifies mitigations for the major sources of workflow variability (listed in the profile activities section) in order to achieve the profile claim. The mitigation steps are performed by actors: study sponsor, technologist, acquisition device, reconstruction software, image analysis workstation, image analyst, imaging facility coordinator, nuclear medicine physician, and medical physicist. The mitigation specifications are shown in tables under each heading in the profile, listing the actors

**TABLE 1**  
High-Level Outline of Profile

Item	Details
Executive summary	
Overview	
Summary for clinical trial use	
Intended audiences	
Clinical context and claims	
Claim	
Considerations for claim	
Clinical trial use	
Profile activities	
Subject handling	
Image data acquisition	
Image data reconstruction and postprocessing	
Image analysis	
Image interpretation and reporting	
Quality control	
Conformance procedures	Image acquisition site
	PET acquisition device
	Reconstruction software
	Image analysis workstation
	Software version tracking
References	
Appendices	

**TABLE 2**  
Example from Profile of Mitigating Steps

Parameter	Entity/actor	Specification
PET scanner calibration	Technologist	Must perform daily/weekly/monthly scanner quality assurance and vendor-recommended maintenance procedures (e.g., replace weak transmission sources for dedicated PET scanner); must ensure that output values are acceptable and manually entered on form/electronic database
PET scanner calibration constancy check	Technologist	Must perform constancy phantom (e.g., <sup>68</sup> Ge cylinder) scan (preferably NIST-traceable or equivalent to gather information on uniformity as well) at least weekly and after each calibration
Radionuclide calibrator	Physicist	Must be calibrated to <sup>18</sup> F using NIST-traceable source or equivalent either by site or by calibrator manufacturer

NIST = National Institute of Standards and Technology.

Only shaded rows are mandatory for profile conformance; white row is recommended and may be mandatory in future profile updates.

and what activities they are expected to perform. When all actors successfully complete their mitigation steps, the site has achieved compliance and can expect to achieve the profile's specified precision. A series of appendices then provides additional detail and information.

The mitigating steps in the profile tables are normative items or requirements that must be performed for the site to claim profile conformance. Surrounding the tables is descriptive text that gives more explanation and examples. Table 2 provides an example from the profile.

## PROFILE CLAIM

### Claim Description

The claim is the fundamental basis of the profile and describes the precision of the biomarker measurements when conformance is achieved (a technical performance claim). The SUVR was chosen as the biomarker because of its logistic feasibility in multisite trials and its use in large reference studies such as the one supported by the Alzheimer Disease Neuroimaging Initiative (ADNI) (58). Because of the fundamental kinetic properties of radiopharmaceuticals, changes in SUVR may not only represent a change in amyloid burden but also include changes in perfusion (9) or tissue clearance (59). This variability contributes to and is embedded in the precision stated in the claim, "Brain amyloid burden as reflected by the SUVR is measurable using <sup>18</sup>F-amyloid PET with a within-subject coefficient of variation (wCV) of  $\leq 1.94\%$ " (11). The claim is equally valid when the measured quantity is centiloids (60,61) or distribution volume ratios (DVRs).

The within-subject wCV is a statistical measure of precision. It describes the ability to obtain replicate measurements that agree with one another. It describes not the variability between subjects but the variability within a subject when scanned at time points close enough that no disease progression has occurred (60 d or less (11)). Statistically, it is defined as the SD of replicate measurements on a subject, divided by the mean of those measurements. Ideally, wCV should be as close to zero as possible.

The claim is valid only for longitudinal measurements, not for cross-sectional measurements. A cross-sectional measurement claim requires additional estimation of bias, and this information was not available across scanners at the time of profile development. Although the profile focuses on SUVR measurement, the

potential benefits of the DVR approach are discussed in detail as a profile appendix.

### Claim Application

The wCV stated in the claim can be used to guide the number of subjects included in clinical trials targeting measurement of longitudinal changes in amyloid SUVR. The amount of longitudinal change anticipated or targeted depends on the disease stage of the study population and on the trial objectives. For example, the rates of change expected from an amyloid-removing agent in a prodromal or mild trial with a high amyloid baseline burden may differ from those anticipated in a prevention trial enrolling participants with lower baseline amyloid. Rates of change may also vary between sporadic and familial AD populations.

As a first example, the mean amount of amyloid accumulation in 2 y for a cohort of patients will be estimated. To estimate within  $\pm 1\%$  with 95% confidence, assuming mean SUVRs at baseline of 1.0–1.5 (this mean range is highly dependent on the reference region used), no significant changes in perfusion between scans, and a between-subject SD ranging from 0.05 to 0.30, Supplemental Figure 2 from the profile (11) shows the number of subjects required for 3 different correlation coefficient (*r*) values between paired measurements from a subject.

The number of subjects required is reduced as *r* increases between scan visits. For example, an internal analysis of <sup>18</sup>F-florbetapir data, available through ADNI, at baseline and year 2 suggests that the correlation between scans is higher for certain reference regions than others. Using the composite of cerebellum and white matter or only white matter as reference tissue, *r* was 0.95 or 0.96, respectively, for amyloid-positive subjects (*n* = 207) and 0.94 for subjects close to the positivity threshold (*n* = 51). However, using cerebellar cortex or whole cerebellum as reference tissue, *r* was 0.79 and 0.83, respectively, for amyloid-positive subjects and 0.33 and 0.48, respectively, for subjects close to the positivity threshold.

As a second example, consider a clinical trial comparing the accumulation in amyloid SUVR over time between 2 groups of subjects: those undergoing a new treatment versus a control group. AD patients will be recruited and randomized to either the experimental intervention or the control group. SUVR will be measured in all subjects at baseline and 2 y later. The null hypothesis is that there is no difference in subjects' mean amyloid accumulation between the 2 groups; the alternative hypothesis is that there is a difference

(2-tailed hypothesis). Obuchowski et al. (62) reported the sample size needed to detect a 50% reduction in the rate of accumulation over a 2-y period with 80% power based on the assumed wCV of 1.94%. Fewer than 100 subjects were needed per group, assuming a homogeneous patient sample with low between-subject variability. Additionally, reducing the variance in the measured quantity will help when patient-level correlations of amyloid burden reduction to cognitive changes are desired.

#### Derivation of Technical Performance Claim

The technical performance claim was derived from a metaanalysis of published data of the repeatability of amyloid PET imaging under 2 types of test–retest conditions, coupled with QIBA-sponsored systematic analyses of the quantitative impact of specific sources of variance. The first type of test–retest data consisted of studies in which 2 serial scans were acquired within less than 60 d (63,64). The wCV values in the short-duration test–retest studies ranged from 1.15% in healthy controls using a cerebellar cortex reference region to 1.94% in AD patients using a whole-cerebellum reference region (63,64). The second set of studies compared baseline values in amyloid-negative cognitively normal participants with those acquired after a 2-y period, a typical clinical trial duration (6,7). Since amyloid accumulation is unlikely to occur in most (though not all) amyloid-negative cognitively normal subjects, longitudinal values in this group were examined. These studies provided a practical indicator of longer-term technical variance given a population presumed to be fairly stable with regard to amyloid pathology. In addition, the acquisition and measurement parameters applied in these more recent studies were well characterized and aligned with profile recommendations.

The wCV values derived from studies over a 2-y duration in amyloid-negative cognitively normal controls from the ADNI dataset ranged from 1.25% (white matter reference region) to 1.6% (whole-cerebellum reference region) and in 1 case up to 3.38% (whole-cerebellum reference region, with a different cerebellum boundary definition) (6,7). In these published studies, the mean and SD of the longitudinal change were shown in a table, and the ADNI data acquisition protocol (58) was used to acquire the data, that in many respects are consistent with the profile (as described in the “Relationship to Other Standards” section). The wCV cited in the claim that 1.95% is the highest of the test–retest studies that occurred within 4 wk from first studies and also satisfies the range of 1.25%–1.6% reported in all but a single 2-y study. Conformance to the claim depends on many factors such as radiopharmaceutical,

subject positioning, data acquisition, reconstruction and post-processing. In particular, the choice of the reference region can greatly impact wCV because of the sensitivity of different regions to technical factors. It is important to note that the wCV was less than 1.94% across these 2-y studies only when reference regions incorporating subcortical white matter were used. However, additional QIBA-sponsored studies performed during the development of the profile identified controls to reduce variability when using reference regions such as the cerebellum (65). This and related contributors to variance are described in the “Profile Activities and Key Points” section (6–8,66).

#### PROFILE ACTIVITIES AND KEY POINTS

##### <sup>18</sup>F PET Amyloid Radiopharmaceuticals and Subject Handling

Although a significant body of work was initially performed with the <sup>11</sup>C-amyloid radiopharmaceutical <sup>11</sup>C-Pittsburgh compound B (PiB) (67), the profile was developed using data from the <sup>18</sup>F-amyloid radiopharmaceuticals listed in Table 3, and therefore only these radiopharmaceuticals conform with the profile. That said, there are no technical limitations that prevent the profile from being extended to <sup>11</sup>C-PiB, but its clinical use is limited since there is no Food and Drug Administration approval and an on-site cyclotron is required. The site should administer the activity per its local protocol, provided it meets the specifications listed in the profile and the manufacturer’s specifications. The subject’s head should be positioned at a consistent location within the scanner, with as much axial distance as possible between the edge of the scanner field of view and the subject’s head and cerebellum to minimize slice-to-slice variability due to nonuniform scanner axial sensitivity. To prevent head movement, the head should be secured and subjects should be made as comfortable as possible.

##### Image Data Acquisition

The same scanner, <sup>18</sup>F-amyloid radiopharmaceutical, and protocol should be used to acquire serial within-subject images since any bias due to any of these factors will be consistent from scan to scan. The PET acquisition should be broken into a minimum of 5-min dynamic frames, and the dynamic frames should be assessed for significant head movement since this is a known source of quantitative error in PET (65). It is ideal for each PET image time frame to be coregistered with the CT image before attenuation and scatter correction are performed. If this is not possible and motion exceeds 4 mm or 4°, removal of selected frames or exclusion of the scan should be considered (65). If motion is less, variability

**TABLE 3**

List of <sup>18</sup>F-Amyloid Radiopharmaceuticals and Their Recommended Doses, Uptake Times, and Acquisition Durations

Parameter	Florbetapir*	Flutemetamol†	Florbetaben‡	NAV4694 (80)
Administered activity (MBq)	370 (maximum, 50- $\mu$ g mass dose)	185 (maximum, 20- $\mu$ g mass dose)	300 (maximum, 30- $\mu$ g mass dose)	300
Uptake time (postinjection min)	30–50	90	45–130	50–70
Acquisition duration (min)	10	20	15–20	20

\*Amyvid (Eli Lilly & Co.) (77).

†Vizamyl (GE Healthcare) (78).

‡Neuraceq (Piramal Imaging) (79).

Data are per U.S. package inserts. There might be some slight variations in package insert information depending on country of approval.

due to patient motion can be reduced through postreconstruction motion correction, in which all emission time frames are aligned with one another before a single averaged image is created. Finally, the dynamic time frames can be averaged or summed to form a single static PET image. An additional control specified by the profile to minimize variability is axial scanner uniformity.

The profile also describes the potential benefits obtained from the use of DVRs calculated from dynamic PET images. Emission scan data are acquired from the time of radiopharmaceutical injection through the late-time-frame period. In full dynamic scanning, a parametric image can be created using physiologic modeling techniques. The image can then be measured using the same analysis as specified by the profile. A benefit is that the contribution of local cerebral blood flow rate to the amyloid value can be separated from that due to amyloid burden. This separation can be important when a therapeutic intervention causes blood flow changes or when the population is one for which blood flow declines significantly during a study.

### Image Data Reconstruction and Postprocessing

The reconstruction and postprocessing steps need to conform with the specifications listed in their respective sections in the profile (Table 1). These tasks need to be consistent and not change from scan to scan, including the reconstruction algorithm (68,69).

### Image Analysis

PET amyloid image analysis packages are complex and highly variable; several exist, both commercially and independently developed. Some approaches use a standard anatomic space and transform the PET amyloid data to this space, often using the subject's MR images to improve the transformation (70). Others segment the MR images in native space and apply the boundaries to a coregistered PET image. A widely used analysis is known as the centiloid pipeline (60,61), which has already addressed many standardization issues. To mitigate the variability of these packages and evaluate their conformance, a digital-reference-object (DRO) series of synthetic PET data was derived from human anatomy (71) and includes T1-weighted MRI. Users should use the DRO series (as per the DRO user's guide in appendix F of the profile) to verify correct implementation of volume-of-interest placement for both target and reference regions, SUVR calculations, PET alignment to standardized atlases (when applicable), system linearity, and system reproducibility. The DRO images can be downloaded at a published link (72), and appendix F in the profile explains the rationale behind the DRO and details the conformance process.

Since SUVR is a ratio of target to reference regions, the selection of an appropriate reference region is critical. Reference regions are not prescribed by the profile, but it is imperative that the same region be used across longitudinal studies, and it should be selected to minimize serial or longitudinal variability. For example, the cerebellar cortex can optimize sensitivity because this region typically lacks amyloid, but it can be more vulnerable to subject motion and technical noise given its position near the edge of the axial field of view of the detectors. The cerebellum is positioned in slices of the brain that are more inferior than those of most target amyloid regions. Since scanner sensitivity is not perfectly consistent across the axial field of view, changes in head positioning from one scan to the next, or changes in slice sensitivity, can cause changes in both the numerator (the target region) and the denominator (the reference region) of the amyloid SUVR that do not cancel out and therefore mimic amyloid burden changes. Regions including white

matter or superior slices have been shown to reduce variability in radiopharmaceuticals such as  $^{18}\text{F}$ -florbetapir (6–8,66). Caveats are that the kinetics of white matter can differ from those of the target gray matter, that significant changes in white matter disease or in white matter binding associated with therapeutic intervention may impact longitudinal stability (73), and that benefit may depend on the white matter binding characteristics of the radiopharmaceutical (6–8,66). Although the standard centiloid pipeline (60,61) (which uses the whole cerebellum as a reference region) is compatible with the claim assuming profile conformance is met, Bourgeat et al. (74) reported that when a composite reference region that included subcortical white matter was used in the centiloid pipeline analysis for  $^{18}\text{F}$ -florbetapir longitudinal studies, higher consistency was achieved.

The target regions should be placed consistently. Larger regions (e.g., cortical average) should reduce variability in studies of large groups but can lose sensitivity if amyloid pathology is regionally restricted early in the disease course or in individuals with atypical presentations. Significant subject brain atrophy over serial scans may require region definition boundaries that minimize impact, aided by serial MRI, for the claim to be valid. Because PET scanners with higher resolution can tolerate more atrophy change, the reading physician will need to decide what level of atrophy can be tolerated on the basis of amyloid radiopharmaceutical reading experience and PET scanner resolution. Partial-volume correction for such issues is discussed in the profile but not specified in this version because of lack of a standardized technique and increased SUVR variability.

### Image Interpretation and Reporting

How quantitative response is measured should be specified a priori by the imaging site and should conform with the profile. There is no profile specification for image interpretation, even if based on quantitative SUVRs, since conformance to the profile ensures SUVR precision only across serial PET  $^{18}\text{F}$ -amyloid scans.

### Image Quality Control

The profile provides a quality control section and appendices for ensuring that the equipment (e.g., dose calibrator), scanner, reconstruction, and postprocessing pass the listed specifications. Various common PET phantoms are used for testing and qualifying the PET scanner, and time schedules for checking scanner and equipment calibrations are also specified.

## CONFORMANCE PROCEDURES

### Definitions

It is important to define and distinguish the difference between QIBA conformance with a profile and other organizations' similar definitions.

*Qualified.* *Qualified* indicates formal approval of the imaging site by an appropriate body (e.g., the American College of Radiology Imaging Network, the Centers for Quantitative Imaging Excellence, the Society of Nuclear Medicine and Molecular Imaging Clinical Trials Network, and EARL [EANM Research GmbH], an imaging laboratory or imaging contract research organization) for a specific clinical research study.

*Accredited.* *Accredited* indicates approval by an independent body or group for broad clinical use (requires ongoing quality assurance and quality control); for example, by the American College of Radiology, the Intersocietal Accreditation Commission, and The Joint Commission.

*Conformant.* *Conformant* indicates that the imaging site and equipment meet all the requirements described by the profile to meet the QIBA profile claim.

The profile does specify that the site is either qualified or accredited, so it builds on these procedures. The “Conformance Procedures” section in the profile outlines the specifications in the format of performance assessment tables from an actor point of view:

#### **Image Acquisition Site**

The image acquisition site specifications cover appropriate imaging equipment calibration and quality control processes, proper training of the various site personnel, and compliant scheduling of subject scans.

#### **PET Acquisition Device**

The profile supports PET/CT and PET-only scanners with transmission rods (e.g.,  $^{68}\text{Ge}$ ), both of which must acquire the PET data in 3-dimensional mode (e.g., septa should not be used). PET/MRI scanners are allowed if the repeatability of the SUVR 511-keV  $\mu$ -maps (used for PET attenuation and scatter corrections) from these scanners is conformant with the assumptions underlying the claims.

#### **Reconstruction Software**

The PET data should be reconstructed with full corrections (e.g., for normalization, attenuation, scatter, randoms, decay, and dead time). If available, time of flight can be applied during the reconstruction, but if the point-spread-function filter is available it should not be used.

#### **Image Analysis Workstation**

The conformance of the image analysis workstation should be tested, as described in the “Image Analysis” section above.

#### **Software Version Tracking**

Software versions, phantom imaging performance data, upgrade versions, and the date that updates occurred should all be tracked at the site and preferably stored in the DICOM image header.

#### **APPENDICES IN PROFILE**

The profile contains several appendices:

- A: Acknowledgments and attributions: lists the members of the QIBA amyloid PET biomarker committee and their affiliations.
- B: Background information for claim: gives details of the meta-analysis that was done to derive the claim.
- C: Conventions and definitions: explains the QIBA conventions used in writing profiles, and lists the definitions and abbreviations used in the profile.
- D: Model-specific instructions and parameters: lists equipment (e.g., PET/CT scanners) and the type of quality assurance procedures that should be performed to properly maintain the equipment.
- E: Data fields to be recorded in common-data-format mechanism: lists the meta-information that is necessary for quantitatively accurate PET SUVRs.
- F: Testing of PET display and analysis systems with DRO: is as described in the “Image Analysis” section above.
- G: Best practice guidance for Hoffman brain phantom: includes useful tips and tricks for filling the intricate Hoffman brain phantom, written by authors with extensive experience.

H: Detailed example of Hoffman phantom data analysis: explains the standard analysis used for qualifying PET scanners using data from the Hoffman brain phantom.

I: Kinetic modeling and comparison to SUVR: is as described in the “Image Data Acquisition” section above, which discusses the DVR.

J: Site checklist (appendix J): distills the various mitigations required by the profile into a list, organized by actor. This checklist is based on the questionnaire completed by multiple imaging sites during achievement of the technically confirmed stage. The checklist can provide a basis for imaging site qualification, to which other criteria can be added, depending on the study.

#### **RELATIONSHIP TO OTHER STANDARDS**

A site that is using the ADNI 2 or 3 protocol (75) is close to conforming with the profile (Table 4). The major differences are that the ADNI protocol does not specify accurate SUV or Bq/mL PET image quantification (and therefore lacks related specifications for information entry and equipment); does not specify an acceptable axial uniformity level (should be minimized for accurate serial SUVRs); does not specify how the subject should be positioned in the scanner (head should be centered and serial scans should have subject positioned as identically as possible to the previous scans); does not have a performance assessment for the Image Analysis Workstation; and does not make a claim about SUVR precision for the same subject scanned using the same scanner and protocol.

#### **PROFILE STAGE**

QIBA has a process committee that has adopted the stages of profile development as shown in Table 5. This profile has achieved stage 3—technically confirmed. Stages 4 and 5 can be achieved in the future as the profile is implemented and results are reported at more sites.

#### **INFORMATION GAPS ADDRESSED BY GROUNDWORK PROJECTS**

During writing of the profile, 3 major previously unknown sources of variability in SUVR were identified, and projects funded by grants from the RSNA in association with this working group were completed to characterize them: the impact of the different Image Analysis Workstation processing algorithms on SUVR (71); the impact of patient motion both between the CT and PET acquisitions and during the PET acquisition (65); and the impact of the PET reconstruction algorithm (68,69).

#### **FUTURE DEVELOPMENTS**

The profile can be updated to new versions, and proven technology and advances can be incorporated in the profile specifications. These include PET/MRI scanners (future versions may include specific requirements); partial-volume effect correction (e.g., for atrophy), once accepted and shown not to increase biomarker variability; potentially, body mass index (it is currently unknown how body mass index may affect the claim; studies are needed to determine whether wCV depends on body mass index and, if so, at what value of body mass index the claim is no longer valid); new PET  $^{18}\text{F}$ -amyloid radiopharmaceuticals, as they become widely used; and pooling of different amyloid tracers (centiloids (60,61) may be able to achieve this goal).

**TABLE 4**  
Differences Between Profile Specifications and ADNI 2 Protocol Specifications

Actor	Profile section for reference	ADNI 2 (58)
Site administrator	3.6.1.1: site accreditation/qualification maintenance	Same
Site administrator	3.6.2: imaging facility personnel	Same
Medical physicist	3.6.3: amyloid PET acquisition scanner	Same
Medical physicist	3.6.3.1.1: radionuclide calibrator	Same
Medical physicist	3.6.3.1.2: scales and stadiometers	Not required
Medical physicist	3.6.3.1.4: clocks and timing devices	Not required
Medical physicist	3.6.4.1: uniformity and calibration	Not required
Medical physicist	3.6.4.2: resolution	Same
Medical physicist	3.6.4.3: noise	Same
Medical physicist	3.6.4.4: amyloid PET specific phantom measurements	Same
Medical physicist	4.1: performance assessment: image acquisition site	Same
Technologist	3.1.3.1.2: radiopharmaceutical activity calculation or schedule	Dose structured report not required
Technologist	3.1.3.1.3: radiopharmaceutical administration route	Excludes saline flush and checking for infiltration
Technologist	3.2.1.1: timing of image data acquisition	Same
Technologist	3.2.1.2: subject positioning	Does not cover strict serial scan positioning
Technologist	3.2.1.3: scanning coverage and direction	Same
Technologist	3.2.1.4: scanner acquisition mode parameters: PET acquisition	Same except does not cover if scan is stopped and restarted
Technologist	3.2.1.4: scanner acquisition mode parameters: CT acquisition	Not required
Technologist	3.3.1: imaging data reconstruction	Same except point spread function is allowed
Image Analyst	4.4: performance assessment: image analysis workstation	Not required

A separate profile has been recommended for <sup>18</sup>F PET tau radiopharmaceuticals, with the profile serving as a starting base because of a similar workflow, including site qualification, phantoms, and equipment calibration; patient management during scans; sources of technical variability in measurement; image quality control; image processing alignment and spatial registration; and SUV<sub>r</sub> versus DVR.

The unique aspects of a tau-specific profile include a different set of radiopharmaceuticals and acquisition parameters; implications for clinical use; radiopharmaceutical-specific differences in the tau variants measured and in off-target binding; target regions, reference regions, and optimal measurement methods; radiopharmaceutical-specific differences; considerations in the longitudinal acquisition

**TABLE 5**  
QIBA Profile Development Stages

Profile stages	Description
Public comment	Biomarker committee experts have drafted profile and believe it is practical and expect it to achieve claimed performance
Consensus	Wider community has read profile and judged it to be practical and expect it to achieve claimed performance
Technically confirmed	Several sites have performed profile and found it to be practical and expect it to achieve claimed performance (status of the profile)
Claim confirmed	Some sites have performed profile and found that it achieved claimed performance
Clinically confirmed	Many sites have performed profile and demonstrated claimed performance is widely achievable



time window related to equilibrium; and potentially greater bias in SUVR versus DVR.

## PROFILE WRITING AND IMPLEMENTATION BARRIERS

There are several specific challenges in developing and implementing the profile.

First, the supported amyloid radiopharmaceuticals have different pharmacokinetics and vary in their image acquisition parameters, sensitivity, dynamic range, and manufacturer recommendations for measurement approaches (76). Including data from all supported amyloid radiopharmaceuticals and diverse members on the biomarker committee overcame this barrier.

Second, QIBA profiles have often used published literature as a basis for establishing the variability in the longitudinal claim. Most early amyloid PET studies used methods and scanners that can increase variability. Focus was placed on recommending methods and scanners that could be reasonably controlled and factored into the claim and on finding which references were applicable.

Another challenge was in deciding between full dynamic (DVR) and late-time-frame (SUVR) image acquisition. Although full dynamic acquisitions enable separation of amyloid measurement from blood flow, these long, labor-intensive protocols are not practical in many clinical settings and clinical trials. Therefore, the focus was late-time-frame SUVR, but an appendix was created to communicate the caveats of late-time-frame measurement and the potential benefits of full dynamic scans.

In addition, because of the lack of wide reimbursement for PET amyloid scans, the commercial availability of amyloid radiopharmaceuticals can be a barrier to clinical use. Anti-amyloid treatments will be successful only on patients with biomarker-verified amyloid-positive tests, which may help drive reimbursement.

Finally, achieving profile conformance takes extra effort and training by the sites for routine clinical use. This implementation effort can be justified if PET amyloid imaging is required before and during expensive AD treatments or if extra reimbursement is given for quantitative PET amyloid imaging.

## CONCLUSION

The QIBA amyloid profile provides recommendations for image acquisition, processing, and measurement approaches supporting a claim regarding technical variability in longitudinal amyloid measurement. This information can aid in the design of statistically powered clinical trials and in the assessment of longitudinal changes in the clinic. Although it is not QIBA's mission to enforce profile compliance or to govern the requirements of granting agencies, profiles can be used as a guideline for applicants and for reviewer assessments of proposed study designs, with the main objective of minimizing sample size. Given the recent market availability of anti-amyloid therapeutics, and the importance of amyloid as an early biomarker in the diagnosis of AD, the profile recommendations can provide an important guide for the consistent, objective monitoring of disease progression and treatment response.

## DISCLOSURE

This work was financially supported by the RSNA including QIBA leadership and staff time. This project was funded in whole or in part with federal funds from the National Institute of Biomedical Imaging and Bioengineering, National Institutes of Health, and

Department of Health and Human Services, under contracts HHSN268201300071C, HHSN268201500021C, P50AG005681, P01AG003991, U19AG03243808, U01AG042791, and UL1TR000448. No other potential conflict of interest relevant to this article was reported.

## ACKNOWLEDGMENTS

The QIBA PET amyloid biomarker committee members who developed and wrote the profile are all volunteers and come from academic, clinical, government, and industry sectors. Without their expertise, experience, time, and effort, the creation of the profile and the advancement of quantitative PET amyloid imaging would not be possible. Dr. Rathana Subramanian and his team performed the meta-analysis work for the claim. We are grateful to the Imaging Research Laboratory at the University of Washington, Department of Radiology, and Dr. Larry Pierce and Darrin Byrd for spending countless hours developing the PET brain DRO—a major achievement for the profile and the PET amyloid field. Dr. Rachid Fahmi from Siemens Healthineers was instrumental in testing and improving the DRO. Julie Lisiecki coordinated all working group meetings and provided documentation supporting profile development, with additional support from Joseph Koudelik. The reviewer of this article made it a stronger publication through helpful criticisms and insights. Finally, we thank the QIBA biomarker committee that authored the  $^{18}\text{F}$ -FDG PET/CT as an imaging biomarker measuring response and the Cancer Therapy profile for developing the PET base profile and supporting this committee.

## KEY POINTS

**QUESTION:** How can a PET amyloid imaging site decrease SUVR variability when performing longitudinal scanning of the same patient?

**PERTINENT FINDINGS:** Conforming with the QIBA PET amyloid profile can decrease the wCV (e.g., variability) to no more than 1.94%.

**IMPLICATIONS FOR PATIENT CARE:** As AD treatments improve, visual PET amyloid assessments become more ambiguous, and decreasing the PET SUVR variance may allow for earlier detection of  $\beta$ -amyloid plaques and more effective anti-amyloid treatments.

## REFERENCES

- McKhann GM, Knopman DS, Chertkow H, et al. The diagnosis of dementia due to Alzheimer's disease: recommendations from the National Institute on Aging and the Alzheimer's Association workgroup. *Alzheimers Dement*. 2011;7:263–269.
- Jack CR Jr, Bennett DA, Blennow K, et al. NIA-AA research framework: toward a biological definition of Alzheimer's disease. *Alzheimers Dement*. 2018;14:535–562.
- Nicoll JA, Wilkinson D, Holmes C, Steart P, Markham H, Weller RO. Neuropathology of human Alzheimer disease after immunization with amyloid-beta peptide: a case report. *Nat Med*. 2003;9:448–452.
- Mintun MA, Lo AC, Duggan Evans C, et al. Donanemab in early Alzheimer's disease. *N Engl J Med*. 2021;384:1691–1704.
- van der Kall LM, Truong T, Burnham SC, et al. Association of beta-amyloid level, clinical progression, and longitudinal cognitive change in normal older individuals. *Neurology*. 2021;96:e662–e670.
- Chen K, Roontiva A, Thiyyagura P, et al. Improved power for characterizing longitudinal amyloid-beta PET changes and evaluating amyloid-modifying treatments with a cerebral white matter reference region. *J Nucl Med*. 2015;56:560–566.

7. Brendel M, Hogenauer M, Delker A, et al. Improved longitudinal [<sup>18</sup>F]-AV45 amyloid PET by white matter reference and VOI-based partial volume effect correction. *Neuroimage*. 2015;108:450–459.
8. Chiao P, Bedell BJ, Avants B, et al. Impact of reference and target region selection on amyloid PET SUV ratios in the phase 1b PRIME study of aducanumab. *J Nucl Med*. 2019;60:100–106.
9. van Berckel BN, Ossenkuppe R, Tolboom N, et al. Longitudinal amyloid imaging using <sup>11</sup>C-PIB: methodologic considerations. *J Nucl Med*. 2013;54:1570–1576.
10. Quantitative Imaging Biomarkers Alliance. Radiological Society of North America website. <https://www.rsna.org/QIBA>. Accessed October 5, 2022.
11. Profiles. Radiological Society of North America website. <https://qibawiki.rsna.org/index.php/profiles>. Updated October 5, 2022. Accessed October 5, 2022.
12. Integrating the healthcare enterprise. IHE website. [https://www.ihe.net/wp-content/uploads/2018/07/ihe\\_radiology\\_users\\_handbook\\_2005edition.pdf](https://www.ihe.net/wp-content/uploads/2018/07/ihe_radiology_users_handbook_2005edition.pdf). Published 2005. Accessed October 5, 2022.
13. Barret O, Alagille D, Sanabria S, et al. Kinetic modeling of the tau PET tracer <sup>18</sup>F-AV-1451 in human healthy volunteers and Alzheimer's disease subjects. *J Nucl Med*. 2017;58:1124–1131.
14. Blautzik J, Brendel M, Sauerbeck J, et al. Reference region selection and the association between the rate of amyloid accumulation over time and the baseline amyloid burden. *Eur J Nucl Med Mol Imaging*. 2017;44:1364–1374.
15. Bourgeat P, Doré V, Doecke J, et al. Non-negative matrix factorisation improves centiloid robustness in longitudinal studies. *Neuroimage*. 2021;226:117593.
16. Edison P, Hinz R, Ramlackhansingh A, et al. Can target-to-pons ratio be used as a reliable method for the analysis of [<sup>11</sup>C]PIB brain scans? *Neuroimage*. 2012;60:1716–1723.
17. Fleisher AS, Rountiva A, Reschke C, et al. Improving the power to track fibrillar amyloid PET measurements and evaluate amyloid modifying treatments using a cerebral white matter reference region of interest. In: *Alzheimer's Association International Conference (AAIC)*. Elsevier; 2014:P4-298.
18. Hahn A, Schain M, Erlandsson M, et al. Modeling strategies for quantification of in vivo <sup>18</sup>F-AV-1451 binding in patients with tau pathology. *J Nucl Med*. 2017;58:623–631.
19. Heeman F, Hendriks J, Lopes Alves I, et al. [<sup>11</sup>C]PIB amyloid quantification: effect of reference region selection. *EJNMMI Res*. 2020;10:123.
20. Joshi A, Kennedy IA, Mintun M, Pontecorvo M, Navitsky MA, Devous MD. Measuring change in beta amyloid burden over time using florbetapir PET and a subcortical white matter reference region. In: *Alzheimer's Association International Conference (AAIC)*. Elsevier; 2014:P4-316.
21. Klein G, Sampat M, Staewen D, Scott D, Suhy J. Comparative assessment of SUVR methods and reference regions in amyloid PET studies. In: *Alzheimer's Association International Conference (AAIC)*. Elsevier; 2015:P1-035.
22. Koeppe RA. Basic principles and controversies in PET amyloid imaging. Presented at: Human Amyloid Imaging (HAI) Conference, February 24, 2012, Miami Beach, FL, HAI Abstract Book, 2012.
23. Landau SM, Breault C, Joshi AD, et al.; Alzheimer's disease neuroimaging initiative. Amyloid- $\beta$  imaging with Pittsburgh compound B and florbetapir: comparing radiotracers and quantification methods. *J Nucl Med*. 2013;54:70–77.
24. Landau SM, Fero A, Baker SL, et al. Measurement of longitudinal  $\beta$ -amyloid change with <sup>18</sup>F-florbetapir PET and standardized uptake value ratios. *J Nucl Med*. 2015;56:567–574.
25. Lodge MA, Rahmim A, Wahl RL. Simultaneous measurement of noise and spatial resolution in PET phantom images. *Phys Med Biol*. 2010;55:1069–1081.
26. Lundqvist R, Lilja J, Thomas BA, et al. Implementation and validation of an adaptive template registration method for <sup>18</sup>F-flutemetamol imaging data. *J Nucl Med*. 2013;54:1472–1478.
27. Makris NE, Huisman MC, Kinahan PE, Lammertsma AA, Boellaard R. Evaluation of strategies towards harmonization of FDG PET/CT studies in multicentre trials: comparison of scanner validation phantoms and data analysis procedures. *Eur J Nucl Med Mol Imaging*. 2013;40:1507–1515.
28. Pontecorvo MJ, Devous MD Sr, Navitsky M, et al. Relationships between flortaucipir PET tau binding and amyloid burden, clinical diagnosis, age and cognition. *Brain*. 2017;140:748–763.
29. Schmidt ME, Chiao P, Klein G, et al. The influence of biological and technical factors on quantitative analysis of amyloid PET: points to consider and recommendations for controlling variability in longitudinal data. *Alzheimers Dement*. 2015;11:1050–1068.
30. Schwarz CG, Senjem ML, Gunter JL, et al. Optimizing PiB-PET SUVR change-over-time measurement by a large-scale analysis of longitudinal reliability, plausibility, separability, and correlation with MMSE. *Neuroimage*. 2017;144:113–127.
31. Shcherbinin S, Schwarz AJ, Joshi A, et al. Kinetics of the tau PET tracer <sup>18</sup>F-AV-1451 (T807) in subjects with normal cognitive function, mild cognitive impairment, and Alzheimer disease. *J Nucl Med*. 2016;57:1535–1542.
32. Shokouhi S, McKay JW, Baker SL, et al. Reference tissue normalization in longitudinal <sup>18</sup>F-florbetapir positron emission tomography of late mild cognitive impairment. *Alzheimers Res Ther*. 2016;8:2.
33. Thurfjell L, Lilja J, Lundqvist R, et al. Automated quantification of <sup>18</sup>F-flutemetamol PET activity for categorizing scans as negative or positive for brain amyloid: concordance with visual image reads. *J Nucl Med*. 2014;55:1623–1628.
34. Tryputsen V, DiBernardo A, Samtani M, Novak GP, Narayan VA, Raghavan N. Optimizing regions-of-interest composites for capturing treatment effects on brain amyloid in clinical trials. *J Alzheimers Dis*. 2015;43:809–821.
35. Abella M, Alessio AM, Mankoff DA, et al. Accuracy of CT-based attenuation correction in PET/CT bone imaging. *Phys Med Biol*. 2012;57:2477–2490.
36. Rowe CC, Doré V, Jones G, et al. <sup>18</sup>F-florbetaben PET beta-amyloid binding expressed in centiloids. *Eur J Nucl Med Mol Imaging*. 2017;44:2053–2059.
37. Su Y, Flores S, Horneck RC, et al. Utilizing the centiloid scale in cross-sectional and longitudinal PiB PET studies. *Neuroimage Clin*. 2018;19:406–416.
38. Johnson KA, Minoshima S, Bohnen NI, et al. Appropriate use criteria for amyloid PET: a report of the Amyloid Imaging Task Force, the Society of Nuclear Medicine and Molecular Imaging, and the Alzheimer's Association. *Alzheimers Dement*. 2013;9:e-1–e-16.
39. Johnson KA, Minoshima S, Bohnen NI, et al. Update on appropriate use criteria for amyloid PET imaging: dementia experts, mild cognitive impairment, and education. *J Nucl Med*. 2013;54:1011–1013.
40. Schmidt ME, Matthews D, Andrews R, Mosconi L. Positron emission tomography in Alzheimer disease: diagnosis and use as biomarker endpoints. In: McArthur RA ed. *Translational Neuroimaging: Tools for CNS Drug Discovery, Development, and Treatment*. Academic Press; 2013:131–194.
41. Medicines in development: Alzheimer's disease. PhRMA website. <http://phrma-docs.phrma.org/sites/default/files/Alzheimer%27s%202013.pdf>. Published 2013. Accessed October 6, 2022.
42. Becker GA, Masanori I, Barthel H, et al. PET quantification of <sup>18</sup>F-florbetaben binding to  $\beta$ -amyloid deposits in human brains. *J Nucl Med*. 2013;54:723–731.
43. Bullich S, Barthel H, Koglin N, et al. Validation of non-invasive tracer kinetic analysis of <sup>18</sup>F-florbetaben PET using a dual time-window acquisition protocol. *J Nucl Med*. 2018;59:1104–1110.
44. Cselényi Z, Farde L. Quantification of blood flow-dependent component in estimates of beta-amyloid load obtained using quasi-steady-state standardized uptake value ratio. *J Cereb Blood Flow Metab*. 2015;35:1485–1493.
45. Forsberg A, Engler H, Blomquist G, Långström B, Nordberg A. The use of PiB-PET as a dual pathological and functional biomarker in AD. *Biochim Biophys Acta*. 2012;1822:380–385.
46. Frokjaer VG, Pinborg LH, Madsen J, et al. Evaluation of the serotonin transporter ligand <sup>123</sup>I-ADAM for SPECT studies on humans. *J Nucl Med*. 2008;49:247–254.
47. Gjedde A, Aanerud J, Braendgaard H, Rodell AB. Blood-brain transfer of Pittsburgh compound B in humans. *Front Aging Neurosci*. 2013;5:70.
48. Hsiao IT, Huang CC, Hsieh CJ, et al. Correlation of early-phase <sup>18</sup>F-florbetapir (AV-45/Amyvid) PET images to FDG images: preliminary studies. *Eur J Nucl Med Mol Imaging*. 2012;39:613–620.
49. Lopresti BJ, Klunk WE, Mathis CA, et al. Simplified quantification of Pittsburgh compound B amyloid imaging PET studies: a comparative analysis. *J Nucl Med*. 2005;46:1959–1972.
50. Nelissen N, Van Laere K, Thurfjell L, et al. Phase 1 study of the Pittsburgh compound B derivative <sup>18</sup>F-flutemetamol in healthy volunteers and patients with probable Alzheimer disease. *J Nucl Med*. 2009;50:1251–1259.
51. Price JC, Klunk WE, Lopresti BJ, et al. Kinetic modeling of amyloid binding in humans using PET imaging and Pittsburgh compound-B. *J Cereb Blood Flow Metab*. 2005;25:1528–1547.
52. Rostomian AH, Madison C, Rabinovici GD, Jagust WJ. Early <sup>11</sup>C-PIB frames and <sup>18</sup>F-FDG PET measures are comparable: a study validated in a cohort of AD and FTLN patients. *J Nucl Med*. 2011;52:173–179.
53. Sepulveda-Falla D, Matschke J, Bernreuther C, et al. Deposition of hyperphosphorylated tau in cerebellum of PS1 E280A Alzheimer's disease. *Brain Pathol*. 2011;21:452–463.
54. Sevigny J, Chiao P, Bussière T, et al. The antibody aducanumab reduces A $\beta$  plaques in Alzheimer's disease. *Nature*. 2016;537:50–56.
55. Slifstein M. Revisiting an old issue: the discrepancy between tissue ratio-derived binding parameters and kinetic modeling-derived parameters after a bolus of the serotonin transporter radioligand <sup>123</sup>I-ADAM. *J Nucl Med*. 2008;49:176–178.
56. Tolboom N, Yaqub M, Boellaard R, et al. Test-retest variability of quantitative [<sup>11</sup>C]PIB studies in Alzheimer's disease. *Eur J Nucl Med Mol Imaging*. 2009;36:1629–1638.
57. Wong DF, Rosenberg PB, Zhou Y, et al. In vivo imaging of amyloid deposition in Alzheimer disease using the radioligand <sup>18</sup>F-AV-45 (florbetapir F 18). *J Nucl Med*. 2010;51:913–920.
58. Alzheimer's Disease Neuroimaging Initiative. ADNI website. <http://adni.loni.usc.edu/>. Accessed October 6, 2022.
59. Carson RE, Channing MA, Blasberg RG, et al. Comparison of bolus and infusion methods for receptor quantitation: application to [<sup>18</sup>F]cyclofoxy and positron emission tomography. *J Cereb Blood Flow Metab*. 1993;13:24–42.

60. Klunk WE, Koeppe RA, Price JC, et al. The centiloid project: standardizing quantitative amyloid plaque estimation by PET. *Alzheimers Dement*. 2015; 11:1–15.e1–4.
61. Rowe CC, Jones G, Dore V, et al. Standardized expression of <sup>18</sup>F-NAV4694 and <sup>11</sup>C-PiB beta-amyloid PET results with the centiloid scale. *J Nucl Med*. 2016;57: 1233–1237.
62. Obuchowski NA, Mozley PD, Matthews D, Buckler A, Bullen J, Jackson E. Statistical considerations for planning clinical trials with quantitative imaging biomarkers. *J Natl Cancer Inst*. 2019;111:19–26.
63. Joshi AD, Pontecorvo MJ, Clark CM, et al. Performance characteristics of amyloid PET with florbetapir F 18 in patients with Alzheimer’s disease and cognitively normal subjects. *J Nucl Med*. 2012;53:378–384.
64. Vandenberghe R, Van Laere K, Ivanoiu A, et al. <sup>18</sup>F-flutemetamol amyloid imaging in Alzheimer disease and mild cognitive impairment: a phase 2 trial. *Ann Neurol*. 2010;68:319–329.
65. Andrews R, Matthews D, Smith AM. The quantitative impact of emission-transmission scan misalignment and region selection upon amyloid measurement accuracy. In: *11<sup>th</sup> Human Amyloid Imaging: Conference Program and Abstracts*. World Events Forum; 2017:73.
66. Matthews D, Marendic B, Andrews R, et al., for the Alzheimer’s Disease Neuroimaging Initiative. Longitudinal amyloid measurement for clinical trials: a new approach to overcome variability. In: *8<sup>th</sup> Human Amyloid Imaging: Conference Program and Abstracts*. World Events Forum; 2014:88–89.
67. Klunk WE, Engler H, Nordberg A, et al. Imaging brain amyloid in Alzheimer’s disease with Pittsburgh compound-B. *Ann Neurol*. 2004;55:306–319.
68. Matthews D, Andrews R, Smith A. The impact of PET reconstruction method on measured amyloid SUVR. In: *12<sup>th</sup> Human Amyloid Imaging: Conference Program and Abstracts*. World Events Forum; 2018:96.
69. Smith AM, Matthews D, Andrews R. Assessment of PET amyloid quantification differences by varying the reconstruction protocol. In: *2017 IEEE Nuclear Science Symposium and Medical Imaging Conference (NSS/MIC)*. IEEE; 2017:1–6.
70. Talairach J, Tournoux P. *Co-Planar Stereotaxic Atlas of the Human Brain: An Approach to Medical Cerebral Imaging*. Thieme Medical Publishers; 1988:66.
71. Perlman ES, Smith AM, Minoshima S, et al. QIBA PET amyloid biomarker committee: overview and status update. RSNA website. [https://qibawiki.rsna.org/images/0/06/PET-Amyloid-Poster\\_QIBA\\_Kiosk\\_RSNA2015.pdf](https://qibawiki.rsna.org/images/0/06/PET-Amyloid-Poster_QIBA_Kiosk_RSNA2015.pdf). Published 2015. Accessed October 6, 2022.
72. Digital Reference Object. University of Washington website. [http://depts.washington.edu/petctdro/DRObrain\\_main.html](http://depts.washington.edu/petctdro/DRObrain_main.html). Published June 21, 2016. Accessed October 6, 2022.
73. Kameyama M, Ishibash K, Wagatsuma K, Toyohara J, Ishii K. A pitfall of white matter reference regions used in [<sup>18</sup>F] florbetapir PET: a consideration of kinetics. *Ann Nucl Med*. 2019;33:848–854.
74. Bourgeat P, Li S, Sosun D, et al. Centiloid harmonization strategies across longitudinal studies: evaluation on AIBL, ADNI and OASIS3. *Alzheimers Dement*. 2021; 17(suppl 1):e053660.
75. PET acquisition. ADNI website. <http://adni.loni.usc.edu/methods/pet-analysis-method/pet-analysis/>. Accessed October 6, 2022.
76. Bischof GN, Bartenstein P, Barthel H, et al. Toward a universal readout for <sup>18</sup>F-labeled amyloid tracers: the CAPTAINS study. *J Nucl Med*. 2021;62:999–1005.
77. Amyvid [package insert]. Eli Lilly & Co.; 2012.
78. Vizamyl [package insert]. GE Healthcare, Medi-Physics, Inc.; 2013.
79. Neuraceq [package insert]. Piramal Imaging, S.A.; 2014.
80. Rowe CC, Pejoska S, Mulligan RS, et al. Head-to-head comparison of <sup>11</sup>C-PiB and <sup>18</sup>F-AZD4694 (NAV4694) for beta-amyloid imaging in aging and dementia. *J Nucl Med*. 2013;54:880–886.

---

---

# Clinical Decision Support for Axillary Lymph Node Staging in Newly Diagnosed Breast Cancer Patients Based on <sup>18</sup>F-FDG PET/MRI and Machine Learning

Janna Morawitz<sup>1</sup>, Benjamin Sigl<sup>2</sup>, Christian Rubbert<sup>1</sup>, Nils-Martin Bruckmann<sup>1</sup>, Frederic Dietzel<sup>1</sup>, Lena J. Häberle<sup>3</sup>, Saskia Ting<sup>4</sup>, Svyetlana Mohrmann<sup>5</sup>, Eugen Ruckhäberle<sup>5</sup>, Ann-Kathrin Bittner<sup>6</sup>, Oliver Hoffmann<sup>6</sup>, Pascal Baltzer<sup>2</sup>, Panagiotis Kapetas<sup>2</sup>, Thomas Helbich<sup>2</sup>, Paola Clauser<sup>2</sup>, Wolfgang P. Fendler<sup>7</sup>, Christoph Rischpler<sup>7</sup>, Ken Herrmann<sup>7</sup>, Benedikt M. Schaarschmidt<sup>8</sup>, Andreas Stang<sup>9</sup>, Lale Umutlu<sup>8</sup>, Gerald Antoch<sup>1</sup>, Julian Caspers\*<sup>1</sup>, and Julian Kirchner\*<sup>1</sup>

<sup>1</sup>Department of Diagnostic and Interventional Radiology, Medical Faculty, University of Duesseldorf, Duesseldorf, Germany;

<sup>2</sup>Department of Biomedical Imaging and Image-Guided Therapy, Division of General Radiology, Medical University of Vienna, Vienna, Austria;

<sup>3</sup>Institute of Pathology, Medical Faculty, Heinrich Heine University and University Hospital Duesseldorf, Duesseldorf, Germany;

<sup>4</sup>Institute of Pathology, University Hospital Essen, West German Cancer Center, University of Duisburg–Essen and the German Cancer Consortium (DKTK), Essen, Germany;

<sup>5</sup>Department of Gynecology and Obstetrics, University Hospital Essen, University of Duisburg–Essen, Essen, Germany;

<sup>6</sup>Department of Gynecology and Obstetrics, University Hospital Essen, University of Duisburg–Essen, Essen, Germany;

<sup>7</sup>Department of Nuclear Medicine, University Hospital Essen, University of Duisburg–Essen and German Cancer Consortium (DKTK), Essen, Germany;

<sup>8</sup>Department of Diagnostic and Interventional Radiology and Neuroradiology, University Hospital Essen, University of Duisburg–Essen, Essen, Germany; and

<sup>9</sup>Institute of Medical Informatics, Biometry, and Epidemiology, Essen University Medical Center, Essen, Germany

---

In addition to its high prognostic value, the involvement of axillary lymph nodes in breast cancer patients also plays an important role in therapy planning. Therefore, an imaging modality that can determine nodal status with high accuracy in patients with primary breast cancer is desirable. Our purpose was to investigate whether, in newly diagnosed breast cancer patients, machine-learning prediction models based on simple assessable imaging features on MRI or PET/MRI are able to determine nodal status with performance comparable to that of experienced radiologists; whether such models can be adjusted to achieve low rates of false-negatives such that invasive procedures might potentially be omitted; and whether a clinical framework for decision support based on simple imaging features can be derived from these models. **Methods:** Between August 2017 and September 2020, 303 participants from 3 centers prospectively underwent dedicated whole-body <sup>18</sup>F-FDG PET/MRI. Imaging datasets were evaluated for axillary lymph node metastases based on morphologic and metabolic features. Predictive models were developed for MRI and PET/MRI separately using random forest classifiers on data from 2 centers and were tested on data from the third center. **Results:** The diagnostic accuracy for MRI features was 87.5% both for radiologists and for the machine-learning algorithm. For PET/MRI, the diagnostic accuracy was 89.3% for the radiologists and 91.2% for the machine-learning algorithm, with no significant differences in diagnostic performance between radiologists and the machine-learning algorithm for MRI ( $P = 0.671$ ) or PET/MRI ( $P = 0.683$ ). The most important lymph node feature was tracer uptake, followed by lymph node size. With an adjusted threshold, a sensitivity of 96.2% was achieved by the random forest classifier, whereas specificity, positive predictive value, negative predictive value, and accuracy were 68.2%, 78.1%, 93.8%, and 83.3%, respectively. A decision tree based on 3 simple imaging

features could be established for MRI and PET/MRI. **Conclusion:** Applying a high-sensitivity threshold to the random forest results might potentially avoid invasive procedures such as sentinel lymph node biopsy in 68.2% of the patients.

**Key Words:** breast cancer; lymph node metastases; machine learning; PET/MRI

**J Nucl Med 2023; 64:304–311**

DOI: 10.2967/jnumed.122.264138

---

**W**ith more than 2.3 million cases in 2020, breast cancer represents the world's most prevalent cancer (1). In primary breast cancer, axillary lymph node involvement is the most important predictor of overall survival and recurrence in breast cancer patients (2) and has a decisive influence on the therapy regime. Whereas a few years ago mastectomy and extensive axillary dissection were performed in most clinically node-positive patients, advances in imaging, among other factors, have helped to make therapeutic options for local control much less invasive (3,4). When imaging procedures such as sonography and mammography do not reveal affected axillary lymph nodes, sentinel lymph node biopsy is now the gold standard for clinically node-negative patients (5). With regard to the planned therapy, this is decisive, because depending on these findings, axillary dissection and axillary radiation are further therapy options (6). Nearly 60% of breast carcinoma patients do not have lymph node metastases at the time of initial diagnosis (7). These patients, in particular, would benefit from deescalation of invasive procedures. Although the recently introduced Node-RADS (Reporting and Data System) classification tries to standardize reporting of possible lymph node metastases (8), no universal consensus exists on objective criteria for evaluation of metastatic disease in the axillary lymph nodes of breast cancer patients, and N staging by imaging remains a challenge (7,9,10).

---

Received Mar. 16, 2022; revision accepted Aug. 19, 2022.

For correspondence or reprints, contact Janna Morawitz (janna.morawitz@med.uni-duesseldorf.de).

\*Contributed equally to this work.

Published online Sep. 22, 2022.

COPYRIGHT © 2023 by the Society of Nuclear Medicine and Molecular Imaging.

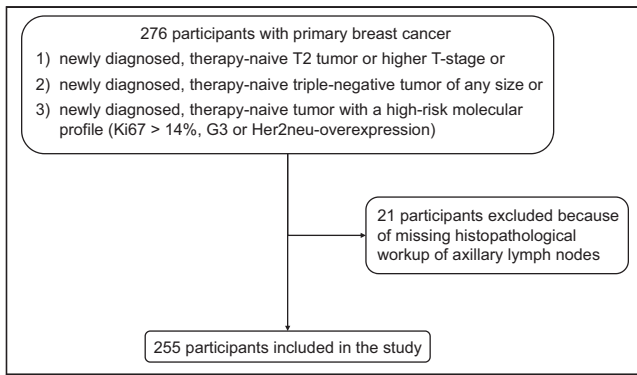


**FIGURE 1.** Flowchart of included and excluded participants. G3 = grade 3; Her2neu = human epidermal growth factor receptor type 2.

In recent years, artificial intelligence and machine learning have emerged strongly into the medical imaging field (11). Thus, incorporating machine-learning models into imaging-based decision-support tools has great potential to enhance diagnostic workup in breast cancer patients.

Therefore, the aim of this study was to investigate whether, in newly diagnosed breast cancer patients, machine-learning prediction models based on simple and easily assessable imaging features on MRI or PET/MRI are able to detect lymph node metastases with performance comparable to that of experienced radiologists; whether such models can be adjusted to achieve low rates of false-negatives such that invasive procedures might potentially be omitted; and whether a clinical framework for decision support based on simple imaging features can be derived from these models.

## MATERIALS AND METHODS

Because of the multiple aims of this study, the workflow was structured into 3 consecutive steps involving different methods. All calculations were based on the assessment of predefined imaging features of axillary lymph nodes by radiologists. First, machine-learning-based prediction models applying random forest classifiers were developed using the imaging features derived from the radiologist reader assessments, and their predictive performance on an independent test sample was compared with that of radiologists. Second, the random forest classifiers were adjusted to

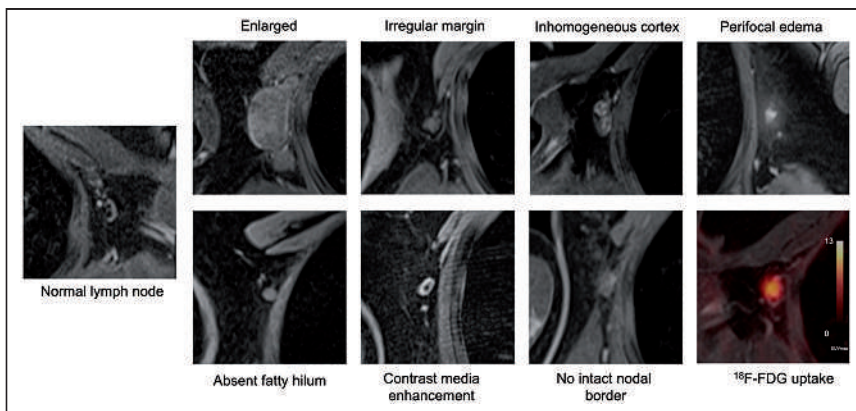


**FIGURE 2.** Examples of morphologic and metabolic features for assessment of axillary lymph nodes in axial T1-weighted, volume-interpolated breath-hold examination, fat-saturated, contrast-enhanced images. Enlarged lymph node has short-axis diameter of 31 mm. Lymph node with increased  $^{18}\text{F}$ -FDG uptake has  $\text{SUV}_{\text{max}}$  of 13.1.

minimize false-negative results by receiver-operating-characteristic (ROC) area-under-the-curve (AUC) optimization. Third, to facilitate a simple decision framework for everyday clinical routine, a simple decision tree classifier was trained on the imaging features independently of the optimized random forest classifiers trained beforehand.

## Participant Population, Inclusion Criteria, and Imaging Protocol

The study sample consisted of 2 samples: a training sample derived from 2 centers (University Hospital Duesseldorf and University Hospital Essen) and a testing sample from a third center (Medical University of Vienna, General Hospital).

For the training sample, 255 participants were prospectively included (Fig. 1). All had newly diagnosed, therapy-naïve breast cancer with at least one of the following criteria for a worse prognosis: a newly diagnosed, therapy-naïve T2 tumor or a higher T stage; a newly diagnosed, therapy-naïve triple-negative tumor of any size; or a newly diagnosed, therapy-naïve tumor with a high-risk molecular profile (Ki-67 > 14%, grade 3, or overexpression of human epidermal growth factor receptor type 2). All participants underwent whole-body  $^{18}\text{F}$ -FDG PET/MRI. Some participants have been reported before (7,12,13). This study was approved by the local ethics committees (study 6040R, 17-7396-BO + 510-2009). The test sample consisted of 48 participants. All PET/MRI examinations were performed on an integrated hybrid 3.0-T PET/MRI system (Biograph mMR; Siemens Healthcare) (14).

## Image Analysis

Imaging data from the training and test samples were analyzed by 1 reader, whereas data from the test sample were additionally rated by a second reader. MRI or PET/MRI datasets were analyzed in random order using an Osirix workstation (Pixmeo SARL). Readers were unaware of participant identity and all clinical information except for the diagnosis of breast cancer. For every participant, the presence or absence of axillary lymph node metastasis was evaluated on MRI and subsequently on PET/MRI separately. This assessment was of predefined imaging features of the most suggestive axillary lymph node for each participant. The morphologic features for the assessment of lymph node metastases were short-axis diameter in millimeters, irregular margin (yes/no), inhomogeneous cortex (yes/no), intact nodal border (yes/no), perifocal edema (yes/no), absence of fatty hilum (yes/no), and contrast medium enhancement (yes/no) (Fig. 2). On PET/MRI, tracer uptake in terms of the  $\text{SUV}_{\text{max}}$  of the selected lymph node was assessed by manually drawing a region of interest around the respective lymph node. A lymph node  $\text{SUV}_{\text{max}}$  ratio was calculated, with the blood pool  $\text{SUV}_{\text{max}}$  of the ascending aorta as the denominator. Considering all criteria together, each reader then made a final evaluation of the lymph node status, although an absolute number of positive findings did not have to be present to evaluate the lymph node as benign or malignant.

## Reference Standard

In all participants, the histopathologic findings for the axillary lymph nodes served as the reference standard. If available, sentinel lymph node biopsy or axillary dissection was used. Otherwise, histopathologic results were derived from pretherapeutic ultrasound-guided core-needle biopsy of the suggestive lymph node. If no sufficient pretherapeutic sampling of lymph nodes was available, sentinel lymph node excision or axillary dissection after neoadjuvant systemic therapy was used as the reference standard. In these cases,

**TABLE 1**  
Participant Demographics and Tumor Characteristics

Parameter	Training sample	Testing sample	<i>P</i>
Total participants	255	48	
Mean age ( $\pm$ SD)	51.2 $\pm$ 11.9 y	52.2 $\pm$ 12.2 y	0.689
Lymph node status (reference standard)			
Negative	154 (60.4%)	26 (54.2%)	0.420
Positive	101 (39.6%)	22 (45.8%)	
Menopause status			
Premenopausal	111 (43.5%)	18 (37.5%)	0.737
Perimenopausal	25 (9.8%)	5 (10.4%)	
Postmenopausal	119 (46.7%)	25 (52.1%)	
Ki-67			
Positive > 14%	226 (88.6%)	41 (85.4%)	0.528
Negative < 14%	29 (11.4%)	7 (14.6%)	
Progesterone status			
Positive	169 (66.3%)	29 (60.4%)	0.433
Negative	86 (33.7%)	19 (39.6%)	
Estrogen status			
Positive	187 (73.3%)	28 (58.3%)	<0.01
Negative	68 (26.7%)	20 (41.7%)	
HER2neu expression			
0	97 (38.0%)	23 (47.9%)	0.479
1+	73 (28.6%)	14 (29.2%)	
2+	34 (13.3%)	5 (10.4%)	
3+	51 (20.0%)	6 (12.5%)	
Tumor grade			
1	10 (3.9%)	4 (8.3%)	0.025
2	137 (53.7%)	16 (33.3%)	
3	108 (42.4%)	28 (58.3%)	
Histology			
No special type	222 (87.1%)	42 (87.5%)	< 0.01
Lobular invasive	25 (9.8%)	0 (0%)	
Other	8 (3.1%)	6 (12.5%)	

HER2neu = human epidermal growth factor receptor type 2.  
Data are number and percentage, except for age.

additional histopathologic preparations were evaluated, using focal fibrosis or focal necrosis as retrospective indicators of previously viable lymph node metastasis (15,16).

### Model Development

Predictive models were developed for MRI and PET/MRI separately using random forest classifiers. For each modality, a random forest classifier was trained using the imaging features derived from the reader assessment as input features and the dichotomous reference standard (benign or malignant) as output.

To further optimize the classification of the models for sensitivity and minimize false-negatives (to identify a rule-out criterion), an adjusted random forest model was developed by adjusting the classification threshold of a trained random forest model on an independent validation set that was split from the training sample beforehand

(80:20 stratified split) so that sensitivities of more than 0.95 were achieved on this validation set.

To additionally create more clinically interpretable classifiers, simple decision-tree classifiers with a maximum depth of 3 were additionally built using Gini impurity as the optimization criterion.

The model was developed using the scikit-learn library (version 0.24.2) in Python 3.9.

### Statistics

For statistical analyses, SPSS Statistics (version 21; IBM) was used. Demographic participant data were reported using descriptive statistics. The Cohen  $\kappa$  was used to calculate interrater reliability between the 2 readers regarding prediction of lymph node status (metastatic vs. non-metastatic) on MRI and PET/MRI. The diagnostic performance of the radiologists and machine-learning models for lymph node status on

**TABLE 2**

Diagnostic Performance of MRI and PET/MRI in Assessment of Lymph Node Status of Radiologists and Random Forest Classifier Within Testing Sample

Assessor	MRI	PET/MRI
<b>Radiologists</b>		
Sensitivity	84.6 (65.1–95.6)	92.3 (74.9–99.1)
Specificity	90.9 (70.8–98.9)	86.4 (65.1–97.1)
PPV	91.7 (74.4–97.7)	88.9 (73.5–96.8)
NPV	83.3 (66.8–92.6)	90.5 (71.3–97.3)
Accuracy	87.5 (74.8–95.3)	89.6 (77.3–96.5)
<b>Random forest algorithm</b>		
Sensitivity	88.5 (69.9–97.6)	88.5 (69.9–97.6) (reader 1), 88.5 (69.9–97.6) (reader 2)
Specificity	86.4 (65.1–97.1)	86.4 (65.1–97.1) (reader 1), 81.8 (59.7–94.8) (reader 2)
PPV	88.5 (72.6–95.7)	88.5 (72.6–95.7) (reader 1), 85.2 (70.1–93.4) (reader 2)
NPV	86.4 (68.3–94.9)	86.4 (68.3–94.9) (reader 1), 85.7 (67.0–94.7) (reader 2)
Accuracy	87.5 (74.8–96.3)	87.5 (74.8–96.3) (reader 1), 85.4 (72.2–93.9) (reader 2)

Data are percentages, with 95% CIs in parentheses.

MRI and PET/MRI was assessed by determining sensitivity, specificity, positive predictive value (PPV), negative predictive value (NPV), accuracy, and ROC AUC. A McNemar test was used to compare the diagnostic performance of the radiologists with that of the machine-learning models. A Pearson  $\chi^2$  test was used to compare the tumor characteristics between the training and validation samples. Statistical significance was defined as a *P* value of less than 0.05.

**RESULTS**

**Participant Demographics and Reference Standard**

In this study, 255 female participants (mean age, 51.2 ± 11.9 y) from 2 centers were included for the training sample (Fig. 1). According to the reference standard, 101 of the 255 (39.6%) were node-positive and 154 (60.4%) were node-negative.

For the testing sample, 48 female participants (mean age, 52.2 ± 12.2 y) from a third center were evaluated. According to the reference standard, 26 of the 48 (54.2%) were node-negative and 22 (45.8%) were node-positive. The demographics and tumor characteristics of all participants are in Table 1.

**Radiologist Performance**

On the basis of MRI data, the radiologist was able to determine the correct lymph node status in 218 of 255 participants (85.5%) in the training set. This yielded a diagnostic performance indicated by sensitivity, specificity, PPV, NPV, and accuracy of 74.3%, 92.9%, 87.2%, 84.6%, and 85.5%, respectively, for the training sample (Supplemental Table 1; supplemental materials are available at <http://jnm.snmjournals.org>). Corresponding results for radiologist performance (identical results for both readers) based on MRI in the testing sample were 84.6%, 90.9%, 91.7%, 83.3%, and 87.5% (Table 2).

When taking PET/MRI into account, the radiologist was able to determine the correct lymph node status in 221 of 255 participants (86.7%), and sensitivity, specificity, PPV, NPV, and accuracy were 84.0%, 88.4%, 82.4%, 89.5%, and 86.7%, respectively, for the training sample (Supplemental Table 1). In the testing sample,

radiologist performance on PET/MRI data was 92.3%, 86.4%, 88.9%, 90.5%, and 89.6%, respectively (Table 2).

With regard to the individual features, there were isolated differences in the subjective evaluation of lymph nodes by the raters (irregular margin,  $\kappa = 0.919$ ; inhomogeneous cortex,  $\kappa = 0.879$ ; perifocal edema,  $\kappa = 0.776$ ; absence of fatty hilum,  $\kappa = 0.865$ ; contrast medium enhancement,  $\kappa = 0.947$ ; absent intact nodal border, 0.957; all *P* < 0.001), but together these led to an equal evaluation of lymph node status, so that the interrater reliability with regard to lymph node status was excellent ( $\kappa = 1.0$ , *P* < 0.001).

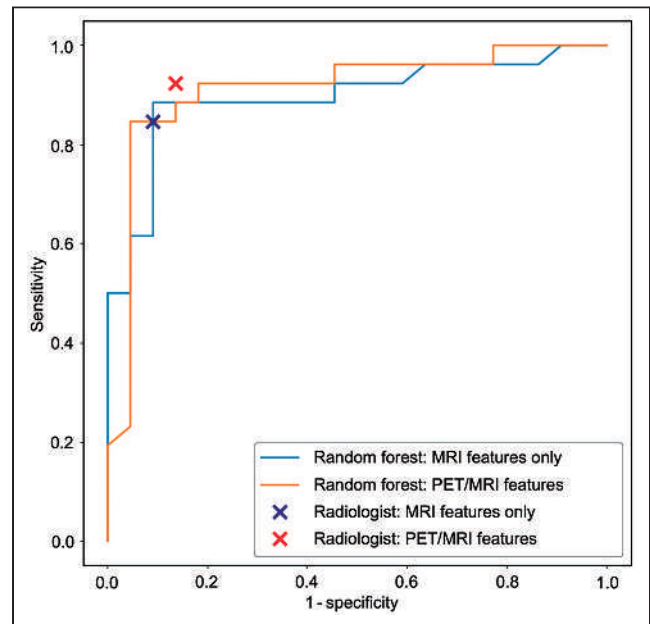


**FIGURE 3.** ROC AUC for random forest model performance on testing data and for prediction of lymph node status by radiologists on MRI and PET/MRI. LN = lymph node.

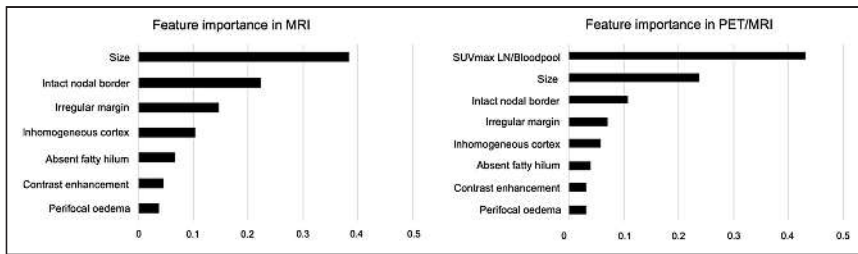


**FIGURE 4.** Importance of different morphologic and metabolic features of lymph nodes.

### Random Forest Algorithm Performance

The trained random forest classifiers yielded an accuracy of 88.3% for MRI and of 99.2% for PET/MRI on the training data, which is indicative of a very good model fit to the training data (Supplemental Table 1). When applied to the independent datasets of the testing sample, the respective random forest classifier was able to determine the correct lymph node status in 42 of 48 participants (87.5%) (23 true-positive and 19 true-negative) for MRI features, whereas 3 participants were rated false-positive and 3 participants false-negative (both readers, Table 2). The performance was unchanged when applying the PET/MRI-based random forest classifier to the testing sample, with 42 of 48 correct classifications (87.5%) (23 true-positive and 19 true-negative), whereas 3 participants were rated false-positive and 3 participants false-negative on the basis of the lymph node assessment of reader 1. On the basis of the lymph node assessment of reader 2, there were 41 of 48 correct classifications (85.4%) (23 true-positive and 18 true-negative), whereas 4 participants were rated false-positive and 3 participants false-negative. Sensitivity, specificity, PPV, and NPV for both classifiers on PET/MRI were 88.5%, 86.4%, 88.5%, and 86.4%, respectively, for reader 1 and 88.5%, 81.8%, 85.2%, 85.7%, 85.4%, respectively, for reader 2 (Table 2).

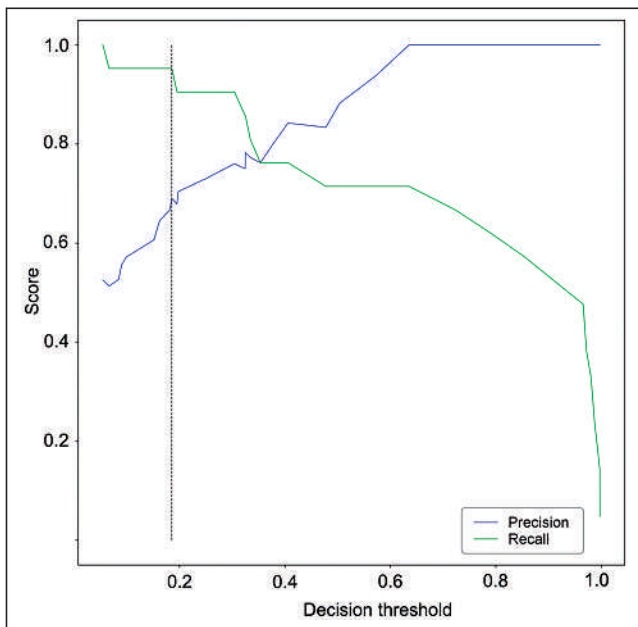


**FIGURE 5.** Precision and recall scores as function of decision threshold on internal validation sample.  $x$  represents threshold values, and  $y$  is score of precision or recall. Adjusted decision threshold for optimized sensitivity is indicated by dashed line.

### Comparison of Radiologist Performance and Random Forest Algorithm

In the testing sample, the highest ROC AUC was achieved by the random forest classifier based on PET/MRI data, with a value of 91.2% (95% CI, 82.8%–99.6%), followed by an ROC AUC of 89.5% (95% CI, 80.4%–98.7%) by the random forest classifier based on MRI data (Fig. 3).

There were no significant differences in the assessment of lymph node status between the radiologists and the random forest classifier,

either for MRI features ( $P = 0.67$ ) or for PET/MRI features ( $P = 0.68$ ).

### Feature Importance

The most important feature in MRI was size, followed by intact nodal border and irregular margin, whereas the most important features for predicting the nodal status in PET/MRI were tracer uptake as indicated by the ratio of the  $SUV_{max}$  of the lymph node to the  $SUV_{max}$  of the ascending aorta, followed by size and intact nodal border (Fig. 4).

### Decision Threshold Adjustment

To minimize the classifier's false-negatives with regard to clinical need, we adjusted the decision threshold of the random forest classifier on PET/MRI data as a trade-off between precision (i.e., PPV) and recall (i.e., sensitivity). The default decision threshold in the random forest classifier was 0.5. Figure 5 shows precision and recall as a function of decision values in the internal validation sample. The optimal decision threshold for this purpose was obtained at 0.19. A sensitivity (recall) of 96.2% was achieved, with only 1 false-negative in the test sample, whereas specificity, PPV, NPV, and accuracy were 68.2%, 78.1%, 93.8%, and 83.3%, respectively, at this threshold. Applying these results to everyday routines in our cohort would mean that it would be possible to save 68.2% (15/22) of the women from an unnecessary biopsy, although 3.8% (1/26) of the affected women would be missed (Tables 3 and 4).

### Decision Tree for Clinical Decision Support

The decision tree classifier for distinguishing benign from malignant lymph nodes achieved an accuracy of 89.6% and an ROC AUC of 87.6% (95% CI, 77.6%–97.5%) for MRI in the testing sample and an accuracy of 89.6% and ROC AUC of 89.0% (95% CI, 79.7%–98.4%) for PET/MRI data in the testing sample.

These decision trees can support clinical decision making based on 3 simple imaging features each (Fig. 6A). For MRI, the root node indicative of the most important feature is size, which is consistent with the feature importance from random forests. Here, a short-axis diameter of at least 7.5 mm serves as a cutoff for highly suggestive lymph nodes. ROC AUC evaluation of this feature alone shows a sensitivity of 71.6% and specificity of 86.4% ( $J = 0.580$ ).

**TABLE 3**  
Confusion Matrix for Adjusted Threshold

Actual	Predicted	
	Negative	Positive
Negative	15	7
Positive	1	25



**TABLE 4**  
Performance Metrics for Adjusted Threshold

Metric	Data
Sensitivity	96.2% (80.4%–99.9%)
Specificity	68.2% (45.1%–86.1%)
PPV	78.1% (65.9%–86.9%)
NPV	93.8% (68.2%–99.1%)
Accuracy	83.3% (69.8%–92.5%)

Data in parentheses are ranges.

for this cutoff. A cutoff of 12.5 mm led to a specificity of 100% but a sensitivity of 34.3% ( $J = 0.343$ ) (Fig. 6B). The decision tree and these cutoffs were determined from the training data. The combination of an  $^{18}\text{F}$ -FDG uptake more than 1.3-fold that in the aorta ascendens and a short-axis diameter of 7.5 mm is sufficient to characterize a lymph node as malignant.

The confusion matrices and performance metrics for the decision trees are shown in Tables 5 and 6. The performance of the decision trees on the training data is shown in Supplemental Table 2. Supplemental Table 3 shows the detection rates for lymph nodes on  $^{18}\text{F}$ -FDG PET/MRI per nodal stage (cN0–cN3c).

## DISCUSSION

Our study demonstrated that lymph node metastases in patients with newly diagnosed breast cancer can be diagnosed using simple

**TABLE 5**  
Confusion Matrices for Decision Trees

Actual	Predicted			
	MRI		PET/MRI	
	Negative	Positive	Negative	Positive
Negative	20	2	21	1
Positive	3	23	4	22

imaging features from MRI and PET/MRI, both by radiologists and by machine-learning-based prediction models, with comparably high accuracies. However, our results indicate that a machine-learning-based prediction model can be advantageous in a clinical setting because it provides the opportunity for decision threshold adjustments. Compared with the current gold standard, in which every clinically node-negative patient would undergo sentinel lymph node biopsy, use of the random forest classifier on PET/MRI data would make it possible to prevent unnecessary biopsy in 68.2% of the women, although 3.8% of the women would be missed. This ability is important for such a model to be suitable for the clinical setting, in which diagnostic imaging might potentially omit invasive procedures such as lymph node biopsy when false-negatives can reliably be reduced. Furthermore, we derived a decision tree for clinical decision support based on simple imaging features from MRI and PET/MRI, which can assist clinicians in the diagnostic workup with regard to lymph node involvement in breast cancer. Although application of the model evaluated here does not, per se, save time in the evaluation

of lymph node criteria, the clear cascade of the 3 easily assessable imaging features can be helpful for the radiologist when classifying axillary lymph nodes in daily routine.

Different machine-learning algorithms for the detection of axillary lymph node metastases have previously been shown to provide diagnostic performance comparable to or better than that of experienced physicians in other specialties (17), but only a few applications have been introduced into everyday routine.

This study further rated the relevance of various imaging features of lymph nodes. Although the size of a lymph node, as characterized by the short-axis diameter, is a generally accepted criterion for assessing metastatic status (8), diagnostic accuracy can be increased by adding factors such as contour and signal intensity. Nevertheless, the feature importance of the random forest classifier and the good performance of the simple decision tree classifier indicate that only a few features are necessary to predict lymph node malignancy with high accuracy. Our findings are in line with those of Ramírez-Galván et al. (18), who found lymph node size to be the most important morphologic feature. However, according to our investigation, a short-axis diameter of at least 7.5 mm seems to be most

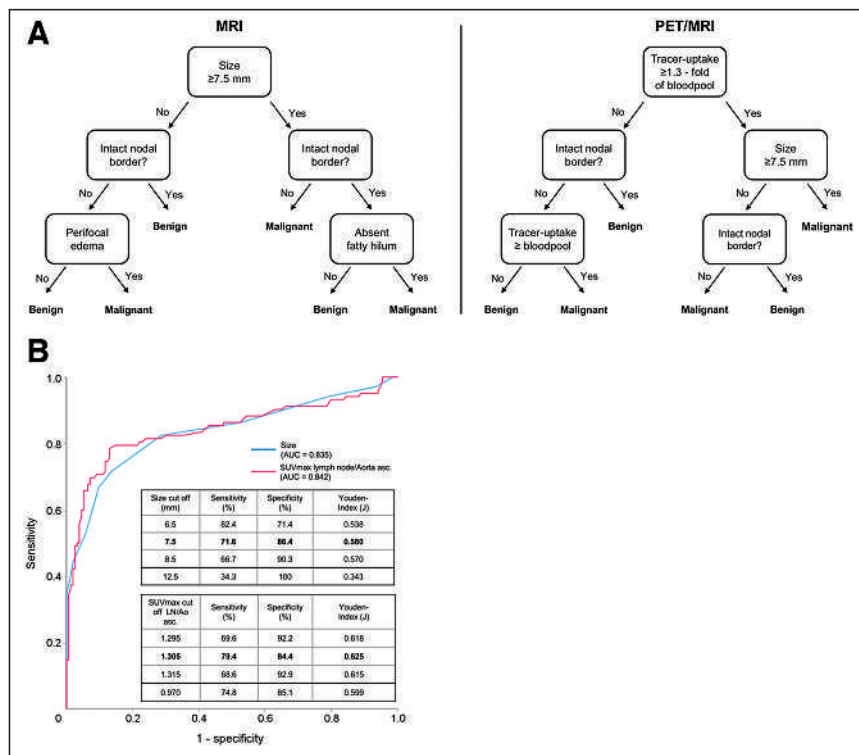


**FIGURE 6.** (A) Decision tree for predicting lymph node status in MRI and PET/MRI. (B) ROC AUC for size and for SUV<sub>max</sub> ratio of lymph node to mediastinal blood pool for prediction of lymph node status. Ao = aorta; LN = lymph node.

**TABLE 6**  
Performance Metrics for Decision Trees

Metric	Data
<b>MRI</b>	
Sensitivity	88.5% (69.9%–97.6%)
Specificity	90.9% (70.8%–98.9%)
PPV	92.0% (75.3%–97.8%)
NPV	87.0% (69.5%–95.1%)
Accuracy	89.6% (77.3%–96.5%)
<b>PET/MRI</b>	
Sensitivity	84.6% (65.1%–95.6%)
Specificity	95.5% (77.2%–99.9%)
PPV	95.7% (76.3%–99.3%)
NPV	84.0% (68.0–92.9. %)
Accuracy	89.6% (77.3%–96.5%)

Data in parentheses are ranges.

suitable for prediction of axillary lymph node involvement by breast cancer, whereas a diameter of at least 12.5 mm can be seen even as evidence of malignancy (Fig. 6B).

As with other cancer entities, there is no consensus about uptake thresholds in breast cancer to define a lymph node as benign or malignant (19), but an SUV<sub>max</sub> threshold of 1.8–2.0 has reported to be a helpful criterion to diagnose malignancy (20,21). Our study demonstrated that uptake in the lymph node below that in the mediastinal blood pool is a reliable feature of benignity, whereas uptake at least 1.3 times that in the mediastinal blood pool should be considered malignant.

Using the adjusted threshold of the random forest classifier, the rate of false-negatives might be substantially decreased to a range that would be acceptable for clinical purposes. The single participant missed by our machine-learning algorithm after adjustment of the threshold had a histopathologically proven micrometastasis (1 mm). The clinical impact of micrometastases does not appear to be comparable to that of macrometastases, with micrometastasis outcome being comparable to that of node-negative patients (22). Thus, machine-learning algorithms may be expected to play a crucial role in reducing invasive procedures in the future.

This study had some limitations. Because only therapy-naïve patients were examined at baseline staging, no general statements can be made on regressively altered lymph nodes after therapy or on response to therapy. The reference standard was in part based on posttherapeutic specimens from axillary nodes and different methods of sample acquisition, including axillary dissection and ultrasound-guided biopsy. These differences may have had an impact on definition of the reference standard. The imaging features used as input for the machine-learning-based prediction models still rely on subjective assessments of radiologists. Nevertheless, we could show that these imaging features are easy assessable and have a high interrater reliability. In addition, the size of the validation cohort was only moderate; further studies with a larger population are needed.

## CONCLUSION

This study showed, first, that a random forest classifier based on simple imaging features provides diagnostic performance comparable

to that of an experienced radiologist; second, that <sup>18</sup>F-FDG PET uptake and lymph node size assessed on MRI are the most informative features in determining the metastatic status of an axillary lymph node; third, that a combination of 3 features can be helpful for differentiating between malignant and benign axillary lymph nodes in newly diagnosed breast cancer in daily routine; and fourth, that—accepting a low specificity—a sensitivity of more than 95% can be achieved with an adjusted random forest classifier on <sup>18</sup>F-FDG PET/MRI data, which can exclude lymph node involvement with high confidence and might play a central role in reducing invasive procedures in the future. Thus, the combination of the 3 imaging features, in particular, may be applied for daily use by the radiologist, as these can be determined and evaluated quickly and reliably, although the decision tree should not be the only basis for therapy planning. For therapy decision making, the adjusted random forest model is more reliable for differentiation between malignant and benign lymph nodes because of its higher sensitivity. Nevertheless, the adjusted random forest model needs to be confirmed in large, prospective studies to minimize the number of unnecessary invasive procedures and, if successful, will then have great impact.

## DISCLOSURE

The study was funded by the Deutsche Forschungsgemeinschaft (DFG: the German Research Foundation) (BU3075/2-1 and KI2434/1-2). No other potential conflict of interest relevant to this article was reported.

## KEY POINTS

**QUESTION:** Can machine-learning prediction models perform comparably to experienced radiologists in determining nodal status on PET/MRI examinations of patients with newly diagnosed breast cancer?

**PERTINENT FINDINGS:** Machine learning performed comparably to experienced radiologists in identifying axillary lymph node metastases on PET/MRI in patients with primary breast cancer. The most important lymph node feature was tracer uptake, followed by lymph node size. A combination of 3 features was helpful for differentiation between malignant and benign axillary lymph nodes in newly diagnosed breast cancer, leading to an easily applicable decision tree in everyday clinical routine.

**IMPLICATIONS FOR PATIENT CARE:** With the help of machine learning, axillary lymph node metastases can reliably be excluded on PET/MRI, sparing 68.2% of the patients an invasive procedure such as sentinel lymph node biopsy.

## REFERENCES

- Breast cancer. World Health Organization website. <https://www.who.int/news-room/fact-sheets/detail/breast-cancer>. Published March 26, 2016. Accessed November 30, 2022.
- Chang JM, Leung JWT, Moy L, Ha SM, Moon WK. Axillary nodal evaluation in breast cancer: state of the art. *Radiology*. 2020;295:500–515.
- Giuliano AE, Ballman KV, McCall L, et al. Effect of axillary dissection vs no axillary dissection on 10-year overall survival among women with invasive breast cancer and sentinel node metastasis: the ACOSOG Z0011 (Alliance) randomized clinical trial. *JAMA*. 2017;318:918–926.
- Giuliano AE, Hunt KK, Ballman KV, et al. Axillary dissection vs no axillary dissection in women with invasive breast cancer and sentinel node metastasis: a randomized clinical trial. *JAMA*. 2011;305:569–575.

5. Duraes M, Guillot E, Seror J, Pouget N, Rouzier R. Sentinel lymph node biopsy and neoadjuvant treatment in breast cancer [in French]. *Bull Cancer*. 2017;104:892–901.
6. Yan M, Abdi MA, Falkson C. Axillary management in breast cancer patients: a comprehensive review of the key trials. *Clin Breast Cancer*. 2018;18:e1251–e1259.
7. Morawitz J, Bruckmann N-M, Dietzel F, et al. Determining the axillary nodal status with four current imaging modalities including <sup>18</sup>F-FDG PET/MRI in newly diagnosed breast cancer: a comparative study using histopathology as reference standard. *J Nucl Med*. 2021;62:1677–1683.
8. Elsholtz FHJ, Asbach P, Haas M, et al. Introducing the node reporting and data system 1.0 (Node-RADS): a concept for standardized assessment of lymph nodes in cancer. *Eur Radiol*. 2021;31:6116–6124.
9. Zhao M, Wu Q, Guo L, Zhou L, Fu K. Magnetic resonance imaging features for predicting axillary lymph node metastasis in patients with breast cancer. *Eur J Radiol*. 2020;129:109093.
10. Atallah D, Moubarak M, Arab W, Kassis NE, Chahine G, Salem C. MRI-based predictive factors of axillary lymph node status in breast cancer. *Breast J*. 2020;26:2177–2182.
11. Ehteshami Bejnordi BE, Veta M, van Diest PJ, et al. Diagnostic assessment of deep learning algorithms for detection of lymph node metastases in women with breast cancer. *JAMA*. 2017;318:2199–2210.
12. Bruckmann NM, Kirchner J, Umutlu L, et al. Prospective comparison of the diagnostic accuracy of <sup>18</sup>F-FDG PET/MRI, MRI, CT, and bone scintigraphy for the detection of bone metastases in the initial staging of primary breast cancer patients. *Eur Radiol*. 2021;31:8714–8724.
13. Morawitz J, Kirchner J, Martin O, et al. Prospective correlation of prognostic immunohistochemical markers with SUV and ADC derived from dedicated hybrid breast <sup>18</sup>F-FDG PET/MRI in women with newly diagnosed breast cancer. *Clin Nucl Med*. 2021;46:201–205.
14. Kirchner J, Grueneisen J, Martin O, et al. Local and whole-body staging in patients with primary breast cancer: a comparison of one-step to two-step staging utilizing <sup>18</sup>F-FDG-PET/MRI. *Eur J Nucl Med Mol Imaging*. 2018;45:2328–2337.
15. Newman LA, Pernick NL, Adsay V, et al. Histopathologic evidence of tumor regression in the axillary lymph nodes of patients treated with preoperative chemotherapy correlates with breast cancer outcome. *Ann Surg Oncol*. 2003;10:734–739.
16. Takahashi Y, Soh J, Shien K, et al. Fibrosis or necrosis in resected lymph node indicate metastasis before chemoradiotherapy in lung cancer patients. *Anticancer Res*. 2020;40:4419–4423.
17. Golden JA. Deep learning algorithms for detection of lymph node metastases from breast cancer: helping artificial intelligence be seen. *JAMA*. 2017;318:2184–2186.
18. Ramírez-Galván YA, Cardona-Huerta S, Elizondo-Riojas G, Álvarez-Villalobos NA, Campos-Coy MA, Ferrara-Chapa CM. Does axillary lymph node size predict better metastatic involvement than apparent diffusion coefficient (ADC) value in women with newly diagnosed breast cancer? *Acta Radiol*. 2020;61:1494–1504.
19. Yu C, Xia X, Qin C, Sun X, Zhang Y, Lan X. Is SUVmax helpful in the differential diagnosis of enlarged mediastinal lymph nodes? A pilot study. *Contrast Media Mol Imaging*. 2018;2018:3417190.
20. Rosen EL, Eubank WB, Mankoff DA. FDG PET, PET/CT, and breast cancer imaging. *Radiographics*. 2007;27(suppl 1):S215–S229.
21. Carkaci S, Adrada BE, Rohren E, et al. Semiquantitative analysis of maximum standardized uptake values of regional lymph nodes in inflammatory breast cancer: is there a reliable threshold for differentiating benign from malignant? *Acad Radiol*. 2012;19:535–541.
22. Wada N, Imoto S. Clinical evidence of breast cancer micrometastasis in the era of sentinel node biopsy. *Int J Clin Oncol*. 2008;13:24–32.

---

---

# Fetal Dose from PET and CT in Pregnant Patients

Christiane Sarah Burton<sup>1</sup>, Kirk Frey<sup>2</sup>, Frederic Fahey<sup>3</sup>, Mark S. Kaminski<sup>4</sup>, Richard K.J. Brown<sup>5</sup>, Judith M. Pohlen<sup>2</sup>, and Barry L. Shulkin<sup>1</sup>

<sup>1</sup>St. Jude Children's Research Hospital, Memphis, Tennessee; <sup>2</sup>Michigan Medicine, Ann Arbor, Michigan; <sup>3</sup>Children's Hospital, Boston, Massachusetts; <sup>4</sup>University of Michigan, Ann Arbor, Michigan; and <sup>5</sup>University of Utah School of Medicine, Salt Lake City, Utah

---

When pregnancy is discovered during or after a diagnostic examination, the physician or the patient may request an estimate of the radiation dose received by the fetus as per guidelines and standard operating procedures. This study provided the imaging community with dose estimates to the fetus from PET/CT with protocols that are adapted to University of Michigan low-dose protocols for patients known to be pregnant. **Methods:** There were 9 patients analyzed with data for the first, second, and third trimesters, the availability of which is quite rare. These images were used to calculate the size-specific dose estimate (SSDE) from the CT scan portion and the SUV and <sup>18</sup>F-FDG uptake dose from the PET scan portion using the MIRD formulation. The fetal dose estimates were tested for correlation with each of the following independent measures: gestational age, fetal volume, average water-equivalent diameter of the patient along the length of the fetus, SSDE, SUV, and percentage of dose from <sup>18</sup>F-FDG. Step-wise multiple linear regression analysis was performed to assess the partial correlation of each variable. To our knowledge, this was the first study to determine fetal doses from CT and PET images. **Results:** Fetal self-doses from <sup>18</sup>F for the first, second, and third trimesters were 2.18 mGy (single data point), 0.74–1.82 mGy, and 0.017–0.0017 mGy, respectively. The combined SSDE and fetal self-dose ranged from 1.2 to 8.2 mGy. These types of images from pregnant patients are rare. **Conclusion:** Our data indicate that the fetal radiation exposure from <sup>18</sup>F-FDG PET and CT performed, when medically necessary, on pregnant women with cancer is low. All efforts should be made to minimize fetal radiation exposure by modifying the protocol.

**Key Words:** PET/CT; radiation physics; MIRD; PET; fetal dose; imaging

**J Nucl Med 2023; 64:312–319**  
DOI: 10.2967/jnumed.122.263959

---

**D**iagnostic imaging that uses ionizing radiation may sometimes be necessary for a pregnant patient despite the potential risk to the fetus. Typically, when such diagnostic information is needed, it is relating to the health of the mother. When radiologists or nuclear medicine physicians need to decide if the diagnostic benefits will outweigh the risks of radiation, it is important they have a reasonable estimate of radiation dose to the fetus. When pregnancy is discovered during or after a diagnostic examination, the physician or the patient may request an estimate of the radiation dose received by the

fetus. The risks of fetal adverse outcomes, including childhood cancer induction, are small at a dose of 100 mGy and negligible at doses of less than 50 mGy (1,2). In the case of hybrid imaging in which both modalities involve radiation, the fetal dosimetry resulting from both modalities should be considered. One example is PET/CT, where the CT scan provides anatomic information and the PET scan provides information on radionuclide uptake at the tumor site. Fetal dose estimates from CT have been based primarily on Monte Carlo simulations of geometric patient models (3–5). PET studies of pregnant patients are extremely uncommon, and even <sup>18</sup>F-FDG PET studies accidentally performed on pregnant patients are rare (6–11). Therefore, providing fetal dose estimates from the CT and <sup>18</sup>F-FDG PET images themselves and from dose reports would be helpful to the medical imaging community. In this study, fetal dose estimates for PET/CT scans were based on a series of pregnant patients in their first, second, and third trimesters. These images were used to calculate the size-specific dose estimate (SSDE) (12) from the CT scan portion and to calculate the SUV and <sup>18</sup>F-FDG uptake dose from the PET scan portion using the MIRD formulation. This study provided the imaging community with dose estimates to the fetus from PET/CT based on patient data, the availability of which is quite rare.

## MATERIALS AND METHODS

### Pregnant Patient Population

In total, 9 <sup>18</sup>F-FDG PET/CT scans performed on pregnant patients over an 11-y period at the University of Michigan were analyzed. The axial range of these scans covered the full uterus. The gestational ages of the fetuses of these patients ranged from 3 to 40 wk. The cohort included 2 patients in the first trimester of pregnancy, 2 in the second trimester, and 5 in the third trimester. Some patients were scanned multiple times during pregnancy and the postpartum period to ascertain diagnostic information pertaining to the patient. The postpartum scans were included in this study as a way of comparing what dose a fetus might get from a PET/CT scan using standard protocols for nonpregnant patients.

### CT Fetal Dose Estimation

The CT portion of the scans was acquired with 120-kVp and 130-kVp acquisition protocols, with the slice thickness varying from 2 to 5 mm. The patients were originally scanned with one of the following scanners: Siemens Biograph Vision 6 PET/CT, Siemens Biograph 40 True Point PET/CT, and Siemens Emotion Duo CT/CPS 1062 PET. No oral contrast agent was used for the CT examinations. The PET/CT images of the pregnant mothers' anatomy were at least from the top of the cranium to the upper thigh of the mother. The gestational age was estimated from the clinical data.

CT axial scans of the same 9 patients were collected on Siemens systems. These images were analyzed retrospectively, and the scan parameters were obtained from the Digital Imaging and Communications in

---

Received Feb. 2, 2022; revision accepted Aug. 23, 2022.  
For correspondence or reprints, contact Christiane Sarah Burton (christiane.burton@stjude.org).  
Published online Sep. 8, 2022.  
COPYRIGHT © 2023 by the Society of Nuclear Medicine and Molecular Imaging.

Medicine (DICOM) header shown in Table 1. There are 2 patients who were scanned twice with the fetus at different gestational ages.

These CT scans were performed using techniques yielding low doses as shown in Table 1. For all 9 patients, there was no automatic tube current modulation; therefore, a constant tube current and kilovoltage were used. For patients 1–5, scanned before 2011, the CT dose index–volume (CTDI<sub>vol</sub>) was not reported since this quantity was not a Food and Drug Administration requirement at the time. The CTDI<sub>vol</sub> was calculated using the output values for a 32-cm phantom of 6.7 mGy/100 mAs in the center and 12.8 mGy/100 mAs at the periphery for the Emotion Duo (13) and Biograph 6 (14) scanners. The pitch factor could not be located in the DICOM header for scans from these scanners, so we assumed it to be 1.0.

The CT dose to the fetus was based on the SSDE method used to calculate organ dose (8,15–23). A recent study by Hardy et al. (24) showed a reasonable accuracy (±25%) with SSDE as a surrogate of fetal dose. The normalized dose coefficient (NDC) scales the CTDI<sub>vol</sub> to make it reflect the dose the patient actually receives. The NDC is calculated directly from the patient size surrogates, which include the effective diameter or water-equivalent diameter (D<sub>W</sub>). The preferred patient size surrogate is the D<sub>W</sub> since it directly incorporates attenuation properties from the patient scan. D<sub>W</sub> represents the diameter of a cylinder of water that contains the same total x-ray attenuation as that contained within the patient’s axial cross section and depends on both the cross-sectional area of the patient and the attenuation of the contained tissues. The method of calculating D<sub>W</sub> described in American Association of Physicists in Medicine report 220 (12) was implemented using the following equation:

$$D_W = \sqrt{\frac{4}{\pi} \left( \frac{CT(x,y)}{1,000} + 1 \right)} \times A_{ROI}, \quad \text{Eq. 1}$$

where  $\overline{CT}$  represents the mean CT number within the reconstructed field of view and  $A_{ROI}$  is the product of the number of pixels in the region of interest (ROI) and the pixel area. Our ROI was inscribed inside the reconstructed DICOM images for each patient. Since the DICOM images are square matrices, we inscribed a circle inside each DICOM image with a diameter equal to the entire width of the image. D<sub>W</sub> was calculated from CT axial images as previously described. Corrections were applied to images that were not reconstructed at isocenter (25). In some cases, when the reconstructed image center was not at isocenter, this ROI could contain padding values of –3,024 Hounsfield units. Therefore, we applied a remapping of all the values inside the circle used to calculate the mean CT number, which mapped all signals equal to –3,024 to –1,000 Hounsfield units to simulate air. The use of padding values is common to most CT vendors, but the padding value may differ. Failure to correct for this would decrease the D<sub>W</sub> values. We did not perform any thresholding or connected-component analysis of the axial image data before calculating D<sub>W</sub>. The D<sub>W</sub> uses the mean Hounsfield units of the patient habitus, taking into consideration the attenuation properties of the patient. The D<sub>W</sub> was then used to calculate the NDC using equation A-1 from the American Association of Physicists in Medicine task group report 204, replicated in equation 2 here:

$$NDC = a \times \exp(-b \times D_W), \quad \text{Eq. 2}$$

where constant  $a = 3.70469$  and constant  $b = 0.03671937$ . The SSDE is simply the product of the NDC and CTDI<sub>vol</sub> as shown in equation 3:

$$SSDE = NDC \times CTDI_{vol}, \quad \text{Eq. 3}$$

where the CTDI<sub>vol</sub> for a 32-cm phantom was taken from the patients’ dose reports. The average SSDE was taken along the

**TABLE 1**  
Patient Data

Patient no.	System	kV	mA	ms	Slice thickness (mm)	Pitch	CTDI <sub>vol</sub>	Weight (kg)	Recon. kernel	D <sub>W</sub> (cm)		Gestational age (wk)	Patient perimeter (cm)	Topogram	
										Fetus	Overall			kV	mA
1*	Emotion Duo	130	79	800	5	1.0	6.74	74.5	B40s	34.9	33.6	17	92.5	130	30
2*	Emotion Duo	130	47	800	5	1.0	4.01	66.7	B40s	37.0	35.3	33	102.4	130	30
3	Emotion Duo	130	47	800	5	1.0	4.01	53.9	B40s	33.0	32.4	12	81.4	NA	NA
4	Emotion Duo	130	47	800	5	1.0	4.01	72.6	B40s	36.5	32.4	36	99.2	NA	NA
5 <sup>†</sup>	Biograph 6	130	75	600	5	1.0	4.79	58.6	B30s	35.1	32.4	28	84.3	NA	NA
6	Biograph 40	120	60	500	5	1.0	2.45	54.4	B30s	35.4	33.0	36	87.8	120	29
7 <sup>‡</sup>	Biograph 40	120	40	500	2	1.0	1.63	69.0	I31f5	37.4	33.6	14	99.2	120	20
8 <sup>‡</sup>	Biograph 40	120	40	500	2	1.0	1.63	79.8	I31f5	38.5	34.8	26	85.6	120	20
9 <sup>§</sup>	Biograph 40	120	40	500	3	1.0	1.46	88.9	I30f3	39.1	33.5	20	109.0	120	20
10*	Emotion Duo	130	156	800	5	1.0	13.35	68.1	B40s	0	35.43	Postpartum	92.1	130	30
11 <sup>§</sup>	Biograph 6	130	164	600	4	1.0	12.65	88.53	B31s	0	37.42	Postpartum	111.1	NA	NA
12 <sup>‡</sup>	Biograph 40	120	84	500	3	1.0	2.98	74.39	I30f3	0	37.10	Postpartum	103.2	120	35
13 <sup>†</sup>	Biograph 6	130	162	600	4	1.0	9.73	62.4	B30s	0	34.97	Postpartum	92.09	NA	NA
14 <sup>†</sup>	Biograph 6	130	182	600	4	1.0	10.49	59.9	B30s	0	34.66	Postpartum	86.94	NA	NA

\*Same patient scanned at 17 wk, 33 wk, and in postpartum period.

<sup>†</sup>Same patient was scanned at 28 wk and twice in postpartum period.

<sup>‡</sup>Same patient was scanned at 14 wk, 26 wk, and in postpartum period.

<sup>§</sup>Same patient was scanned at 20 wk and in postpartum period.

Recon. = reconstruction; NA = not applicable.

Patients 8 and 9 are same patient who came in for 2 separate scans.

**TABLE 2**  
<sup>18</sup>F-FDG Uptake MIRD Calculation Using RADAR with Interpolation Between 12, 24, and 36 Weeks

Patient no.	Gestational age (wk)	SSDE (mGy)	<sup>18</sup> F-FDG fetal self-dose (mGy)	<sup>18</sup> F-FDG fetal total dose (mGy)	SSDE + <sup>18</sup> F-FDG fetal self-dose (mGy)	Fetal self-dose to total fetal dose (%)
1	17	6.9	1.28	1.38	8.2	92.8
2	33	3.8	0.0063	0.0099	3.8	63.6
3	12	4.4	2.18	2.35	6.6	93.6
4	36	3.9	0.0017	0.0034	3.9	50.0
5	28	4.9	0.014	0.021	4.9	67.6
6	36	2.0	0.0017	0.0034	2.0	50.0
7	14	1.2	1.82	1.96	3.0	92.9
8	26	1.2	0.0017	0.025	1.2	68.0
9	20	1.0	0.74	0.80	1.7	92.2
10	Postpartum	13.47	4.9 (12)	5.2 (12)	18.37 (12)	92.8 (12)
			0.045 (24)	0.065 (24)	13.52 (24)	68.5 (24)
			0.0038 (36)	0.0075 (36)	13.47 (36)	51.2 (36)
11	Postpartum	11.87	9.2 (12)	9.9 (12)	21.07 (12)	92.8 (12)
			0.085 (24)	0.12 (24)	11.96 (24)	68.5 (24)
			0.0073 (36)	0.014 (36)	11.88 (36)	51.2 (36)
12	Postpartum	2.83	5.0 (12)	5.4 (12)	7.83 (12)	92.8 (12)
			0.046 (24)	0.067 (24)	2.88 (24)	68.5 (24)
			0.0039 (36)	0.0077 (36)	2.84 (36)	51.2 (36)
13	Postpartum	9.99	5.1 (12)	5.4 (12)	15.09 (12)	92.8 (12)
			0.047 (24)	0.068 (24)	10.04 (24)	68.5 (24)
			0.0040 (36)	0.0078 (36)	9.99 (36)	51.2 (36)
14	Postpartum	10.89	5.3 (12)	5.7 (12)	16.19 (12)	92.8 (12)
			0.049 (24)	0.071 (24)	10.94 (24)	68.5 (24)
			0.0042 (36)	0.0082 (36)	10.89 (36)	51.2 (36)

Injection activity for postpartum scans was used to calculate fetal dose at 12, 24, and 36 wk as indicated in parentheses.

**TABLE 3**  
SUV<sub>mean</sub>, SUV<sub>max</sub>, and 95th Percentile SUV over Entire Fetal Volume

Patient no.	Gestational age (wk)	SUV <sub>mean</sub>	SD*	SUV <sub>max</sub>	95th percentile SUV
1	17	2.30	0.98	7.67	4.20
2	33	4.61	0.98	9.13	6.51
3	12	1.28	0.31	2.64	1.8
4	36	2.71	1.02	9.36	5.18
5	28	2.11	1.01	6.61	4.08
6	36	2.50	1.18	11.71	4.80
7	14	1.24	0.73	7.83	2.66
8	26	1.73	1.45	15.03	4.49
9	20	1.62	0.85	7.28	3.27

\*Summed in quadrature.

length of the fetus. The absorbed dose to the uterus was used as a surrogate for the absorbed dose to the embryo/fetus as is common practice in medical radiation dosimetry (22,23). The CT localizer radiograph (or topogram) technique (kVp and mA) is reported in Table 1. The dose range for the topograms was 0.08–0.13 mGy.

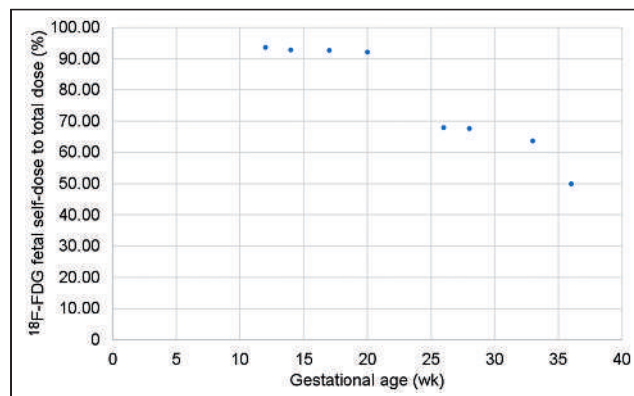


**FIGURE 1.** <sup>18</sup>F-FDG fetal self-dose to fetal total dose from organs of patient.

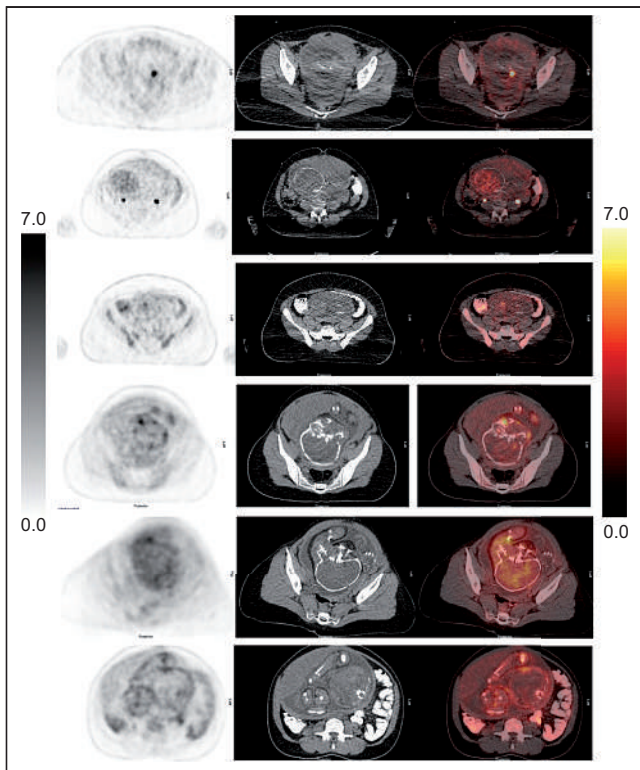


**FIGURE 2.** Examples of single PET (left), CT (middle), and PET/CT (right) images for 6 patients in cohort with high concentration of  $^{18}\text{F}$ -FDG in fetal heart at gestational ages (from top to bottom) of 12 wk, 20 wk (second and third from top), and 36 wk (bottom three) to demonstrate first trimester, second trimester, and third trimester pregnancies, respectively.  $^{18}\text{F}$ -FDG uptake in fetus is seen in PET images.

### $^{18}\text{F}$ -FDG Fetal Dose Estimation

The  $^{18}\text{F}$ -FDG dose administered for all 9 patients in this study was 130 MBq (3.5 mCi). At the time of the injection, the physicians knew that the patients were pregnant, which is the reason for such a low injection dose. All pharmacokinetic and dosimetric estimates for  $^{18}\text{F}$ -FDG, including placental crossover, are shown in Table 2 (26).

For  $^{18}\text{F}$ -FDG dose calculations, the fetuses in the first, second, and third trimesters were rounded to gestational ages of 3, 6, and 9 mo. The  $^{18}\text{F}$ -FDG fetal self-dose and total dose from both maternal organs and the fetal self-dose were calculated using a table of specific absorption fractions (27) for the following organs: adrenals, brain, breasts, gallbladder wall, lower large intestine wall, small intestine, stomach, upper large intestine wall, heart wall, kidneys, liver, lungs, muscle, ovaries, pancreas, red marrow, bone surfaces, skin, spleen, thymus, thyroid, urinary bladder wall, uterus, fetus, and placenta.

The SUV is a simple metric for assessing the amount of activity present in the fetus. The SUV was determined using Hermes software by drawing a contour ROI about the fetus in all slices of the PET image where the fetus was present. The mean, maximum, and

peak (95% percentile) values were determined over the entire volume of the fetus.

### Statistical Analysis

The fetal dose estimates were tested for correlation with each of the following independent measures: gestational age, fetal volume, average  $D_w$  of the patient along the length of the fetus, SSDE, SUV, and percentage of dose from  $^{18}\text{F}$ -FDG. Stepwise multiple linear regression analysis was performed to assess the partial correlation of each variable.

### RESULTS

All data were collected under an institutional review board–approved protocol in a retrospective manner in which the need for patient consent was waived. Table 3 shows the following information gathered from the PET scan:  $\text{SUV}_{\text{mean}}$ , SD,  $\text{SUV}_{\text{max}}$ , and 95th percentile SUV, all over the entire volume of the fetus. Table 2 shows the SSDE for 4 cases after 2011, the  $^{18}\text{F}$  fetal self-dose,  $^{18}\text{F}$  fetal total dose, total dose from SSDE and  $^{18}\text{F}$  to fetus, and percentage of fetal self-dose to total dose. Figure 1 shows the  $^{18}\text{F}$ -FDG fetal self-dose to fetal total dose from organs, including the fetus, of the patient.

### DISCUSSION

To our knowledge, this was the largest series of pregnant patients for whom fetal radiation dose from  $^{18}\text{F}$ -FDG and SSDE was calculated. Our data add considerably to the existing literature about fetal radiation exposure from  $^{18}\text{F}$ -FDG PET and CT dose studies of pregnant patients. These patients were not accidentally exposed to  $^{18}\text{F}$ -FDG during their pregnancy but rather underwent intentional studies that were performed after adequate consideration of the risks and benefits of  $^{18}\text{F}$ -FDG PET in these pregnant patients with malignancy.  $^{18}\text{F}$ -FDG is known to cross the placental membrane and accumulate in the fetus (8,22,28–30), and we were able to clearly identify  $^{18}\text{F}$ -FDG activity in the fetus inside the gravid

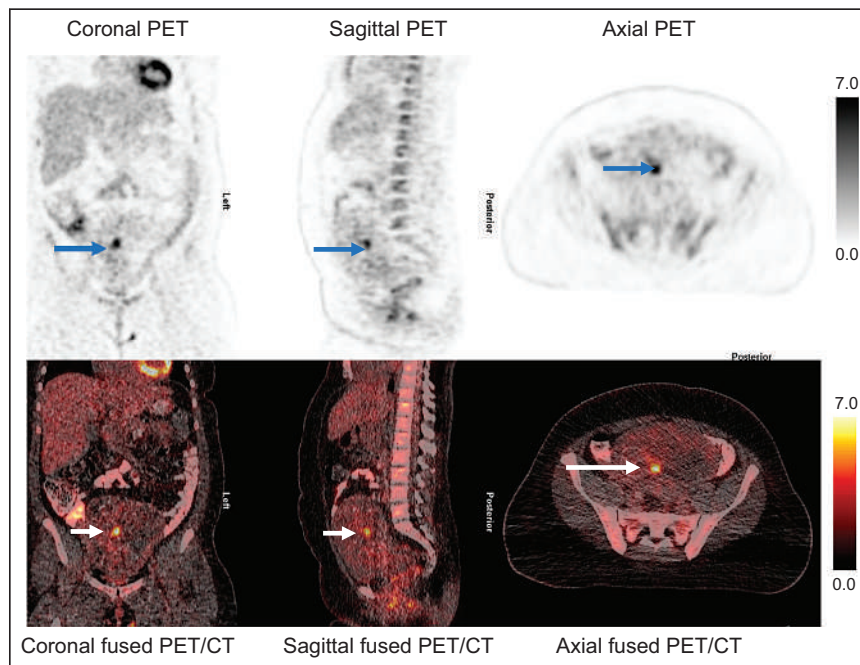


**FIGURE 3.** Example of concentrated uptake of  $^{18}\text{F}$ -FDG in fetal heart (arrows) for patient in second trimester at 20 wkT.

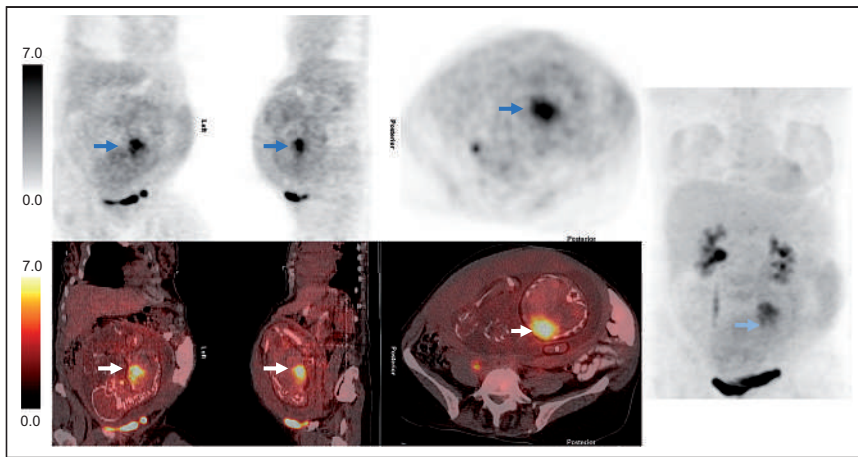


**FIGURE 4.** Example of concentrated uptake of  $^{18}\text{F}$ -FDG in fetal heart (arrows) for patient in second trimester at 26 wk.

uterus, confirming the ability of  $^{18}\text{F}$ -FDG to cross the placenta and accumulate in the fetus. There is no scientific literature documenting fetal toxicity associated with  $^{18}\text{F}$ -FDG in pregnant women or nonhuman primates. All our patients delivered healthy babies at term.

For visual inspection, Figure 2 shows examples of a single CT and corresponding PET image of the fetus for pregnant patients in the first, second, and third trimesters.

Our results show that fetal doses from a combined dose from  $^{18}\text{F}$ -FDG and SSDE range from 1.2 to 8.2 mGy and that the SSDE alone ranges from 1.0 to 2.0 mGy, as shown in Table 2. These doses are significantly below the threshold of 50–100 mGy considered for deterministic effects to the fetus, although fetal dose in this range does not conclusively result in an adverse impact on the fetus (31). Generally, most of the diagnostic studies performed during a mother's pregnancy are below this threshold. However, there is no threshold for stochastic effects, but a discussion about the probability of various deterministic and stochastic effects occurring because of fetal exposure to radiation from CT or  $^{18}\text{F}$ -FDG PET in pregnancy is beyond the scope of this article.

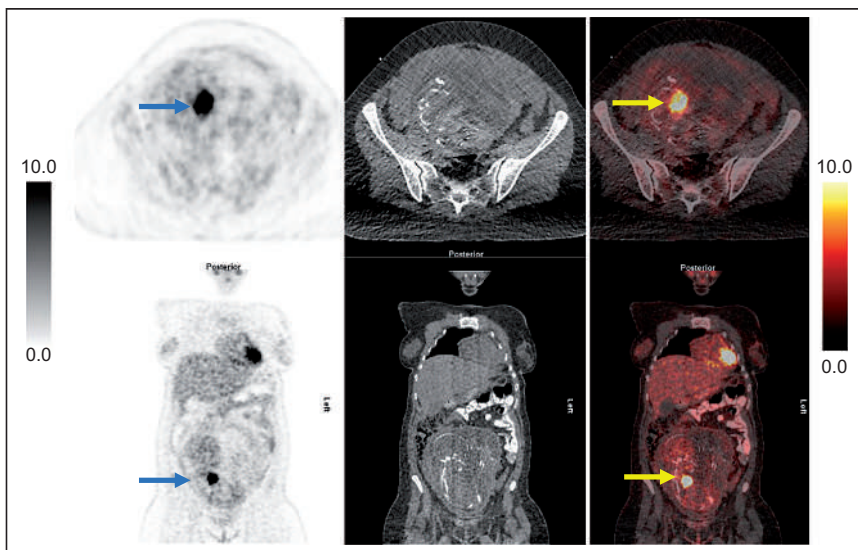


**FIGURE 5.** Example of concentrated uptake of  $^{18}\text{F}$ -FDG in fetal heart (arrows) for patient in second trimester at 28 wk (entering third trimester).

It is not uncommon for a pregnant mother to be imaged using CT by itself. According to a large, multicenter study of advanced medical imaging in pregnancy. The CT imaging rates in the United States increased from 2.0 examinations per 1,000 pregnancies in 1996 to 11.4 per 1,000 pregnancies in 2007, remained stable through 2010, and decreased to 9.3 per 1,000 pregnancies by 2016 (32). Fetal dose estimates from CT have been based primarily on Monte Carlo simulations of geometric patient models. One method is the CTExpo software (version 1.5.1; Medizinische Hochschule) (32), in which organ dose estimates are based on simulations performed by Zankl et al. at the German National Research Center, with the Eva geometric phantom model representing a

standard-sized female patient (3,4). Felmlee et al. demonstrated estimates of CT dose index using Monte Carlo simulations on an anthropomorphic phantom (5). Using Monte Carlo simulations, Ratnapalan et al. (33) and Lazarus et al. (34) reported that normalized fetal CT dose ranges from 7.3 to 14.3 mGy/100 mAs and that mean dose is 17.1 mGy (range, 8–44 mGy), respectively. Goldberg-Stein et al. looked at a series of 54 patients and estimated mean fetal dose to be 24.8 mGy (range, 6.7–56 mGy) (35). Doses to the fetus from a single-acquisition abdominal–pelvic CT examination have ranged between 10 and 50 mGy in phantom and clinical studies. Hurwitz et al. (36) estimated fetal dose as 1.52–3.22 cGy using physical measurements from internal dosimeters in an anthropomorphic phantom that was modified to represent a newly pregnant patient and a patient who was 3 mo pregnant. Since the patients in our study were known to be pregnant before the scan, the scanner technique may have been set to give the lowest possible  $\text{CTDI}_{\text{vol}}$ , which was indicative of the automatic exposure control's being turned off. Although  $\text{CTDI}_{\text{vol}}$  is often provided, the uniform cylindrical phantom does not represent the gross anatomy of

a pregnant patient. SSDE, a quantity that describes the absorbed dose to the patient, scales the  $\text{CTDI}_{\text{vol}}$  with a factor based on the patient's size and attenuation (12,37). This metric will be required to be reported by vendors soon, though it will likely be an average SSDE over the entire patient range. Hardy et al. (24) calculated the  $\text{CTDI}_{\text{vol}}$ -to-fetal-dose coefficients for tube current-modulated and fixed tube current CT examinations of pregnant patients of various gestational ages and reported the SSDE. To estimate SSDE to an organ, Moore et al. (23) provided a method that utilized the conversion factor for the uterus. Existing methods to estimate fetal dose for pregnant patients undergoing CT examinations assume early term pregnancy in a single-sized patient model with an average, non-varying maternal anatomy. These dose estimates do not consider natural variations such as fetal presentation and gestational age. Differences in these attributes can



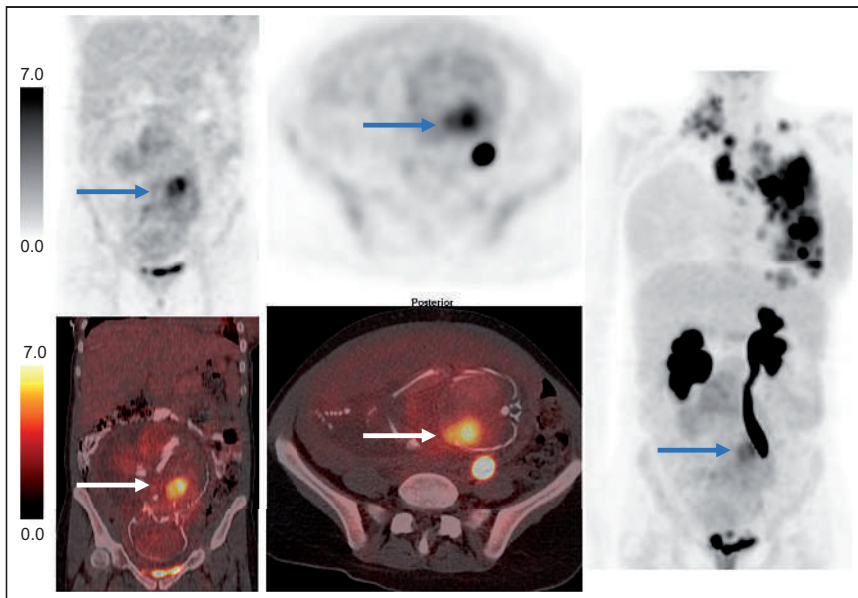


**FIGURE 6.** Example of concentrated uptake of  $^{18}\text{F}$ -FDG in fetal heart (arrows) for patients well into third trimester at 33 wk.

cause overestimation or underestimation of up to 100% (38). Angel et al. (39) used Monte Carlo simulations to estimate fetal dose in CT for a range of gestational ages and patient sizes and found no significant correlation between gestational age and fetal dose. For various fetal ages and maternal body habitus, the fetal dose estimates were between 1.1 and 21.9 mGy for CT.

$^{18}\text{F}$ -FDG PET studies of pregnant patients are extremely uncommon, and even  $^{18}\text{F}$ -FDG PET studies accidentally performed on pregnant patients are rare (6–11). Because adequate and accurate data regarding  $^{18}\text{F}$ -FDG uptake by the fetus are not available other than the very few case reports of accidental exposure, it is difficult to get

This model provides 2 dosimetry tables (45,46) to perform these calculations, and the user inputs the initial activity. The first is from International Commission on Radiological Protection (ICRP) publication 128 (2015), which bases its dosimetry model on anthropomorphic phantoms and bases its effective doses on organ-weighting factors from ICRP publication 60. The tables contain a mix of published estimates from ICRP (publications 53, 80, and 106) and dosimetry provided by Stabin et al. (26). The second is dose estimates from the Radiation Dose Assessment Resource (RADAR) (2017) generated using a set of anthropomorphic phantoms (26) based on the recommended body and organ masses given in ICRP

an estimate of fetal radiation exposure from  $^{18}\text{F}$ -FDG PET in pregnant patients. As a result, most estimates of fetal dose from  $^{18}\text{F}$ -FDG PET are based on models of exposure of the fetus to radiation from the mother and do not consider self-dose from the fetus itself. Those studies that have been published are based mostly on data from nonhuman primates and mathematic models (8–11). Recent case reports by Zanotti-Fregonara et al. (28,40) have raised the possibility that  $^{18}\text{F}$ -FDG dose to the fetus in early pregnancy may be higher than estimated by current dosimetric standards. Hence, there is a need to have more data to establish the accurate fetal dose exposure. A few studies have looked at fetal dose from mothers having a PET scan using  $^{18}\text{F}$ -FDG (41–44). The Society of Nuclear Medicine and Molecular Imaging has provided a nuclear medicine radiation dose tool for  $^{18}\text{F}$ -FDG examinations for different patient models, including pregnant women in the early stage of pregnancy and at 3, 6, and 9 mo into pregnancy.

publication 89 (2003). This study uses PET scans of pregnant patients to calculate the SUV, fetal self-dose, and total fetal dose from the organs of the patient, and from our findings, we determined that  $^{18}\text{F}$ -FDG dose is exceedingly low. The fetal heart contains the highest concentration of  $^{18}\text{F}$ -FDG uptake, as shown in Figures 3–7, which show examples of  $^{18}\text{F}$ -FDG in the fetal heart for patients in their second and third trimesters. Supplemental Figure 1 shows a patient who is well into her third trimester with  $^{18}\text{F}$ -FDG in the fetal heart, like that shown in Figure 7 (supplemental materials are available at <http://jnm.snmjournals.org>). Figure 2A shows a higher concentration of  $^{18}\text{F}$ -FDG uptake in the fetal heart.

For PET/CT, the total estimated radiation dose to the fetus is the sum of CT exposure, maternal  $\gamma$ -irradiation, and fetal  $\beta$ - and  $\gamma$ -irradiation. One method for calculating fetal dose estimates for CT is the ImPACT CTDosimetry dose calculator (CTDosimetry.xls, version 0.99; ImPACT) (47), which is based on Monte Carlo simulations performed by the National

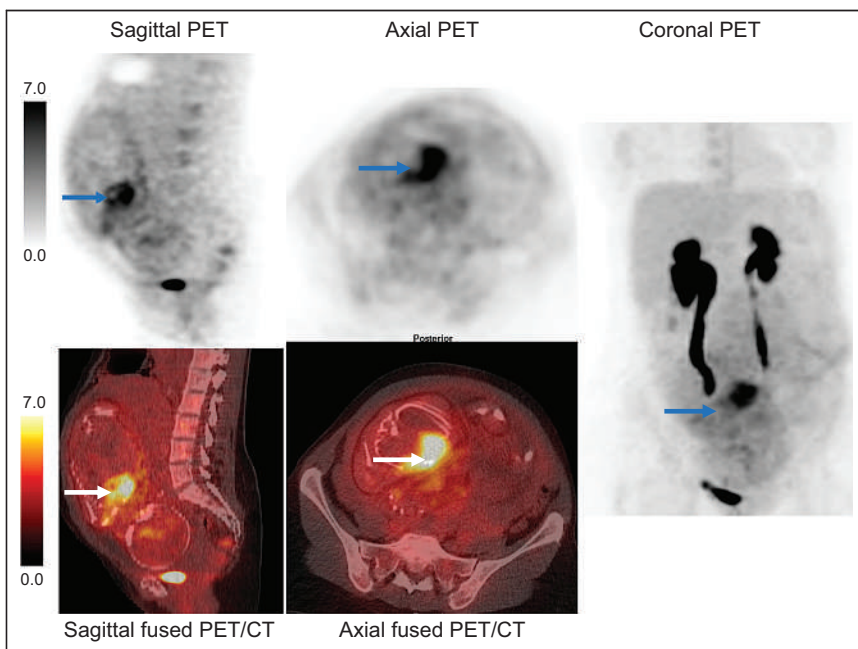


**FIGURE 7.** Example of concentrated uptake of  $^{18}\text{F}$ -FDG in fetal heart (arrows) for patients well into third trimester at 36 wk.

Radiological Protection Board (48) with a geometric MIRD phantom model (49).

A limitation to our study is that, although we believe our sample of pregnant patients to be the largest ever reported, it is still relatively small. Another limitation is that we considered the fetus to be an oval shape in PET images for calculating SUV. It was difficult to contour the perimeter of the fetus, especially for the first trimester; however, this oval was confined as much as possible to the fetus for each PET slice. We also rounded the gestational age upward to 3, 6, and 9 mo for the MIRD calculations. Lastly, we did not attempt to estimate the dose uncertainties for this study.

## CONCLUSION

To our knowledge, this was the first study to determine fetal doses from CT and PET images of pregnant patients. These types of images from pregnant patients are rare. Fetal self-dose from  $^{18}\text{F}$  for the first, second, and third trimesters was 2.18, 0.74–1.82, and 0.017–0.0017 mGy, respectively. The range of SSDE for the CT scan and fetal self-dose for the PET scan was 1.2–8.2 mGy. Our data indicate that fetal radiation exposure from  $^{18}\text{F}$ -FDG PET and CT performed, when medically necessary, on pregnant women with cancer is low. All efforts should be made to minimize fetal radiation exposure while maintaining diagnostic accuracy by modifying the protocol.

## DISCLOSURE

No potential conflict of interest relevant to this article was reported.

## KEY POINTS

**QUESTION:** Is there a risk to the fetus for pregnant patients undergoing a PET/CT scan?

**PERTINENT FINDINGS:** In a study involving 9 pregnant patients who underwent PET/CT, our data suggest that the fetal radiation exposure from  $^{18}\text{F}$ -FDG PET and CT performed, when medically necessary, on pregnant women with cancer is low. The fetal self-dose from  $^{18}\text{F}$ -FDG for the first, second, and third trimesters was 2.18, 0.74–1.82, and 0.017–0.0017 mGy, respectively, and the range of SSDE and fetal self-dose was 1.2–8.2 mGy.

**IMPLICATIONS FOR PATIENT CARE:** Although use of PET/CT on pregnant patients is not encouraged, the data suggest that if a scan is needed to assess the health of the patient, the dose to the fetus would not put the fetus at risk. All efforts should be made to minimize fetal radiation exposure by modifying the protocol.

## REFERENCES

- ICRP publication 84: pregnancy and medical radiation. *Ann ICRP*. 2000;30(1):1.
- Radiation and pregnancy: a fact sheet for clinicians. CDC website. <https://www.cdc.gov/nceh/radiation/emergencies/prenatalphysician.htm>. Published 2000. Accessed December 14, 2022.
- Kramer R. *The Calculation of Dose from External Photon Exposures Using Reference Human Phantoms and Monte Carlo Methods*. Vol. 1. Forschungszentrum für Umwelt und Gesundheit GmbH; 1982.
- Zankl M, Panzer W, Drexler G. *The Calculation of Dose from External Photon Exposures Using Reference Human Phantoms and Monte Carlo Methods*. Part 6. Forschungszentrum für Umwelt und Gesundheit GmbH; 1991. GSF 30/91.
- Felmler JP, Gray JE, Leetzow ML, Price JC. Estimated fetal radiation dose from multislice CT studies. *AJR*. 1990;154:185–190.
- Hutchins E, Wallis J. Diagnosis: metastatic melanoma in a pregnant patient. Malinckrodt Institute of Radiology website. <http://gamma.wustl.edu/pt114te198.html>. Published August 25, 2005. Accessed December 6, 2022.
- ten Hove CH, Zijlstra-Baalbergen JM, Comans EFI, van Elburg RM. An unusual hot spot in a young woman with Hodgkin's lymphoma. *Haematologica*. 2008;93:e14–e15.
- Benveniste H, Fowler JS, Rooney WD, et al. Maternal-fetal in vivo imaging: a combined PET and MRI study. *J Nucl Med*. 2003;44:1522–1530.
- Stabin MG. Proposed addendum to previously published fetal dose estimate tables for  $^{18}\text{F}$ -FDG. *J Nucl Med*. 2004;45:634–635.
- Russell JR, Stabin MG, Sparks RB. Placental transfer of radiopharmaceuticals and dosimetry in pregnancy. *Health Phys*. 1997;73:747–755.
- Russell JR, Stabin MG, Sparks RB, Watson E. Radiation absorbed dose to the embryo/fetus from radiopharmaceuticals. *Health Phys*. 1997;73:756–769.
- Boone JM. Reply to "Comment on the 'Report of AAPM TG 204: Size-Specific Dose Estimates (SSDE) in Pediatric and Adult Body CT Examinations'" [AAPM report 204, 2011]. *Med Phys*. 2012;39:4615–4616.
- Radiation and pregnancy: information for clinicians. Centers for Disease Control and Prevention website. [https://www.cdc.gov/nceh/radiation/emergencies/pdf/303779-a\\_2019\\_radiation-and-pregnancy\\_508.pdf](https://www.cdc.gov/nceh/radiation/emergencies/pdf/303779-a_2019_radiation-and-pregnancy_508.pdf). Published 2019. Accessed December 6, 2022.
- Efficiency in CT: SOMATOM Emotion—2-slice configuration: syngoCT 2006A. Siemens website. <https://5.imimg.com/data5/SELLER/Doc/2020/12/YA/LW/WZ/7182657/emotion-duo-dual-slice-siemens-ct-scan-machines.pdf>. Published 2006. Accessed December 6, 2022.
- Wang J, Duan X, Christner JA, Leng S, Yu L, McCollough CH. Attenuation-based estimation of patient size for the purpose of size specific dose estimation in CT. Part I. Development and validation of methods using the CT image. *Med Phys*. 2012;39:6764–6771.
- Leng S, Shiung M, Duan X, Yu L, Zhang Y, McCollough CH. Size-specific dose estimates for chest, abdominal, and pelvic CT: effect of inpatient variability in water-equivalent diameter. *Radiology*. 2015;276:184–190.
- Anam C, Haryanto F, Widita R, Arif I, Dougherty G, McLean D. The impact of patient table on size-specific dose estimate (SSDE). *Australas Phys Eng Sci Med*. 2017;40:153–158.
- Kalra MK, Maher MM, Toth TL, et al. Techniques and applications of automatic tube current modulation for CT. *Radiology*. 2004;233:649–657.
- Anam C, Haryanto F, Widita R, Arif I, Dougherty G, McLean D. Estimation of eye radiation dose during nasopharyngeal CT examination for an individual patient. *Int J Information*. 2016;19:3951–3962.
- Burton CS, Szczykutowicz TP. Evaluation of AAPM reports 204 and 220: estimation of effective diameter, water-equivalent diameter, and ellipticity ratios for chest, abdomen, pelvis, and head CT scans. *J Appl Clin Med Phys*. 2018;19:228–238.
- Nickel M. *Pharmacokinetic Modeling for Optimization of Radioimmunotherapy: Macroscopic and Microscopic Approach*. Master's thesis. Lund University; 2005.
- Adelstein SJ. Administered radionuclides in pregnancy. *Teratology*. 1999;59:236–239.
- Moore BM, Brady SL, Mirro AE, Kaufman RA. Size-specific dose estimate (SSDE) provides a simple method to calculate organ dose for pediatric CT examinations. *Med Phys*. 2014;41:071917.
- Hardy AJ, Angel E, Bostani M, Cagnon C, McNitt-Gray M. Estimating fetal dose from tube current-modulated (TCM) and fixed tube current (FTC) abdominal/pelvic CT examinations. *Med Phys*. 2019;46:2729–2743.
- ACR Practice Guideline for Imaging Pregnant or Potentially Pregnant Adolescents and Women with Ionizing Radiation. ACR; 2008:3.
- Stabin MG, Xu XG, Emmons MA, Segars WP, Shi C, Fernald MJ. RADAR reference adult, pediatric, and pregnant female phantom series for internal and external dosimetry. *J Nucl Med*. 2012;53:1807–1813.
- Stabin MG. Internal dosimetry in pediatric nuclear medicine. In: Treves ST, ed. *Pediatric Nuclear Medicine*. Springer; 1995:556–581.
- Zanotti-Fregonara P, Jan S, Taieb D, et al. Absorbed  $^{18}\text{F}$ -FDG dose to the fetus during early pregnancy. *J Nucl Med*. 2010;51:803–805.
- Alibazoglu H, Kim R, Ali A, Green A, La Monica G. FDG uptake in gestational sac. *Clin Nucl Med*. 1997;22:557.
- Zanotti-Fregonara P, Jan S, Champion C, et al. In vivo quantification of  $^{18}\text{F}$ -FDG uptake in human placenta during early pregnancy. *Health Phys*. 2009;97:82–85.
- Kwan ML, Miglioretti DL, Marlow EC, et al. Trends in medical imaging during pregnancy in the United States and Ontario, Canada, 1996 to 2016. *JAMA Netw Open*. 2019;2:e197249.
- Stamm G, Nagel HD. CT-Expo: a novel program for dose evaluation in CT. *ROFO Fortschr Geb Rontgenstr Nuklearmed*. 2002;174:1570–1576.
- Ratnapalan S, Bona N, Chandra K, Koren G. Physicians' perceptions of teratogenic risk associated with radiography and CT during early pregnancy. *AJR*. 2004;182:1107–1109.
- Lazarus E, DeBenedictis C, North D, Spencer PK, Mayo-Smith WW. Utilization of imaging in pregnant patients: 10-year review of 5270 examinations in 3285 patients—1997–2006. *Radiology*. 2009;251:517–524.

35. Goldberg-Stein S, Liu B, Hahn PF, Lee SI. Body CT during pregnancy: utilization trends, examination indications, and fetal radiation doses. *AJR*. 2011;196:146–151.
36. Hurwitz LM, Yoshizumi T, Reiman RE, et al. Radiation dose to the fetus from body MDCT during early gestation. *AJR*. 2006;186:871–876.
37. McCollough C, Bakalyar DM, Bostani M, et al. Use of water equivalent diameter for calculating patient size and size-specific dose estimates (SSDE) in CT: the report of AAPM task group 220. *AAPM Rep*. 2014;2014:6–23.
38. Osei EK, Faulkner K. Fetal position and size data for dose estimation. *Br J Radiol*. 1999;72:363–370.
39. Angel E, Wellnitz CV, Goodsitt MM, et al. Radiation dose to the fetus for pregnant patients undergoing multidetector CT imaging: Monte Carlo simulations estimating fetal dose for a range of gestational age and patient size. *Radiology*. 2008;249:220–227.
40. Zanotti-Fregonara P, Champion C, Trébossen R, Maroy R, Devaux J-Y, Hindié E. Estimation of the  $\beta^+$  dose to the embryo resulting from  $^{18}\text{F}$ -FDG administration during early pregnancy. *J Nucl Med*. 2008;49:679–682.
41. Takalkar AM, Khandelwal A, Lokitz S, Lilién DL, Stabin MG.  $^{18}\text{F}$ -FDG PET in pregnancy and fetal radiation dose estimates. *J Nucl Med*. 2011;52:1035–1040.
42. Zanotti-Fregonara P, Laforest R, Wallis JW. Fetal radiation dose from  $^{18}\text{F}$ -FDG in pregnant patients imaged with PET, PET/CT, and PET/MR. *J Nucl Med*. 2015;56:1218–1222.
43. Zanotti-Fregonara P, Koroscil TM, Mantil J, Satter M. Radiation dose to the fetus from [ $^{18}\text{F}$ ]-FDG administration during the second trimester of pregnancy. *Health Phys*. 2012;102:217–219.
44. Gill MM, Sia W, Hoskinson M, Niven E, Khurana R. The use of PET/CT in pregnancy: a case report of malignant parathyroid carcinoma and a review of the literature. *Obstet Med*. 2018;11:45–49.
45. Mattsson S, Johansson L, Liniecki J, et al. Radiation dose to patients from radiopharmaceuticals: a compendium of current information related to frequently used substances. *Ann ICRP*. 2015;44(suppl):7–321.
46. Stabin MG, Siegel JA. RADAR dose estimate report: a compendium of radiopharmaceutical dose estimates based on OLINDA/EXM version 2.0. *J Nucl Med*. 2018;59:154–160.
47. CTdosimetry: CT scanner matching data, tables of CTDI values in air, CTDI<sub>w</sub>, and phantom factor values. ImpACT website. <http://www.ImpACTscan.org>. Published 2000. Accessed December 14, 2022.
48. Shrimpton PC, Jones DG. Normalised organ doses for x ray computed tomography calculated using Monte Carlo techniques and a mathematical anthropomorphic phantom. *Radiat Prot Dosimetry*. 1993;49:241–243.
49. Snyder WS, Fisher HL Jr, Ford MR, Warner GG. Estimates of absorbed fractions for monoenergetic photon sources uniformly distributed in various organs of a heterogeneous phantom. *J Nucl Med*. 1969;8(suppl 3):7–52.

---

---

# First-in-Humans Evaluation of Safety and Dosimetry of $^{64}\text{Cu}$ -LLP2A for PET Imaging

Richard Laforest<sup>\*1,2</sup>, Anchal Ghai<sup>\*2</sup>, Tyler J. Fraum<sup>1,2</sup>, Reiko Oyama<sup>2</sup>, Jennifer Frye<sup>2</sup>, Helen Kaemmerer<sup>2</sup>, Greg Gaehle<sup>2</sup>, Tom Voller<sup>2</sup>, Cedric Mpooy<sup>3</sup>, Buck E. Rogers<sup>1,3</sup>, Mark Fiala<sup>4</sup>, Kooresh I. Shoghi<sup>1,2,5</sup>, Samuel Achilefu<sup>1,2</sup>, Michael Rettig<sup>1,4</sup>, Ravi Vij<sup>1,4</sup>, John F. DiPersio<sup>1,4</sup>, Sally Schwarz<sup>2</sup>, Monica Shokeen<sup>1,2,5</sup>, and Farrokh Dehdashti<sup>1,2</sup>

<sup>1</sup>Alvin J. Siteman Cancer Center, Washington University School of Medicine, St. Louis, Missouri; <sup>2</sup>Edward Mallinckrodt Institute of Radiology, Washington University School of Medicine, St. Louis, Missouri; <sup>3</sup>Department of Radiation Oncology, Washington University School of Medicine, St. Louis, Missouri; <sup>4</sup>Division of Oncology, Department of Medicine, Washington University School of Medicine, St. Louis, Missouri; and <sup>5</sup>Department of Biomedical Engineering, Washington University in St. Louis, St. Louis, Missouri

There remains an unmet need for molecularly targeted imaging agents for multiple myeloma (MM). The integrin very late antigen 4 (VLA4), is differentially expressed in malignant MM cells and in pathogenic inflammatory microenvironmental cells. [ $^{64}\text{Cu}$ ]Cu-CB-TE1A1P-LLP2A ( $^{64}\text{Cu}$ -LLP2A) is a VLA4-targeted, high-affinity radiopharmaceutical with promising utility for managing patients diagnosed with MM. Here, we evaluated the safety and human radiation dosimetry of  $^{64}\text{Cu}$ -LLP2A for potential use in MM patients. **Methods:** A single-dose [ $^{64}\text{Cu}$ ]Cu-LLP2A (Cu-LLP2A) tolerability and toxicity study was performed on CD-1 (Hsd:ICR) male and female mice.  $^{64}\text{Cu}$ -LLP2A was synthesized in accordance with good-manufacturing-practice-compliant procedures. Three MM patients and six healthy participants underwent  $^{64}\text{Cu}$ -LLP2A-PET/CT or PET/MRI at up to 3 time points to help determine tracer biodistribution, pharmacokinetics, and radiation dosimetry. Time-activity curves were plotted for each participant. Mean organ-absorbed doses and effective doses were calculated using the OLINDA software. Tracer bioactivity was evaluated via cell-binding assays, and metabolites from human blood samples were analyzed with analytic radio-high-performance liquid chromatography. When feasible, VLA4 expression was evaluated in the biopsy tissues using 14-color flow cytometry. **Results:** A 150-fold mass excess of the desired imaging dose was tolerated well in male and female CD-1 mice (no observed adverse effect level). Time-activity curves from human imaging data showed rapid tracer clearance from blood via the kidneys and bladder. The effective dose of  $^{64}\text{Cu}$ -LLP2A in humans was  $0.036 \pm 0.006$  mSv/MBq, and the spleen had the highest organ uptake,  $0.142 \pm 0.034$  mSv/MBq. Among all tissues, the red marrow demonstrated the highest residence time. Image quality analysis supports an early imaging time (4–5 h after injection of the radio-tracer) as optimal. Cell studies showed statistically significant blocking for the tracer produced for all human studies ( $82.42\% \pm 13.47\%$ ). Blood metabolism studies confirmed a stable product peak (>90%) up to 1 h after injection of the radiopharmaceutical. No clinical or laboratory adverse events related to  $^{64}\text{Cu}$ -LLP2A were observed in the human participants. **Conclusion:**  $^{64}\text{Cu}$ -LLP2A exhibited a favorable dosimetry and safety profile for use in humans.

**Key Words:** radiochemistry; radiopharmaceuticals; dosimetry; first-in-humans; safety; translational imaging

**J Nucl Med 2023; 64:320–328**

DOI: 10.2967/jnumed.122.264349

**R**ecent advances in molecularly targeted radiopharmaceuticals have been nothing short of transformative. In oncology, PET imaging using molecularly targeted radiolabeled molecules is a vital approach toward managing patients effectively and improving outcomes. Widespread development of diverse disease-specific small molecules, peptides, and antibodies as imaging vectors has thrust discovery of new oncogenic molecular mechanisms and biomarkers.

PET imaging performed with the metabolic radiopharmaceutical,  $^{18}\text{F}$ -FDG, has been the leading nuclear medicine tracer for oncologic studies, as demonstrated by its wide availability and frequent use (1). Of note, as compared with solid tumors, in hematologic malignancies  $^{18}\text{F}$ -FDG PET/CT remains the mainstay for imaging of extramedullary infiltration, relapse, and assessment of inflammatory activity in leukemia as well as in  $^{18}\text{F}$ -FDG-avid lymphoma (2). There is increasing evidence of superior accuracy when nuclear imaging is synergized with liquid biopsies (3). Multiple myeloma (MM) is the second most common hematologic cancer, can cause debilitating end-organ symptoms, and remains largely incurable. It is a disease of malignant plasma cells that originate in the bone marrow (BM). Myeloma is commonly preceded by either or both precursor states: monoclonal gammopathy of undetermined significance and smoldering MM. Although the precursor states are not symptomatic; they are not benign either, and they present with a variable progression rate to overt myeloma. The unstable genome (4); inter-, intra-, and spatial tumoral heterogeneity (5); and age, race, and immunosuppressive BM microenvironment all contribute to the complexity and nonuniformity of myeloma pathogenesis. Consequently, the therapy options for MM encompass a combination of corticosteroids, immunomodulatory agents, proteasome inhibitors, immune- and cell-based therapies, and BM transplantation (6).

One of the overt features of MM is the presentation of diffuse infiltration and punctate focal lesions in the BM (7). Molecular PET and functional MRI are highly informative in the management of patients with MM, from initial diagnosis to therapy and longitudinal tumor monitoring (8), especially in the context of bone and BM involvement (9). Anatomic and functional imaging

Received May 4, 2022; revision accepted Aug. 11, 2022.

For correspondence or reprints, contact Farrokh Dehdashti (dehdashti@wustl.edu) or Monica Shokeen (mshokeen@wustl.edu).

\*Contributed equally to this work.

Published online Aug. 25, 2022.

Immediate Open Access: Creative Commons Attribution 4.0 International License (CC BY) allows users to share and adapt with attribution, excluding materials credited to previous publications. License: <https://creativecommons.org/licenses/by/4.0/>. Details: <http://jnm.snmjournals.org/site/misc/permission.xhtml>.

COPYRIGHT © 2023 by the Society of Nuclear Medicine and Molecular Imaging.

play a forefront role in the detection of minimal residual disease and relapse and in therapy response as well (10).  $^{18}\text{F}$ -FDG PET/CT works adequately in patients in whom  $^{18}\text{F}$ -FDG-avid myeloma lesions manifest (11). Despite its frequent use in the clinic, a known limitation of  $^{18}\text{F}$ -FDG PET in MM is the inconsistent expression of glucose transporter 1 and hexokinase 2 enzyme in myeloma cells (12).  $^{18}\text{F}$ -FDG uptake can additionally change during the course of disease progression and after therapy (12,13). Collectively, the tumor microenvironment in MM can significantly affect  $^{18}\text{F}$ -FDG signal specificity in the BM, leading to either an overestimation or an underestimation of disease burden. Therefore, development of new molecularly targeted tracers for imaging and therapy of MM that can supplement these limitations is the logical next step. It is encouraging to witness an exciting array of new tracers (14) in MM targeted toward metabolism and altered proteins such as CD38, CXCR4, and BCMA (15–18).

Myeloma cells thrive on the pathogenic interactions with the cellular and noncellular components of the BM. One of the molecules that contributes significantly to the vicious cycle of the MM–BM interaction is the integrin very late antigen 4 (VLA4). VLA4 is overexpressed on MM cells relative to other cells and is an established marker of cell adhesion–mediated drug resistance. We recently described the transcriptomic and biologic effects of VLA4 modulation in myeloma cells (19). Encouragingly, there is a well-characterized preclinical PET probe, [ $^{64}\text{Cu}$ ]Cu-CB-TE1A1P-LLP2A ( $^{64}\text{Cu}$ -LLP2A), specific to the activated conformation of VLA4 (20,21). We have previously demonstrated the utility of  $^{64}\text{Cu}$ -LLP2A-PET in diverse human and mouse models of MM (19,22–24).

After rigorous characterization; *in vitro* and *in vivo* evaluations; and rodent dosimetry, toxicity, and safety studies, we initiated and completed the first-in-humans evaluation of  $^{64}\text{Cu}$ -LLP2A with the primary goal of evaluating the safety and dosimetry of this tracer. The secondary goal was to determine the optimal imaging time point in humans. Furthermore, this foundational study informs optimization of the next generation of VLA4-targeted radiotracers for achieving a precise signal-to-background ratio in the BM.

## MATERIALS AND METHODS

LLP2A-CB-TE1A1P (LLP2A) peptide was purchased from Auspep Pty (Tullamarine). All other chemicals were purchased from Sigma Aldrich unless otherwise noted.  $^{64}\text{Cu}$  was purchased from Washington University School of Medicine and was produced on a TR-19 biomedical cyclotron (Nuclear System Co.) at the Washington University School of Medicine. The institutional review board approved the study, and all participants gave written informed consent. All data in the tables and all radiopharmaceutical doses mentioned are correct.

### Good-Manufacturing-Practice-Compliant Synthesis of $^{64}\text{Cu}$ -LLP2A for Human PET Imaging

$^{64}\text{Cu}$ -LLP2A was synthesized according to the good-manufacturing-practice-compliant procedure in a chemistry hot cell. Details are provided in the supplemental materials and Supplemental Figure 1 (supplemental materials are available at <http://jnm.snmjournals.org>).

### Prerelease and Postrelease Quality Control Specifications

$^{64}\text{Cu}$ -LLP2A was released for clinical use after prerelease quality control specifications were met. Pre- and postrelease conditions are described in the supplemental materials and Supplemental Figure 2.

### Preclinical Studies

**Cell Uptake Assay.** A whole-cell uptake assay was performed as previously described to calculate the percentage specific uptake of

$^{64}\text{Cu}$ -LLP2A in the murine MM cell line, 5TGM1 (24). Additional details are provided in the supplemental methods.

**Toxicity Studies on Mice.** The toxicity of [ $^{nat}\text{Cu}$ ]Cu-LLP2A (Cu-LLP2A) was evaluated in male and female CD-1 IGS mice. Details are in the supplemental methods.

## Clinical Studies

**Patient Population.** We studied 6 healthy participants and 3 participants with a confirmed diagnosis of MM (Table 1). This study (NCT03804424) was approved by the Institutional Review Board and the Radioactive Drug Research Committee at Washington University School of Medicine and was conducted under investigational new drug application 136782 submitted to the U.S. Food and Drug Administration. All patients gave written informed consent before participation. The inclusion criteria for patients with MM included an age of 18 y or older and clinically or pathologically defined MM in accordance with the criteria of the International Myeloma Working Group. All types of active myeloma were eligible, including both newly diagnosed and previously treated. Healthy volunteers were eligible if the study principle investigator assessed them as being healthy, if they were at least 18 y old, and if they had no known hematologic disorder (e.g., anemia or leukemia).

For safety evaluation, the vital signs of all participants were measured (blood pressure, heart and respiratory rate, and temperature) and they underwent clinical laboratory testing (standard hematologic and comprehensive metabolic panels that included measurement of hemoglobin, white blood cells, neutrophils, lymphocytes, platelets, creatinine, blood urea nitrogen, calcium, sodium, potassium, carbon dioxide, alanine transaminase, aspartate aminotransferase, alkaline phosphatase, total bilirubin, and albumin), urinalysis, and electrocardiography before  $^{64}\text{Cu}$ -LLP2A administration and at 60 min after injection or before discharge. All participants were additionally monitored for adverse reactions (e.g., dyspnea, chest tightness, fever, and rigors) during administration of  $^{64}\text{Cu}$ -LLP2A.

**PET Imaging Procedures.** PET imaging was performed with a Siemens mMR, Biograph 40HD PET/CT, or Biograph Vision scanner. The scanners were independently calibrated against a National Institute of Standards and Technology–traceable  $^{68}\text{Ge}$  source and then were cross calibrated to the dose calibrator using an F08 water cylinder. Participants entering the study were asked to undergo  $^{64}\text{Cu}$ -LLP2A-PET at up to 3 separate time points to calculate human dosimetry. Two of the MM participants underwent  $^{64}\text{Cu}$ -LLP2A-PET/MRI, and one of the MM participants underwent  $^{64}\text{Cu}$ -LLP2A-PET/CT. All healthy participants underwent  $^{64}\text{Cu}$ -LLP2A-PET/MRI, and 1 healthy participant underwent CT ( $^{64}\text{Cu}$ -LLP2A-PET/CT) at the third imaging time point. All participants were injected with  $^{64}\text{Cu}$ -LLP2A at median dose of 352.24 MBq (range, 247–433 MBq). Three participants underwent a single-station 60-min dynamic study immediately after administration of  $^{64}\text{Cu}$ -LLP2A over the known site of the tumor (1 MM participant) or over the lower lumbar spine and pelvis (2 healthy participants). Dynamic imaging was followed by static body imaging (typically mid brain to lower thighs) at 2 time points. The remaining 6 participants did not undergo dynamic imaging but rather underwent static body imaging at 3 time points between 0 and 26 h after injection.  $^{64}\text{Cu}$ -LLP2A-PET/MR or PET/CT images were evaluated to determine the imaging time after administration of  $^{64}\text{Cu}$ -LLP2A that yields the best-quality images and the best tumor-to-nontumor ratio for visual and quantitative analysis of the images.  $^{64}\text{Cu}$ -LLP2A-PET images were correlated with all available imaging studies to assess lesion uptake of  $^{64}\text{Cu}$ -LLP2A in known lesions seen on the radiologic studies.

PET/MRI in all participants consisted of a 2-point DIXON MRI for attenuation correction and body emission scans (2–5 min per bed position). In all participants who underwent simultaneous PET/MRI, additional sequences were performed: T1-weighted turbo-spin echo (TSE), T2-weighted fat suppression post-contrast imaging, diffusion-weighted

**TABLE 1**  
Participant Characteristics

Subject no.	Sex	Age (y)	Weight (kg)	Dose injected (MBq)	Scanner	Participant status*	Preinjection mDRD glomerular filtration rate <sup>†</sup> (mL/min/1.73 m <sup>2</sup> )
MMDN01	F	44	68	257.5	mMR	Healthy	69.8
MMDN02	M	30	90.7	357	mMR	Healthy	82
MMDN03	F	25	61.2	347	mMR; Bio40 PET/CT	Healthy	76.3
MMDN04	F	25	63	370	mMR	Healthy	90
MMDN05	M	25	77.1	433	mMR	Healthy	112.9
MMDN06	F	27	66.7	361.5	mMR	Healthy	91.3
MMDM01	F	83	54	377	mMR	MM: untreated; plasma cell burden, 24%; ISS, I; R-ISS, II; subtype, IgA κ; cytogenetics, t (14,16)	70.5
MMDM02	M	63	77.1	366	mMR	MM: untreated; plasma cell burden, 22%; ISS, UNK; R-ISS, UNK; subtype, IgG κ; no high-risk abnormalities	52.5
MMDM03 <sup>‡</sup>	M	68	136.1	301.2	Vision PET/CT	MM: relapsed; plasma cell burden, 20%; ISS, 3; R-ISS, 3; subtype, IgG λ; cytogenetics, t (4,14)	40.3

\*MM status includes BM plasma cell infiltration, clinical parameters, disease stage, and subtype.

<sup>‡</sup>Prior treatments for MMDM03 include (1) bortezomib, lenalidomide, and dexamethasone; melphalan autologous stem cell transplantation; and lenalidomide maintenance; (2) lenalidomide and dexamethasone; daratumumab, bortezomib, and dexamethasone; and pomalidomide and dexamethasone; (3) daratumumab, carfilzomib, and dexamethasone; and (4) elotuzumab, pomalidomide, and dexamethasone.

<sup>†</sup>Glomerular filtration rate reference: <https://www.mdcalc.com/mdrd-gfr-equation>.

mDRD = modification of diet in renal disease equation; ISS = MM international staging system; R-ISS = revised MM international staging system; UNK = unknown.

imaging (DWI)/apparent diffusion coefficient (ADC) dynamic imaging, and contrast-enhanced (DCE) imaging.

PET/CT consisted of a spiral CT scan for attenuation correction (120 kVp, 50 effective mAs at a 4-mm slice thickness) from the top of the skull through the upper thighs with the subject supine. Emission images beginning at the skull and proceeding through the lower thighs were obtained (at a rate of 1–10 min per bed position, depending on the time after injection) over 6–7 bed positions with a total imaging duration of no more than 1 h. Images were reconstructed with 3-dimensional ordered-subsets expectation maximization with 3 iterations, 21 subsets, and a postreconstruction gaussian filter of 4 mm.

**Image Analysis.** Two nuclear medicine physicians and 1 physicist reviewed the images. Similar findings were found by all 3 reviewers, independently. The quantitative analysis was performed primarily by 1 individual, with cross-validation and contributions from the other 2 experts. PET images of the healthy participants were evaluated to assess the biodistribution of <sup>64</sup>Cu-LLP2A. The images of the patients diagnosed with MM were evaluated qualitatively in comparison with the healthy participants with the following grading scale: no uptake (tumor ≤ background), minimal uptake (tumor = background), moderate uptake (tumor > background), and intense uptake (tumor ≫ background). The images were evaluated semiquantitatively by measurement of the

tumor SUV<sub>max</sub>. A region of interest was drawn around the entire lesion, with knowledge of the tumor location. In patients with no focal lesions and positive BM biopsy results for the iliac bone for MM, we determined SUV<sub>max</sub>, SUV<sub>mean</sub>, and the iliac bone (or tumor)-to-spleen (and liver) ratio. The SUV for BM uptake was measured as the average of lumbar vertebrae 3–5 in most participants (supplemental materials). For radiation dosimetry estimation, volumes of interest (VOIs) were traced on the organs on the PET images with visible uptake. The liver, spleen, and kidney average organ activity concentration was measured by drawing a VOI that encompassed most of the organs as visible on the PET images at each imaging time point. The blood-pool activity was measured from a VOI traced with the left ventricle of the heart. Red marrow activity was measured from the tracer's VOIs on the marrow uptake seen on lumbar vertebrae 2–4. The total organ activity was then scaled by the standard male or female organ masses as defined by the International Commission on Radiological Protection (25). Total urinary bladder content was measured from a VOI encompassing the whole bladder as seen on the PET images.

**Organ Time-Integrated Activity and Radiation Dose.** Organ time-integrated activity was calculated on a per-patient basis by analytic integration of mono- or dual-exponent fits for the liver, spleen, kidneys, marrow, and blood-pool time-activity curves. The heart

content time-integrated activity was computed from the blood time-integrated activity and the total blood volume and heart chamber volume for the adult male or female as defined in International Commission on Radiological Protection publication 106 (25). The cumulative urine data (from both imaging and urine collection) were plotted as a function of time and were fitted for each patient with an uptake function of the form ( $A = A_0(1 - \exp(-A_1 t))$ ), where  $A_0$  is the filling fraction and  $A_1$  is related to the filling half-life by the relation  $\ln(2)/A_1$ . The filling fraction and filling half-life were then entered in the MIRD bladder voiding model along with a voiding interval of 2 h to yield the bladder content time-integrated activity (26). Aggregated time-activity curves are presented in Figure 1. The male and female radiation doses, the average organ radiation doses per sex, and the effective dose were generated (Table 2). The organ residence times calculated from the human dosimetry data are presented in Table 3. Additional details are included in the supplemental materials.

**Blood Metabolism Study.** To determine the stability of  $^{64}\text{Cu}$ -LLP2A and to measure the metabolites of  $^{64}\text{Cu}$ -LLP2A in human samples, whole blood samples were collected and analyzed by analytic radio-high-performance liquid chromatography. Additional details are in the supplemental methods.

**Flow Cytometry Study.** Two of the 3 participants with MM agreed to provide blood and BM samples for an institutional banking study of plasma cell dyscrasias. For this study, a sample from one of the MM patients was analyzed. Details are provided in the supplemental methods.

### Statistical Analysis

Student *t* tests were used to evaluate differences in tracer uptake between patients with MM and healthy participants. Demographic and clinical characteristics were summarized by descriptive statistics. A *P* value of less than 0.05 was deemed statistically significant.

## RESULTS

### Cell-Binding Assays

The whole cell uptake of  $^{64}\text{Cu}$ -LLP2A at 37°C in VLA4-expressing 5TGM1 cells was determined as part of the postrelease quality control after each radiolabeling study. Cell uptake of  $^{64}\text{Cu}$ -LLP2A was significantly reduced in the presence of the blocking agent (unlabeled LLP2A) ( $n = 9$ ; percentage blocking, 82.42 ± 13.47) (Supplemental Fig. 3).

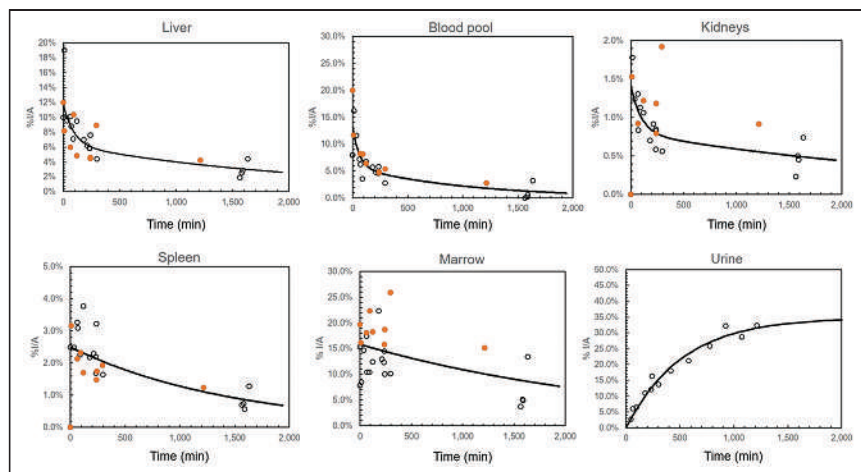


**FIGURE 1.** Aggregated time-activity curves. Orange circles indicate MM participants; black circles indicate healthy participants. %I/A = percentage injected activity.

### Animal Toxicity Studies

A single intravenous injection of 0.0103 mg of Cu-LLP2A per mouse was well tolerated in male and female CD-1 IGS mice and was considered a level with no observed adverse effects (Supplemental Fig. 4). Additional details are provided in the supplemental results.

### Human Imaging

Six healthy volunteers and 3 participants with a confirmed MM diagnosis (median age, 30 y; range, 25–83 y) participated in the study. On the basis of no-observed-adverse-effect-level data, the maximum administered amount of VLA4-targeted radiotracer,  $^{64}\text{Cu}$ -LLP2A, was calculated to be 15  $\mu\text{g}$ , and the mean radioactivity administered per patient was 352.24 MBq (9.5  $\mu\text{g}$ ), with a maximum specific activity of 572.7 MBq/nmol. The radiochemical purity of more than 90% was confirmed by radio-high-performance liquid chromatography for all participant imaging sessions.

Qualitative analysis showed that the best-quality images were obtained between 1 and 5 h after injection of the radiotracer. The images that were collected the next day, typically at around 24 h, were of relatively lower counts and higher image noise (Fig. 2). At an average of 240 min, the mean ± SD for the  $\text{SUV}_{\text{max}}$  of iliac bones in healthy volunteers ( $n = 5$ ) was  $12.05 \pm 2.0$ , whereas it was  $25.62 \pm 9.38$  for myeloma patients ( $n = 3$ ) (2-tailed;  $P < 0.03$ ) (Fig. 3). The BM  $\text{SUV}_{\text{max}}$  was measured as the average of lumbar vertebra 3–5 for most patients (Supplemental Fig. 5). Two participants had a new diagnosis of MM; both had negative findings on  $^{18}\text{F}$ -FDG PET/CT for diffuse or focal areas of increased uptake. However, one of these participants had a lytic lesion in the right iliac bone that was not  $^{18}\text{F}$ -FDG-avid and demonstrated focally intense  $^{64}\text{Cu}$ -LLP2A uptake. The scan of this MM participant (MMDM02) demonstrated diffuse moderate T1 hypointensity of the marrow in the spine and pelvis, similar to intervertebral disks and skeletal muscle, indicating diffuse marrow infiltration (Fig. 4). The second MM patient (MMDM01), who underwent PET/MRI, had recurrent MM with an increase in immunoglobulin M while on a regimen of elotuzumab. This subject had negative results on  $^{18}\text{F}$ -FDG PET/CT and on a bone survey. However, the MRI scan for MMDM01 showed heterogeneous mild T1 hypointensity of marrow in the spine and pelvis but not as T1 hypointense as in the intervertebral disks and skeletal muscle, a finding that might be attributable to red marrow and not sufficient to be called diffuse marrow infiltration on MRI.  $^{64}\text{Cu}$ -LLP2A-PET demonstrated an overall diffuse, moderately increased uptake throughout the BM in all of these 3 myeloma participants.

### Safety Evaluation

The mean and SD of the administered mass of  $^{64}\text{Cu}$ -LLP2A was  $9.52 \pm 1.33 \mu\text{g}$  (range, 6.9–11.7  $\mu\text{g}$ ). There were no adverse or clinically detectable pharmacologic effects in any of the participants. No changes in vital signs or in the results of laboratory studies or electrocardiography were observed. A comprehensive list of safety evaluation parameters and results is summarized in Supplemental Figure 6.

### Serum and Plasma Stability Study

Stability of  $^{64}\text{Cu}$ -LLP2A in blood samples was determined. Radioactive fragments (metabolites) were evaluated in the

**TABLE 2**  
Organ Radiation Dose (*n* = 9)

Organ	Sex											
	MMDM01 (F)	MMDM02 (M)	MMDM032 (M)	MMDN012 (M)	MMDN022 (M)	MMDN03 (F)	MMDN04 (F)	MMDN052 (M)	MMDN06 (F)	Average	M	F
Adrenals	0.029	0.024	0.022	0.027	0.026	0.023	0.018	0.017	0.011	0.022 ± 0.006	0.023 ± 0.004	0.020 ± 0.008
Brain	0.020	0.017	0.015	0.020	0.020	0.015	0.012	0.013	0.004	0.015 ± 0.005	0.017 ± 0.003	0.013 ± 0.006
Breasts	0.018	0.000	0.000			0.014	0.012		0.004	0.010 ± 0.008		0.012 ± 0.006
Gallbladder wall	0.026	0.022	0.021	0.028	0.026	0.021	0.017	0.017	0.009	0.021 ± 0.006	0.023 ± 0.004	0.018 ± 0.007
Lower large intestine wall	0.026	0.022	0.020	0.025	0.024	0.021	0.017	0.017	0.009	0.020 ± 0.005	0.022 ± 0.003	0.018 ± 0.007
Small intestine wall	0.025	0.022	0.020	0.026	0.025	0.019	0.015	0.016	0.008	0.020 ± 0.006	0.022 ± 0.004	0.017 ± 0.007
Stomach wall	0.023	0.021	0.019	0.025	0.024	0.018	0.015	0.015	0.006	0.018 ± 0.006	0.021 ± 0.004	0.016 ± 0.007
Upper large intestine wall	0.025	0.021	0.019	0.025	0.024	0.020	0.016	0.016	0.007	0.019 ± 0.006	0.021 ± 0.004	0.017 ± 0.007
Heart wall	0.029	0.026	0.023	0.028	0.026	0.024	0.018	0.016	0.009	0.022 ± 0.007	0.024 ± 0.005	0.020 ± 0.009
Kidneys	0.042	0.063	0.052	0.043	0.084	0.048	0.042	0.028	0.044	0.050 ± 0.016	0.054 ± 0.021	0.044 ± 0.003
Liver	0.073	0.035	0.044	0.064	0.039	0.068	0.054	0.037	0.055	0.052 ± 0.014	0.044 ± 0.012	0.063 ± 0.009
Lungs	0.022	0.019	0.017	0.023	0.022	0.018	0.014	0.014	0.006	0.017 ± 0.005	0.019 ± 0.003	0.015 ± 0.007
Muscle	0.021	0.018	0.017	0.022	0.021	0.016	0.013	0.014	0.005	0.016 ± 0.005	0.018 ± 0.003	0.014 ± 0.006
Ovaries	0.026	0.000	0.000			0.021	0.017		0.009	0.015 ± 0.010		0.018 ± 0.007
Pancreas	0.027	0.023	0.022	0.029	0.027	0.022	0.017	0.018	0.009	0.021 ± 0.006	0.024 ± 0.004	0.019 ± 0.007
Red marrow	0.165	0.123	0.113	0.088	0.081	0.121	0.070	0.064	0.112	0.104 ± 0.032	0.094 ± 0.024	0.117 ± 0.039
Skeleton	0.158	0.093	0.085	0.080	0.076	0.117	0.074	0.055	0.092	0.092 ± 0.030	0.078 ± 0.014	0.110 ± 0.037
Skin	0.017	0.016	0.014	0.019	0.018	0.013	0.011	0.012	0.004	0.014 ± 0.005	0.016 ± 0.003	0.011 ± 0.006
Spleen	0.132	0.123	0.124	0.220	0.138	0.170	0.111	0.116	0.141	0.142 ± 0.034	0.144 ± 0.043	0.138 ± 0.025
Testes		0.017	0.016	0.021	0.020			0.013		0.018 ± 0.003	0.018 ± 0.003	
Thymus	0.021	0.019	0.017	0.022	0.021	0.016	0.013	0.014	0.004	0.016 ± 0.005	0.018 ± 0.003	0.014 ± 0.007
Thyroid	0.020	0.018	0.016	0.022	0.021	0.015	0.012	0.013	0.004	0.016 ± 0.006	0.018 ± 0.003	0.013 ± 0.007
Urinary bladder wall	0.070	0.058	0.064	0.062	0.051	0.129	0.127	0.098	0.186	0.094 ± 0.045	0.067 ± 0.018	0.128 ± 0.047
Uterus	0.025	0.000	0.000	0.000	0.000	0.021	0.017	0.000	0.010	0.008 ± 0.010		0.018 ± 0.006
Lens of eyes	0.029	0.023	0.021	0.026	0.024	0.023	0.018	0.017	0.012	0.021 ± 0.005	0.022 ± 0.004	0.021 ± 0.007
Total body	0.029	0.023	0.021	0.026	0.025	0.023	0.018	0.016	0.012	0.021 ± 0.005	0.022 ± 0.004	0.020 ± 0.007
Effective dose equivalent (Sv/MBq)	0.058	0.047	0.044	0.051	0.045	0.054	0.040	0.035	0.046	0.047 ± 0.007	0.044 ± 0.006	0.049 ± 0.008
Effective dose (Sv/MBq)	0.046	0.038	0.036	0.040	0.035	0.043	0.030	0.029	0.032	0.036 ± 0.006	0.035 ± 0.004	0.038 ± 0.008

MM participants are MMDM01, MMDM02, and MMDM03; healthy participants are MMDN01, MMDN02, MMDN03, MMDN04, MMDN05, and MMDN06. Data are Sv/MBq.



**TABLE 3**  
Residence Times Calculated from Human Dosimetry Data ( $n = 9$ )

Organ	MMDM01 (F)	MMDM02 (M)	MMDM03 (M)	MMDN01 (M)	MMDN02 (M)	MMDN03 (F)	MMDN04 (F)	MMDN05 (M)	MMDN06 (F)
Liver	1.05	0.62	0.82	1.23	0.71	1.00	0.80	0.71	0.83
Kidneys	0.10	0.20	0.16	0.12	0.28	0.13	0.12	0.08	0.13
Bladder content	3.21	3.29	4.34	1.08	2.10	6.72	9.25	7.46	12.48
Spleen	0.23	0.19	0.27	0.48	0.18	0.31	0.20	0.25	0.26
Red marrow	4.75	3.11	2.89	2.02	1.83	2.93	1.89	1.54	1.56
Heart content	0.072	0.053	0.061	0.055	0.041	0.067	0.042	0.015	0.035
Total	9.41	7.47	8.54	4.99	5.15	11.16	12.30	10.05	15.28
MIRD 2-h void	0.19	0.20	0.24	0.10	0.15	0.43	0.48	0.43	0.68
Excreted	3.02	3.09	4.10	0.99	1.95	6.29	8.77	7.03	11.79
Remainder	8.91	10.85	9.78	13.34	13.18	7.17	6.02	8.27	3.05

MM participants are MMDM01, MMDM02, and MMDM03; healthy participants are MMDN01, MMDN02, MMDN03, MMDN04, MMDN05, and MMDN06. Data are hours.

serum and plasma samples obtained from participants after they were injected with the radiotracer. Analytic radio-high-performance liquid chromatography was used to collect fractions, which were

measured (radioactive counts) using the  $\gamma$ -counter. Data were normalized before plotting and analysis. Our original intent was to perform metabolite analysis from 0 to 4 h; however, the assay sensitivity was determined to be best for the time point at 1 h after injection. The low radioactivity counts after 1 h are likely due to the tracer's small size and pharmacokinetics (rapid blood clearance). The rapid blood clearance diluted the signal to close to the baseline noise beyond 1 h. For patient convenience, we made the decision to limit the metabolite blood sampling to 1 h and amended the protocol accordingly. We previously performed ex vivo stability testing on human serum and demonstrated radiopharmaceutical stability up to 24 h. Here, the data showed that more than 90% of  $^{64}\text{Cu}$ -LLP2A was stable at 1 h, with the measured retention time of 5.5–7 min. The remaining radioactivity was accounted for by free  $^{64}\text{Cu}$  (elution time, 2–3 min) (Supplemental Fig. 7).

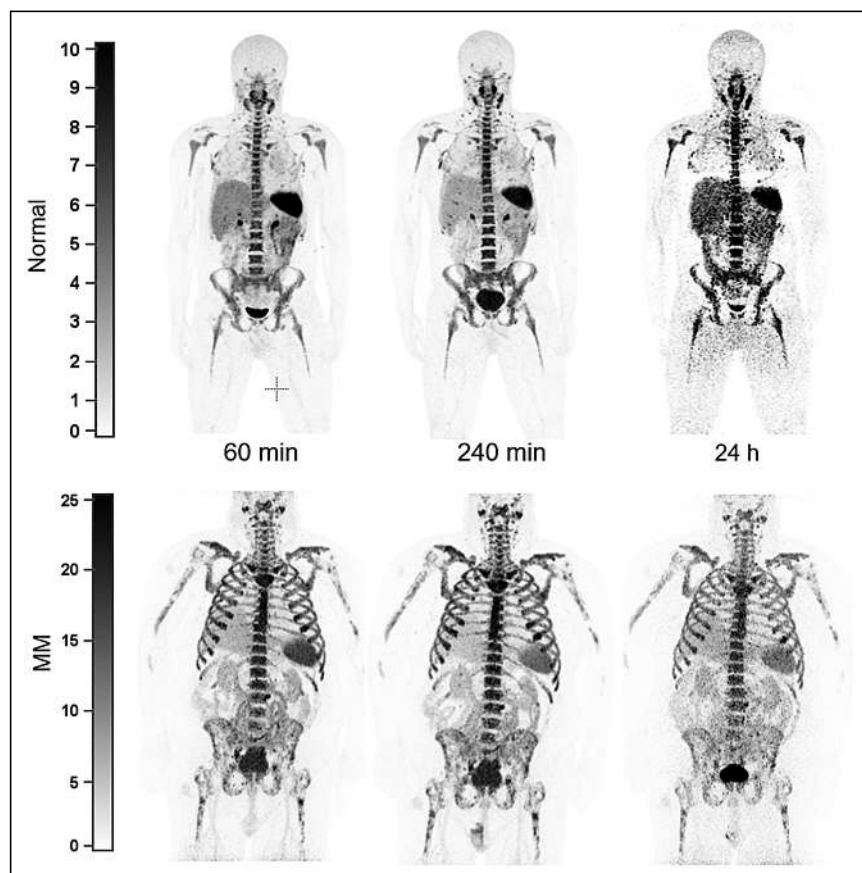


**FIGURE 2.** Anterior maximum-intensity-projection  $^{64}\text{Cu}$ -LLP2A-PET images of healthy volunteer (MMDN05) and subject with MM (MMDM03) at similar time points after tracer injection. Best-quality images were obtained 1–5 h after injection of radiotracer. Later time points ( $\sim 24$  h) exhibited relatively lower count and high image noise. Unit of measurement for intensity bars = SUV.

#### Flow Cytometry Study

The expression of activated VLA4 on hematopoietic cell populations within the BM or peripheral blood of 3 healthy participants from MM tissue bank (UPN1954, UPN2055, and UPN2140) and a patient with MM (MMDM02) (baseline and after disease progression 4 mo later) was examined by flow cytometry using LLP2A-Cy5 (19). Using a 14-color flow cytometry panel, we identified 18 different hematopoietic cell populations within these 7 samples (Supplemental Fig. 8). The BM mononuclear cells exhibited similar cellular distributions with the exception of fewer mature B cells in the patient with MM than in the healthy

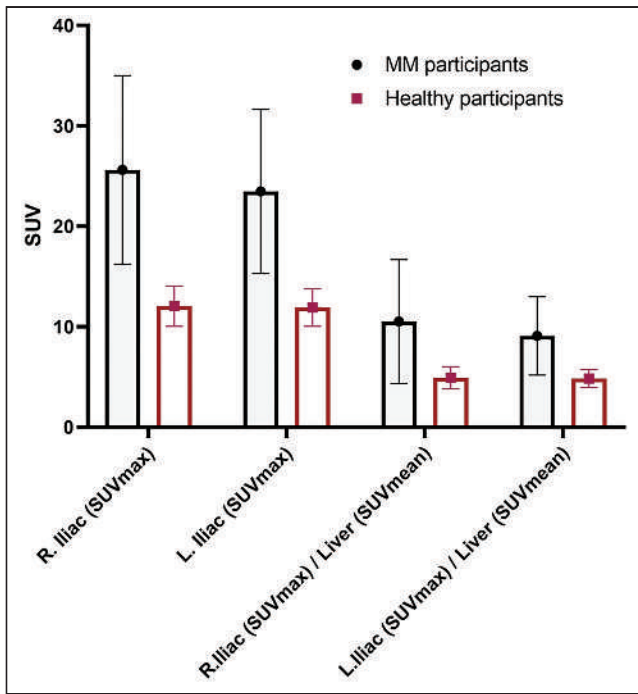


**FIGURE 3.** Comparison of  $^{64}\text{Cu}$ -LLP2A  $\text{SUV}_{\text{max}}$  of iliac bones in healthy and MM participants at average of 240 min after injection of radiotracer. Mean and SD for  $\text{SUV}_{\text{max}}$  were  $12.05 \pm 2.0$  for healthy participants ( $n = 5$ ) and  $25.62 \pm 9.38$  for MM patients ( $n = 3$ ) (\*\* $P < 0.03$ , 2-tailed).

participants (Fig. 5A; Supplemental Fig. 9). In contrast, the peripheral blood samples from the patient with MM were enriched for CD138-positive plasma cells expressing high levels of CD16 and activated VLA-4, as measured with LLP2A-Cy5 (Fig. 5B; Supplemental Fig. 10). As we previously described, subsets of B cells, T cells, natural killer T cells, and myeloid cells expressing activated VLA-4 (LLP2A<sup>hi</sup>) were identified in both the healthy control and the MM samples (19).

## DISCUSSION

The landscape of MM pathogenesis and progression varies from patient to patient. Tumor heterogeneity, development of resistance

to drugs, relapse of refractory disease, persistence of minimal residual disease, and variability in response are some of the hallmarks of MM. Molecular imaging has the ability to address some of the critical issues in management of MM patients by providing an accurate assessment of disease burden spatially, unambiguous staging, and quantitative and qualitative assessment of sites of disease, as well as detection of residual disease after treatment (27). Some outstanding challenges remain in the myeloma diagnostic tool kit: tissue biopsies are prone to sampling errors, serum assays can be confounding in cases of nonsecretory and heavily treated myelomas, conventional radiologic modalities are not sensitive for detecting osteolytic lesions, and molecular imaging using  $^{18}\text{F}$ -FDG has inherent limitations in MM. In recent years, different groups have assessed the utility of myeloma-specific agents targeted to myeloma proteins such as CD38 and CXCR4. Metabolic tracers such as  $^{18}\text{F}$ -FACBC (28) and  $^{11}\text{C}$ -acetate (29) have also been explored as alternatives to  $^{18}\text{F}$ -FDG. Although promising, the short 20-min radioactive half-life of  $^{11}\text{C}$  makes it a challenging radionuclide for routine use. The 12.7-h radioactive half-life of the positron emitter  $^{64}\text{Cu}$ , on the other hand, is a more viable option for wide clinical use.

Over 80% of myeloma patients present with skeleton-related events, and a significant number also experience pathologic fractures (30). Therefore, focusing on markers involved in the adherence, survival, and progression of myeloma cells in the BM is highly relevant. MM cells interact with the VCAM-1 expressed on the BM stromal cells and soluble fibronectin via VLA4 (31). Several studies have independently shown that VLA4 is overexpressed in MM cells relative to other cells and is an established marker of cell adhesion-mediated drug resistance.

Here, we describe, for the first time to our knowledge, the production of a VLA4-targeted clinical-grade tracer,  $^{64}\text{Cu}$ -LLP2A, under good-manufacturing-practice conditions in a cyclotron facility for use in human participants. The results of toxicity studies on rodents (no observed adverse effect level), and subsequently in patients, demonstrate the safety of injecting up to 15  $\mu\text{g}$  of this tracer into patients. This level is not a limiting dose, but a reasonable starting point based on robust rodent imaging, toxicity, dosimetry, and safety data. The prerelease acceptance criteria, which included factors such as the pH, more than 90% radiochemical purity, more than 99% radionuclide purity, and an acceptable endotoxin result ( $<175$  endotoxin units per total batch volume) was met for each imaging study. The postrelease quality control cell data also met the

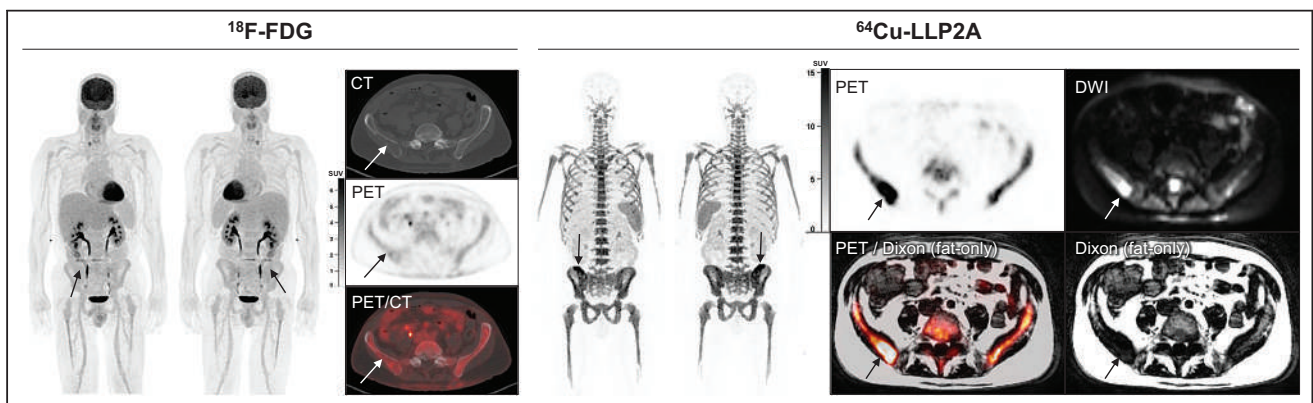


**FIGURE 4.** MM patient underwent PET imaging with  $^{64}\text{Cu}$ -LLP2A and  $^{18}\text{F}$ -FDG. On PET/CT, osteolytic lesion in right iliac bone (arrows) of MM patient had  $^{18}\text{F}$ -FDG uptake similar to background marrow. On PET/MRI, this same lesion (arrows) had  $^{64}\text{Cu}$ -LLP2A uptake above background marrow, corresponding to fat-replacing lesion on fat-only Dixon images and hyperintense lesion on DWI. In this lesion,  $^{64}\text{Cu}$ -LLP2A  $\text{SUV}_{\text{max}}$  was 29.5 with  $\text{SUL}_{\text{peak}}$  (per PERCIST) of 18.7; in comparison,  $^{18}\text{F}$ -FDG  $\text{SUV}_{\text{max}}$  was 2.9 with  $\text{SUL}_{\text{peak}}$  (per PERCIST) of 2.1. DWI = diffusion-weighted imaging.

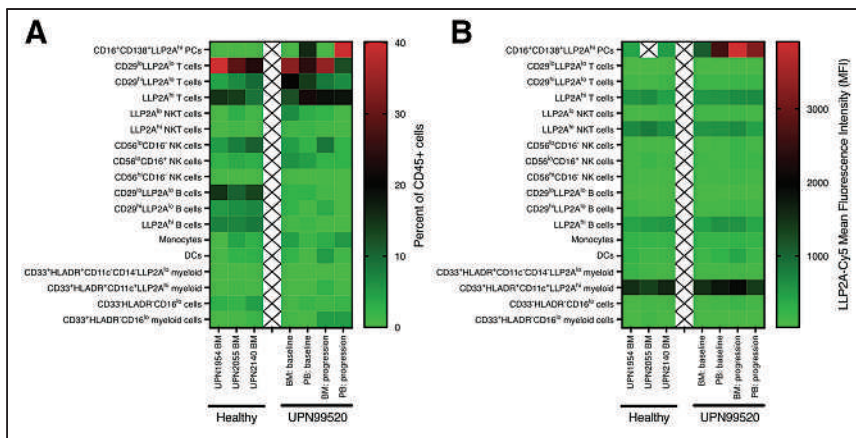


**FIGURE 5.** Flow cytometry analysis of LLP2A-Cy5 staining of human BM and peripheral blood cell subsets. (A) Heat map showing percentage of different cell subsets found within BM or peripheral blood (PB) of healthy participants from MM tissue bank (UPN1954, UPN2055, and UPN2140) or one of the MM patients (UPN99520/MMDM02) at baseline and after disease progression 4 mo later. (B) Heat map showing mean fluorescence intensity of LLP2A-Cy5 staining of different cell subsets.

acceptance criteria for each study participant. These data validated the robustness of the tracer production and retention of bioactivity after the radiolabeling procedure.

Six healthy participants and 3 participants with a confirmed diagnosis of MM were injected with  $^{64}\text{Cu}$ -LLP2A. Metabolite analysis in these patients demonstrated that the tracer was more than 90% stable up to 1 h, with free copper identified as the only remaining metabolite. Accurate stability analysis beyond 1 h was not feasible because of sensitivity limitations. The calculated effective dose of  $^{64}\text{Cu}$ -LLP2A (0.036 mSv/MBq) is within the range of other reported copper radiopharmaceuticals (e.g.,  $^{64}\text{Cu}$ -SARTATE [0.0204 mSv/MBq] (32),  $^{64}\text{Cu}$ -ATSM [0.036 mSv/MBq] (33),  $^{64}\text{Cu}$ -DOTA-AE105 [0.0284 mSv/MBq] (34), and  $^{64}\text{Cu}$ -DOTATATE [0.0315 mSv/MBq] (35). The organ with the highest dose is the spleen, at a sex-averaged value of 0.142 mSv/MBq, followed by the red marrow (0.104 mSv/MBq) and bladder wall (0.094 mSv/MBq). As a comparison, the effective dose for  $^{18}\text{F}$ -FDG, the most widely used radiopharmaceutical for oncologic imaging, is 0.019 mSv/MBq (25).

The tracer pharmacokinetics in humans closely followed the rodent data, with rapid washout from blood and clearance via kidneys and bladder. As expected, there was relatively high uptake in the BM. The residence time in the BM was generally higher in women than in men and, overall, was higher in MM participants than in healthy participants. The SUV analysis of the BM in the iliac bones showed significantly higher values in the MM participants than in the healthy participants. The SD of SUVs was also higher in the MM participants across all time points. This finding points to the inhomogeneity and patchiness of the malignant BM in the MM patients as compared with healthy individuals (36). Comparison of image quality from early and late time points supports the selection of early time points—that is, 4–5 h after injection of the radiotracer—as optimal. This timing is advantageous for the convenience of myeloma patients, as they prefer same-day imaging because of the morbidity associated with the myeloma disease burden.

Takahashi et al. have demonstrated a quantitative metabolic parameter for  $^{18}\text{F}$ -FDG PET for assessing the intensity of bone involvement in MM (37). Li et al. proposed  $^{18}\text{F}$ -FDG uptake higher than liver as the positivity cutoff to discriminate between physiologic and pathologic uptake in the BM and defined 4 BM

$^{18}\text{F}$ -FDG uptake patterns (normal, focal, diffuse, and mixed) as reliable prognostic predictors of MM (38). In our study, we focused on the iliac bone  $\text{SUV}_{\text{max}}$  and  $\text{SUV}_{\text{mean}}$  and on SUVs normalized to liver and spleen. SUVs from the spine BM showed borderline statistical significance between MM and healthy participants (higher SUVs in MM participants). Further studies on a larger cohort are required to propose robust qualitative and quantitative metrics for  $^{64}\text{Cu}$ -LLP2A-PET. Other key variables to consider are the disease stage (precursor, newly diagnosed, relapsed, refractory, remission, or residual), genetic fingerprint, spatial distribution, BM inhomogeneity, age, and sex, as all these factors are known to impact myeloma pathogenesis (39).

## CONCLUSION

In this trial, we demonstrated that  $^{64}\text{Cu}$ -LLP2A can readily be synthesized with high quality and specific activity, is safe in humans, and has an acceptable radiation dosimetry, on a par with other  $^{64}\text{Cu}$ -labeled imaging agents and about twice higher than  $^{18}\text{F}$ -FDG, mainly because of the longer half-life of  $^{64}\text{Cu}$ . We demonstrated that phenotyping of the imaging signal using flow cytometry is complex yet feasible. Among the various discerning imaging features, the imaging data showed that there was uptake of  $^{64}\text{Cu}$ -LLP2A in the BM of healthy participants, as expected. To address this aspect of background uptake, we are working toward optimizing the imaging parameters to enhance the signal-to-background ratio in the malignant BM. The optimization approaches involve modulation of the imaging dose and molar activity as well as use of time-of-flight scanners for precise and sensitive imaging. Furthermore, in vitro and ex vivo studies evaluating the mechanisms of uptake, activation, retention, and efflux will be used to reduce background uptake. In our future  $^{64}\text{Cu}$ -LLP2A-PET imaging trials, we plan to incorporate a systems biology approach to integrate longitudinal clinical data with the imaging results.

## DISCLOSURE

This study was supported in part by U54CA199092, R42CA257797, R01 CA248493, R35 CA210084, R50CA211466, and R01CA176221. We thank the Mallinckrodt Institute of Radiology for pilot funds, the Foundation for Barnes–Jewish Hospital, and the Response Assessment Shared Resource Cores of the Alvin J. Siteman Cancer Center, supported in part by P30 CA91842. Monica Shokeen and Samuel Achilefu are cofounders of Sarya, LLC. No other potential conflict of interest relevant to this article was reported.

## ACKNOWLEDGMENTS

We thank the Washington University School of Medicine isotope production team for  $^{64}\text{Cu}$ . We thank the nurse coordinators and CCIR technical team for their exceptional assistance. We thank the patients who provided samples to the MM Tissue Bank Study at Washington University that were used in this study. We profusely thank the volunteers who participated in the imaging study. Professor Shokeen thanks Professors Katherine Weilbaeher, Carolyn Anderson and Michael Tomasson for their expertise and encouragement.

## KEY POINTS

**QUESTION:** Is  $^{64}\text{Cu}$ -LLP2A-PET safe for use in humans?

**PERTINENT FINDINGS:** This first-in-humans imaging trial demonstrated that  $^{64}\text{Cu}$ -LLP2A-PET is safe for use in MM patients. Preliminary findings support early imaging time points, which are amenable to patient comfort.

**IMPLICATIONS FOR PATIENT CARE:**  $^{64}\text{Cu}$ -LLP2A-PET can inform on the unique biology of VLA4-positive malignant cells in MM patients, thus having potential to enhance diagnosis and guide therapy.

## REFERENCES

1. Peacock JG, Christensen CT, Banks KP. RESISTing the need to quantify: putting qualitative FDG-PET/CT tumor response assessment criteria into daily practice. *AJNR*. 2019;40:1978–1986.
2. Valls L, Badve C, Avril S, et al. FDG-PET imaging in hematological malignancies. *Blood Rev*. 2016;30:317–331.
3. Lennon AM, Buchanan AH, Kinde I, et al. Feasibility of blood testing combined with PET-CT to screen for cancer and guide intervention. *Science*. 2020;369:eabb9601.
4. Alagpulinsa DA, Szalat RE, Poznansky MC, Shmookler Reis RJ. Genomic instability in multiple myeloma. *Trends Cancer*. 2020;6:858–873.
5. Morgan GJ, Walker BA, Davies FE. The genetic architecture of multiple myeloma. *Nat Rev Cancer*. 2012;12:335–348.
6. Callander NS, Baljevic M, Adekola K, et al. NCCN Guidelines<sup>®</sup> insights: multiple myeloma, version 3.2022: featured updates to the NCCN guidelines. *J Natl Compr Canc Netw*. 2022;20:8–19.
7. Lecouvet FE, Vekemans M-C, Van Den Berghe T, et al. Imaging of treatment response and minimal residual disease in multiple myeloma: state of the art WB-MRI and PET/CT. *Skeletal Radiol*. 2022;51:59–80.
8. Charalampous C, Goel U, Broski SM, et al. Utility of PET/CT in assessing early treatment response in patients with newly diagnosed multiple myeloma. *Blood Adv*. 2022;6:2763–2772.
9. Hillengass J, Usmani S, Rajkumar SV, et al. International myeloma working group consensus recommendations on imaging in monoclonal plasma cell disorders. *Lancet Oncol*. 2019;20:e302–e312.
10. Zamagni E, Tacchetti P, Barbato S, Cavo M. Role of imaging in the evaluation of minimal residual disease in multiple myeloma patients. *J Clin Med*. 2020;9:3519.
11. Davies FE, Rosenthal A, Rasche L, et al. Treatment to suppression of focal lesions on positron emission tomography-computed tomography is a therapeutic goal in newly diagnosed multiple myeloma. *Haematologica*. 2018;103:1047–1053.
12. Rasche L, Angtuaco E, McDonald JE, et al. Low expression of hexokinase-2 is associated with false-negative FDG-positron emission tomography in multiple myeloma. *Blood*. 2017;130:30–34.
13. van Lammeren-Venema D, Regelink JC, Riphagen II, Zweegman S, Hoekstra OS, Zijlstra JM.  $^{18}\text{F}$ -fluoro-deoxyglucose positron emission tomography in assessment of myeloma-related bone disease: a systematic review. *Cancer*. 2012;118:1971–1981.
14. Matteucci F, Paganelli G, Martinelli G, Cerchione C. PET/CT in multiple myeloma: beyond FDG. *Front Oncol*. 2021;10:622501.
15. Ghai A, Maji D, Cho N, et al. Preclinical development of CD38-targeted [ $^{89}\text{Zr}$ ]Zr-DFO-daratumumab for imaging multiple myeloma. *J Nucl Med*. 2018;59:216–222.
16. Ulaner GA, Sobol NB, O'Donoghue JA, et al. CD38-targeted immuno-PET of multiple myeloma: from xenograft models to first-in-human imaging. *Radiology*. 2020;295:606–615.
17. Buck AK, Haug A, Dreher N, et al. Imaging of C-X-C motif chemokine receptor 4 expression in 690 patients with solid or hematologic neoplasms using  $^{68}\text{Ga}$ -PentixaFor PET. *J Nucl Med*. March 3, 2022 [Epub ahead of print].
18. Thomas E, Mathieu C, Moreno-Gaona P, et al. Anti-BCMA immuno-nanoPET radiotracers for improved detection of multiple myeloma. *Adv Healthc Mater*. 2022;11:e2101565.
19. Hathi D, Chanswangphuwana C, Cho N, et al. Ablation of VLA4 in multiple myeloma cells redirects tumor spread and prolongs survival. *Sci Rep*. 2022;12:30.
20. DeNardo SJ, Liu R, Albrecht H, et al.  $^{111}\text{In}$ -LLP2A-DOTA polyethylene glycol-targeting  $\alpha_4\beta_1$  integrin: comparative pharmacokinetics for imaging and therapy of lymphoid malignancies. *J Nucl Med*. 2009;50:625–634.
21. Shokeen M, Zheleznyak A, Wilson JM, et al. Molecular imaging of very late antigen-4 ( $\alpha_4\beta_1$  integrin) in the premetastatic niche. *J Nucl Med*. 2012;53:779–786.
22. Soodgupta D, Hurchla MA, Jiang M, et al. Very late antigen-4 ( $\alpha_4\beta_1$  integrin) targeted PET imaging of multiple myeloma. *PLoS One*. 2013;8:e55841.
23. Ghai A, Fettig N, Fontana F, et al. In vivo quantitative assessment of therapeutic response to bortezomib therapy in disseminated animal models of multiple myeloma with [ $^{18}\text{F}$ ]FDG and [ $^{64}\text{Cu}$ ]Cu-LLP2A PET. *EJNMMI Res*. 2021;11:97.
24. Soodgupta D, Zhou H, Beaino W, et al. Ex vivo and in vivo evaluation of overexpressed VLA-4 in multiple myeloma using LLP2A imaging agents. *J Nucl Med*. 2016;57:640–645.
25. ICRP publication 106: radiation dose to patients from radiopharmaceuticals—addendum 3 to ICRP publication 53. *Ann ICRP*. 2008;38:(1–2).
26. Thomas SR, Stabin MG, Chen CT, Samarantunga RC. MIRD pamphlet no. 14 revised: a dynamic urinary bladder model for radiation dose calculations. Task group of the MIRD committee, Society of Nuclear Medicine. *J Nucl Med*. 1999;40:102S–123S.
27. Cowan AJ, Green DJ, Kwok M, et al. Diagnosis and management of multiple myeloma: a review. *JAMA*. 2022;327:464–477.
28. Morath V, Heider M, Mittelhäuser M, et al. Initial evaluation of [ $^{18}\text{F}$ ]FACBC for PET imaging of multiple myeloma. *EJNMMI Res*. 2022;12:4.
29. Chen M, Zhu W, Du J, et al.  $^{11}\text{C}$ -acetate positron emission tomography is more precise than  $^{18}\text{F}$ -fluorodeoxyglucose positron emission tomography in evaluating tumor burden and predicting disease risk of multiple myeloma. *Sci Rep*. 2021;11:22188.
30. Terpos E, Berenson J, Cook RJ, Lipton A, Coleman RE. Prognostic variables for survival and skeletal complications in patients with multiple myeloma osteolytic bone disease. *Leukemia*. 2010;24:1043–1049.
31. Abe M, Hiura K, Ozaki S, Kido S, Matsumoto T. Vicious cycle between myeloma cell binding to bone marrow stromal cells via VLA-4-VCAM-1 adhesion and macrophage inflammatory protein-1 $\alpha$  and MIP-1 $\beta$  production. *J Bone Miner Metab*. 2009;27:16–23.
32. Hicks RJ, Jackson P, Kong G, et al.  $^{64}\text{Cu}$ -SARTATE PET imaging of patients with neuroendocrine tumors demonstrates high tumor uptake and retention, potentially allowing prospective dosimetry for peptide receptor radionuclide therapy. *J Nucl Med*. 2019;60:777–785.
33. Laforest R, Dehdashti F, Lewis JS, Schwarz SW. Dosimetry of  $^{60/61/62/64}\text{Cu}$ -ATSM: a hypoxia imaging agent for PET. *Eur J Nucl Med Mol Imaging*. 2005;32:764–770.
34. Persson M, El Ali HH, Binderup T, et al. Dosimetry of  $^{64}\text{Cu}$ -DOTA-AE105, a PET tracer for uPAR imaging. *Nucl Med Biol*. 2014;41:290–295.
35. Pfeifer A, Knigge U, Mortensen J, et al. Clinical PET of neuroendocrine tumors using  $^{64}\text{Cu}$ -DOTATATE: first-in-humans study. *J Nucl Med*. 2012;53:1207–1215.
36. Sachpekidis C, Merz M, Raab M-S, et al. The prognostic significance of [ $^{18}\text{F}$ ]FDG PET/CT in multiple myeloma according to novel interpretation criteria (IMPETUs). *EJNMMI Res*. 2021;11:100.
37. Takahashi MES, Mosci C, Souza EM, et al. Proposal for a quantitative  $^{18}\text{F}$ -FDG PET/CT metabolic parameter to assess the intensity of bone involvement in multiple myeloma. *Sci Rep*. 2019;9:16429.
38. Li J, Tan H, Xu T, Shi H, Liu P. Bone marrow tracer uptake pattern of PET-CT in multiple myeloma: image interpretation and prognostic value. *Ann Hematol*. 2021;100:2979–2988.
39. Rasche L, Chavan SS, Stephens OW, et al. Spatial genomic heterogeneity in multiple myeloma revealed by multi-region sequencing. *Nat Commun*. 2017;8:268.

---

---

# Lesion Quantification Accuracy of Digital $^{90}\text{Y}$ PET Imaging in the Context of Dosimetry in Systemic Fibroblast Activation Protein Inhibitor Radionuclide Therapy

David Kersting<sup>1,2</sup>, Walter Jentzen<sup>1,2</sup>, Daniel Jeromin<sup>1,2</sup>, Ilektra-Antonia Mavroei<sup>2,3</sup>, Maurizio Conti<sup>4</sup>, Florian Büther<sup>5</sup>, Ken Herrmann<sup>1,2</sup>, Christoph Rischpler<sup>1,2</sup>, Rainer Hamacher<sup>2,3</sup>, Wolfgang P. Fendler<sup>1,2</sup>, Robert Seifert<sup>1,2,5</sup>, and Pedro Fragoso Costa<sup>1,2</sup>

<sup>1</sup>Department of Nuclear Medicine, West German Cancer Center (WTZ), University Hospital Essen, University of Duisburg-Essen, Essen, Germany; <sup>2</sup>German Cancer Consortium (DKTK), Partner Site University Hospital Essen, Essen, Germany; <sup>3</sup>Department of Medical Oncology, West German Cancer Center (WTZ), University Hospital Essen, University of Duisburg-Essen, Essen, Germany; <sup>4</sup>Siemens Medical Solutions USA, Inc., Knoxville, Tennessee; and <sup>5</sup>Department of Nuclear Medicine, University Hospital Muenster, University of Muenster, Muenster, Germany

Therapy with  $^{90}\text{Y}$ -labeled fibroblast activation protein inhibitors ( $^{90}\text{Y}$ -FAPIs) was recently introduced as a novel treatment concept for patients with solid tumors. Lesion and organ-at-risk dosimetry is part of assessing treatment efficacy and safety and requires reliable quantification of tissue uptake. As  $^{90}\text{Y}$  quantification is limited by the low internal positron–electron pair conversion rate, the increased effective sensitivity of digital silicon photomultiplier-based PET/CT systems might increase quantification accuracy and, consequently, allow for dosimetry in  $^{90}\text{Y}$ -FAPI therapy. The aim of this study was to explore the conditions for reliable lesion image quantification in  $^{90}\text{Y}$ -FAPI radionuclide therapy using a digital PET/CT system. **Methods:** Two tumor phantoms were filled with  $^{90}\text{Y}$  solution using different sphere activity concentrations and a constant signal-to-background ratio of 40. The minimum detectable activity concentration was determined, and its dependence on acquisition time (15 vs. 30 min per bed position) and smoothing levels (all-pass vs. 5-mm gaussian filter) was investigated. Quantification accuracy was evaluated at various activity concentrations to estimate the minimum quantifiable activity concentration using contour-based and oversized volume-of-interest-based quantification approaches. A  $\pm 20\%$  deviation range between image-derived and true activity concentrations was regarded as acceptable. Tumor dosimetry for 3 patients treated with  $^{90}\text{Y}$ -FAPI is presented to project the phantom results to clinical scenarios. **Results:** For a lesion size of 40 mm and a clinical acquisition time of 15 min, both minimum detectable and minimum quantifiable activity concentrations were 0.12 MBq/mL. For lesion sizes of greater than or equal to 30 mm, accurate quantification was feasible for detectable lesions. Only for the smallest 10-mm sphere, the minimum detectable and minimum quantifiable activity concentrations differ substantially (0.43 vs. 1.97 MBq/mL). No notable differences between the 2 quantification approaches were observed. For the investigated tumors, absorbed dose estimates with reliable accuracy were achievable. **Conclusion:** For lesion sizes and activity concentrations that are expected to be observed in patients treated with  $^{90}\text{Y}$ -FAPI, quantification with reasonable accuracy is possible. Further dosimetry studies are needed to thoroughly investigate the efficacy and safety of  $^{90}\text{Y}$ -FAPI therapy.

**Key Words:**  $^{90}\text{Y}$ ; PET; minimum detectable activity; quantification accuracy; FAPI therapy

**J Nucl Med 2023; 64:329–336**

DOI: 10.2967/jnumed.122.264338

---

**T**he high-energy  $\beta$ -particle emitter  $^{90}\text{Y}$  is a radionuclide that is used in oncologic radionuclide therapy regimens. Typical applications include local radioembolization of hepatocellular carcinoma by selective internal radiation therapy (1) or systemic therapies using, for example, somatostatin receptor agonists like  $^{90}\text{Y}$ -DOTATATE/DOTATOC to target neuroendocrine tumors after intravenous injection (2). Recently, systemic treatments of sarcoma or pancreatic cancer patients using  $^{90}\text{Y}$ -labeled fibroblast activation protein (FAP) inhibitors ( $^{90}\text{Y}$ -FAPIs) were introduced (3,4). The target molecule, fibroblast activation protein  $\alpha$ , is a cell surface dipeptidyl peptidase expressed by cancer-associated fibroblasts in the tumor microenvironment of various solid tumors as well as cancer cells such as sarcoma and mesothelioma (5).

Intratherapeutic  $^{90}\text{Y}$  bremsstrahlung whole-body scintigraphy or SPECT imaging is established and well tolerated by patients for rapidly verifying tracer accumulation in the tumor tissue and for investigating tracer biodistribution (6). However, these imaging modalities do not allow reliable quantification of  $^{90}\text{Y}$  activity concentrations, which is mandatory for intratherapeutic lesion dosimetry in systemic radionuclide therapy (7). Limiting factors are, for example, an inaccurate compensation of scattered and septal penetrating photons of the continuous bremsstrahlung energy spectrum and the difficulty of choosing an appropriate energy window, as no discrete  $\gamma$ -photons are emitted (7,8). In  $^{90}\text{Y}$ -FAPI therapy, lesion dosimetry is required for dose-response investigations and can be part of the decision-making process regarding the application of further therapeutic cycles.

As an alternative to bremsstrahlung imaging,  $^{90}\text{Y}$  PET can be performed (9) to provide higher visual image quality and higher detectability for small lesions (6,8). Moreover, the possibility of reliable  $^{90}\text{Y}$  PET quantification for selective internal radiation therapy was demonstrated (10). However, tumor activity concentrations in selective internal radiation therapy are typically high ( $>1$  MBq/mL) (11), whereas in systemic radionuclide therapies, considerably lower

---

Received Apr. 30, 2022; revision accepted Aug. 13, 2022.  
For correspondence or reprints, contact David Kersting (david.kersting@uni-due.de).

Published online Aug. 18, 2022.

COPYRIGHT © 2023 by the Society of Nuclear Medicine and Molecular Imaging.

activity concentrations are accumulated by the tumor tissue (3). As  $^{90}\text{Y}$  PET imaging is limited by poor counting statistics due to internal positron–electron pair conversion occurring in only 0.00326% of pairs per decay (11), quantification of low activity concentrations is extremely challenging (12).

The recently introduced digital silicon photomultiplier-based PET/CT systems offer higher effective sensitivity and higher spatial and coincidence timing resolutions than previous-generation systems. Therefore, image quality and lesion detectability are improved, particularly for small lesions with low tracer uptake (13–17). The improvements were described for different radionuclides, including  $^{18}\text{F}$  (positron branching ratio, 97%) and  $^{68}\text{Ga}$  (positron branching ratio, 89%), and for the nonstandard tracer  $^{124}\text{I}$  (23%). Recently, first applications of digital  $^{90}\text{Y}$  PET in the context of selective internal radiation therapy were described (12,18) but—to our knowledge—no performance evaluation for systemic radionuclide therapy has been performed yet.

The aim of this study was to explore the conditions for reliable lesion image quantification in  $^{90}\text{Y}$ -FAPI radionuclide therapy using a digital PET/CT system.

## MATERIALS AND METHODS

### Study Design

The study consisted of 2 parts: a phantom study and a clinical case study. A National Electrical Manufacturers Association (NEMA) tumor phantom and an anthropomorphic abdominal tumor phantom were scanned under different conditions to estimate the size-dependent minimum detectable activity concentration (MDAC), minimum quantifiable activity concentration (MQAC), and quantification accuracy. Two approaches for partial-volume effect correction were compared. Additionally, tumor dosimetry for 3 patients treated with  $^{90}\text{Y}$ -FAPI was performed and evaluated, considering the results of the phantom data. A condensed version of the methods used is given in this article; full experimental details are presented as supplemental materials (supplemental materials are available at <http://jnm.snmjournals.org>).

### Simple Approaches to Correct for Partial-Volume Effects

In clinical tumor dosimetry, the mean imaged activity concentration within the tumor boundary is commonly used to derive the (mean) tumor absorbed (radiation) dose. When the mean activity concentration is used, a partial-volume effect correction is necessary unless the objects are extremely large, that is, an equivalent sphere diameter of greater than or equal to 47 times the PET spatial resolution (19). Two simple approaches were applied in this study to correct for this effect. In the first, the contour-based approach, measured sphere recovery coefficient (RC) values were used to correct the mean imaged activity concentration within the lesion boundary. RC values were derived from the NEMA tumor phantom. The second approach, the oversized volume-of-interest (VOI)-based approach, included the total activity within the lesion volume using an oversized VOI, whose borders had an approximate distance of 1 time the PET spatial resolution of the actual geometric (CT-derived) boundary of the lesion. It was assumed that this oversized VOI contained the main activity to compensate for partial-volume effects; however, to compensate for a contribution from background activity, a background subtraction was performed as previously described (20).

### Phantoms

**Setup and Preparation.** The NEMA tumor phantom is a torso-shaped phantom containing 6 spheres (with diameters of 9.7, 12.6, 17.4, 22.2, 27.7, and 37.0 mm). The anthropomorphic abdominal tumor phantom (Abdo-Man) (21) contains a refillable liver insert, in which 4 spheres (diameters of 10.0, 20.0, 30.0, and 40.0 mm) are attached. It was selected from the phantoms available at our institution

(University Hospital Essen) to resemble the human body scattering geometry more realistically than the NEMA tumor phantom. Moreover, an investigation of quantification accuracy with the NEMA phantom would have been biased for the contour-based method, as the RC values were determined using images of the same phantom.

On the basis of clinical data, spheric inserts and the cavity were filled with  $^{90}\text{Y}$  solution at a representative initial sphere activity concentration of about 3.3 MBq/mL and a signal-to-background ratio of about 40. The initial activity concentration was determined as the mean of measurements using 3 different calibrated vial geometries in 2 different dose calibrators; the maximum error of the initial activity concentration was estimated to be  $\pm 7\%$  at the 95% confidence level (Supplemental Table 1). Activity concentrations at the PET start time were 3.36, 1.96, 1.22, 0.73, 0.34, 0.20, 0.12, and 0.05 MBq/mL for the NEMA tumor phantom and 3.33, 1.97, 1.23, 0.73, 0.34, 0.20, 0.12, and 0.06 MBq/mL for the anthropomorphic tumor phantom.

**PET Acquisition and Image Reconstruction.** Phantom PET data were acquired using a single bed position on a digital Biograph Vision 600 PET/CT scanner (Siemens Healthineers; detailed specifications are given in Supplemental Table 2), which exhibits a time-of-flight resolution of 210 ps (22). Initially, the NEMA tumor phantom was scanned for 6 h to determine RC values at high counting statistics. Thereafter, PET data for both phantoms were acquired for 30 min and used to reconstruct 30- and 15-min acquisition time PET images.

Images were reconstructed with the time-of-flight option and with point spread function modeling as previously recommended for quantitative  $^{90}\text{Y}$  PET imaging on the Biograph Vision scanner (12). Two postreconstruction smoothing filter levels (all-pass and 5-mm gaussian filters) were applied. The images had a voxel size of  $3.30 \times 3.30 \times 3.00$  mm, and the measured system spatial resolution (average full width at half maximum) (23) was 6.0 mm for a 5-mm gaussian smoothing filter.

### Patients

**Patient Characteristics.** Retrospective analysis of clinical data was approved by the local ethics committee (permit no. 20-9558-BO). Datasets for 3 patients who had progressive, advanced-stage solitary fibrous tumor (SFT) and received  $^{90}\text{Y}$ -FAPI-46 therapy (first cycle) under compassionate access after clinical indication were included. The decision about radionuclide treatment was made by a multidisciplinary tumor board. All patients had either previously shown progressive disease during established treatment options or were not eligible for other established treatment concepts. The administered therapeutic activities were 8.90 GBq (patient 1), 3.82 GBq (patient 2), and 3.67 GBq (patient 3).

**PET Acquisition and Image Reconstruction.** PET/CT examinations were scheduled as described in a previous study (3). Because of symptomatic patients and logistical reasons, serial PET/CT acquisitions were performed at slightly different time points: 17, 22, and 41 h after injection for patient 1; 2, 20, and 43 h after injection for patient 2; and 1, 4, and 20 h after injection for patient 3. PET data acquisition and image reconstruction were performed as described for phantoms (15-min acquisition time per bed position and 5-mm gaussian smoothing filter).

### Phantom Analysis

**MDAC.** The images of the NEMA tumor phantom at various activity concentrations were used to determine the MDAC as previously described (13,24). In brief, the visual detectability of each sphere was determined in a human observer study. Next, the signal-to-noise ratio (SNR) of each sphere was determined to estimate the SNR threshold indicating detectability. Finally, the MDAC was calculated for each sphere. The MDAC was defined as the activity concentration at the threshold SNR.

**Quantification Accuracy Evaluation.** To evaluate the lesion quantification accuracy, the activity concentration ratio of PET-imaged measurements to (decay-corrected) dose calibrator–derived measurements

was investigated. A  $\pm 20\%$  deviation range of the activity concentration ratio was regarded as acceptable considering the uncertainty for the  $^{90}\text{Y}$  activity concentration dose calibrator measurement, the  $^{18}\text{F}$  PET cross-calibration measurement (25), and the frequency of the positron–electron pair conversion (26–29).

**MQAC.** The results of the quantification accuracy evaluations were used to estimate the MQAC, that is, the minimum activity concentration for which the quantification appears to be reliable. In its derivation, the values for the quantification accuracy should lie within the  $\pm 20\%$  deviation range.

### Patient Analysis

In the patient analysis, key quantities related to the estimation of the tumor absorbed dose were derived. The procedure used was previously described (3). In brief, the tumor volumes were estimated by manual segmentation (VOI technique) using the respective CT images, and the VOIs were used to determine the tumor uptake values at 3 imaging time points. Mean tumor activity concentrations were determined using both the contour-based approach and the oversized VOI-based approach. The resulting uptake curves were parameterized by fitting a monoexponential function to the measured uptake values to determine the effective half-lives. The time-integrated activity coefficients (residence times) were determined and used to estimate the tumor absorbed doses with the sphere model of OLINDA/EXM (30). A logarithmic approach was applied for interpolation between tumor absorbed doses in the OLINDA tables.

### Software/Statistics

PET image analysis and VOI segmentation were performed using PMOD 4.202 (PMOD Technologies); MATLAB R2021a (The MathWorks) was used for data handling and computations. The tumor

absorbed dose was calculated using OLINDA/EXM 2.2 software (Hermes Medical Solutions AB). Graphics were created using BioRender.com (BioRender; www.BioRender.com).

## RESULTS

### Recovery Coefficients

Fitting parameters for calculating measured and fitted RC values are listed in Supplemental Table 3. The agreement between fitted and measured RC values was high (maximum percentage deviation of  $-6\%$ ), indicating a small contribution of the fitting process to the total error of the quantification approaches.

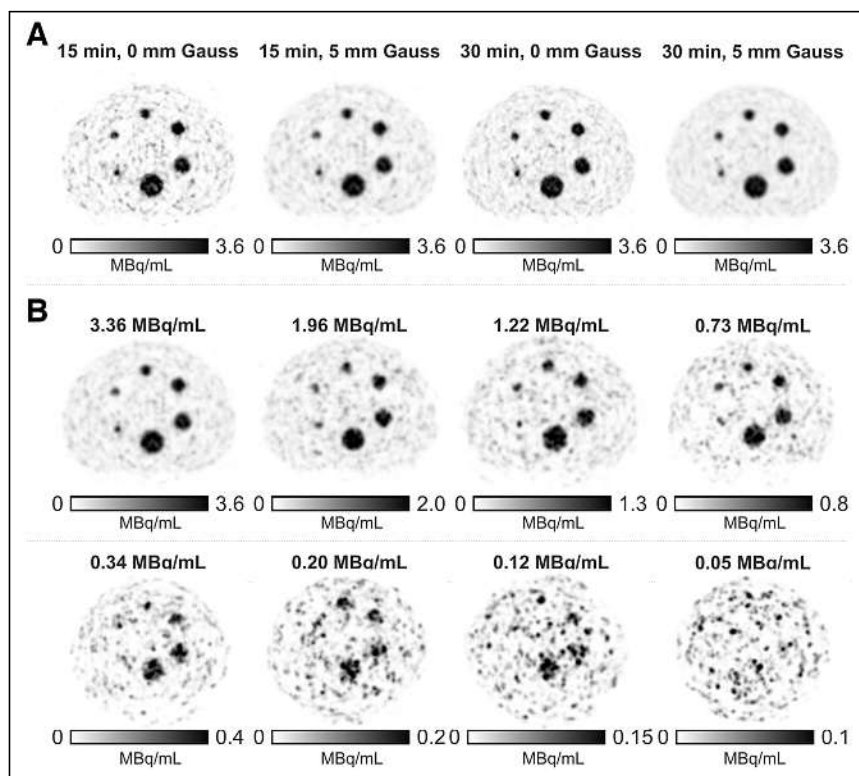
### MDAC

Figure 1 shows exemplary PET images for the NEMA tumor phantom. The human observer study revealed an SNR threshold of greater than or equal to 6 for distinguishing between spheres that were not detected and spheres that were detected (Supplemental Fig. 1). The MDAC for each sphere size is shown in Table 1. The SNR is presented as a function of the activity concentration for all acquisition conditions in Supplemental Figure 2. The 5-mm smoothed images provided improved detectability for smaller spheres, and the MDAC was smaller by a mean factor of 0.54 in comparison with the results for images without gaussian smoothing. For a 30-min acquisition time, the MDAC was reduced by a factor of 0.53 compared with that for a 15-min acquisition time.

As the detectability was higher for the 5-mm gaussian filter, the following evaluation of the anthropomorphic phantom and patient examples was restricted to this filter level. Moreover, an acquisition time of 30 min per bed position is excessively long and not feasible for patients who are in pain and undergoing  $^{90}\text{Y}$ -FAPI-46 therapy (typically, a PET scan comprises at least 2 bed positions); therefore, only an acquisition time of 15 min (per bed position) was further evaluated.

Figure 2 shows exemplary PET maximum-intensity projections (MIPs) of the anthropomorphic abdominal tumor phantom. Only detectable spheres were included in the quantification accuracy analysis (detectable was defined as an activity concentration greater than or equal to the size-dependent MDAC; the MDAC for the 9.7-, 17.4-, 27.7-, and 37.0-mm spheres in the NEMA tumor phantom were used for the 10.0-, 20.0-, 30.0-, and 40.0-mm spheres in the anthropomorphic abdominal tumor phantom).

Quantification accuracy results from the contour-based and oversized VOI-based quantification approaches are shown in Figure 3. For the 40- and 30-mm spheres, accurate quantification was feasible for detectable lesions using both approaches. The oversized VOI-based approach revealed slightly more accurate results for the 30-mm sphere. For the 20-mm sphere and activity concentrations of less than or equal to 1.23 MBq/mL, quantification accuracy for the contour-based method was slightly below the  $-20\%$  deviation threshold, whereas accurate quantification was feasible down to activity concentrations of greater than or equal to 0.34 MBq/mL using the



**FIGURE 1.** PET images of NEMA tumor phantom showing different investigated emission times and gaussian filter levels at highest sphere activity concentration of 3.36 MBq/mL (A) and different investigated sphere activity concentrations for 15-min acquisition time and 5-mm gaussian smoothing level (B).

**TABLE 1**  
Estimated MDAC for Investigated Sphere Diameters, Acquisition Time Durations, and Smoothing Levels

Sphere diameter (mm)	Estimated MDAC (MBq/mL)			
	All-pass filter		5-mm gaussian smoothing filter	
	15 min	30 min	15 min	30 min
9.7	0.71	0.44	0.43	0.33
12.6	0.51	0.23	0.30	0.17
17.4	0.37	0.15	0.16	0.07
22.2	0.37	0.18	0.18	0.09
27.7	0.29	0.16	0.15	0.08
37.0	0.27	0.14	0.12	0.06

oversized VOI-based approach. For the smallest (10-mm-diameter) sphere, quantification accuracy was limited for activity concentrations of less than or equal to 1.23 MBq/mL, and the contour-based approach revealed slightly more accurate results. In general, a trend toward an underestimation of the activity concentration was observed for low activity concentrations.

### MQAC

The MQAC ranged from 0.12 MBq/mL for the 40-mm sphere to 1.97 MBq/mL for the 10-mm sphere. Detailed results are presented in Table 2.

### Patient Tumor Dosimetry

Lesion dosimetry was performed for 3 tumor sites in 3 patients with thoracic/pleural SFT. In patient 1, a left paracardial supra-diaphragmatic SFT was evaluated; in patient 2, a right lateral SFT of the third thoracic vertebra was evaluated; and in patient 3, a left lateral SFT of the aortic arch was evaluated (Figs. 4–6). Almost all activity concentration measurements were considered reliable

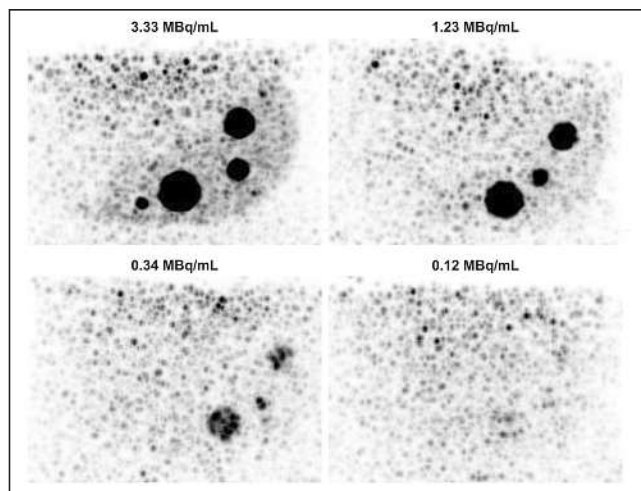


**FIGURE 2.** PET MIP images of anthropomorphic abdominal tumor phantom at 4 different activity concentration levels. Images were reconstructed using 15-min acquisition data and smoothed with 5-mm gaussian filter. In the MIP images, the largest sphere is marginally discernible at 0.12 MBq/mL.

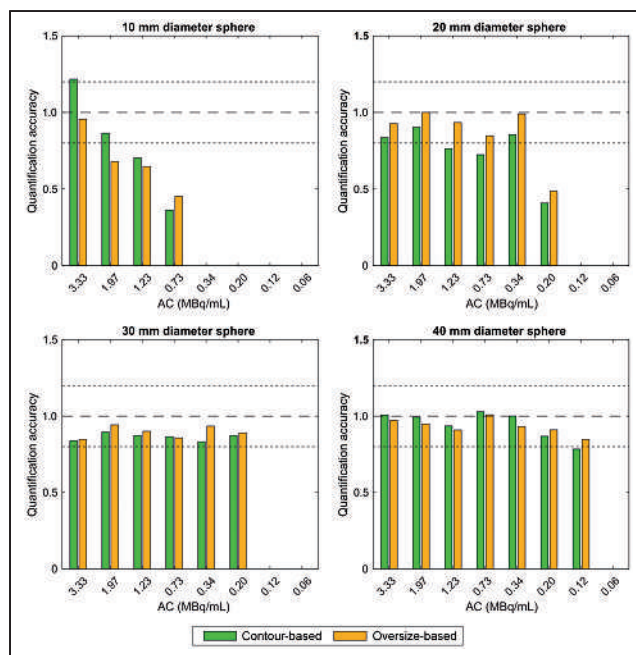


**FIGURE 3.** Contour-based and oversized VOI-based quantification accuracy using anthropomorphic tumor phantom. Dashed horizontal lines indicate  $\pm 20\%$  error margins. Missing bars correspond to spheres regarded as “not detected” and as such not considered for quantification accuracy evaluation. Only PET images with 5-mm gaussian filter and acquisition time of 15 min (per bed position) were analyzed. AC = activity concentration.

(Fig. 7). The activity concentration at the last measurement in patient 1 was below the MQAC for the largest sphere investigated in the phantom study (sphere diameter of 40 mm), which is why we did not use the data point for the lesion dosimetry estimation.

The relevant key dosimetry data derived from both the oversized VOI-based and the contour-based quantification approaches are listed in Table 3. The tumor absorbed dose estimation ranged from 0.6 to 12.0 Gy/GBq. Overall good agreement (absolute percentage deviation of  $<20\%$ ) of the relevant quantities was observed between the 2 approaches, except for the effective half-life of the tumor in patient 1 (8.4 vs. 12.2 h).

### DISCUSSION

FAP-targeted radionuclide therapy is emerging for patients with solid tumors and, recently, several case reports and case series using different ligands and radionuclides were published (31–33). For example,  $^{90}\text{Y}$ -FAP therapy was described for the treatment of sarcoma and pancreatic cancer patients (3,4) as well as a patient

**TABLE 2**  
Estimated MQAC of Reliability at Lesion Sizes Derived From Images Reconstructed with 15-min Acquisition Time Data and Smoothed with 5-mm Gaussian Filter

Lesion diameter (mm)	MQAC (MBq/mL)
10	1.97
20	0.34
30	0.20
40	0.12



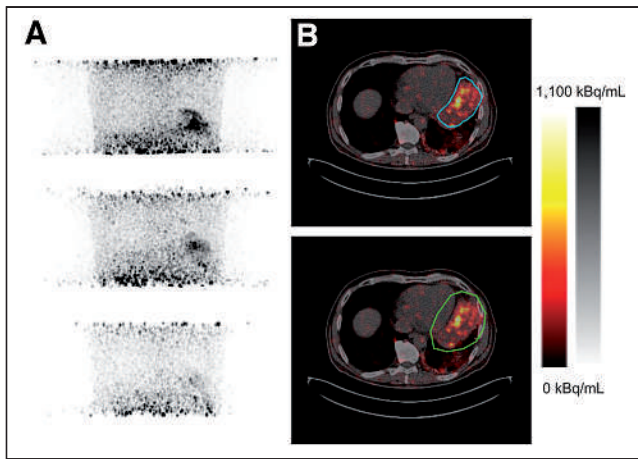


**FIGURE 4.** PET/CT imaging and lesion delineation for patient 1.  $^{90}\text{Y}$ -FAPI-46 PET MIP images (A) and axial PET/CT images (B) show contour-based VOI (blue) and oversized VOI (green). Only first 2 PET data points were considered for tumor absorbed dose estimation.

with both breast and colorectal cancers (34). Safety and efficacy studies, including dosimetry, have been reported for  $^{177}\text{Lu}$ -labeled FAP-targeted radionuclide therapy (32,35). Given that  $^{90}\text{Y}$ -based dosimetry for systemic radioligand therapy is not as well established and documented as  $^{177}\text{Lu}$ -based dosimetry, it is even more important to establish the basis for accurate radionuclide quantification. Doing so will have relevance in pharmacovigilance processes of authorization (such as the evaluation of safety) in the form of dosimetry for organs at risk and efficacy in the form of tumor dosimetry for investigating the dose effects of novel  $^{90}\text{Y}$  radioligand therapy agents.

In the present study, we applied a heuristic approach for reliable lesion quantification in  $^{90}\text{Y}$ -FAPI therapy. To the best of our knowledge, no reports on reliable PET-derived  $^{90}\text{Y}$  tumor quantification for activity concentration ranges as they appear in systemic radionuclide therapies have yet been published. The phantom evaluation (Figs. 1 and 2) showed that for detectable lesions greater than or equal to 30 mm in diameter, reliable quantification is feasible (Fig. 3). For the 20-mm-diameter sphere, the difference between the MQAC and the MDAC was small (0.34 vs. 0.16 MBq/mL).

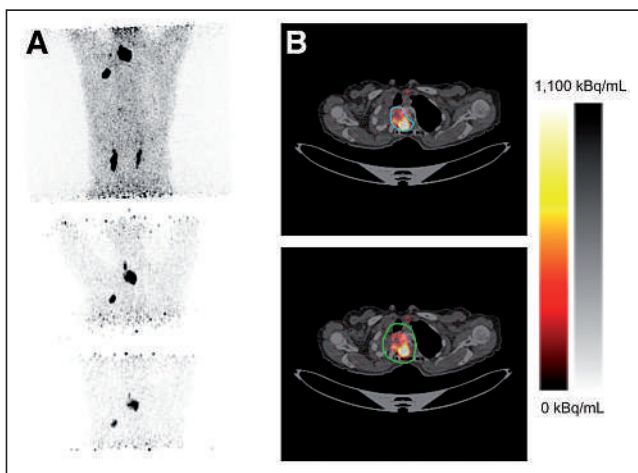


**FIGURE 5.** PET/CT imaging and lesion delineation for patient 2.  $^{90}\text{Y}$ -FAPI-46 PET MIP images (A) and axial PET/CT images (B) show contour-based VOI (blue) and oversized VOI (green).

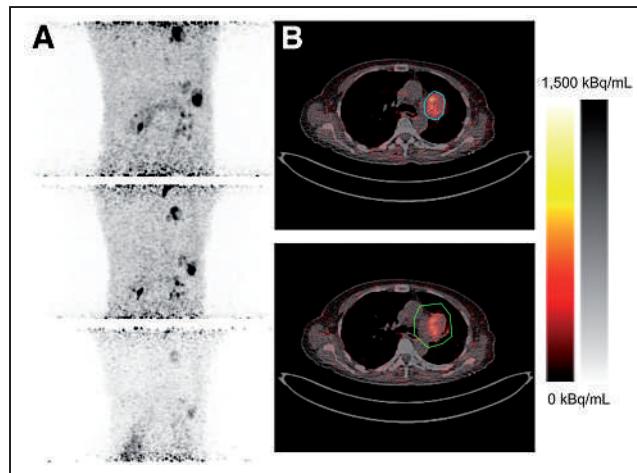


**FIGURE 6.** PET/CT imaging and lesion delineation for patient 3.  $^{90}\text{Y}$ -FAPI-46 PET MIP images (A) and axial PET/CT images (B) show contour-based VOI (blue) and oversized VOI (green).

Only for the smallest sphere (10-mm diameter) was the MQAC notably higher than the MDAC (1.97 vs. 0.43 MBq/mL). Possible explanations are the low absolute amount of  $^{90}\text{Y}$  activity resulting in poor counting statistics and the proximity to the 40-mm sphere (also, see a comparison of MDACs between NEMA and anthropomorphic phantoms in the supplemental materials and Supplemental Table 4).

In current clinical scenarios, patients undergoing  $^{90}\text{Y}$ -FAPI-46 therapy will most likely exhibit larger tumor masses, as this therapy is offered in end-stage diseases when established therapy options have already been exhausted (3,4). In the evaluated patients (Figs. 4–7), the accumulated tumor activity concentration was, except for 1 data point, larger than the size-dependent MQAC of 0.12 MBq/mL (40-mm-diameter lesion). We therefore assume that reliable quantification in the context of intratherapeutic tumor dosimetry is feasible in  $^{90}\text{Y}$ -FAPI-46 therapy using a digital PET/CT system. The tumor absorbed dose estimation ranged from 0.6 to 12.0 Gy/GBq (Table 3).

As cancer-associated fibroblasts were described to be nonuniformly distributed in the tumor microenvironment (36),  $^{90}\text{Y}$ -FAPI accumulation will most likely follow that pattern and lead to nonuniform tumor uptake in PET imaging. Because the high  $\beta$ -particle energy of  $^{90}\text{Y}$  leads to a high particle range, tumor cells surrounding FAP-expressing cancer-associated fibroblasts will be targets of crossfire and bystander radiation (37). Therefore,  $^{90}\text{Y}$ —which deposits its energy at a distance of up to 1 cm—may be more suitable for FAPI radionuclide therapy than  $^{177}\text{Lu}$ —with an energy deposition in close proximity to the source (38). However, the consequences of nonuniform FAPI uptake for the quantification of accumulated activity, dosimetry, and the dose response remain unclear. In the present study, quantification approaches were projected without adjustments from the homogeneous conditions of the phantom study to the patient images. Therefore, accumulated activity was measured as the mean activity concentration. This approach might be appropriate given a high level of influence of crossfire and bystander effects, which might lead to a homogenization of the radiation dose. Voxel-based dosimetry might be an alternative to take into account a nonuniform activity distribution (39); however, its clinical relevance might be limited by the low accumulated activity concentrations in systemic  $^{90}\text{Y}$  radionuclide therapy.

Future evaluations of clinical data will be necessary to investigate possible effects on determined tumor doses and, especially,

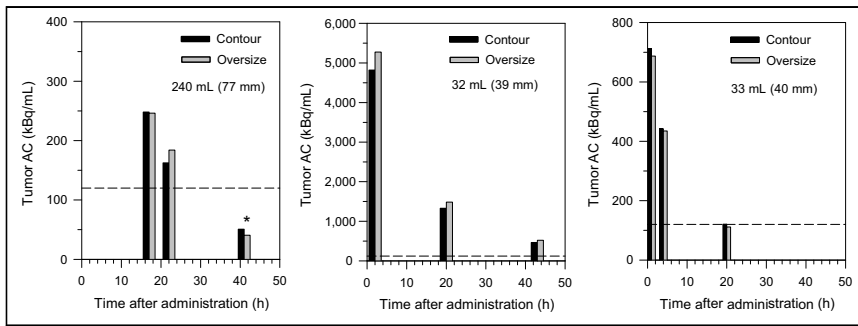


**FIGURE 7.** Tumor activity concentration (AC) derived from either contour-based or oversized VOI-based approach as function of time after administration (3 time points). Values within parentheses are respective equivalent sphere diameters. ACs above horizontal dashed lines indicate reliable quantification based on Figure 3. Asterisk indicates value that appears to be “unreliable” in terms of quantification (see text for details).

dose-response effects to select the optimal quantification approach. With increasing application of  $^{90}\text{Y}$  FAPI therapy, sufficient data will probably be available for a systematic evaluation. At the moment, the number of investigated patients with sufficient follow-up data is limited. In the present study, we investigated the quantification accuracy of a current-generation PET scanner as a basis for future clinical evaluations.

The comparison of 15- and 30-min acquisition times per bed position revealed a lower MDAC for the 30-min acquisition time, by a factor of approximately 2 (Table 1). Thus, an approximate linear correlation between MDAC and acquisition time was observed. This finding is in line with the results of a previous study using a different radionuclide (13). Typically, PET scans in patients receiving  $^{90}\text{Y}$ -based therapy are performed using at least 2 bed positions (3). Therefore, in most patients, an extension of the acquisition time will most likely not be tolerable. Moreover, detectability was improved when a 5-mm gaussian filter was applied (Table 1). In a systematic comparison of previous-generation Siemens PET/CT systems for quantitative  $^{90}\text{Y}$  imaging, the use of a gaussian filter was left to the user’s decision (40). We therefore propose an acquisition time of 15 min for clinical imaging protocols and the application of a 5-mm gaussian filter.

Both evaluated quantification methods exhibit limitations and advantages. On the one hand, the contour-based approach is more reproducible, but it has no background activity concentration correction. On the other hand, although the oversized VOI-based approach will represent

the lesion activity surrounded by a uniform and low activity concentration background, accounting for a nonuniform background might be challenging, making the quantification prone to error. Regarding quantification accuracy in phantom data and estimated activity concentrations in patient data, both methods yielded comparable results (Figs. 3 and 7), probably because of a low and visually uniform background. Larger differences might be possible for tumor lesions close to a region with high physiologic tracer accumulation, such as the kidney.

Only a few previous studies investigating  $^{90}\text{Y}$  PET imaging in the context of systemic radionuclide therapy were published, and none of these used a digital PET system. Fabbri et al. (41) identified an MDAC of

0.20 MBq/mL for the 3 largest spheres of the NEMA tumor phantom using a previous-generation time-of-flight-capable PET scanner. In that study, 30-min acquisitions with no background activity were reconstructed with 3-dimensional ordered-subset expectation maximization using 2 iterations and 4 subsets and a 5-mm gaussian filter. In the present study, for a 30-min acquisition time, the MDAC was smaller (0.06–0.09 MBq/mL) (Table 1). The improvement is explained by the improved time-of-flight resolution of the digital PET system and is comparable to the improvement that we observed in a direct comparison of 2 PET/CT systems for  $^{124}\text{I}$  (13). Of note, Fabbri et al. (41) did not investigate quantification accuracy. Walrand et al. (42) also investigated previous-generation PET systems (42); they predicted a reliable estimation of the mean absorbed kidney dose after  $^{90}\text{Y}$ -DOTATOC therapy using a kidney phantom filled with an activity concentration of about 0.33 MBq/mL—substantially larger than the MQAC for the largest sphere in the present study (0.12 MBq/mL). Moreover, the investigated kidney cortex had a volume of 107 mL—considerably larger than the largest sphere in the present study (sphere volume of 33.5 mL).

Future improvements might be possible through the application of total-body PET/CT scanners (43), which cover an extended field of view and allow complete acquisition of all necessary PET data in a patient scan using a single bed position. Moreover, increased sensitivity may allow for shorter acquisition times (44) or, alternatively, improved accuracy of detection and quantification of lesions at lower activity concentrations.

**TABLE 3**  
Key Dosimetry Quantities for Estimating Tumor AD per Administered Activity Using Contour-Based and Oversized VOI-Based Approaches

Patient	V (mL)	d (mm)	Contour-based			Oversized VOI-based		
			TIAC (min)	$T_{\text{eff}}$ (h)	AD (Gy/GBq)	TIAC (min)	$T_{\text{eff}}$ (h)	AD (Gy/GBq)
1	240	77	17	8.4	0.62	17	12.2	0.60
2	32	39	42	12.3	10.90	47	12.4	12.00
3	33	40	4	7.5	0.98	4	7.3	0.93

AD = absorbed dose; VOI = volume of interest; V = tumor volume; d = equivalent sphere diameter; TIAC = time-integrated activity coefficient;  $T_{\text{eff}}$  = effective half-life.

## CONCLUSION

For  $^{90}\text{Y}$ -treated lesions with a diameter of greater than or equal to 40 mm—typical in patients receiving FAPI radionuclide therapy—reliable quantification was possible for activity concentrations of at least 0.12 MBq/mL using a digital PET system. For lesions with a diameter of greater than or equal to 30 mm, the minimum detectable activity and minimum quantifiable activity were in good agreement, suggesting that dosimetry can be performed for detectable lesions. Further dosimetry studies are needed to thoroughly investigate the efficacy and safety of novel  $^{90}\text{Y}$ -FAPI radionuclide therapies.

## DISCLOSURE

This work was supported by the Universitätsmedizin Essen Clinician Scientist Academy (UMEA)/German Research Foundation (DFG [Deutsche Forschungsgemeinschaft]) under grant FU356/12-1 to David Kersting and Rainer Hamacher and by a Universitätsmedizin Essen Clinician Scientist Academy (UMEA) grant to Robert Seifert. David Kersting reports a research grant from Pfizer outside the submitted work. Walter Jentzen received research funding from Siemens Healthineers. Maurizio Conti is a full-time employee of Siemens Medical Solutions USA, Inc. Ken Herrmann reports personal fees from Bayer, personal fees and other fees from Sofie Biosciences, personal fees from SIRTEX, nonfinancial support from ABX, personal fees from Adacap, personal fees from Curium, personal fees from Endocyte, grants and personal fees from BTG, personal fees from IPSEN, personal fees from Siemens Healthineers, personal fees from GE Healthcare, personal fees from Amgen, personal fees from Novartis, personal fees from ymabs, personal fees from Aktis Oncology, personal fees from Theragnostics, and personal fees from Pharma15 outside the submitted work. Christoph Rischpler reports a research grant from Pfizer, consultancy for Adacap and Pfizer, and speaker honoraria from Adacap, Alnylam, BTG, GE Healthcare, Pfizer, and Siemens Healthineers outside the submitted work. Rainer Hamacher received travel grants from Lilly, Novartis, and PharmaMar as well as fees from Lilly outside the submitted work. Wolfgang P. Fendler reports fees from Sofie Bioscience (research funding), Janssen (consultant, speakers bureau), Calyx (consultant), Bayer (speakers bureau), and Parexel (image review) outside the submitted work. No other potential conflict of interest relevant to this article was reported.

## ACKNOWLEDGMENT

We thank Ulrich Graf (Sirtex Medical Europe GmbH) for providing the anthropomorphic abdominal tumor phantom (Abdo-Man).

## KEY POINTS

**QUESTION:** Does digital PET allow reliable quantification for lesion dosimetry in  $^{90}\text{Y}$ -FAPI radionuclide therapy?

**PERTINENT FINDINGS:** For lesion sizes and activity concentrations that are expected to be observed in patients treated with  $^{90}\text{Y}$ -FAPI, quantification with reasonable accuracy is possible.

**IMPLICATIONS FOR PATIENT CARE:** Reliable lesion dosimetry in  $^{90}\text{Y}$ -FAPI radionuclide therapy is mandatory for dose-response evaluations and for decisions about treatment continuation.

## REFERENCES

1. Dancey JE, Shepherd FA, Paul K, et al. Treatment of nonresectable hepatocellular carcinoma with intrahepatic  $^{90}\text{Y}$ -microspheres. *J Nucl Med.* 2000;41:1673–1681.
2. Strosberg J, El-Haddad G, Wolin E, et al. Phase 3 trial of  $^{177}\text{Lu}$ -Dotatate for midgut neuroendocrine tumors. *N Engl J Med.* 2017;376:125–135.
3. Ferdinandus J, Costa PF, Kessler L, et al. Initial clinical experience with  $^{90}\text{Y}$ -FAPI-46 radioligand therapy for advanced-stage solid tumors: a case series of 9 patients. *J Nucl Med.* 2022;63:727–734.
4. Fendler WP, Pabst KM, Kessler L, et al. Safety and efficacy of  $^{90}\text{Y}$ -FAPI-46 radioligand therapy in patients with advanced sarcoma and other cancer entities. *Clin Cancer Res.* 2022; Epub ahead of print.
5. Liu F, Qi L, Liu B, et al. Fibroblast activation protein overexpression and clinical implications in solid tumors: a meta-analysis. *PLoS One.* 2015;10:e0116683.
6. Brosch J, Gosewisch A, Kaiser L, et al. 3D image-based dosimetry for yttrium-90 radioembolization of hepatocellular carcinoma: impact of imaging method on absorbed dose estimates. *Phys Med.* 2020;80:317–326.
7. Elschot M, Vermolen BJ, Lam MG, de Keizer B, van den Bosch MA, de Jong HW. Quantitative comparison of PET and Bremsstrahlung SPECT for imaging the in vivo yttrium-90 microsphere distribution after liver radioembolization. *PLoS One.* 2013;8:e55742.
8. Kubik A, Budzynska A, Kacperski K, et al. Evaluation of qualitative and quantitative data of Y-90 imaging in SPECT/CT and PET/CT phantom studies. *PLoS One.* 2021;16:e0246848.
9. Wright CL, Zhang J, Tweedle MF, Knopp MV, Hall NC. Theranostic Imaging of yttrium-90. *BioMed Res Int.* 2015;2015:481279.
10. Lhomme R, van Elmbt L, Goffette P, et al. Feasibility of  $^{90}\text{Y}$  TOF PET-based dosimetry in liver metastasis therapy using SIR-Spheres. *Eur J Nucl Med Mol Imaging.* 2010;37:1654–1662.
11. Pasciak AS, Bourgeois AC, McKinney JM, et al. Radioembolization and the dynamic role of  $^{90}\text{Y}$  PET/CT. *Front Oncol.* 2014;4:38.
12. Kunnen B, Beijst C, Lam M, Viergever MA, de Jong H. Comparison of the Biograph Vision and Biograph mCT for quantitative  $^{90}\text{Y}$  PET/CT imaging for radioembolisation. *EJNMMI Phys.* 2020;7:14.
13. Kersting D, Jentzen W, Fragoso Costa P, et al. Silicon-photomultiplier-based PET/CT reduces the minimum detectable activity of iodine-124. *Sci Rep.* 2021;11:17477.
14. Weber M, Jentzen W, Hofferber R, et al. Evaluation of [ $^{68}\text{Ga}$ ]Ga-PSMA PET/CT images acquired with a reduced scan time duration in prostate cancer patients using the digital Biograph Vision. *EJNMMI Res.* 2021;11:21.
15. Weber M, Jentzen W, Hofferber R, et al. Evaluation of  $^{18}\text{F}$ -FDG PET/CT images acquired with a reduced scan time duration in lymphoma patients using the digital Biograph Vision. *BMC Cancer.* 2021;21:62.
16. Fragoso Costa P, Jentzen W, Sußelbeck F, et al. Reduction of emission time for [ $^{68}\text{Ga}$ ]Ga-PSMA PET/CT using the digital Biograph Vision: a phantom study. *Q J Nucl Med Mol Imaging.* July 26, 2021 [Epub ahead of print].
17. Kersting D, Jentzen W, Sraieb M, et al. Comparing lesion detection efficacy and image quality across different PET system generations to optimize the iodine-124 PET protocol for recurrent thyroid cancer. *EJNMMI Phys.* 2021;8:14.
18. Labour J, Boissard P, Baudier T, et al. Yttrium-90 quantitative phantom study using digital photon counting PET. *EJNMMI Phys.* 2021;8:56.
19. Jentzen W. Experimental investigation of factors affecting the absolute recovery coefficients in iodine-124 PET lesion imaging. *Phys Med Biol.* 2010;55:2365–2398.
20. Walrand S, Jamar F, Mathieu I, et al. Quantitation in PET using isotopes emitting prompt single gammas: application to yttrium-86. *Eur J Nucl Med Mol Imaging.* 2003;30:354–361.
21. Gear JI, Cummings C, Craig AJ, et al. Abdo-Man: a 3D-printed anthropomorphic phantom for validating quantitative SIRT. *EJNMMI Phys.* 2016;3:17.
22. van Sluis J, de Jong J, Schaar J, et al. Performance characteristics of the digital Biograph Vision PET/CT system. *J Nucl Med.* 2019;60:1031–1036.
23. Jentzen W, Weise R, Kupferschlager J, et al. Iodine-124 PET dosimetry in differentiated thyroid cancer: recovery coefficient in 2D and 3D modes for PET/(CT) systems. *Eur J Nucl Med Mol Imaging.* 2008;35:611–623.
24. Øen SK, Aasheim LB, Eikenes L, Karlberg AM. Image quality and detectability in Siemens Biograph PET/MRI and PET/CT systems: a phantom study. *EJNMMI Phys.* 2019;6:16.
25. Keller SH, Jakoby B, Svalling S, Kjaer A, Hojgaard L, Klausen TL. Cross-calibration of the Siemens mMR: easily acquired accurate PET phantom measurements, long-term stability and reproducibility. *EJNMMI Phys.* 2016;3:11.
26. Dryák P, Solc J. Measurement of the branching ratio related to the internal pair production of Y-90. *Appl Radiat Isot.* 2020;156:108942.
27. Chisté V, Bé MM.  $^{90}\text{Y}$ : comments on evaluation of decay data. Decay Data Evaluation Project website. [http://www.nucleide.org/DDEP\\_WG/Nuclides/Y-90\\_com.pdf](http://www.nucleide.org/DDEP_WG/Nuclides/Y-90_com.pdf). Updated November 2016. Accessed March 3, 2022.

28. Staníček J. Emission of positrons in beta-decay of  $^{90}\text{Sr}$  +  $^{90}\text{Y}$ . *Acta Phys Univ Comen.* 2007;XLVIII–XLIX:51–56.
29. Selwyn RG, Nickles RJ, Thomadsen BR, DeWerd LA, Micka JA. A new internal pair production branching ratio of  $^{90}\text{Y}$ : the development of a non-destructive assay for  $^{90}\text{Y}$  and  $^{90}\text{Sr}$ . *Appl Radiat Isot.* 2007;65:318–327.
30. Stabin MG, Sparks RB, Crowe E. OLINDA/EXM: the second-generation personal computer software for internal dose assessment in nuclear medicine. *J Nucl Med.* 2005;46:1023–1027.
31. Assadi M, Rekabpour SJ, Jafari E, et al. Feasibility and therapeutic potential of  $^{177}\text{Lu}$ -fibroblast activation protein inhibitor-46 for patients with relapsed or refractory cancers: a preliminary study. *Clin Nucl Med.* 2021;46:e523–e530.
32. Ballal S, Yadav MP, Moon ES, et al. First-in-human results on the biodistribution, pharmacokinetics, and dosimetry of [ $^{177}\text{Lu}$ ]Lu-DOTA.SA.FAPi and [ $^{177}\text{Lu}$ ]Lu-DOTAGA.(SA.FAPi)<sub>2</sub>. *Pharmaceuticals (Basel).* 2021;14:1212.
33. Fu K, Pang Y, Zhao L, et al. FAP-targeted radionuclide therapy with [ $^{177}\text{Lu}$ ]Lu-FAPi-46 in metastatic nasopharyngeal carcinoma. *Eur J Nucl Med Mol Imaging.* 2022;49:1767–1769.
34. Rathke H, Fuxius S, Giesel FL, et al. Two tumors, one target: preliminary experience with  $^{90}\text{Y}$ -FAPi therapy in a patient with metastasized breast and colorectal cancer. *Clin Nucl Med.* 2021;46:842–844.
35. Kuyumcu S, Kovan B, Sanli Y, et al. Safety of fibroblast activation protein-targeted radionuclide therapy by a low-dose dosimetric approach using  $^{177}\text{Lu}$ -FAPi04. *Clin Nucl Med.* 2021;46:641–646.
36. Sahai E, Astsaturov I, Cukierman E, et al. A framework for advancing our understanding of cancer-associated fibroblasts. *Nat Rev Cancer.* 2020;20:174–186.
37. Freudenberg R, Wendisch M, Kotzerke J. Geant4-Simulations for cellular dosimetry in nuclear medicine. *Z Med Phys.* 2011;21:281–289.
38. Brady D, O’Sullivan JM, Prise KM. What is the role of the bystander response in radionuclide therapies? *Front Oncol.* 2013;3:215.
39. Chiesa C, Bardies M, Zaidi H. Voxel-based dosimetry is superior to mean absorbed dose approach for establishing dose-effect relationship in targeted radionuclide therapy. *Med Phys.* 2019;46:5403–5406.
40. Willowson KP, Tapner M, Team QI, Bailey DL. A multicentre comparison of quantitative  $^{90}\text{Y}$  PET/CT for dosimetric purposes after radioembolization with resin microspheres: the QUEST Phantom Study. *Eur J Nucl Med Mol Imaging.* 2015;42:1202–1222.
41. Fabbri C, Bartolomei M, Mattone V, et al.  $^{90}\text{Y}$ -PET/CT imaging quantification for dosimetry in peptide receptor radionuclide therapy: analysis and corrections of the impairing factors. *Cancer Biother Radiopharm.* 2015;30:200–210.
42. Walrand S, Jamar F, van Elmbt L, Lhommel R, Bekonde EB, Pauwels S. 4-Step renal dosimetry dependent on cortex geometry applied to  $^{90}\text{Y}$  peptide receptor radiotherapy: evaluation using a fillable kidney phantom imaged by  $^{90}\text{Y}$  PET. *J Nucl Med.* 2010;51:1969–1973.
43. Zhang YQ, Hu PC, Wu RZ, et al. The image quality, lesion detectability, and acquisition time of  $^{18}\text{F}$ -FDG total-body PET/CT in oncological patients. *Eur J Nucl Med Mol Imaging.* 2020;47:2507–2515.
44. Alberts I, Hunermond JN, Prenosil G, et al. Clinical performance of long axial field of view PET/CT: a head-to-head intra-individual comparison of the Biograph Vision Quadra with the Biograph Vision PET/CT. *Eur J Nucl Med Mol Imaging.* 2021;48:2395–2404.

# First-in-Humans PET/MRI of In Vivo GD2 Expression in Osteosarcoma

Nils Florian Trautwein<sup>1,2</sup>, Gerald Reischl<sup>2,3</sup>, Christian Seitz<sup>4</sup>, Helmut Dittmann<sup>1</sup>, Ferdinand Seith<sup>4</sup>, Sophia Scheuermann<sup>5</sup>, Tobias Feuchtinger<sup>6</sup>, Frank Dombrowski<sup>7</sup>, Rupert Handgretinger<sup>5</sup>, Jörg Fuchs<sup>8</sup>, Bernd Pichler<sup>2,3,9</sup>, Christian la Fougère<sup>1,3,9</sup>, and Johannes Schwenck<sup>1,2,3</sup>

<sup>1</sup>Department of Nuclear Medicine and Clinical Molecular Imaging, University of Tübingen, Tübingen, Germany; <sup>2</sup>Werner Siemens Imaging Center, Department of Preclinical Imaging and Radiopharmacy, University of Tübingen, Tübingen, Germany; <sup>3</sup>Cluster of Excellence iFIT (EXC 2180) "Image-Guided and Functionally Instructed Tumor Therapies," University of Tübingen, Tübingen, Germany; <sup>4</sup>Department of Radiology, University of Tübingen, Tübingen, Germany; <sup>5</sup>Department of Pediatric Hematology and Oncology, University of Tübingen, Tübingen, Germany; <sup>6</sup>Department of Pediatric Hematology, Oncology, Hemostaseology, and Stem Cell Transplantation, University of Munich, Munich, Germany; <sup>7</sup>Department of Pathology, University of Greifswald, Greifswald, Germany; <sup>8</sup>Department of Pediatric Surgery, University of Tübingen, Tübingen, Germany; and <sup>9</sup>German Cancer Consortium, Partner Site Tübingen, Tübingen, Germany

**O**steosarcoma is a malignant bone tumor with very limited therapeutic options (1). However, targeting the frequently overexpressed disialoganglioside GD2 was successful in preclinical studies with bispecific GD2 antibodies (2), and a clinical trial is ongoing using the clinically approved GD2 antibody dinutuximab in osteosarcoma patients (NCT02484443). Recently, we developed the radiolabeled antibody [<sup>64</sup>Cu]Cu-DOTAGA-ch14.18/CHO to evaluate GD2 expression by PET (3).

Here, we assessed the in vivo GD2 expression in a heavily pretreated woman with progressive pulmonary osteosarcoma metastasis for potential therapy stratification (compassionate use according to German Medicinal Products Act AMG §13.2b). PET/MRI was performed 19 h after injection of 234 MBq of [<sup>64</sup>Cu]Cu-NOTA-ch14.18/CHO and revealed increased tracer retention with a high signal-to-background ratio bilaterally in the pulmonary metastases (SUV<sub>max</sub>, 9.8; Fig. 1). The background uptake in normal lung tissue and blood pool was reasonably low, whereas retention in the liver was relatively high. An intense GD2 expression was confirmed in a resected pulmonary metastasis by GD2 immunohistochemistry and by cyclic immunofluorescence staining.

To the best of our knowledge, we present here the first report of clinical GD2

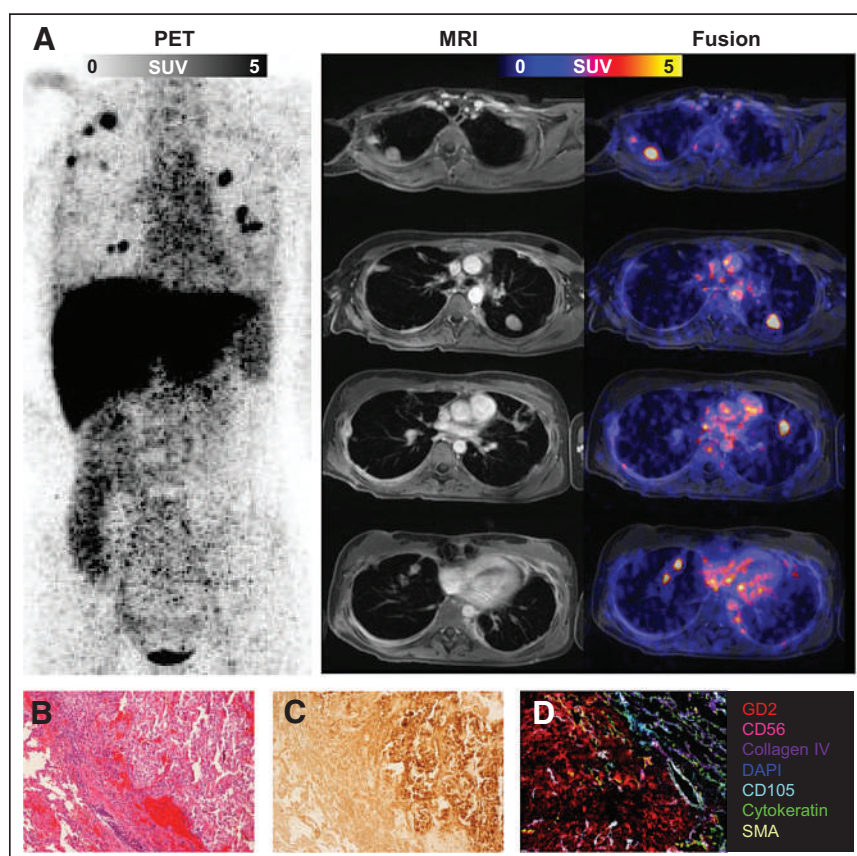


**FIGURE 1.** (A) Maximum-intensity projection (left) and representative transaxial slices (right) of [<sup>64</sup>Cu]Cu-NOTA-ch14.18/CHO-PET/MRI. (B) Hematoxylin and eosin staining. (C) GD2 immunohistochemistry. (D) Cyclic immunofluorescence staining of resected pulmonary osteosarcoma metastasis.

Received Jul. 19, 2022; revision accepted Jul. 29, 2022.  
For correspondence or reprints, contact Christian la Fougère (christian.lafougere@med.uni-tuebingen.de).  
Published online Sep. 15, 2022.  
COPYRIGHT © 2023 by the Society of Nuclear Medicine and Molecular Imaging.  
DOI: 10.2967/jnumed.122.264626

PET/MRI in an osteosarcoma patient with pulmonary metastasis. Our findings demonstrate that GD2 expression can be assessed noninvasively in vivo using [<sup>64</sup>Cu]Cu-NOTA-ch14.18/CHO-PET/MRI, which might open new possibilities for therapy stratification

in GD2-expressing tumor entities such as osteosarcoma or melanoma.

#### **DISCLOSURE**

This work was supported by the Deutsche Forschungsgemeinschaft (DFG, German Research Foundation, Germany's Excellence Strategy EXC2180-390900677). No other potential conflict of interest relevant to this article was reported.

#### **REFERENCES**

1. Gill J, Gorlick R. Advancing therapy for osteosarcoma. *Nat Rev Clin Oncol*. 2021; 18:609–624.
2. Roth M, Linkowski M, Tarim J, et al. Ganglioside GD2 as a therapeutic target for antibody-mediated therapy in patients with osteosarcoma. *Cancer*. 2014;120: 548–554.
3. Schmitt J, Schwenck J, Maurer A, et al. Translational immunoPET imaging using a radiolabeled GD2-specific antibody in neuroblastoma. *Theranostics*. 2022;12: 5615–5630.

## Dosimetry in Radiopharmaceutical Therapy

**TO THE EDITOR:** Regarding “Dosimetry in Radiopharmaceutical Therapy” (1), in general this is a very good paper, and I am pleased to see attention being drawn to this important topic. Unfortunately, however, it ends on the familiar sour note that we should not do any dosimetry at this time, as it may not be perfect, and we should wait and wait until there is absolute proof of its usefulness.

First, as a minor point, the 1962 Benua “dose to blood” method (2) is completely outdated, being superseded by several detailed dosimetry models for the red marrow (3). Dose to blood itself is not relevant to internal dose calculations; this was a poor early surrogate for the truly important dose to active red marrow and ignores valiant efforts by many (Spiers, Eckerman, Bolch, and others) to develop good marrow dose models. The Eckerman model is implemented in the easy-to-use OLINDA/EXM software (4). The Benua method should not be cited as a recommended standard dosimetry method.

Second, the authors state that “Treating patients according to [prescribed tumor-absorbed dose] is a concept extended from [external-beam radiotherapy] practice. However, there are few dose–response data available for [radiopharmaceutical therapy] on which to base treatment prescription.” They also state that “dosimetry is not performed because dose–response data are lacking, and dose–response data are lacking because dosimetry is not performed.” The authors conclude that “If dosimetry is to become more than an academic exercise, we need to show that it makes a significant difference to clinical outcomes with [radiopharmaceutical therapy]. Ultimately, the only acceptable way of achieving this is through multicenter randomized controlled clinical trials comparing dosimetry-based prescriptions with one-size-fits-all activity-based prescriptions.” The authors did not mention Garin et al., who said, “Compared with standard dosimetry, personalized dosimetry significantly improved the objective response rate in patients with locally advanced hepatocellular carcinoma.” (5). As the authors note, we cannot mature in our understanding of dose–response relationships with no understanding whatsoever of what the potential radiation doses are. Our colleagues in external-beam radiotherapy knew years ago that dosimetry was essential to radiation therapy. Their methods were not perfect at the start but have improved over the years. If we continue to refuse to even start, we will never progress. Furthermore, for any future therapy applications of radiation in these patients, radiation doses from prior therapies are needed.

Thus, as noted some years ago (6), radiopharmaceutical therapy patients are clearly being treated at a lower standard of care than external-beam radiotherapy patients. I ask anyone advocating against calculation of patient-individualized dosimetry of cancer patients whether they would accept this if it were their spouse, child, or other loved one receiving therapy without optimization of their therapy, which requires patient-individualized dosimetry. We need to break this vicious cycle of endless, pointless discussions while inaction dominates and patients are given substandard medical care.

## REFERENCES

1. O’Donoghue J, Zanzonico P, Humm J, Kesner A. Dosimetry in radiopharmaceutical therapy. *J Nucl Med.* 2022;63:1467–1474.
2. Benua RS, Cicale N, Sonenberg M. The relation of radiation dosimetry to results and complications in the treatment of metastatic thyroid cancer. *AJR.* 1962;87:171–182.
3. Stabin MG, Eckerman KF, Bolch WE, Bouchet LG, Patton PW. Evolution and status of bone and marrow dose models. *Cancer Biother Radiopharm.* 2002;17:427–433.
4. Stabin MG, Sparks RB, Crowe E. OLINDA/EXM: the second-generation personal computer software for internal dose assessment in nuclear medicine. *J Nucl Med.* 2005;46:1023–1027.
5. Garin E, Tselikas L, Guiu B, et al. Personalised versus standard dosimetry approach of selective internal radiation therapy in patients with local advanced hepatocellular carcinoma (DOSISPERE-01): a randomized multicentre open-label phase 2 trial. *Lancet Gastroenterol Hepatol.* 2021;6:17–29.
6. Stabin MG. The case for patient-specific dosimetry in radionuclide therapy. *Cancer Biother Radiopharm.* 2008;23:273–284.

**Michael Stabin**

*RADAR, Inc.*

*E-mail: stabinmg17@gmail.com*

Published online Nov. 10, 2022.  
DOI: 10.2967/jnumed.122.265056

## Reply: Dosimetry in Radiopharmaceutical Therapy

**REPLY:** We are grateful for the commentary on our paper (1) by Dr. Stabin and agree with almost everything he says (2). We would, however, take issue with his characterization of our conclusions, especially the “sour note that we should not do any dosimetry at this time . . . .” This is certainly not the conclusion we intended to convey and is difficult to reconcile with the fact that the paper is devoted largely to how to do dosimetry.

We probably all agree that the main goal of performing dosimetry is to improve clinical outcomes. This means it must, in some way, affect the treatment prescription. A patient-individualized, dosimetry-driven treatment prescription will almost certainly be different from a standard “one-size-fits-all” treatment prescription. Most medical physicists and nuclear medicine physicians likely agree that an individualized approach would be better, but it remains to be determined how much better in terms of objective clinical endpoints such as progression-free survival and overall survival. Other stakeholders (e.g., medical oncologists, pharma sponsors, medical insurers, administrators, and perhaps even patients themselves) may resist the additional time and effort, expense, and logistic complexity unless there is a demonstrable and significant cost benefit. Compelling data from randomized, multicenter clinical trials comparing a dosimetry-based prescription with simpler alternatives are therefore

essential for broad acceptance of dosimetry-based radiopharmaceutical therapy. Although specialists in our field may not need convincing, the greater community very much does.

#### REFERENCES

1. O'Donoghue J, Zanzonico P, Humm J, Kesner A. Dosimetry in radiopharmaceutical therapy. *J Nucl Med.* 2022;63:1467–1474.
2. Stabin M. Dosimetry in radiopharmaceutical therapy [letter]. *J Nucl Med.* 2023;64:339.

**Joe O'Donoghue**  
**Pat Zanzonico**  
**John Humm**  
**Adam Kesner\***

*Memorial Sloan Kettering Cancer Center*  
*New York, New York*

\*E-mail: kesnera@mskcc.org

---

Published online Nov. 10, 2022.  
DOI: 10.2967/jnumed.122.265078



## Nuclear Medicine: The Essentials

H. Jadvar and P.M. Colletti

*Wolters Kluwer, 2021, 310 pages, \$110.99*

In contrast to the discipline of conventional radiology, to which medical school students, trainees, and many practitioners of medicine are heavily exposed, the field of nuclear medicine is somewhat specialized and requires special training for optimal understanding of its role in various domains in medicine. Therefore, there is a dire need for a simplified exposure to the specialty that provides some practical knowledge about the field and its unique role in the day-to-day practice of medicine. “The Essentials” series is a collection of radiology textbooks that follow such a standardized format. The series is designed to provide a practical tool for those who wish to gain a broad base of knowledge on various specialties in medical imaging. The content is confined to the essentials of the specialty and can be understood by the novice. However, enough details are included to be useful for those who teach the specialty and to provide a reference for health-care providers practicing the specialty of imaging. “The Essentials” books are compact in size and allow for residents and other interested groups to grasp practical knowledge about the various procedures that are offered by this specialty. Furthermore, the self-assessment sections provide multiple-choice questions at the end of each chapter. As such, this additional training is of particular benefit for those who are preparing for an image-rich computer-based examination for professional and maintenance certifications.

Currently, the field of nuclear medicine is the fastest-growing discipline in medical imaging. The recent introduction of novel radiopharmaceuticals for imaging and targeted therapy is revolutionary; therefore, educating trainees and the community at large about their applications in many disciplines is essential at this time. These include innovations in high-technology instruments related to digital and time-of-flight cameras, total-body PET instruments, PET/CT, PET/MRI, and SPECT/CT. This textbook provides a concise yet comprehensive overview of the field of molecular imaging that fits the criteria intended for “The Essentials” series. Each chapter describes the basics of physics, instrumentation, quality control, radiochemistry, radiation safety, and other essential information about each procedure.

The table of contents includes radiochemistry, instrumentation, physics, and radiation safety as introductions to technical bases for

performing various procedures. The clinical section deals with assessment of diseases and disorders of various organs and anatomic structures (thyroid, parathyroid, and neuroendocrine glands; central nervous system; skeleton; lungs; gastrointestinal tract; kidneys; and lymph nodes). Also, chapters are devoted to radiotheranostics, the essentials of pediatric nuclear medicine, quality assurance, and procedures on pregnant and lactating patients. Overall, the book includes 19 chapters.

The chapters are organized in a logical manner and describe in some detail the imaging techniques that practitioners of the discipline follow. Therefore, readers who may not be familiar with the role of nuclear medicine procedures will be able to comprehend the scope of this discipline in clinical settings. No critically important topics are missing from this comprehensive book.

The chapters are written by highly qualified and expert contributing authors with longstanding experience in their respective disciplines. The main authors, Drs. Jadvar and Colletti, have substantially contributed by writing several chapters of this book.

Overall, this book provides a well-balanced view of current applications of conventional nuclear medicine and PET. Therefore, the book is a strong medium for introducing physicians and scientists to ongoing activities in the field and their relevance to the day-to-day practice of medicine. There are no serious weaknesses to the overall content of the book. Additionally, the figures and tables are of high quality. Most of the figures in the book are selected from the authors’ own clinical files and are of high quality.

In conclusion, *Nuclear Medicine: The Essentials* provides a comprehensive and excellent review of the current practice of the field. Therefore, this book will be of great interest to trainees, technologists, and scientists, as well as to practitioners of this rapidly evolving specialty. As such, the book is highly recommended for those who wish to refresh their understanding of the field and its various applications in medicine.

**Abass Alavi**

*Hospital of the University of Pennsylvania  
Philadelphia, Pennsylvania*

*E-mail: abass.alavi@penmedicine.upenn.edu*

---

Published online Sep. 8, 2022.  
DOI: 10.2967/jnumed.122.264788

## Richard C. Reba, MD, 1932–2022

**R**ichard C. Reba, MD, a past president of SNMMI, died in Frederick, MD, on December 30, 2022. He received his MD in 1957 from the University of Maryland College of Physicians and Surgeons. While serving in the U.S. Army Medical Corps, he became a research fellow under Henry N. Wagner, Jr., MD, at the Johns Hopkins Hospital, and later a senior investigator in the Division of Nuclear Medicine and chief of the Department of Isotope Metabolism at Walter Reed Army Institute of Research. He served in 1965 and 1966 as chief of Medical Services at the 85th Evac Hospital in Qui Nhon, Vietnam.

During his long career, Dr. Reba held faculty positions at Johns Hopkins, Washington Hospital Center, George



Washington University, the University of Chicago, and Georgetown University. His research foci included development and application of SPECT and PET radiopharmaceuticals, and, in the 1980s, he carried out pioneering SPECT imaging of neuroreceptors in humans. He provided expert advice to the National Institutes of Health, the International Atomic Energy Agency, and government advisory committees and was the author/coauthor of 330 scientific papers.

Dr. Reba was the 1993 president of what was then the Society of Nuclear Medicine and worked to identify practice guidelines and criteria for scientific assessment, educate nuclear medicine professionals, and advance health care reform.

## Michel Meignan, MD, PhD, 1947–2022

**M**ichel Meignan, MD, PhD, died on October 15, 2022, at the age of 75, after a long battle against cancer. He was head of the nuclear medicine department at Henri Mondor Hospital (Assistance Publique Hôpitaux de Paris; Créteil, France) from 1997 to 2013. He was trained at the University of Paris, and his early work concentrated on respiratory physiopathology using  $^{81m}\text{Kr}$  ventilation/perfusion scintigraphy. From 2005 onward, he focused on PET/CT evaluation of treatment response in lymphoma. In particular, he set up a network for centralized review of PET/CT scans and led the imaging section of the Lymphoma Study Association, an international multidisciplinary cooperative group. His leadership led to harmonization of PET/CT interpretation criteria, implementation of PET/CT-guided therapeutic strategies, and development of new prognostic biomarkers. Professor Meignan initiated the pioneering workshops on PET in Lymphoma and Myeloma, a unique forum for researchers from around the world. His conviction and remarkable ability to unite international experts contributed considerably to dissemination of knowledge



about metabolic imaging of lymphomas. He published more than 240 scientific articles.

A professor emeritus since 2016, he was until recently the imaging lead on the organizing committee for revision of the Lugano classification for management of patients with lymphoma. He remained committed to teaching and the clinic and inspired colleagues in multiple fields. He was an extraordinary mentor, keen to nurture new talent. Professor Meignan will be remembered as an attentive, inventive, rigorous, honest, and erudite man.

**Sally Barrington**

*King's College, London, UK*

**Irène Buvat**

*Institut Curie, Paris, France*

**Anne-Ségolène Cottreau**

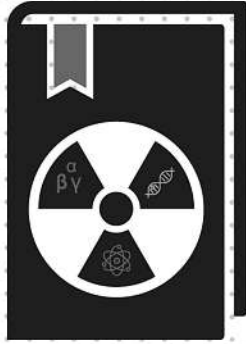
*René Descartes University, Paris, France*

**Andrea Gallamini**

*Centre Antoine-Lacassagne, Nice, France*

**Catherine Thieblemont**

*Hôpital Saint-Louis, Paris, France*



## 80 Hour Radionuclide Authorized User TRAINING COURSE

Debuting this spring, the ASNC/SNMMI 80 Hour Authorized User Training Course features more than 40 expert lecturers from across nuclear medicine.

The course is designed to train authorized users and define the responsibilities inherent to the role while also meeting NRC-specified knowledge requirements for 80 hours of didactic training highlighted by real-world clinical scenarios.

This new course will be available as a standalone program in addition to special packages developed for training programs.

LEARN MORE: [www.snmmi.org/80HourCourse](http://www.snmmi.org/80HourCourse)



REGISTRATION OPENS THIS FEBRUARY!



Register Today

[WWW.SNMMI.ORG/AM2023](http://WWW.SNMMI.ORG/AM2023)



